THE
SHOCK AND VIBRATION BULLETIN

Part 4,
Measurements and Criteria Development,
Isolation and Damping.

AUGUST 1976

293 p.

A Publication of
**THE SHOCK AND VIBRATION
INFORMATION CENTER**
Naval Research Laboratory, Washington, D.C.

Office of
The Director of Defense
Research and Engineering

DDC
DEC 17 1976
F

389004

SYMPOSIUM MANAGEMENT

THE SHOCK AND VIBRATION INFORMATION CENTER

Henry C. Pusey, Director
Rudolph H. Volin
J. Gordan Showalter
Barbara Szymanski
Carol Healey

Bulletin Production

Graphic Arts Branch, Technical Information Division,
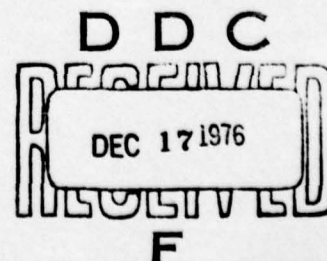Naval Research Laboratory

THE
SHOCK AND VIBRATION
BULLETIN

AUGUST 1976

The 46th Symposium on Shock and Vibration was held
at the Royal Inn at the Wharf, San Diego, California on
October 20-23, 1975. The Naval Electronics Laboratory
Center and the Naval Undersea Center, San Diego,
California were the hosts.

White Section ☑
Buff Section ☐
☐

BY
DISTRIBUTION/AVAILABILITY CODES

Dist.   AVAIL. and/or SPECIAL

A

Office of
The Director of Defense
Research and Engineering

D D C

DEC 17 1976

F

CONTENTS

PAPERS APPEARING IN PART 4

Partial Contents:

PAPERS APPEARING IN PART 2

KEYNOTE ADDRESS
 Rear Admiral Samuel L. Gravely, Jr., Commandant 11th Naval District, San Diego, California

Invited Papers

S AND V IN T AND E
 Captain Louis Colbus, USN, Ship Evaluation Division, COMOPTEVFOR, Norfolk, Virginia

REVIEW OF NUCLEAR BLAST AND SHOCK ENVIRONMENT SIMULATION
 Dr. Eugene Sevin, Defense Nuclear Agency, Washington, D. C.

METRICATION IN THE NAVY
 Mr. John Haas, Chairman, Navy Metrication Group, Naval Ship Engineering
 Center, Hyattsville, Maryland

Panel Session

VIBRATION REQUIREMENTS FOR RELIABILITY DEMONSTRATION TESTS

Shock Testing and Analysis

EARTHQUAKE TEST ENVIRONMENT - SIMULATION AND PROCEDURE FOR COMMUNICATIONS
 EQUIPMENT
 N. J. DeCapua, M. G. Hetman, and S. C. Liu, Bell Telephone Laboratories,
 Whippany, New Jersey

AN ALTERNATE APPROACH TO MODAL DAMPING AS APPLIED TO SEISMIC-SENSITIVE
 EQUIPMENT
 L. A. Bergman and A. J. Hannibal, Lord Kinematics, Erie, Pennsylvania

ACTUATOR DEVELOPMENT FOR SYSTEM-LEVEL SHOCK TESTING
 G. Richard Burwell, Boeing Aerospace Company, Seattle, Washington

BOUNDED IMPACT A REPEATABLE METHOD FOR PYROTECHNIC SHOCK SIMULATION
 R. T. Fandrich, Jr., Harris Electronic Systems Division, Melbourne, Florida

DYNAMIC RESPONSE OF ELECTRICAL CABLES TO SHOCK MOTION
 R. W. Doll, TRW Defense and Space Systems Group, Redondo Beach, California

DEVELOPMENT OF A SHRAPNEL CONTAINMENT SYSTEM FOR EXPLOSIVE-TO-ELECTRIC
TRANSDUCERS
P. H. Prasthofer, Exxon Production Research Company, Houston, Texas

ANALYSIS OF CONCRETE ARCH MAGAZINE USING FINITE ELEMENT TECHNIQUES
J. M. Ferritto, Civil Engineering Laboratory, Naval Construction Battalion Center,
Port Hueneme, California

PAPERS APPEARING IN PART 5

MEASUREMENTS AND CRITERIA DEVELOPMENT

BOUNDARY LAYER FLUCTUATING PRESSURE DATA OBTAINED IN A HIGH BACKGROUND NOISE ENVIRONMENT ON A SMALL SCALE WIND TUNNEL MODEL

G. L. Getline
General Dynamics Convair Division
San Diego, California

Because flow visualization studies on a small wind tunnel model of a new Navy fighter design indicated the possibility of aerodynamic flow separation over the cockpit canopy in the transonic flight regime and under some maneuvering conditions , it was decided to instrument an available small scale (1/14.92) model in order to obtain boundary layer fluctuating pressure data in the transonic and supersonic flight regimes. These data could then be used to provide estimates of cockpit interior noise levels for the full scale aircraft during high speed flight.

Three technical areas which required circumspection in attainment of program objectives were:

a. Obtaining of a very high frequency (up to 80 KHz) fluctuating pressure data in the presence of a high background noise environment.

b. Demonstration that the test data was representative of boundary layer pressure fluctuations and did not merely reflect ambient wind tunnel noise and turbulence.

c. Conversion of wind tunnel model data to the full scale aircraft with appropriate aerodynamic scaling parameters.

The above technical areas are discussed in detail. It is concluded that is feasible to obtain valid, high frequency boundary layer fluctuating pressure data at low cost on small scale models in unmodified wind tunnels with characteristically high level background noise and turbulence.

INTRODUCTION

During preliminary design studies of a lift-lift/cruise engine V/STOL fighter aircraft, it was realized that because of the close proximity of the vertical lift engines immediately behind the cockpit it might be necessary to crop the trailing edge of the canopy for clearance. Possible flow separation due to the extreme "boat tail" of the canopy was of concern for three reasons; namely, increased drag, degradation of rudder control effectiveness and increased noise levels in the cockpit. Subsequent flow visualization studies on a small wind tunnel model of the aircraft indicated incipient aerodynamic flow separation over the cropped canopy in the transonic flight regime and under some maneuvering

conditions. It was decided, therefore, to obtain boundary layer fluctuating pressure data on another model with a modified canopy. These data would establish the onset of flow separation, if it occurred, and also could be used as a basis for estimates of cockpit interior noise levels for the full-scale aircraft during high speed flight.

PROGRAM CONSTRAINTS

It must be realized that this was not a research program wherein special instrumentation could be procured or fabricated, and that tests would not be conducted in a special "quiet" wind tunnel. Acoustic instrumentation would be "off-the-shelf" and acoustic test data would be obtained as a by-product with

1

aerodynamic data in commercial wind tunnels with their inherent background noise and turbulence. Thus, there were three, distinct technical areas which required considerable care in fulfillment of program objectives:

a. The obtaining of very high frequency boundary layer fluctuating pressure data in the presence of a high background noise and turbulence environment.

b. Demonstration that the test data were representative of boundary layer pressure fluctuations and did not merely reflect ambient wind tunnel noise and turbulence.

c. Conversion of wind tunnel model data to the full-scale aircraft with appropriate aerodynamic scaling factors.

These areas are discussed in the following paragraphs.

TECHNICAL DISCUSSION

Tests were run in the Convair supersonic wind tunnel at San Diego, California and in the CALSPAN transonic tunnel at Buffalo, New York. The aircraft model was 1/14.92 scale. Ideally, to obtain full scale acoustic data up to the maximum specified preferred frequency of 11,200 Hz, with the octave band center frequency at 8000 Hz, model data would have had to be obtained at frequencies up to 167,000 Hz. However, in order to preclude excessive costs related to special instrumentation and data reduction procedures, and because it would provide acoustically significant information, it was decided to obtain model data only up to about one-half of the above frequency. That is, full scale data would be generated up to 5600 Hz, with the octave band center frequency at 4000 Hz, which could be reasonably extrapolated up to the maximum frequency.

The model canopy was instrumented with 4, Celesco Industries Type LC-70 piezoelectric microphones. The microphones were flush mounted as shown in Figure 1 and data were recorded on a multi-track magnetic tape recorder as shown in Figure 2. As indicated previously, note was made of the required trade-off between special instrumentation requirements and frequency response limitations. This is explained as follows. The flush mounted microphones were installed so as to sense the pressure fluctuations in the broad band random pressure field of the boundary layer as it was convected downstream over the canopy. Experimental and theoretical investigations have shown that the finite size of a pressure transducer limits its

response in the upper frequency range. This occurs because frequency and spatial extent are related so that high frequency corresponds to small spatial extent. Thus, at some frequency determined by the ratio of microphone diameter to boundary layer displacement thickness, $D/\delta*$, cancellation between positive and negative pressure begins to occur over the transducer surface, as described in Reference 2. Referring to Figure 3, it is seen that to avoid any significant reduction in measured frequency pressure responses the microphone diameter, D, would have to be less than 10 percent of the boundary layer displacement thickness, $\delta*$. For the tests reported herein, this would define a microphone diameter of less than 0.003 inch. Such a small microphone would have very low sensitivity and would require special, low-noise pre-amplifiers which were not available. Since, from the availability and cost standpoints, a larger more sensitive microphone was indicated, and response-frequency corrections would have to be made anyway, it was decided, based on past experience with these instruments, to use the Celesco LC-70 transducers. These had sufficient sensitivity so that no special pre-amplification was required. Further, with the resonant frequency of the transducer at 150 KHz, useful data could be obtained up to 70-75 Hz.

Because dynamic pressure transducers (microphones) will sense any kind of pressure fluctuations, most all boundary layer fluctuating pressure measurements in wind tunnels have been made in specially constructed or modified facilities designed to provide low background noise and unperturbed flow, as described in Reference 2. (Note: Both References 1 and 2 have extensive bibliographies related to measurements and procedures.) The data reported herein, however, were obtained in unmodified, operational wind tunnels with characteristic ambient noise and turbulence levels. Data were available which described the noise and turbulence levels of the Convair supersonic and the CALSPAN transonic tunnels. Review of the spectral distribution of the noise-turbulence levels in both the above tunnels showed that most of the energy was at very low frequencies. For example, in the Convair tunnel the energy peaks strongly at 50-60 Hz, while at CALSPAN the energy peaks below 500 Hz, Figure 4. In both tunnels energy peaks are associated with discrete tones related to design and operation of the transonic-supersonic test sections, etc. Considering the small scale (1/14.92) of the model and the corresponding frequency separation between model scale and full scale, i.e., a frequency of 1500 Hz in model scale would correspond to a full scale frequency of 100 Hz, it was concluded that it would be feasible to obtain
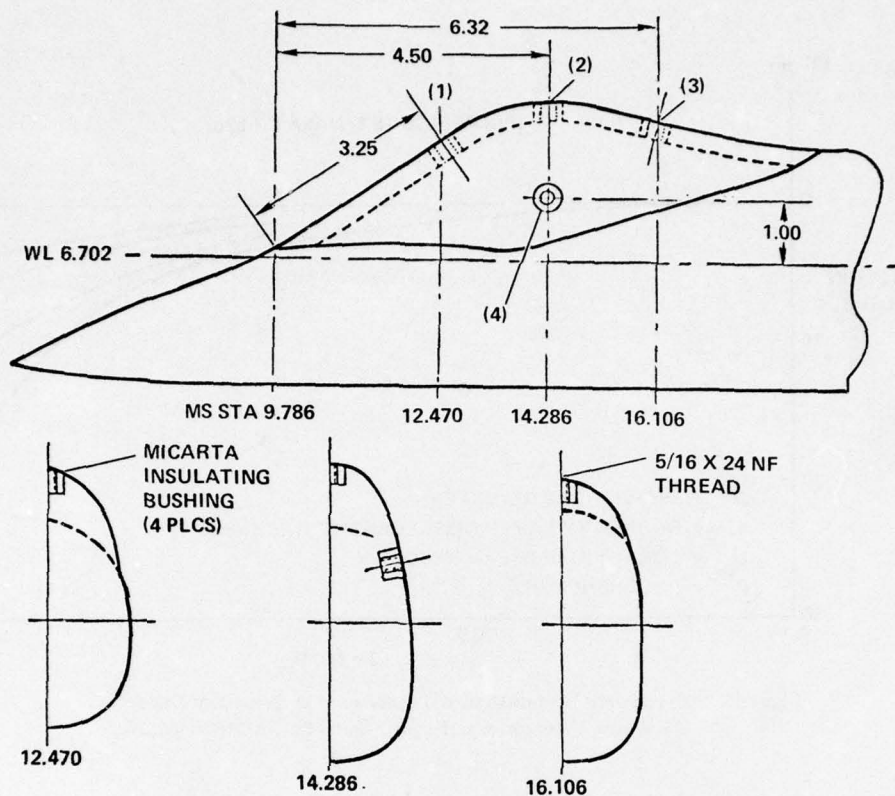
Figure 1. Location of Celesco LC-70 Transducers in Canopy
(Acoustic Area = 0.034 sq. in. /Transducer)
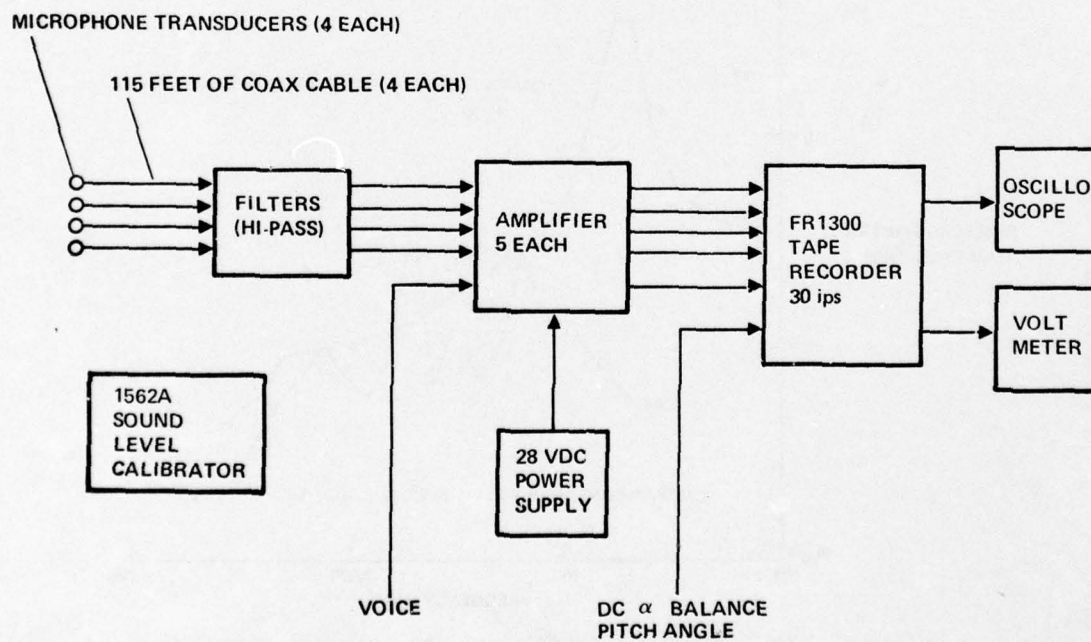
Figure 2. Instrumentation Block Diagram

(FROM FIGURE 5, NASA CR-626)

DECIBEL REDUCTION
IN MEASURED LEVEL

+10

0

-10

-20

-30

D/δ*

0.1

0.2

0.5

1.0 TO ∞

D = MICROPHONE DIAMETER
δ* = BOUNDARY LAYER DISPLACEMENT THICKNESS
U_∞ = LOCAL FREESTREAM VELOCITY
f = FREQUENCY (Hz)

0.1   0.5   1   5   10

$2\pi fD/U_\infty$
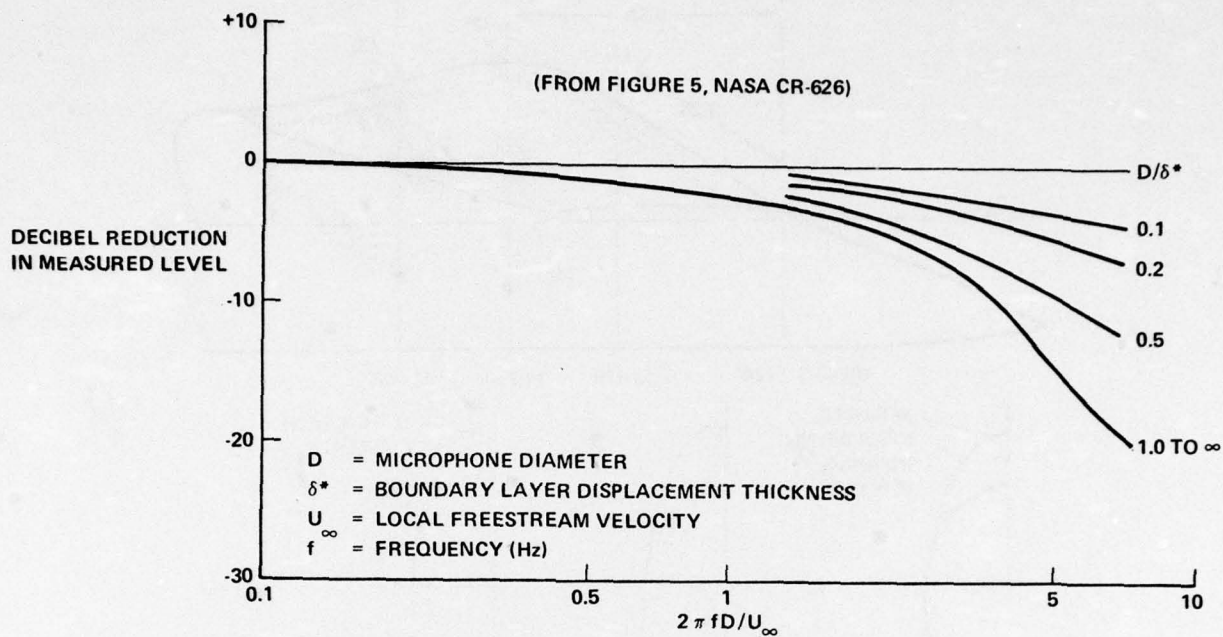
Figure 3. Frequency Response of a Transducer to Boundary Layer
Pressure Fluctuations (From Figure 5, NASA CR-626)

PRESSURE SPECTRAL
DENSITY (PSI^2/Hz)

10^{-4}

10^{-5}

10^{-6}

10^{-7}

CONVAIR BLOWDOWN TUNNEL (MACH 0.9)

CV

CAL

CALSPAN CONTINUOUS FLOW TUNNEL (MACH 0.8)

10   100   1,000   10,000

FREQUENCY (Hz)
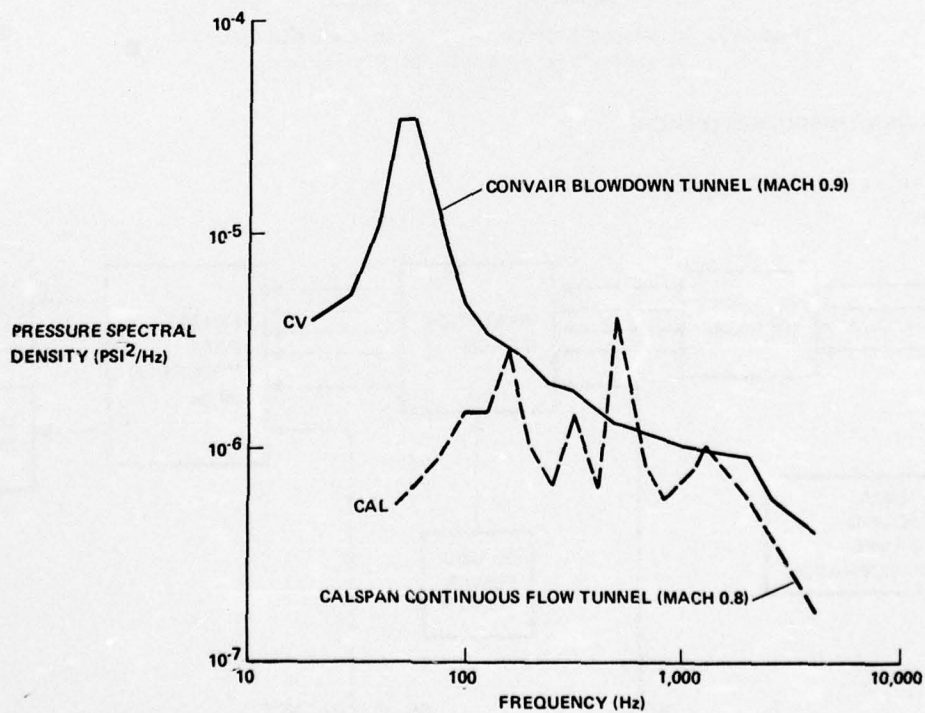
Figure 4. Wind Tunnel Background Noise and Turbulence (Data From
5° Half-Angle Cone Model)

4

meaningful flow noise data on the model canopy and interpret it in terms of the full scale aircraft. In order to assure that the magnetic tape data recording system would not be saturated by low frequency background noise and turbulence, high-pass filters which rolled off sharply below 1 KHz were interposed between the microphone and amplifiers. It was also concluded that it would be necessary to demonstrate that data obtained really represented canopy boundary layer pressure fluctuations and not merely full scale wind tunnel turbulence.

Figure 5a compares free stream overall turbulence pressures, in rms psi, measured in the CALSPAN tunnel with pressures measured on the canopy at several Mach numbers. All test data shown herein are with the model at the appropriate cruise angle of attack for each Mach number. However, data were also obtained at large positive and negative angles of attack. It is noted that while the turbulence pressures increase with increasing Mach number, canopy pressures decrease with increasing Mach number, which is characteristic of boundary layer pressure fluctuations, as noted in Figures 5b and 6

and Reference 3. Figure 5b compares the ratio of overall fluctuating pressure to dynamic head, $\bar{p}/q$, for several Mach numbers, for data taken on the wall of the CALSPAN tunnel test section (Reference 4) and the model canopy. Both curves are characteristic of boundary layer pressure fluctuations. It is no coincidence that the two curves lie very close to one another. All research workers note that the parameter $\bar{p}/q$, collapses boundary layer pressure fluctuating pressure data as well as any other more sophisticated parameter, although it is admittedly not perfect. This states, in effect, that for any given conditions of dynamic head and Mach number, the energy in a fully developed turbulent boundary layer is essentially constant - regardless of the thickness of the boundary layer. What does vary with boundary layer thickness is the spectral distribution of the energy. That is, thick boundary layers are characterized by more of the total energy at lower frequencies, while thin boundary layers are characterized by more energy at the higher frequencies. High and low frequencies are generally defined in terms of a "characteristic" frequency, eg, U_∞/δ^*, where U_∞ is the local freestream velocity and δ^* is the boundary
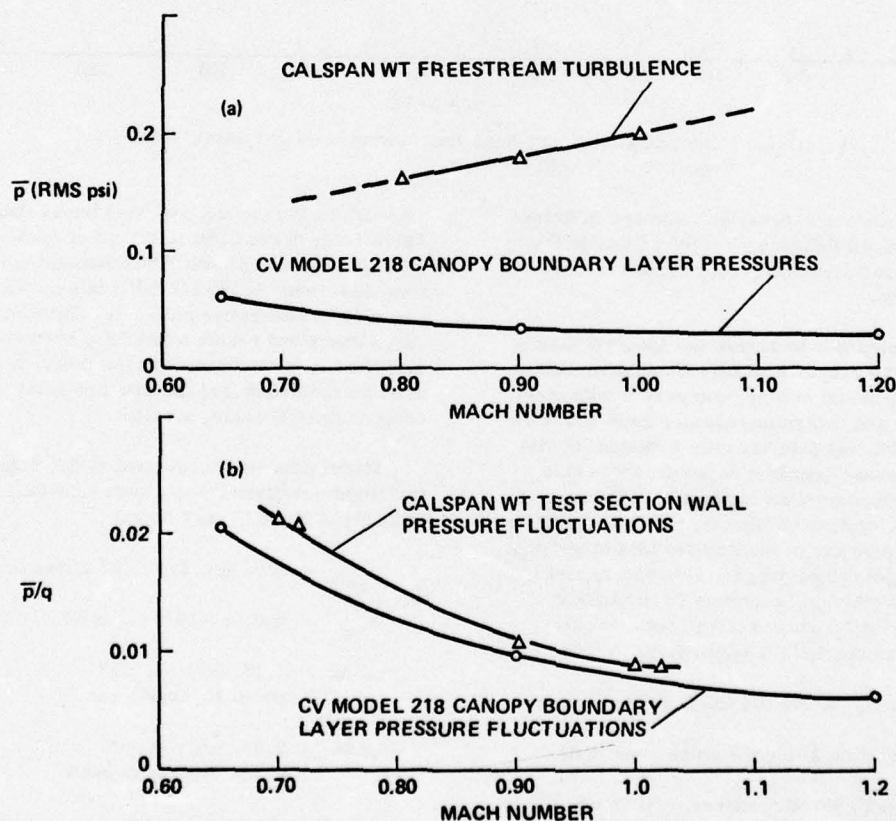
Figure 5. Comparison Between Freestream Turbulence and Boundary Layer Fluctuating Pressures in CALSPAN Wind Tunnel
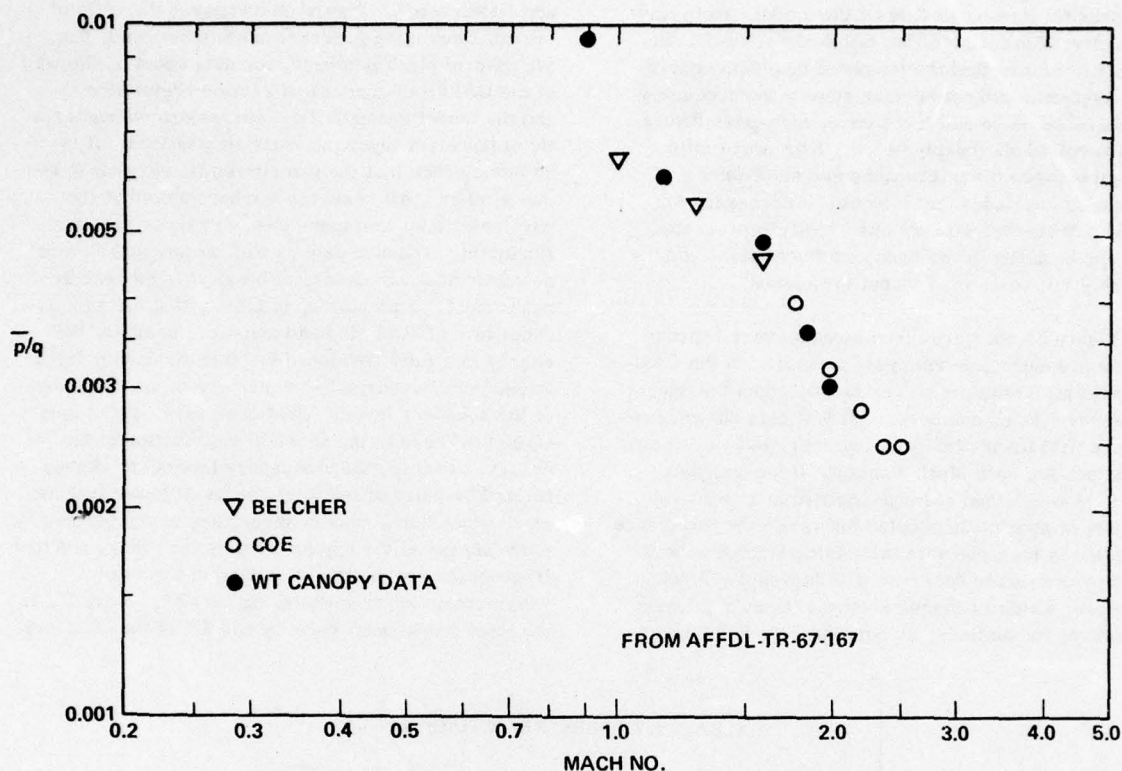
Figure 6. Fluctuating Pressure Non-Dimensionalized by Dynamic Head Versus Mach Number

layer displacement thickness, as indicated in Reference 3. It is noted that this directly relates to the microphone size versus frequency response situation discussed above.

The next step was to review the spectral distribution of boundary layer pressure fluctuation data obtained on the model canopy, compare it with other published data and determine whether from this viewpoint meaningful test data had been obtained in this program. Because boundary layer pressure data have been obtained over an extremely wide range of aerodynamic operating conditions, as shown in Table 1, it was necessary to normalize the data in order to make meaningful comparisons. This was accomplished as described in Reference 1, by plotting $L_f - (L_{OA} - 10 \log f_o)$ in dB versus frequency in terms of a characteristic frequency, f_o, where

$$f_o = 0.1 \, U_\infty / \delta^* \text{ Hz } (U_\infty \text{ and } \delta^* \text{ defined above});$$

L_f = spectrum sound pressure level in dB

L_{OA} = overall sound pressure level in dB

Figure 7 superimposes test data obtained in this

program on the envelope of wind tunnel data noted in Table 1. It is seen that the mean of the Convair data falls about in the middle of the data spread obtained from Reference 1. F-102 full scale data are also shown for comparative purposes. By all the procedures described herein which have been used to evaluate the test data obtained on the model canopy, it must be concluded that the data are valid and applicable to the full scale, aircraft.

Model data were converted to full scale data for two flight conditions, i.e., corresponding to maximum Mach number, as follows:

q_{max} = 2000 psf, M = 1.17 at sea level

M_{max} = 2.0, q = 1240 psf at 37,500 ft altitude

At M = 1.17, $\bar{p}/q$ = 0.0062 → L_{OA} = 149.5 dB (from Figures 5 and 6)

at M = 2.00, $\bar{p}/q$ = 0.0031 → L_{OA} = 139.5 dB (from Figures 5 and 6)

In converting the model data to full scale data, corrections were made for boundary layer displacement

Table 1. Measurements of Boundary Layer Pressure Fluctuations

INVESTIGATOR	TUNNEL SIZE + TYPE	MACH NO.	REYNOLDS NO.	MIC. DIAM. $\overline{\delta*}$
JORGENSEN, DONALD W. (REF. 7)	CONTINUOUS 18 IN. x 15 IN.	0.04 0.18	(x) 5.9×10^5 2.4×10^6	6.7 11.4
HARRISON, M. (REF. 8)	CONTINUOUS 15 IN. x 20 IN.	0.04 0.18	(x) 1×10^6 4×10^6	1.2
BAROUDI, LUDWIG, + RIBNER (REF. 9)	CONTINUOUS 8 IN. x 12 IN.	0.04 0.15		0.092
BAKEWELL, H.P. JR., et al (REF. 6)	CONTINUOUS 3-½ IN. DIAM.	0.1	(x) 4×10^6	0.31
WILMARTH + WOOLDRIDGE (REF. 10)	CONTINUOUS 60 IN. x 84 IN.	0.2	(x) 3.1×10^7 3.8×10^7	4.0
BULL, WILBY + BLACKMAN (REF. 11)	CONTINUOUS 9 IN. x 6 IN.	0.3 0.5	(x) 0.5×10^7 3×10^7	0.15 0.51
MURPHY, J.S., et al (REF. 12)	BLOWDOWN 12 IN. x 12 IN.	0.59	(θ) 1.3×10^4	2.77
SERAFINI, J. S. (REF. 13)	CONTINUOUS 8 IN. x 18 IN.	0.6	(x) 1×10^7 1.4×10^8	0.195 1.33
MAESTRELLO, L. (REFS. 14 AND 15)	CONTINUOUS 7.3 IN. x 3.5 IN.	0.63 0.78		0.45
WILLIAMS, D. J. M. (REF. 16)	CONTINUOUS 6 IN. X 2-½ IN.	1.2 1.5		5 8
KISTLER + CHEN (REF. 17)	CONTINUOUS 18 IN. x 20 IN.	3.5	(θ) 1.55×10^4	1.1
MURPHY, J. S., et al (REF. 12)	BLOWDOWN 12 IN. x 12 IN.	3.46	(θ) 4.9×10^4	0.43
WESTLEY, R. (REF. 18)	BLOWDOWN 5 IN. x 5 IN.	2.91 3.96		
SPEAKER + AILMAN (REF. 19)	BLOWDOWN 12 IN. x 12 IN.	0.42 3.45	(θ) 1.6×10^4 5.3×10^4	0.17 1.3

(x) REYNOLDS NUMBER BASED ON DISTANCE FROM INCEPTION OF TURBULENCE.

(θ) REYNOLDS NUMBER BASED ON MOMENTUM THICKNESS.

NOTE: TABLE TAKEN FROM NASA CR-626

thickness and characteristic frequency. This was required because the Reynolds numbers associated with the model tests were not representative of the full scale flight conditions. Corrections were made on the basis of data contained in Reference 1.

Figure 8 is a plot of predicted, average octave band sound pressure levels (flow noise levels) over the wind screen and canopy of the full scale aircraft at maximum dynamic pressure and maximum Mach number. The upper limit of each curve represents the spectral distribution derived by the decomposition of the overall levels noted above.

The lower limit of each curve, and corresponding overall level, was obtained by summation of spectral data based on the mean curve of Figure 6. The small data spread is considered acoustically acceptable.

With respect to the basic question of possible flow separation over the canopy, test data indicated that there was no problem at normal aircraft attitudes. In all cases, separation did not occur until the model was rotated to large angles of attack, ie, -10 to +18 degrees or more, associated with

stall of the entire aircraft. Separation was indicated by a sudden jump in response amplitudes with a concurrent shift in energy toward lower frequencies.

CONCLUSIONS

The feasibility of obtaining valid boundary layer fluctuating pressure data on small scale models in unmodified wind tunnels with characteristic background noise and turbulence has been demonstrated. It is fully realized, however, that the successful accomplishment of this task relied on the fundamental work of all those researchers who have precisely measured and defined the unique properties of convected, fluctuating pressure fields and turbulence. Further, without such a foundation it would be extremely difficult for those of us involved with the development of flight vehicles of all kinds to carry out our tasks in a timely and cost effective manner.

REFERENCES

1. "A Review of Flight and Wind Tunnel Measurements of Boundary Layer Pressure Fluctuations and Induced Structural Response," NASA CR-626, dated Oct. 1966.

2. "Wall-Pressure Fluctuations and Pressure-Velocity Correlations in a Turbulent Boundary Layer," NASA TR R-165, dated 1963.

3. "Prediction of Boundary Layer Pressure Fluctuations," AFFDL-TR-67-167, dated April 1968.

4. "Transonic Flow Quality Improvements in a Blowdown Wind Tunnel," J.M. Cooksey and J.W. Arnold, Journal of Aircraft, Vol. 10, No. 9, dated September 1973.
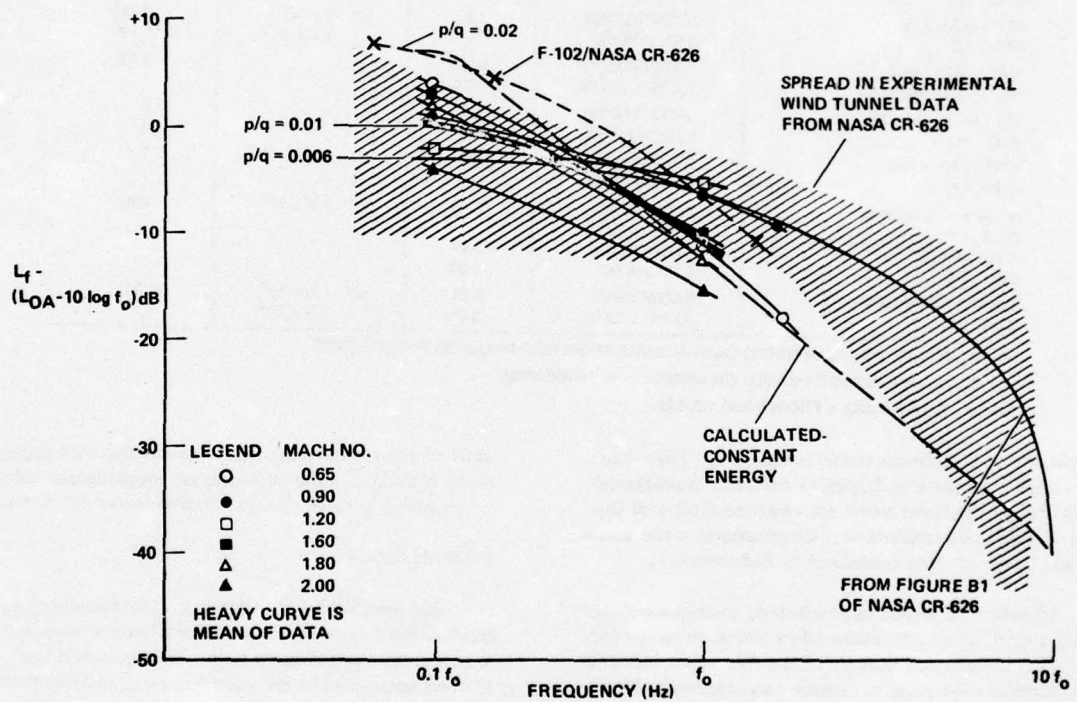
Figure 7. Model 218 Canopy – Boundary Layer Pressure Spectra
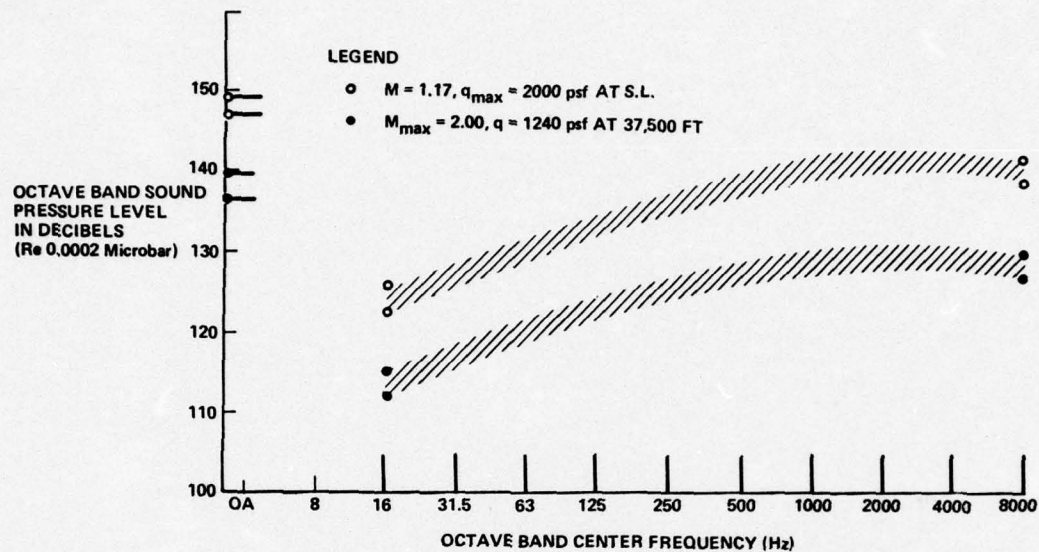
Figure 8.   Average External Flow Noise Levels (Over Canopy at
Max Mach and Max q Conditions)

9

DYNAMIC MEASUREMENT OF LOW-FREQUENCY
COMPONENTS OF TRACK-INDUCED RAILCAR WHEEL ACCELERATIONS

S. A. Macintyre, C. T. Jones, R. E. Scofield
ENSCO, Inc.
Springfield, Virginia 22151

Track-induced accelerations to a railcar cover a broad frequency band consisting of both short-duration high-level shocks and low-level low-frequency vibrations. In order to measure the low-frequency vibrations without the high-level shocks saturating the measuring device, a wide dynamic measurement range is required. However, commercially available accelerometers with such a range lack the resolution for measuring low-level vibration.

This paper describes how a limited range high-resolution servo-accelerometer can be used in railcar applications. The accelerometer is mounted to an underdamped spring mass mechanical isolator and an LRC circuit is tuned to inversely match the resonant response of the isolator so that the overall transfer function is essentially flat for all frequencies less than the isolator resonant frequency. The LRC network and the isolator prevent saturation of the accelerometer for frequencies equal to or greater than the resonant frequency of the isolator.

The development of the system transfer function, a description of the physical system, and laboratory test results are also discussed.

BACKGROUND

The U.S. Department of Transportation (DOT), Federal Railroad Administration (FRA) has for some time been sponsoring research into the dynamic behavior of railcars and trains in an effort to improve ride quality and operating safety. Typically, a test vehicle is instrumented with transducers and subjected to dynamic inputs. Its response is recorded, and an analysis of the data aimed at characterizing the vehicle's motions is performed. Some of these tests are performed under controlled conditions, while others are carried out under field conditions with an instrumented vehicle in a revenue train.

In order to characterize the dynamic response of a test vehicle, the input displacements, accelerations, and velocities must be accurately defined. For a railcar, these inputs are from track and are transmitted through the wheels and axles to the suspension system. Measurements of track gage, profile, alignment, and crosslevel may be used to determine the displacement inputs to the wheels. The FRA has developed precise methods for measuring these parameters and successfully utilized this type of data to relate ride quality to track geometry. Because of the

physical limitations of track geometry measuring equipment, displacement inputs at all wheels cannot easily be made. Therefore, the complete dynamic response of a vehicle cannot be characterized without utilizing mathematical models and simulation techniques. Although the goal of such research is the development of a model which duplicates a vehicle's correct response, such a model cannot be verified unless the vehicle's responses to its operating environment are known.

An alternate and more usual approach to dynamic vehicle testing is to measure the vehicle's acceleration response under the same test conditions described earlier. Except in the case of component fatigue, acceleration is a more meaningful measurement since it is indicative of the forces acting on the test vehicle. Using this method the dynamic input to the railcar is considered to be track-induced wheel accelerations. Under normal circumstances, this poses no measurement problem. Piezoelectric, piezoresistive, or strain gage accelerometers can be mounted to the vehicle's axles. These accelerometers have both wideband frequency response and large dynamic range, and can withstand the high shock and vibration environment. In many situations

11

the measurement of the low-frequency components of track-induced railcar wheel accelerations is of primary interest, but this involves a much more difficult measuring task. The profile geometry of a typical U.S. railroad track can be represented by two rectified sine waves shifted 90° with respect to one another with joints between rail sections spaced 12 m apart. This is illustrated in Fig. 1. A railcar traveling over such a track experiences two types of acceleration inputs: inpulses from the joints (intersection of two rail sections), and vibrations from the track profile and alignment variations. The vertical impulse and high-frequency accelerations can be as great as a few hundred g's (1 g = 981 cm/sec^2), with impulse durations in milliseconds. The vertical vibration acceleration inputs are of a much lower level and generally vary from 0.1 to 10 g's in the frequency range from 0 to 30 Hz. The high-level high-frequency vibrations tend to mask the low-level low-frequency vibrations, thus making measurements of the low-frequency components extremely difficult.

The lateral wheel accelerations are lower in level than the vertical accelerations. A range of 0.01 to 1.0 g is typical, with the impulse accelerations also falling within this range. Misalignment with respect to the vertical and cross-axis sensitivity of the lateral accelerometer will cause some of the vertical acceleration to be included in the lateral accelerometer signal. Because of the high level of the vertical acceleration, this cross-axis signal can be equal to or greater than the actual lateral acceleration. Therefore, in order to accurately measure the low-frequency low-level vertical and lateral accelerations, some means of attenuating the high-frequency impulse accelerations must be utilized.

This paper describes a technique for accomplishing these measurements. Conceptually, the method utilizes two servoaccelerometers mounted on a linear spring-mass-damper mechanical isolator designed to attenuate the high-frequency

vertical accelerations applied through the wheel. Minimization of the impulse amplification necessitates the use of a small damping ratio. This causes a frequency-dependent amplification of the input vertical acceleration experienced by the mass, with the maximum amplification occurring at the resonant frequency of the mechanical system. If a standard servoaccelerometer mounted to the mass is used to measure vertical acceleration, it would require a dynamic range that included the expected amplified acceleration at the resonant frequency. Since this amplified acceleration can be 2 to 4 times greater than the actual input acceleration, resolution suffers. To prevent this acceleration amplification from saturating the accelerometer, to flatten the overall frequency response, and to maintain good resolution in the low-frequency band, a combination inductor-resistor-capacitor (LRC) network can be placed in the servoaccelerometer feedback loop and tuned to minimize the effect of the mechanical acceleration amplification in the overall system transfer function. The effect of the LRC network is to adjust the feedback current to the torque coil of the accelerometer suspension system such that the accelerometer's range changes with frequency in proportion to the changes in mechanical transmissibility.

PRELIMINARY ANALYSIS

In order to design a system which can accurately measure the low-frequency acceleration environment of a rail vehicle, it is necessary to have some prior knowledge of the magnitude and frequency content of the environment over a broad frequency spectrum. Since the environment is comprised of a number of complex inputs that are associated with track geometry, wheel contour, truck structural resonances, truck hunting, etc., characterization of this environment by purely analytic techniques is a monumental task. It was therefore decided to simply characterize the deterministic portion of the track input by analytic means for the purpose of identifying the resolution requirements of the measurement instrument and to obtain information pertaining to those inputs of a high-frequency content by field measurement techniques.

A simple but effective representation of the rail profile experienced on typical bolted rail has the form:

$$f(t) = A\left|\sin\pi\frac{vt}{\lambda_o}\right| = \left|A \sin\pi t/T\right| \qquad (1)$$

where λ_o = wavelength (m) (12 m for bolted rail)

T = period of function $f(t)$

v = velocity of the railcar (m/sec)

A = vertical displacement amplitude (cm)

The fundamental frequency of the function $f(t)$ is therefore

$$f_o = 1/T = v/\lambda_o \qquad (2)$$
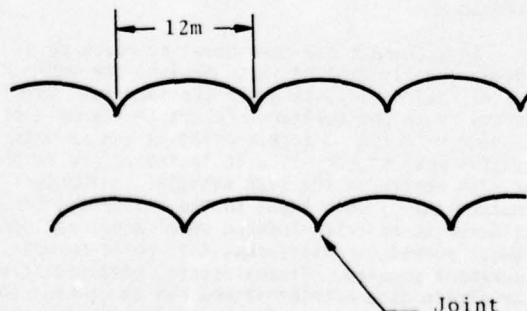
Fig. 1. Schematic representation of typical U.S. railroad track

12

The Fourier expansion* of the function $f(t)$ reveals that peak acceleration amplitude at frequencies

$$f_n = n \frac{v}{\lambda_o} = \frac{n}{T} \qquad (3)$$

have the form

$$A_n = \frac{2A}{\pi} \frac{1}{1-4n^2} \left(\frac{n}{T}2\pi\right)^2 = \frac{8\pi A n^2}{T(1-4n^2)} \left(\frac{cm}{sec^2}\right) \quad (4)$$

where f_n = nth harmonic frequency

$\quad$ A_n = amplitude of nth harmonic

$\quad$ $n = 1, 2, 3, \ldots$

This equation shows that the acceleration magnitude is essentially proportional to the displacement amplitude and independent of frequency for $n \gg 1$. For values of A equaling 3 to 5 cm (typical range for profile variations), the acceleration amplitude is quite low, requiring an accelerometer of high resolution.

Field measurement techniques were used to determine the magnitude and frequency content of those accelerations outside the bandwidth of interest which might mask the low-frequency data. In general, these accelerations can be primarily attributed to discontinuities in the rail (jointed rail) and structural characteristics of the truck. In order to obtain amplitude and frequency information for this type of input,

——————————
*Derivation is given in Appendix A.

five accelerometers--three vertical and two lateral--were coupled to the axle of a railcar. The characteristics of the five accelerometers are shown in Table 1.

The railcar was run at various speeds over typical track, and the outputs of the accelerometers were measured on an analog FM recorder. Power spectral density plots (Fig. 2) indicated that the power was distributed over a broad frequency band, while analog traces (Fig. 3) indicated that peak accelerations of up to 25 g's were common. This data was then digitized and utilized as the input to a computer-simulated model of the mechanical isolator/accelerometer transfer function. A recursive numerical filter technique was used to simulate the appropriate transfer functions, and the 150-g strain gage accelerometer data was used as the primary input to the program.

Based on the above analysis and field test results, it was determined that a linear mechan-

TABLE 1

Accelerometer Characteristics

Type	Position	Range (g's)	Approx. Natural Frequency (Hz)
Servo	Vert.	50	200
Servo	Vert.	50	1000
Servo	Horiz.	50	200
Strain gage	Vert.	150	1000
Strain gage	Horiz.	50	600
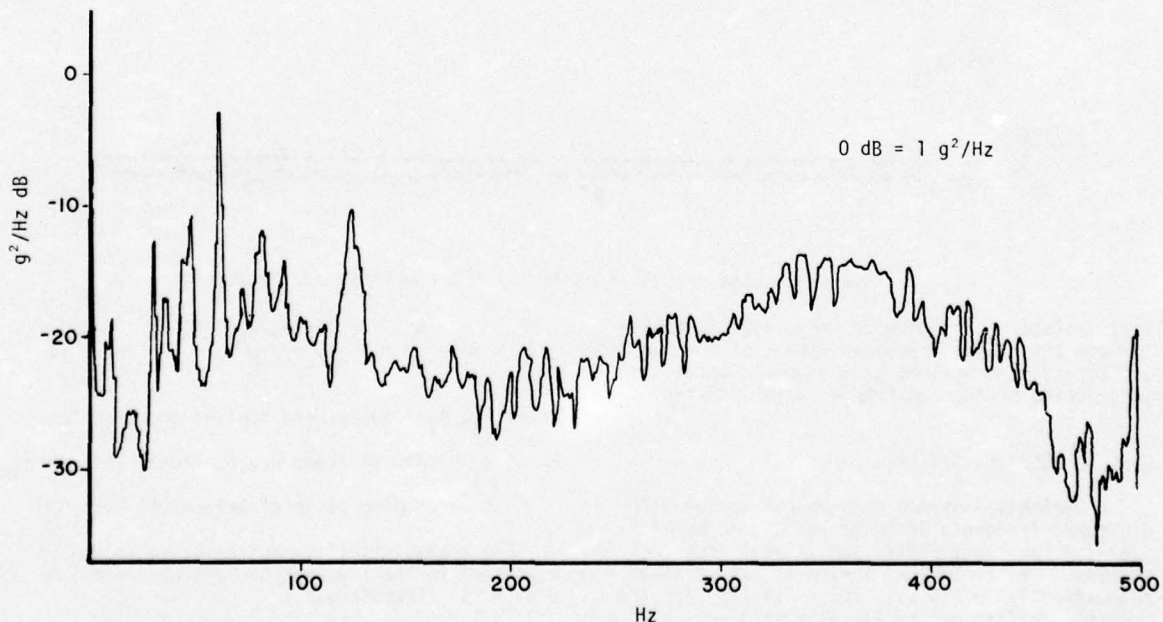
Fig. 2. Power spectral density plot of vertical acceleration for journal half-ring

+25 g

KISTLER
F_C = 1000 Hz
Range = ±50 g

-25 g

+25 g

SCHAEVITZ
F_C = 200 Hz
Range = ±50 g

-25 g

+25 g

STATHAM
F_C = 600 Hz
Range = ±50 g

-25 g

+75 g

STATHAM
F_C = 900 Hz
Range = ±150 g

-75 g
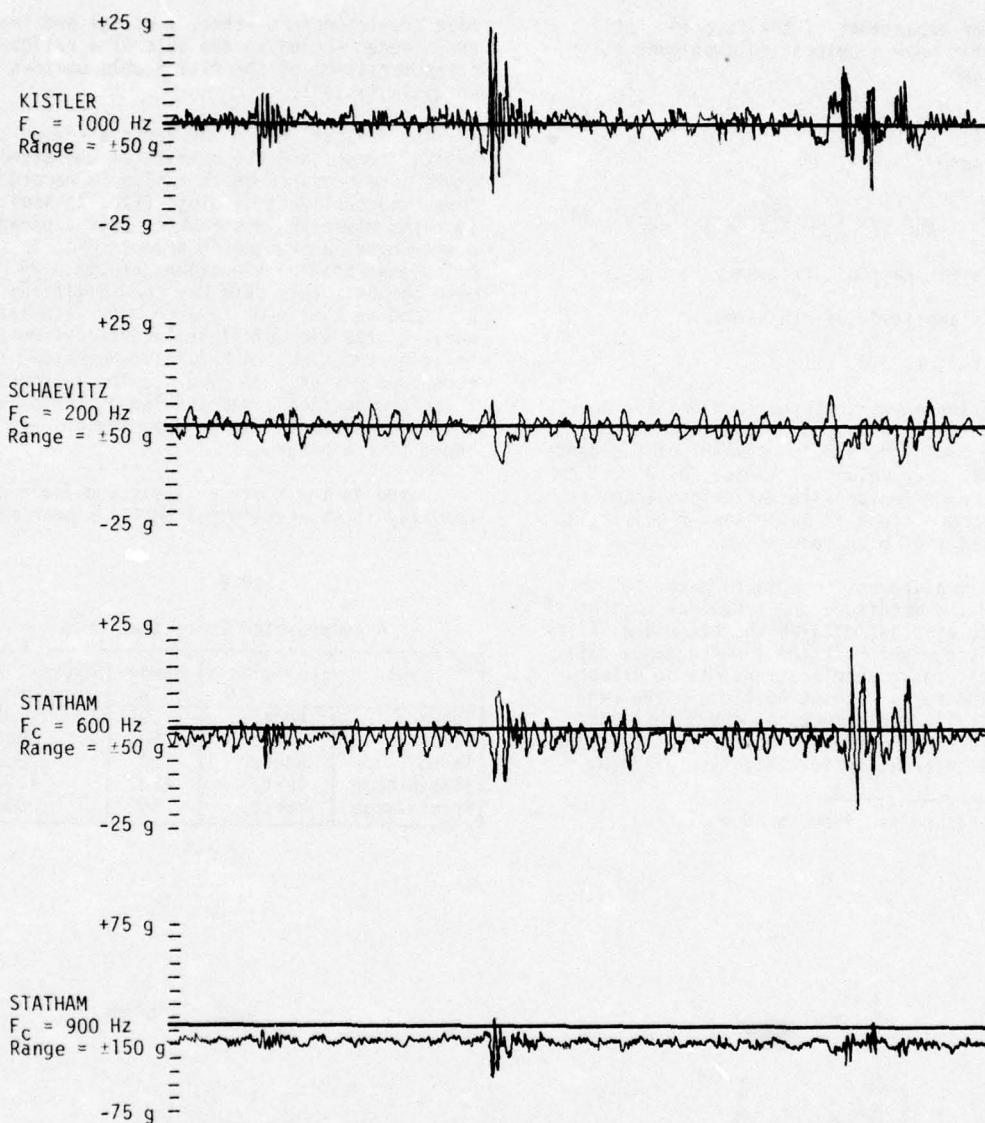
Fig. 3. Typical analog traces of railcar journal bearing accelerometers

ical isolator would be necessary in order to attenuate the higher frequency vibration components sufficiently to prevent accelerometer saturation and masking of the low-frequency information.

GENERAL SOLUTION CONCEPT

A mechanical spring-mass-damper system with a natural frequency of 30 Hz was chosen as an isolator for the vertical and lateral accelerometers. The mechanical system is illustrated schematically in Fig. 4. The derivation for the transmissibility of the isolator is given in Appendix B and, expressed in Laplace transform notation, can be written as

$$H(s) = \frac{A_o}{A_i} = \frac{\omega_n^2 \ (1+2\delta s/\omega_n)}{s^2+2\delta\omega_n s+\omega_n^2} \tag{5}$$

Where A_o, A_i = output and applied accelerations

ω_n = natural frequency of mechanical system

δ = damping ratio of mechanical system

The transmissibility and phase angle may be expressed in the frequency domain by replacing s with jα. Therefore,

14
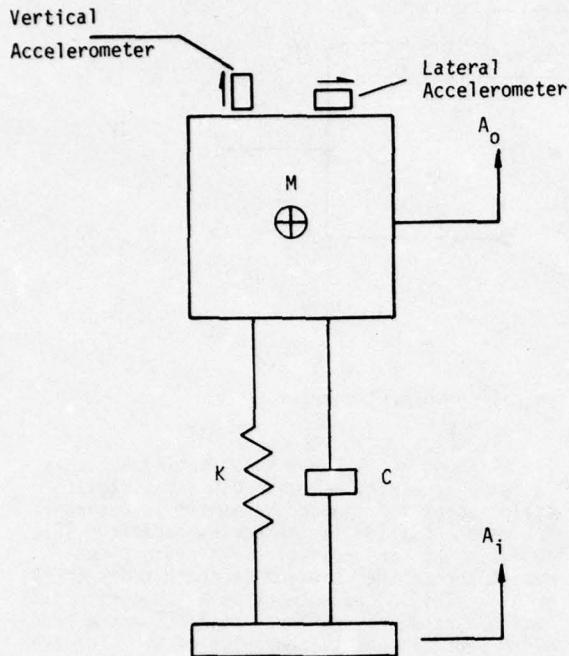
Fig. 4. Schematic representation of spring-mass-damper mechanical isolator

$$H(j\alpha) = \frac{(1+2\delta j\alpha)}{(1-\alpha^2) + (2\delta j\alpha)} \qquad (6)$$

$$\phi = \tan^{-1}(2\delta\alpha) - \tan^{-1}[2\delta\alpha/(1-\alpha^2)]$$

where $\alpha = \omega/\omega_n$. At resonance ($\alpha = 1$), the absolute value and phase angle of the transmissibility are

$$|H(j\alpha)| = \frac{(1+4\delta^2)^{1/2}}{2\delta} \qquad (7)$$

$$\phi = \tan^{-1}(2\delta)-90°$$

Inspection of Equation (7) indicates that for $\delta \leq 1$, the transmissibility of the isolator is greater than 1, which causes the output acceleration to be greater than the input acceleration. Therefore, it appears that a large value of δ should be chosen in order to minimize the transmissibility at resonance. Unfortunately, the response of the mechanical isolator to impulses* is proportional to $2\delta\omega_n$. Thus, a high value of δ will cause an amplification of the impulse for a constant natural frequency.

A good compromise between an optimally flat frequency response and minimized sensitivity to impulses is a $\delta = 0.25$. Under this condition the accelerometers mounted on the mass will be subjected to a frequency-dependent amplified in-

*A discussion of the impulse response of the mechanical isolator is given in Appendix C.

put acceleration. A plot of the transmissibility versus frequency for a $\delta = 0.25$ is given in Fig. 5. At the resonant frequency, the acceleration experienced by the mass is 2.24 times greater than the input acceleration. In order to reestablish a flat frequency response and maintain good resolution without saturating the vertical accelerometer, the sensitivity of the accelerometer can be tailored to compensate for the frequency response of the mechanical system.

A schematic diagram for a typical servo-accelerometer is given in Fig. 6. If mechanical damping (e.g., an oil bath) is ignored, the block diagram for the accelerometer can be represented by Fig. 7. The first block represents the relative transmissibility of the mechanical sensor. The second block represents an amplifier that converts the mechanical displacement into a voltage. The last block represents the conversion of the voltage into an acceleration which is fed back to the mechanical system in a manner that opposes the input (A_0) acceleration. A detailed discussion and derivation of the accelerometer transfer function are given in Appendix D. This transfer function is

$$\frac{V_0}{A_0} = S(s) = \left|\frac{R}{F}\right| \frac{\omega_c^2}{s^2+2\delta'\omega_c s+\omega_c^2} \qquad (8)$$

where ω_c = corner frequency of accelerometer (assuming mechanical natural frequency is small)

δ' = damping ratio of accelerometer

F = scale factor constant

R = feedback resistor

Typically ω_c and δ' are 750 radians per second (~120 Hz) and 0.707, respectively.
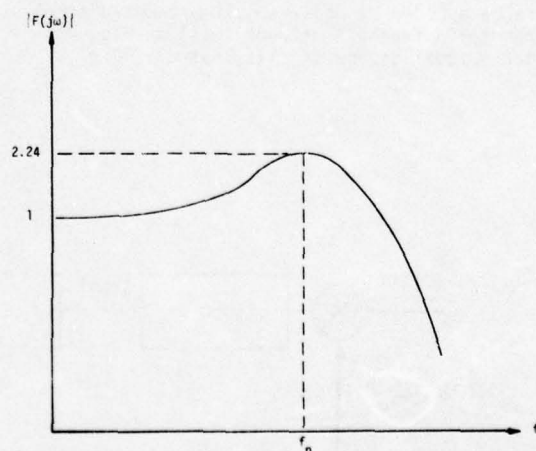
Fig. 5. Transmissibility versus frequency for mechanical isolator with a $\delta = 0.25$

Fig. 6. Schematic diagram of typical servoaccelerometer

The normalized overall system transfer function (including the isolator) from applied acceleration to the output voltage of the accelerometer is

$$\Psi(s) = \frac{S(s)}{(R/F)} = \left[\frac{\omega_n^2(1+2\delta s/\omega_n)}{s^2+2\delta\omega_n s+\omega_n^2}\right]\left(\frac{\omega_c^2}{s^2+2\delta'\omega_c s+\omega_c^2}\right)$$

(9)

At an input acceleration frequency of zero, the normalized transmissibility of the system is unity. At the resonant frequency of the isolator (assuming $\omega_n \ll \omega_c$) the normalized transmissibility is

$$|\Psi(j\omega_n)| = \frac{(1+4\delta^2)^{1/2}}{2\delta}$$

(10)

which is essentially the transmissibility of the isolator. Therefore, a standard servoaccelerometer will be subjected to an amplified input acceleration and possibly saturation unless a sacrifice in resolution is made. This sacrifice can be avoided by modifying the standard accelerometer's feedback network (L(s) in Fig. 7). Such a modification is illustrated in Fig. 8.

Although R_1 is shown substituting R_3, this is not a necessity unless a different static scale factor for the accelerometer is desired. The major addition is the series capacitor (C), inductor (L), and resistor (R_2) network connected across the standard feedback resistor (R_1 or R_3). This added network is a tuned circuit having a resonant frequency at $1/\sqrt{LC}$ and a bandwidth proportional to the value of R_2. For frequencies below and above the LR_2C network's resonant frequency, the impedance of the network is much much higher than R_1 and, therefore, has no effect on the accelerometer's response. At resonance, the impedance of the network is equal to R_2, causing an overall feedback impedance of $R_1R_2/(R_1 + R_2)$. This, in turn, increases the feedback to the force balance coil and, therefore, increases the accelerometer's range proportionately.*

The normalized transfer function for the system with the LR_2C network in the accelerometer's feedback is given by

---
*The sensitivity of the accelerometer is directly proportional to the feedback resistance, as indicated in Equation (8).
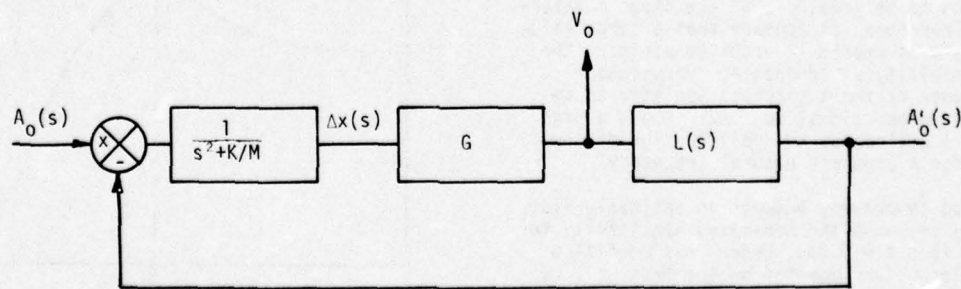
Fig. 7. Block diagram of servoaccelerometer

16

$$\Psi'(s) = \left[\frac{\omega_c^2(s^2+2\delta_1\omega_1 s+\omega_1^2)}{s^4+s^3(2\delta_1\omega_1+2\delta'\omega_c)+s^2(\omega_1^2+\omega_c^2+2\delta_1\omega_1 2\delta'\omega_c)+s(2\delta_2\omega_1\omega_c^2+2\delta'\omega_1^2\omega_c)+\omega_1^2\omega_c^2}\right]\left[\frac{\omega_n^2(1+2\delta s/\omega_n)}{s^2+2\delta\omega_n s+\omega_n^2}\right] \quad (11)$$

where $\omega_1 = \dfrac{1}{\sqrt{LC}}$ = LRC network resonant frequency

$$\delta_1 = \frac{R_2}{2\omega_1 L}$$

$$\delta_2 = \frac{R_1+R_2}{2\omega_1 L} \quad\quad (12)$$

ω_c, δ' = resonant frequency and damping ratio for the servoaccelerometer

The three parameters ω_1, δ_1, and δ_2 can be chosen such that $\Psi'(s)$ is maximally flat over the frequency range of interest. For convenience and since maximum feedback is required at the resonant frequency of the mechanical isolator, ω_1 is chosen to equal ω_n. Additionally, δ_1 is chosen to equal δ (the damping ratio of the mechanical isolator). The third value δ_2 is determined by requiring the overall system transfer function to be down 3 dB at the resonance of the mechanical isolator; that is,

$$|\Psi'(j\omega_n)| = 0.707$$

Therefore,

$$\delta^2 = \delta\beta^2 + [0.5(1+4\delta^2) - 4(\delta\delta'\beta)^2]^{1/2} \quad (13)$$

where $\beta = \omega_n/\omega_c$. Equations (12) and (13) can be used to calculate values of L, R_2, and C that will satisfactorily compensate for the mechanical isolator's transmissibility characteristics.

As an example, the system to be used for measuring the low-frequency components of
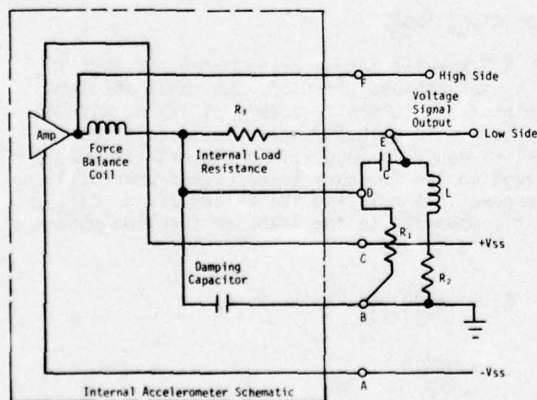
Fig. 8. Accelerometer feedback network for compensating isolator transmissibility

track-induced railcar wheel acceleration has the following characteristics:

ω_n = 188 radians/second

$\omega_c = \omega_1$ = 754 radians/second

$\delta = \delta_1 = 0.250$

$\delta' = 0.707$

Therefore $\delta_2 = 0.80$.

Plots of $\Psi'(\alpha)$, $H(\alpha)$, and $X(\alpha)$, the modified accelerometer response, are given in Fig. 9. The dip in the $X(\alpha)$ response near $\alpha = 1$ is the result of the LR_2C feedback. The drop in $X(\alpha)$ for $\alpha > 4$ is the effect of the normal corner frequency of the servoaccelerometer. The overall system transfer function $\Psi'(\alpha)$ is flat over the bandwidth of interest (0 to 30 Hz) and shows no sign of peaking.

MECHANICAL SYSTEM DESIGN

The mechanical system used for this instrumentation application is basically a damped spring-mass system that is mounted directly to the journal bearing adapter of a standard freight car truck. The bearing adapter is a saddle which fits over the roller bearing; thus, its motion conforms almost exactly to the motion of the train's axles (Fig. 10).

The sensor assembly consists of both a lateral and a vertical servoaccelerometer mounted to the mass of the isolation mechanism. The mass is suspended on vertical guide rods which isolate the mass platform from high-frequency vertical inputs but which allow the platform to follow lateral motion with virtually no attenuation. The mass is guided by four superprecision Thompson Industry linear ball bearings which ride on stainless steel, case-hardened, ground, polished shaftways. The mass is suspended in its housing by four compression springs which are located both above and below the mass and held in position by the shaft rods.

The spring-mass mechanism is fluid damped viscously. Thus, the damping forces are proportional to the relative velocity between the mass and the outer housing. The damper is a solid disk that is rigidly connected to the outer housing through a polished stainless steel guide rod. The piston remains stationary within the cavity that is centrally located in the mass block. The shaft is secured to the outer housing by a rubber bushing which acts as
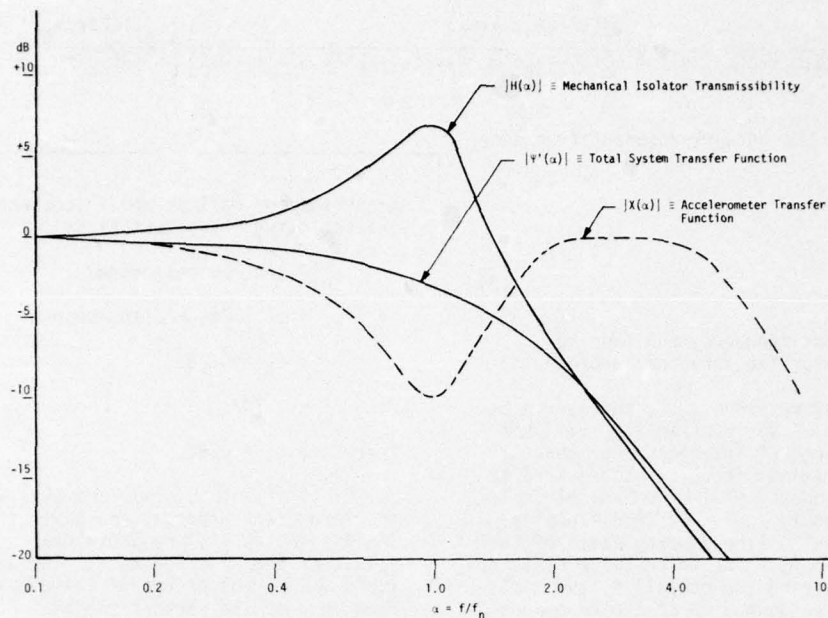
Fig. 9. Accelerometer response plots

a spring in series with the damper piston. The stiffness of the spring, which is placed in series with the piston rod, is five times stiffer than the combined stiffness of the springs which suspend the mass within the housing. The purpose of this second spring is to reduce the severity of instantaneous velocity inputs which may be transmitted to the mass platform.

The damper is centrally located in the mass equidistant between both guide rods and springs. This allows the forces in the mechanism to be uniformly distributed about the center of the mass, thus insuring that the mass will slide freely without binding. The piston plunger is attached to the top of the outer housing so that the guide rod can be brought out of the top of

Fig. 10. Typical 2-axle railcar truck

the damper cavity. There is no static pressure on the fluid. The damping fluid is confined within the mass platform, an arrangement which has several other important advantages: (1) a separate fluid housing is not required; (2) the fluid is insulated from the outside environment; thus, the operating temperature of the damping fluid will be somewhat independent of the outside temperature; and (3) the fluid is isolated from the input motion. The vertical and lateral accelerometers are mounted on support brackets which are bolted to opposite ends of the mass platform.

LABORATORY TESTS

A Schaevitz servoaccelerometer was used in this application. This off-the-shelf accelerometer has a corner frequency of 120 Hz with a damping ratio of 0.707. Its full-scale acceleration range is 10 g's. An LRC network was placed in the feedback as described previously. The equations relating the values of the circuit components to the transfer function parameters are

$$R_2 = \frac{R_1}{(\delta_2/\delta-1)} \; , \quad R_2{}' = R_2 - R_L$$

$$L = \frac{R_2}{\delta\omega_n}$$

$$C = \frac{1}{L\omega_n{}^2}$$

18

The value of R_1 is determined by the desired static full range of the accelerometer. R_L is the internal resistance of the inductor and must be considered as a part of R_2. Therefore, the resistor for the network would be R_2'.

For $R_1 = 5 \times 10^3$ ohms, $\omega_n = 188$ radians/second, $\delta = 0.25$, and $\delta_2 = 0.80$. The values of the circuit components then become

$$R_2 = 2.27 \times 10^3 \text{ ohms}$$

$$L = 48.3 \text{ henrys}$$

$$C = 0.59 \text{ microfarad}$$

The modified accelerometer was tested in the laboratory. A constant level acceleration was applied to the unit, and the frequency was swept from 5 to 1,000 Hz. A comparison of the calculated response versus the measured response indicated agreement to within 5 percent. Variations could be accounted for by the effects of internal torque coil resistance, differences between the accelerometer's theoretical and actual physical characteristics, and experimental error. With more critical adjustment of the LRC values, the measured response could be made to approximate more closely the calculated response.

The isolator assembly was bolted to the head of a vertical shaker, and transmissibility curves were developed for various viscosities of the damper fluid, ranging from air to 12,500 centistokes. Four springs, with a total spring constant of 144 lbs. per inch, were installed in the mechanism for all tests. Comparison of the theoretically derived transmissibility of the isolator with the test results indicated close agreement. Since the 3,000-centistoke viscosity closely approximated a damping ratio of 0.25, it was chosen for the final mechanism design.

CONCLUSIONS

The next step will be to test the assembled unit containing the modified accelerometer on a vertically excited shaker table. From the transmissibility characteristics measured individually for the mechanical isolator and modified accelerometer, it can be concluded that the fully assembled mechanism will exhibit a flat transfer function. The tests should verify that this is the case.

It should be emphasized that the technique described in this paper does not involve simply tailoring the signal from the accelerometer to nullify the effects of the mechanical system's frequency-dependent transmissibility. If this were done, the accelerometer would still require a range wide enough to measure the amplified signal at the resonant frequency of the mechanical isolator in order to prevent saturation. This method involves the dynamic changing with frequency of the accelerometer range such that

the mechanically amplified input acceleration is measured by an accelerometer having a proportionally expanded range.

APPENDIX A

FOURIER SERIES EXPANSION OF RAIL PROFILE

Any periodic function can be expressed as a series of harmonics of its fundamental frequency ($f_o = 1/T$, where T is the period). That is,

$$h(t) = \sum_{n=0}^{\infty} \left(a_n \cos \frac{2\pi n t}{T} + b_n \sin \frac{2\pi n t}{T} \right) \quad \text{(A-1)}$$

where

$$a_n = \frac{2}{T} \int_0^T f(t) \cos \frac{n2\pi t}{T} \, dt \quad \text{(A-2)}$$

$$b_n = \frac{2}{T} \int_0^T f(t) \sin \frac{n2\pi t}{T} \, dt \quad \text{(A-3)}$$

If the profile of a typical bolted rail can be considered periodic with a spatial period equal to one track length, then it can be represented by a Fourier series. A function which has been used effectively to represent the vertical profile of a typical bolted rail is

$$f(x) = A \left| \sin \frac{\pi x}{\lambda_o} \right| \quad \text{(A-4)}$$

where x = position along rail

λ_o = one rail length (12 m)

Equation (A-4) can be expressed in terms of time by considering a railcar that travels along the rail at some velocity v. Therefore, at any time t

$$x = x_o + vt \quad \text{(A-5)}$$

and $\sin \frac{\pi x}{\lambda_o} = \sin \frac{\pi(x_o + vt)}{\lambda_o}$. By choosing $x_o = 0$, the corresponding vertical profile time function is

$$f(t) = A \left| \sin \frac{\pi v t}{\lambda_o} \right| = A \left| \sin \frac{\pi t}{T} \right| \quad \text{(A-6)}$$

where $T = \frac{\lambda_o}{v}$ = period of f(t)

v = vehicle velocity (m/sec)

A = profile amplitude (cm)

λ_o = spatial wavelength (m)

By substituting Equation (A-6) into Equations (A-2) and (A-3), the Fourier series coefficients are:

$$a_n = \frac{4}{T} \int_0^{T/2} \sin \frac{\pi t}{T} \cos \frac{n2\pi t}{T} \, dt; \quad b_n = 0 \quad \text{(A-7)}$$

The coefficient b_n is zero, since $f(t)$ is a positive function; therefore, the integral is zero over the integration interval. By performing the integration of Equation (A-7),

$$a_n = \frac{2A}{\pi(1-4n^2)} \text{ at } f_n = \frac{n}{T} \qquad (A-8)$$

At a frequency of f_n, the acceleration amplitude corresponding to the profile amplitude is

$$A_n = \frac{2A}{\pi(1-4n)} \left(\frac{2\pi n}{T}\right)^2 \qquad (A-9)$$

If the λ_0/v is substituted into Equation (A-9), the relationship between acceleration amplitude and railcar velocity results. That is,

$$A_n = \frac{2A}{\pi(1-4n^2)} \left(\frac{2\pi n v}{\lambda_0}\right)^2 \qquad (A-10)$$

APPENDIX B

DERIVATION OF SPRING MASS-DAMPER TRANSMISSIBILITY RELATIONSHIP

The equation of motion for the mechanical isolator illustrated in Fig. 4 can be written as

$$(x_i - x_o)K + (\dot{x}_i - \dot{x}_o)C = M\ddot{x}_o \qquad (B-1)$$

where x_i = input displacement* (cm)

x_o = output displacement (displacement of mass)

K = spring constant (kg/cm)

M = mass (kg)

C = damping coefficient (kg/cm/sec)

and the dot over the variables indicates differentiation with respect to time. For the steady-state case (after transients have decayed), Equation (B-1) can be expressed in Laplace notations as

$$[X_i(s) - X_o(s)]K + [X_i(s) - X_o(s)]sC = MX_o s^2 \qquad (B-2)$$

where s is the complex Laplace variable.

Equation (B-2) can be rearranged to obtain system transmissibility:

$$\frac{X_o(s)}{X_i(s)} = \frac{K + Cs}{Ms^2 + Cs + K} \qquad (B-3)$$

Although Equation (B-3) is the transmissibility for displacement inputs, it is also the transmissibility for acceleration inputs, since

_____

*Displacements are relative to an inertial reference.

$$*\mathcal{L}(\ddot{x}_i) = s^2 X_i(s) = A_i(s)$$

$$\mathcal{L}(\ddot{x}_o) = s^2 X_o(s) = A_o(s)$$

and therefore

$$\frac{A_o(s)}{A_i(s)} = \frac{s^2 X_o(s)}{s^2 X_i(s)} = \frac{X_o(s)}{X_i(s)}$$

Therefore,

$$\frac{A_o(s)}{A_i(s)} = \frac{\omega_n^2(1 + 2\delta s/\omega_n)}{s^2 + 2\delta\omega_n s + \omega_n^2}$$

where $\omega_n = \sqrt{\frac{K}{M}}$ = natural frequency of system

$$\delta = \frac{C}{2\sqrt{KM}} = \text{damping ratio}$$

APPENDIX C

IMPULSE RESPONSE OF A LINEAR SPRING-MASS-DAMPER ISOLATOR

In Appendix B, the general equation for the steady-state transmissibility of a spring-mass-damper isolator was developed. This equation applies for steady-state vibrations after transients have decayed. But the transient response of a system is equally important, since it indicates how the system will respond to shocks (impulses of high amplitude but of short duration). The general equation of motion for the isolator is

$$(x_i - x_o)K + (\dot{x}_i - \dot{x}_o)C = M\ddot{x}_o \qquad (C-1)$$

where x_i, x_o, K, C, and M are defined in Appendix B. For an initially relaxed system ($x_i = x_o = \dot{x}_i = \dot{x}_o = 0$), the transmissibility of the system can be expressed in Laplace transform as (see Appendix B for derivation)

$$\frac{A_o(s)}{A_i(s)} = \frac{\omega_n^2(1 + 2\delta s/\omega_n)}{s^2 + 2\delta\omega_n s + \omega_n^2} \qquad (C-2)$$

The response of this system for an impulse [$i(t)$] is simply the inverse transformation of the system's transmissibility.** Therefore,

$$A_o^i(t) = \mathcal{L}^{-1}\left[\frac{\omega_n^2(1 + 2\delta s/\omega_n)}{s^2 + 2\delta\omega_n s + \omega_n^2}\right] \qquad (C-3)$$

where the i superscript indicates the system's impulse response and $\mathcal{L}^{-1}$ indicates the inverse Laplace transform of the function inside the

_____

*$\mathcal{L}(f)$ is the standard symbol used to indicate a Laplace transformation of the function f.

**See "Analysis of Linear Systems," by David K. Cheng, Addison-Wesley Publishing Co., 1961, pages 229-234.

brackets. The response function, which depends on the value of the damping ratio δ, is given in Equations (C-4), (C-5), and (C-6) for the three ranges of damping ratio.

$$\delta < 1 \quad A_o^i(t) = \frac{\omega_n \varepsilon^{-\delta \omega_n t}}{(1-\delta^2)^{1/2}} \sin \left[\omega_n (1-\delta^2)^{1/2} t + \theta\right]$$
(C-4)

$$\theta = \text{arc-tan} \left(\frac{2\delta\sqrt{1-\delta^2}}{1-2\delta^2}\right)$$

$$\delta = 1 \quad A_o^i(t) = \omega_n \varepsilon^{-\omega_n t}(2-\omega_n t)$$
(C-5)

$$\delta > 1 \quad A_o^i(t) = \frac{\omega_n \varepsilon^{-\delta \omega_n t}}{\sqrt{\delta^2-1}} \{(1-2\delta^2)\sin h$$

$$\left[\omega_n (\delta^2-1)^{1/2} t\right] + 2\delta\sqrt{\delta^2-1} \cos h$$

$$\left[\omega_n (\delta^2-1)^{1/2} t\right]\}$$
(C-6)

The response at time $t = 0$ is equal to $2\delta\omega_n$ for all three ranges of δ. Thus, a high value of damping ratio and/or natural frequency causes the system to be more sensitive to shock than low values of these parameters.

The impulse response can also be used to determine the system's response for any arbitrary input by making use of the convolution integral as shown in Equation (C-7).

$$A_o(t) = \int_o^t A_i(\tau)A_o^i(t-\tau)d\tau$$
(C-7)

APPENDIX D

SERVOACCELEROMETER TRANSFER FUNCTION

Referring to Fig. 7, the transfer function between the input acceleration (A_o) and output voltage (V_o) can be written in Laplace transform notation as

$$\frac{V_o(s)}{A_o(s)} = \frac{G}{s^2+GL(s)+\omega_r}$$
(D-1)

where $\omega_r = \sqrt{K/M}$ = resonant frequency of sensor mechanical suspension

G = displacement to voltage conversion constant (volts/cm)

For a standard accelerometer in which a torque coil is used to produce a force balance, a current is fed back from the amplifier by means of a resistor in series with the torque

coil and connected to zero volt. Electrical damping is achieved by connecting a capacitor across the feedback resistor. In this case $L(s)$ has the form

$$L(s) = \frac{F(1+\tau s)}{R}$$
(D-2)

where τ = RC = time constant of feedback network

R = feedback resistor

C = feedback capacitor

F = conversion constant $[(m/sec^2)/ampere]$

If Equation (D-2) is substituted into Equation (D-1), the transfer function becomes

$$\frac{V_o(s)}{A_o(s)} = \left(\frac{R}{F}\right) \frac{\omega_c^2}{s^2+2\delta'\omega_c s+\omega_c+\omega_r^2}$$
(D-3)

where $\omega_c = \sqrt{\frac{GF}{R}}$ = accelerometer corner frequency

$$\delta' = \frac{RC\omega_c}{2} = \text{accelerometer damping ratio}$$

In general, $\omega_c \gg \omega_r$ and can be dropped from Equation (D-3). Typically,

ω_c = 754 radians/second

ω_r = 6 radians/second

δ' = 0.707

R = 5,000 ohms

C = 0.4 microfarad

The coil resistance has been neglected in this analysis, since it produces a second resonance at a much higher frequency than ω_c and has minimal effect upon the accelerometer's overall frequency response.

DEVELOPMENT AND APPLICATION OF A MINIATURE RECORDER/ANALYZER

FOR MEASUREMENT OF THE TRANSPORTATION ENVIRONMENT

Matthew A. Venetos
Air Force Packaging Evaluation Agency
Wright-Patterson Air Force Base, Ohio

and

John J. Lorusso
Bolt Beranek and Newman, Inc.
Cambridge, Massachusetts

This paper describes the design of a miniature recorder/analyzer system developed primarily for the measurement of the environment experienced by packaged items during handling, shipment, and storage. Significant features of this solid state device are: real time data analysis, metal oxide semiconductor memory, small size, low power requirements, rugged construction, and extensive measurement capability. Environmental parameters measured include impact shock, temperature and humidity. Applications of the recorder are described for monitoring shipments of cushion packs, jet engines, and nuclear cargo.

In 1973 the Air Force Packaging Evaluation Agency (AFPEA) contracted with Bolt Beranek and Newman, Inc., to develop a miniature transportation environment recorder to determine the environments and hazards that packaged items experience in handling, shipment and storage.

Prior to the development of this recorder, several devices existed for investigating transportation environments. In brief, these devices were of either the simple shock threshold indicating type or the more sophisticated peak reading recorders which generally utilize magnetic tape as the recording medium. Since both types will subsequently be discussed in some detail, comment at this point will be confined to their limitations. By their very nature, the threshold shock indicators can provide only an approximate and very limited picture of the shock environment. Although the magnetic tape, peak reading recorders give a more precise measure of the shock environment, their relatively large volume and weight as well as significant power requirements preclude their use in all but the largest shipping containers. In addition, significant time and effort can be involved in data retrieval and processing with this type of recorder.

Therefore, the criteria for design of a new recorder were: (1) real time analysis of data, (2) elimination of magnetic tape recorders as data storage media, (3) significant recorder volume reduction without compromising recorder operational flexibility, (4) the inclusion of temperature and humidity measurement capability, and (5) the ability to withstand hazards consistent with the environment to be measured.

The key to significant reduction in volume of this recorder is the use of metal oxide semiconductor (MOS) technology coupled with the use of a miniature triaxial accelerometer developed by BBN. The recorder circuitry has been optimized to minimize power consumption such that, using internal batteries, the recorder can operate continuously for over two weeks. The total volume of the recorder (Figs. 1 and 2) including internal batteries is 2753 cu cm (168 cu in), 12.4cm X 14.9cm X 14.9cm, and its weight is 2.72 kilograms (6 pounds).

The shock data acquired from the triaxial accelerometer is separated by shock polarity for each recorder axis. Data are analyzed in real time and the results stored in MOS memories. The dynamic range of each shock channel is 2.5g to 90g. Twenty-four amplitude windows characterize each shock polarity. The first nineteen windows are 2.5g wide and the next four windows are 10g each, while the last window is an overflow window for shocks greater than 90g. Each amplitude window is capable of storing over 65,000 events. Figure 3 is a typical shock histogram, which presents the
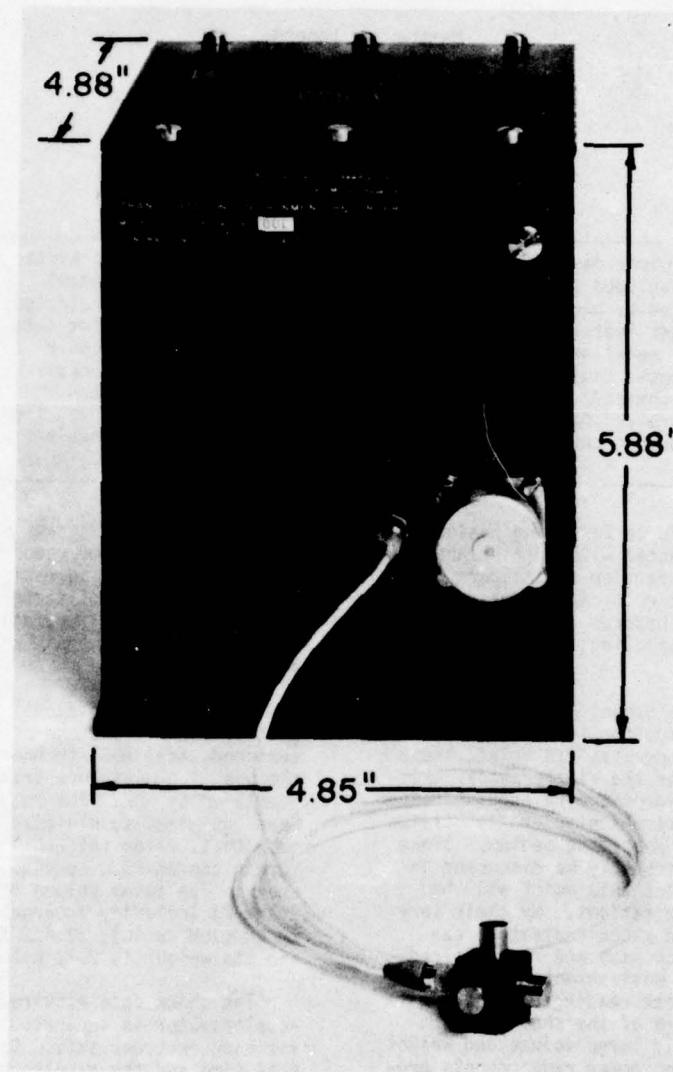
Fig. 1 - Model 711 Transportation Recorder In Optional Remote Triaxial Accelerometer Configuration

DIGITAL READOUT
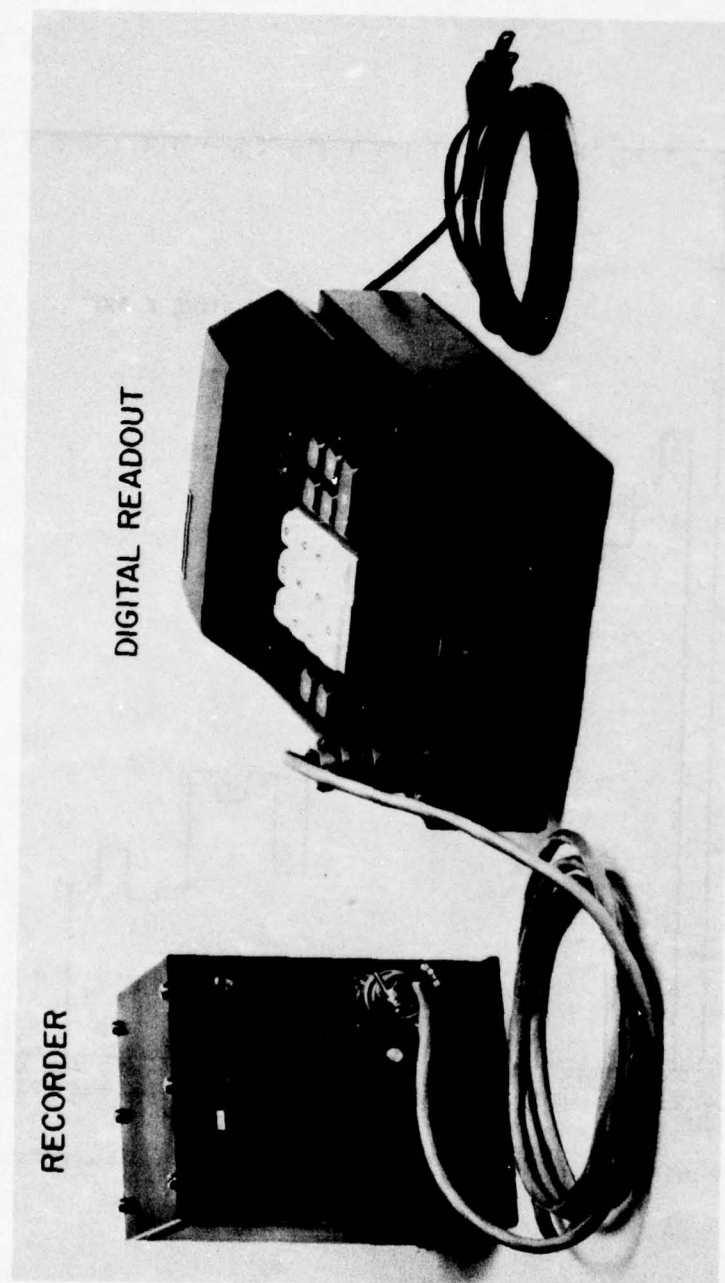
RECORDER

Fig. 2 - Model 711 Recorder and Digital Readout

25
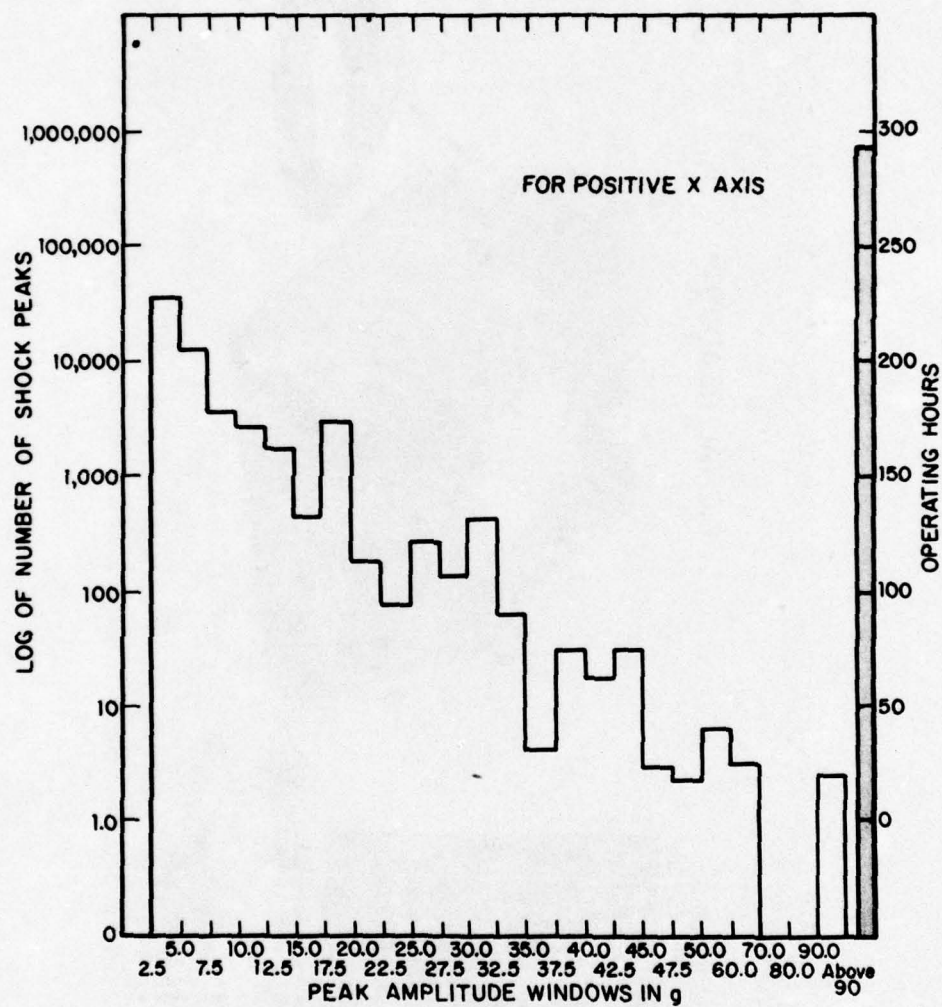
Fig. 3 - Model 711 Transportation Environment Recorder Typical Shock Histogram

logarithm of the number of occurrences of a given shock increment.

The recorder also has the capability of measuring temperature and humidity. The recorder's temperature range extends from -20 to +140°F. Sixteen amplitude windows, each 10°F wide, are employed for temperature measurement. The recorder's relative humidity range is 0 to 100%. Eight amplitude windows are used for the humidity measurement, one 0 to 30% RH and seven for 30 to 100% RH, each 10% wide. Temperature and humidity measurements are made every minute. The recorder also contains an elapsed time clock which measures time in one minute increments. The elapsed time clock makes possible the determination of the percentage of time specific temperature and humidity ranges are experienced.

One of the prime advantages of the recorder is that the data as read out are already analyzed. It is not necessary to perform magnetic tape analysis or to feed data into a computer. The amplitude statistical analysis has already been accomplished. Peripheral data (temperature, humidity, and elapsed time) are also presented in histogram form.

SYSTEM OPERATION:

A typical channel of the recorder may be divided into three major blocks: (1) input signal conditioning, (2) A/D conversion, and (3) memory, as shown in Figure 4. Six shock channels - 3 axes with two polarities each, and two peripheral data channels for temperature and humidity, have been implemented in the recorder.

The analog signal conditioning circuitry converts a shock peak to a digital signal, which ultimately increments an amplitude window in memory proportional to the peak value of the shock.

The shock signal from the accelerometer is amplified and bandpass-limited ($0.8H_z$ to $200\ H_z$) in the preamplifier. Threshold circuitry decides whether either positive or negative shock peak are above the system threshold of 2.5g. If the threshold is exceeded, peak detector circuitry is powered up and the peak value of the shock stored. When the magnitude of the signal presented to the threshold circuitry falls below the system threshold, A/D conversion logic is powered up. The magnitude of the shock stored in the peak detector circuitry is compared to the D/A ramp signal and a digital pulse increments the appropriate window in the MOS memory. Shock data is analyzed in real time resolving events as often as 4 msec. It is important to note that data may be simultaneously processed on all three axes without degradation of resolution.

Temperature and humidity are sampled once every minute. The temperature signal conditioning consists of a thermistor bridge whose output is linearly related to temperature. The humidity tranducer requires rather complex signal conditioning. The transducer must be excited with a low frequency A.C. signal. Its transfer characteristic is logarithmic, so a log full wave average detector is required to provide an output linearly proportional to relative humidity. Since the transducer is temperature sensitive, a correction must be added to compensate for ambient temperature.

In order to accommodate the requirement for two different "window" sizes in the shock amplitude analysis, the staircase voltage from the DAC has two different magnitudes as shown in Figure 5. For the first 19 steps, the step amplitude is proportional to 2.5g. For the last five steps, the step amplitude is proportional to 10g. The staircase also provides a uniform 16 step staircase for conversion of temperature and humidity data.

A typical memory has been organized into 64, 16-bit words. Words 0 to 23 are designated for positive peaks, words 24 to 47 for negative peaks and words 48 to 63 for peripheral data, such as temperature. The DAC ramp and memory operate in synchronous mode so that the appropriate amplitude window in memory is incremented during each conversion cycle.

One of the prime considerations during the hardware design was minimization of power consumption since this directly affected the experimental flexibility and ultimately the physical size and weight of the recorder. The analog circuitry is configured such that only preamplifiers and threshold detectors are powered when shocks are below threshold. A/D conversion circuitry is powered only when a shock above threshold is encountered.

The majority of power consumption in the recorder is due to the memory. Three MOS 1024 bit dynamic shift registers are utilized as memory storage elements. These devices are a series of P-channel MOS field effect transistor (FET) devices connected in a bucket-brigade configuration. Two properties of MOS IC technology made possible the design of dynamic shift registers: (1) the high impedance associated with the gate circuit permits temporary storage of charge on the parasitic capacitances, and (2) MOS technology permits realization of bidirectional transmission gates that have zero offset. With the transmission gate, a gate-node may be easily connected to or disconnected from other points in the circuit. A series of 1024 transmission gates are configured in a single package. To retain the data stored in the register, the rate at which the data are circulated (or clocked) must not fall below some minimum value, typically 1 kH_z at room temperature. The minimum data rate is proportional to ambient temperature. In order to assure 4 msec resolution of shock data, the memory must recirculate in 4 msec. This means that the memory must be clocked at $\frac{1024}{4\ msec} = 256\ kH_z$.
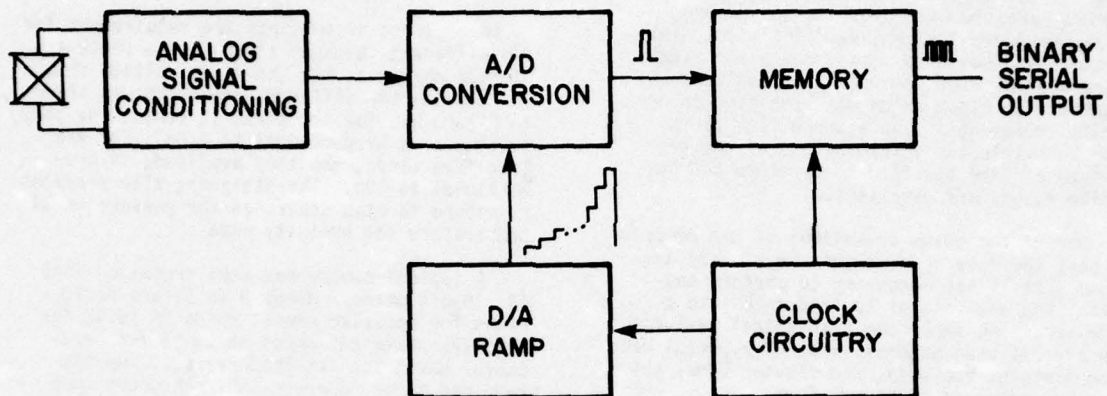
Fig. 4 - Typical Channel of the Recorder
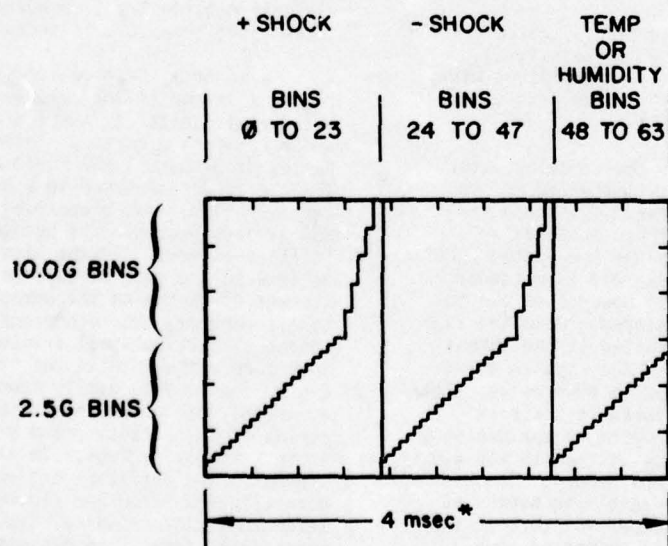
*THE A/D CONVERSION IS SYNCHRONIZED
WITH THE SHIFT REGISTER MEMORY

Fig. 5 - DAC Staircase

28

Since the power consumption for the MOS shift registers is directly proportional to the rate at which they are clocked, significant power would be required to operate the memory continuously at that rate.

In order to minimize power consumption a dual mode clocking scheme was designed as shown in Figure 6. When shock data are above the threshold of the recorder, thus requiring real time processing, the dynamic shift registers are clocked at 256 kHz. When processing is completed, the clock retires to the minimum operating data rate. Since this rate is temperature dependent, the clocking circuitry has been designed to compensate for this characteristic. This technique guarantees the integrity of the processed data while reducing the power consumption by an order of magnitude.

In summary, an amplitude statistical recorder has been successfully implemented for investigating environmental exposure of packages in transit as well as in the design and evaluation of packaging systems. Further, it may be utilized for the evaluation of handling procedures and on-site quality control. Other application areas include vibration, noise and meteorological measurements in which the data may be adequately represented by an amplitude probability function. In many cases with such a device experiments could run unattended, and little or no data reduction would be required for presentation of experimental results.

Before discussing specific applications for the recorder described above, consideration will be given to some Air Force requirements for environmental recorders capable of measuring shipping, handling, and storage conditions.

Many every day activities at the Air Force Packaging Evaluation Agency involve "trouble shooting" problems relating to high damage rates reported for previously approved pack designs. Instrumentation of the type described here becomes invaluable in situations such as this for determining whether the containers are experiencing any extraordinary shock and vibration conditions in shipment through the logistic system.

The design of protective packaging systems for fragile, high value Air Force weapon system components requires information on the environmental inputs that packages will be subjected to during shipment in terms of shock, temperature, and humidity.

A continuing need exists for more definitive information on the general shipping environment. Review of the literature reveals a general lack of data regarding the shock environment experienced by packaged items. Generalized information on the shipping environment would improve the realiability of package designs. In addition, this type of information could be used in establishing more realistic performance standards required for approval of both in-house and contractor design packaging systems. It is suspected that considerable savings in packaging materials and labor costs could be achieved by modifying existing specification requirements which may be too conservative, thereby, resulting in overpackaging of military equipment. Conversely, information on the shipping environment would make possible the upgrading of marginal performance standards which may be contributing to high damage rates.

AFPEA has used and is continuing to use some commercially available, relatively inexpensive shock indicator devices for instrumentation of cushion packs. Generally, they consist of a simple spring-mass system in which the spring is tensioned to release when a specific shock threshold has been exceeded. If properly employed, these devices can give valuable information on the shock environment. An extensive evaluation has been made of several types of these shock indicators. Figure 7 is a plot of shock threshold values versus pulse duration for a typical shock indicator. The natural frequency and damping of this shock indicator is such that shock pulses exceeding 20 milliseconds will give relatively accurate readings. However, as indicated in Figure 7, pulse dirations less than 20 milliseconds can result in considerable error. In addition to the high frequency response problem, the primary limitation with this type of shock indicator is the fact that it is a threshold indicating device and therefore will not record the exact magnitude of the shock input.

A Transportation Environmental Measurement and Recording System (TEMARS) manufactured by the Endevco Corporation has been used extensively in monitoring shipments. The TEMARS recorder will measure peak shock inputs up to 30g and also the pulse duration of the input. The TEMARS also provides a record of the cumulative shocks encountered whereas the threshold type indicators are capable of only a single event measurement. Since the TEMARS is approximately 45.7cm (18 in) in cube and weighs 25 kilograms (55 lbs), it obviously cannot be used for the instrumentation of small containers which experience has indicated normally receive the greatest shock inputs.

Prior to using the miniature transportation environment recorder developed by Bolt Beranek and Newman, AFPEA conducted an extensive laboratory evaluation of its shock and vibration performance characteristics.

A vibration resonance search on an electrodynamic vibrator revealed resonant frequencies of 1700Hz which is well above the upper frequency level generally concerned with in packaging development activities.

One of the first applications of the recorders was in the evaluation of the performance
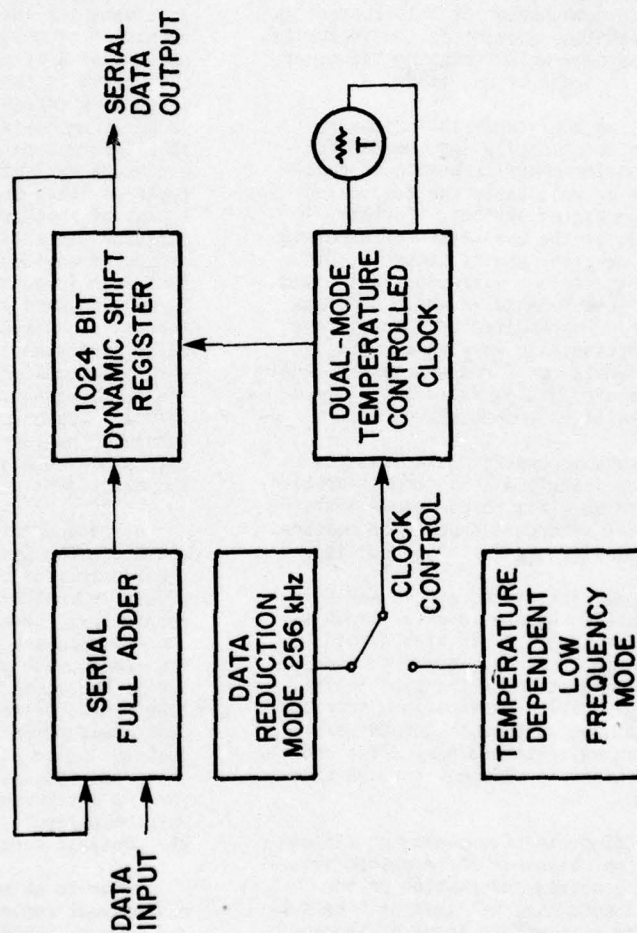
Fig. 6 - Block Diagram - Memory and Temperature Controlled Clock
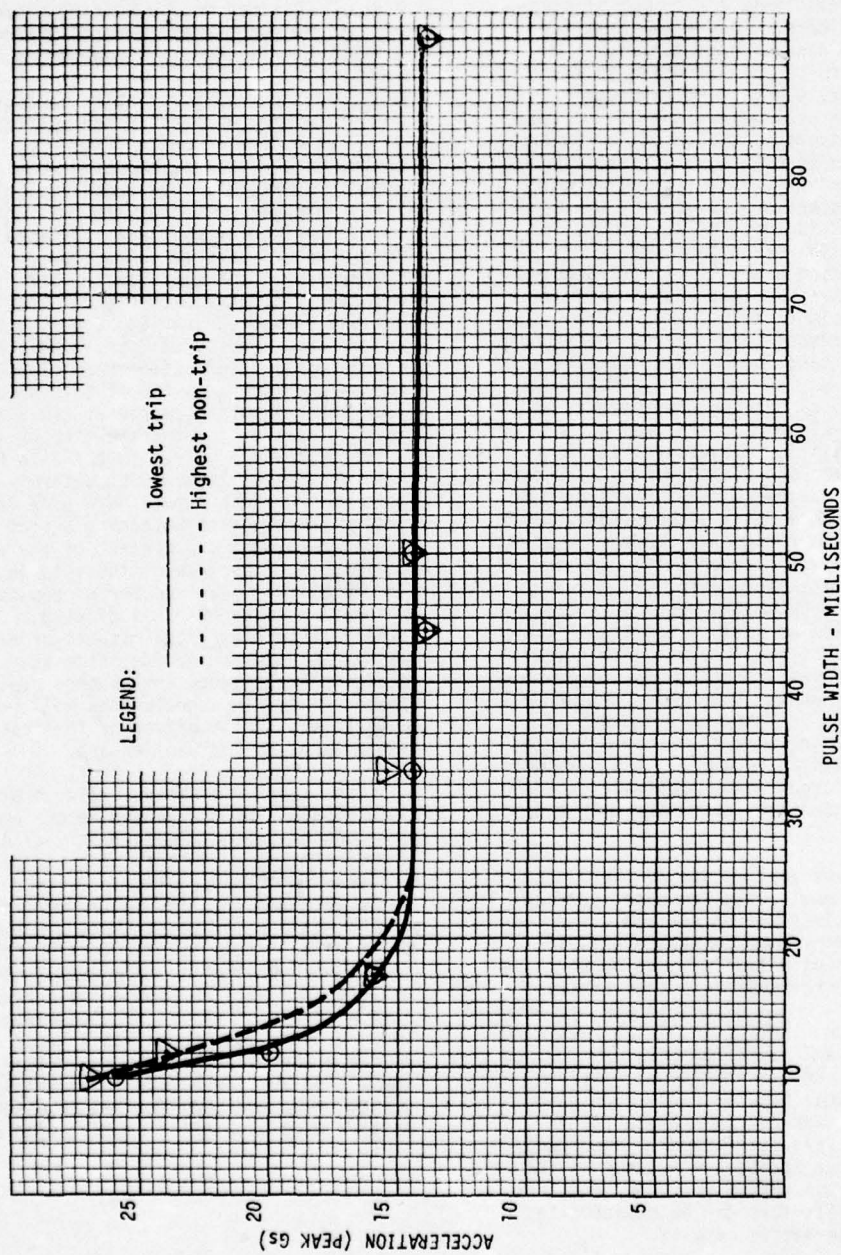
Fig. 7 - 15G "OMNI - G" Shock Indicator

31

of a "family" of standardized cushion packs ("Star" Packs) (Fig. 8) used by the Air Force in the shipment of high value, fragile weapon system components. These standard cushion packs are part of the Air Force Fast Pack concept which makes possible the shipment of items representing a wide range of weights and sizes using a relatively few number of standard type containers. This eliminates the need for custom design packs for each and every item which can be expensive in terms of material, labor, design, and inventory costs. In order for the package designer to be able to effectively use this system of containers, it was necessary to develop a series of pack selection charts (Fig. 9) which would indicate the level of protection provided by the various pack designs in terms of the item's size and weight. These selection charts were developed by making a series of instrumented free fall drop tests. In performing these tests, a drop height of 76.2 cm (30 in) was selected as representative of that which would occur in actual handling situations. The shock recorder was used to verify that the shock inputs and associated drop heights assumed in the development of the selection charts were realistic. Several different sizes of the Star Pack design were instrumented in shipments to various locales throughout the United States; specifically, these shipments were made to our Air Logistic Centers located in Robins, Georgia; Oklahoma City, Oklahoma; San Antonio, Texas; Sacramento, California; and Ogden, Utah. Shipments were made utilizing the postal service as well as commercial carriers contracted to haul cargo to Air Force facilities. The results of the monitored shipments revealed that our assumption of the drop heights occurring in shipment (Fig. 10) were reasonably close to those that actually occurred. As indicated in Figure 11, the maximum shock levels recorded were comparable to those developed in controlled laboratory drop tests (Fig. 9).

Another recent application of the shock recorder was in monitoring "on base" surface movements of nuclear weapon systems. The tie-down configurations used to secure nuclear cargo to the bed of a trailer must be certified prior to use. Determination of the reaction modes which would be developed in the tie-down chains depends on specific knowledge regarding the input shock and vibration developed during road transport. Unfortunately, no specific information of this nature was available in the literature; instead, generalized data developed for a variety of trucks, road conditions, and vehicle speeds are plotted in the form of shock input versus frequency envelops. Use of data in this form can be expected to give highly conservative results.

The shock recorder was mounted on the bed of the trailer at a location above the rear axle (Fig. 12). Two other systems were used together with the shock recorder; these were the TEMARS recorder previously described and an oscillograph recording system. The data recorded with the three systems indicated that the road shock inputs developed during hauling nuclear weapons on several Air Force bases was significantly less than the data obtained from the generalized curves available in the literature. This was not surprising since road conditions on base are generally good and drivers are limited to speeds of 25mph or less.

One of our most recent applications of the miniature recorder was in the monitoring of a J-57 jet engine shipment (Fig. 13). The transportation environment had been identified as one of several possible causes for high defect rates being experienced with this engine which is used primarily by the Air National Guard. The recorder was used to monitor an engine shipment by commercial semitrailer from the Air Logistic Center at Oklahoma City to an Air National Guard base at St. Louis, Missouri, and return. The overall travel distance was approximately 2,000 kilometers (1,250 miles). During the entire course of this shipment only four shock inputs occurred at the 5 to 7-1/2g level. Most of the transient shock inputs were minor and occurred in the 2 to 5g range. From this data, it could be determined that none of the shock inputs were of a level high enough to result in bottoming out of the shock isolation system and contact of the engine against the interface of the shipping container. The relatively small number of counts in the recorder's lower "bins" indicated that no steady state vibrational inputs of significant magnitude occurred during shipment. Several additional shipments are planned over different routes before any conclusions will be drawn with regard to the effect of the transportation environment on the J-57 engine.

One of AFPEA's future projects will involve determination of the general shock environment experienced in world-wide distribution of Air Force materiel. For this effort additional recorders will be required. Based on experience gathered to-date, several modifications of the basic recorder unit are contemplated. These will include another version of the recorder wherein the shock inputs along the three primary axes will be combined electronically into a resultant value. A time delay feature is also being considered which would make possible the separation of the primary impact input from the subsequent low level inputs generated by the tumbling and secondary impacting of a pack after contact with an impact surface.
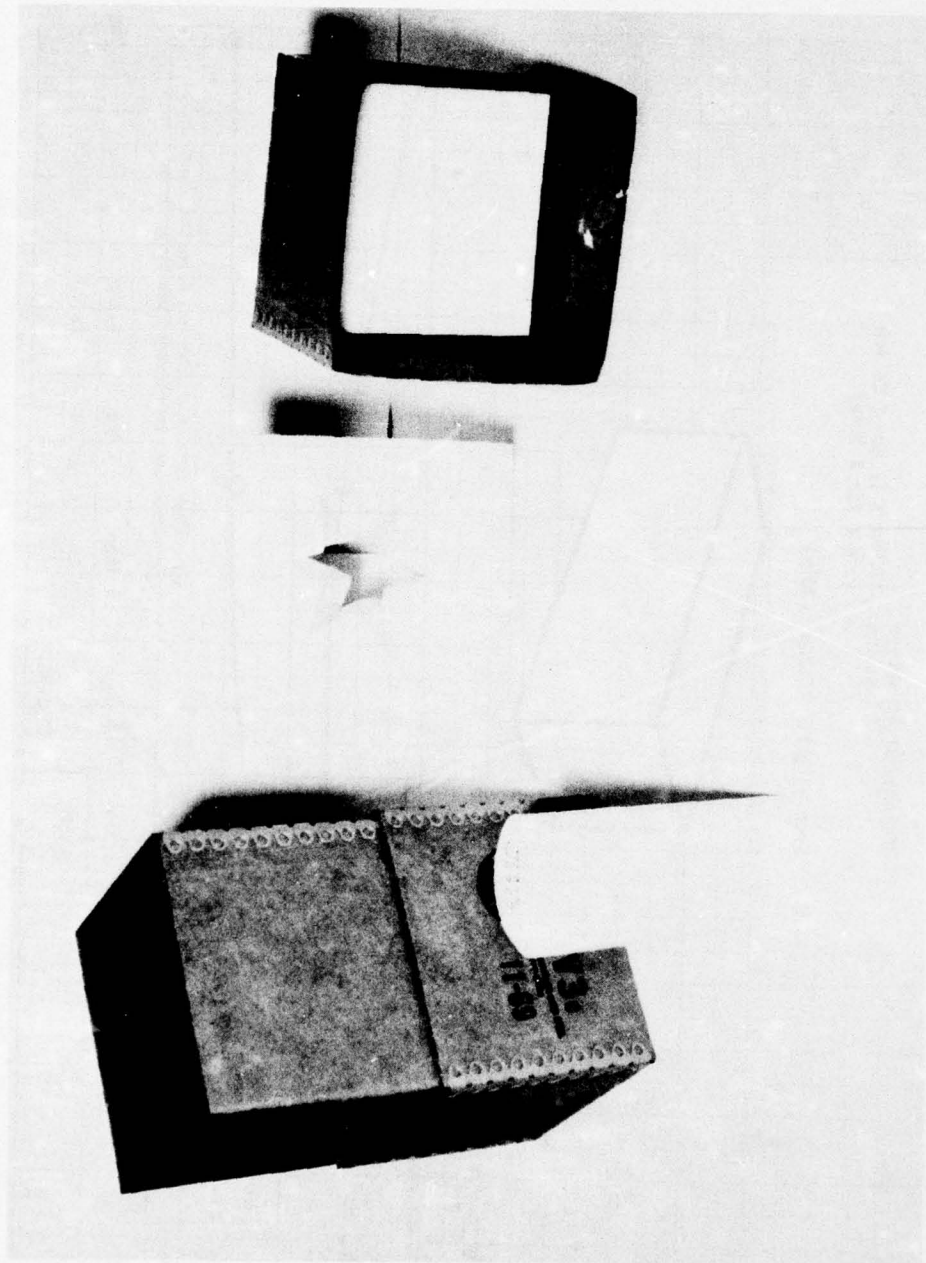
Fig. 8 - "Star" Pack with Polyurethane Cushioning Insert

33

Rectangular Prototype
Dimension: 17.8cm X 17.8cm X 25.4cm
(7in X 7in X 10in)

Drop Height: 76.2cm (30in)

—Peak Acceleration-Top & Bottom Face Drops
—Peak Acceleration-Side Face Drops

PEAK ACCELERATION (G's)

ITEM WEIGHT (POUNDS)

| 2.7kg | 3.6kg | 4.5kg | 5.5kg | 6.4kg | 7.3kg | 8.2kg | 9.1kg | 10.0kg |
| 6.00 | 8.00 | 10.00 | 12.00 | 14.00 | 16.00 | 18.00 | 20.00 | 22.0 |
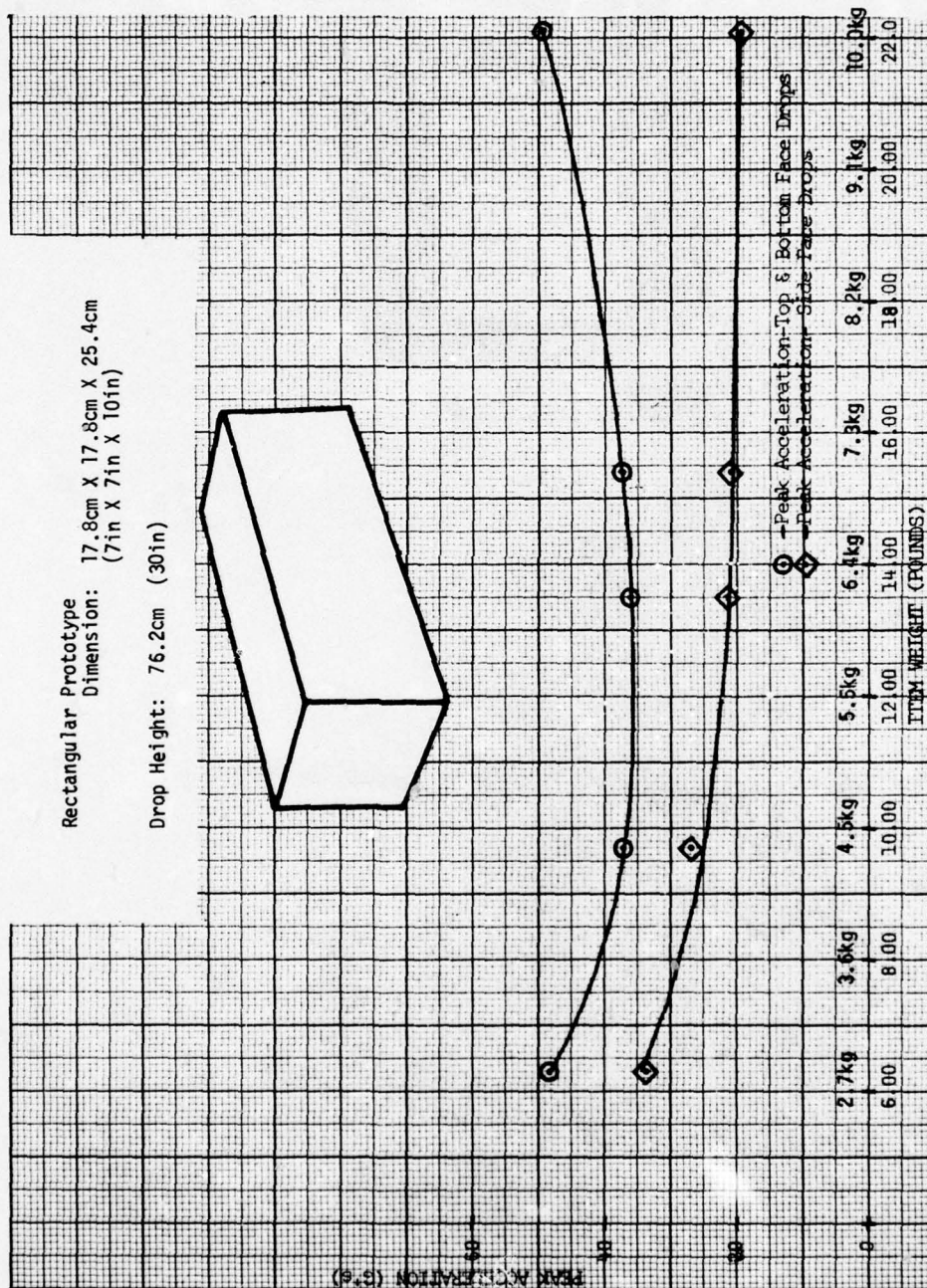
Fig. 9 - Peak G - Item Weight Curves for 35.6cm X 35.6cm X 35.6cm Polyurethane Star Pack

34

TRAVEL MODE	NUMBER OF TRIPS	NO. OF TRIPS WITH 76.2cm DROPS OR BETTER	PERCENTAGE OF TRIPS WITH 76.2cm DROPS OR BETTER	PACK SIZE (cm)
*UPS & PP	15	4	26	25.4 X 25.4 X 30.5
**Logair	13	7	54	25.4 X 25.4 X 30.5
TOTALS	28	11		25.4 X 25.4 X 30.5
UPS & PP	16	7	43	30.5 X 30.5 X 35.6
Logair	8	2	25	30.5 X 30.5 X 35.6
TOTALS	24	9		30.5 X 30.5 X 35.6
UPS & PP	11	5	45	35.6 X 35.6 X 40.6
Logair	11	3	27	35.6 X 35.6 X 40.6
TOTALS	22	8		35.6 X 35.6 X 40.6

*UPS - United Parcel Service
PP - Parcel Post
**Logair - Commercial Air Carrier under Air Force contract.

Fig. 10 - Analysis of Package Drop Heights Occurring in Shipment

35

G	MEMORY I				MEMORY 2				MEMORY 3			
	+	X	-	X	+	Y	-	Y	+	Z	-	Z
2.0 to 5.0	100	48	124	37	200	36	224	27	300	39	324	68
5.0 to 7.5	101	38	125	52	201	43	225	39	301	42	325	52
7.5 to 10.0	102	13	126	18	202	8	226	12	302	19	326	15
10.0 to 12.5	103	1	127	3	203	5	227	7	303	10	327	8
12.5 to 15.0	104	3	128	3	204	7	228	3	304	4	328	3
15.0 to 17.5	105	1	129	2	205	2	229	2	305	3	329	3
17.5 to 20.0	106		130		206	1	230		306	2	330	1
20.0 to 22.5	107	1	131		207		231		307	1	331	
22.5 to 25.0	108		132		208		232		308	1	332	
25.0 to 27.5	109		133		209		233		309		333	
27.5 to 30.0	110		134		210	1	234		310		334	

Fig. 11 - Data Log Sheet of Fast Pack Shipment (35.6cm X 35.6cm X 35.6cm) to Warner-Robins ALC
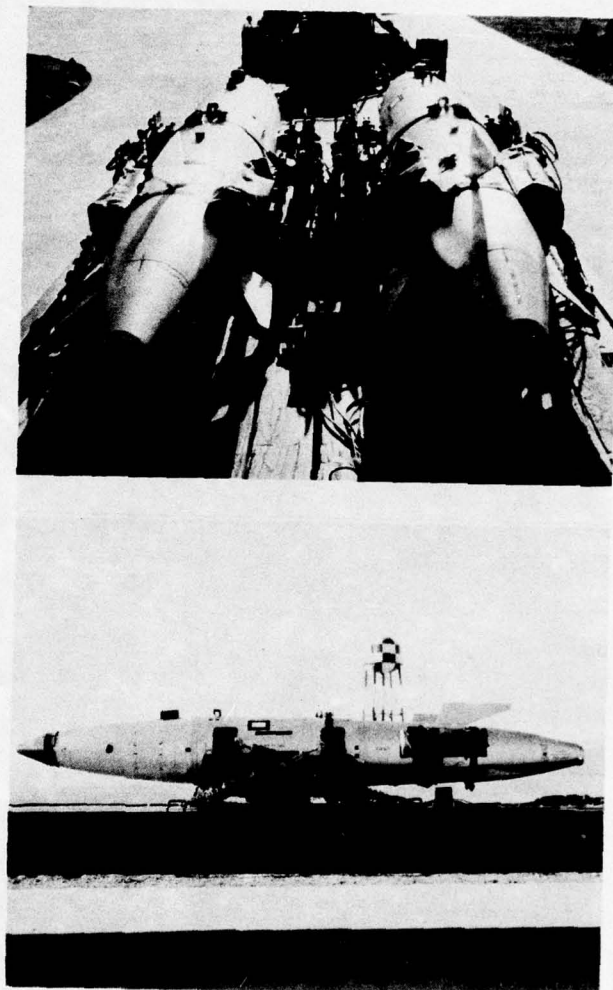
Fig. 12 - "Side By Side" Tie-Down Configuration of B28Y Training Bomb (Inert)
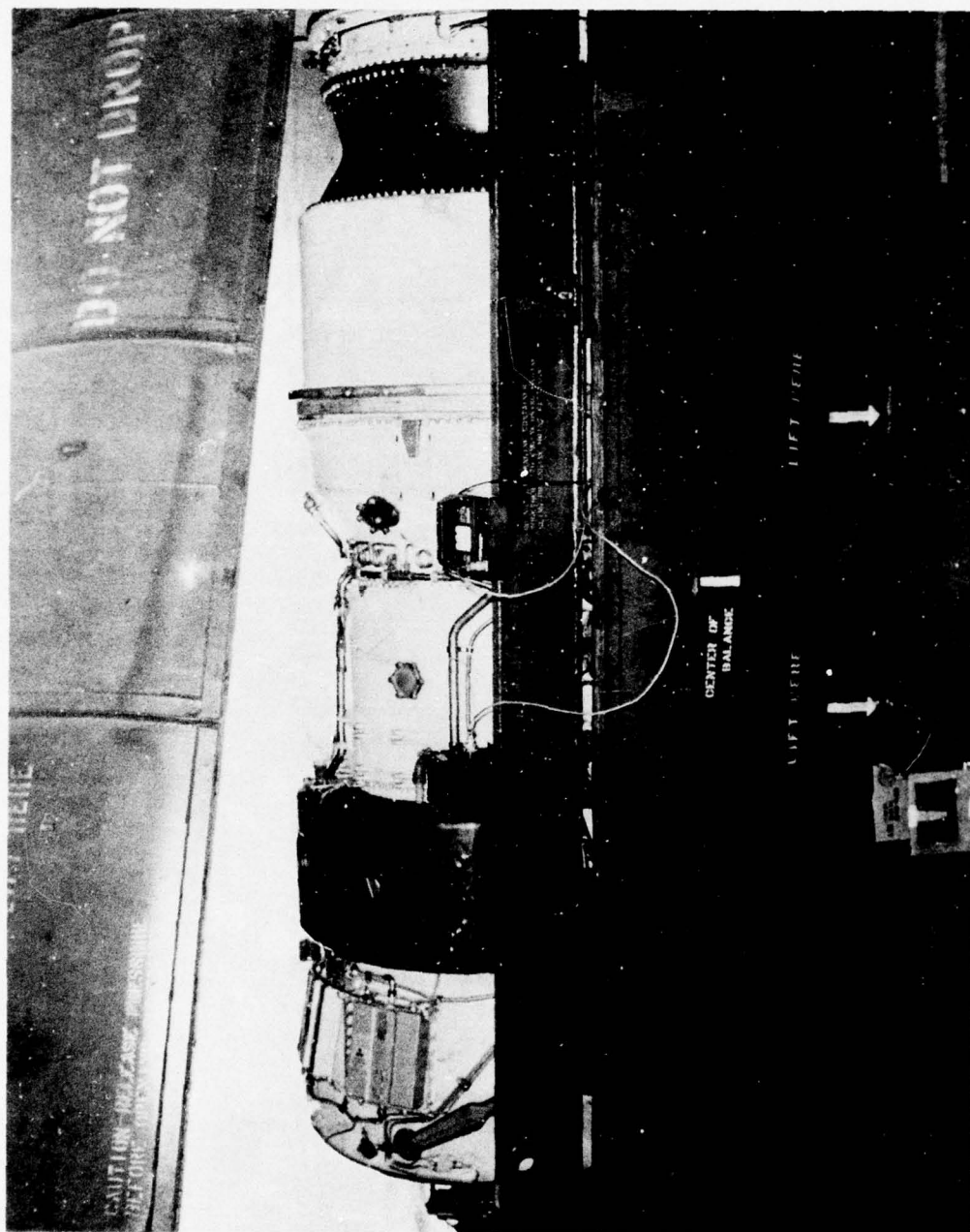
Fig. 13 - J-57 Engine in Shipping Container

38

Discussion

Mr. Paladino (Naval Sea Systems Command): Are
you only concerned with the shock impact type
environment what about the vibration environ-
ment.

Mr. Venetos: We are not just concerned with
the shock environment.

Mr. Paladino: But this recorder can only give
you the impact type enviornment and there is
no way that you can tell what your frequency
and amplitude are in the various modes of
transportation.

Mr. Venetos: That's true but there is a big
lack of information on shock. There is quite
a bit of published data on vibration but almost
nothing on shock.

Mr. Paladino: We had a very unfortunate thing
happen in the Navy many years ago on the USS
Forrestal where the J4 jet engines were stored,
basic ship vibration brinelled the bearings so
when you put the engines into the plane and ran
them they tore themselves apart and I am sure
you can find the same sort of thing if you are
shipping. You will not always ship by land
what about the sea environments?

Mr. Venetos: We are not just concerned with
shock we are concerned with vibration and in
a roundabout way, even with this shock recorder,
you are determining that you either did or
didn't see a lot of high level vibration. For
instance if we ran into a situation where we had
a continuous vibration of relatively high value
this recorder would have run out and we would
have showed full counts in all of the bins.

Mr. Paladino: You are looking at the "g" levels.
What about vibration frequency and amplitude?
If you have a coincidence you get an amplifica-
tion in the equipment you are shipping or if
you have a high q resonance, you don't need a
high amplitude from transportation you can tear
it apart.

Mr. Venetos: I realize that.

Mr. Paladino: We spent ten years in the navy
trying to develop an EVR which is an environ-
mental vibration recorder. We couldn't make
it work because ship vibration tore it apart.

Mr. Venetos: We have had that same situation.
We had a large electron tube which was mounted
on metal springs and the vibration environment
in that situation was most important, because
there was no damping in the spring system and
we had a transmissibility of about 40 to one;
but again there certainly is a need for a good
vibration instrument, I think we have a good
shock instrument.

ADVANCES IN SHIPPING DAMAGE PREVENTION

Henry Caruso and William Silver II
Westinghouse Electric Corporation,
Product Qualification Laboratory;
Baltimore, Maryland

For several years, Westinghouse Electric Corporation has been study-
ing the transportation of loose cargo in tractor-trailers to determine
how products are damaged in shipment and how they can be better de-
signed to resist this damage. During the road test phase of these
studies, the following factors were investigated: suspension system
types, degree of load, rear wheel position, road types, and different
drivers. Analysis of the road data led to two major conclusions. First,
certain suspension systems not only prevent shipment damage, but also
reduce trailer fatigue and tire wear and improve road handling. Second,
a shipping test specification was developed to evaluate package and pro-
duct designs under simulated road conditions. In a typical loose cargo
shipping test, a random vibration input produces a "ride" equivalent to
the worst conditions measured during the road studies. Laboratory
tests are also used to evaluate package designs and the behavior of
reasonable loading configurations. These tests evaluate product, pack-
age, and trailer designs, provide specific recommendations to increase
product survivability and improve package and trailer designs, and
settle claims disputes that result when shipments are damaged.

INTRODUCTION

For several years, Westinghouse Electric
Corporation has been studying the transporta-
tion of loose cargo in tractor-trailers to deter-
mine how products are damaged in shipment
and how they can be better designed to resist
this damage. This work has been the joint
effort of Westinghouse Corporate Traffic De-
partment in Pittsburgh, its Defense and Elec-
tronic Systems Center's Product Qualification
Laboratory, and Jones Motor of Spring City,
Pennsylvania.

ASSUMPTIONS

These were the major assumptions used as
a base for these studies:

1. A very large probability exists that loose
cargo will be transported in a lightly-loaded
trailer.

2. An empty trailer is nearly the same as
a lightly-loaded trailer with the exception that
responsive accelerations generated by bouncing
objects on the trailer bed are eliminated from
the measurement.

3. The light load condition is somewhat
more severe than a heavy load condition, as
will be documented in this paper. (Note: this
is not necessarily true in all cases and further
work is being done to clarify this point.)

4. A test which inputs force to a package
or a set of packages in a manner as close as
possible to the inputs from an empty trailer
bed would constitute a very valid performance
standard.

5. These results would not apply directly
to heavy cargo which was rigidly attached to
the trailer bed.

STUDY PARAMETERS

A number of dual-axle tractor-trailer types were instrumented with accelerometers at several points along the trailer loading bed and on the rear axles. During the road test phase of these studies, each factor that might contribute to shipping damage on long-haul runs was investigated.

ROAD TYPES. Ride characteristics were measured over various road types, including city streets, unimproved back roads, interstate highways, and special test tracks. It was found that high-speed driving over interstate highways produces the worst ride in the trailer. Therefore, all of the data presented in this paper is developed from the worst-case condition.

A continuous three-minute segment of high-speed beltway ride was chosen for continuous analysis. This data was analyzed with a power spectrum density analysis program. A 0.2-Hz bandwidth line resolution was used and the data analyzed from 0.2 to 50 Hz. Sample lengths permitted an analysis of 64 degrees of freedom, thereby establishing a reasonable confidence in the data.

SUSPENSION SYSTEMS. The various types of suspension systems evaluated were: conventional steel leaf springs, air bags, damped coil springs, and rubber isolators. Good correlation was found among data records for similar suspension systems on different trailers.

Figures 1 and 2 compare the power density spectra derived for each of the suspension system types. Figure 1 demonstrates that little energy of significance is present above 50 Hz. Also, these figures show that each of the suspensions have a unique spectrum shape at the first frequency peak. The single steel leaf suspension is clearly inferior to the other types as it permits much more trailer bed vibration at the 4 to 5 Hz resonanace. The air bag peak is very sharp and considerably lower in frequency than the other two systems. The damped coil spring system is quite gentle at the first resonant peak.

All of the suspension types have very similar spectrum shapes for the second resonant peak at about 13 Hz. This mode is dominated by the tire characteristics. It is interesting to note that the air bag system absorbs more of the energy than the other systems. The dashed peaks at the top of figure 1 show the levels that occur on the trailer axle. The spectra for the rear axle data are dominated by these peaks. It is readily apparent that the suspension systems are significantly attenuating this energy before it reaches the trailer bed.

DEGREE OF LOAD. Trailer rides were evaluated with varying degrees of load, from empty (lightly-loaded) to half and full loads. These evaluations demonstrated that the worst ride occurs over the rear axle of a lightly-loaded trailer, as shown in figures 3 and 4. Figures 5 and 6 show the effects of varying degrees of load upon ride quality for conventional steel leaf spring systems as compared with a rubber isolator suspension system.

REAR WHEEL POSITION. Measurements were made with the rear wheels in their forward, rear, and center positions. This information is currently under analysis.

DIFFERENT DRIVERS. The man in the tractor cab was found to have very little effect on the ride quality in the trailer. Road type, speed, suspension system, and degree of load are the determining factors for ride quality.

RESULTS

First, it was found that certain suspension systems will improve trailer ride quality and thereby reduce the likelihood of shipment damage. (As side benefits, trailer and tire life would be extended, road handling improved, and driver fatigue reduced due to improved rear wheel tracking.)

Nearly all of the energy of the trailer bed vibrations concentrates in two fundamental frequency modes. The lower of the two frequency peaks will be influenced by loading on the trailer as long as the load stays in contact with the trailer bed. The energy notch that occurs between 8 and 9 Hz will probably exist for all similar trailers at all load conditions. This information should be of value to package designers since it shows a region where package and product resonances would be more lightly excited than at immediately higher or lower frequencies. The frequency regions above 20 Hz are also quite suitable for fitting package and product resonances.

Second, a random vibration shipping test specification was developed for realistic laboratory simulation of trailer ride quality. This vibration profile, shown in figure 7, envelopes the worst-case condition found in this study: the ride over the rear axle of a lightly-loaded
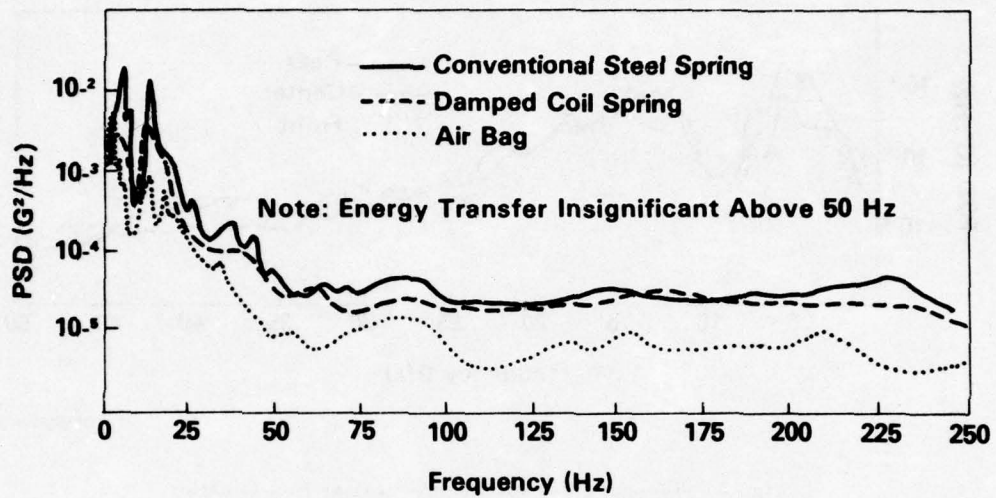
Fig. 1 - Comparison of Suspension Types

Fig. 2 - Comparison of Suspension Types

43

● **Conventional Steel Leaf Springs**

● **Unloaded Trailer**
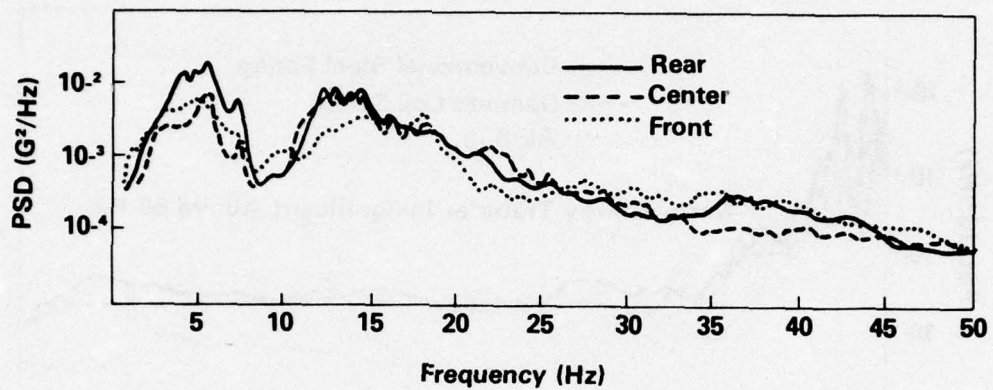
75-0959-VA-2

Fig. 3 - Response Variations vs. Trailer Bed Location

● **Conventional Steel Leaf Springs**

● **Measured over Rear Wheels**
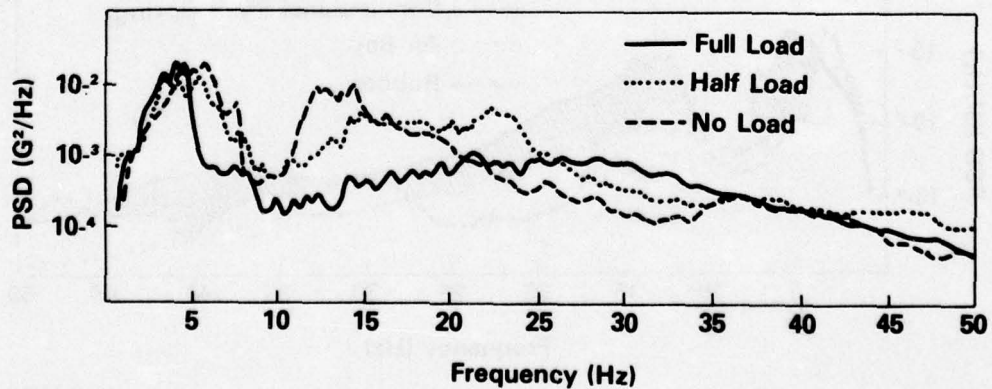
75-0959-VA-3

Fig. 4 - Response Variations vs. Load

44

● **Steel Leaf vs Rubber Isolator**

● **Measured over Rear Wheels**
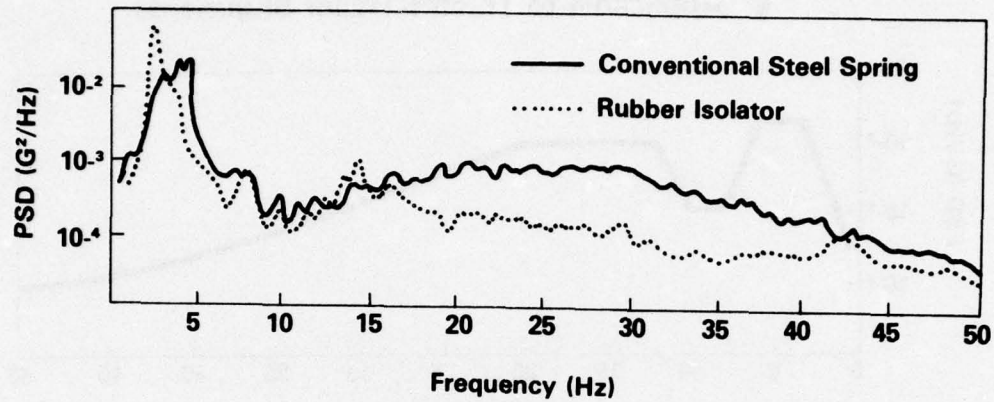
75-0959-VA-4

Fig. 5 - Comparison of Fully-Loaded Trailers

● **Steel Leaf vs Rubber Isolator**

● **Measured over Rear Wheels**
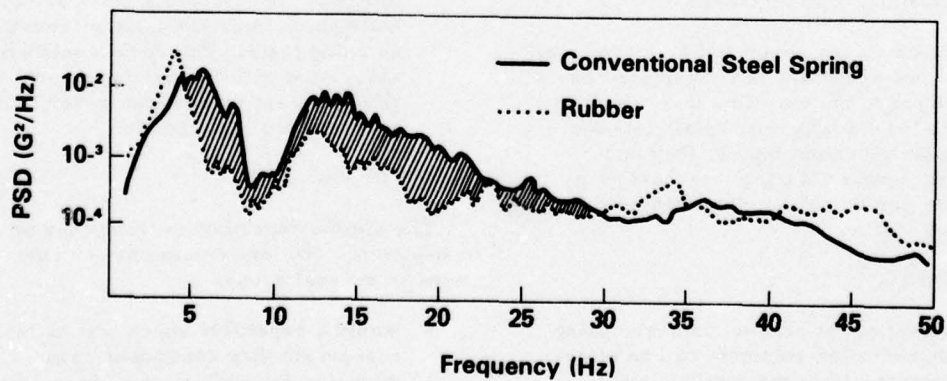
75-0959-VA-5

Fig. 6 - Comparison of Unloaded (Lightly-Loaded) Trailers

45

- **Random Vibration**
- **Simulates Long-Haul Ride**
- **Applicable to Tractor-Trailer Shipments**
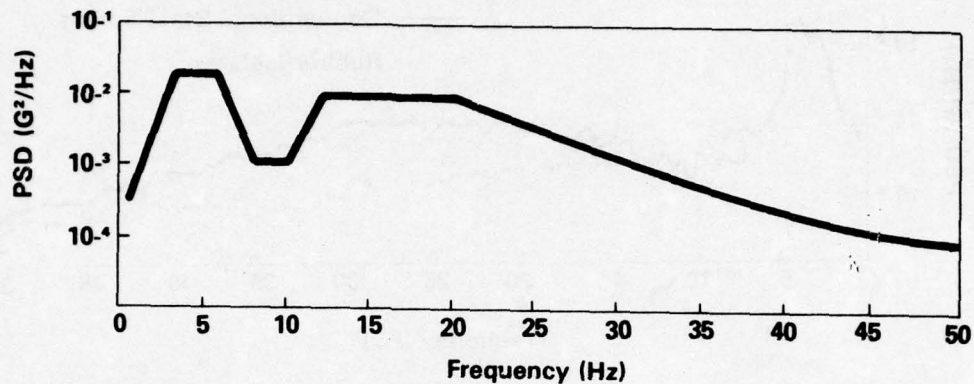
75-0959-VA-6

Fig. 7 - Recommended Transportation Test Spectrum

trailer with conventional steel leaf springs, travelling at high speed over interstate highways. This test is currently in use at Westinghouse' Product Qualification Laboratory.

In a typical loose cargo shipping test, the product is placed on a simulated trailer bed mounted to a vibration exciter. Although barriers are used to limit lateral travel, the product is in no way tied down to the vibration fixture. Laboratory tests can also be used to evaluate package designs and the behavior of reasonable loading configurations.

Acceleration pulses generated by large holes or bumps at low speed are not considered as part of the input to the vibration test. While these shocks individually may be slightly more severe than the vibration inputs, they occur relatively infrequently during long-haul shipments. They can be better simulated with a package drop test.

CONCLUSIONS

- The potential for product damage during long-haul trailer shipment can be effectively evaluated in the test laboratory using the random vibration test profile presented in this paper.

- An ideal comprehensive shipping test procedure would be comprised of:

    1) a random vibration test

    2) a package drop test

    3) a humping shock test (for rail transportation, not discussed here).

- Descriptions of trailer ride quality in terms of peak G-levels alone are of little value in establishing effective shipping tests. Unless G-levels are associated with frequency content, the shipping environment can never be fully understood or appreciated.

WORK IN PROGRESS

The efforts described in this paper are only a beginning. We are continuing our investigations in several areas:

- Would a repetitive shock test be more reasonable than continuous random vibration for evaluating shipment damage susceptibility?

46

- What is the optimum test duration for continuous random vibration? In the case of repetitive shocks, how many pulses would be required?

- At what point does a test's sophistication compromise its effectiveness as an industry-wide standard? Will test laboratories need new equipment or can these tests be specified so that they will be compatible with the majority of existing laboratory operations? In short, when does a realistic test cease to be a reasonable test?

- Is short-haul shipment in single-axle trailers and trucks significantly different from long-haul shipment in dual-axle trailers?

Discussion

Mr. Kilroy (Naval Ordnance Station): Frequently we receive a shipment where the tires in the trailer have almost been deflated so that the whole shipment can pass underneath a bridge. In fact some of the states are considering a law limiting the pressure in tires. Would you comment on that situation?

Mr. Caruso: The tests that we ran were with the trailer's tires inflated at nominal pressures, wo we haven't really evaluated the effects of tire pressure. The second mode was dominated by tire characteristics and it could be changed with a deflated condition but this is something that we would have to study in a little more detail.

COHERENCE METHODS USED TO DEFINE TRANSMISSION PATHS

IN AIRBORNE ANTENNA VIBRATION

Jerome Pearson and Roger E. Thaller
Air Force Flight Dynamics Laboratory
Wright-Patterson AFB, Ohio 45433

Conditional coherence functions are used in a practical mechanical vibration problem to determine which of several possible inputs are the major causes of vibration of an airborne antenna. Pairwise, multiple, and multiple conditional coherence spectra are derived from flight vibration data. The vibratory inputs causing several important antenna responses are identified despite correlations between inputs. These inputs offer the highest potential for reducing the antenna vibration by isolation or decoupling. The results also provide a measure of the vibration reduction which can be achieved by eliminating these inputs.

INTRODUCTION

In solving vibration problems it is frequently desirable to know which of several excitations is causing a particular response, in order to proceed efficiently with isolation or decoupling. The determination of the power spectral densities of the output and the possible inputs can indicate possible transmission paths by revealing common frequencies. These spectra are ambiguous, however, when the output and several inputs all show peaks at the same frequency.

Theoretically a variety of spectra called coherence functions can overcome this ambiguity and can be used to determine the proportion of the output vibration caused by a particular input [1]. Practically, however, the usefulness of this process is degraded by noise in the measured signals, inaccuracy in digitizing, and by any correlations among the various inputs. In recent years the use of high-accuracy analog-to-digital conversions and low-noise recording systems has reduced these first two problems [2] and the use of coherence functions to evaluate the correlations among inputs can eliminate the third problem [3]. These techniques can now be applied to solve practical vibration problems [4-6].

This paper describes a practical application of coherence functions to determine the vibration transmission paths causing the low-frequency vibration of an airborne antenna. This particular antenna has been used by the Air Force Avionics Laboratory to investigate communications between airborne super-high-frequency (SHF) terminals and synchronous satellites. At these frequencies, near 8 GHz, Doppler effects caused by the antenna "boresight" vibration (in the pointing direction) can shift the signal frequency by several kilohertz. The angular vibrations of the antenna in elevation and azimuth cause pointing errors that reduce signal strength. These three vibration responses can severely degrade airborne communications and are limiting factors on system performance. The antenna pedestal linear and angular motions and the aerodynamic noise inside the antenna fairing were considered to be possible sources of the antenna vibration. To measure the antenna vibration and to determine the vibration transmission paths, the Air Force Flight Dynamics Laboratory flight tested the Avionics Laboratory antenna in a transport aircraft. Coherence functions were used to determine the most important excitations so that isolation or decoupling could be applied most efficiently to reduce antenna vibration. The coherence analysis was performed on a part of the data from this flight test program. The program provided data on the antenna vibration environment and the Doppler effects; some of these data have been reported previously [7].

FLIGHT TEST PROGRAM

To measure the effects of vibration on the SHF aircraft-to-satellite communication, a flight test program was conducted. The SHF antenna, shown in Figure 1, was located in a twenty-foot long fiberglass fairing atop a C-135B cargo aircraft. The antenna was a 33" diameter parabolic dish mounted on a forked
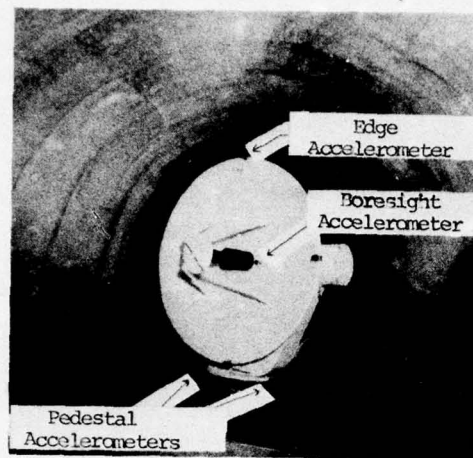
Fig. 1 - SHF antenna and accelerometers mounted on aircraft.

pedestal and driven in elevation and azimuth by servomotors to point toward the satellite. Four crystal accelerometers were attached to the antenna edge to derive the angular accelerations in elevation and azimuth. Another accelerometer was positioned near the axis of the antenna to measure the antenna boresight acceleration, in the direction of the satellite.

The antenna pedestal was attached to the upper skin of the aircraft with a reinforcing plate. The pedestal was instrumented with five accelerometers — a triaxial group to measure vertical, lateral, and longitudinal accelerations, and two others to derive the angular accelerations in pitch and yaw. The antenna fairing was very thin and had a small vent hole to equalize the air pressure; consequently there were high noise levels within the fairing. This acoustic environment was expected to excite the large area of the antenna dish, and therefore a microphone was placed in the forward end of the fairing to measure this environment.

The antenna and pedestal were considered to constitute a linear mechanical system with six inputs — one noise input and five pedestal accelerations (vertical, lateral, longitudinal, pitch, and roll), and three outputs — the antenna boresight, elevation, and azimuth accelerations. A portion of the flight test program was devoted to determining which of these six inputs produced significant antenna vibration responses. To do this, a time history of 570 seconds was recorded during level flight at 33,000 feet altitude, with the antenna facing aft and elevated 20°. The recording system had a signal-to-noise ratio of 42 dB. Automatic gain-changing amplifiers were used to maintain the signals as close as possible to full scale.

DATA ANALYSIS

The spectral analysis of the test data was performed according to the scheme shown in Figure 2. Each of the linear accelerations was first converted to digital form, and then the angular accelerations were computed digitally from pairs of linear accelerations. Using the Fast Fourier Transform, auto power spectral densities and cross power spectral densities were then computed from 2 to 60 Hz. For each normalized spectral density the resolution was 0.783 Hz and the record duration was 163.4 seconds. Fortran IV software was then used to sort these values by frequency and by sensor to form the spectral matrices shown in the figure. These spectral matrices were the inputs for the calculation of a variety of pairwise and multiple coherences, using the program BMD04T [8].

ANALOG TIME HISTORIES
11 Linear Accelerations,
1 Sound Pressure

↓

ANTI-ALIASING FILTERS,
A/D CONVERSION,
COMPUTATION

↓

DIGITAL TIME HISTORIES
4 Linear and 4 Angular
Accelerations,
1 Sound Pressure

↓

FAST FOURIER ANALYSIS

↓

AUTO AND CROSS POWER
SPECTRAL DENSITIES

↓

SOFTWARE

↓

SPECTRAL MATRIX [A]
FOR EACH FREQUENCY:

a_{ij} = auto PSD, $i = j$

= cross PSD, $i \neq j$
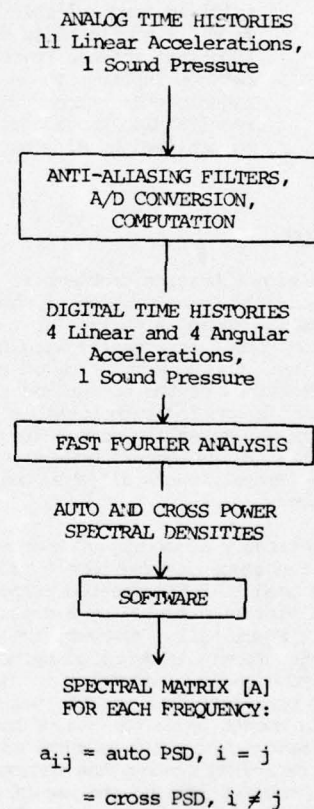
Fig. 2 - Spectral analysis.

The coherence is a spectrum which varies between zero and one. The simple pairwise coherence between a single input and a single output is the square of the cross power spectral density divided by the product of the

50

two auto power spectral densities. Multiple coherences are more complicated functions of these spectral densities which relate a single output to several inputs.

If a system is linear and all inputs are independent, the value of the pairwise coherence between the output and an input is the proportion of the output power that comes from that input. For this system the coherences between the output and all the inputs sum to one. If the inputs are themselves coherent, the simple pairwise coherences do not sum to one, and conditional coherences must be used.

Spectral Matrix [A]
for each frequency:

$$a_{ij} = \text{auto PSD, } i = j$$

$$= \text{cross PSD, } i \neq j$$


```
            BMDO4T
       Invert, drop values
       involving specified
       channels, re-invert


          Conditional
       Spectral Matrices


    BMDO4T              BMDO4T
    Compute             Compute
    Coherences          Coherences


    Conditional         Pairwise and
    Pairwise and        Multiple Coherences
    Multiple
    Coherences
```
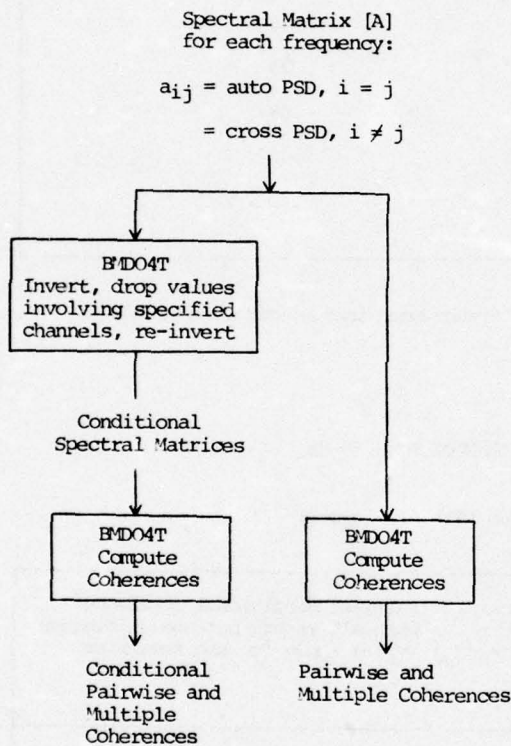
Fig. 3 - Coherence analysis.

The coherence calculations were performed according to the procedure shown in Figure 3. This process allows the calculation of coherences which are conditioned on selected inputs. Conditioning on selected inputs completely eliminates the effect of these inputs. In this paper, the word eliminated is used for the phrase "conditioned on." Prior to calculating the coherences, a separate execution of BMDO4T forms the conditional spectral matrix

by inverting the original matrix, eliminating the values involving specified sensors, and then inverting the resulting matrix. The coherences, called conditional coherences, are then calculated using BMDO4T. The results then show the proportion of the output caused by the specific input, with the effects of all other inputs eliminated. These various types of coherences are discussed more completely by Goodman [9].

This analysis was performed on data from one flight condition. If data from other flight conditions were available, a matrix of coherence functions could be developed and analyzed for distribution and variance, using more sophisticated mathematical techniques [10, 11].

RESULTS

The acceleration spectral densities of the antenna linear vibration in the boresight direction and the angular vibrations in elevation and azimuth were examined for peaks which could degrade the communication. These peak responses were evaluated by the criteria of Reference 7 and several were selected for analysis. Two modes each in elevation, azimuth, and boresight were analyzed.

The elevation response at 7.05 Hz was examined by the coherence method and the results are shown in Table 1. The first entry shows that the multiple coherence of this output with all six chosen inputs is very nearly one (0.93). This indicates that this antenna response is very well accounted for by the chosen inputs and that there are no significant inputs which have been neglected. In order to evaluate the relative contribution of each input, the inputs were eliminated one at a time, and the multiple coherence of the output with the remaining five inputs is shown in the first two columns of the table. The results show that elimination of pedestal roll input results in the lowest coherence. Therefore the pedestal roll is the most important input. The last column of the table shows the pairwise conditional coherences of the output with a single remaining input after all other inputs were eliminated. Row by row comparison of the columns shows a single row (pedestal roll) for which the value in the third column is greater than the value in the second column. This comparison shows that elimination of the pedestal roll produces a smaller coherence than the simultaneous elimination of all remaining inputs. The result of this coherence analysis of the elevation response at 7.05 Hz is that the effect of pedestal roll is significantly more important than the effect of the other inputs.

The elevation response peak at 9.40 Hz is analyzed in Table 2. The multiple coherence of

TABLE 1. ANTENNA ELEVATION MODE AT 7.05 Hz

Multiple Coherence of this Mode with All Inputs: .93

Input	Multiple conditional coherence with all inputs but one (value shown for the eliminated input)	Pairwise conditional coherence with all inputs but one eliminated (value shown for the remaining input)
VERTICAL	.86	.00
LATERAL	.90	.06
LONGITUDINAL	.81	.25
PITCH	.88	.08
ROLL	.50	.70
NOISE	.92	.00

RESULT: Elimination of ROLL reduces the coherence more than elimination of all five other inputs.

TABLE 2. ANTENNA ELEVATION MODE AT 9.40 Hz

Multiple Coherence of this Mode with All Inputs: .97

Input	Multiple conditional coherence with all inputs but one (value shown for the eliminated input)	Pairwise conditional coherence with all inputs but one eliminated (value shown for the remaining input)
VERTICAL	.85	.01
LATERAL	.93	.05
LONGITUDINAL	.19	.59
PITCH	.97	.01
ROLL	.96	.03
NOISE	.95	.01

RESULTS: Elimination of LONGITUDINAL reduces the coherence more than elimination of all five other inputs.

TABLE 3.   ANTENNA AZIMUTH MODE AT 7.05 Hz

Multiple Coherence of This Mode with All Inputs: .68

Input	Multiple conditional coherence with all inputs but one (value shown for the eliminated input)	Pairwise conditional coherence with all inputs but one eliminated (value shown for the remaining input)
VERTICAL	.63	.03
LATERAL	.60	.05
LONGITUDINAL	.38	.02
PITCH	.63	.01
ROLL	.27	.28
NOISE	.63	.01

RESULTS: Elimination of ROLL reduces the coherence more than elimination of all five other inputs.

TABLE 4.   ANTENNA AZIMUTH MODE AT 9.40 Hz

Multiple Coherence of This Mode with All Inputs: .51

Input	Multiple conditional coherence with all inputs but one (value shown for the eliminated input)	Pairwise conditional coherence with all inputs but one eliminated (value shown for the remaining input)
VERTICAL	.18	.00
LATERAL	.35	.00
LONGITUDINAL	.02	.05
PITCH	.51	.00
ROLL	.43	.00
NOISE	.33	.01

RESULTS: Elimination of LONGITUDINAL reduces the coherence more than elimination of all five other inputs.

TABLE 5. ANTENNA BORESIGHT MODE AT 9.40 Hz

Multiple Coherence of this Mode with All Inputs: .99

Input	Multiple conditional coherence with all inputs but one (value shown for the eliminated input)	Pairwise conditional coherence with all inputs but one eliminated (value shown for the remaining input)
VERTICAL	.97	.02
LATERAL	.99	.02
LONGITUDINAL	.50	.91
PITCH	.99	.01
ROLL	.99	.14
NOISE	.95	.02

RESULTS: Elimination of LONGITUDINAL reduces the coherence more than elimination of all five other inputs.

TABLE 6. ANTENNA BORESIGHT MODE AT 16.45 Hz

Multiple Coherence of this Mode with All Inputs: .98

Input	Multiple conditional coherence with all inputs but one (value shown for the eliminated input)	Pairwise conditional coherence with all inputs but one eliminated (value shown for the remaining input)
VERTICAL	.96	.09
LATERAL	.97	.01
LONGITUDINAL	.21	.91
PITCH	.98	.08
ROLL	.98	.08
NOISE	.94	.02

RESULTS: Elimination of LONGITUDINAL reduces the coherence more than elimination of all five other inputs.

this response with all the chosen inputs is again nearly one (0.97) and it is thus explained well by the chosen inputs. The multiple coherences with one input eliminated are all very high unless the pedestal longitudinal input is eliminated. The importance of this input is confirmed by the pairwise coherences with all inputs but one eliminated. Only for the pedestal longitudinal input is the third column greater than the second. We can again conclude that one input is more important than all others combined. For this elevation mode, this input is the pedestal longitudinal vibration.

The antenna azimuth response at 7.05 Hz is analyzed in Table 3. This response shows a multiple coherence of only 0.68 with all the chosen inputs. This means that either an important input has not been considered, or more likely that there is substantial uncorrelated random noise in the signals for this mode. If the signal-to-noise ratios (S/N) of two signals are both 40 dB, the theoretical maximum value of measured pairwise coherence is .98. If the greatest responses are much higher amplitude than secondary responses, the S/N for these secondary responses may be reduced to 20 dB or even 10 dB. In these instances, the highest coherences that can be obtained are 0.83 and 0.58, respectively [9]. The possibility of neglecting an important input is less likely in this case, because the only input not considered was pedestal yaw. The pedestal was mounted on a reinforced horizontal plate, and no significant yaw motion was expected.

The multiple coherences of this mode, with one input eliminated, point to roll as the important input. This is again confirmed by the pairwise coherences with all but one input eliminated. The most important input for this response is evidently pedestal roll.

The antenna azimuth response at 9.40 Hz is analyzed in Table 4. This mode shows the lowest value of multiple coherence (0.51) of any of the important antenna responses. Noise on the signals was certainly a factor in this mode because the peak response was lower than any other mode. The multiple coherences with one input eliminated nevertheless show a pronounced effect of the pedestal longitudinal motion, and this is borne out by the pairwise conditional coherences with all inputs but one eliminated. Because of the relatively low multiple coherence this result is less firmly established than for the other modes.

The two antenna boresight responses at 9.40 and 16.45 Hz are analyzed in Tables 5 and 6 respectively. These modes show very high multiple coherences of .99 and .98, indicating that the responses are very well explained by the chosen inputs. In each case the multiple coherences with all inputs but one show the pedestal longitudinal vibration as the most

important input. Also in each case the pairwise conditional coherences with all inputs eliminated but one confirm this result.

The results of this coherence function analysis of the chief inputs causing the antenna responses are summarized in Table 7. The interesting result is that only two of the six inputs, roll and longitudinal vibration of the pedestal, produced significant vibration responses of the antenna. Furthermore, the modes which caused the greatest errors in pointing and Doppler shift, marked by asterisks, are all due to pedestal longitudinal vibration. The antenna fairing noise was not a major input to any of the antenna responses.

The antenna was pointing aft for all these measurements, which means that the pedestal longitudinal vibration was aligned with the antenna boresight. If the antenna were pointed laterally, the pedestal lateral vibrations could become the most important inputs. Since the antenna pedestal is a long fork with its axis at an angle to the boresight direction, a simple stiffening of the pedestal in this plane might satisfactorily reduce the antenna responses.

TABLE 7. ANTENNA RESPONSES AND VIBRATION SOURCES

MODE	CHIEF SOURCE
Elevation	
7.05 Hz	Pedestal Roll
*9.40 Hz	Pedestal Longitudinal
Azimuth	
7.05 Hz	Pedestal Roll
9.40 Hz	Pedestal Longitudinal
Boresight	
*9.40 Hz	Pedestal Longitudinal
*16.45 Hz	Pedestal Longitudinal

* Most significant responses.

CONCLUSIONS

The theory of the application of coherence functions to vibration studies is well established. They are well suited to random vibration problems and dynamic environment prediction in aerospace vehicles. The results of this study indicate that coherence functions may be used sucessfully in identifying the vibration transmission paths of multiple-input mechanical systems. The two requirements are relatively long, noise-free records and accurate digital conversions and spectral calculations. When these requirements are met the coherence functions can determine the vibration sources and also provide a measure of the confidence in the results. On the basis of these results and the results of References 4-6, coherences functions should be given wider application in random vibration testing.

REFERENCES

1. Julius S. Bendat and Allan G. Piersol, Random Data: Analysis and Measurement Procedures, pp. 136-169. Wiley-Interscience, New York, 1971.

2. Peter R. Roth, "How to Use The Spectrum and Coherence Function," Sound & Vibration, Vol. 5, No. 1, pp. 10-14, Jan 1971.

3. Loren D. Enochson, "Frequency Response Functions and Coherence Functions for Multiple Input Linear Systems," NASA Contractor Report CR-32, April 1964.

4. W. V. Bhat, "Use of Correlation Technique for Estimating In-Flight Noise Radiated by Wing-Mounted Jet Engines on a Fuselage," J. Sound & Vib., Vol. 17, No. 3, pp. 349-355, Mar 1971.

5. C. R. S. Talbot, "Coherence Function Effects on Phase Difference Determination," J. Sound & Vib., Vol. 39, No. 3, pp. 345-358, 8 April 1975.

6. L. L. Koss and R. J. Alfredson, "Identification of Transient Sound Sources on a Punch Press," J. Sound & Vib., Vol. 34, No. 1, pp. 11-33, 8 May 1974.

7. Jerome Pearson and Roger E. Thaller, "Vibration-Induced Doppler Effects on an Airborne SHF Communication System," Shock & Vibration Bulletin No. 45, Part 2, pp. 111-117, June 1975.

8. W. J. Dixon, Ed., BMD - Biomedical Computer Programs, pp. 569-581. University of California Press, Berkeley, 1974.

9. N. R. Goodman, "Measurement of Matrix Frequency Response Functions and Multiple Coherence Functions," Air Force Flight Dynamics Laboratory Technical Report AFFDL-TR-65-56, June 1965.

10. J. C. Lee, P. R. Krishnaiah, and T. C. Chang, "Approximations to the Distributions of the Determinants of Real and Complex Multivariate Beta Matrices," Air Force Aerospace Research Laboratories Technical Report, ARL TR 75-0168, June 1975.

11. P. R. Krishnaiah, J. C. Lee, and T. C. Chang, "Approximations to the Distributions of the Likelihood Ratio Statistics for Testing Certain Structures on the Covariance Matrices of Real Multivariate Normal Populations," Air Force Aerospace Research Laboratories Technical Report, ARL TR 75-0167, June 1975.

DEVELOPMENT OF COMPONENT RANDOM

VIBRATION REQUIREMENTS

CONSIDERING RESPONSE SPECTRA*

C. V. Stahle and H. R. Gongloff
General Electric - Space Division

and

W. B. Keegan
NASA-Goddard Space Flight Center

A method of determining component random vibration requirements
from measured spacecraft test data is presented which enables the
final specifications to be placed on a statistical basis. The statistical
analysis of measurements has become the accepted method of develop-
ing component vibration requirements although several methods are
currently in use. Current procedures lose their statistical significance
and usually employ arbitrary factors to assure the adequacy of the
components for the vibration environment. The purpose of this paper
is to present a method of developing requirements that retains its
statistical significance so that more meaningful requirements are
specified.

The Random Response Spectrum (RRS) of an ensemble of measure-
ments is used to determine the best method of analyzing PSD data. The
RRS is the RMS response of a single-degree-of-freedom oscillator to a
broadband stationary random excitation as a function of oscillator
resonant frequency and is considered to reflect the damaging effects of
the environment. Because it is not practical to develop RRS data for
the large amount of existing measurements, the objective of this study
is to develop a method of statistically analyzing PSD spectra such that
the RRS of the resulting distribution preserves the statistical charac-
teristics of the distribution of the RRS of the original ensemble of
measurements.

Four methods of sampling PSD spectra are evaluated by comparing the
RRS of the resulting PSD with the RRS of the ensemble at several
probability values. Measured spectra during spacecraft testing are
analyzed using sixth-octave frequencies to define frequency bands or
sampling frequencies. The PSD spectra are sampled using (1) the
maximum value in a band, (2) the average value in a band, (3) a re-

duced peak value in a band, and (4) the actual value at discrete frequencies. The sampled values were statistically analyzed and the RRS was computed. The comparison of the sampled RRS with the ensemble RRS at several probability values indicates that Discrete Frequency Sampling (DFS) is the best method. Spectrum smoothing is performed such that the average RRS ratio is within ten percent and the individual values are within 3 dB.

Several sources of significant conservatism in current methods are indicated. As much as a 4 dB margin can be introduced by the sampling method. Spectrum enveloping can add an additional 3 dB.

Using Discrete Frequency Sampling, component random vibration test requirements are developed for various zones within a spacecraft. The component requirements are developed for both random vibration and acoustic excitation.

INTRODUCTION

The purpose of this paper is to present the results of a study to develop an improved method for deriving random vibration specifications for spacecraft components. As continued budget pressures are exerted on space programs, the need for cost effective development methods has intensified. While emphasis in the past has been on maximizing spacecraft reliability, the current trend is to accept increased risk to achieve reduction in cost. All areas are being examined to determine ways in which costs can be reduced. The environmental test portion of spacecraft programs provides an area of potential cost reductions. While environmental testing results in only 5 to 15 percent of total spacecraft costs, it has been recognized that studies in this area are essential [1]. These environmental tests provide the final assurance of flightworthy designs and hardware and have been continually revised as new information has become available. The development methods have been successful although a large number of early failures have still been experienced [2]. To modify present environmental test methods, it is necessary that an orderly evaluation of procedures be implemented and that the risks associated with changes in current test methods be examined and quantified.

The statistical definition of the vibration environment is required to evaluate the cost effectiveness of component requirements. A number of studies in the area of cost effectiveness of environmental testing have been performed. One of the earliest studies was that of Stahle which examined the cost effectiveness of spacecraft vibration qualification testing [3]. More recently, a number of studies have been performed with much of the work being under the direction of NASA-GSFC. A cost effective protoflight concept has been initiated and has proven successful as predicted by the study of Boeckel and Timmins [4]. Studies of test level specification have been performed by Piersol, Young and others to evaluate the percentile of the environment that should be used such that overall program cost is minimized [5,6,7,8]. In these studies, it is necessary to represent the environment statistically.

Methods of deriving component specifications through the statistical analysis of measured data have been in use for some time although the statistical significance of the specifications has not been well understood. Initial work by Condos [9] and Barrett [10] used statistical methods for evaluating random vibration data. The statistical methods provide a systematic

treatment of the variations with time, location, and direction. Peak values in selected frequency bands have been used extensively in the processing of the data so that the resulting spectra are not directly related to the statistical characteristics of the environment. More recently, Keegan [11] used actual spectrum values for deriving specification levels which eliminates some of the conservatism introduced by using peak values. However, with any of the methods the final test spectrum is obtained by fitting a smoothed spectrum shape to the statistically derived spectrum resulting in subjective evaluation by the analyst. The statistical significance of the test requirement, as related to component vibration damage, is clouded by the method of sampling the spectra and the smoothing procedure.

The objective of this investigation is to develop a method of deriving component test requirements from an ensemble of random vibration spectra such that the statistical significance of the requirement is retained.

APPROACH

The approach used in this study to determine the best method of developing component random vibration requirements is shown in Fig. 1. Major emphasis is placed on establishing a method of analyzing the random vibration spectra so that requirements simulating the damage of the actual environment ultimately are obtained. To accomplish this, a new concept, the "Random Response Spectra" (RRS), is introduced to evaluate the damage of the
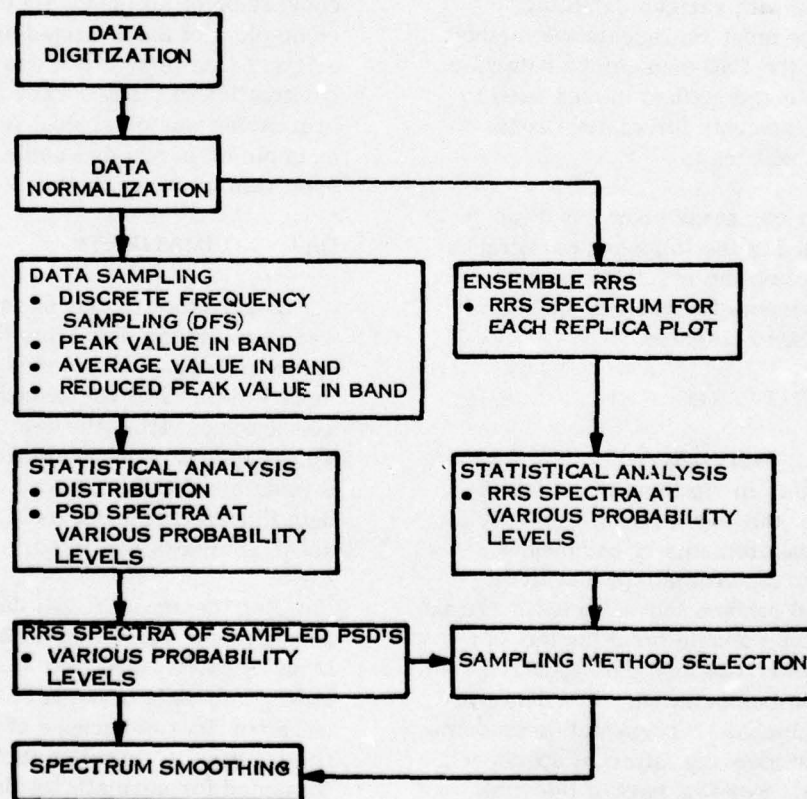
Fig. 1. Flow chart of method development

59

acceleration PSD spectra used to describe the environment. The RRS is similar to the Shock Response Spectrum (SRS) concept. The RRS is defined as the RMS response to a stationary random vibration environment of a single-degree-of-freedom oscillator as a function of the oscillator resonant frequency. The underlying assumption is that the damage to the parts within the component is directly related to the RMS acceleration of the single-degree-of-freedom oscillator and implies that a dominant resonant mode will cause a failure within the component. This assumption parallels that of peak g response in deriving shock requirements from SRS's. By determining the distribution of the RRS's for the original ensemble of random vibration spectra and comparing it to the distribution of the RRS's for the random vibration spectra derived by statistically analyzing the PSD data with various sampling methods, the most representative method of sampling the PSD data can be determined. The selected method is then used to derive requirements for various zones within the spacecraft.

The various steps shown in Fig. 1 are described in the following paragraphs of the paper and the resulting component test requirements for various spacecraft zones are then presented.

DATA DIGITIZATION

The test data analyzed in this study were available in the form of copies of X-Y plots of the acceleration PSD's obtained from measurements at component locations during system spacecraft acoustic and random vibration tests. To put this data into a usable form for the sampling and statistical analyses required some tedious data manipulation. The data were selected to include representative amounts of data from as many different spacecraft as possible. For this part of the study components mounted on structure internal to the spacecraft, i.e., a single spacecraft zone, were selected. As might be expect-

ed, from the variety of spacecraft and the time span of the tests, there was no uniformity to the size or quality of the copies of data plots for this study.

To put the data into a usable form the Applicon Graphic System (AGS/800) was employed to digitize the PSD spectra data. This system provided a semiautomatic technique for converting X-Y plots to a digital magnetic tape compatible with the H6060 computer. Using the Applicon Tabletizer system, the PSD amplitude and frequency were read from the plots by contact of a stylus with an electronic grid. The precalibrated grid system transferred the data point in digital form to a storage bank which later placed the data on magnetic tape for the sampling and statistical analyses. This approach, when developed, provided a rapid reduction and conversion of all data. By comparing Calcomp plots of the digitized spectra with the original data plots, on a one-to-one basis, verification of the accuracy of the data processing was obtained. A typical example of an original and a digitized spectrum is shown in Fig. 2.

DATA NORMALIZATION

Before the various sampling methods were applied the data from the various spacecraft were normalized to reference input levels. For the acoustic test data the average input from the control microphones was normalized to the reference acoustic levels, and for the random vibration test data the average input from the control accelerometers was used.

For the acoustic test data, PSD spectra were selected only if third-octave input test data were available. Furthermore, only data between 75 and 2000 Hz were considered because of test facility limitations. Correction factors were then computed for normalizing the data to the reference acoustic levels given in Table 1. The reference third-octave SPL was applied equally in the three third-octave
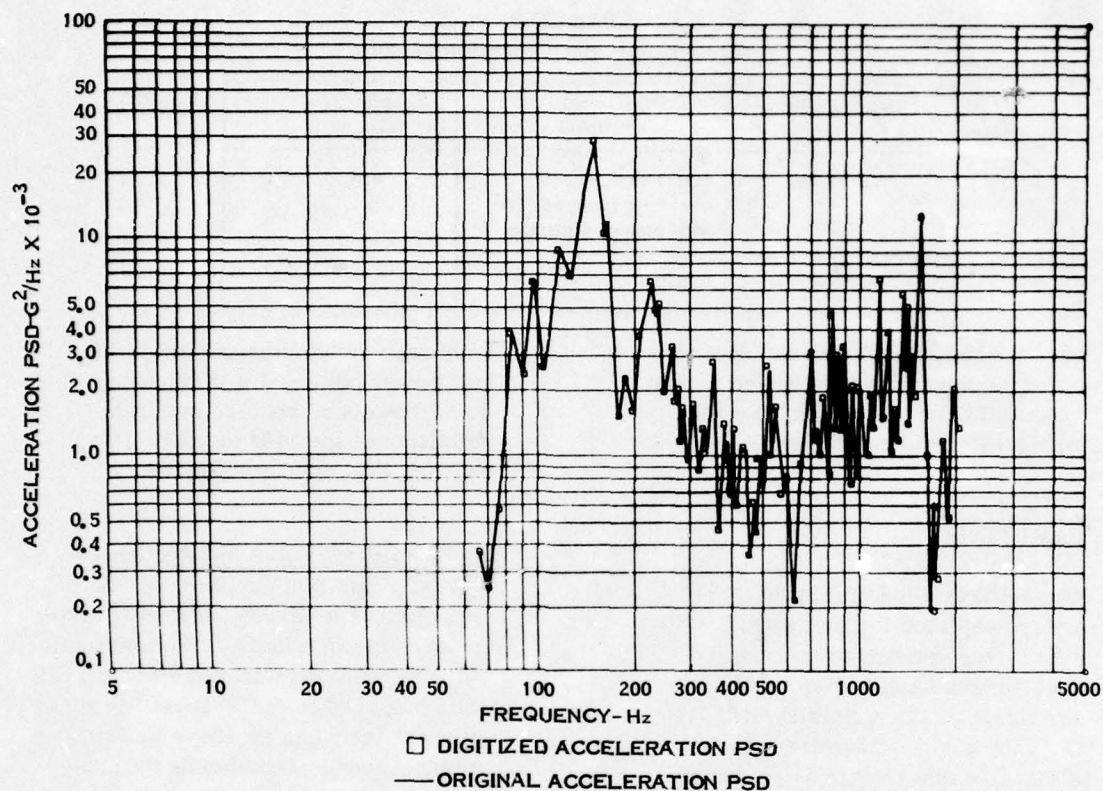
Fig. 2. Original and digitized acceleration PSD

TABLE 1
Reference Acoustic Levels

Octave Band Center Frequency (Hz)	Octave SPL (dB re 20 $\mu N/m^2$)	Reference Third-Octave SPL (dB re 20 $\mu N/m^2$)
63	125	120.2
125	130	125.2
250	133	128.2
500	134	129.2
1000	134	129.2
2000	131	126.2

bands of each octave band. The third-octave test data were then normalized to these third-octave reference acoustic levels. The correction factors were applied at the center frequency of each third-octave band. For other frequencies the correction factors were obtained by linear interpolation. Since one input to the sampling method was log PSD, the correction factor, C.F., was

$$C.F. = \Delta dB/10.$$

where ΔdB is the difference between the reference SPL and the test SPL.

For the random vibration test data, PSD spectra were selected primarily if data were defined between 75 and 2000 Hz, the frequency range used for the acoustic data analysis. Correction factors were computed for normalizing the data to the reference random vibration levels given in Table 2. The average spacecraft control spectrum was compared to the reference

61

TABLE 2
Reference Random Vibration Levels

Frequency Range (Hz)	PSD Level (G^2/Hz)	Acceleration (G_{RMS})
20 to 300	0.001 to 0.040 (Increasing from 20 Hz at a rate of 4 dB/Oct.)	8.5
300 to 2000	0.040	

spectrum. Since log PSD was an input to the sampling method, the correction factor was the logarithm of the ratio of the PSD values of the two spectra at a given frequency.

DATA SAMPLING

Four methods of sampling the PSD spectra were selected for evaluation. With each method, the spectra were sampled using sixth-octave frequencies to define frequency bands or discrete sampling frequencies. The sixth-octave frequencies were selected in that they provide resolution comparable to the resonant bandwidth of systems having typical dynamic magnification factors on the order of 10. The four sampling methods were applied to the replica-digitized data using linear interpolation between data points when required. The four methods were:

1. Discrete Frequency Sampling (DFS). The actual values at the sixth-octave frequencies were sampled in the same manner as the previous work of Keegan.

2. Peak Value in Frequency Bands. The maximum value in each frequency band was selected as in the previous work of Condos and Barrett.

3. Average Value in Frequency Bands. The average value in each band was determined by integrating the PSD curve over the frequency band. It was felt that this may be a good method in that it would average the PSD over a

frequency range comparable to the half power points of a resonance. It does, however, require accurate definition of the PSD to apply it to existing PSD spectrum curves.

4. Reduced Peak Value in Frequency Bands. This method provided a 3 dB reduction of a narrow band PSD maximum value in a band. The maximum value in the band was reduced by 3 dB and compared to the PSD values at two adjacent frequencies above and two adjacent frequencies below the frequency of the maximum value. If the reduced peak value exceeded any of these values, the reduced value was used. If not, the peak value was used. This method has been used at GE and considers resonance on resonance effects as discussed in Ref. [12].

In sampling the data with the various methods, a censor code was used to denote those points falling below the lower limit of the graph. For some data, the PSD curves had a large variation resulting in values below the limits of the graph. For these points, the actual values are not known but it is known that they are less than the limiting value of the spectrum plot. This is referred to as "left hand censored" data in statistical analysis and for these points a censor code was set to denote it. In none of the data were the PSD values permitted to exceed the upper limit of the graph so that only one type of censoring occurred in the data.

ENSEMBLE RANDOM RESPONSE SPECTRA

A Random Response Spectrum (RRS) was calculated for each PSD curve to provide a measure of the damage effects of the environment as a function of the component resonant frequency. The replica digitized PSD curve was multiplied by the square of the single-degree-of-freedom (SDF) transfer function to obtain the PSD of the SDF response. The response values were determined at each frequency at which the input PSD curve was digitized, the sixth-octave resonant frequency and six points near the SDF resonance. For these calculations a nominal damping ratio (C/C_c) of 0.05 was used. The six additional points for calculating the SDF response PSD were $f_n (1 \pm 0.5 \, C/C_c)$, $f_n (1 \pm C/C_c)$ and $f_n (1 \pm 3 \, C/C_c)$. It was felt that this additional frequency resolution was necessary in the vicinity of resonance to minimize the subsequent integration errors. The calculated response PSD was then integrated to determine the RMS response. The RMS response was calculated for a SDF resonant frequency equal to each sixth-octave frequency used to define the RRS curve. This was repeated for each PSD curve from the original ensemble to define a set of 50 RRS spectra for the subsequent statistical analysis.

STATISTICAL ANALYSIS OF SAMPLED DATA

The sampled data in each frequency band or at each frequency were statistically analyzed to determine the distribution that best fit the data and, subsequently, to determine the parameters of the distribution. A general purpose statistical program, STATPAC, was used for the analysis. STATPAC provides a complete package for simple summary statistics and graphical data displays, and for fitting distributions, regression curves and models to data. An important feature of STATPAC is its ability to analyze censored data. It uses the iterative method of maximum likelihood to fit distributions and relations to data. Eight standard distributions are provided for fitting the data.

The lognormal and Weibull distributions were evaluated to determine the distribution that provided the best fit to the data. From previous studies of the statistical distributions of vibration data, either of these two distributions has been found to be applicable. The adequacy of the fit to the data was evaluated by graphical review of the cumulative probability plots and the method of residuals. For the lognormal distribution, a standardized residual is the difference between the common logarithm of the observation and the corresponding estimate of the logarithmic mean divided by the corresponding estimate of the logarithmic standard deviation. Since the logarithmic observations are used, such residuals should look like a sample from the standard normal distribution. Similarly, for the Weibull distribution the standardized residuals will have an extreme value distribution. After fitting distributions to several sets of data, the resulting residuals can be pooled together to provide a better indication of the fit of the data to the distribution. Graphical inspections of the results are highly informative and indicate peculiarities in the data and the adequacy of the fit for subsequent engineering applications.

Typical cumulative probability plots of the data fitted to a lognormal and Weibull distribution are shown in Fig. 3. The curves are for the RRS at 500 Hz and should plot as straight lines with the probability scales used. The maximum likelihood fit of each distribution is shown along with the 95 percent confidence limits. From an overall viewpoint, it is evident that the lognormal distribution provides the best fit to the data since the Weibull distribution has large deviations from the estimated distribution for the smaller values.
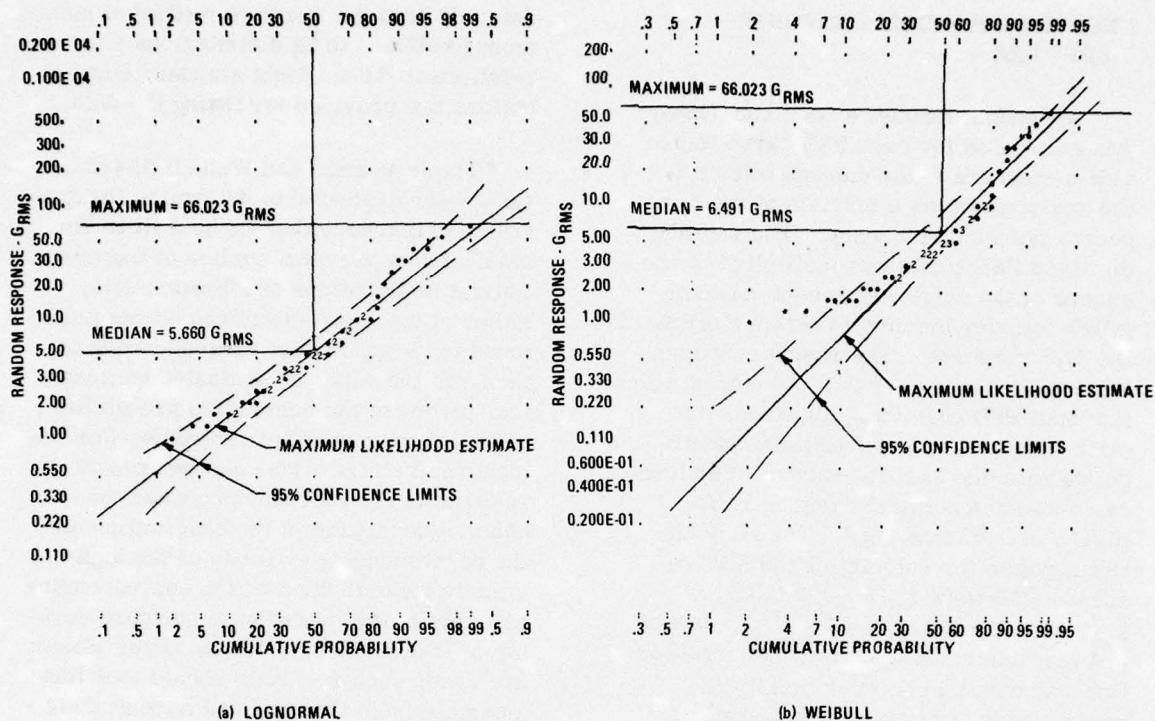
Fig. 3. Lognormal and Weibull cumulative probability plots (Zone 3 acoustics RRS at 500 Hz)

The cumulative probability plots of the residuals obtained by fitting lognormal and Weibull distributions to the data at ten frequencies from 250 Hz to 700 Hz are shown in Fig. 4 and provide a better indication of the distributions than the plots at specific frequencies. While approximately 50 data points are used for analysis at each frequency, 500 data points are used in the pooled residual plots. Again, on an overall basis, the lognormal distribution provides a better fit to the data. In the range between the 90th and 99th percentiles, which is of primary interest in specification development, the lognormal distribution provides a conservative estimate of the values while the Weibull distribution underestimates the values. The lognormal fit is good at values below the 95th percentile but tends to significantly overestimate the values at higher percentiles. These trends are typical for the PSD data obtained with the various sampling methods as well as the RRS data shown in Fig. 4.

On the basis of the statistical analysis of the PSD and RRS data the maximum likelihood estimate of the lognormal distribution was selected to represent the statistical characteristics of the environment. This provides a good fit to the data at all percentiles and provides an apparently conservative estimate of the environment at the higher percentiles. Some caution should be used, however, in using the results for the very high percentiles (e.g., the 99th percentile) in that the distribution becomes excessively conservative.

The lognormal parameters of the PSD spectra for each of the four sampling methods were determined. In each frequency band defined by the sixth-octave frequencies or at each sixth-octave frequency, the sampled data obtained for each method were statistically analyzed to determine the logarithmic mean and log-

64
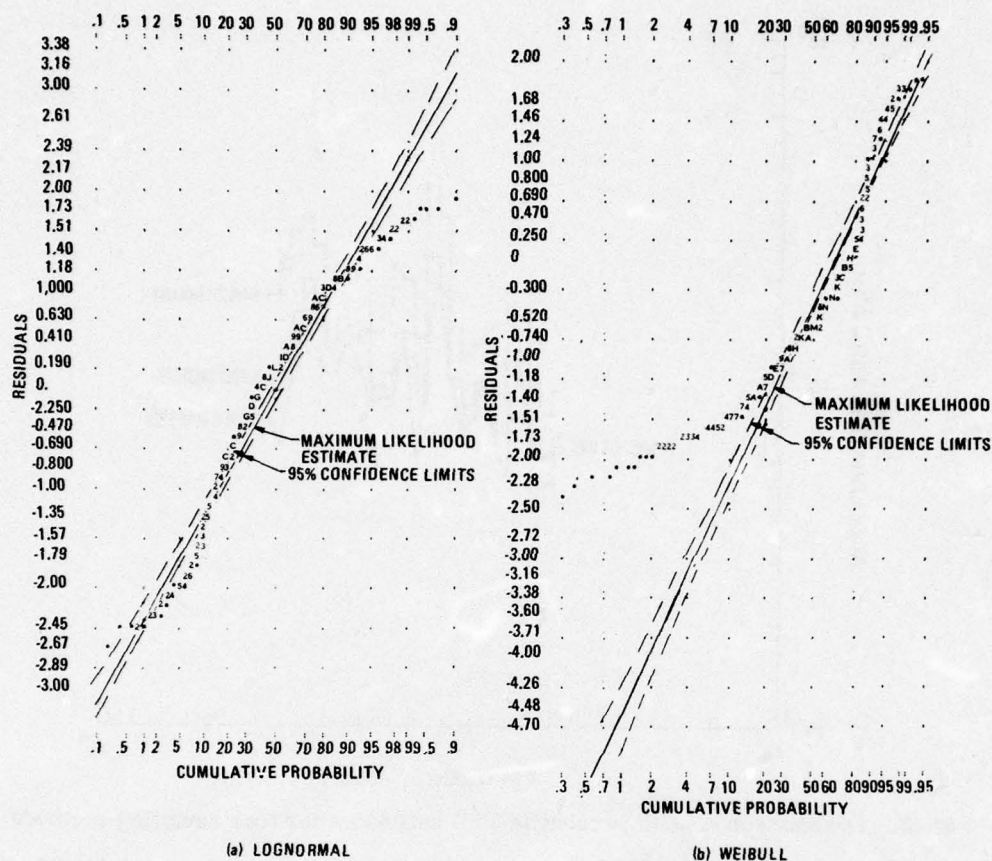
Fig. 4. Lognormal and Weibull cumulative probability plots (Zone 3 acoustics RRS residuals for 10 bands, 250 to 700 Hz)

arithmetic standard deviation of the maximum likelihood lognormal distribution. From this statistical analysis, PSD spectra at the 50, 90, 95 and 97.7 percentiles were determined for each sampling method. A comparison of the 95th percentile PSD spectra obtained with each of the four sampling methods is shown in Fig. 5. For the sampling methods using values in frequency bands, the spectrum is represented by a constant value in each band. For Discrete Frequency Sampling the values are treated as point estimates joined together by straight lines.

The lognormal parameters of the RRS determined from the ensemble of PSD

curves were determined in a similar manner. At each sixth-octave frequency, the values of the RRS obtained from the calculation of the SDF response to the replicated PSD curves were analyzed using STATPAC to determine the logarithmic mean and logarithmic standard deviation of the maximum likelihood lognormal distribution. From these parameters, the 50, 90, 95 and 97.7 percentiles of the RRS were determined.

RANDOM RESPONSE SPECTRA OF SAMPLED PSD'S

The Random Response Spectra (RRS) of the sampled PSD spectra at four probability levels were determined. For each

65
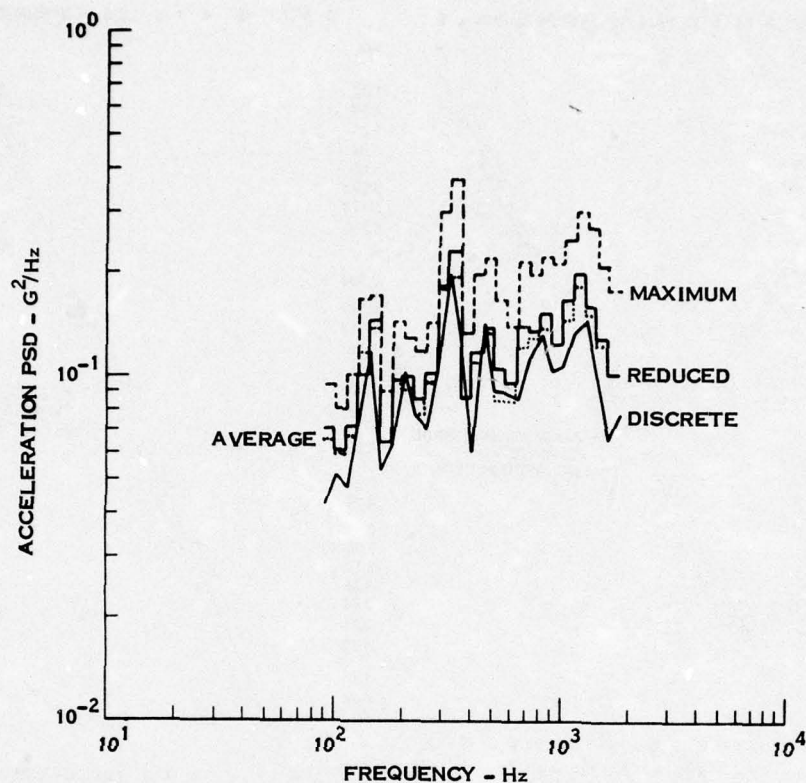
Fig. 5. Comparison of 95th percentile PSD estimates for four sampling methods

sampling method, PSD spectra having probabilities of 50, 90, 95 and 97.7 percent were determined. Using each PSD spectrum the resulting RRS was calculated in the same manner as the ensemble RRS. These RRS spectra are considered to provide a measure of the damage that would result if a selected sampling method were used to process the PSD data and develop the component test requirements. The final test requirement is determined by smoothing the spectra. The errors introduced by this smoothing operation are considered in the last step after the various sampling methods have been evaluated.

SAMPLING METHOD SELECTION

The best of the four sampling methods was selected by comparing the RRS obtained from the sampled PSD curves with the RRS obtained from the ensemble. The comparison was made at the 50, 90, 95 and 97.7 percentiles to evaluate the errors introduced by each sampling method as a function of probability values. The comparison was made using the ratio of the RRS values and the probability errors. The average values of the RRS ratio and the average values of the probability error are shown in Table 3 for each of the four sampling methods.

The average ratio of the sampled RRS to the ensemble RRS indicates that the Discrete Frequency Sampling (DFS) spectrum provides the best spectrum for high probabilities and that a large amount of conservatism is introduced by using the maximum values in the frequency bands. Examination of Table 3 indicates that Discrete Frequency Sampling provides an average RRS ratio that has less than ten percent error at the high percentiles. The average value, reduced peak

66

TABLE 3
Comparison of Sampling Methods

Per-centile	Average RRS Ratio				Average Probability Error			
	DFS	Average	Reduced Peak	Maximum	DFS	Average	Reduced Peak	Maximum
50	0.775	0.821	0.825	1.039	-0.0922	-0.0714	-0.0696	0.0126
90	0.931	1.019	1.048	1.295	-0.0123	0.00204	0.00665	0.0347
95	0.986	1.093	1.132	1.392	-0.00175	0.00667	0.00973	0.0234
97.7	1.045	1.178	1.227	1.501	0.00171	0.00586	0.00753	0.0132

value and maximum value sampling appear to rate in the order shown. The error in the average RRS ratio, considering equal weighing of the 90, 95 and 97.7 percentile values, is -1.3 percent for discrete frequency sampling, 9.7 percent for average value sampling, 13.6 percent for reduced peak sampling and 39.6 percent for maximum value sampling. A large amount of conservatism is indicated when maximum value sampling is used, e.g., the RRS response of a component to the 95th percentile spectrum is approximately 40 percent higher than it should be. Although the average RRS ratio was used for this evaluation, the values at the various frequencies compare quite well as indicated by the comparison of the sampled and ensemble RRS curves, Fig. 6. The variations in the PSD spectrum are smoothed significantly by the RRS, which responds to all PSD frequencies. The shape of the RRS curve obtained from the sampled PSD compares closely with that obtained from the ensemble. This was true for all four sampling methods.

The average probability error provides an indication of the statistical errors introduced by the sampling method. The statistical parameters of the ensemble RRS were used to determine the probability value of the sampled RRS at each sixth-octave frequency. Considering a component failure to result from a principal resonance which can occur at any frequency with equal probability (mutually

exclusive, equally likely event), the probability of a component failure can be obtained by averaging the values of the RRS at each frequency. These RRS values were then averaged and compared to the probability value of the sampled PSD. For example, the average probability value of the RRS obtained from the 95 percentile Discrete Frequency Sampling PSD was 94.825 percent. Again, large conservatism is evident for the maximum value sampling, e.g., the 95 percentile sampled spectrum has an average probability of 97.34 percent. The average probability errors show the same trend as indicated by the average RRS ratios.

The Discrete Frequency Sampling was selected for subsequent data processing based on the results of this comparison. The comparison of the four sampling methods shows it to introduce relatively small errors into the method of specification development, whereas relatively large errors are introduced by the other methods. An added benefit is the ease with which it can be applied to data processing.

SPECTRUM SMOOTHING

The errors and conservatism introduced by deriving smooth PSD test spectra from the statistically derived PSD spectra were evaluated. As in the sampling method evaluation, the RRS was used as the means of evaluating the smoothed
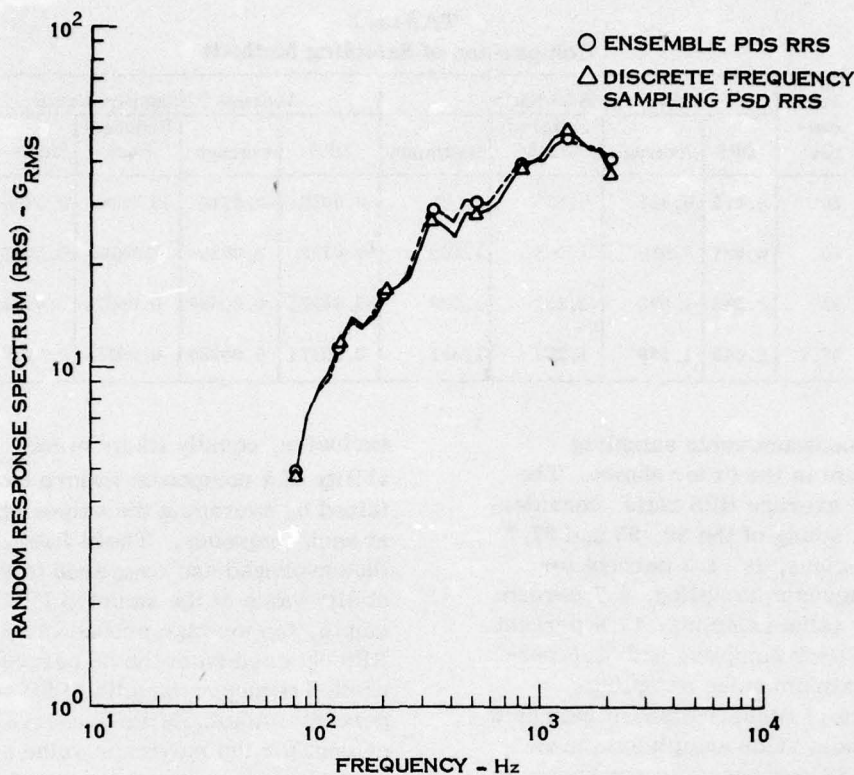
Fig. 6. Comparison of 95th percentile RRS spectra for discrete frequency
sampling and ensemble

spectra. The RRS obtained from the PSD spectra using Discrete Frequency Sampling was used as the reference with the goal of obtaining smoothed PSD spectra that would closely match it at all frequencies. Although the PSD spectra are characterized by many peaks and valleys, the RRS's are relatively smooth such that this goal was felt to be realistic. An approximately equal damage potential should result when a good match is achieved. The RRS ratio and the probability error were used to evaluate the effects of spectrum smoothing in a manner similar to that used in the sampling method evaluation.

The initial comparison evaluated the effects of enveloping the statistically derived PSD spectrum. The method of

smoothing often used in the past consists of enveloping the spectrum as shown in Fig. 7. Although this is known to be conservative, it is intended to account for frequency shifts in the spectrum and, because of the dependence of component response on the PSD at its resonant frequencies, has not been considered to be unduly conservative in the past. The 95th percentile spectrum was selected for enveloping and the smoothed spectrum was also used for comparisons at other probability values by using the average logarithmic standard deviation to vary the magnitude. The resulting average RRS ratio, probability error, RMS variations and ranges are shown in Table 4 for the four probability values selected for these comparisons. The average RRS ratio indicates that a margin of approximately 30 percent results from the enveloping pro-

68
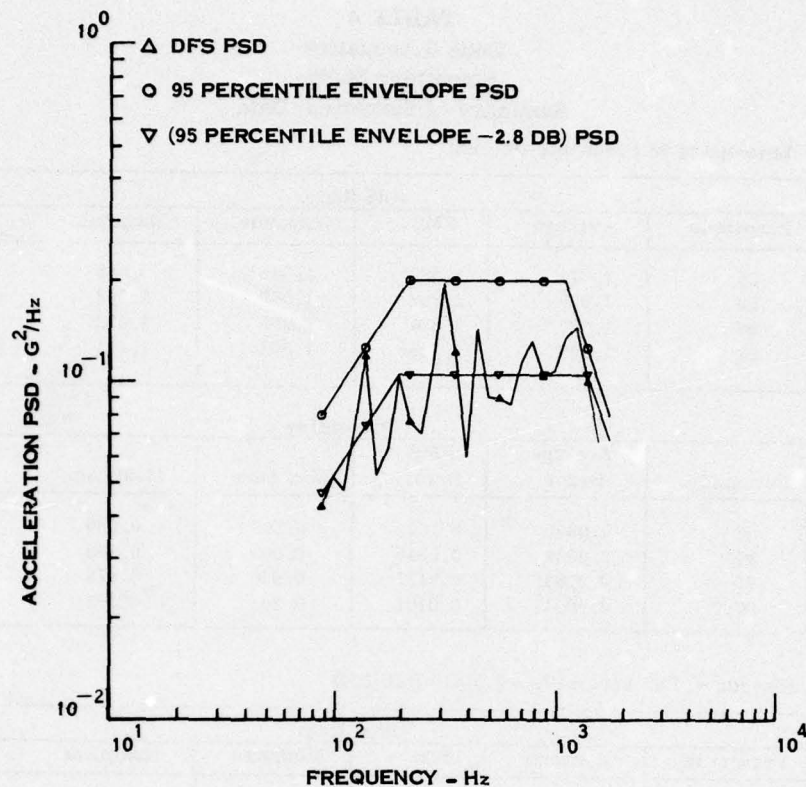
Fig. 7. Comparison of 95th percentile PSD spectra with smoothing

cess and that the 95th percentile envelope really reflects a 96.9 percentile value. A comparison of the RRS from the sampled PSD and the RRS from the smoothed spectrum, Fig. 8, shows a definite bias across the frequency range. Maximum and minimum margins show a variation from 8 to over 50 percent. Additional spectrum smoothing was subsequently investigated to determine methods of more closely matching the RRS of the sampled PSD.

By reducing the values of the smoothed spectrum by 2.8 dB, a good fit of the smoothed RRS spectrum to the sampled RRS spectrum was obtained. The smoothed PSD is compared with the envelope PSD and the sampled spectrum in Fig. 7 and the RRS ratio and probability errors are given in Table 4. As indicated by the

results, the average RMS response acceleration was within five percent of the desired values. A small negative probability error also occurred at all percentile values. The resulting RRS showed excellent agreement with the reference spectrum as shown in Fig. 8. The margin was reduced to a maximum of 14 percent and a minimum of -16 percent as indicated by the range of the RRS ratio for the 95th percentile. The range of probability values shows a relatively small variation with the 95th percentile spectrum varying from the 96th to the 93rd percentile. These spectra were considered to provide an accurate description of the environment and to eliminate excessive conservatism introduced by the smoothing process. These results served as a basis for developing criteria for subsequent spectrum smoothing.

69

TABLE 4
Zone 3 Acoustics
Smoothing Study
Summary of Statistical Data

Envelope of 95 Percentile DFS PSD

	RRS Ratio			
Percentile	Average	RMS	Minimum	Maximum
50	1.371	1.422	1.005	2.085
90	1.330	1.337	1.067	1.562
95	1.327	1.334	1.080	1.532
97.7	1.329	1.338	1.092	1.571

	Probability			
Percentile	Average Error	RMS Error	Minimum	Maximum
50	0.0800	0.104	0.502	0.690
90	0.0329	0.0345	0.909	0.948
95	0.0188	0.0197	0.956	0.978
97.7	0.00945	0.0101	0.981	0.992

(Envelope of 95 Percentile - 2.8 dB) DFS PSD

	RRS Ratio			
Percentile	Average	RMS	Minimum	Maximum
50	1.039	1.079	0.729	1.596
90	1.005	1.010	0.847	1.196
95	1.003	1.006	0.838	1.141
97.7	1.003	1.007	0.814	1.140

	Probability			
Percentile	Average Error	RMS Error	Minimum	Maximum
50	-0.00845	0.0797	0.387	0.624
90	-0.00153	0.0132	0.876	0.920
95	-0.000361	0.00623	0.934	0.959
97.7	-0.0000548	0.00381	0.968	0.983

Spectrum smoothing criteria using the RRS ratio and the probability error were established for subsequent test requirement derivations. An average RRS ratio of 1.0, with a +10 percent tolerance, was selected. In addition, a $\pm$ 3 dB tolerance was placed on the individual RRS ratios, i.e., for any sixth-octave frequency, the RRS ratio was required to be between 0.707 and 1.414. Additionally, it was desired to achieve an average probability error that was as small as practical, and preferably one that was positive. This criteria was not always satisfied. The use of a maximum of two plateaus in the smoothed spectra was selected as a practical limit to spectrum shaping. All smoothing was performed on the 95 per-
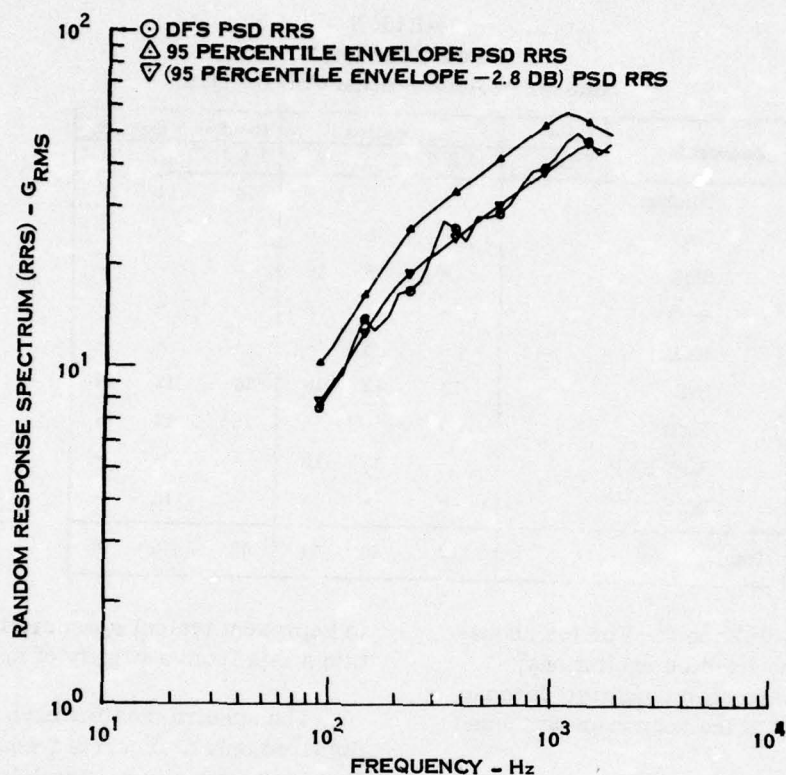
Fig. 8. Comparison of 95th percentile RRS spectra with smoothing

centile DFS PSD. The shape of this spectrum was maintained and the levels adjusted by using the average logarithmic standard deviation of the sampled spectra. The results showed this to provide a satisfactory spectrum shape for the 90 to 97.7 percentiles of interest in specifying component test requirements and simplifies the requirements. Results of the smoothing process are given in the next section of this paper.

APPLICATION OF METHOD

The method of Discrete Frequency Sampling (DFS) described in the preceding paragraphs was used to derive smoothed test requirements from the available data. Table 5 summarizes the data used in this study for acoustics and random vibration excitations. The number of acceleration PSD spectra for the various zones from

the various spacecraft tests is given. The data utilized were placed into structural groupings called zones, which are defined in the same manner as in Ref. [11].

Zone 1 - primary structure within two feet of the spacecraft/launch vehicle interface

Zone 2 - primary structure greater than two feet from the spacecraft/launch vehicle interface

Zone 3 - secondary structure internal to the spacecraft

Zone 4 - secondary structure external to the spacecraft

It is felt that these classifications adequately cover the data. Experience has shown that a large percentage of compon-

71

TABLE 5
Data Summary
Number of Acceleration PSD Spectra

Spacecraft	Type	Acoustics			Random Vibration		
	Zone	1 & 2	3	4	1 & 2	3	4
Nimbus		–	–	–	16	12	16
OSO		–	8	–	–	–	–
SMS		–	8	10	–	–	–
OAO		–	1	8	–	–	–
RAE		–	8	–	–	–	–
IUE		12	12	16	16	12	16
ERTS		–	–	–	16	12	16
S193-EXP		–	13	10	–	–	–
ISEE		–	–	–	–	12	–
Total		12	50	44	48	48	48

ents is mounted in Zone 3. For the acoustics and random vibration excitations, Zones 1 and 2 have been combined because of the similarity of the responses to these excitations.

The number of PSD spectra selected is only a portion of the data available. Approximately 50 spectra were considered to be an adequate sample size to decribe the statistical distribution in a zone. Examination of Table 5 indicates sufficient data were available to assure a statistically significant sample of data for all zones except Zones 1 and 2 acoustics, which had 12 measurements. This reflects the tendency to mount components on secondary structure, so that the limited amount of data in this category does not appear critical. Again, the data were selected

to represent typical spacecraft and to obtain a mix from a variety of spacecraft.

The spectra data for each zone were digitized only at discrete frequencies. For each zone a maximum likelihood lognormal distribution was fitted to the data to obtain the statistical properties, logarithmic mean and logarithmic standard deviation. PSD spectra were determined for four percentiles (50, 90, 95 and 97.7) for the Discrete Frequency Sampling (DFS) data obtained from the statistical analysis. The smoothing procedure was applied to the 95 percentile DFS PSD to obtain a smoothed test spectrum for each zone. The recommended random vibration smoothed test spectra for acoustic and random inputs are shown in Figs. 9 and 10, respectively, for Zones 1 and 2, 3, and 4. The values for the recommended smoothed test spectra are given in Table 6.
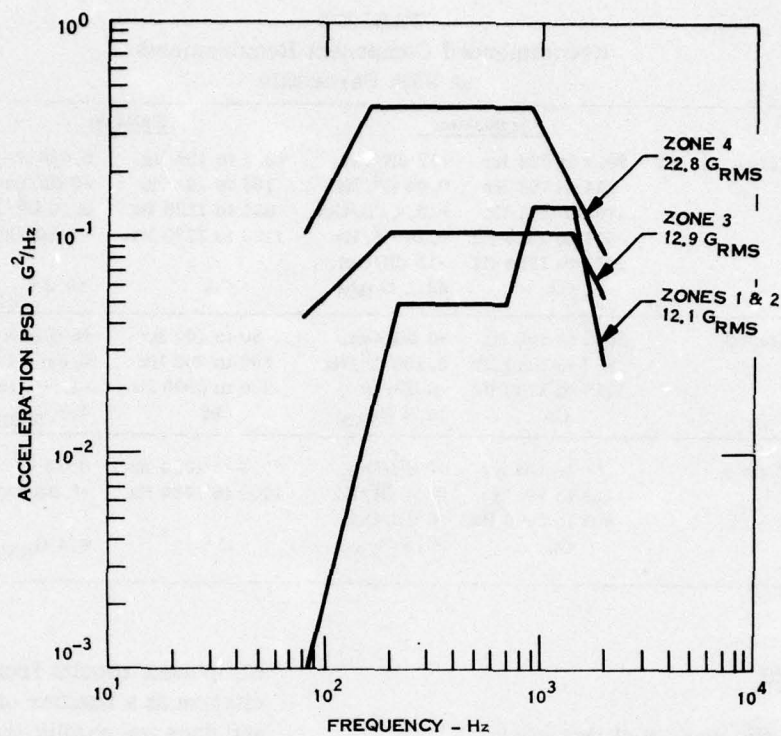
Fig. 9. Acoustics spectra, Zones 1 and 2, 3, 4
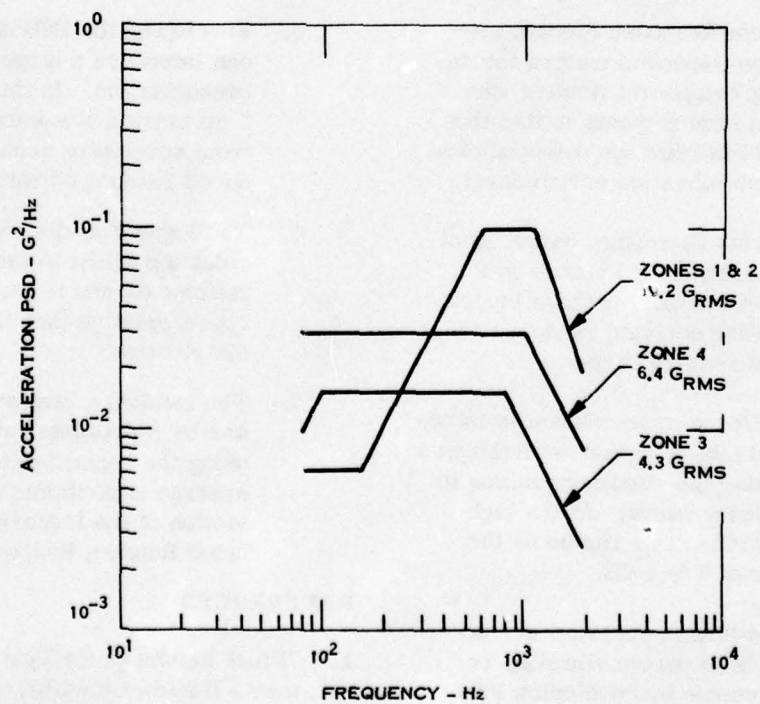
Fig. 10. Random vibration spectra, Zones 1 and 2, 3, 4

73

TABLE 6
Recommended Component Requirements
at 95th Percentile

		Acoustics		Random
Zones 1 and 2	89.1 to 224 Hz	+12 dB/Oct.	89.1 to 158 Hz	0.00627 G^2/Hz
	244 to 708 Hz	0.05 G^2/Hz	158 to 631 Hz	+6 dB/Oct.
	708 to 891 Hz	+13.4 dB/Oct.	631 to 1120 Hz	0.10 G^2/Hz
	891 to 1410 Hz	0.14 G^2/Hz	1120 to 1780 Hz	-9 dB/Oct.
	1410 to 1780 Hz	-15 dB/Oct.		
	OA	12.1 G_{RMS}	OA	10.2 G_{RMS}
Zone 3	89.1 to 200 Hz	+3 dB/Oct.	80 to 100 Hz	+6 dB/Oct.
	200 to 1410 Hz	0.105 G^2/Hz	100 to 800 Hz	0.0155 G^2/Hz
	1410 to 1780 Hz	-6 dB/Oct.	800 to 2000 Hz	-6 dB/Oct.
	OA	12.9 G_{RMS}	OA	4.3 G_{RMS}
Zone 4	80 to 158 Hz	+6 dB/Oct.	89.1 to 1000 Hz	0.03 G^2/Hz
	158 to 891 Hz	0.41 G^2/Hz	1000 to 1780 Hz	-6 dB/Oct.
	891 to 2000 Hz	-6 dB/Oct.		
	OA	22.8 G_{RMS}	OA	6.4 G_{RMS}

CONCLUSIONS

Based on the results of this study, the following conclusions are made:

1. Random Response Spectra provide an improved method for deriving component random vibration requirements in that they reflect the damage potential of a random vibration environment.

2. Discrete Frequency Sampling of acceleration PSD curves is the best of the four methods investigated for deriving random vibration requirements.

3. Significant conservatism is introduced into vibration requirements by using the maximum values in frequency bands. At the high percentiles this can be on the order of 2 to 4 dB.

4. It is neither necessary nor desirable to derive vibration requirements by enveloping PSD spectra. The response of the component results from the excitation at a number of frequencies and does not exhibit the large variations of the PSD spectra.

5. Enveloping the PSD spectrum can introduce a large amount of conservatism. In this study, a 3 dB margin was found to result from enveloping acoustically induced random vibration spectra.

6. The lognormal distribution provides a good fit to the random vibration data and is generally more representative than the Weibull distribution.

7. The random vibration environment can be represented statistically by using the logarithmic mean and average logarithmic standard deviation of the lognormal distributed Random Response Spectrum.

REFERENCES

1. "Final Report of the Test Requirements Review Committee", Informal GSFC Report, Sept. 1973.

2. Timmins, A. R. and Heuser, R. E., "A Study of First Day Space Malfunctions", NASA TND-6474, Sept. 1971.

3. Stahle, C. V., "A Method for Determining the Applicability of System Level Spacecraft Vibration Qualification Testing", Thesis for Drexel Institute of Technology, College of Engineering Graduate Studies, 1966.

4. Boeckel, J. H. and Timmins, A. R., "Test Plan Optimization for An Explorer-Size Spacecraft", NASA TND-5283, July 1969.

5. Choi, S. C. and Piersol, A. G., "Selection of Test Levels for Space Vehicle Component Vibration Tests", Journal Electronics Division (ASQC), 4, No. 3, July 1966.

6. Piersol, A. G. and Maurer, J. R., "Investigation of Statistical Techniques to Select Optimal Test Levels for Spacecraft Vibration Tests", NASA CR-115778, GSFC, Oct. 1970.

7. Young, J. P., "Cost Optimization of Spacecraft Test Levels", Proc of IES 20th Annual Meeting, May 1974.

8. Piersol, A. G., "Criteria for the Optimum Selection of Aerospace Component Vibration Test Levels", Proc of IES 20th Annual Meeting, May 1974.

9. McGregor, H. N., et al., "Acoustic Problems Associated With An Underground Launching of a Large Missile", Shock and Vibration Bulletin No. 29, P4, June 1961.

10. Barrett, R. E., "Statistical Techniques for Describing Localized Vibrating Environments of Rocket Vehicles", NASA TND-2158, July 1964.

11. Keegan, W. B., "A Statistical Approach to Deriving Subsystem Specifications", Proc of the IES 20th Annual Meeting, May 1974.

12. Eldred, K., Roberts, W. and White, R., "Structural Vibrations in Space Vehicles", WADD TR 61-62, December 1961.

Discussion

Mr. Scotti (Convair): Did you consider sinu-
soids in your input data? Sometimes you do not
have a completely random type of input. You
may have a pump that drives the structure in
a sinusoidal fashion. What effect does this
have on the analysis?

Mr. Stahle: There are two types of vibration
tests that are generally imposed on components.
The one I was discussing was random vibration,
sinusoidal tests are also imposed on components
and this is not really part of this discussion.
The sine test is directed more toward the
transient excitations in the lower frequency
range.

Mr. Curtis (Hughes Aircraft): I believe all of
your random response spectra used a Q of 10
which probably gives a fair amount of smoothing.
Do you have any feel for the sensitivity to the
employment of other Q's?

Mr. Stahle: We didn't really have time to
investigate the effect of the variation of Q
on the results, but I would expect that it
would have some effect for most of the shock
data processing that has been done. People
have normally used a Q of 10 and we have con-
tinued to perpetuate the work of our predeces-
s~rs.

Mr. Galef (TRW): It occurs to me that you get
essentially the same results if you stuck with
the power spectral density except that instead
of using the narrow band power spectral density
which approaches the mathematical definition,
you use the third octave or a sixth octave
which essentially smears out the peaks and
gives an average. Is this correct?

Mr. Stahle: I don't believe that is at all
correct; as a matter of fact we are using the
transfer function for a signle degree of
freedom oscillator and that is not really the
same as using a wide band analysis, it is a
'econd order system.

76

STATISTICAL DETERMINATION OF RANDOM
VIBRATION REQUIREMENTS FOR
SUBASSEMBLY TESTS

John M. Medaglia
General Electric-Space Division
Philadelphia, Pennsylvania

A statistical method for determining subassembly random vibration requirements which is compatible with the requirements applied to individual electronic component packages has been developed. Quantitative estimates of the damage potential of the subassembly random vibration environment and of the component specification are compared at various probability levels to arrive at a subassembly input requirement. Detailed examples of the application of this technique to the Japanese Broadcast Satellite Experiment Transponder subassembly test are given to clarify the procedure.

INTRODUCTION

This paper presents a statistical method for determining random vibration test requirements for subassembly level testing which is compatible with the requirements applied to individual electronic component packages. This method has been applied to the Japanese Broadcast Satellite Experiment (BSE) Transponder which cannot be adequately tested on a component level of assembly. The BSE Transponder subassembly is a two tiered, 76.5 cm by 137.5 cm structure which supports numerous electronic components and weighs approximately 80 Kg (Fig. 1). The structure is magnesium sheet, stiffened with extruded and formed members. It forms one side of the central box structure of the satellite. There are 25 major components interconnected by waveguide, 21 active devices and over 20 isolators,

filters, and other passive devices included in the waveguide. In addition to the Radio Frequency coupling there are multiple hard-wired feed-back loops making electrical performance evaluation possible only at the subassembly level. Similarly, the mechanical interactions via waveguide and mounting structure make component testing alone inadequate to assure the proper functioning of the subassembly in orbit. In addition, subassembly testing may be more realistic in that areas in the structure of high and low response are maintained.

The vibration input requirements (levels) for a subassembly such as the BSE Transponder differ from the levels required for individual qualification testing of the components within the subassembly. The levels which a component
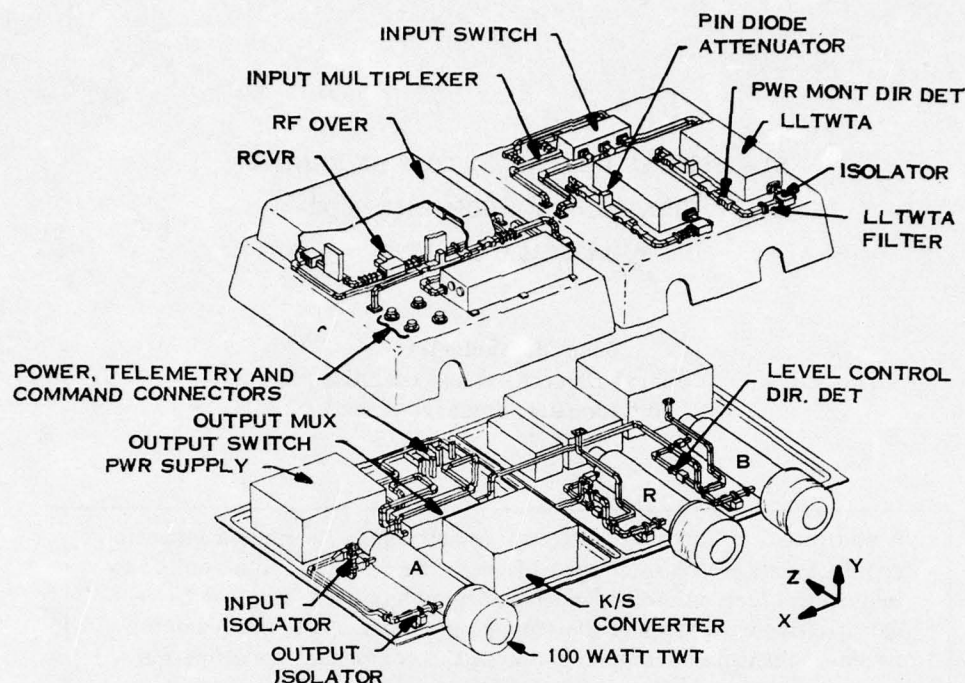
Fig. 1. BSE transponder

(such as the 100 Watt TWT, the power supply, or the PIN diode attenuator labled in Fig. 1) must survive may be defined based on past measurements of the vibration levels at the component mounting interface in the appropriate zone of previous vehicles. The mounting interface for the BSE Transponder components are on the flexible structure of the Transponder subassembly. The subassembly inputs must produce an environment at the components which overall is compatible with the requirements needed to survive flight. Since there are inevitably response magnifications and other characteristics between the subassembly-to-vehicle mounting interface (where the vibration inputs are controlled in the subassembly test) and the component-to-subassembly mounting locations, the inputs to the subassembly must differ from the vibration environment required at the components.

The need for an approach which would result in a response environment on the subassembly which is compatible with component vibration requirements was confirmed and emphasized by the test of the Engineering Model (EM) Transponder. In the EM test, the shapes of the acceleration power spectral density spectra varied widely from one location to another. Fig. 2 is a trace of three acceleration PSD response spectra from one axis of the EM random vibration test. This complex variety of PSD shapes measured by 59 accelerometers in the subassembly could be compared to the component specification only on a statistical basis.

Statistical analyses are widely used to generate component specifications [1, 2, 3, 4]. These methods statistically account for the variations in response (as in Fig. 2) from location to location and structure to structure to produce a realistically conservative estimate of the random vibration environment which a component may have to survive. The acceleration PSD at a given probability level resulting from a pool of data is a complicated shape characterized
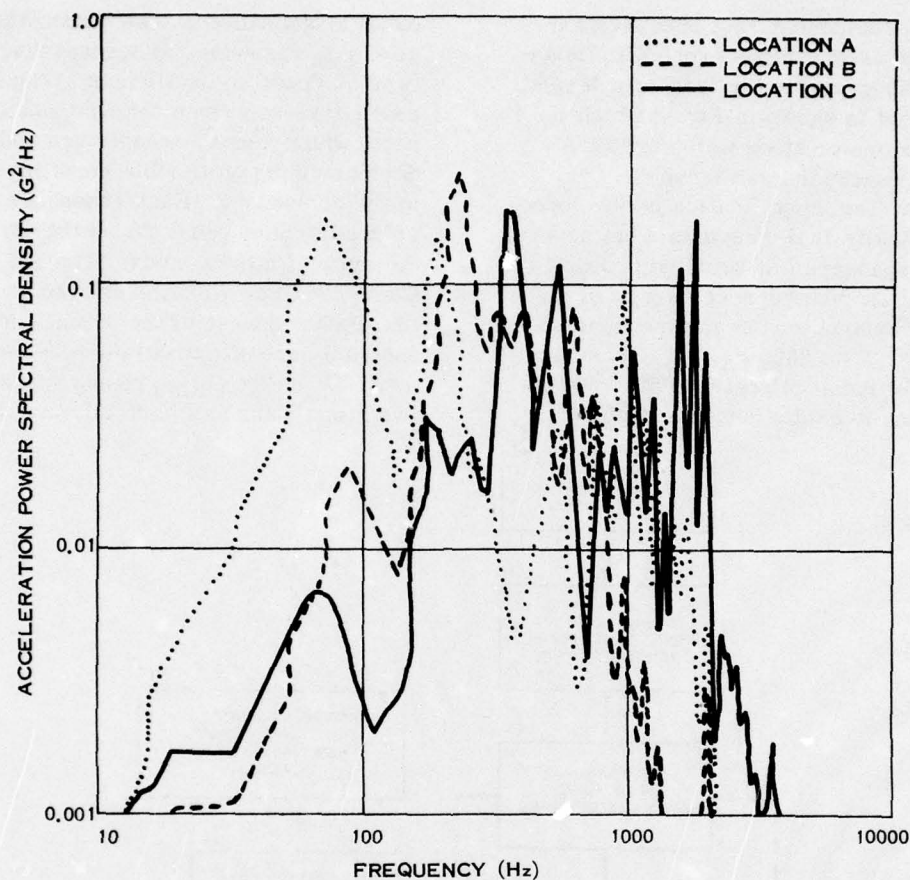
Fig. 2. Example of vibration response variation from location to location.
Data from BSE transponder subassembly random vibration test.

by many sharp peaks and valleys. Usually,
a practical component specification is
chosen by enveloping the peaks with "good
engineering judgement" as the only cri-
teria for the smoothing process. A con-
servatively high acceleration PSD spectrum
is the result. Another method of smoothing
|5| which is perhaps more realistic and
still conservative is to analytically repre-
sent the component internal piece-part re-
sponse to the acceleration PSD stimulus
of the component mounting structure. The
criteria for smoothing becomes a quanti-
tative comparison of the piece-part re-
sponse, or "damage potential", of the sta-
tistically defined acceleration PSD en-
vironment and of the smoothed representa-
tion of the same PSD environment.

The statistical method presented here-
in uses the concept of damage potential for
smoothing and the component specification
as a guide to determine random vibration
requirements for a subassembly. The dam-
age potential of the component environment
produced by the dynamic response charac-
teristics of a specific subassembly is quan-
titatively related to the damage potential of
the component vibration requirements es-
tablished by the usual statistical treatment
of extensive data from many structures.

DESCRIPTION OF METHOD

In general, the damage potential of
the subassembly acceleration PSD response

79

and of the Component Test Specification are compared at various probability levels to establish subassembly test input levels. A flow chart is shown in Fig. 3 which indicates the major steps which are discussed in succeeding paragraphs. The Component Test Specification is developed by statistically analyzing data from several previous spacecraft at selected probability levels and as such represents a realistic PSD environment across the frequency band of interest (20 to 2000 Hz). The damage potential of the acceleration PSD environment acting to excite component piece parts is quantified by calculating the overall G_{RMS} responses of several Single Degree of Freedom oscillators. The SDF oscillators represent the component piece parts which may be transistors and other devices riding on flexible mountings within the component. Each resonance is considered to have equal probability of being the critical failure mode. The PSD of the Component Specification and the acceleration PSD response of the Transponder subassembly are stimuli to the SDF oscillators. When the G_{RMS} responses due to the two stimuli are satisfactorily matched, the

(a) PRELIMINARY PSD INPUT SHAPES

(b) SUBASSEMBLY DYNAMIC RESPONSE CHARACTERISTICS

(c) COMPONENT LOCATIONS SAMPLE RESPONSES

(d) STATISTICAL ANALYSIS OF RESPONSE ENSEMBLE

(e) RRS* OF COMPONENT RESPONSE STATISTICS

(f) COMPONENT VIBRATION SPECIFICATION: STATISTICALLY DEFINED

(g) RRS* OF COMP SPEC AT VARIOUS PROBABILITY LEVELS

(h) RRS* COMPARISON AT VARIOUS PROBABILITY LEVELS

(i) INPUT SPECTRUM RESHAPING VIA COMPONENT RESPONSE STATISTICS

(RESHAPING)

(COMPARISON)

RRS* ENSEMBLE OF COMPONENT RESPONSE REPLICAS

STATISTICAL ANALYSIS OF RRS* ENSEMBLE

* RRS – RANDOM RESPONSE SPECTRA OF THE SDF ENSEMBLE REPRESENTATION OF COMPONENT PIECE PART RESPONSE TO THE COMPONENT ENVIRONMENT ("DAMAGE POTENTIAL")

Fig. 3. Flow chart of main steps in procedure

80

subassembly input levels are defined. This method deals with matching the statistically defined subassembly composite response to the component specification and not with matching of each individual component location on the structure to the component specification. Points on the subassembly with high and low response are considered to represent actual flight conditions.

There were several distinct steps in developing the random vibration test input specifications for the BSE Transponder. They involved replication of the EM test data and test inputs, definition of the damage potential of an acceleration PSD environment, and comparison of the acceleration PSD environments and their damage potentials at various probability levels. The blocks of the flow diagram in Fig. 3 which are connected by solid lines represent the method after simplifications which were discovered in the course of developing the method.

Preliminary acceleration PSD input shapes (Fig. 3a) were established for the Engineering Model (EM) transponder subassembly test. The EM test inputs were defined by enveloping the acceleration PSD responses of the transponder analytical model and selecting a smooth input which was intended to cause the responses to approximate the component random vibration specification.

Subassembly dynamic response characteristics (Fig. 3b) were measured in the EM random vibration test. No individual component location acceleration PSD response matched the Component Specification PSD shape, but this was expected. The correlation of the EM acceleration PSD response envelope and the acceleration PSD of the Component Test Specification was far from exact. Evaluation of the effect of the complex subassembly responses on the components required statistical analysis and some method of

assessing the damage potential of the acceleration PSD environment. The data from the EM Transponder was used to statistically develop random vibration test requirements for succeeding Transponders which included an estimate of damage potential. The data were replicated in detail by digitization of the acceleration PSD response plots from the real time analyzer with an Applicon Tabletizer. There were 59 response accelerometers. The average acceleration PSD input for each axis was also replicated. A total of 180 acceleration PSD plots were replicated from the three-axis EM Transponder test. The most complicated plot took 139 digitized points to replicate. The least complicated took 73 points. Commonly, 90 to 120 points were required to replicate most plots.

Component location response (Fig. 3c) plots from the EM transponder test were converted to matrix form for manipulation. As part of the conversion process the responses were normalized to the smoothed input for each axis. The replica of the average acceleration PSD input was ratioed with the smoothed (nominal) input shape to produce the normalization factors. This simplified later reshaping of the data. The PSD replicas were analytically sampled at the 1/6 octave points to produce the populations for statistical evaluation at 41 discrete frequencies.

Statistical analysis (Fig. 3d) of the ensemble of EM response plots was done by axis. The PSD responses at each discrete frequency were fit to lognormal distributions which have proved satisfactory in other studies of random response data [1, 2, 3, 5] by Condos, Barett, Keegan, Stahle, and Gongloff. The BSE Transponder data were also satisfactorily fit to the lognormal distributions, especially above the fundamental frequency of the subassembly. The mean and standard deviation at the 41 discrete frequency points for the acceleration PSD samples were calculated to de-

81

fine the subassembly composite component response.

The Random Response Spectra (Fig. 3e) produced by the component response statistical definition were calculated. The RRS was an estimate of the damage potential of the environment to which the components are subjected. Damage potential was calculated using the SDF oscillator ensemble as representative of piece-part responses. To account for the possibility that any frequency could stimulate a failure mode, the 20-2000 Hz spectrum was divided at the 1/6 octave points to produce 41 SDF oscillators. The same damping factor was assigned to each oscillator. The stimuli to the ensemble of SDF oscillators were the acceleration PSD shape projected from the statistical composite of the subassembly response and the acceleration PSD shape of the component specification. The square of the 1-G transfer function of each oscillator was multiplied by the PSD shape of the stimulus. This oscillator PSD response was integrated to find its overall G_{RMS}. Thus, 41 G_{RMS} levels were calculated to represent the damage potential of the component acceleration PSD environment for each probability level selected for comparison.

The Component Specification (Fig. 3f) was derived from a statistical composite of the vibration environment measured in several previous spacecraft. A component individually tested to the Specification for the central zone in a hard mount to the shaker could be expected to survive at any location in the zone even though the vibration environment at each location could be quite different. This is indicated in Fig. 2. Therefore each component would be tested to an overly conservative level in some frequency bands as compared to the environment at the specific location where it was actually mounted.

At various probability levels, the damage potential of the component specification was calculated (Fig. 3g) and compared (Fig. 3h) with the damage potential of the Engineering Model Transponder acceleration PSD composite response (Fig. 4). The ratio of these G_{RMS} damage potentials at the 95th percentile (Fig. 5) was squared and used to reshape (Fig. 3i) the Transponder input and response. The G_{RMS} ratio squared was less than the ratio of the PSD shapes and was smoother because it is the integration of the SDF response. When the damage potentials of the PSD response and the component specification were satisfactorily matched, the iterative process was done and the new input defined. The matching criteria were that (using the component specification as the reference point) the average G_{RMS} ratio should be between 1.0 and 1.1, the peak ratio should be between 0.7 and 1.4 and the average probability error should be slightly positive.

The squares of the 95th percentile G_{RMS} ratios were used to select new acceleration PSD input levels. The squares of the 95th percentile G_{RMS} ratios were indirectly applied to the statistical means of the subassembly composite response data via the ratio of the new input level to the preliminary input level. It was not necessary to go back to each response plot nor to repeat the statistical analysis. The assumption was that there was a linear relationship between the transponder inputs and responses for the range of reshaping needed. The standard deviation of the response would remain constant. Therefore, the influence of new input shapes could be seen by reshaping the statistical means of the response data. However, a smooth input shape was desired, so direct multiplication of the preliminary input by the square of the ratio was not practical. Instead, smoothed input spectra based on the square of the ratio were used.

G_RMS (XPSD + COMP SPEC) 4 PERCENTILES
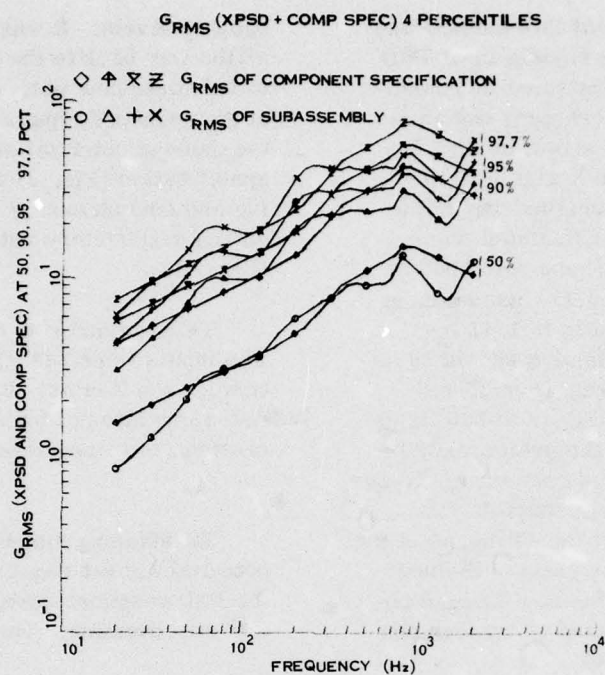
Fig. 4. Comparison of the damage potentials of the subassembly X axis response before reshaping and of the component specification

X AXIS DAMAGE POTENTIAL (G_RMS) COMPARISON AT 95.0 %
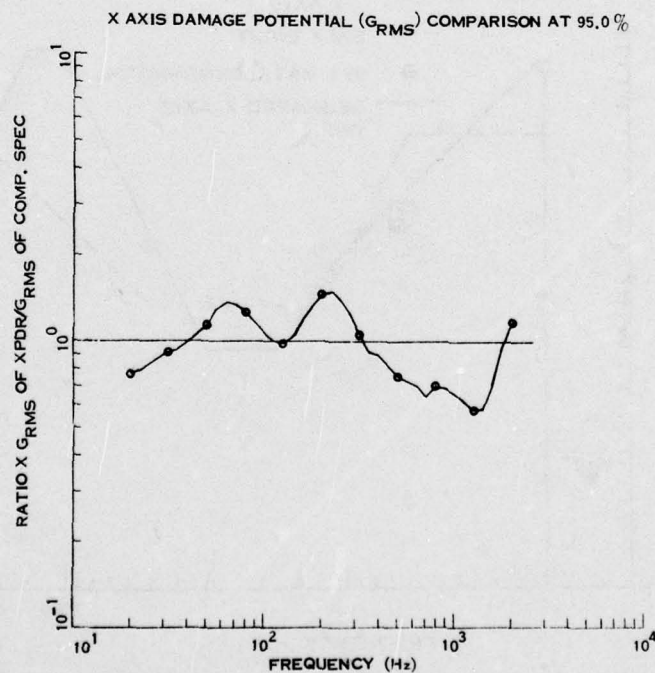
Fig. 5. Ratio of the damage potentials of the subassembly X axis response before reshaping and of the component specification at the 95th percentile.

A major advantage of this method was the ease in specifying a smooth input PSD shape. This is best illustrated by considering a few details of reshaping one axis. The square of the ratio shown in Fig. 5 was used to reshape the X axis PSD input. Fig. 6 shows the original input, the new shape benchmarks calculated from the ratio and the 1st reshape smoothed in around the benchmarks. For example, at 230 Hz in Fig. 5, the ratio is 1.47 indicating that a lower stimulus should be applied to the subassembly. Therefore a benchmark is shown in Fig. 6 at 230 Hz at 0.0046 G^2/Hz which is the preliminary input of 0.01 divided by 1.47 squared. To see the effect of the new input shape it was necessary to only adjust the 41 means of the EM PSD response by the ratio of the new input to the old. Then the new damage potentials could be calculated at various pro-

bability levels. It was not necessary to go all the way back to the individual replicas or to calculate new fits. The damage potential of the reshaped input was then compared to the damage potential of the component specification (Fig. 7) and the above reshaping and comparison process was repeated until a satisfactory ratio was achieved (Fig. 8).

This method converged very rapidly. The inputs were reshaped in only one iteration for the X-axis. It also took only one reshaping attempt for the Y axis. Two iterations were required for the Z axis.

Satisfactory matching of the damage potential did not require close matching of the PSD response envelope to the component test specification. The PSD levels which
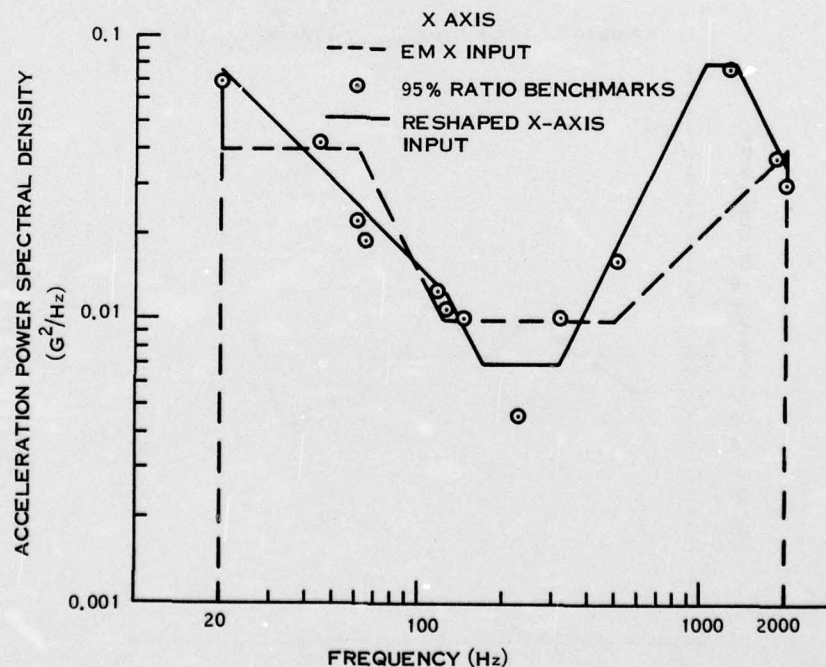
Fig. 6. X axis subassembly random vibration test input requirement before and after reshaping

84

X G_{RMS} COMPARISON AT FOUR PERCENTILES

◇ ⊕ ✗ ⩾ G_{RMS} OF COMPONENT SPECIFICATION

○ △ + ✗ G_{RMS} OF SUBASSEMBLY
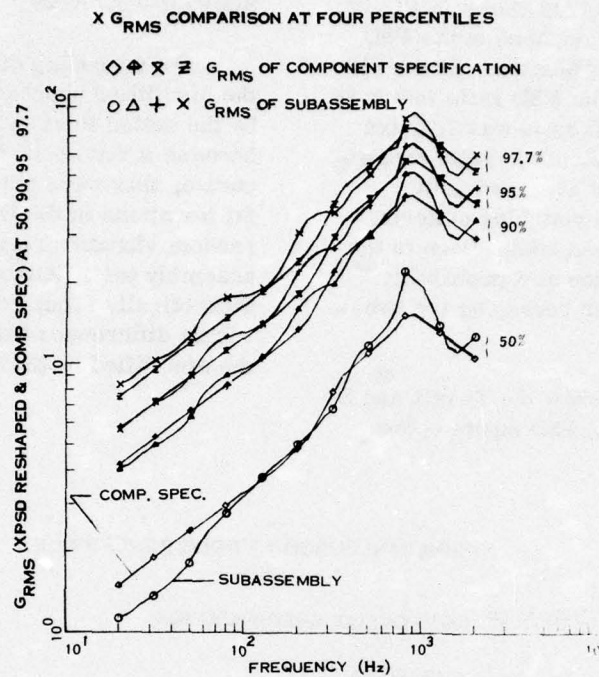
Fig. 7. Comparison of X axis damage potentials (G_{RMS}) of subassembly after reshaping and of the component specification

DAMAGE POTENTIAL (G_{RMS}) COMPARISON AT 95 %
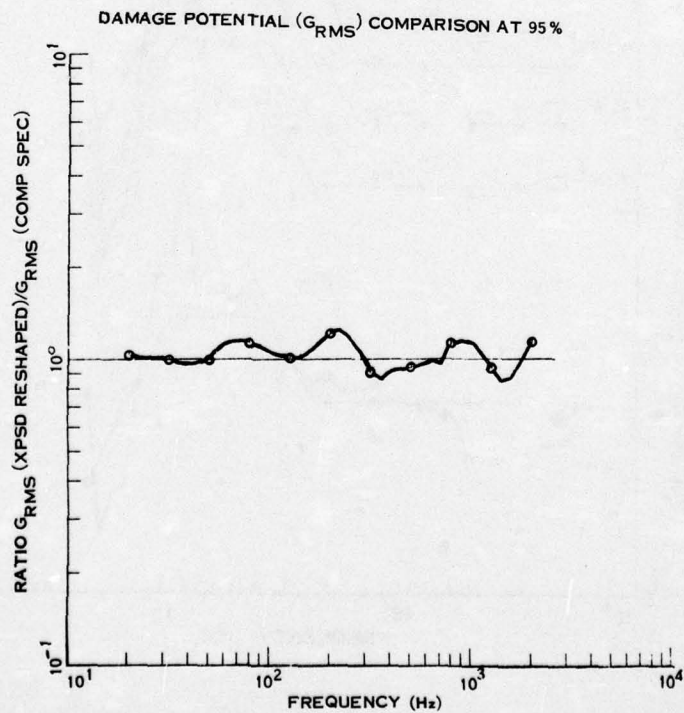
Fig. 8. Ratio of the damage potential of the X axis subassembly response after reshaping divided by the damage potential of the component specification

85

produced the G_{RMS} levels shown in Fig. 7 are shown in Fig. 9 compared to the PSD of the component specification. At the 95th percentile the minimum PSD ratio was 0.46 and the maximum PSD ratio was 2.3, but the G_{RMS} "damage potential" ratio ranged from .86 to 1.26, and averaged 1.04. Therefore, it met the matching criteria. Table 1 lists the X-axis comparison to the component specification at 4 probability levels before and after reshaping the subassembly inputs.

Figs. 10 and 11 show the Y-axis and Z-axis subassembly test PSD inputs before and after reshaping.

SIMPLIFICATIONS

The preceding discussion presented the simplified approach. The steps implied by the dotted lines in Fig. 3 were left out because it was found that although more accurate, they were not essential to successful iterations in the flow of determining the random vibration requirements of a subassembly test. Although these steps are theoretically required, there were no significant differences between the results of the simplified method and this method.
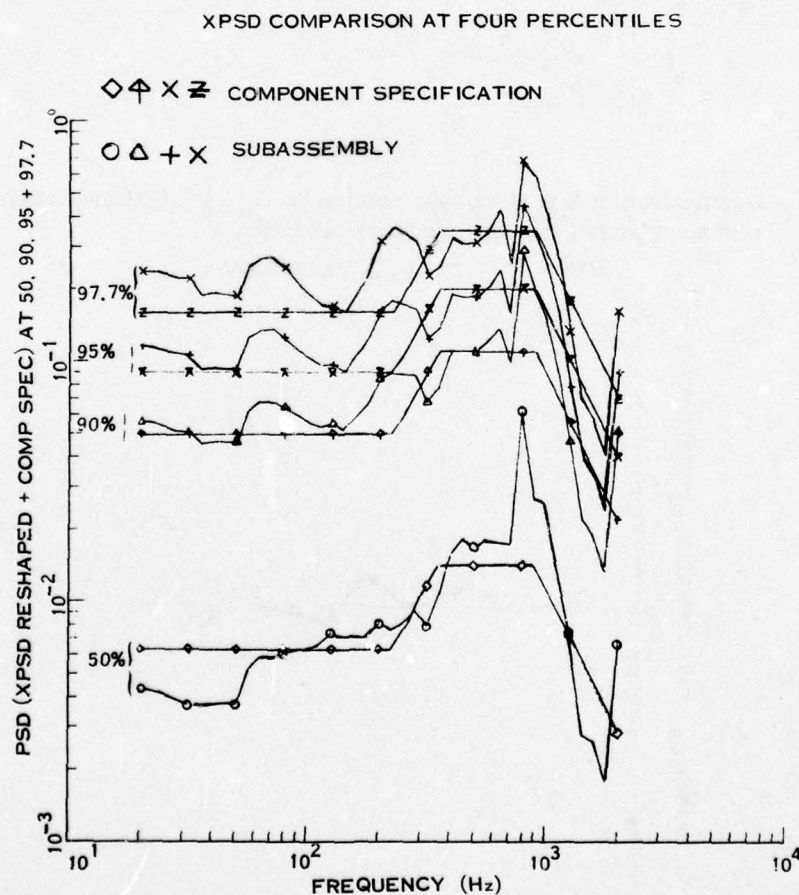
Fig. 9. Comparison of subassembly X axis response PSD after reshaping and PSD of component specification

86

TABLE 1
X-Axis Comparisons

Comparison	%	Avg Probability Error	Avg. Ratio	Max Ratio	Min Ratio
Damage Potential of Subassembly	50	-.0691	.885	1.223	.595
(Before Reshaping)	90	-.0300	.951	1.42	.588
Divided by Damage Potential of	95	-.0187	.975	1.496	.5744
Component					
Specification	97.7	-.0109	.999	1.57	.564
Damage Potential of Subassembly	50	-.02	.976	1.47	.715
(After Reshaping) Divided by	90	.002365	1.023	1.203	.87
Damage Potential of Component	95	.003354	1.0412	1.26	.86
Specification	97.7	.00251	1.061	1.32	.846
PSD of Subassembly	50	.00706	1.907	4.39	.488
(After Reshaping) Divided by	90	.00533	1.173	2.62	.468
PSD of Component	95	.00405	1.215	2.3	.461
Specification	97.7	.00223	1.27	2.29	.453

Fig. 10. Y axis subassembly random vibration test input requirement before and after reshaping

87
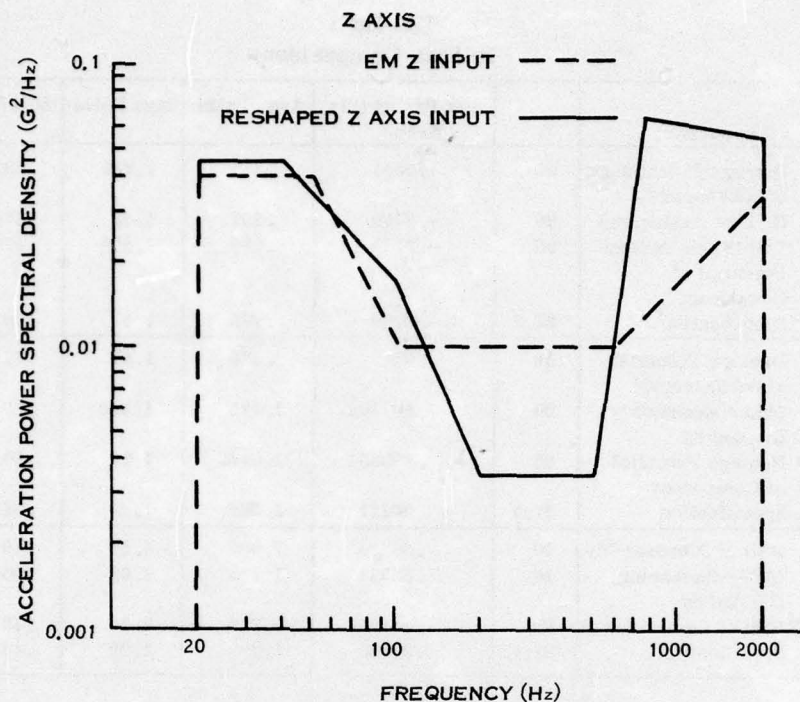
Fig. 11. Z axis subassembly random vibration test requirement before and after reshaping

A Random Response Ensemble was calculated consisting of the damage potentials of each of the 59 accelerometer response replicas. Plot by plot, the 59 replica PSD's were used to excite the SDF oscillators. Thus, a 59 x 41 matrix of G_{RMS} damage estimates was calculated. This ensemble of 59 damage potentials was statistically analyzed using a best fit to a lognormal distribution. Utilizing the resultant statistical mean and standard deviation, the replica damage potential estimate could be projected to any probability level and compared to the damage potential of the component specification. For reshaping, each of the 59 response replicas would have to be reshaped, based on a linear extrapolation of the effect of reshaping the average subassembly stimulus. The 59 RRS calculations would be repeated, as would the statistical analysis. (Reshaping of the inputs

would be accomplished with the benchmark procedure described previously). This repetition of RRS calculations and statistical analyses would be time-consuming and expensive.

However, it was found that calculations of damage potential from the replica, repetition of the statistical analyses and even replication of the test data were unnecessary. The damage potential calculated from the statistical composite of the discrete frequency sampling of the replicas was practically the same as the damage potential calculated from the replicas themselves. This is shown in Fig. 12. The sampling points were taken at the 1/6 octave frequencies without regard to peaks in the PSD replica. The good correlation (Fig. 12) confirms the

G_{RMS} OF YPSD SAMPLE + REPLICA
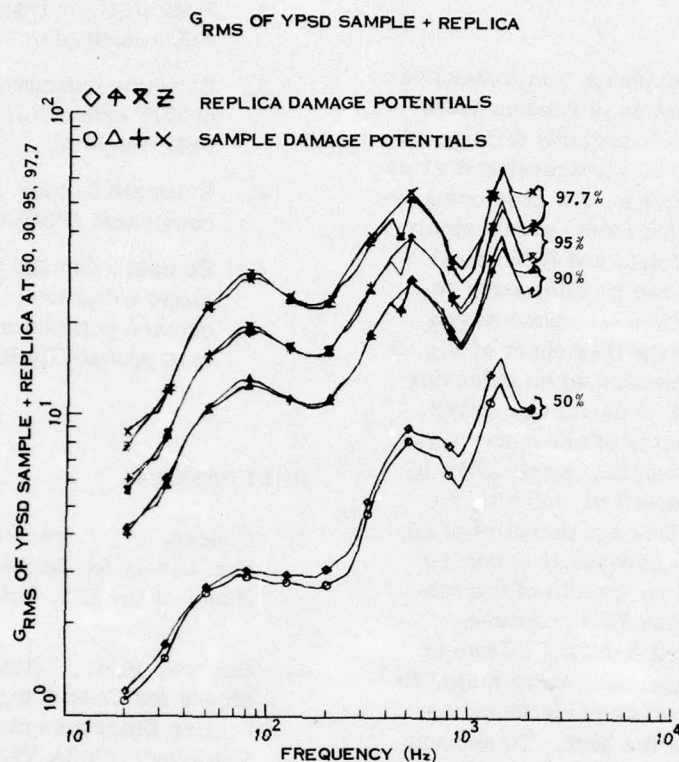
Fig. 12. Comparison of damage potential calculated from Y PSD replicas and from Y PSD as sampled at the 1/6 octave frequencies

adequacy of 1/6 octave sampling for these data. Thus one statistical analysis of the PSD samples and one calculation of the SDF RRS at each probability level can replace many (59) calculations of the SDF RRS and extra statistical analyses.

Replication could be eliminated because a procedure of digitization at discrete frequency sampling could be substituted for the analytic sampling of replicas. Careful consideration must be given to the number of points sampled. Results would not be good if too few frequencies were sampled. Sampling apparently may be done dogmatically, without regard to highs and lows in the individual plots if there are sufficient data and a sufficient number of sampling points. This is indicated by the success of the analytic sampling used on the BSE Transponder data (Fig. 12).

PSD comparisons between the subassembly data and the component specification PSD were made at every step of the development of the random vibration test requirements for the BSE Transponder subassembly test. These comparisons were of some interest and confirmed at each step that nothing unreasonable had happened to the PSD composite because of errors in data or the reshaping procedure. However, it was really the damage potential comparisons that were used for reshaping. Therefore the effort spent comparing PSD's could have been reduced and checks for good procedure could be accomplished just by printing and/or plotting the PSD of the subassembly before its damage potential estimate was calculated. Indeed, this was the output of the computer code used in this study and comparisons of PSD involved extra runs of the programs and the effort of producing all the attendant data.

CONCLUSIONS

This method provides a comprehensive approach to specification of random vibration test levels for subassembly testing. A good engineering model structural test gives the most reliable guidance for developing inputs for a qualification model subassembly test. Replication of data and RRS calculation of each replica can be eliminated resulting in the simplified technique shown by the solid lines of the flow chart of Fig. 3. Effort should be concentrated on achieving a satisfactory match of damage potential. Matching PSD shapes is of secondary importance, less meaningful, more difficult, and follows as a spin-off of matching the damage potential. Damage potential of the subassembly can be adequately estimated from the statistical composite of the subassembly acceleration PSD response. This method included fixturing effects on the subassembly response, so no major fixturing changes should be made from one subassembly test to the next. To account for unit to unit variations and experimental inaccuracies the random vibration requirements determined by this method should be given the same tolerances as any random vibration test specification. This method follows a rational approach to approximate realistic test conditions for a subassembly and does not precribe response limit criteria. Therefore, this method will not obfuscate the dynamics of a subassembly, but rather allow more normal behavior. Responses which may excede previous expectations are not hidden.

Summary of Method:

1. Sample the plots of acceleration PSD responses on subassembly at discrete frequencies.

2. Statistical analysis of sampled PSD responses.

3. Estimate damage potential (RRS of SDF ensemble) of subassembly PSD composite.

4. Estimate damage potential of component (PSD) specification.

5. Compare damage potentials and shape subassembly inputs until damage potentials agree at various probability levels.

REFERENCES

1. Condos, F., "Prediction of Vibration Levels for Space Launch Vehicles" Proc. of the IES, July 1962.

2. Barrett, R. E., "Statistical Techniques for Describing Localized Vibrating Environments of Rocket Vehicles", NASA TND-2158, July 1964.

3. Keegan, W. B., "A Statistical Approach to Deriving Subsystem Specifications", Proc. of the IES 20th Annual Meeting, May 1974.

4. "Test Requirements for Space Vehicles", MIL-STD-1540A (USAF) April 1974.

5. Stahle, C. V., Gongloff, H. G., and Keegan, W. B., "Development of Component Random Vibration Requirements Considering Response Spectra", 46th Shock and Vibration Symposium, October 1975.

Discussion

Mr. Maloney (General Dynamics/Pomona): Have
you had any experience using these less con-
servative methods in terms of the testing and
reliability of the hardware? *For instance*,
have you found fewer failures in tests or have
you experienced more failures in service using
these less conservative methods?

Mr. Medaglia: This is a brand new treatment
of developing a test specification we have no
results for comparison.

DEVELOPMENT OF SHIP SHOCK LOADS TEST
FOR THE RGM-84A MISSILE (HARPOON)

Thomas L. Eby

Pacific Missile Test Center
Point Mugu, California

The environmental design criteria for the HARPOON missile specified ship shock loads for the three principle missile axes. The shock load is specified as a trapezoidal acceleration pulse of thirty-five milliseconds in duration, with ten millisecond ramps to the peak acceleration level. This paper discusses the development of the device used to verify these missile design load requirements. The design verification test was developed and performed using a large shock facility at the Pacific Missile Test Center. The specified shock pulse shape was obtained by using a combination of Belleville (disc) springs as the impact energy transferring device.

INTRODUCTION

The environmental design criteria for the HARPOON missile specified ship shock loads for the three principle missile axes. The shock load is specified as a trapezoidal acceleration pulse of thirty-five milliseconds in duration with ten millisecond ramps to the peak acceleration level. This specification is to be the input to the missile (where the missile attaches to the launcher).

The lateral direction of shock specifies a nine g peak acceleration and the vertical and longitudinal directions of shock specify a fifteen g peak acceleration (Figure 1).

This paper dicusses the development of the buffer device used to generate the shock pulses and the results obtained from the tests. The buffer device was developed and used in conjunction with a large shock test facility at the Pacific Missile Test Center. This shock facility is a dual mode shock machine which functions as a drop tester and as a pneumatically operated hammer tester (Figure 2). This test utilized the hammer mode because it more closely resembles ship shock motion.

PROCEDURES

Preliminary Analysis

To determine the type of mechanism which is to be used to produce the shock pulses, the initial velocity of the dual mode machines's hammer must be known. The conservation of energy and the conservation of momentum equations were used to solve for the initial hammer velocity.

$$M_h V_h + M_t V_t = M_h V_h' + M_t V_t'$$

$$eV_h - eV_t = -V_h' + V_t'$$

Where:

M_h = mass of the dual mode hammer mechanism

M_t = mass of the test item, table and fixture

V_h = initial velocity of hammer mechanism

V_t' = final velocity of hammer mechanism

V_t = initial velocity of test item, table and fixture

V_t' = final velocity of test item, table and fixture

e = coefficient of restitution

In this set of equations the masses are known, the initial velocity of the test item is known and for simplicity the coefficient of restitution is assumed to be 1.0. There are two equations and three unknowns, so the velocity of the test item at the end of the thirty-five millisecond shock pulse was determined by graphical integration of the shock pulse specification. Integrating the shock pulse specification once with respect to time gives a velocity of 368.1 cm/s for the fifteen g specification and 220.8 cm/s for the nine g specification. These velocities are ideal velocities to have at the end of the thirty-five millisecond shock.

Thus, for the fifteen g shock,

$$2041 \text{ kg } (V_h) + 1678 \text{ kg } (0) = 2041 \text{ kg } (V_h') + 1678 \text{ kg } (368.1 \text{ cm/s})$$

$$1.0 (V_h - 0) = - V_h' + 368.1 \text{ cm/s}$$

$$V_h = V_h' + 1678 \text{ kg}/2041 \text{ kg } (368.1 \text{ cm/s})$$

$$2V_h = 368.1 \text{ cm/s } (1.82)$$

$$V_h = 335.36 \text{ cm/s}$$
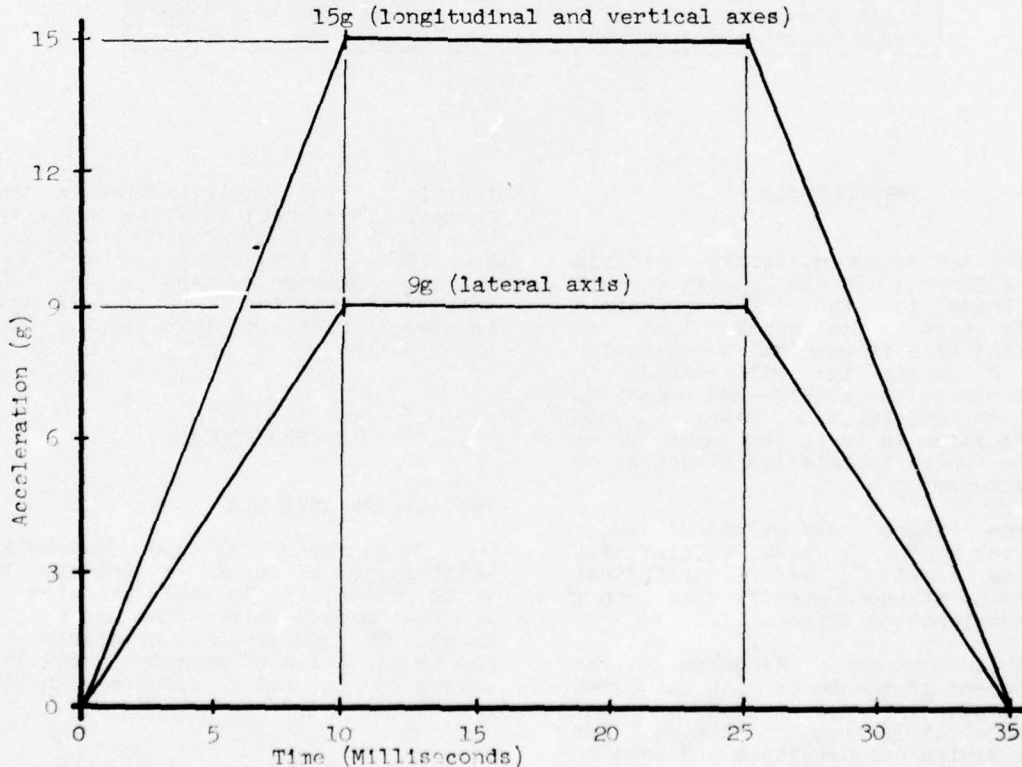
Figure 1. Ship Shock Pulse Specifications.
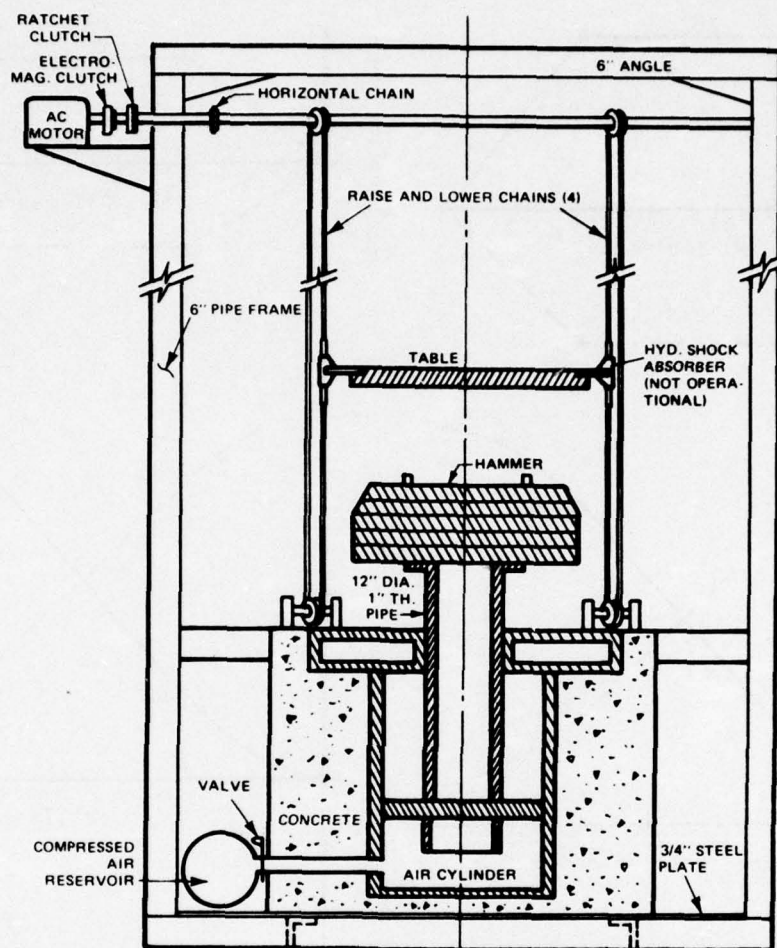
Figure 2. Dual Mode Shock Machine (Schematic).

And,

$$V_h' = 368.1 \text{ cm/s} - 335.36 \text{ cm/s}$$

$$V_h' = 32.71 \text{ cm/s}$$

And for the nine g shock,

$$1.0 (V_h - 0) = -V_h' + 220.83 \text{ cm/s}$$

$$V_h = V_h' + 0.82 (220.83 \text{ cm/s})$$

$$2V_h = 220.83 \text{ cm/s} (1.82)$$

$$V_h = 200.96 \text{ cm/s}$$

$$V_h' = 19.87 \text{ cm/s}$$

The motion of the system was determined by graphical techniques. Integrating the shock pulse specifications twice with respect to time yields the displacement of the test item and associated equipment. Integrating the deceleration of the hammer after impact twice with respect to time yields the hammer displacement (Figures 3 and 4). For simplicity the hammer deceleration is assumed to be the same shape and duration as the test item shock specification, but is reduced by the factor; mass of the test

95
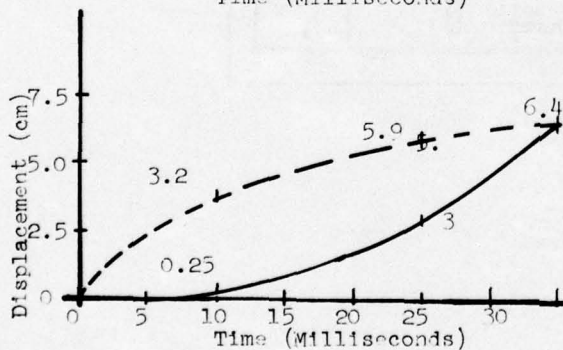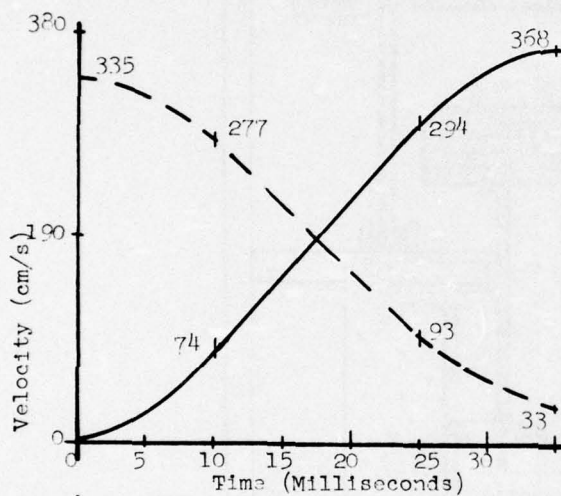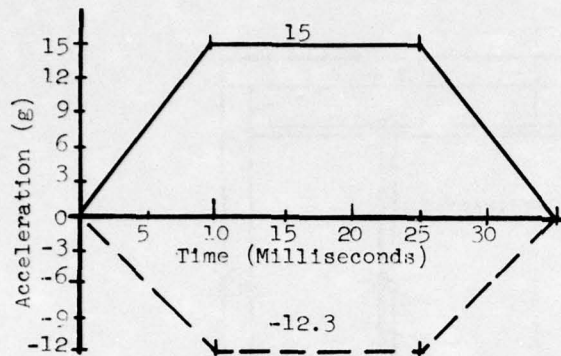
Figure 3. 15g Ideal System Motion.

Figure 4. 9g Ideal System Motion.
--- Hammer
— Test Item

item, table and fixture divided by the mass of the hammer mechanism of the dual mode shock machine. From the two displacement/time curves a differential displacement between the two moving bodies can be plotted for any time after impact. This then is used to plot a load/deflection curve from which desired spring characteristic can be

determined (Figure 5). It is seen in Figure 5 that the same device can be used to generate both levels of shock.

The specified shock pulse shape and duration can be generated using a series combination of Belleville (disc) springs as the impact energy transferring device. Commercially

96
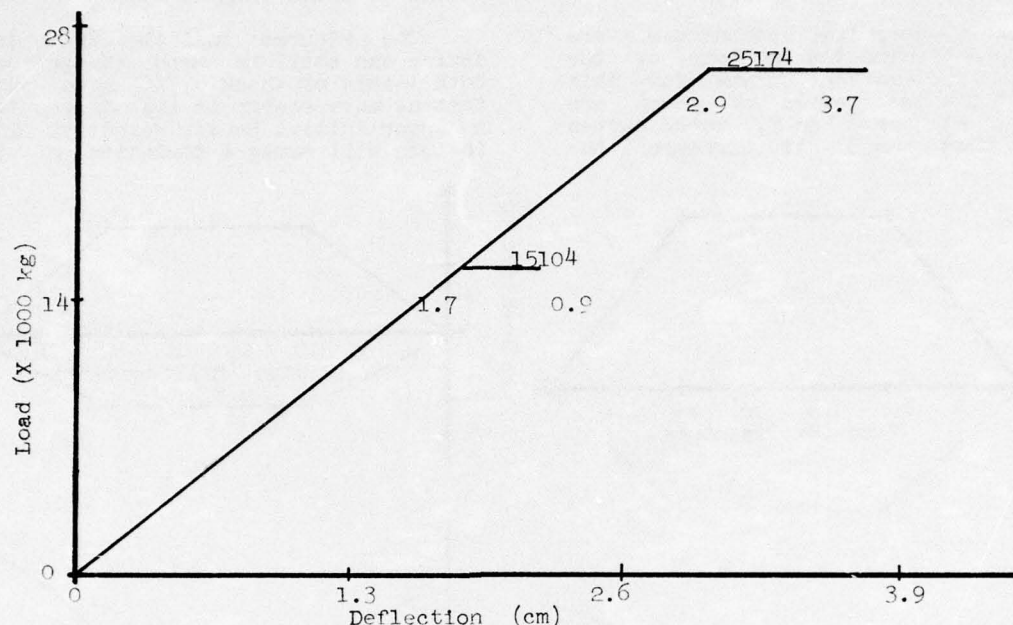
Figure 5. Load/Deflection of System for 15 and 9 g Shock (Ideal).

available disc springs were chosen to build the device. The springs are 250 mm outside diameter, 127 mm inside diameter, 1.27 cm thick and 1.95 cm high. These type of springs can have linear or nonlinear characteristics which make them ideal for generating the specified shock pulse. In general the springs become softer as more load is applied and the nonlinearity can be more pronounced depending on the physical dimensions of the springs. The series combination consists of two sets of nested disc springs, the first set is to produce the ramps and the second set is preloaded to work in conjunction with the first set to develop the peak acceleration level.

Practical Analysis

The previous solutions were for the simple ideal case. In this system there are losses due to friction pneumatic forces, etc., which make the ideal solution impractical. A more realistic value for the coefficient of restitution would be less than 1.0 because some appreciable amount of energy is lost using the steel springs and the coefficient of restitution is now assumed to be 0.95.

Again, solving the conservation of energy and the conservation of momentum equations simultaneously, the initial velocity of the hammer is calculated. The mass of the hammer mechanism now includes the buffer device.

For the fifteen g shock the velocities are;

2267 kg $(V_h) + 1678$ kg $(0) = 2267$ kg $(V_h') + 1678$ kg $(256.29$ cm/s$)$

$0.95 V_h = - V_h' + 368.1$ cm/s

$V_h = 328.44$ cm/s

And,

$V_h' = 39.63$ cm/s

And for the nine g shock,

$1.95 V_h = 220.83$ cm/s (1.74)

$V_h = 197.05$ cm/s

97

$V_h' = 23.78$ cm/s

Again, graphical techniques were used to determine the motions of the system. The motion curves for this case of the two levels of shock are shown in Figures 6 and 7. These curves were then used to produce the

load/deflection curve for the two levels of shock (Figure 8).

The Figures indicate the same device can still be used to generate both levels of shock. It also shows that as more energy is lost it requires a larger initial hammer velocity. This in turn will cause a deviation of the
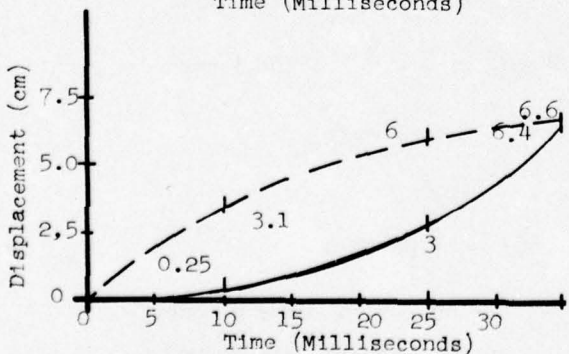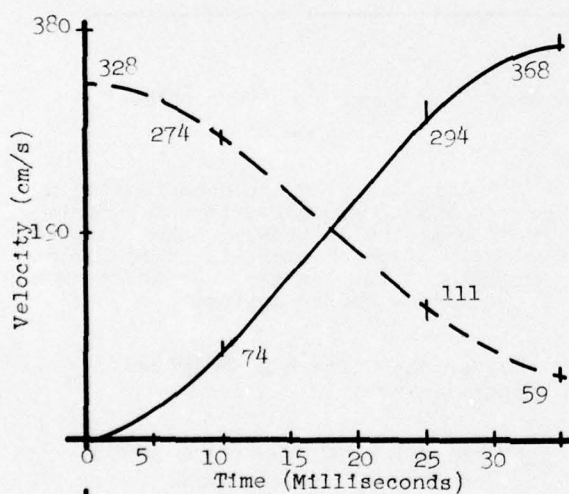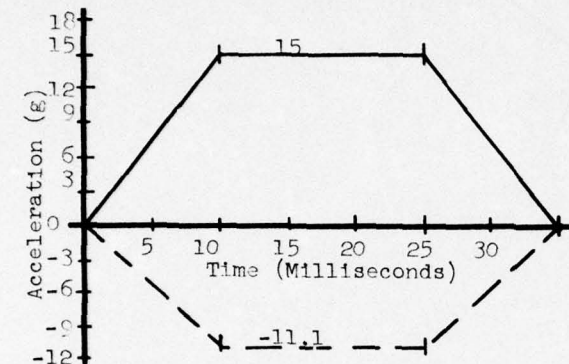
Figure 6. 15g e=0.95 System Motion.
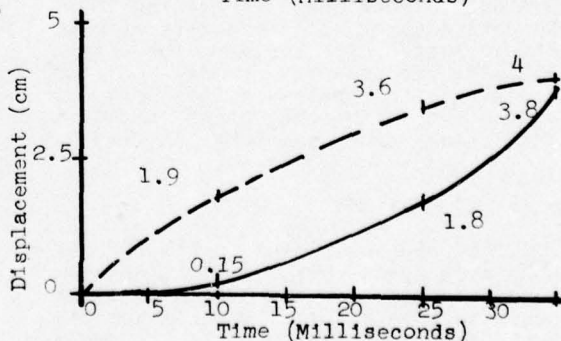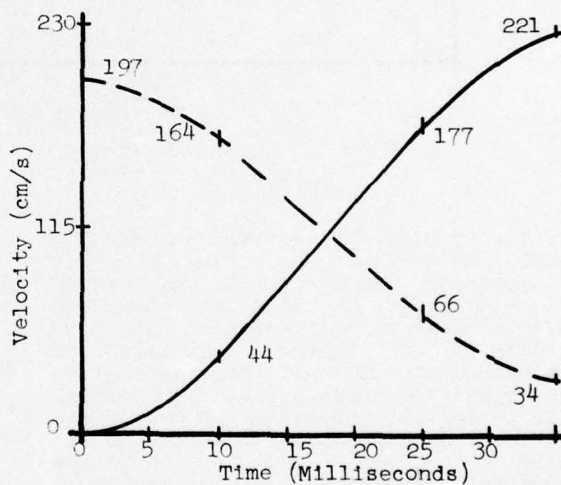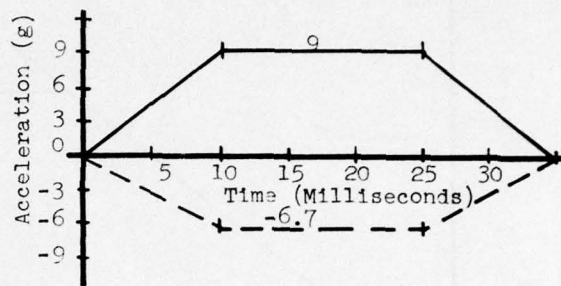
Figure 7. 9g e=0.95 System Motion.
--- Hammer
—— Test Item
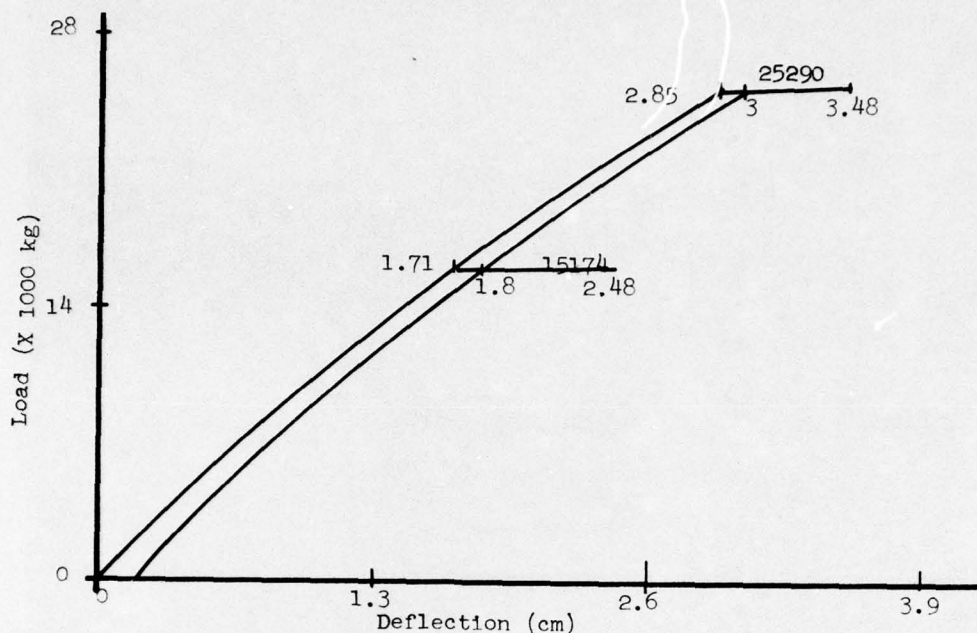
Figure 8. Load/Deflection of System 15 and 9 g Shock (e=0.95).

pulse. Also, the deflection of the buffer device has not returned to zero at the end of the thirty-five millisecond shock and some additional acceleration will occur after that time although it is not significant. This amount is not significant because the hammer is being stopped by the pneumatic forces and within a few milliseconds the two bodies will have separated and gravity will stop the test item and associated equipment.

ASSEMBLY AND GUIDE MECHANISM

Since the spring dimensions are known, a mechanism to assemble and guide them was designed and built at the Pacific Missile Test Center. The device (Figure 9) is a threaded steel bar from which the inside diameters of the springs will guide. It was decided to guide on the inside diameter to minimize weight and physical size. Two distinct sections are visible, the lower portion is for the preloaded spring section and the upper portion is for the unloaded spring section. A

mounting plate for attaching the mechanism to the top of the hammer mechanism of the dual mode shock machine and a retaining ring and impact surface at the top of the mechanism hold all the springs in one complete unit. The lower set of springs are preloaded to the desired load characteristics depending on which shock is to be performed. The impact of the mechanism and the dual mode machines's table results in the initial compression of the upper springs until the preload level of the lower springs is overcome. At this point the entire spring arrangement acts as a single series of springs until the energy of impact is transferred.

PERFORMING THE TESTS

To perform the tests, the table containing the test item is raised to a predetermined height (obtained from previous testing; the maximum amount of energy is received from the hammer for a certain table height and air

99
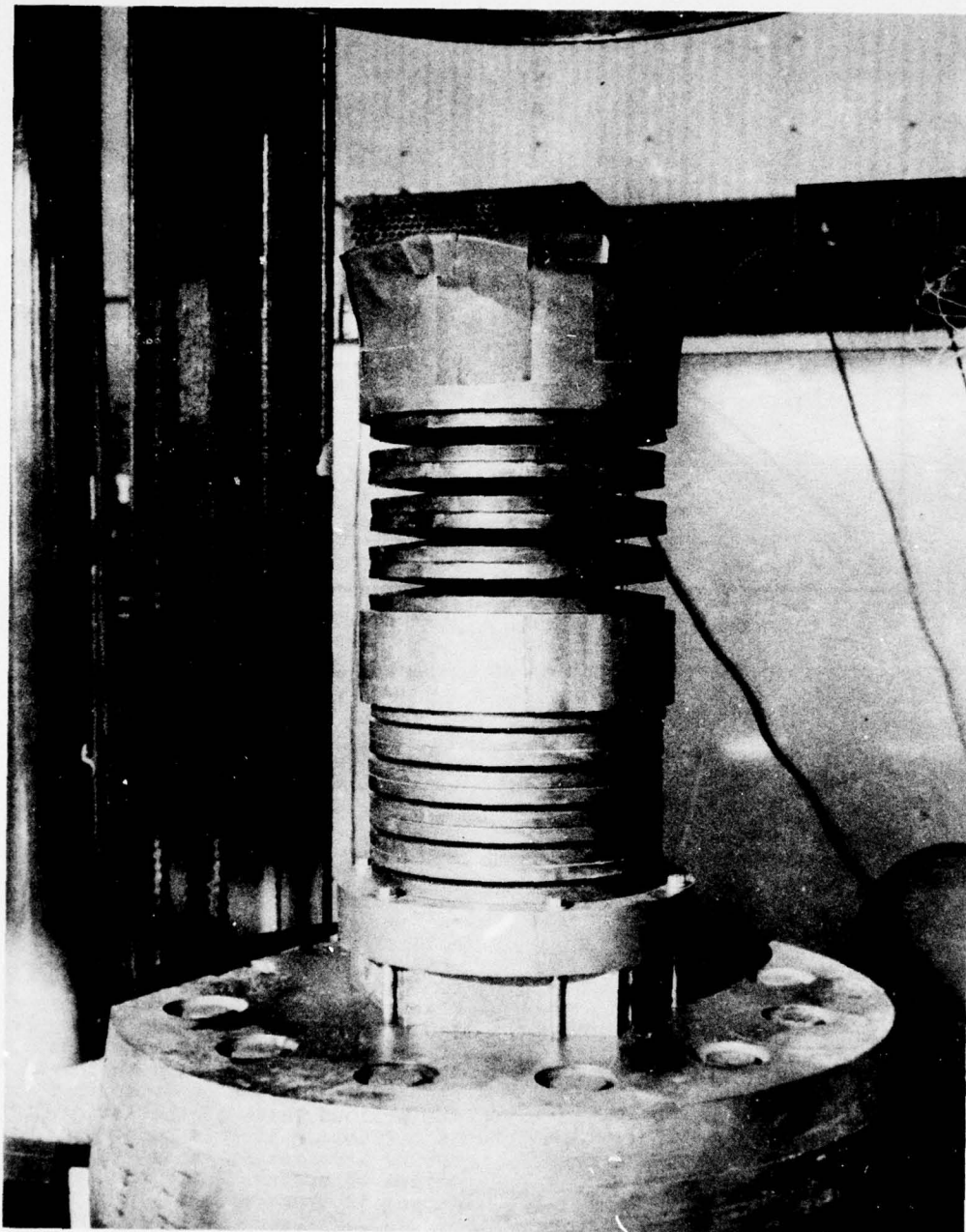
Figure 9. Assembly and Guide Mechanism Mounted on Dual Mode Shock Machine.

reservoir pressure), pressurizing the air reservoir to the corresponding pressure and releasing the air to the piston cylinder assembly of the dual mode shock machine. This causes the hammer mechanism (piston cylinder assembly) and buffer device to rise and strike the table, in turn transferring

the energy to the test item.

RESULTS

A test vehicle was used in the vertical axis to verify the analytical and graphical work. This inert vehicle was also used to resolve test configuration, test eccentricities and instrumentation problems. Piezoelectric accelerometers were used in these verification tests. Because of the seeming inability of the piezoelectric accelerometers to respond to this low frequency data, piezoresistive (strain gage) accelerometers were also used for the actual testing of the missile scheduled for the ship shock loads tests. These accelerometers will be located at the input to the missile (launcher rail mock-ups of the HARPOON fixture designed by Kimball Industries). The test configurations for the vertical and longitudinal axes are shown in Figures 10 and 11 and depict the fixture, missile, spring mechanism and dual mode shock machine.

The correct parameters for the shock machine were determined from the initial tests using the inert test vehicle. For the fifteen g shock the plenum (air reservoir) pressure is 552 kPa and the table height is 37.8 cm. For the nine g shock the plenum pressure is 448 kPa and the table height is 30.6 cm.

The test data compares favorably with design criteria. The tolerance of the shock pulse is to be within 15% of the maximum acceleration level and the duration within 10% of that specified. Figures 12 through 19 are oscillographs of the ship shock test for the three principle missile axes. Figures 12 and 13 are of the longitudinal axis, front attachment point. The shock is of the proper time duration with the desired ten millisecond ramps, but the amplitude is slightly on the low side and there is very little difference between the piezoelectric and piezoresistive accelerometer responses.

Figures 14 and 15 are of the vertical axis, front attachment point. The ten millisecond ramps are not as discernible, but the shape is a trapezoidal shape. There is noticeably more ringing in this axis probably due to the mass distribution over the dual mode shock machine. The amplitude is also somewhat low in this axis.

Figures 16 and 17 are of the lateral axis, front attachment point. The launcher rail mock-up failed in this axis doing minor damage to the missile fins and wings. The missile checked out electrically and it was decided not to run the test again because the rail had failed.

Figure 10. Test Item Mounted on the Dual Mode Machine in the Vertical Axis.

102
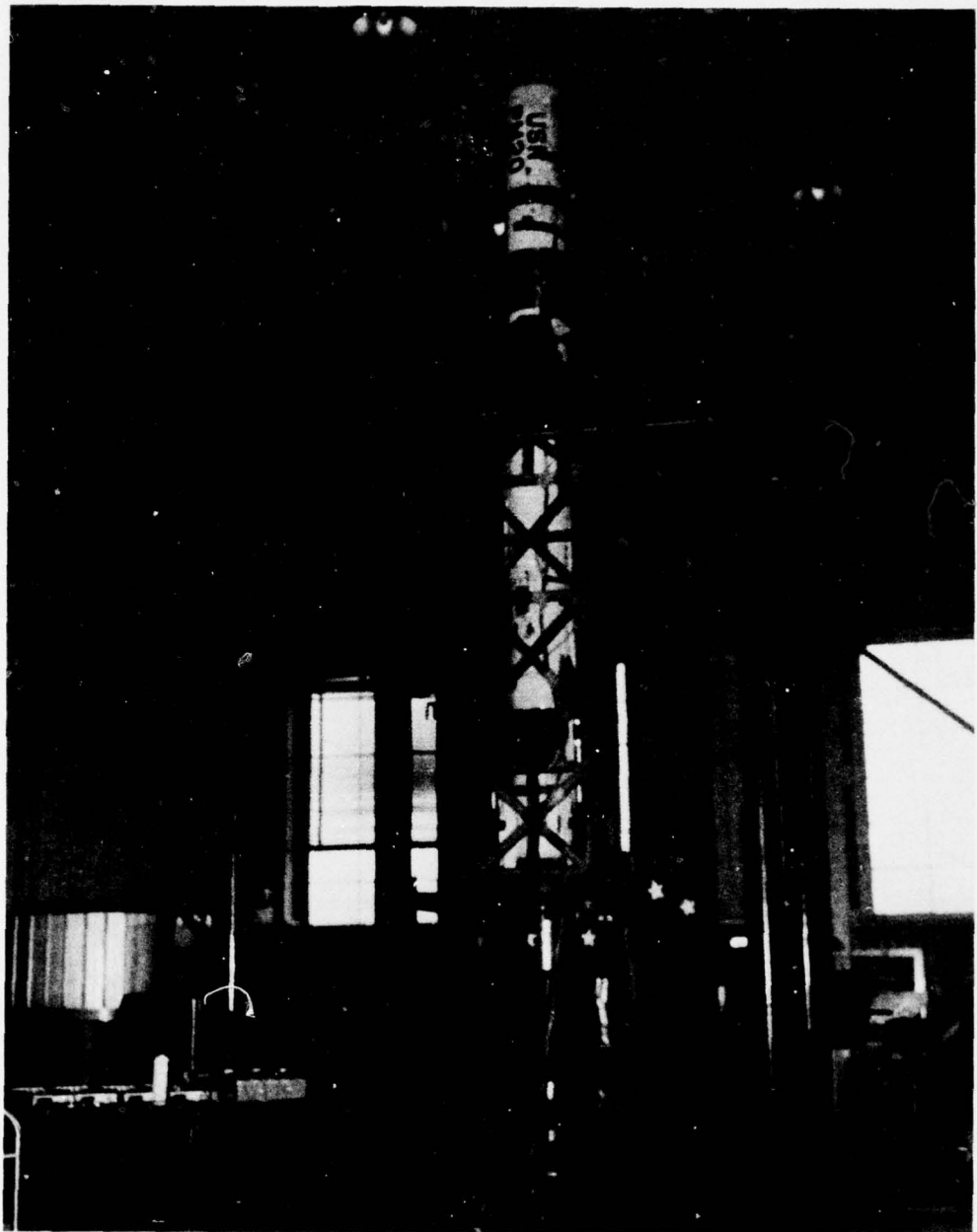
Figure 11. Test Item Mounted on the Dual Mode Machine in the Longitudinal Axis.

103
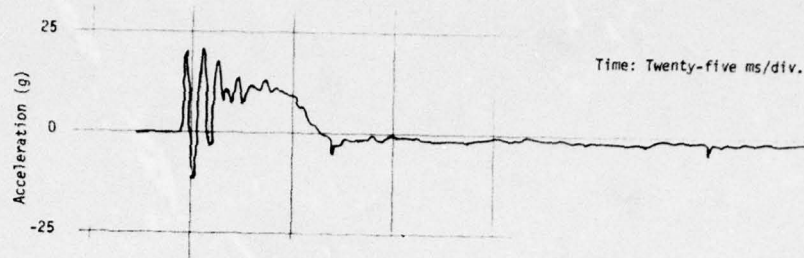
Figure 12.   x-Axis;   Front Launcher Lug;   Piezoresistive Accelerometer.
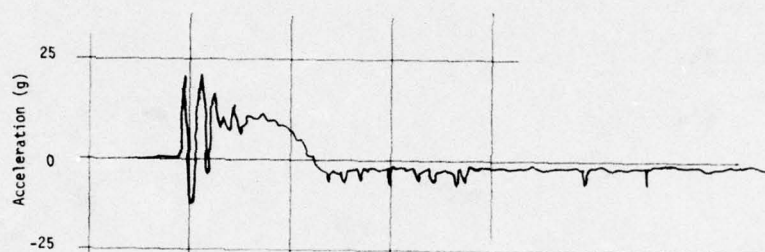
Figure 13.   x-Axis;   Front Launcher Lug;   Piezoelectric Accelerometer.
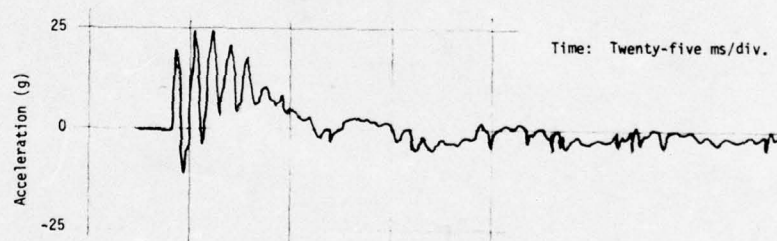
Figure 14.   y-Axis;   Front Launcher Lug;   Piezoresistive Accelerometer.
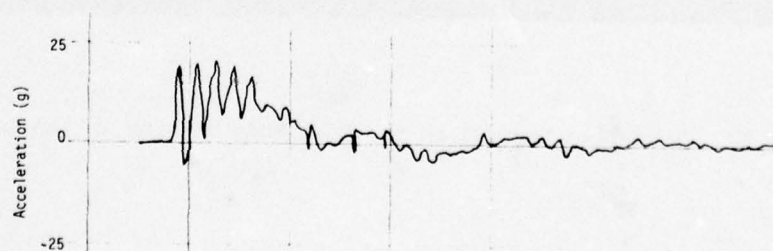
Figure 15.   y-Axis;   Front Launcher Lug;   Piezoelectric Accelerometer.

104
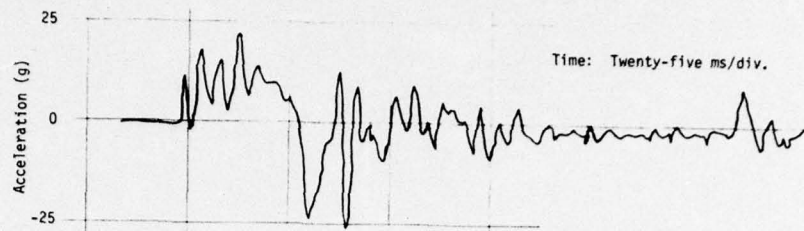
Figure 16.   z-Axis; Front Launcher Lug; Piezoresistive Accelerometer.
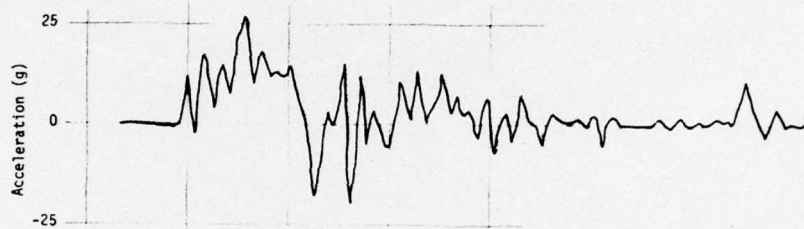
Figure 17.   z-Axis; Front Launcher Lug; Piezoelectric Accelerometer.
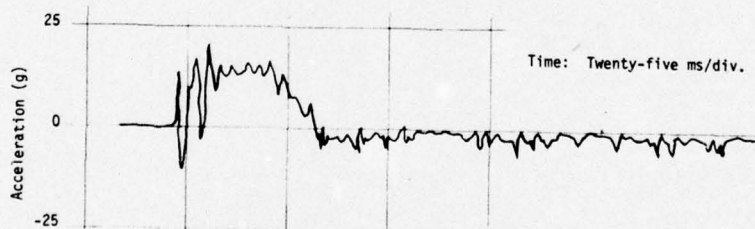
Figure 18.   y-Axis; Booster Launcher Lug; Piezoresistive Accelerometer.

Figure 19.   z-Axis; Booster Launcher Lug; Piezoelectric Accelerometer.

105

EVALUATION OF THE HARPOON MISSILE AIRCRAFT LAUNCH
EJECTION SHOCK ENVIRONMENT

James A. Zara, John L. Gubser
McDonnell Douglas Astronautics Corporation
St. Louis, Missouri

Allan G. Piersol
Bolt, Beranik and Newman Corporation
Canoga Park, California

and

W. N. Jones
Naval Weapons Center
China Lake, California

A series of ground launch ejections of a Harpoon missile were performed to establish and evaluate the Harpoon ejection shock environment. The acceleration response of the missile was measured at 30 locations during various simulated ejections from an MAU-9A and an Aero-7A rack. The data were reduced to acceleration shock spectra covering a frequency range from 100 to 10,000 Hz. The results of the study produced considerable information concerning launch ejection shock environments of general interest. For example, the shock spectra of the response at all locations typically displayed a sharp increase in level in the frequency range around 800 Hz, which corresponds to the estimated frequency of the first flexural ring mode of the missile shell. This frequency appears to be a significant dividing line for various other response characteristics. Specifically, increasing the ejector foot-missile clearance increased the response shock spectrum levels at frequencies above 800 Hz, but did not significantly increase the levels at lower frequencies. On the other hand, the response levels along the three orthogonal axes were not significantly different, on the average, at frequencies below 800 Hz, but were significantly different at the higher frequencies, with the highest response occurring in the vertical direction and the lowest in the axial direction. There was no significant difference in the missile response during ejections from the MAU-9A and Aero-7A rack. However, increasing the force of the ejection cartridges did significantly increase the shock response of the missile at frequencies below 800 Hz. Finally, the shock response of the missile decreased greatly with distance from the point of impact. For example, the peak acceleration levels at locations only 10 inches from the point of impact were less than 20%, on the average, of the levels measured at the point of impact.

INTRODUCTION

The dynamic response experienced by externally carried aircraft stores during launch ejection can pose a major reliability hazard to store equipment and structure. To assess this hazard to the Harpoon missile, an extensive test program was performed at the Pacific Missile Test Center Ground Ejection Test Facility, Point Mugu, Calif. using various ejection rack-cartridge configurations. The principal purpose of the test program was to evaluate the Harpoon launch ejection shock environment relative to the design criteria for this missile. However, the test data provided substantial amounts of information of general interest for aircraft stores which are force-ejected. This paper summarizes those results which are believed to be of general interest. The complete results of the study will be published at a later date as a U.S. Navy technical publication.

TEST CONFIGURATIONS AND PROCEDURES

The Harpoon missile (AGM-84A) is an antiship missile designed to be launched from aircraft, surface ships, and submarines. A diagram of the air-launched missile configuration is shown in Figure 1. The missile has a low-level cruise trajectory, active radar guidance, and terminal maneuvering to assure maximum weapon effectiveness. During cruise, it is powered by a turbojet sustainer engine.
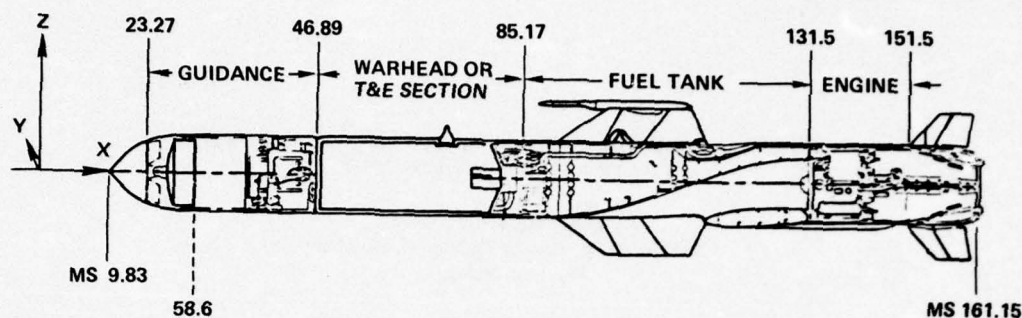
FIGURE 1. Diagram of the Harpoon Missile.

Test Missile Configuration

The missile configuration used for the tests simulated a prototype vehicle in size, weight, and center of gravity. No attempt was made to simulate wire bundles, valves, tubing, and other plumbing components; nor was secondary structure included, except where it was required to mount equipment packages. These items contribute very little mass and stiffness, and hence their absence should not significantly influence the shock response. All major equipment items were included in the test configuration. Some of the major components were structurally and mechanically the same as the real installation, but not necessarily a functional device. Other major items were simulated with the same mass, center of gravity, and mounting configuration as the component being represented.

Data Transducers

All acceleration measurements were made using Endevco Type 2292 and 2225 shock accelerometers in conjunction with Endevco Type 2713, 2718, and 2740 charge amplifiers. The accelerometers were mechanically mounted both externally and internally on the test missile, as shown in Figures 2 and 3. In addition to the accelerometers, a pressure transducer was used to measure ejector rack breech pressure. Breakwires were used to record the time of rack hook release. The times at which the ejector foot impacted and separated from the missile were monitored using an electrical contact strip.

Ejection Racks

Two different ejection racks were used for the tests; an Aero-7A-1 rack and an MAU-9A/A rack. Both rack assemblies consist of the following: a dual cartridge breech assembly, a hook assembly, a star assembly group, and a sway brace assembly. Both racks accept the same cartridge combinations; one Mk 2 Mod 0 and one Mk 1 Mod 2 cartridge

(hereafter referred to as the high-force cartridges) or two Mk 2 Mod 0 cartridges (hereafter referred to as low-force cartridges). Nominal force-time histories for the two cartridge combinations are shown in Figure 4.

Test Facility

The ejection tests were conducted on the Ground Ejection Test Facility at the Pacific Missile Test Center, Point Mugu, Calif. The missile was allowed to free-fall approximately 6 feet after ejection before being arrested by nylon rope. All of the signal conditioning equipment was adjacent to the stand and hard-wired to the missile. The data were recorded in a data acquisition van located adjacent to the test stand. Figure 5 illustrates the test setup.

Test Procedure

The missile was installed on the ejection rack simulating an actual aircraft installation. The cartridges were installed, the rack was armed, and a firing countdown initiated. The tape recorders were turned on approximately 5 seconds before the ejection. After each ejection the missile was inspected for damage and was then reinstalled on the ejection rack. The restraining ropes were replaced, the instrumentation was again checked out, precalibrated, etc., and the above sequence was repeated.

Eleven ejections were performed including calibration and instrumentation evaluation tests. Six of these tests provided data of interest for this paper, as detailed in Table 1. The other ejections were for calibration and instrumentation checkout.

Analysis Procedures

The acceleration transients measured at various locations on the Harpoon missile during the simulated ejections were evaluated in terms of significant transient events and peak

108
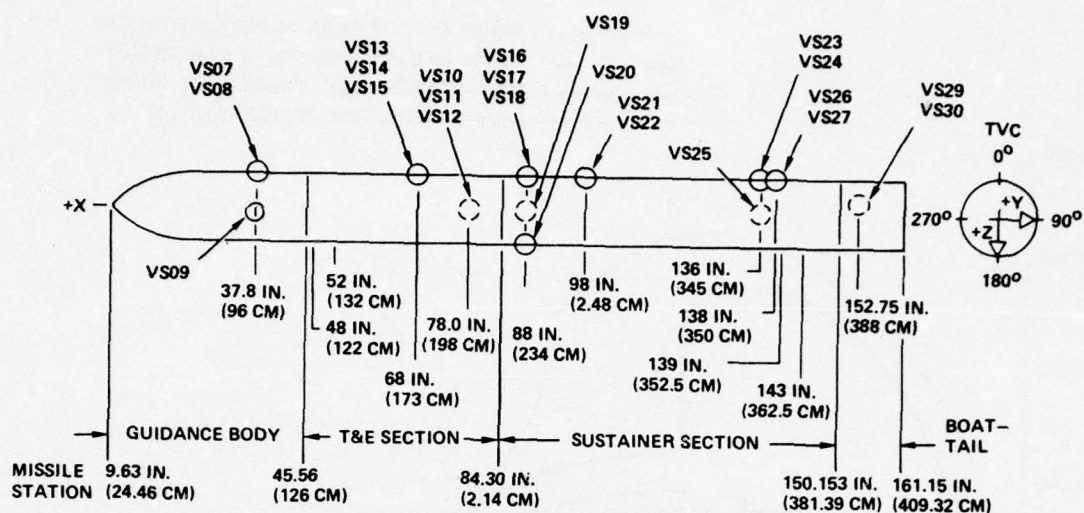
FIGURE 2. Location of External Accelerometers for Harpoon Ejection Tests.
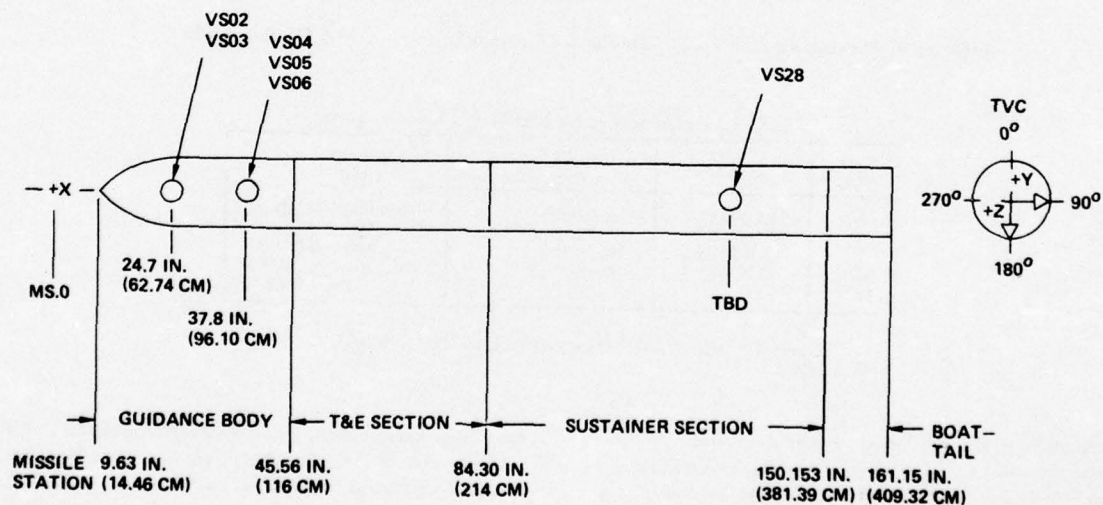
FIGURE 3. Location of Internal Accelerometers for Harpoon Ejection Tests.
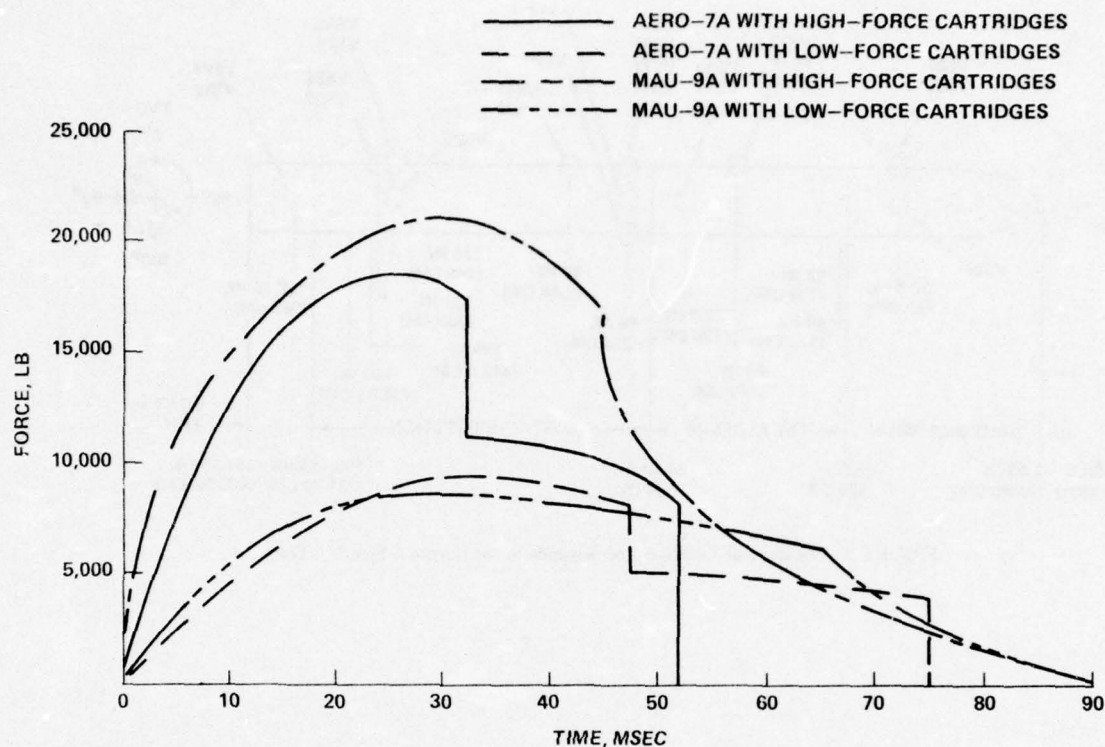
FIGURE 4. Nominal Ejection Force Time History for Aero-7A and MAU-9A Ejection Racks.

Table 1. Test Sequence for HARPOON Ejection Tests.

Test No.	Rack Used	Ejector Foot Clearance	Cartridges Used
4-5	MAU-9A/A	normal*	Two MK 2 MOD 0
6	MAU-9A/A	1/4 inch (.64 cm)	Two MK 2 MOD 0
9	AERO-7A-1	normal	Two MK 2 MOD 0
10-11	AERO-7A-1	normal	One MK 2 MOD 0 & One MK 1 MOD 2

*Normal clearance generally less than 1/16 inch (.16 cm)
(first detent).

acceleration levels. Beyond these direct analyses, the time history records were reduced to response (shock) spectra for more detailed evaluation using a Spectral Dynamics 320 shock spectrum analyzer. The shock spectra calculations were performed using two damping factors, 5% critical (damping ratio Q= 10) and 0.5% critical (Q= 100). Energy spectra were also computed and evaluated for selected cases, but these results are omitted from this paper for brevity and will be published in the U.S. Navy technical publication.

EXPERIMENTAL RESULTS

The basic results of the test effort consist of acceleration time histories, peak acceleration values, and shock spectra at the various measurement locations. Peripheral results include measurements of the rack cylinder pressure, the time of contact and separation between the rack ejector foot and the missile, and the time of the ejection rack hook release. Pertinent characteristics of these results are summarized in the following sections.

Time Histories and Related Parameters

Figure 6 shows a typical time history of the vertical acceleration response measured on the Harpoon structure near the point of the ejector foot impact during an ejection from the MAU-9A rack using the low-force cartridges. Note that the time history displays three distinct transient events, the first
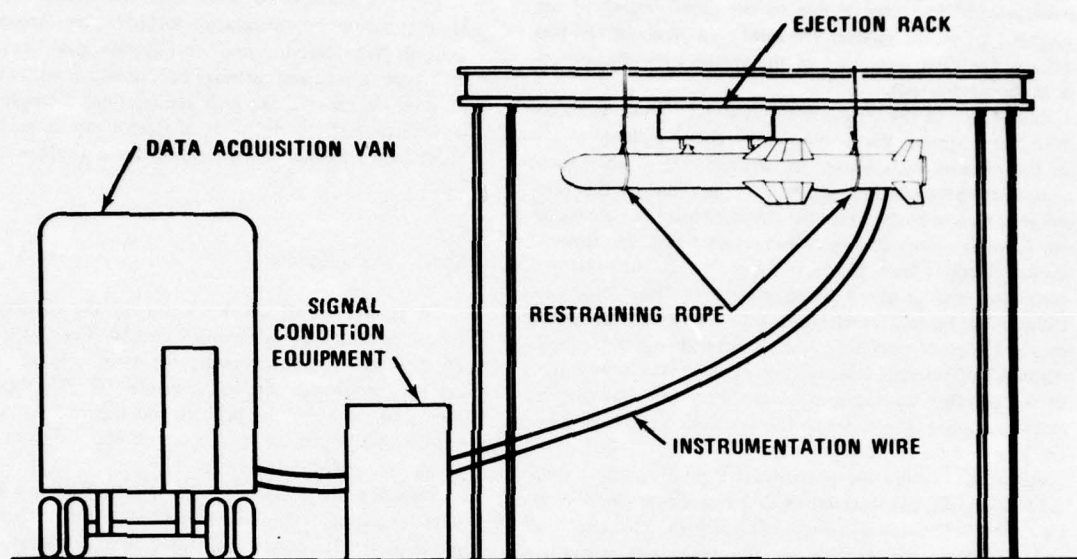
FIGURE 5. Harpoon Ejection Test Stand and Setup.
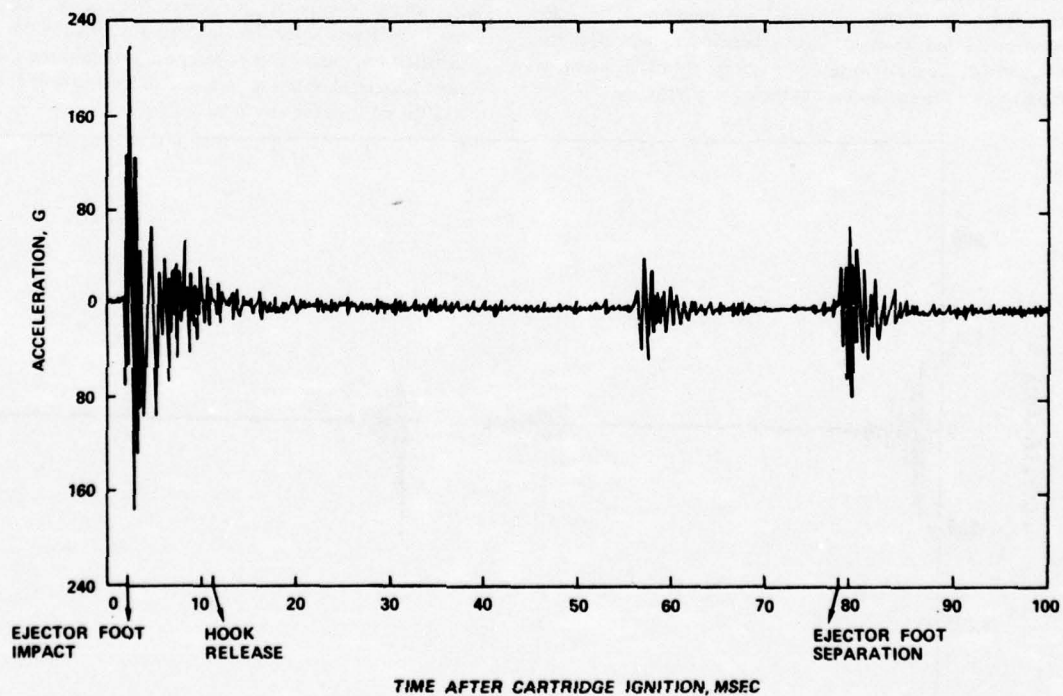
FIGURE 6. Acceleration Time History at Ejector Foot Location (VS18)
During Ejection Test No. 4 (MAU-9A Rack With Low-Force Cartridges).

111

initiating at about 2 msec, the second at about 56 msec, and the third at about 78 msec after cartridge ignition. The first event at about 2 msec is due to the initial impact of the ejector foot on the missile. The third event at about 78 msec reflects the final separation of the missile from the contact with the ejector foot.

The source of the second event at about 56 msec is uncertain, but it appears that it may be related to a discontinuity in the ejection rack thrust, or perhaps even a momentary separation between the ejector foot and the missile. The event is present in the time histories at all locations during all ejections. It occurs at about 47 msec after cartridge ignition during ejections from the Aero-7A rack with the low-force cartridges, and at about 39 msec with the high-force cartridges. The vertical acceleration time history for the latter case at the point of ejector foot impact is shown in Figure 7. Although of uncertain origin, this event between the initial impact and final separation is assumed to be physically significant and hence is included in the calculation of shock spectra.

At locations more widely separated from the point of ejector foot impact, the acceleration time histories are more complex. This is illustrated in Figure 8, which shows the vertical acceleration response measured on the guidance section structure during the same ejection that produced the data in Figure 6. Note that the same three events seen in Figure 6 are present at this location as well, but the responses have lower peak levels and are more spread in time. In particular, the initial transient starting at about 2 msec appears to maintain its strength up to about 15 msec, and then builds up again between 20 and 25 msec. This is believed to represent the influence of flexural waves propagating from the point of impact down the missile shell at their group velocity.

Peak Acceleration Results

The peak values of the acceleration time histories recorded at the various measurement locations are presented in Table 2. Note that the peak acceleration levels vary greatly with type of rack and cartridge size, as well as with structural location. In general, the peak accelerations diminish rapidly with distance from the point of ejector foot impact, as will be discussed further in the section titled Evaluation of Results.

Shock Spectra Results

A typical set of shock spectra for the acceleration response is presented in Figures 9 and 10. The two spectra in Figure 9 are maximax results for two different damping ratios, specifically, $Q = 10$ and $Q = 100$. The spectra in Figure 10 represent the positive and negative shock spectra for $Q = 100$. All of the spectra were computed from the time history presented in Figure 7.

Referring first to Figure 9, the spectra display a sharp rise with frequency in the range around 800 Hz. The first flexural mode of the Harpoon missile shell structure is estimated to be at about this frequency. Hence, the spectral characteristics of the shock response are consistent with the dynamic properties of the missile.

Now referring to Figure 10, it is seen that the positive and negative shock spectra of the transient are similar at frequencies above 300 Hz. At the lower frequencies, the positive spectrum levels sometimes exceed the negative levels by a significant amount. This reflects the fact that the basic transient associated with the rack ejector foot striking the missile is in the positive (downward) direction.
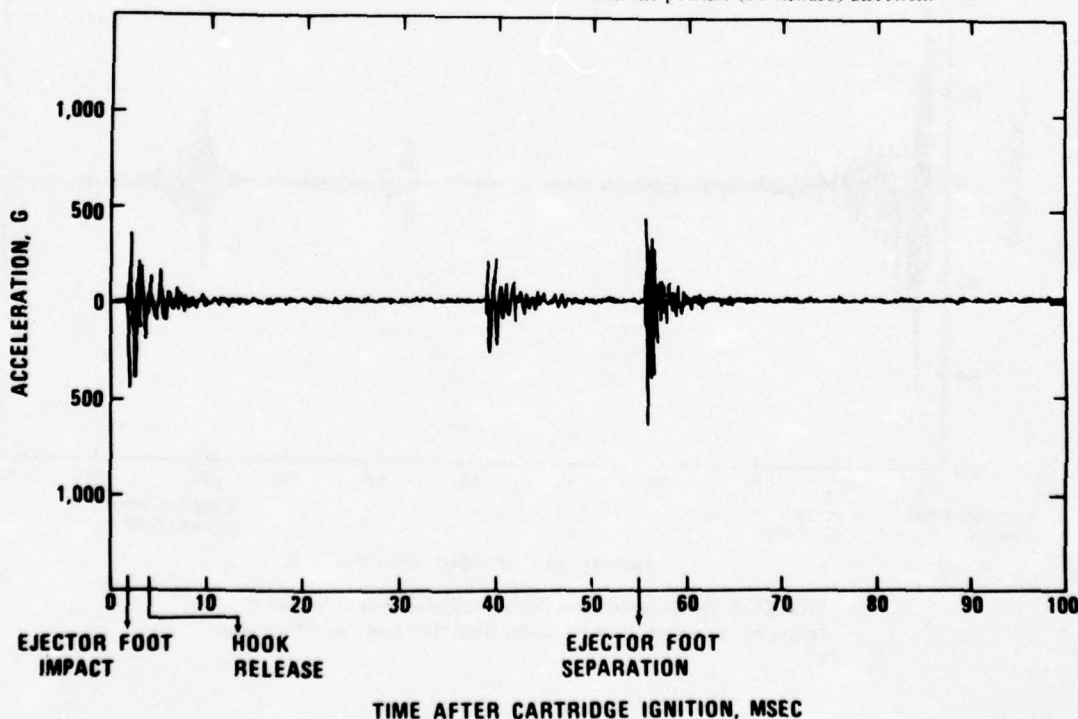
FIGURE 7. Acceleration Time History at Ejector Foot Location (VS18) During Test No. 11 (Aero-7A Rack With High-Force Cartridges).

112
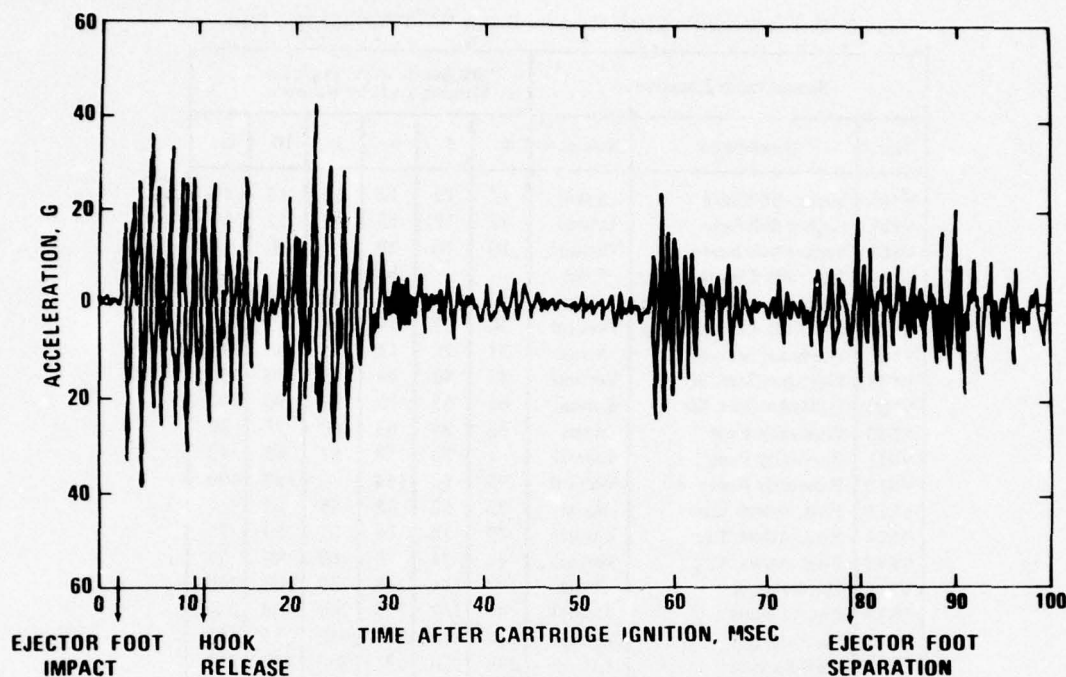
FIGURE 8. Acceleration Time History at Guidance Section Location (VS08)
During Ejection Test No. 4 (MAU-9A Rack With Low-Force Cartridges).

EVALUATION OF RESULTS

Various aspects of the test results are of interest, including
(1) variations among repeated trial ejections, (2) variations
with ejector foot clearance, (3) variations with rack type,
(4) variations with cartridge size, (5) variations with measure-
ment direction, and (6) variations with measurement loca-
tion. Such variations were investigated using the shock
spectra results and the peak acceleration data summarized in
Table 2. To permit the evaluations to be performed in an
efficient manner, the shock spectra of interest were first con-
verted to average levels in contiguous 1/3-octave bandwidths.
Both the shock spectra values and the peak acceleration val-
ues were also converted to dB referenced to 1 g
(dB = 20 log g). This was done so a given percentage differ-
ence in acceleration values would be weighted equally in the
statistical studies, independent of the absolute acceleration
values. All statistical evaluations were performed using the
well-known University of California at Los Angeles Biomedi-
cal Department (BMD) statistical data analysis programs.

It should be mentioned that many of the evaluations in-
volve comparisons of different cases based upon average
shock spectra values. These average spectra were computed
separately for each 1/3-octave band by averaging over all lo-
cations where data were available for the cases being com-
pared in that plot. Due to the wide dynamic range of the
shock spectra data, accurate shock spectra values were not
always retrieved at all locations, particularly in the frequency
range below 1,000 Hz. Since this problem was most common
at those locations displaying relatively low response levels,
the average values computed in the frequency range below
1,000 Hz often tend to be biased upwards. However, in any

given figure to follow, the same locations were used for all
cases of interest to compute the average values in a given
1/3-octave band, and hence the results within that figure are
directly comparable.

Variations Among Repeated Ejection Tests

Referring back to Table 1, the test missile was subjected to
two identical ejections tests for each of two ejection rack-
cartridge configurations (MAU-9A rack with low-force car-
tridges and Aero-7A rack with high-force cartridges).
Referring to Table 2, the peak acceleration values measured
at the various locations on the Harpoon structure during
these repeated ejections under identical conditions display
reasonable agreement, on the average, as demonstrated in
Table 3. In both comparisons, the difference in the average
peak acceleration levels is not sufficient to be considered
statistically significant at the $a = 1\%$ level of significance,
based upon a conventional student "t" test of differences.

Now considering the shock spectra data, the shock spectra
values measured at specific locations on the missile some-
times differ between repeated tests by up to 2:1 (6 dB) at
certain frequencies. On the average, however, the shock spec-
tra for repeated tests are in good agreement (within antici-
pated statistical variations), at least in the frequency range
below 4,000 Hz. This is demonstrated in Figure 11, which
presents the average of the shock spectra values measured at
all locations for which data were available on the missile
during Tests No. 4 and 5 for Q = 10 and Q = 100. At frequen-
cies above 4,000 Hz, discrepancies between the average shock

113

Table 2. Peak Acceleration Levels Measured During HARPOON Ejection Tests.

Measurement Location			Peak Acceleration in g's For Various Tests by Number					
No.	Description	Direction	4	5	6	9	10	11
VS01	Seeker Bulkhead	Axial	12	12	12	13	15	19
VS02	Seeker Bulkhead	Lateral	12	12	15	15	13	14
VS03	Seeker Bulkhead	Vertical	10	10	20	–	30	20
VS04	MGU Flt. Control Ring	Axial	–	–	83	–	–	–
VS05	MGU Flt. Control Ring	Lateral	40	50	57	108	58	27
VS06	MGU Flt. Control Ring	Vertical	30	23	19	60	55	45
VS07	Guidance Sect. Str.	Axial	24	22	52	55	45	45
VS08	Guidance Sect. Str.	Vertical	43	40	64	65	110	98
VS09	Guidance Sect. Str.	Lateral	88	65	75	87	90	100
VS10	Proximity Fuse	Axial	52	34	63	60	75	50
VS11	Proximity Fuse	Lateral	–	30	50	57	63	40
VS12	Proximity Fuse	Vertical	90	84	144	–	160	100
VS13	Fwd. Attach Lug	Axial	32	42	38	55	60	–
VS14	Fwd. Attach Lug	Lateral	19	16	36	35	50	33
VS15	Fwd. Attach Lug	Vertical	42	34	78	60	94	55
VS16	Ejector Foot	Axial	100	116	248	250	260	240
VS17	Ejector Foot	Lateral	140	152	250	280	450	300
VS18	Ejector Foot	Vertical	218	176	368	500	625	650
VS19	T&E Sect. Str.	Lateral	248	200	576	600	420	970
VS20	T&E Sect. Str.	Vertical	205	224	315	400	660	–
VS21	Aft. Attach Lug	Axial	92	86	118	137	110	93
VS22	Aft. Attach Lug	Vertical	92	100	150	142	130	–
VS23	Engine Sect. Str.	Axial	30	22	42	33	30	80
VS24	Engine Sect. Str.	Vertical	52	40	80	85	65	70
VS25	Engine Sect. Str.	Lateral	72	46	100	65	55	50
VS26	Engine Sect. Str.	Axial	38	35	54	40	50	–
VS27	Engine Sect. Str.	Vertical	48	52	80	90	70	60
VS28	Sustainer Engine	Vertical	7	9	16	13	20	–
VS29	Control Fin Actuator	Axial	33	24	54	–	40	33
VS30	Control Fin Actuator	Radial	60	44	108	57	–	50

spectra values of up to 3.5 dB are observed. These discrepancies are slightly outside the range of expected statistical variations and may represent the sensitivity of the high-frequency response of the missile to the exact manner in which the ejector foot initially strikes the missile structure. In any case, the repeatability of the test results is considered acceptable.

Variations with Ejector Foot Clearance

Of the three ejection tests performed with the MAU-9A rack using the low-force cartridges (Tests No. 4, 5, and 6), Test No. 6 was conducted with the clearance between the ejector foot and the missile increased to 1/4 in. (.64 cm) from the normal 1/16 in. (0.16 cm) or less. The peak acceleration data in Table 2 indicate a significant increase in levels due to the increased ejector foot clearance. Specifically, the average of the peak acceleration with the increased clearance is 37.1 dB, as compared to 33.0 dB with normal clearance. However, most of this increased structural response with increased clearance occurs in the frequency range above

800 Hz. This fact is illustrated in Figure 12, which presents the average shock spectra of the response accelerations during Tests No. 4 and 5 versus Test No. 6 for Q = 10 and Q = 100. Note that the shock spectrum levels for the increased clearance case are no more than 1.8 dB higher than for the normal clearance case at frequencies below 800 Hz. Above 800 Hz, however, the levels for the increased clearance case are over 5 dB higher at some frequencies, well beyond the limits of anticipated statistical variations. It must be concluded that the shock response of the missile structure at frequencies above 800 Hz is dependent upon the clearance between the ejector foot and the missile.

Variations With Q Factor

Shock spectra values for any given transient are, of course, a function of the damping ratio used; a smaller damping ratio (larger Q) will produce larger shock spectra values. This dependence on Q for the Harpoon shock data is illustrated in Figure 13, which presents the average spectra for all locations

114
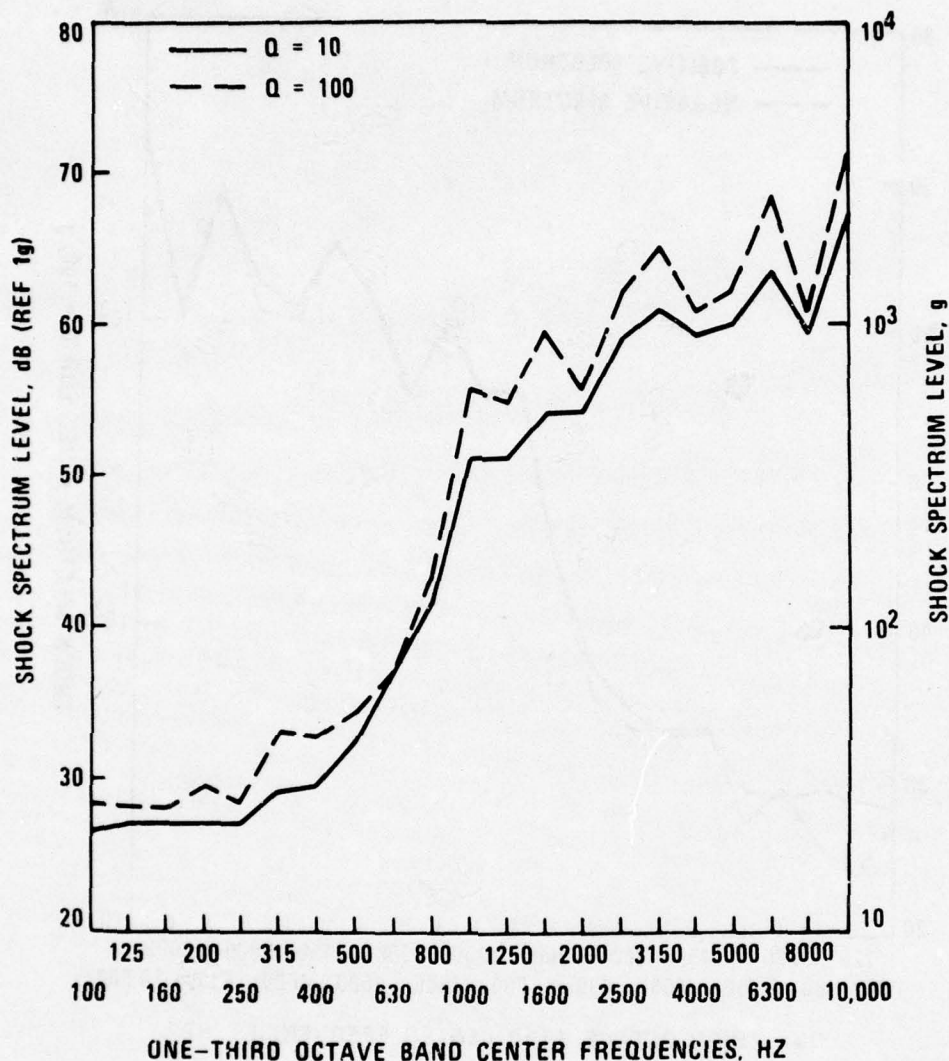
FIGURE 9. Maximax Shock Spectra for Q = 10 at Ejector Foot Location
(VS18) During Ejection Test No. 11 (Aero-7A Rack With High-Force Cartridges).

during Tests No. 4 and 5 computed for Q = 10 and Q = 100. Note that there is no significant statistical error in the indicated difference between the Q = 10 and Q = 100 curves, since both curves were computed from identical time history records.

From Figure 13 it is seen that the Q = 100 shock spectrum values exceed the Q = 10 values by less than 1.5 dB at frequencies below about 800 Hz. At higher frequencies, however, the difference increases to about 4.5 dB. This result indicates that the Harpoon structure tends to "ring" for a longer period of time at the higher frequencies; i.e., the

structural response to the ejection shock tends to decay much more rapidly at the lower frequencies. This is generally characteristic of the response of lightly damped structures to sharp impact loads.

Variations With Measurement Direction

Using the data from Tests No. 4, 5, and 6, the differences in the average shock spectra levels along the three orthogonal axes of the Harpoon during ejection from the MAU-9A rack

115
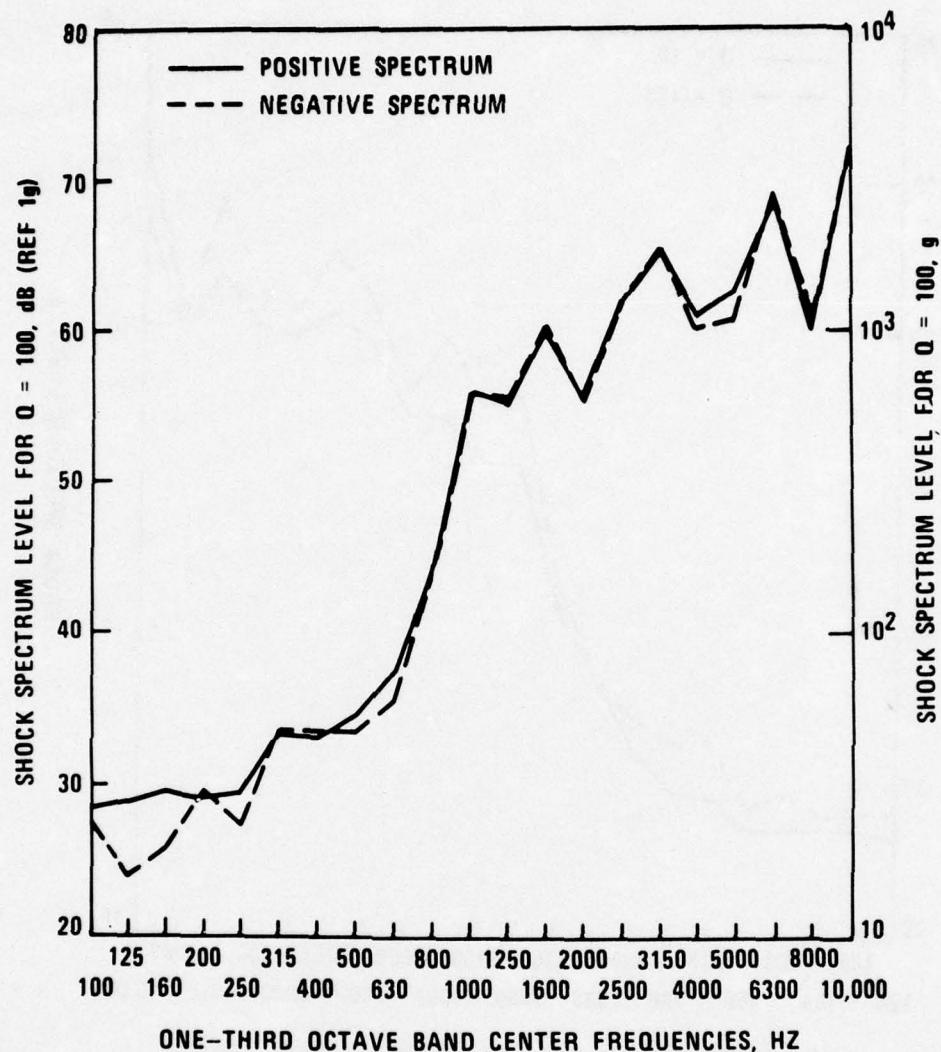
FIGURE 10. Positive and Negative Shock Spectra for Q = 100 at Ejector Foot Location (VS18) During Ejection Test No. 11 (Aero-7A Rack With High-Force Cartridges).

using the low-force cartridges are shown for Q = 100 in Figure 14. These results indicate that the shock spectrum levels at most frequencies are lowest in the axial direction and highest in the vertical direction, as would be expected for a cylindrical structure subjected to a shock load normal to its axis. However, the differences in the spectra values among the three orthogonal axes are not great, particularly at the lower frequencies. For example, in the frequency range below 800 Hz, the differences among the three axes are always less than 3 dB, as compared to anticipated statistical variations of about 2 dB for each measurement.

Variations With Type of Rack

In Figure 15 the average shock spectra values computed using Q = 10 for ejections from the MAU-9A rack with the low-force cartridges are compared to similar data for an ejection from the Aero-7A rack. Note that the general shapes of the average shock spectra for the two cases are similar, but the spectra values for the Aero-7A rack ejection are consistently higher by 1 to 3 dB at all frequencies, except for the lowest band at 100 Hz. Although this discrepancy is usually within the range of anticipated statistical variations for any

Table 3. Comparison of Peak Acceleration Levels
For Repeated Ejection Tests.

Test No.	Test Config- uration*	Average of Peak Acceler- ations (dB)	Average Differ- ence (dB)	Standard Deviation (dB)	Sample Size	Significant Difference at 1% Level (dB)
4	1	33.46	0.81	1.75	28	0.91
5		32.65				
10	2	37.80	0.94	3.51	23	2.05
11		36.86				

*1. MAU-9A rack with low force cartridges and normal
ejector foot clearance.
2. Aero-7A rack with high force cartridges and normal
ejector foot clearance.

given frequency band, the consistency of the discrepancy over all frequencies suggests the shock loads were actually higher by a small amount (1.3 dB on the average) for the Aero-7A ejection. It should be noted, however, that the MAU-9A ejections (Tests No. 4 and 5) were performed with an electrical contact strip mounted on the ejector foot to identify the times of contact and separation of the ejector foot and missile. This instrumentation was not used for the Aero-7A ejection being considered (Test No. 9). Evaluations of calibration ejection test data with and without the strip suggest that the presence of the strip might account for the minor differences indicated in Figure 15.

Variations With Size of Cartridges

The average shock spectra values computed using Q = 10 for an ejection from the Aero-7A rack with the low-force cartridges are compared to similar data for an ejection with the high-force cartridge combination in Figure 16. It should be mentioned that the dynamic range of the analysis for these measurements was quite good, and hence even the low-frequency values represent an accurate average of almost all the 30 measurements made of the missile structure.

It is clear from Figure 16 that the missile shock response is more severe for the ejection with the high-force cartridges, particularly in the frequency range below 800 Hz. Specifically, the average shock spectrum levels are consistently about 4 dB higher in this frequency range when the high-force cartridges are used. Noting that the nominal ejection force with the high-force cartridges is about twice as great as for the low-force cartridges, one might have expected the shock response levels to have doubled, i.e., to have increased by 6 dB. The lack of full 6-dB increase in levels with the doubling of ejection force probably reflects the influence of nonlinearities in the response of the missile structure to intense shock loads.

Variations With Structural Locations

The 30 measurements of the missile shock response during the various ejection tests were made at 10 specific structural locations over the length of the missile, as illustrated in Figures 2 and 3. It is now of interest to evaluate how the missile shock response varies from one location to another. This variation is illustrated in terms of peak acceleration levels measured at different locations versus the missile station number for the locations in Figure 17. The peak acceleration levels averaged over the available measurements at each location are shown separately for the three basic ejection rack-cartridge configurations tested.

The results in Figure 17 clearly demonstrate that the missile shock response diminishes very rapidly with axial distance from the point of impact, as would be expected. For example, from the point of ejector foot impact to the proximity fuse, a distance of only 10 inches, the peak acceleration levels during ejections from the Aero-7A rack drop by 16 dB (a ratio of over 6:1). From the ejector foot to the seeker bulkhead, the drop is over 28 dB (a ratio of 25:1). In other words, the seeker section at Station No. 25 sees acceleration peaks that are only 4% as great as those measured at the Station No. 88, the point of impact. About 10 dB of this reduction occurs over the last 10 inches between the guidance section and the seeker section.

This notable variation in the shock response with structural location is also illustrated by the shock spectra data shown in Figures 18a and 18b. Here, the shock spectra average over the available measurements at each location are shown for the ejection from the Aero-7A rack using the high-force cartridges. Note that the shock spectra for locations at Station No. 88 (the ejector foot and the test and evaluation section structure) far exceed the shock spectra at all other locations at all frequencies. The seeker section at the forward end of the missile displays a uniquely low shock
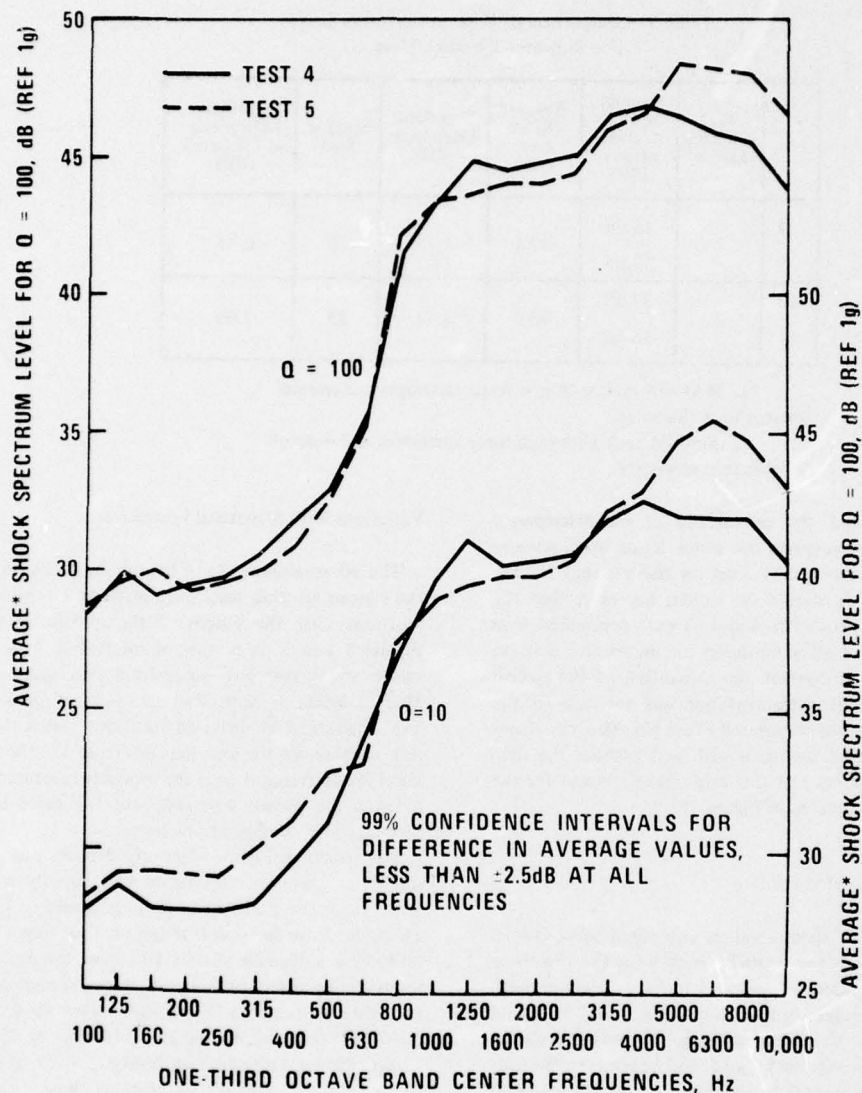
117

FIGURE 11. Shock Spectra Average Over All Locations for Repeated Ejections
From MAU-9A Rack Using Low-Force Cartridges.

response spectrum at frequencies above 200 Hz. The shock spectra at other locations scatter in between these two extremes.

CONCLUSIONS

The specific conclusions to be drawn from this study of the Harpoon missile response to simulated launch ejection shock loads may be summarized as follows:

1. The response of the missile is sensitive to the pre-ejection clearance between the ejector foot and the missile. Specifically, the average shock spectra of the acceleration response at frequencies above 800 Hz were up to 6 dB (100%) higher when the clearance was increased from normal (less than 1/16 in. (0.16 cm)) to 1/4 in. (0.62 cm).

2. The acceleration response shock spectrum levels computed for Q = 100 exceed those computed for Q = 10 by about 1 dB at frequencies below 800 Hz and about 4 dB at frequencies above 800 Hz.

FIGURE 12. Shock Spectra Average Over All Locations for Ejection From MAU-9A
Rack Using Low-Force Cartridges With Normal and Increased Ejector Foot Clearance.

3. The shock spectra of the acceleration responses are generally highest in the direction of separation and lowest in the axial direction. However, the differences among the three orthogonal axes are not significant in the frequency range below 800 Hz. At the higher frequencies, the vertical response is up to 4 dB (60%) higher than the axial response.

4. The response of the missile is about the same for ejection from the MAU-9A rack and the Aero-7A rack using similar cartridge configurations.

5. The response of the missile is higher when ejection cartridges of greater force are used. Specifically, when the nominal force of the ejection cartridges was doubled, the

119
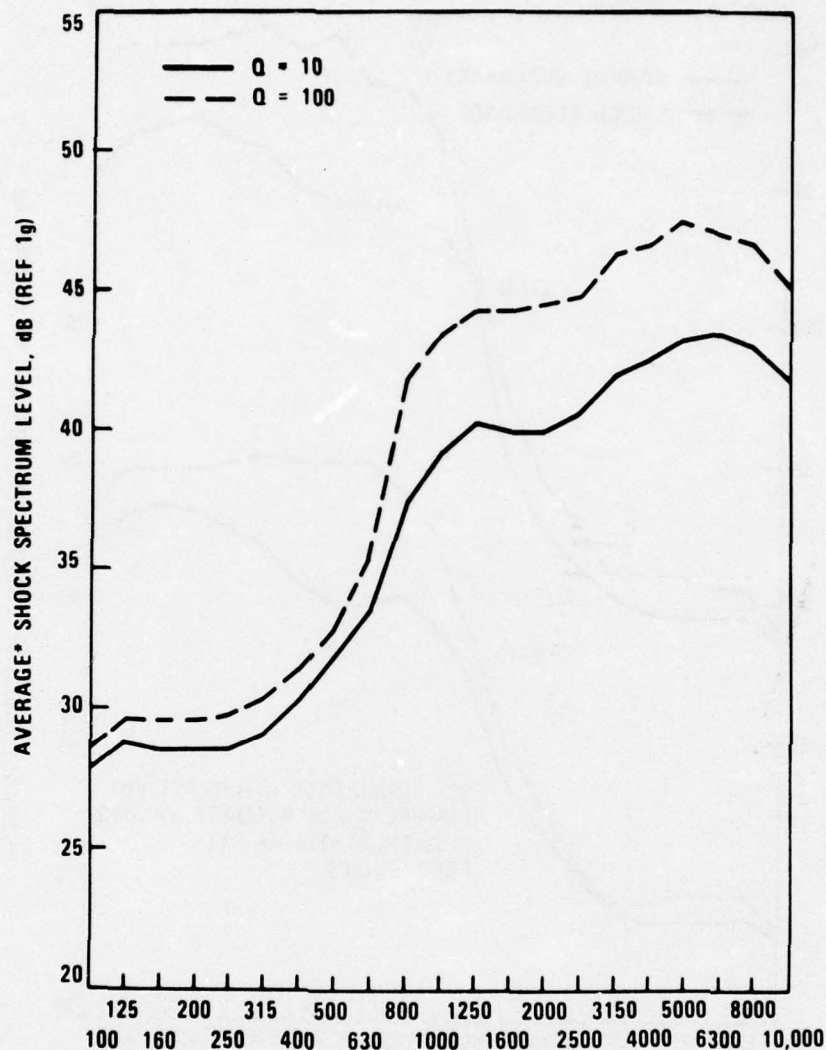
*NOTE: AVERAGE VALUES AT FREQUENCIES BELOW 1,000 HZ COMPUTED
OVER THOSE LOCATIONS OF MOST INTENSE RESPONSE ONLY.

FIGURE 13. Q = 10 and Q = 100 Shock Spectra Averaged Over All Locations
for Ejections From MAU-9A Rack Using Low-Force Cartridges.

average shock spectrum of the acceleration responses increased by about 4 dB (60%) in the frequency range below 800 Hz. At the higher frequencies, however, the shock spectrum levels increased by less than 2 dB (25%).

6. The response of the missile falls off dramatically with distance from the ejector foot impact location. For example, the peak acceleration levels at a location only 10 inches (25.4 cm) from the point of impact were about 16% of those measured at the impact location. The lowest levels were measured in the seeker section near the nose of the missile,

where the peak acceleration was only 4% of that measured at the impact location. In terms of shock spectra, the levels in the seeker section were 20 to 30 dB lower than at the ejector foot impact location, indicating that the ejection shock is strongly attenuated with distance.

The above specific conclusions apply rigorously to the Harpoon missile only. However, most of the conclusions could probably be applied to a new missile of similar construction, assuming that differences in key structural parameters are properly taken into account. For example, the

AVERAGE* SHOCK SPECTRUM LEVEL FOR Q = 100, dB (REF 1g)

—— VERTICAL
— — LATERAL
•••••• AXIAL

99% CONFIDENCE INTERVALS FOR
INDIVIDUAL AVERAGE VALUES;
LESS THAN ±2dB AT MOST
FREQUENCIES

ONE-THIRD OCTAVE BAND CENTER FREQUENCIES, Hz
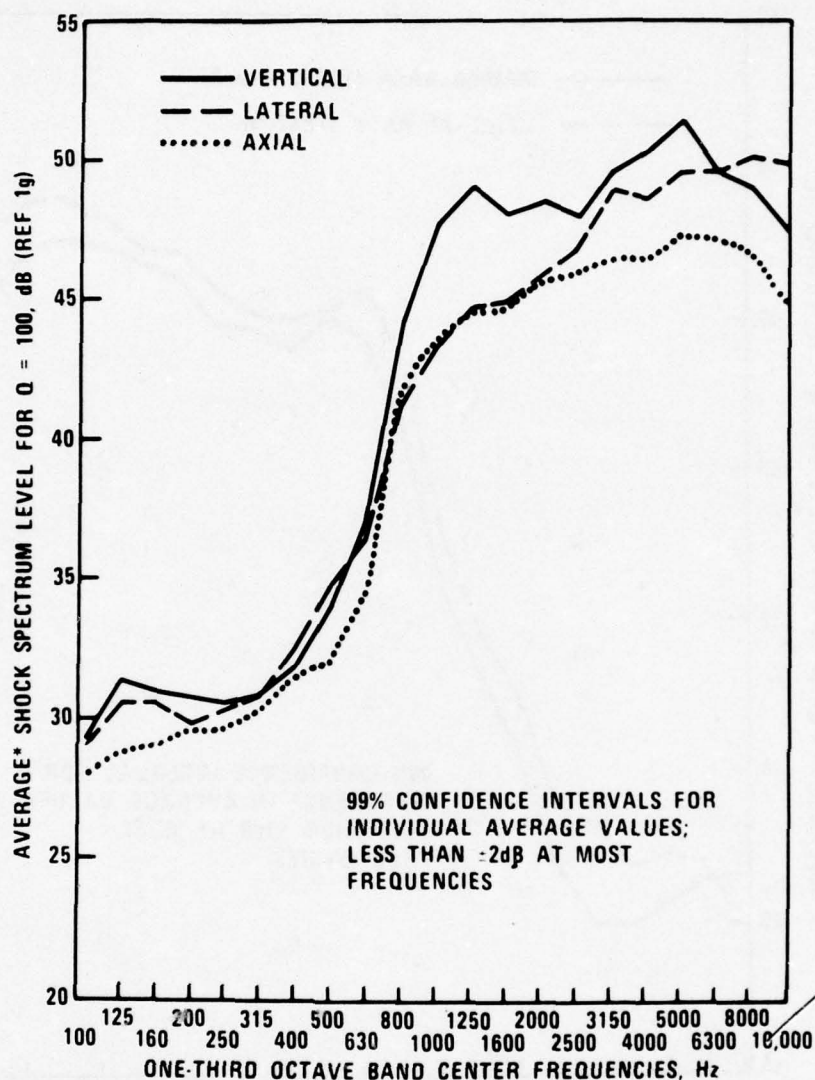
*NOTE: AVERAGE VALUES OF FREQUENCIES BELOW 1,000 Hz COMPUTED
OVER THOSE LOCATIONS OF MOST INTENSE RESPONSE ONLY.

FIGURE 14. Q = 100 Shock Spectra Averaged Over All Locations Along Each
Orthogonal Axis for Ejections From MAU-9A Rack Using Low-Force Cartridges.

first flexural ring mode of the missile shell (about 800 Hz for Harpoon) appears to constitute an important parameter in establishing the response characteristics of the missile, as measured by a shock spectrum. Hence, conclusions 1, 2, 3, and 6 might be assumed in the preliminary design of a new missile by replacing the 800 Hz frequency with the estimated frequency of the first flexural ring mode of the new missile.

121
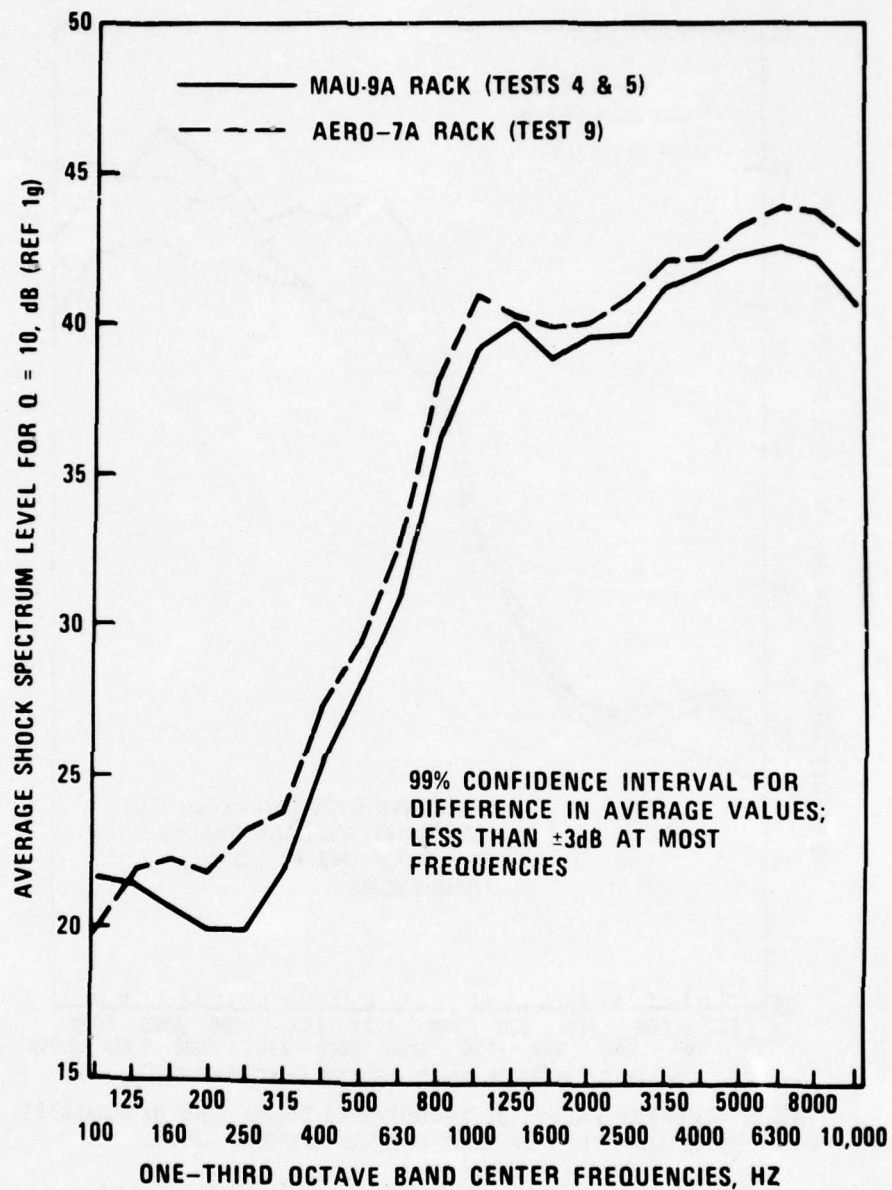
FIGURE 15. Q = 10 Shock Spectra Averaged Over All Locations for Ejections From MAU-9A and Aero-7A Racks Using Low-Force Cartridges.

122
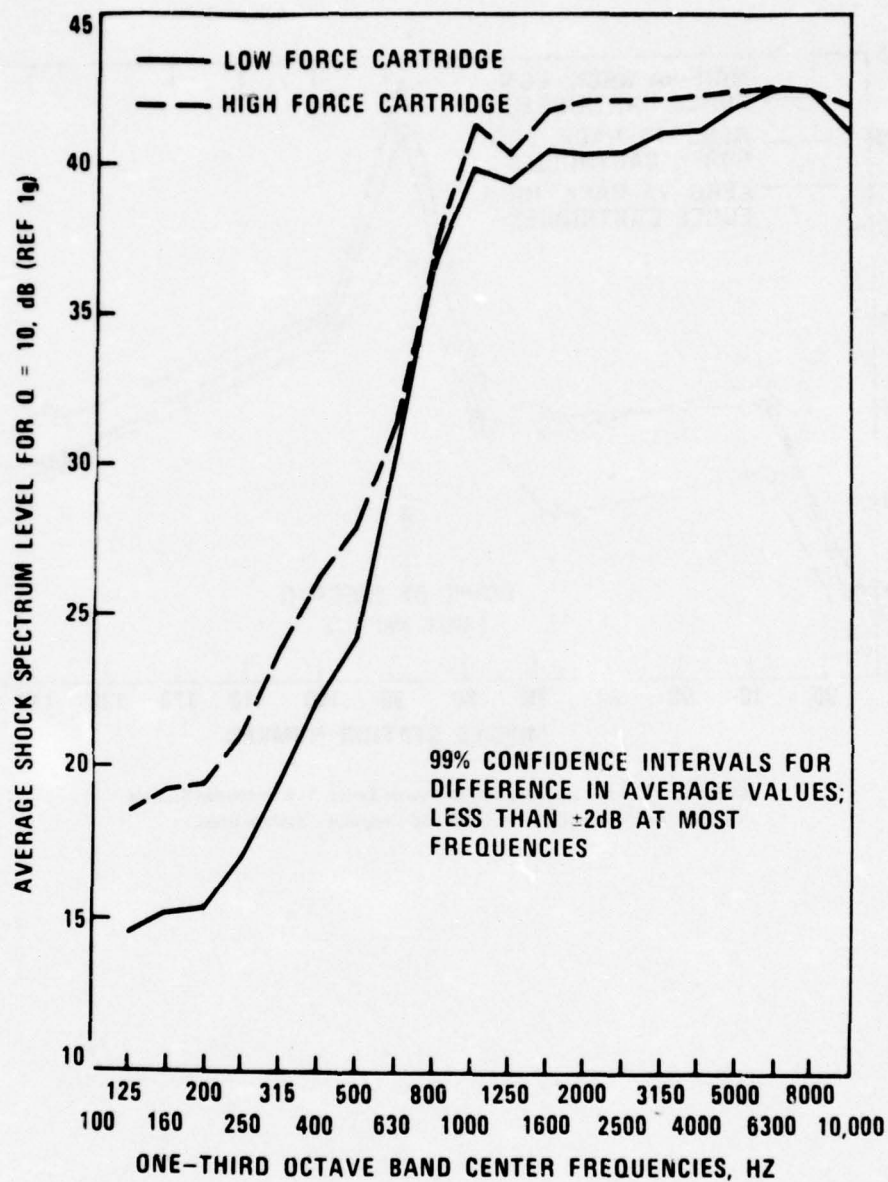
FIGURE 16. Q = 10 Shock Spectra Averaged Over All Locations for Ejections From Aero-7A Rack Using Low-Force and High-Force Cartridge Combinations.

123
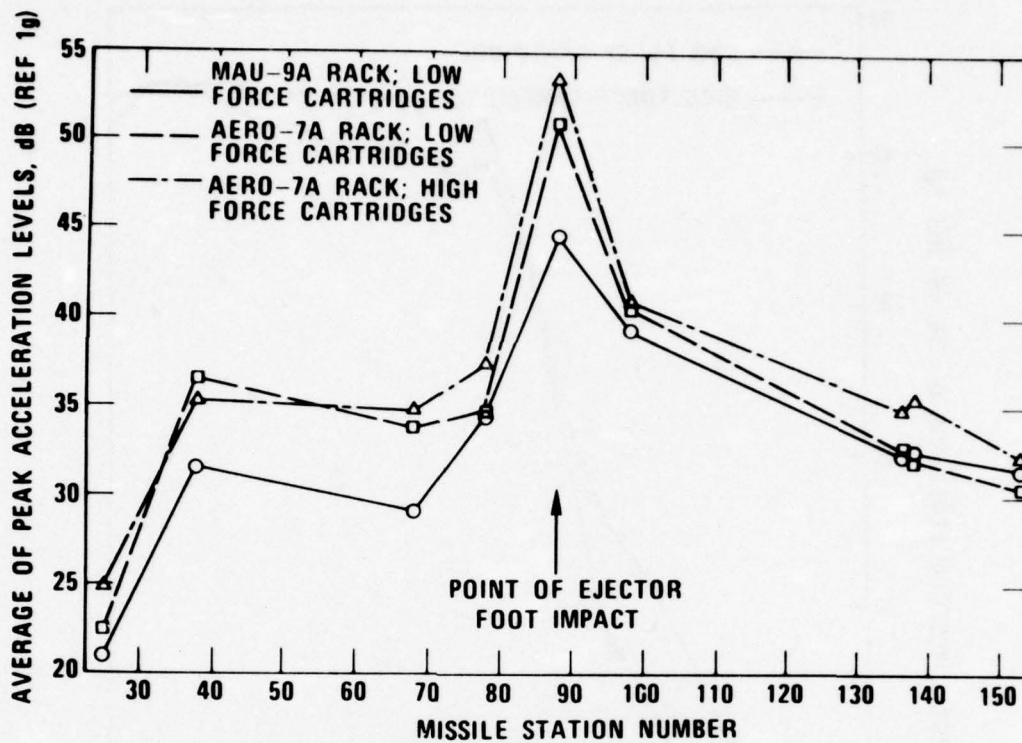
FIGURE 17. Peak Acceleration Response Levels Versus Missile Station Number for Various Ejection Rack and Cartridge Combinations.
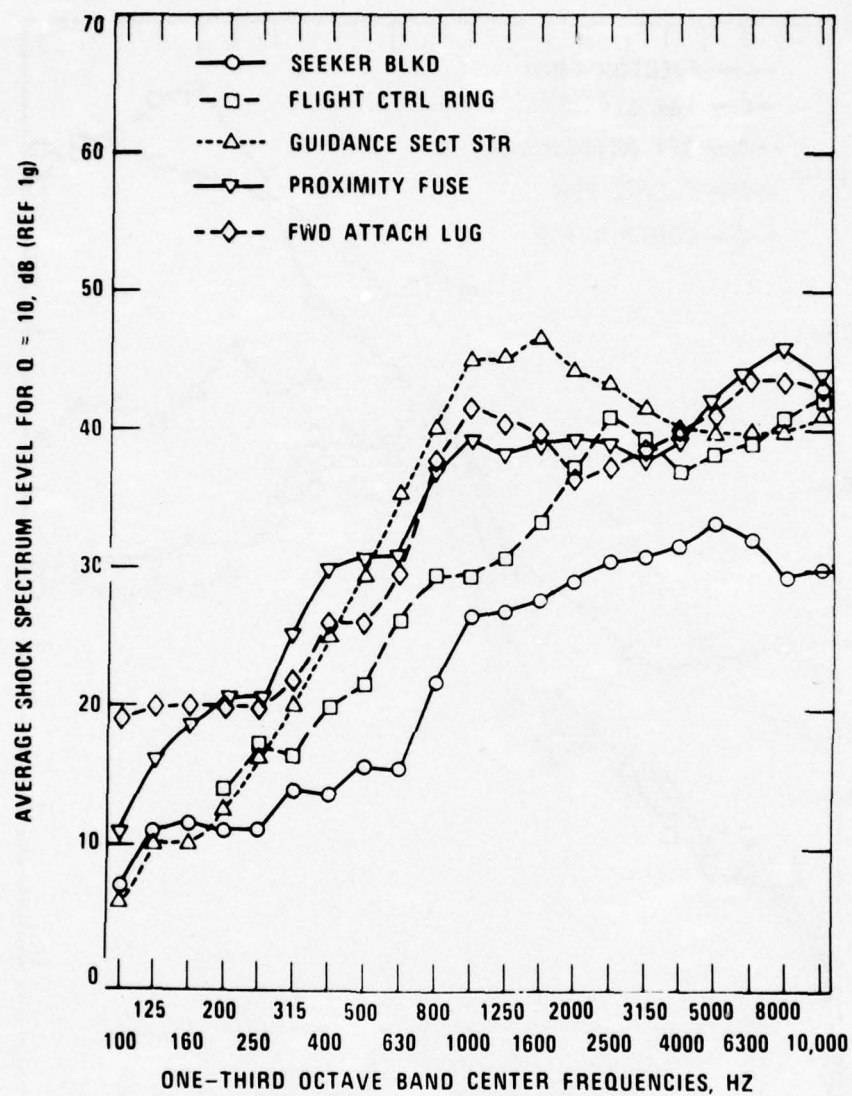
FIGURE 18a. Q = 10 Shock Spectra Averaged Over Three Axes at Various
Locations for Ejection From Aero-7A Rack Using High-Force Cartridges.

125
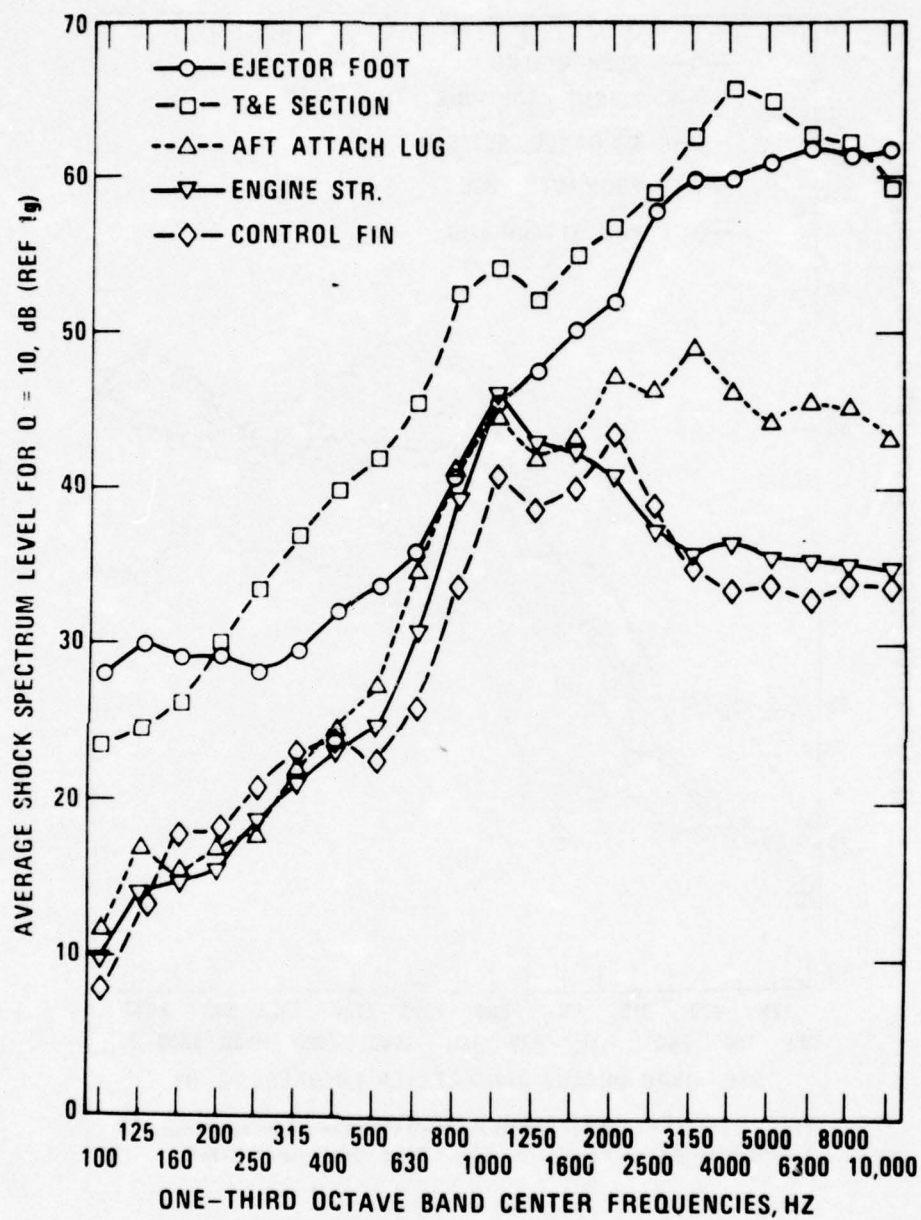
FIGURE 18b. Q = 10 Shock Spectra Averaged Over Three Axes at Various Locations for Ejection From Aero-7A Rack Using High-Force Cartridges.

126

Discussion:

Mr. Mustain (Rockwell International Space
Division): You showed a Q of 10 at one time
and then another time you showed a Q of 100
and that kind of mixes up your information,
if you were to write a specification for that
what would you use?

Mr. Zara: I would use a Q of 10 which is
5% damping.

ISOLATION AND DAMPING

THE MEASUREMENT OF DAMPING AND THE DETECTION OF

DAMAGES IN STRUCTURES BY THE RANDOM

DECREMENT TECHNIQUE

J. C. S. Yang and D. W. Caldwell
Mechanical Engineering Department
University of Maryland
College Park, Maryland

A technique called random decrement has been developed, which makes possible the computation of damping values and the detection of damage in structures when only response data is available. Damping ratios were computed using this technique for several modes of randomly excited panels, beams, and bones. These damping ratios compared satisfactorily to damping ratios which were computed from the power spectral density method. Standard randomdec signatures were established for all the structures. Damages were detected by observing the changes in the established signatures. Notches which simulated cracks were induced into two of the beams. The effects of these notches on the beams' signatures are presented.

INTRODUCTION

When a physical structure is subjected to random forces, internal vibrations are set up within the structure as it absorbs the energy imparted to it. In some cases, the energy imparted may cause stresses which exceed the strength limitations of the structure and which may result in a failure of the structure. To prevent the failure of a structure, structural damping needs to be more thoroughly investigated. Small cracks and localized failures of the structural elements often have a significant effect on the vibration response characteristics of the structure long before they are significant enough to be visually detectable. Damping is one of the characteristics which changes. Damping is the means by which structures absorb energy and significant changes in damping are therefore very meaningful. The precise measurement of damping is therefore highly important to the economic design and reliable analysis of large structures.

Various attempts have been made to provide means for obtaining structural damping information used in the design of structures and used in the monitoring of the response to the applied forces. Although various types of apparatus and techniques are available for measuring structural responses to random vibrations, the data obtained is usually so complicated that an observer cannot readily determine when a significant change in the structural response occurs. Most of these techniques are only suitable for use under controlled laboratory conditions and are of little use for structures in service.

A simple, direct, and precise method is needed for translating the structural response time history into a form meaningful to the observer. The method chosen to examine the structure should be sensitive to changes in the natural frequencies and the damping. Power spectral density has been considered, with damping measured by the half-power point bandwidth method, but this was found to have a large measurement variance, especially when the bandwidth was small. In addition, when two modes are close, this method cannot be applied. Erroneous answers were obtained when assumed linear systems were actually nonlinear, a problem which could not be detected unless the input was also measured. The autocorrelation function was investigated as an alternative wherein damping data was obtained from the logarithmic decrement. The problem with the use of autocorrelation signatures is that the level of the curve is dependent on the intensity of the random input, and in a natural environment this can seldom be measured or controlled. If the structure is a linear system, the level changes can be compensated for by normalizing the curves, but if the structure is nonlinear (as is often the case), a different signature will be obtained with each level of excitation. Therefore, correlation functions can only be used with linear systems and by knowing the input.

Another area that needs development is the detection of crack initiation and growth. Present methods of crack detection include visual inspection and acoustic emissions. Although acoustic emissions can detect flaws in assembly line comparisons, it is highly unlikely that

129

under conditions of high ambient noise level such as is encountered in aircraft flight that this method can be applied. In addition, it is obvious that visual inspections are useless when cracks develop within the interior of a structural material.

In the present report a technique called "Random Decrement" is presented which makes possible the computation of damping values and the detection of damage in structures when only response data is available.

RANDOMDEC ANALYSIS

A technique called "Random Decrement" analysis has been developed and explored initially by Cole [1], which advances the state-of-the-art in the detection of crack development and extension in structures subjected to random excitation when only response data is available. A brief summary of the method is given here.

The techniqe, or method of analysis, requires as input the time history of the response of a system subjected to random excitation. This time history is divided into short segments, with each segment starting with an amplitude Y_s. This amplitude is usually chosen to be some fraction of the standard deviation of the signal. The segments are ensemble averaged to yield the signature $\delta(\tau)$ which is a time variation of the parameter, say acceleration, strain, etc., composing the time history. The averaging process removes the effect of the random excitation and leaves a signature representing the free vibration characteristics of the structure. The averaging process also yields a signature with an initial slope of zero since the segments are divided equally into segments of positive and negative initial slopes. The method of extracting a randomdec signature is shown in Figure 1.

The degree to which the random excitation is removed from the signature depends on the number of segments averaged. Generally, good repeatability is obtained with about 500 segments. If high frequencies are being studied, say 5 KHz, a few seconds of data are needed to obtain an accurate signature.

An important part of the analysis is the filtering that is done to isolate certain frequency ranges. The time history is usually bandpass filtered; so the resulting signature shows the characteristics of the structure for that frequency bandwidth. To obtain damping, only the natural mode of interest is analyzed. This effectively reduces the response to that of a single degree of freedom system. Once the signature is obtained, damping can be found by the classical logarithmic decrement method. In addition, because of the fixed selection level, Y_s, it was shown that the scale and form of this signature is always the same even though the random excitation may change intensity. This independence of input intensity makes this method very attractive to use as a failure

detector.

To detect flaws, a standard randomdec signature is established for the undamaged structure. Then, a flaw such as a fatigue crack will introduce an additional degree of freedom for the structure and the frequency of the flaw mode will decrease as flaw size increases. Thus when the flaw frequency couples with the modes within the analyzed bandwidth, the signature will change shape. An additional mechanism which causes distortion of the signature shape is the frictional damping caused by the interaction of the crack faces. One important characteristic of this method is that it requires no knowledge of the structural excitation other than the fact that it is random.

EXPERIMENTAL PROCEDURE

A. Analog Signal Recording

Three different types of structures were tested: rectangular cross-section beams, bones, and thin square panels. Table 1 contains descriptions of the specimens. Several different bones were tested. However, their first natural frequencies were at about 2 000 Hz. The digitizing rate used was too slow to obtain randomdec signatures of sufficient smoothness to measure damping for this high frequency. Therefore, a mass was mounted on top of the bones to lower their first natural frequencies.

Each beam was clamped horizontally in the center and mounted on an exciter. Accelerometers were used to pick up the input excitation and the output response of the beam to flexural vibration. An example of a mounted beam is shown in Figure 2.

Each bone was mounted vertically on a cylindrical hollowed out aluminum base which was bolted to the shaker, see Figure 3. Accelerometers were positioned inside the aluminum base and on the top end of the bone to pick up the input excitation and to sense the response of the bones to the longitudinal vibrations.

The panels were bolted with approximately clamped boundary conditions between two like reverberation chambers. The mounted panels can be seen in Figure 4. The panels were excited with a diffuse sound field with a sound pressure level of 105 dB re 0.0002 microbar. The excitation was provided by a loudspeaker located within one of the chambers. A condenser microphone was also placed within this chamber to record the signal which is representative of the random acoustical pressure variations occurring on the side of the panel. A miniature accelerometer was used to sense the response. This small, light (0.4 gram) accelerometer was utilized in order to minimize the effect of loading the structures.

A random noise generator, connected to a power amplifier was used to drive the shaker and loudspeaker. Each excitation signal used

was band-limited white noise. The white noise was low pass filtered at a cutoff frequency of about 3,500 Hz. This filtering was done to prevent the folding over of frequencies above the nyquist frequency during later digitization, and also to usefully utilize the tape recorder's full dynamic range.

Before the input and output signals were tape recorded, they were passed through Audio Frequency Spectrometers. These spectrometers were used to condition the signals and provide a rough look at the content of their frequency spectrums which were displayed by a Level Recorder. These spectrums were used to identify resonances and examine the low pass filter characteristics. Subsequently, the input and output signals were recorded on the tape recorder.

B. Digital Signal Processing and Damping Measurement

Because a digital computer cannot be used to store and operate on a continuous-time signal, it was necessary to change the analog signals into discrete-time signals. The analog to digital converter which was used had a sampling rate of 10,000 samples per second.

Power spectral density of both the input excitation and the output response was calculated. Each power spectral density resulted from 18 averaged 1024 point fast Fourier transforms. Subsequently from these results the structure's transfer function was calculated and graphically displayed. From the transfer function plot, the natural frequencies and half power bandwidths of the resonances were measured. The damping ratios were then calculated.

The same data as above was also used to calculate the randomdec signatures. Before applying the randomdec procedure to the data, the frequencies outside the narrowband time history of interest were excluded. This was accomplished by the convolution of a digital filter within the randomdec program with the data. After the narrowband data had been calculated, their mean and standard deviation were computed. The mean value was used to change the data values to have a zero mean. If this had not been done the signature would not have ended at zero as in Figure 1. A fraction of the standard deviation was used as the selected threshold level. Each time the signal values were found to cross this level, a new segment was summed to previous segments, thus calculating the randomdec signature. When the digital values of the signature were computed, a plot routine within the program displayed the curve. From this decaying sinusoidal signature, the damping ratio for various numbers of cycles were calculated by the logarithmic decrement method. The damped natural frequency was calculated from an average of the periods of oscillation.

C. Detection of Damage

To see the effect that damage might have on a structure's standard signature, notches which were assumed to simulate cracks were cut into Beams 3 and 4 as shown in Figure 5. The notches were cut with a saw blade which was approximately 0.10 cm wide. Both beams were notched 1.27 cm from the supporting fixture.

The notch in Beam 4 was cut into the full 1 inch width of the beam to a depth of 0.05 cm. Signatures from the beam's response were computed with this notch and also for five more saw cuts which extended the notch to the total depth of 0.30 cm.

Beam 3 was used to find the effect which a notch cut into a beam's side would have on it's signature. This was not expected to have quite the pronounced result on the signature as might be expected from Beam 4. However, torsional modes should be introduced by this type notch. Six damage signatures were taken for this beam from the effects of six 0.20 cm saw cuts, which made the total notch width 1.50 cm.

RESULTS

The computer generated power spectral density and transfer function curves of the response and the excitation of a typical damped beam are shown in Figure 6 and 7. The narrowband response of one of the resonant peaks of the response was used to create the randomdec signature as shown in Figure 8. Comparisons of the transfer function and the randomdec signature damping ratio results for all the specimens are given in Table 2.

Figure 9 shows three randomdec signatures extracted from different sections of the same time history. Each of these signatures contain approximately 500 segments. These curves show the portion of the length of Beam 4's standard signature which can be considered stable enough from which to detect damage. Figures 10 and 11 show the randomdec signatures as beams 3 and 4 are damaged.

DISCUSSION AND CONCLUSIONS

The limitations imposed by the sampling rate of the digitizer and the digital filter characteristics at low frequencies considerably reduced the number of damping ratio comparisons which were available. However, the results from Table 2 show that for most of the comparisons which were made, the damping ratios taken from the randomdec signatures and transfer function plots differed by less than a factor of two. Furthermore, the few comparisons which did differ by more than a factor of two were associated with very low values of damping.

131

A comparison of values of the resonant frequencies obtained from the transfer function plots with those calculated from the periods of the randomdec signatures show that all but one differed by less than 6 percent. Considering that the randomdec signatures were calculated from only response data while it was necessary to also use the excitation data for the calculation of the transfer function, these results are very good. This is especially true for the panels since the excitation spectrum was very non-uniform.

Figure 9 shows the results of extracting three randomdec signatures from different portions of the same narrowband time history. It can be seen that for approximately the first 8 milliseconds all the signatures are almost identical. This portion of the signature can be used as a standard from which damage can be detected.

Figures 10 and 11 show the signatures resulting from the damaged beams. Both figures show that the effects of the saw cut in each beam had a significant effect on the standard signatures.

The satisfactory results obtained from the experimental comparisons indicate that the randomdec technique is a valid method of measuring damping. Also, the randomdec signatures of the damaged beams demonstrate its ability to detect the induced flaws.

ACKNOWLEDGEMENT

REFERENCE

Cole, Henry A., Jr., "On-Line Failure Detection and Damping Measurement of Aerospace Structures by Random Decrement Signatures," NASA CR 2205, Mar. 1973.

Figure 2. Mounted Beam on Shaker
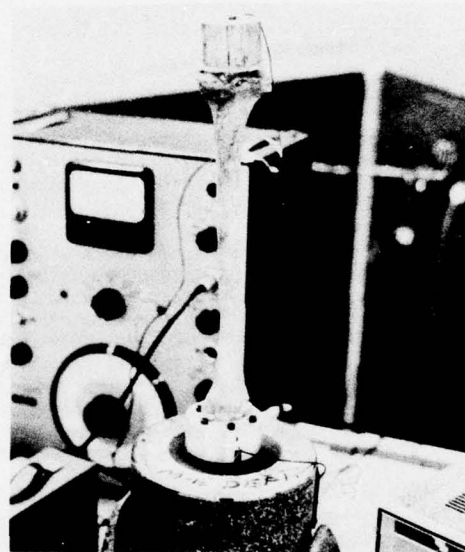
Figure 3. Mounted Bone on Shaker
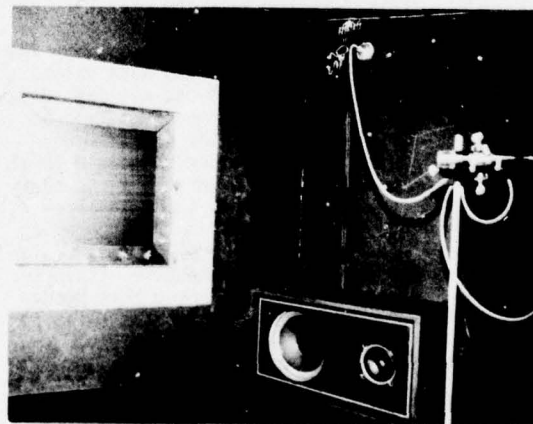
Figure 4. Mounted Panel in Chamber

Figure 1. Extraction of a Randomdec Signature from Response Data
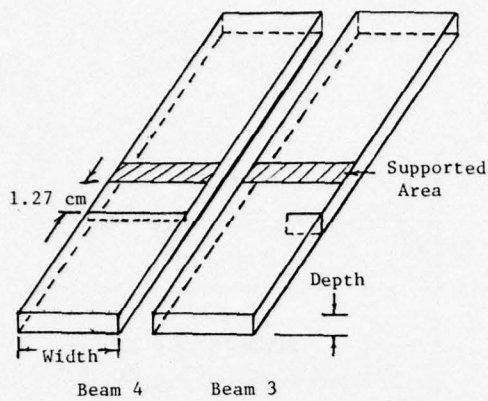
Figure 5.   Notched Beams
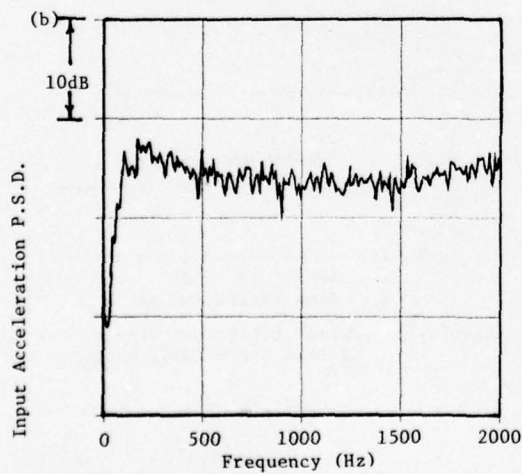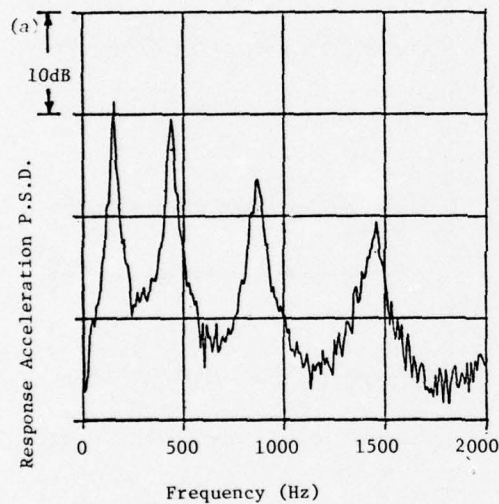
Figure 6.   Typical Power Spectral
            Density Plots
            (a) Response (b) Input
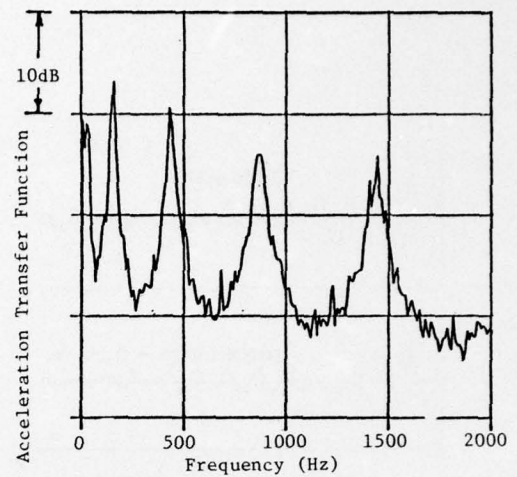
Figure 7.   Typical Transfer Function Plot
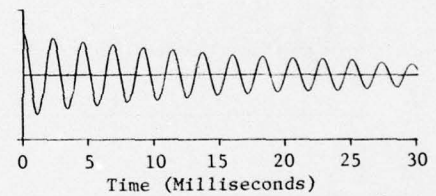
Figure 8.   Typical Randomdec Signature from
            Narrowband Response Time History
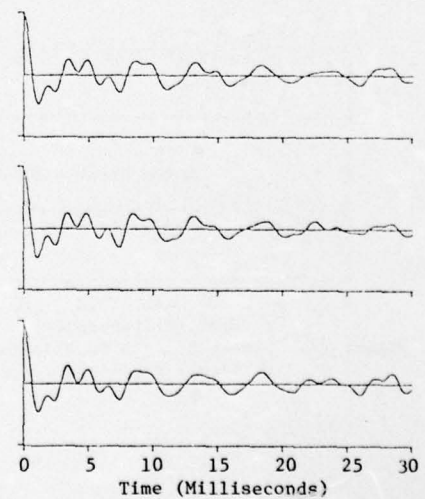
Figure 9.   Three Randomdec Signatures from
            Different Records of Undamaged
            Beam 4 Response

133

UNDAMAGED

NOTCH DEPTH = 0.10 cm

NOTCH DEPTH = 0.60 cm

0   5   10   15   20   25   30
Time (Milliseconds)
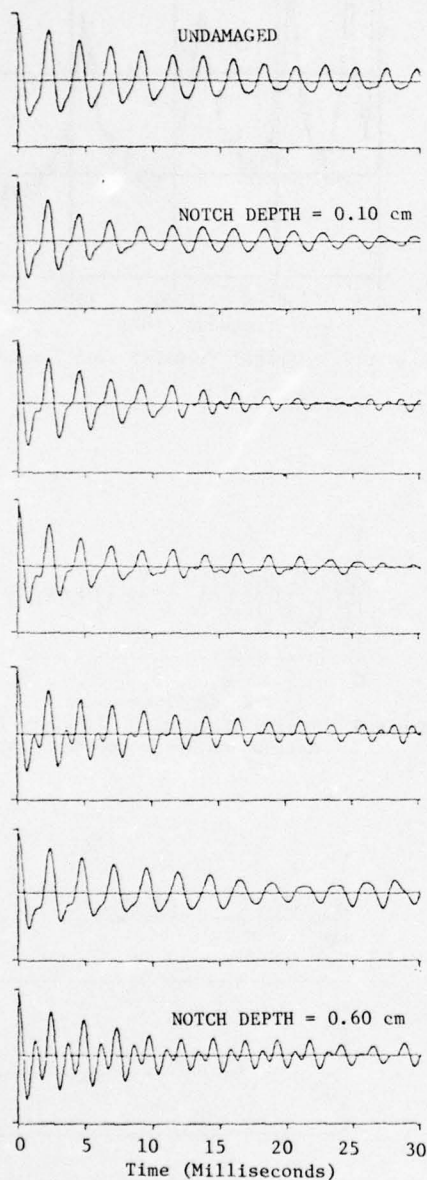
Figure 10.   Damage Effects on Signature
of Beam 3 Broadband Response

UNDAMAGED

NOTCH DEPTH = 0.05 cm

NOTCH DEPTH = 0.30 cm

0   5   10   15   20   25   30
Time (Milliseconds)
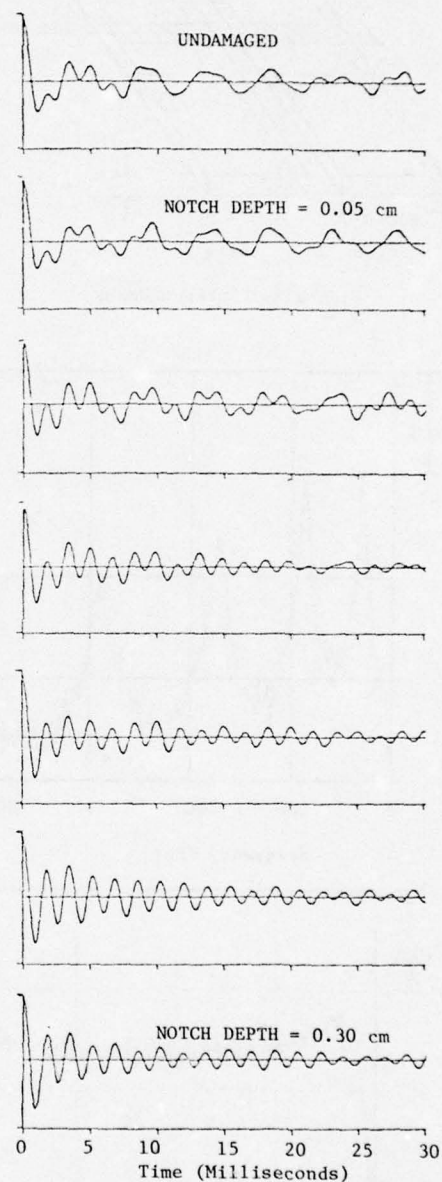
Figure 11.   Damage Effects on Signature
of Beam 4 Broadband Response

134

TABLE 1. Descriptions of Beams and Panels

Beams

Number	Material	Length (cm)	Thickness (cm)	Width (cm)
1	Aluminum	42.5	0.124	2.54
2	Aluminum	42.5	0.325	2.54
3	Plexiglass	42.5	0.318	2.54
4	Plexiglass	42.5	0.432	2.54
5	Glass	34.9	0.635	2.54
6	Glass	37.5	0.635	2.54

Panels*

Number	Material	Thickness (cm)	Lamina Lay Up (degrees)
1	Aluminum	0.084	Homogenous
2	Hercules 3501/ AS Graphite/ Epoxy	0.099	0/90/0/90/90/0/90/0
3	Hercules 3501/ AS Graphite/ Epoxy	0.112	45/-45/45/-45/-45/45/-45/45
4	Hercules 3501/ AS	0.109	22.5/-22.5/22.5/-22.5/-22.5/ 22.5/-22.5/22.5

*All panels are 30.5 cm x 30.5 cm

TABLE 2. Consolidation of Results

Specimen	Cut-Off Freqs. (Hz)	Transfer f(Hz)	Function ζ	Randomdec f_d(Hz)	Signature ζ_{Avg}	Comparison $\frac{f}{f_d}$	$\frac{\zeta}{\zeta_{Avg}}$
Beam 1	350-600	455	.025	458	.014	.994	1.79
Beam 1	750-1050	900	.013	896	.013	1.004	1.00
Beam 2	250-550	380	.026	387	.003	.982	8.67
Beam 2	800-1300	1060	.008	1076	.001	.985	8.00
Beam 3	300-650	433	.032	441	.016	.982	2.00
Beam 3	650-1100	868	.033	879	.022	.987	1.50
Beam 4	400-900	613	.022	622	.029	.985	.76
Beam 4	900-1500	1225	.017	1225	.020	1.000	.85
Beam 5	900-1300	1065	.019	1099	.001	.969	19.00
Beam 6	800-1100	868	.004	909	.002	.955	2.00
Bone 1	500-1500	985	.019	1039	.019	.948	1.00
Panel 1	135-190	166	.051	164	.036	1.012	1.42
Panel 2	140-190	175	.017	173	.019	1.011	.89
Panel 3	190-250	224	.040	193	.042	1.160	.95
Panel 4	190-270	215	.061	200	.039	1.075	1.56

Discussion

Mr. Liebowitz (David Taylor Naval Ship Research
and Development Center): Since damping is most
significant at the resonance frequencies I
would presume that you would be concerned with
damping at those frequencies. The crack in
effect must change the properties of the
material, why not use the ordinary damping
methods, high q or logarithmic decrement at the
resonance frequencies, and observe the changes
in the properties of the material, and therefore
the resonances themselves at these frequencies
by ordinary methods? What is the advantage of
using the random approach?

Mr. Yang: There are those who use ordinary
methods in the sense of looking at the reso-
nances and their problems and I am sure they
realize how to recognize the changes in the
variations. Also some of the other regular
methods require the knowledge of the input as
long as it is random in nature, it cannot be
sinusoidal. That is one of the big advantages
of this method in the sense that you have many
problems that are due to the environment such
as wind loading or trucks going over a bridge;
it is difficult to get the input so this random
decrement method is independent of the input
loading and it only requires the response curve
of the structure.

Mr. Leibowitz: The response has frequency
components related to the excitation function
and the component you are looking for in the
output has to exist in the input; therefore
it is dependent upon the frequency component
that you are looking for being in that
input to the degree that it is dependent upon
input function. If it isn't there you can't
observe it.

Mr. Yang: This method is dependent upon the
input only in a sense that it has to be random
in nature, preferably white noise because it
would give you better results. For some of the
tests we used the excitation of a vibrator
and for the tests on bridges the excitation
was provided by trucks going by, even though
you have different loading for rush hours as
opposed to no rush hours; however we don't
care, as long as we have the reponse.

RESPONSE ANALYSIS OF A SYSTEM WITH DISCRETE DAMPERS

G. K. Hobbs, D. J. Kuyper, and J. J. Brooks
Santa Barbara Research Center
Goleta, California

This paper describes the analytical design of a spaceborne structural system which limits vibrational response through the use of discrete dampers. The analytical techniques used are described, and analytical and experimental results are compared. Excellent correlation is shown.

INTRODUCTION

The NASA-sponsored SMS Spacecraft is a synchronous meteorological satellite having as the primary instrument the Visible/Infrared Spin-Scan Radiometer (VISSR). The VISSR system provides meteorological maps of the earth and clouds from geostationary orbit. The satellite is spin-stabilized on an axis parallel to the earth's (Fig. 1). As indicated in the figure, a mapping raster is formed by a combination of the satellite spin motion and a step action of the scanner optics. One west-to-east raster line is formed for each rotation of the spinning satellite.

The radiometer uses visible channels combined with infrared channels to provide both day and night operation. The infrared channels use HgCdTe detectors which must be cooled to less than 90°K for operational use. A two-stage passive radiation cooler is used to obtain the low temperature.

RADIATION COOLER DESCRIPTION

The radiation cooler which supports and cools the two infrared detectors is optically aligned to the radiometer telescope axis (Fig. 2). The major cooler components are an ambient housing and sun shield, intermediate stage, and cold stage. The sun shield specularly reflects to space unwanted solar energy entering the cooler during summer solstice (Fig. 1). The intermediate stage supports the

cold stage (detector stage), and thermally decouples the cold stage from ambient source radiation. High-emittance radiators on both stages emit long-wavelength energy to low-temperature space, thereby lowering the temperature of each stage until thermal equilibrium is reached.

The cooler interstage support members have severely contradictory design requirements. Interstage heat transfer (radiation, conduction) must be reduced to very low levels if the detectors are to reach their operational temperature, but a rigid interstage support structure is needed to raise the cooler vibration mode frequencies above the principal launch excitation frequencies. Also, large thermal gradients between stages (250°K, overall) must be accommodated during operation, while maintaining detector optical alignment.

A glass-epoxy composite material was selected for the interstage support members, because of its high strength/conductivity ratio. The interstage support members were arranged like pretensioned spokes in a wheel. The use of six tension members per stage maintained a statically determinant system (Fig. 3).

Each member was fabricated in a configuration much like a rubber band — a continuous structure wrapped around a cylindrical support at each end. This configuration was selected to minimize the stress concentration at the end attachments. The unidirectional glass-epoxy bands were fabricated from continuous "S"

CW

Radiation Cooler

VISSR 45° Scan Mirror (Scans 20° in 0.192-mr Steps)

Solar Rays

Spacecraft Spin Axis (100 rpm)

Fig. 1 - Spin-scan geometry

Intermediate Stage Radiator High ϵ Surface

Radiation Shields Specular Low ϵ Surface

Cold Stage Radiator High ϵ Surface

Solar Rays

Sun Radiation Shield

Cold Stage Damper Assembly (Figure 5)

Sun Shield Elastomeric Mounts (Figure 6)

Intermediate Stage

Intermediate Stage Support Bands

Cold Stage

Ambient Housing

Cold Stage Support Bands

Telescope Tube

Adapter Cone

Fig. 2 - Radiation cooler structural schematic
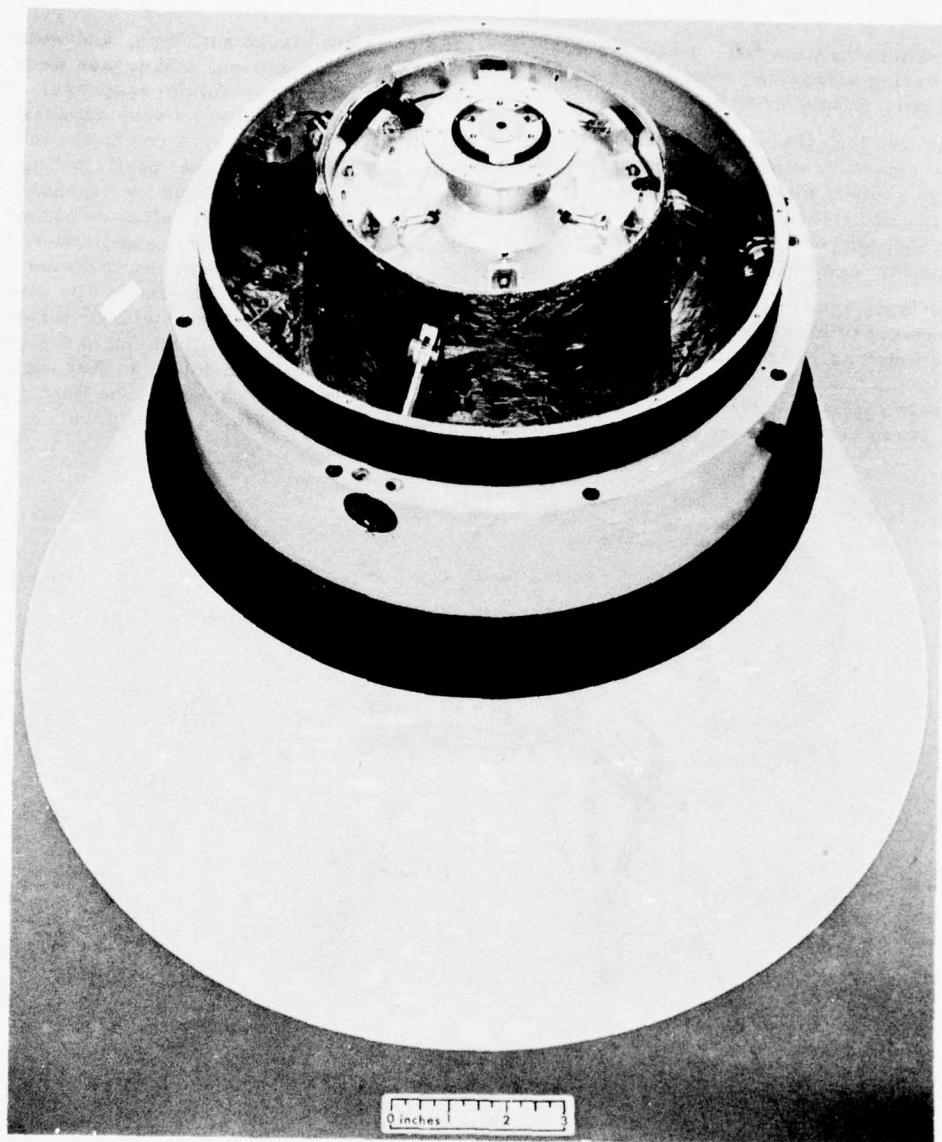
Fig. 3 - View of cooler from detector end

glass rovings pre-impregnated with epoxy resin. This design yielded a typical strength of about 1.5×10^{10} dynes/cm^2, with a tensile modulus of about 6.2×10^{11} dynes/cm^2.

The intermediate-stage lateral axis rotational modes were uncoupled from lateral axis excitation by proportioning the stiffness of the band pairs. The elastic axis of the support system and the center of gravity of the suspended mass were made to coincide. Thus, the

design of one band in each pair was controlled by stiffness criterion rather than by a thermal conductance/strength criterion. Since the stiffest band was the longer one of the pair, the thermal penalty for this advantage was not severe.

Creep relaxation during service was not found to be a problem, but the duration and level of vibration exposure were found to be critical to the fatigue life of the fiberglass

139

bands. Random vibration fatigue damage accumulated during extensive ground tests was found to be particularly critical.

Fatigue was thus the controlling failure mode in the selection of pre-load stress levels for the stage support members. Fatigue endurance and ultimate strength are directly related; the goal of high fatigue endurance was served by designing for high ultimate strength.

The analysis and test of a structural model cooler showed very high dynamic magnification factors, as much as 100 to 1 between stages. Survival of launch was not expected. Discrete dampers were inserted into the mathematical model and parametric analyses run to determine

the optimum placement, type, and value of the dampers. In addition, stiffnesses were varied in the search for minimum response. The structure was found to be very sensitive to small parameter changes due to the interplay between the five principal participating modes of vibration and the frequency dependent input vibration levels. Final selection of damping was to use an elastomeric auxiliary mass damper on the cold stage and to mount the sun shield on elastomeric mounts. The elastomeric mounts allowed the sun shield to vibrate out of phase with the ambient housing at the critical frequency and, in so doing, to flex the elastomer and dissipate energy. The final configuration is shown in Fig. 3 and Fig. 4.

1. INTERMEDIATE STAGE RADIATOR	10. INTERMEDIATE STAGE HEATER
2. INTERMEDIATE STAGE SUPPORT BANDS	11. INTERMEDIATE STAGE ASSEMBLY
3. INTERMEDIATE STAGE SHIELD	12. AMBIENT HOUSING
4. COLD STAGE HEATER	13. SUPERINSULATION
5. COLD STAGE SUPPORT BANDS	14. ELASTOMERIC MOUNTS (12)
6. DETECTOR/DEWAR ASSEMBLY	15. SUN SHIELD
7. COLD STAGE ASSEMBLY	16. WARM AND COLD FILTERS
8. COLD STAGE DAMPER	17. DETECTOR FIELD OF VIEW
9. COLD STAGE RADIATOR	18. CABLE ASSEMBLY

Fig. 4 - Cooler cutaway drawing and terminology

140

DYNAMIC ANALYSIS

A finite element computer program, Matrix Analysis Routine for Structures (MARS), was used for preliminary analysis of the radiation cooler. A model consisting of some 144 degrees of freedom and 135 elements consisting of cones, cylinders, beams, plates, and infinite stiffness extensions was used to determine all modes of vibration below 2000 Hz. Due to elastic and mass symmetry, no lateral-axial or lateral-torsional coupling existed in the model. This allowed simplification of the analysis to a smaller model for each direction, namely lateral-rotational and axial.

A method of including discrete dampers was sought as analysis and test of prototype coolers showed very high dynamic magnification factors in the modes of interest. These modes involved stretching of the fiberglass bands and flexing of the adapter cone, both of which dissipated very little energy due to the low loss coefficients for beryllium and filament-wound fiberglass.

Very little energy dissipation was available from bolted joints, because optical alignment criteria dictated slip-free joint design. The total permanent shift of the cold stage relative to the ambient housing could not exceed 0.002 cm after all vibration testing was completed. Also, any cold-stage shift during cooldown could not exceed this amount.

The input from the spacecraft was expected to drop substantially above 200 Hz, so a further simplification of the models was possible; i.e., to only simulate the first five modes in each model. These simplifications made it possible to include discrete dampers and calculate the energy dissipated in them using simplified techniques.

A number of techniques for adding damping to the system were considered and are listed below along with the reasons for rejecting those not used:

Constrained Layer Damping

In this technique, a high damping elastomer material is applied to parts of the structure undergoing large strains. No really suitable place on the cooler was found to apply such a material.

Inertial Dampers

An investigation was made into the possibility of attaching a container of soft lead shot to the cold stage which would dissipate energy by inelastic collisions between the shot. Calculations indicated that about 0.045 kg of shot would provide the minimum needed amount of damping. This damper type was not pursued further since objection was raised to having unrestrained masses on the spacecraft.

Inertial Coulomb Dampers

Calculations showed that a 0.045-kg mass restrained by a friction device adjusted to slip at a predetermined acceleration would provide as much damping as the shot. This approach was not pursued further since development of a reliable friction mechanism was considered to be more involved than the development of other damping devices.

Tuned Dampers

Tuned dampers are best used where the impressed frequency is a constant since the damper is effective only at the absorber frequency. If the absorber is tuned for a particular natural frequency, the natural frequencies are changed by the addition of the absorber which defeats the purpose. Even it if were possible to tune an absorber to a natural frequency, an absorber would be required for each troublesome frequency. If the absorber masses were to be mounted with an elastomer, the nonlinear characteristics would affect the tuning according to the temperature and amplitude. Also, once the cooler is mounted to the VISSR, and the VISSR to the spacecraft, the natural frequencies will be different. For the above reasons, true tuned dampers were not considered to be appropriate candidates for suppressing the cold stage response.

Broad-Band Dampers

A broad-band damper consists of a mass supported by a spring element and to which a damping element of some sort is also attached as shown below:
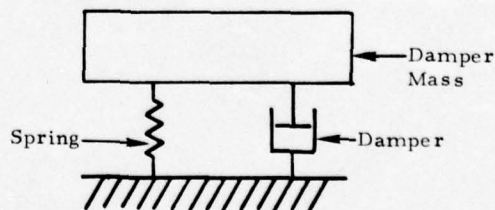
The damper mass can be an extra mass added to the system, or an existing mass remounted on a spring-damper set. The spring can be any one of a number of linear, or nonlinear, elements and the damper could be viscous, hydraulic, friction, etc.

The broad-band damper reduces vibration amplitudes simply by dissipating energy across the damper element, and the greater the amount of energy dissipated, the lower the amplitude. To maximize the energy dissipation, the motions across the damper are maximized. This is done by choosing the damper spring/mass ratio to be less than the lowest troublesome eigenvalue of the system without the damper. This puts the damper mass out of phase with the mass to which it is attached in the frequency range of interest, thereby maximizing the motions across the damper.

While the broad-band damper cannot produce results as dramatic as that of a damper tuned to a given impressed frequency, it has the advantage of not having to stay in careful tune. It was decided to develop broad-band dampers for the cooler using viscoelastic elements.

Dampers Selected for the Cooler

Two types of dampers were used on the flight coolers. The cold-stage damper was mounted on the body of the cold stage. The other type, identified as the ambient housing damper, used viscoelastic elements interposed between the sun shield and ambient housing of the cooler.

The cold-stage damper used an auxiliary mass of about 0.045 kg, supported by three symmetrically placed visoelastic rubber elements as shown in Fig. 5. These elements were designed to yield the same spring rate in all axes, thus imparting this quality to the assembled damper. Each rubber element was divided into two working parts. One part, which resembled a rubber shear bushing with cored out holes, provided shear deflection in the direction of the thrust axis. The other part resembled a rubber sandwich and provided shear deflection in either lateral axis.

The amount of rubber shear straining under vibratory load was of critical importance to damper performance; i.e., the available damping was a strong function of the amount of shear strain. Both working parts of the rubber element were thus proportioned to yield the
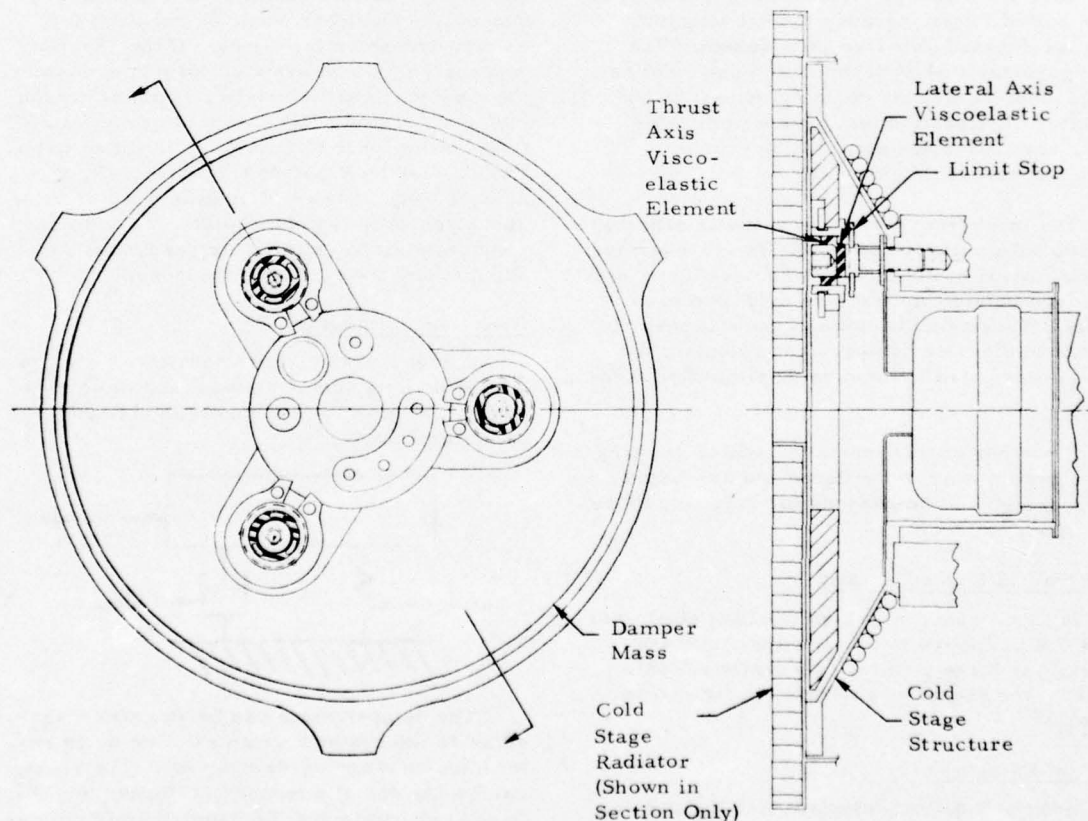
Fig. 5 - Cold stage damper assembly

142

desired shear strains within the range of predicted vibratory amplitudes.

Limit stops which controlled the deflections of the cold-stage damper mass were provided. These stops were not needed for normal operation, but were provided for safety in the event of a failure of one or more of the rubber elements. The stops restrained relative deflections of the mass in excess of 0.05 cm in each axis.

The ambient housing damper consisted of twelve viscoelastic rubber elements which supported an existing cooler mass, the sun shield as shown in Fig. 6. The rubber elements were of conventional shear bushing design and provided maximum damping in the thrust axis. The shield center of gravity was displaced from a lateral plane containing the viscoelastic elements so that under lateral axis excitation, a pitching motion was induced in the shield which was reacted by axial motions of the viscoelastic elements. Thus, a small amount of damping was also realized in the lateral axis.

The proportions of the ambient housing damper viscoelastic elements were adjusted to yield the desired spring rate and shear strains for good damping performance. Limit stops were provided for safety in the event of rubber element failure. These stops were also needed during thrust axis excitation at low frequencies, to prevent possible overtravel of the sun shield.

Both damper types used a flight-qualified, damped, silicone rubber of 65 Shore A hardness as the viscoelastic material. This material was transfer-molded under conditions of elevated pressure and temperature, and cured in place to form a vulcanized bond to the metal components also included in the mold (see Fig. 7). The process yielded the highest bond strength attainable in practice.

Test Setups

Fig. 8 schematically shows the test setups used to vibrate the cooler in the thrust and lateral axes. The cooler was mounted upside down relative to its position in the spacecraft/launch vehicle with the adapter cone included

Note: 12 viscoelastic elements are used in the complete damper assembly.
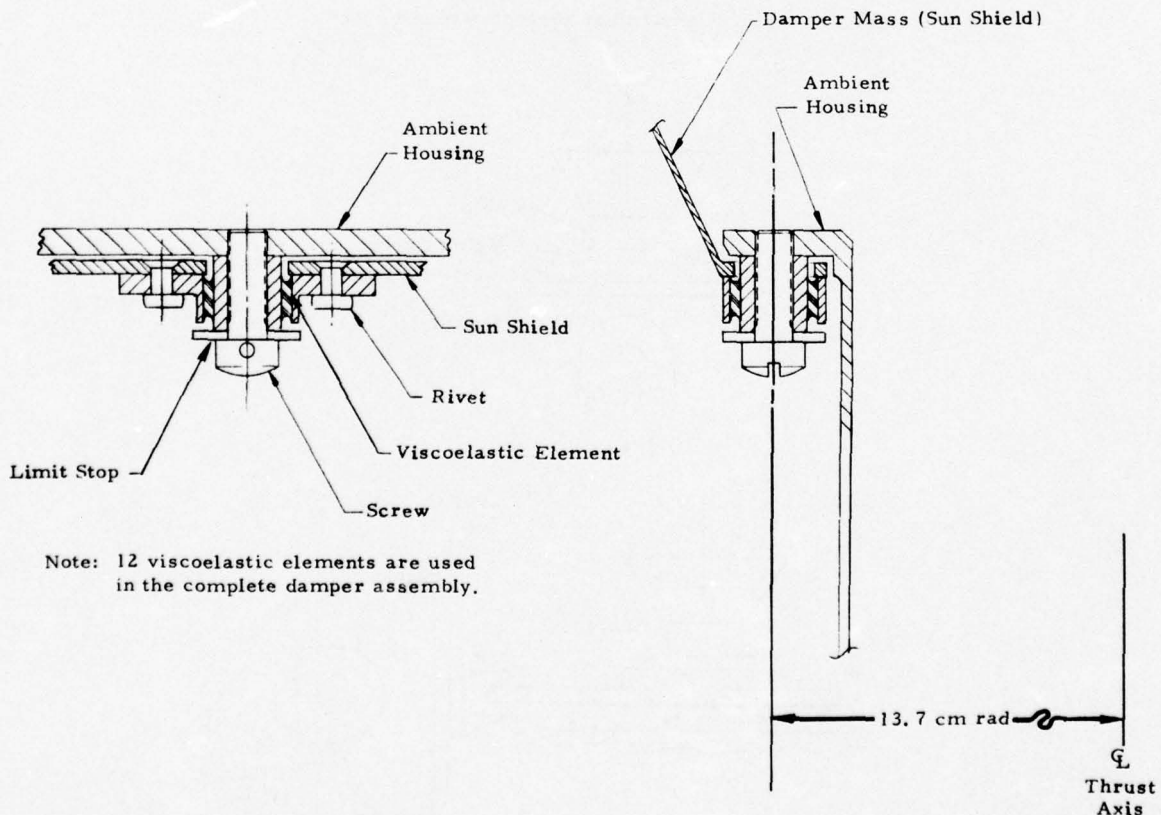
Fig. 6 - Ambient housing elastomeric mount
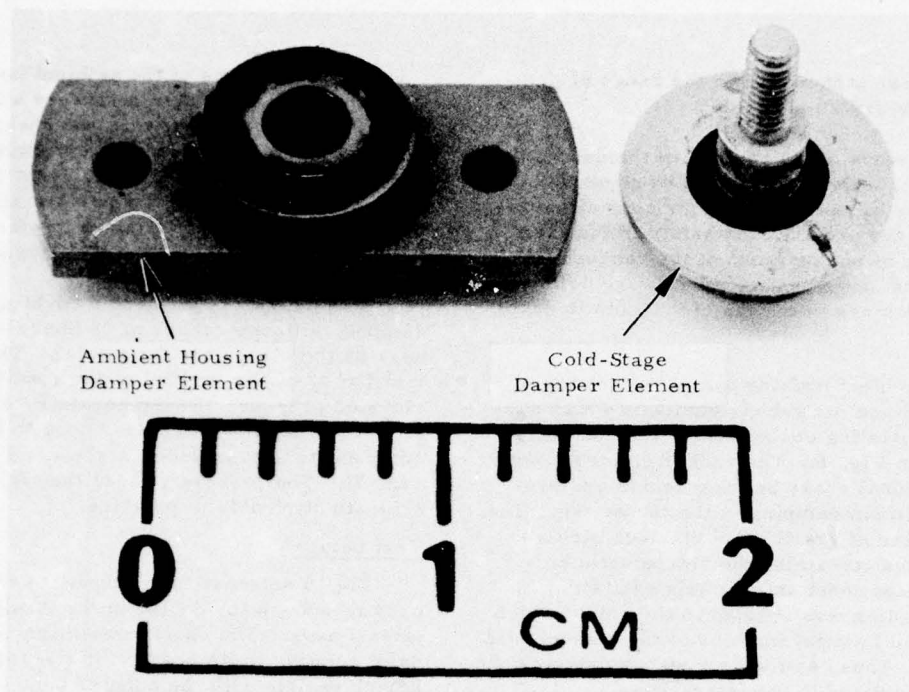
Fig. 7 - Vibration damper viscoelastic elements
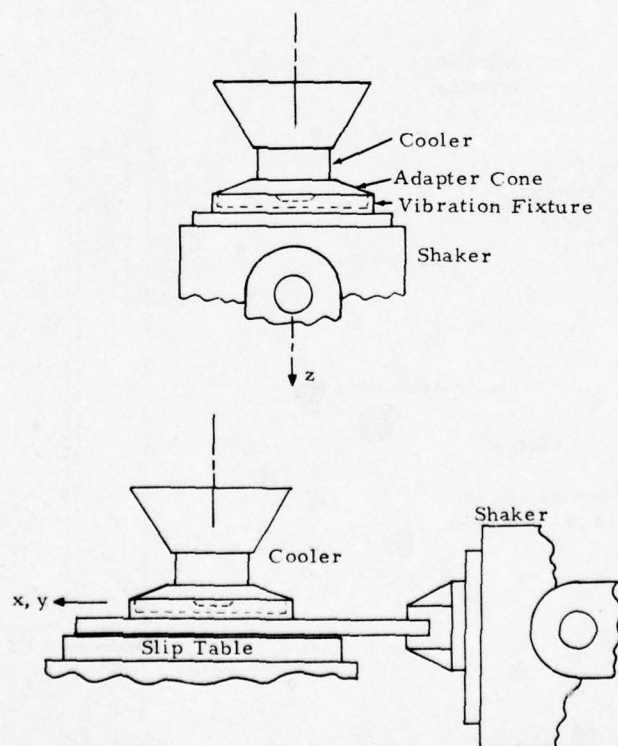
Fig. 8 - Radiation cooler vibration setups

between the cooler and vibration fixture. The absence of the telescope tube in the thrust axis is relatively unimportant since it is quite stiff in that direction. However, the adapter cone is flexible enough that it should be included in the setup. The telescope tube is not as stiff in the lateral direction, and its dynamic excursions were included in the vibration input levels using data obtained from the vibration of the entire instrument with a prototype cooler installed.

Analytical Models

It is helpful to consider the cooler as lumped masses interconnected by elastic (or viscoelastic) elements in discussing cooler dynamics. Fig. 9 and Fig. 10 show lumped parameter models for the thrust and lateral axes. The principal masses and elastic elements are labeled.
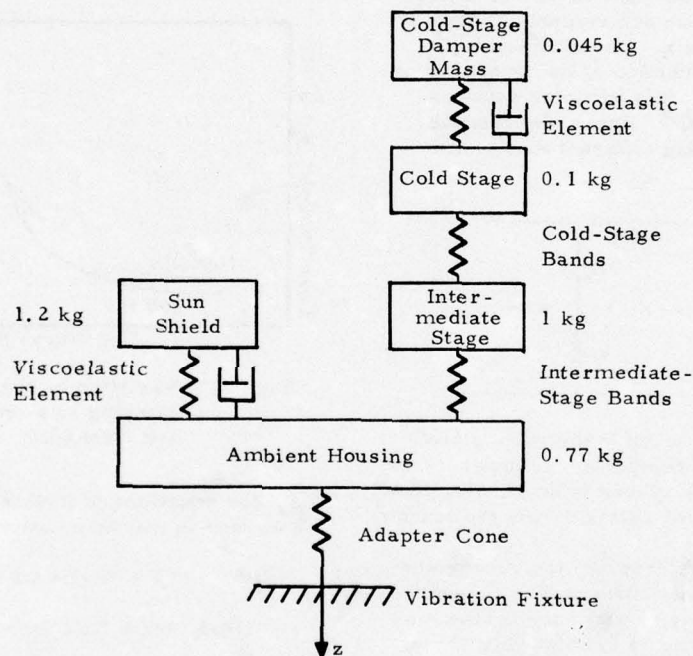
Fig. 9 - Thrust axis lumped parameter model
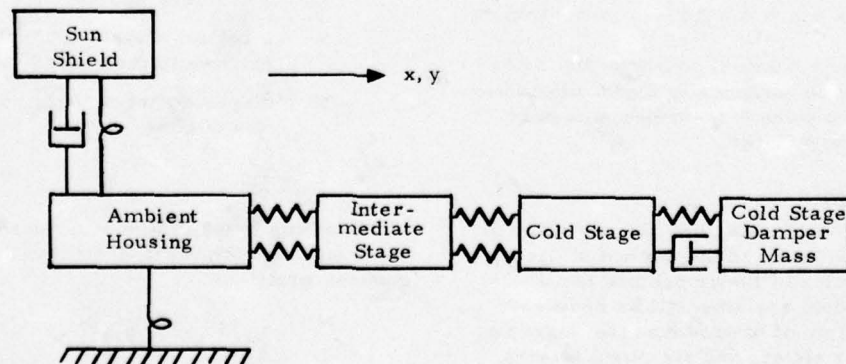
Fig. 10 - Lateral axis lumped parameter model

The ambient housing dampers and the adapter cone are shown as moment springs to indicate that they have no appreciable lateral flexibility, but do have flexibility in rotation.

The ambient housing and cold-stage damper elements are not intended to be depicted as linear viscoelastic elements. They are, in fact, quite nonlinear. The SE565 silicone rubber used in the dampers takes some set if a load is applied in one direction, and will not completely recover to its original condition if the load is removed. It can easily be restored to its original shape by applying a reverse load. Another nonlinear characteristic of this rubber is the dependence of stiffness and damping on the magnitude of the strain. The stiffness and damping are also a function of the frequency of vibration. However, this behavior could be modeled with a series of linear viscoelastic Kelvin elements having different elastic and viscous values:
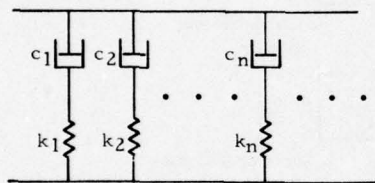
Stiffness and damping in the rubber are also a function of its temperature; however, the variation for silicone rubber is small over the $5°$ to $45°C$ range which exists during the launch.

If we analytically describe the rubber shear modulus as a complex number, $G^* = G' + iG''$, in which G' is the elastic part, and G'' the viscous part, the behavior is qualitatively shown in Fig. 11. The figure illustrates the increase of shear stiffness with frequency and the decrease with strain. The dynamic modulus is several times higher than the static modulus determined by a Shore A hardness measurement.

The nonlinear characteristics of the rubber make it difficult to analytically model the cooler and they produce some extraordinary results which will be shown later.

Analysis Technique

As an aid to understanding the operation of a broad-band damper and the method of design, the characteristics of linear damped multi-degree-of-freedom systems will be reviewed. Consider a system of lumped masses interconnected by linear elastic and viscous elements.
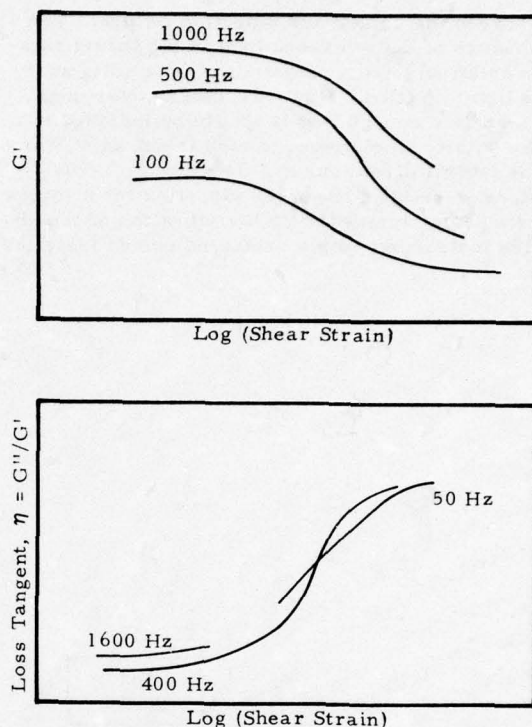
Fig. 11 - Variation of shear stiffness and damping as a function of strain and frequency

The equations of motion of this system may be written in matrix notation as:

$$M[\ddot{z} + \ddot{\gamma}(t)] + C\dot{z} + Kz = 0 \qquad (1)$$

$$M\ddot{z} + C\dot{z} + Kz = -M\ddot{\gamma}(t) \qquad (2)$$

where M = a diagonal mass matrix

C = a viscous damping matrix

K = a stiffness matrix

z = a column matrix of displacements relative to the ground

γ = displacement of the ground, a function of time

$\dot{z}$ = $\dfrac{dz}{dt}$

Electing to take the modal approach to solve equation (2), we deal first with the homogeneous equation:

$$M\ddot{z} + C\dot{z} + Kz = 0 \qquad (3)$$

This set of second order equations may be reduced to first order equation by letting [1]

$$z_2 = z \qquad (4)$$

$$z_1 = \dot{z}_2 \qquad (5)$$

Forming a new system of equations, we have

$$z_1 - \dot{z}_2 = 0$$

$$M\dot{z}_1 + C\dot{z}_2 + Kz_2 = 0 \qquad (6)$$

Equation (6) can be written in combined matrix notation as

$$R\dot{Z} + SZ = 0 \qquad (7)$$

where $R = \begin{bmatrix} [0] & [M] \\ [M] & [C] \end{bmatrix}$

$S = \begin{bmatrix} -[M] & [0] \\ [0] & [K] \end{bmatrix}$

$Z = \begin{Bmatrix} \{\dot{z}\} \\ \{z\} \end{Bmatrix}$

Matrices R and S are symmetric and are of size $2N \times 2N$, where N is the number of degrees of freedom. Reduction of the order of the differential equations has resulted in doubling the number of equations. To obtain the homogeneous solution, let

$$Z = e^{\alpha t}\Phi \qquad (8)$$

and substitute into (7)

$$\alpha R\Phi + S\Phi = 0 \qquad (9)$$

where $e^{\alpha t}$ is a scalar function of time, and

Φ is a vector of displacements.

The solution of (9) will yield 2N eigenvalues and eigenvectors,

$$\alpha_n \text{ and } \Phi = \begin{Bmatrix} \alpha_n \phi_n \\ \phi_n \end{Bmatrix}, \quad n = 1, 2N. \qquad (10)$$

For a system which is stable and has less than critical damping, the roots, α_n, and the eigenvectors, ϕ_n, will occur in complex conjugate pairs. α_n has the form

$$\alpha_n = -\zeta_n + i\omega_n, \quad \alpha_{n+1} = -\zeta_n - i\omega_n \qquad (11)$$

The corresponding complex eigenvectors can be written

$$\phi_n = \overline{\phi}_n e^{i\theta_n}, \quad \phi_{n+1} = \overline{\phi}_n e^{-i\theta_n} \qquad (12)$$

where $\overline{\phi}_n$ is the absolute magnitude of ϕ_n.

Substituting α and ϕ into (8) for the n and n+1 modes, we have

$$Z_n = e^{(-\zeta_n + i\omega_n)t}\overline{\phi}_n e^{i\theta_n} + e^{(-\zeta_n - i\omega_n)t}\overline{\phi}_n e^{-i\theta_n}$$

$$= e^{-\zeta_n t}[e^{i(\omega_n t + \theta_n)} + e^{-i(\omega_n t + \theta_n)}]\overline{\phi}_n \qquad (13)$$

Using the Euler identity, $e^{\pm i\theta} = \cos\theta \pm i\sin\theta$, we get

$$Z_n = 2\overline{\phi}_n e^{-\zeta_n t}\cos(\omega_n t + \theta_n) \qquad (14)$$

This expression is mathematically identical to the expression for the free vibration of a damped simple oscillator. We conclude that a linear multidegree-of-freedom system having viscous damping has natural modes of vibration whose amplitudes are modified in direct proportion by a modal damping factor analogous to the fraction of critical damping for a simple oscillator. Thus, a damper placed somewhere in the system damps each entire mode and not just the motion of the masses to which it is attached. Broad-band damping, then, is simply applying damping to the system at points where the maximum amount of energy dissipation can be obtained. The most effective points are chosen by examining the mode shapes of the system. We, therefore, continue our discussion of linear damped systems.

One may proceed to develop orthogonality relations for equation (9), and then to develop the particular solution to the equations of motion (2). Carrying it through, one eventually finds it possible to combine the 2N equations into N equations and arriving at solution forms which are analogous to those for a damped single degree of freedom. Contrary to the characteristics of an undamped multidegree-of-freedom system, the eigenvectors are not in phase unless the damping has special proportionality.

The rigorous procedure described above can become rather involved, and it is usual in the case where the damping in the system is small to ignore the damping in finding the eigenvalues and eigenvectors, and then to add it in at the last moment in the solution. It is assumed that for small damping the eigenvalues will be little different from the undamped ones, and that the same is true for the eigenvectors, and further, that the eigenvector phase angles will be small enough to ignore. It is further argued that describing the damping of most systems with linear viscous elements is such a gross approximation that the refinement provided by the rigorous approach is more fanciful than real. Having so reasoned, we drop the damping matrix and forcing function from equation (2) and obtain

$$M\ddot{z} + Kz = 0 \tag{15}$$

These equations yield a set of eigenvalues, λ, and eigenvectors, Φ. λ is a diagonal matrix of eigenvalues, ω_n^2, and the modal columns of Φ are composed of the eigenvectors, ϕ_{in}, where i denotes the mass points, and n the mode.

Expand z in a modal series:

$$z = \Phi\xi \tag{16}$$

where ξ = a column of modal functions of time, $\xi_n(t)$.

Still leaving out the damping, the equations of motion become:

$$M\Phi\ddot{\xi} + K\Phi\xi = -M\ddot{\gamma} \tag{17}$$

Replacing $K\Phi$ by $M\Phi\lambda$,

$$M\Phi\ddot{\xi} + M\Phi\lambda\xi = -M\ddot{\gamma} \tag{18}$$

$$\Phi^T M\Phi\ddot{\xi} + \Phi^T M\Phi\lambda\xi = -\Phi^T M\ddot{\gamma} \tag{19}$$

The equations of motion have been uncoupled because of modal orthogonality.

Let $\overline{M}$ = a diagonal matrix of the generalized masses.

$$\overline{M}[\ddot{\xi} + \lambda\xi] = -\Phi^T M\ddot{\gamma} \tag{20}$$

$$\ddot{\xi} + \lambda\xi = -\overline{M}^{-1}\Phi^T M\ddot{\gamma} \tag{21}$$

Let

$$p = \overline{M}^{-1}\Phi^T M \tag{22}$$

$$\ddot{\xi} + \lambda\xi = -p\ddot{\gamma} \tag{23}$$

For a sinusoidal forcing function,

$$\ddot{\gamma} = \ddot{\Gamma}e^{i\Omega t} \tag{24}$$

the particular solution is

$$\xi = \frac{p\ddot{\Gamma}e^{i\Omega t}}{\omega^2\left[1 - \left(\frac{\Omega}{\omega}\right)^2\right]} \tag{25}$$

$$z = \Phi\xi = \frac{\Phi p\ddot{\Gamma}e^{i\Omega t}}{\omega^2\left[1 - \left(\frac{\Omega}{\omega}\right)^2\right]} \tag{26}$$

$$\ddot{z} = \frac{\Phi p\ddot{\Gamma}e^{i\Omega t}}{1 - \left(\frac{\Omega}{\omega}\right)^2} \tag{27}$$

At this point damping will be artificially re-introduced in the form of a fraction of

critical modal damping, β_n. The preceding equation becomes,

$$\ddot{z} = \frac{\Phi p}{\left\{\left[1 - \left(\frac{\Omega}{\omega}\right)^2\right]^2 + \left(\frac{2\Omega}{\omega}\beta\right)^2\right\}^{\frac{1}{2}}} \tag{28}$$

Equation (28) provides a means by which the modal damping can be estimated from vibration data. At $\Omega = \omega_n$, it is assumed that other modes are not contributing significantly, and that the accelerometer readings represent the mode shape. With these assumptions and choosing point i as a reference, equation (28) becomes

$$\ddot{z}_{in} = \frac{\phi_{in}p_n\ddot{\Gamma}}{2\beta_n} \tag{29}$$

As an example, the lowest Z-axis cooler mode occurred at 240 Hz for a prototype model, and the cold-stage magnification was 65:1. Normalizing the mode shape on the cold stage, we have

$$\frac{\ddot{z}_{41}}{\ddot{\Gamma}} = \frac{(1.0)(3.1)}{2\beta_1} \tag{30}$$

$$\therefore \beta_1 = 0.024$$

The above procedure also requires a knowledge of the phasing of the various masses. The phasing found in analytical studies was used in this case.

Before proceeding to the design of the dampers, it will be helpful to derive some additional relationships between the energy dissipated by a viscous damper and modal damping.

If a viscous damper of damping constant, c, is cycled sinusoidally at frequency, Ω, through amplitude, δ, the energy dissipated per cycle is

$$U = \pi c\Omega\delta^2 \tag{31}$$

For a simple damped oscillator having a mass, m, and natural frequency, ω, we can substitute for c in terms of the fraction of critical damping.

$$c = 2m\omega\beta \tag{32}$$

$$U = 2\pi m\omega\Omega\beta\delta^2 \tag{33}$$

Drawing the analogy between a simple oscillator and a multidegree-of-freedom system vibrating in its nth mode at impressed frequency, Ω, we have

$$U_n = 2\pi\overline{M}_n\omega_n\Omega\beta_n\xi_n^2 \tag{34}$$

148

where, from (25) and (28)

$$\xi_n = \frac{p_n \ddot{\Gamma} e^{i\Omega t}}{\omega_n^2 \left\{ \left[1 - \left(\frac{\Omega}{\omega_n} \right)^2 \right]^2 + \left(\frac{2\Omega}{\omega_n} \beta_n \right)^2 \right\}^{\frac{1}{2}}} \qquad (35)$$

At resonance, (35) becomes

$$\xi_n = \frac{p_n \ddot{\Gamma} e^{i\Omega t}}{\omega_n^2 2\beta_n} \qquad (36)$$

and (34) becomes

$$U_n = 2\pi \overline{M}_n \beta_n \omega_n^2 \xi_n^2 = 2\pi \overline{M}_n \beta_n \dot{\xi}_n^2 \qquad (37)$$

The last step is to establish a relationship between the damping in an elastomer and the modal damping factor.

The viscoelastic shear properties of elastomers are often described by a complex shear modulus, $G^* = G' + iG''$. It can be shown that at a given frequency and strain amplitude, G^* can be modeled by an elastic spring and a viscous damper element in parallel. G^* is sometimes written as

$$G^* = G'(1 + iG''/G') = G'(1 + i\eta) \qquad (38)$$

where η is called the loss factor, or loss tangent.

Also, it can be shown that

$$\eta = \frac{\text{energy dissipated per cycle}}{2\pi \text{ energy stored}} \qquad (39)$$

$$= U_n / 2\pi V_n$$

$$U_n = 2\pi V_n \eta = 2\pi \overline{M}_n \beta_n \omega_n^2 \xi_n^2 \qquad (40)$$

$$\beta_n = \frac{V_n \eta}{\overline{M}_n \omega_n^2 \xi_n^2} \qquad (41)$$

V_n refers to the energy stored in the viscoelastic element; i.e., the real part, say K', which is

$$K' = \text{constant} \times G' \qquad (42)$$

If the viscoelastic element is connected between coordinates i and j, (41) can be written

$$\beta_n = \frac{\frac{1}{2} K'_{ij} (z_{jn} - z_{in})^2 \eta}{\overline{M}_n \omega_n^2 \xi_n^2}$$

$$= \frac{\frac{1}{2} K'_{ij} (\phi_{jn} \xi_n - \phi_{in} \xi_n)^2 \eta}{\overline{M}_n \omega_n^2 \xi_n^2}$$

$$= \frac{\frac{1}{2} K'_{ij} (\phi_{jn} - \phi_{in})^2 \eta}{\overline{M}_n \omega_n^2} \qquad (43)$$

This expression allows us to estimate the modal damping provided by the inclusion of a viscoelastic element provided its properties are known and that the mode shape is known. It also provides us a method for designing the damping for a structure:

1. Analytically determine the damper stiffness which produces the most desirable mode shapes.

2. Assuming that a certain elastomer strain level will be achieved, use the corresponding value of η and the modal data to estimate β_n and the response levels.

3. Having the response level estimate, design the elastomer element to give the required stiffness and strain amplitude.

Implementation of Damping

Having ascertained that damping addition to the cooler was necessary, the proper location for the damping was investigated. A series of analytical investigations was made in which dampers of various types were placed in the dynamical model in likely positions. One position chosen was the ambient housing/sun shield interface where an elastomeric mount was chosen. The selection of material and geometry required numerous model variations and experimental tests to verify the damping properties of the material used (SE 565 silicone rubber). In all calculations, the frequency dependent properties of the elastomer were used and the temperature was taken to be 22°C. An example of analytical results for the maximum cold-stage response when only viscoelastic elements were placed on the housing/shield interface is shown in Fig. 12 where the mount stiffness is the variable.

A test set of mounts was fabricated using the optimum stiffness calculated and the response at the cold stage versus input level is plotted in Fig. 13.

The amplification would be expected to decrease with increasing amplitude due to larger strains in the elastomer and so no peak would exist. The peak that exists is due to stiffness change with strain and the resulting modal response changes with strain. Such behavior is common when using elastomeric dampers.
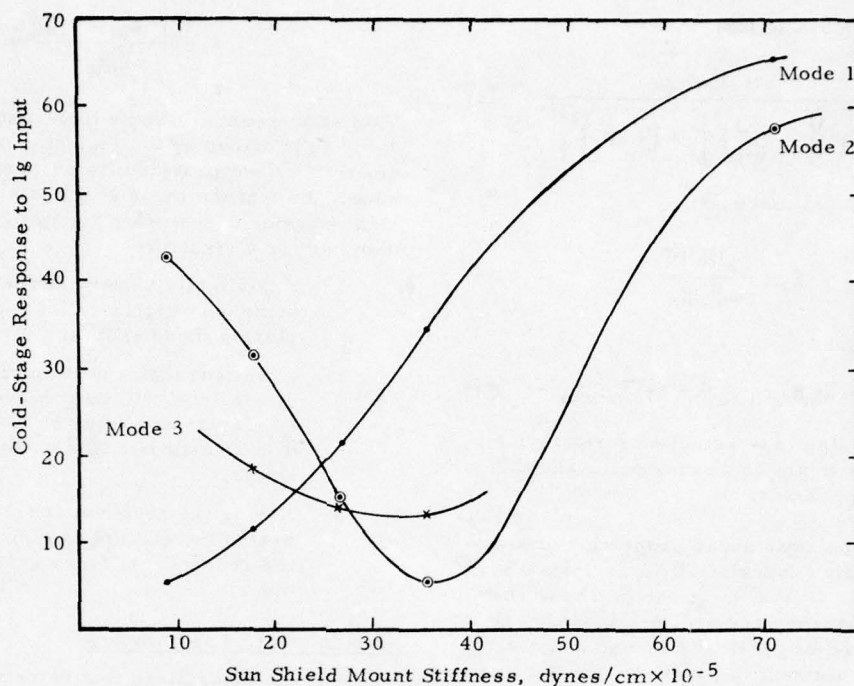
Fig. 12 - Calculated cold-stage response versus sun shield mount stiffness
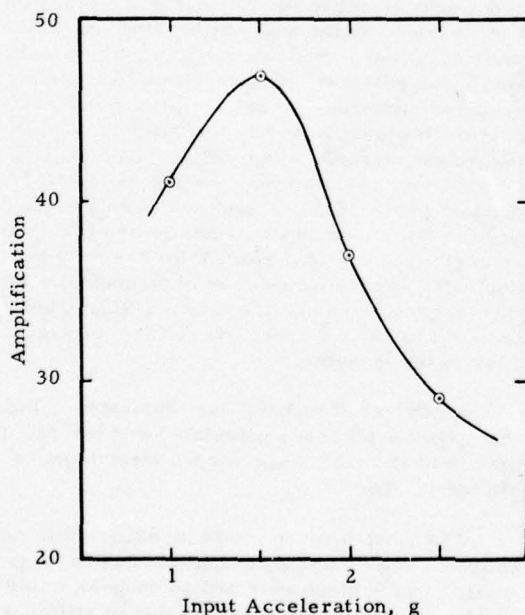
Fig. 13 - Cooler cold-stage amplification,
Z-axis, elastomeric mounts
between ambient housing and
shield

Similar tests were run with dampers on the cold stage of the cooler resulting in the final configuration discussed previously which consisted of SE 565 mounts for the sun shield and a damper mass on the cold stage supported on SE 565 mounts. Comparative test response results for the undamped cooler and two configurations with damping are shown in Table 1.

The percent of critical modal damping has been calculated using the previously derived equations and neglecting modes other than the primary response mode at each frequency. Results are shown in Table 2. Note that additional modes are introduced by adding dampers, as the suspended mass itself contributes an additional degree of freedom.

The estimated modal damping values show that, overall, the cold-stage damper and the ambient-housing damper are each effective as the other, but that, in particular, the cold-stage damper is more effective in the lower modes, and the ambient-housing damper is more effective for the higher ones.

150

TABLE 1

Effects of Cold-Stage and Ambient-Housing Dampers on
Intermediate-Stage and Cold-Stage Response to 1g Input

Condition	Thrust, Z				Lateral, Y			
	Intermediate Stage (g)	f (Hz)	Cold Stage (g)	f (Hz)	Intermediate Stage (g)	f (Hz)	Cold Stage (g)	f (Hz)
No dampers	41	260	94	370	35	240	39	240
Cold-stage dampers	25	260	44	260	19	240	16	240
Cold-stage and ambient-housing dampers	9	320	28	320	16	220	15	305

TABLE 2

Approximate Thrust Axis Modes and Modal Damping

Dampers	Mode Frequency (Hz)	Modal Damping (%)	Approximate Mode Shapes				
			Ambient Housing	Sun Shield	Intermediate Stage	Cold Stage	Damper Mass
None	260	1.3	0.24	0.34	0.47	1	---
	370	0.7	0.101	0.14	0.04	-1	---
Cold-stage damper only	180	23	0.19	0.29	0.23	0.51	1
	260	2.2	0.29	0.43	0.56	1	-0.46
	400	1.6	0.08	0.18	-0.11	-1	0.40
Cold-stage and ambient-housing dampers	135	13	0.33	1.02	0.34	0.5	1
	190	3.6	0.23	-0.65	0.26	0.54	1
	320	3.4	0.15	-0.076	0.31	1	-0.33
	420	4.6	0.067	-0.013	0.15	1	-0.25

Note: The approximate mode shapes are the relative responses of the masses at the reso-
nance peaks gathered from low-level sine sweep plots and are not pure modes since
there is some significant contribution from other modes. Algebraic signs were de-
termined on the basis of analytical studies.

CONCLUSIONS

Analytical techniques for systems with dis-
crete dampers have been presented and the use
of the techniques for a particular system has
been demonstrated. The frequency and ampli-
tude dependent properties of the elastomers
used as damping elements have been included
in the analytical procedures presented. Test
results from hardware analyzed and modified
using the techniques have shown the addition

of discrete dampers to be effective in reducing
modal responses of a system with only very
slight additions of weight.

REFERENCES

1. K. A. Foss, "Coordinates which Uncouple
the Equations of Motion of Damped Linear
Dynamic Systems," MIT ASRL Report
25-20.

Discussion

Mr. Henderson (Air Force Materials Lab):
Presumeably this involves some experimental
measurements is that correct?

Mr. Hobbs: Yes.

Mr. Henderson: Did you simulate the actual
temperatures during your experiments?

Mr. Hobbs: Yes, we did. These elastomers are
quite sensitive to temperature. Their damping
and stiffness are very radically a function
of temperature, however we are not using tuned
dampers in the normal sense. We ran into that
same problem when we used tuned dampers. Since
we used dampers that are tuned to resonate at
about half the natural frequency that we are
trying to clobber, we don't have that sensitive
a problem.

Mr. Henderson: This is of a lot of interest
to me because about ten years ago I was on a
personal kick trying to get people out of the
frame of mind of thinking of some of elastomer-
ic tuned dampers as discrete frequency devices
and we found some applications where this same
kind of thing was very useful to us.

Mr. Joe (Rohr Corporation): You have some mass
formula, you know it is pretty complicated, do
you actually optimize the system?

Mr. Hobbs: Yes, we optimized the system. We
selected, for the allowable damper masses that
we had because we had a total weight budget,
the stiffness of the elastomeric mount that we
would like to put it on to maximize the dis-
placement of that elastomeric mount, that is to
pump as much strain energy into it as possible.
We then selected the area of elastomeric
material we would put in and using these
equations we calculated the percent of modal
damping, we calculated the modal response and
went around in an iterative fashion; it
usually took two iterations. We tried to
optimize the damper mass, the damper stiffness,
and the frequency to which they were tuned.

Mr. Hannibal (Lord Kinematics): In the
determination of the modal damping from discrete
dampers what would be wrong with going into
state space and obtaining your modal damping
from your state space, from the discrete
elements instead of in the fashion that you did?

Mr. Hobbs: Nothing at all but the prime
advantage to going to state space is if you
had a linear viscoelastic element you could
then do the whole thing in closed form; however
we took into account the variation of the
damping and stiffness coefficients with fre-
quency, amplitude, and temperature.

THE APPLICATION OF ELASTOMERIC LEAD-LAG
DAMPERS TO HELICOPTER ROTORS

D. P. McGuire
Lord Kinematics
Erie, Pennsylvania

A ground resonance analysis has been developed for fully articulated or soft in-plane helicopter rotors with elastomeric lead-lag dampers. This analysis includes a suitable mathematical model of an ideal viscoelastic material. By applying the method of multiblade coordinates, the four-degree-of-freedom analysis can be applied to any rotor with three or more blades. Stability boundaries are plotted for a hypothetical rotor system with viscous and elastomeric dampers. The non-linear characteristics of two highly-damped elastomers were determined experimentally as functions of dynamic amplitude. The changes in the stability boundaries at various amplitudes are plotted using the measured material characteristics. The magnitude of these changes is shown to be within acceptable design limits.

NOTATION

C_B blade viscous damping coefficient (daN-m-sec)

C_y effective fuselage damping coefficient (daN-sec/m)

e drag hinge offset (m)

$G*$ complex modulus of a viscoelastic material

G' elastic modulus (real component of $G*$)

G'' damping modulus (imaginary component of $G*$)

g loss factor ($g = \tan\delta = G''/G'$)

I_B blade moment of inertia around drag hinge (kg-m^2)

K_B spring restraint around drag hinge (daN-m/rad)

K_y effective fuselage spring restraint (daN/m)

M_B blade mass (kg)

M_y effective fuselage mass at hub (kg)

N number of rotor blades

δ phase angle between complex force and displacement

Λ_1 blade lag frequency parameter $\Lambda_1 = e\sigma_B/I_B$

Λ_3 effective fuselage mass parameter $\Lambda_3 = N\sigma_B^2/M_y I_B$

$\overline{\lambda}_B$ blade damping parameter $\overline{\lambda}_B = C_B/\omega_y I_B$

$\overline{\lambda}_y$ effective fuselage damping parameter $\overline{\lambda}_y = C_y/\omega_y M_y$

σ_B blade mass moment around drag hinge (kg-m)

Ω rotor speed (RPM)

ω_y effective fuselage natural frequency $\omega_y = \sqrt{K_y/M_y}$

ω_o in-plane natural frequency of blade, non-rotating $\omega_o = \sqrt{K_B/I_B}$

INTRODUCTION

Ground resonance is a potentially destructive instability which can occur in helicopters with fully articulated or soft in-plane rotors. The dynamics of this phenomenon have been adequately described and analyzed in previous technical papers [1,2] The instability occurs when the in-plane motions of the rotor blades create non-symmetrical blade patterns resulting in an offset of the rotor center of gravity. Coupling of these motions with the natural roll mode of the fuselage, combined with the input energy available from rotation of the rotor can make the system unstable. Practical design of helicopter rotors requires sufficient damping of both the blade and the landing gear to prevent instability. The Coleman analysis [1] has outlined simplified methods for determining the amount of damping required. Hydraulic or friction dampers have commonly been used to provide the required energy dissipation. Both of these types of dampers have a history of poor service life due to leakage and wear. The use of a highly damped elastomer to perform this function offers significant advantages in terms of eliminating maintenance and improving reliability. Elastomeric dampers can provide long service life without maintenance, since they are not subject to wear or leakage. Laboratory testing has indicated service lives in excess of 4500 flight-hours can be achieved. Also, their gradual mode of deterioration requires only visual inspection and allows for replacement "on condition" rather than at specified overhaul intervals. Elastomeric dampers have been in production for the Aerospatiale SA-341 Gazelle since 1970. Other applications include the Hughes YAH-64 (AAH) and their 5-bladed Model 500D. In addition, several prototype damper configurations have been designed, fabricated and flight tested.

Since elastomers are viscoelastic materials, they exhibit both spring and damper characteristics. The spring restraint of the blade provided by an elastomeric lead-lag damper can be an advantage. Lag motions due to steady loads, such as aerodynamic drag, are reduced significantly. Blade centering devices, which are frequently used with hydraulic dampers, are not required because of the self-centering action of the elastomeric damper. By increasing the in-plane natural frequency of the blade, the spring restraint reduces the amount of damping required to prevent ground resonance. In effect, the elastomeric damper converts a fully articulated rotor to a soft in-plane rotor.

In some specific applications, the use of an elastomeric lead-lag damper has eliminated the need for discrete landing gear dampers. The minimal damping provided by the conventional skid gear was sufficient.

The versatility of elastomers allows the rotor designer new freedom in determining the location and configuration of the damper. Some of the variety of configurations which have been manufactured by Lord are shown in Figure 1. The broad range of elastomers available also permits tailoring the damper characteristics for specific applications.
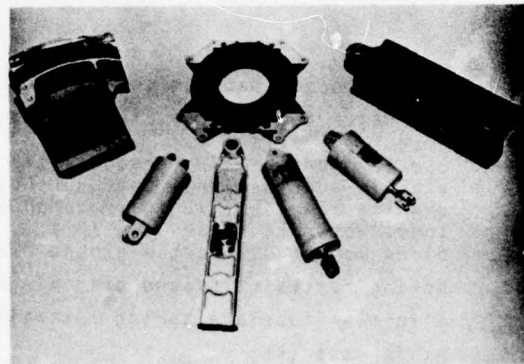
Figure 1. Elastomeric damper configurations for helicopter rotors.

Elastomeric dampers have also demonstrated retrofit potential as direct replacements for friction or hydraulic dampers on existing helicopter rotors. Figure 2 shows the installation of an elastomeric lead-lag damper on the Hughes Model 500C as a direct substitute for a friction damper.
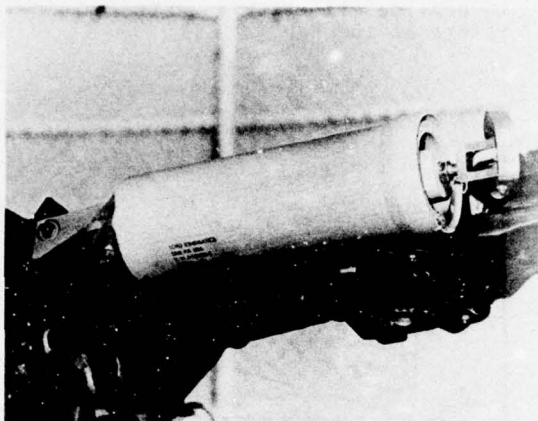
Figure 2. Retrofit installation of an elastomeric lead-lag damper on the Hughes Model 500C

The application of elastomeric dampers to helicopter rotors involves some design decisions which are not defined in the Coleman analysis. The purpose of this paper is to describe the design considerations and analytical methods necessary to define the dynamic characteristics required for an elastomeric lead-lag damper. The ground resonance stability analysis has been modified to include an ideal model of a viscoelastic material. Differences in the stability boundaries caused by the use of hysteresis damping and the changes in material characteristics are considered.

MODELS OF VISCOELASTIC MATERIALS

Viscoelastic materials, by definition, exhibit both spring and damper characteristics. When subjected to sinusoidal motion, hysteresis of the elastomer provides a damping force proportional to the amplitude of motion, but in phase with velocity. Many complex mathematical models have been proposed to describe the behavior of such materials. None of them have proven totally satisfactory. The simplest models represent ideal linear viscoelastic materials whose spring and damping characteristics are constant. There are two methods for mathematically representing materials with damping force proportional to displacement:

a) The complex modulus method

b) The equivalent viscous damping method.

The complex modulus method represents the shear modulus of a viscoelastic material as a complex quantity ($G*$) (Figure 3). The real part of this quantity, which is in phase with the displacement, represents the spring or elastic modulus (G'). The imaginary part is 90° out of phase with the displacement and represents the damping modulus (G''). The complex modulus ($G*$) is the vector sum of the elastic and damping components. The complex or total force is out of phase with the displacement by an angle δ which is determined by the ratio of the damping modulus to the elastic modulus. This ratio, G''/G', is defined as the loss tangent ($\tan \delta$) or loss factor (g) and is a fundamental material property. The concept of a complex modulus can be extended to include the spring rates and forces produced by a given configuration of the viscoelastic material as complex quantities. The complex stiffness ($K* = K'+jk''$) can then be introduced into the differential equations of motion directly as the coefficient of the displacement. The use of this model to represent hysteresis damping in a dynamic system introduces complex coefficients which may not be desireable if all other coefficients are real.

$$G* = G' + jG''$$
$$|G*| = \sqrt{G'^2 + G''^2}$$
$$\tan \delta = G''/G'$$
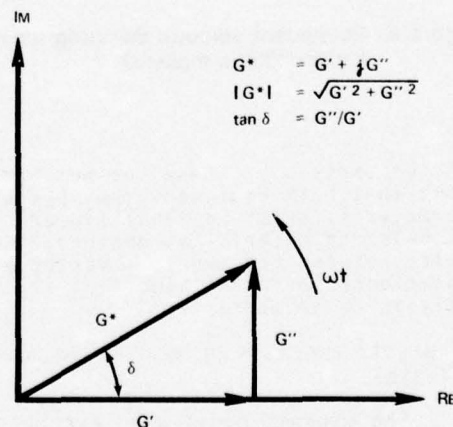
Figure 3. Complex modulus model of a viscoelastic material

The second method for modeling an ideal linear viscoelastic material is to define an equivalent viscous damping coefficient which will provide the same energy dissipation as the viscoelastic material. The damping force provided by a viscous damper is proportional to velocity, and at any. given amplitude is equal to: $F_D = C\dot{x} = C\omega X\cos(\omega t)$. The hysteresis damping force is proportional to the displacement, but 90° out of phase: $F_D = K''X\sin(\omega t - 90°) = K''X\cos(\omega t)$. Equating these two expressions and solving for C yields $C_{eq} = K''/\omega$ (Figure 4). This expression indicates that at constant frequency there is dynamically no difference between a viscous and an ideal hysteretic damper. However, at constant amplitude and variable frequency, the differences are significant. Being inversely proportional to frequency, the equivalent viscous damping coefficient approaches infinity as ω approaches zero and approaches zero as ω approaches infinity.

modes of the fuselage are transferred to provide effective translational values at the hub.
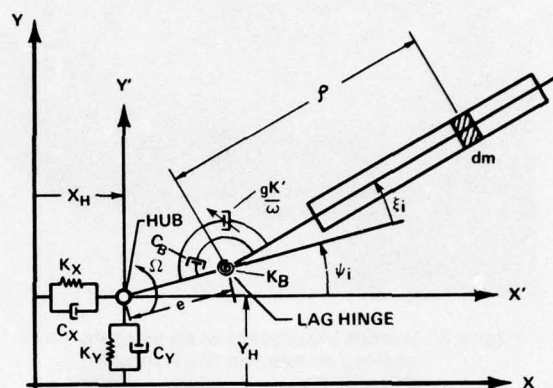
Figure 5. Dynamic model of the helicopter rotor and fuselage including elastomeric lead-lag dampers

Figure 4. Equivalent viscous damping model of a viscoelastic material

Comparison of these two methods shows that both represent the physical characteristics of an ideal linear viscoelastic material as desired. The choice between the two is a matter of convenience in the mathematical analysis to be performed.

STABILITY ANALYSIS OF ROTOR/FUSELAGE SYSTEM

The dynamic model used for this analysis (Figure 5) represents the helicopter fuselage on its landing gear as a damped spring-mass system with two translational degrees of freedom, longitudinal and lateral. Parameters for the pitch and roll

As in previous analyses, [1][2][3], it is assumed that only in-plane motions of the blades and hub are significant in determining the ground resonance characteristics. The system then consists of two degrees of freedom at the hub and a lead-lag degree of freedom for each rotor blade. The total system has (N+2) degrees of freedom where N is the number of blades. By assuming that the rotor has three or more blades and that it is isotropic, the method of multiblade coordinates can be applied to reduce the rotor to two degrees of freedom. These two degrees of freedom represent the longitudinal and lateral displacements of the rotor center of gravity relative to its center of rotation. Thus, rotor/fuselage systems with any number of blades greater than two can be analyzed in four degrees of freedom. The additional rotor blade degrees of freedom are not considered in this analysis. They represent modes which are decoupled relative to the fuselage because they are reactionless at the rotor hub.

The equations of motion were derived for the four degree of freedom system incorporating the equivalent viscous damping model of the elastomeric damper. They were then expanded to provide the characteristic equation. A computer program was written which solves repetitively for the roots of the characteristic polynomial with various values of the system parameters. By examining the eigenvalues, stability boundaries can be plotted as functions of these system parameters. The parameters of concern are the rotor speed, (Ω) the landing gear damping coefficient, (C_y), the blade spring restraint (K_B) and the blade damping coefficient, (C_B). The program allows any number of these parameters to be varied. In addition to plotting the stability boundaries, the system natural frequencies and modal damping factors can be plotted as functions of rotor speed. With this information, the degree of stability at any rotor speed can also be determined.

The equations of motion were also transformed to state variable form to allow the time response and frequency response of specific systems to be analyzed using available computer programs.

The stability boundaries were determined for a baseline system with conventional viscous damping and without spring restraint of the blade (Table I). The system parameters are similar to those used in Reference 3, but were modified to set Λ_1, and Λ_3, as defined in Reference 1, equal to .10 and .025 respectively. The stability boundaries for this system are plotted in Figure 6 as functions of landing gear damping and rotor speed for three different values of the blade damping coefficient. The axes of these charts are scaled in dimensionless terms by using the undamped lateral natural frequency of the effective fuselage mass as a reference. The normalized variables are defined as:

$$\bar{\Omega} = \frac{\Omega}{\omega_y} \qquad \bar{\lambda}_y = \frac{C_y}{\omega_y M_y} \qquad \bar{\lambda}_B = \frac{C_B}{\omega_y I_B}$$

The stability boundaries for this system are consistent with those determined in Reference 2. The unstable region contracts rapidly with increased blade damping.

TABLE I

System Parameters

Number of Blades	N	= 3
Blade Mass	m_B	= 94.9 kg
Blade Mass Moment	σ_B	= 254.0 kg-m
Blade Mass Moment of Inertia	I_B	= 1084.7 kg-m^2
Drag Hinge Offset	e	= .427 m
Blade Spring Restraint	K_B	= 0 daN-m/radian
Damper Loss Factor	g	= 0
Blade Viscous Damping Coefficient	C_B	= 202.2 daN-m-sec./radian
Effective Fuselage Mass at hub	m_y	= 3283.6 kg
Effective Fuselage Spring Rate at hub	k_y	= 124,048 daN/m
Effective Fuselage Viscous Damping Coefficient at hub	c_y	= 2554 daN-sec/m
Rotor Speed (Operating)	Ω	= 267 RPM
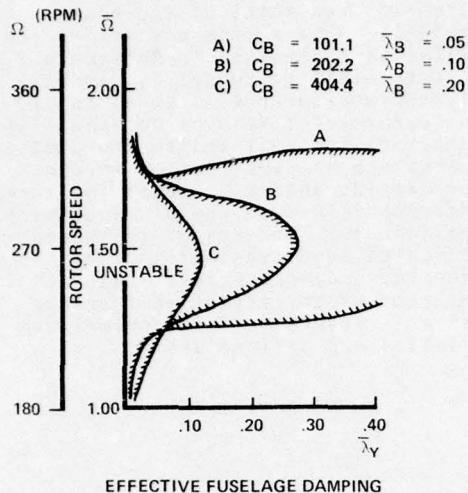
Figure 6. Stability boundaries for baseline system with three values for the blade viscous damping coefficient and without a spring restraint of the blade ($K_B = 0$)

To compare the effect of using hysteresis damping, which is proportional to displacement, rather than viscous damping, which is proportional to velocity, a spring restraint ($K_B = 10600$ daN-m/radian) was added to the blade. This gave a non-rotating in-plane natural frequency of $\omega_o = .35\Omega$. For typical elastomeric damper applications ω_o is in the range of .45 to .65Ω. A lower value was used for this comparison so that the effect of the spring restraint would not mask the effect of using hysteresis damping. A loss factor of g = .277 was selected to provide an equivalent viscous damping coefficient $C_B = 202.2$ daN-m-sec. ($\bar{\lambda}_B = .10$) at the center of instability. Thus, at this rotor speed the systems are identical. Figure 7 shows that the stability boundaries for the hysteresis and viscous damped systems are virtually congruent. This can be explained by the previously stated fact that the two types of damping are mathematically identical at constant frequency. Over the unstable range of rotor speeds the shift in the in-plane natural frequency

of the blade is small, and for practical purposes constant. Thus, the difference between hysteresis and viscous damping is very slight. At rotor speeds far from the center of instability, or with very small blade restraint or damping the difference may be more significant.
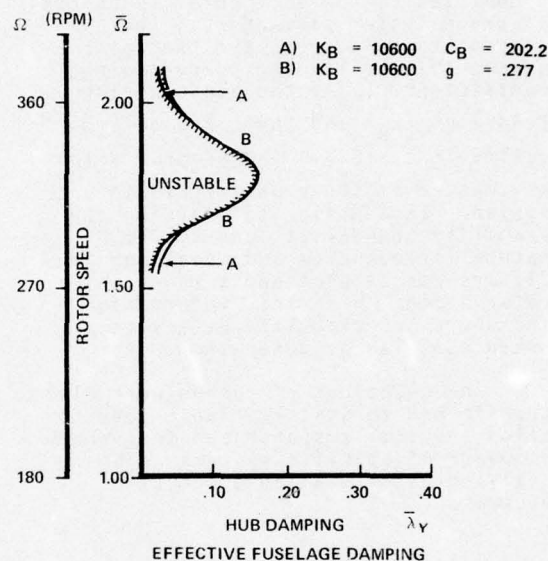
Figure 7. Stability boundaries for viscous and elastomeric blade damping with the same blade spring restraint

Figure 8 shows the stability boundaries for the elastomerically damped system with loss factors of g = .1, .2 and .4. The same blade spring restraint ($K_B = 10600$ daN-m/radian) was used. These curves could represent the use of three different elastomers in a given damper configuration. The variation in the size of the stability regions demonstrates the range of damping factors available through the use of different elastomers. Contraction of the unstable region at higher loss factors parallels the effect of increasing the damping coefficient in the viscous system.

A) K_B = 10600   g = .1
B) K_B = 10600   g = .2
C) K_B = 10600   g = .4

EFFECTIVE FUSELAGE DAMPING
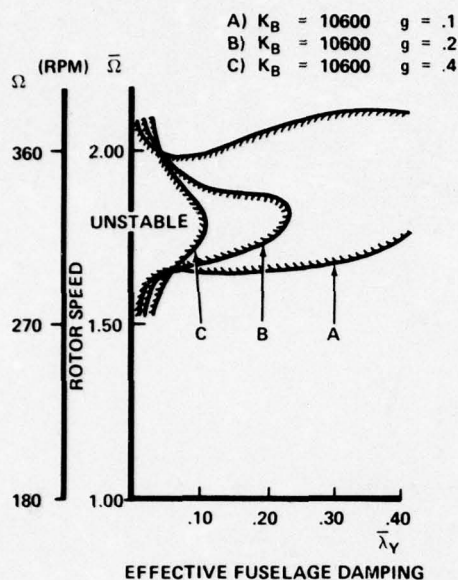
Figure 8. Stability boundaries for elastomeric blade damping with different loss factors (g)

THE EFFECT OF NONLINEAR MATERIAL
CHARACTERISTICS ON THE STABILITY
BOUNDARIES

The mathematical models and dynamic analysis up to this point have assumed an ideal linear viscoelastic material. That is, G' and G" are considered constant regardless of the environmental or dynamic conditions to which the material is subjected. As discussed previously, real viscoelastic materials can be highly nonlinear. While their dynamic characteristics are dependent upon many factors such as temperature and frequency, the most significant variation occurs as a function of dynamic amplitude. In the application of elastomeric lead-lag dampers, it is important to know the effect of changes in the damper characteristics on the stability boundaries. To determine this, the dynamic characteristics (G' and G") of two highly damped elastomers were measured as functions of dynamic amplitude. Both materials, BTR[R] and BTR IV, which are proprietary to Lord Kinematics, have been used in elastomeric dampers. In elastomeric damper

applications, BTR[R] has a loss factor of .35 to .5 while BTR IV ranges from .2 to .3. Due to the strain limitations of the elastomer, the maximum dynamic amplitudes in elastomeric damper applications are typically on the order of five times the design amplitude. The dynamic characteristics, G' and G", were measured over this amplitude range by the vector subtraction method [5]. The test data for BTR[R] and BTR IV are shown in Figures 9 and 10 respectively. The characteristics for each material at angular amplitudes of $\xi = \pm.5°$, $+1°$ and ± 2.5 were then substituted into the analysis and the stability boundaries plotted. Table II shows the spring rate and loss factor values used in the analysis. The stability boundaries for BTR[R] and BTR IV are plotted in Figures 11 and 12 respectively. As expected, the critical speed is shifted downward and the size of the unstable region increases at the higher amplitudes. The magnitude and trend of the change is such that it can be compensated for by designing the damper to insure stability at the highest amplitude. The system will then have a surplus of damping at all lower amplitude at the expense of a small increase in damper loads.

Damper configurations with nonlinear load-deflection characteristics are being considered to reduce this amplitude sensitivity.
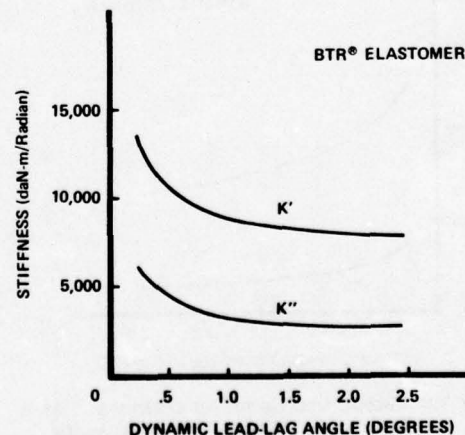
Figure 9. Elastic and damping stiffness as a function of dynamic amplitude for BTR® elastomer

159

TABLE II

BTR Elastomer

Dynamic Lead-Lag Angle	K_B (daN-m/rad.)	K''_B (daN-m/rad.)	g
$\pm$ .5°	10,600	4,462	.421
$\pm$ 1.0°	8,857	3,313	.374
$\pm$ 2.5°	7,808	2,756	.352

BTR IV Elastomer

Dynamic Lead-Lag Angle	K_B (daN-m/rad.)	K''_B (daN-m/rad.)	g
$\pm$ .5°	10,600	2,766	.261
$\pm$ 1.0°	8,807	2,043	.232
$\pm$ 2.5°	6,592	1,437	.218
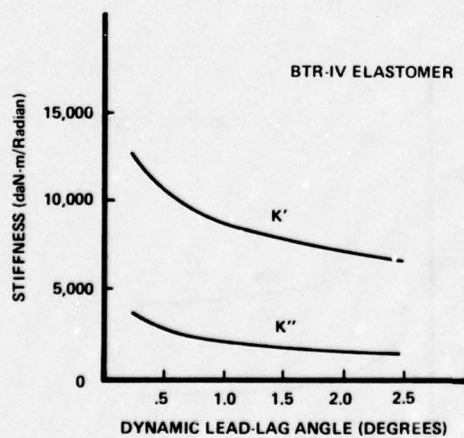
Figure 10. Elastic and damping stiffnesses as a function of dynamic amplitude for BTR IV elastomer
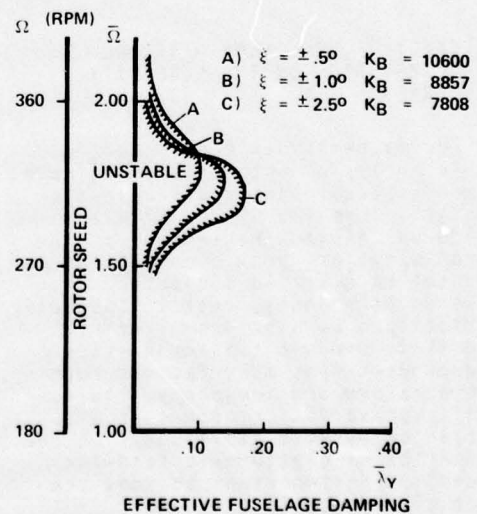
Figure 11. Stability boundaries for various dynamic amplitudes (BTR elastomer)

160

Ω (RPM) $\bar{\Omega}$

	A	$\xi = \pm .5°$	$K_B = 10600$
	B	$\xi = \pm 1.0°$	$K_B = 8807$
	C	$\xi = \pm 2.5°$	$K_B = 6592$

UNSTABLE

EFFECTIVE FUSELAGE DAMPING
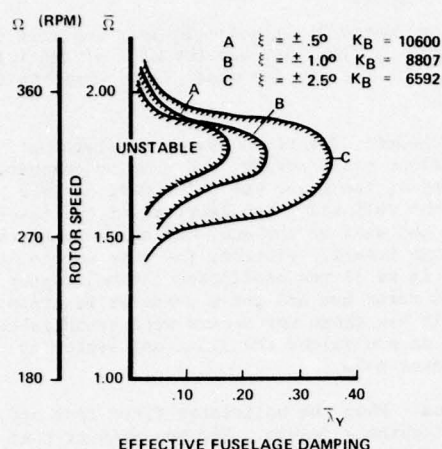
Figure 12. Stability boundaries for various dynamic amplitudes (BTR IV elastomer)

CONCLUSIONS

1. A ground resonance stability analysis for helicopters incorporating a model of an ideal *linear viscoelastic blade restraint* has been developed. This analysis is useful in determining the stability boundaries for helicopters with elastomeric lead-lag dampers.

2. For practical design purposes the difference between the viscous and hysteretic types of damping is not dynamically significant. The simplified Coleman analysis can be used to estimate the required characteristics for an elastomeric lead-lag damper, provided proper consideration is given to the higher in-plane natural frequency of the blade.

3. The change in the dynamic characteristics of an elastomeric damper at higher amplitude lowers the critical rotor speed for ground resonance and increases the size of the unstable region. The magnitude of this effect is predictable and has been accommodated within acceptable design limits.

REFERENCES

1. Coleman, R. P., and Feingold, A. M., Theory of Self-Excited Mechanical Oscillations of Helicopter Rotors with Hinged Blades, NACA TR1351, 1958.

2. Gabel, R., and Capurso, V., Exact Mechanical Instability Boundaries as Determined from the Coleman Equation, Journal of the American Helicopter Society, Vol. 7, No. 1, January 1962.

3. Hammond, C. E., An Application of Floquet Theory to Prediction of Mechanical Instability, Journal of the American Helicopter Society, Vol. 19, No. 4, October, 1974.

4. Potter, J. L., Improving Reliability and Eliminating Maintenance with Elastomeric Dampers, Journal of the American Helicopter Society, Vol. 18, No. 1, January, 1973 (Lord Library No. 56).

5. Painter, G. W., The Measurement of the Dynamic Modulus of Elastomers by the Vector Subtraction Method, ASTM Bulletin, October, 1951 (Lord Library No. 13).

Discussion

Mr. Henderson (Air Force Materials Laboratory): I realize that the materials that you are looking at are filled silicone materials and have broad temperature range applications, but have you considered the effects of changes in temperature on the dynamic behavior of the lead lag dampers?

Mr. McGuire: Yes, that has been evaluated. The environment of the lead lag damper is not particularly severe temperature wise the range which is required for helicopter applications is -65F to 160F (219K to 345K), the silicone material shows a variation in characteristics over this range but the variation in spring and damping rates with temperature is not as severe as the strain sensitivity of the material. The same approach could be used to analyze the shift in stability boundaries with variations in temperatures the critical condition was due to the strain sensitivity. The largest changes occurred with amplitude and that is why this was treated in this paper.

Mr. Lepor (Naval Undersea Center): Do you also isolate your gearbox as part of the damping requirement?

Mr. McGuire: No, transmission isolation is really a different problem. The Hughes AH does not incorporate discrete transmission isolators the gearbox and the rotor system are mounted rigidly to the fuselage but they consider structural stiffnesses and modes which result. The Bell AH on the other hand incorporates a rather complex nodal flex beam system to isolate rotor disturbances. The purpose of the elastomeric lead lag damper is not isolation and it does not serve that function at all. It basically prevents an instability which could otherwise occur.

Mr. Lepor: How does blade slap affect what you have done? If you have a condition of blade slap you have an interaction between your rotor and the other blade?

Mr. McGuire: It doesn't have any other effect on this damper than it would on a viscous or friction damper. It would typically result in increased amplitudes at the damper for some transient condition.

Mr. Lepor: Would damping the blade have any effect on the interior noise level in the cabin?

Mr. McGuire: No, I don't think it would. It probably would be significant. It can influence the torsional dynamics of the drive system and it can also have a significant effect on rotor vibration levels. There is a distinct difference in vibration levels depending upon which type of damper was used relative to friction dampers. But as far as noise isolation I would be kidding to pretend that I had any information that would indicate that it

reduced that.

Mr. Fox (Barry Division): In your analysis on the mass did you just use the mass of the rotor hub or did you use the mass of the whole helicopter?

Mr. McGuire: The fixed system consisted of equivalent mass, spring, and damping parameters defined at the rotor hub which were derived from the roll and pitch inertias of the fuselage, the mass of the hub, and the mass of the fuselage itself. Probably the best way to look at it is as if you oscillated the helicopter at the rotor hub and got a transfer function; that is how these parameters were established. It is an equivalent translational system at the rotor hub.

Mr. Fox: When the helicopter first took off it was pitching sideways. Did you predict that kind of mode?

Mr. McGuire: I think that that was a first flight and control sensitivity is something that a pilot has to get used to and I think that was more of the fact that this was the first time that that helicopter had taken off. I don't think that a pilot that was familiar with the control sensitivities would have encountered that, it was not related to ground resonance.

Mr. Fox: Was the ground resonance like an up and down motion?

Mr. McGuire: No, ground resonance would be a rolling motion. It would typically occur before the helicopter is off the ground and in this case the motion that you saw was probably due to the fact that there was a new pilot at the controls since nobody had flown the helicopter before.

EVALUATION OF ISOLATION MOUNTS IN

REDUCING STRUCTUREBORNE NOISE

Thomas F. Derby

BARRY DIVISION
Barry Wright Corporation
Watertown, Massachusetts

This paper presents an evaluation of the effectiveness of isolators in reducing structureborne noise transmitted from a piece of equipment, through the isolators, to the foundation. The results are based on a theoretical model of equipment, isolator, and foundation represented as internally damped rods. This model is used to represent equipment and foundation structural resonances as well as standing wave effects in the isolator. A computer program is presented that obtains the results in graphical form. Conclusions are drawn, based on the graphical results, as to which quantities should be measured in order to evaluate the effectiveness of isolators and also in regard to the effects of isolator parameters in reducing structureborne noise. The applicability of the analysis to elastomeric and metallic type isolators is also discussed.

INTRODUCTION AND SUMMARY

The increased concerns with reducing structureborne noise caused by shipboard equipment has raised questions concerning the evaluation of isolation mounts.

One problem seems to be what is measured according to MIL-STD-740B and how this relates to what the ultimate purpose of the Navy is in reducing structureborne noise. The reason for MIL-STD-740B is to evaluate the noisiness of a piece of equipment without taking into consideration the foundation on which it is to be mounted. The ultimate problem is the amount of ship deck or hull vibration caused by the machinery.

The purpose of MIL-STD-740B is to evaluate the noisiness of a piece of equipment, not to evaluate isolation mounts. Among other specifications MIL-STD-740B states that: (1) the equipment "shall be tested resiliently mounted regardless of whether or not resilient mountings are used in service"; (2) accelerometers used to measure the acceleration vibration level of the equipment shall be located "directly above the resilient mountings"; (3) "the complete assembly (i.e., equipment on resilient mountings) should be supported on reinforced concrete or cast metal floor which is preferably in direct contact with the ground".

The purpose of the resilient mounts and the massive and rigid foundation specified for testing is to eliminate any effects due to the foundation. It is simulating a piece of equipment freely floating in space so that this situation can be used as a standard evaluation of the noisiness of equipment.

Acceptable acceleration levels are given by Figure 1 of MIL-STD-740B for equipment types 1, 2, and 3. All compressors and internal combustion engines are type 1 equipment. All pumps are type 2 equipment. All other equipment is type 3. Types 1 and 2 acceptable levels are functions of frequency as shown in Figure 1 of MIL-STD-740B. Type 3 acceptable level is 85 db re 10^{-3} cm/sec^2 (approximately 10^{-6} g's) from 25 to 8000 Hz. If the equipment is to be solidly mounted on board ship (it is never solidly mounted for testing according to MIL-STD-740B), then the acceptable acceleration levels are 20 db less than the acceptable levels for resiliently mounted equipment. This difference in acceptable levels between resiliently and solidly mounted equipment is essentially attributing a factor of

ten reduction in vibration to the resilient mountings.

The Navy's primary concern in reducing structureborne noise is illustrated in Figure 1. Vibrations caused by equipment is transmitted through the resilient mountings (if they are present in service) to the ship deck which in turn transmits the vibration to the hull. The hull then radiates this noise through the water where it can be detected and used to locate the ship.
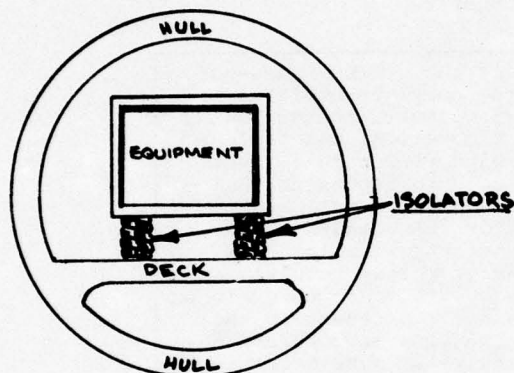
Fig. 1 - Schematic model of equipment mounted on ship deck

The impracticality of having real conditions is recognized because a) ships have not been built, b) different locations on the ship have different structural responses, and c) the same machine can go into different ships and/or different locations on the ship.

Even if real conditions are present there are some questions concerning which response quantities should be used in evaluating the effectiveness of isolation mounts in reducing structureborne noise. Isolation mount effectiveness should be determined by the value of the response ratio, which is defined as the vibrational amplitude of concern when equipment is isolation mounted, divided by this same amplitude when the equipment is hard mounted. Isolation mounts have been evaluated on the basis of the value of the ratio of the acceleration on the foundation side of the mount divided by the acceleration at the equipment side.

The purpose of this paper is twofold: a) to compare structureborne noise, determined according to MIL-STD-740B, to structureborne noise transmitted to a ship deck or hull; and b)

to compare the ratio of accelerations on either side of an isolation mount to the response ratio.

Theoretical results are obtained based on a one directional model of the equipment, isolation mount, and foundation. The mathematical formulation is presented in terms of modified four-pole parameters. The four-pole parameters are determined from the theory of longitudinal vibration of internally damped rods [Ref. 1]. Although this is a simple model, it is felt that its essential feasures (i.e., impedance versus frequency curves having alternate sharp peaks and troughs) are adequate in showing the effects of equipment and foundation structural responses. Also, various isolation mount characteristics are easily accommodated by this model (e.g., a two-stage mounting with a rigid mass included within the isolator).

The theoretical results are presented graphically for various combinations of system parameters. The parameters used are mass, fundamental standing-wave frequency, and damping factor. These results are generated by a computer program which is also presented.

In the next section, a model of the structureborne noise is set up and is mathematically formulated in terms of four-pole parameters. Following this is a section that derives the equations for the four quantities that are used in the analysis. These are the equipment acceleration, the force transmitted to the foundation (or deck), the foundation to equipment acceleration ratio, and the response ratio. The computer program is described in the following section and following this is a section presenting the graphical results obtained from the computer program. A discussion of these results follows this in which conclusions are drawn based on the graphical results. Nonlinear isolator effects are then discussed followed by a section enumerating general conclusions that were drawn from the analysis.

FOUR-POLE PARAMETER ANALYSIS

The transmission of sound from equipment, through an isolator, to a foundation as shown in Figure 2 is modeled as a unidirectional vibration of rods as shown in Figure 3. Using four-pole parameter analysis [Ref. 2], the model is shown in Figure 4. For an individual block as shown in Figure 5, the relationship between input and output forces and velocities is given by
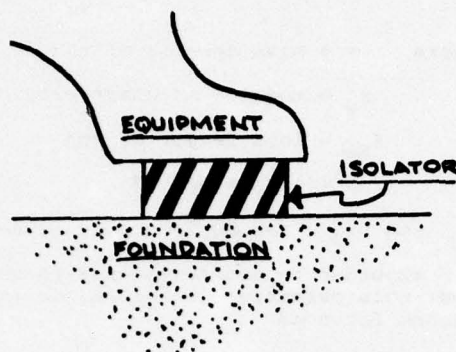
Fig. 2 - Model of equipment,
isolator, and
foundation
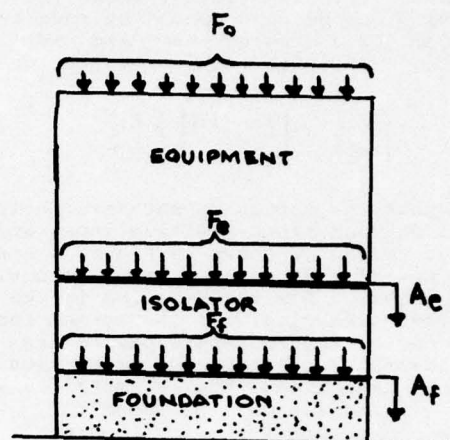
Fig. 3 - Equipment, isolator,
and foundation
modeled as rods
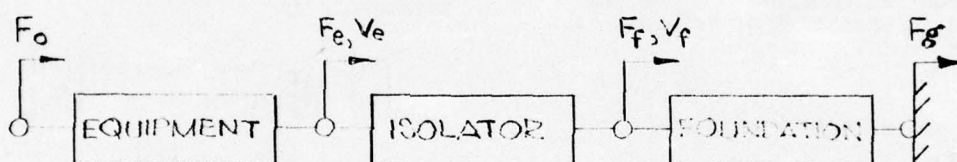
Fig. 4 - Block diagram of equipment, isolator
and foundation
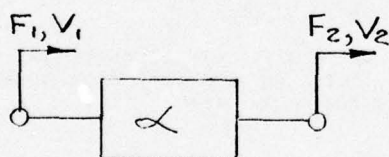
Fig. 5 - Block diagram for
four-pole parameter
analysis

$$\begin{Bmatrix} F_1 \\ V_1 \end{Bmatrix} = \begin{bmatrix} \alpha_{11} & \alpha_{12} \\ \alpha_{21} & \alpha_{22} \end{bmatrix} \begin{Bmatrix} F_2 \\ V_2 \end{Bmatrix} \qquad (1)$$

where the forces F_1 and F_2 are the input and output forces and V_1 and V_2 are the input and output velocities, respectively. The α_{ij}s are the four-pole parameters representing the block.

The four-pole parameters are defined as

$$\alpha_{11} = \frac{F_1}{F_2} \bigg| V_2 = 0 \qquad (2)$$

$$\alpha_{12} = \frac{F_1}{V_2} \bigg| F_2 = 0 \qquad (3)$$

$$\alpha_{21} = \frac{V_1}{F_2} \bigg| V_2 = 0 \qquad (4)$$

$$\alpha_{22} = \frac{V_1}{V_2} \bigg| F_2 = 0 \qquad (5)$$

It is a property of these parameters that

$$\alpha_{11} \alpha_{22} - \alpha_{12} \alpha_{21} = 1 \qquad (6)$$

so that only three parameters are necessary to define a block.

165

Transmission of vibration in the opposite direction to that shown in Figure 5 can be represented by inverting Eq. (1) and using $-V_1$ and $-V_2$ for the velocities. This results in

$$\begin{Bmatrix} F_2 \\ -V_2 \end{Bmatrix} = \begin{bmatrix} \alpha_{22} & \alpha_{12} \\ \alpha_{21} & \alpha_{11} \end{bmatrix} \begin{Bmatrix} F_1 \\ -V_1 \end{Bmatrix} \quad (7)$$

Note that the forces do not have their signs changed since positive input and output forces as shown in Figure 5 are also positive output and input forces, respectively, for transmission in the opposite direction. If the system represented by the four-pole parameters has identical transmission properties in both directions, the α matrices in Eqs. (1) and (7) must be identical, hence

$$\alpha_{22} = \alpha_{11} \quad (8)$$

In this case only two four-pole parameters are necessary to define the system. The four-pole parameters for a damped rod can be obtained from the analysis in Chapter 6 of Reference 1. They are

$$\alpha_{11} = \frac{\tilde{F}_0}{\tilde{F}_1} \quad \text{(Fig. 6.4(c) with M = 0)}$$

$$= \cos(n^*\ell) \quad \text{(Eq. 6.91)} \quad (9)$$

$$\alpha_{12} = \frac{\tilde{F}_0}{j\omega\tilde{\xi}_1} \quad \text{(Fig. 6.4(a) or (b) with M=0)}$$

$$= \frac{j\omega M_r \sin(n^*\ell)}{n^*\ell} \quad \text{(Eqs. 6.91 and 6.92)} \quad (10)$$

$$\alpha_{21} = \frac{j\omega\tilde{\xi}_0}{\tilde{F}_1} \quad \text{(Fig. 6.4(c) with M = 0)}$$

$$= \frac{-(n^*\ell)\sin(n^*\ell)}{j\omega M_r} \quad \text{(Eqs. 6.91 and 6.92)} \quad (11)$$

$$\alpha_{22} = \frac{j\omega\tilde{\xi}_0}{j\omega\tilde{\xi}_1} \quad \text{(Fig. 6.4(a) or (b) with M = 0)}$$

$$= \cos(n^*\ell) \quad \text{Eqs. 6.86 or 6.88)} \quad (12)$$

where M_r is the mass of the rod and ω is frequency (radians/second). The quantity $n^*\ell$ is a complex number and is defined as

$$n^*\ell = \sqrt{\frac{\rho/E_\omega}{1+j\,\delta_{E\omega}}} \; \omega\ell \quad (13)$$

where ρ = mass density of rod

E_ω = modulus of elasticity of rod

$\delta_{E\omega}$ = loss factor of rod

ℓ = length of rod

E_ω and $\delta_{E\omega}$ can be frequency dependent.

In order to nondimensionalize the four-pole parameter equations, define a psuedo force as

$$P_i = j\omega m V_i = m a_i \quad (14)$$

where m is a reference mass and a_i is the acceleration corresponding to the velocity V_i. Eq. (1) can be written in terms of modified four-pole parameters as

$$\begin{Bmatrix} F_1 \\ P_1 \end{Bmatrix} = \begin{bmatrix} \alpha_{11} & \alpha_{12}/j\omega m \\ j\omega m\,\alpha_{21} & \alpha_{22} \end{bmatrix} \begin{Bmatrix} F_2 \\ P_2 \end{Bmatrix}$$
$$= \begin{bmatrix} \beta_{11} & \beta_{12} \\ \beta_{21} & \beta_{22} \end{bmatrix} \begin{Bmatrix} F_2 \\ P_2 \end{Bmatrix} \quad (15)$$

where the β_{ij}s are the modified four-pole parameters.

Using Eqs. (9) through (12) with Eq. (15), the modified four-pole parmeters for a rod are

$$\beta = \begin{bmatrix} \cos(n^*\ell) & \dfrac{(M_r/m)\sin(n^*\ell)}{n^*\ell} \\ \dfrac{-(n^*\ell)\sin n^*\ell}{M_r/m} & \cos(n^*\ell) \end{bmatrix} \quad (16)$$

As a check, the determinant of the above matrix equals 1, and $\alpha_{11} = \alpha_{22}$ since a rod has identical transmission properties in both directions.

There are three undamped natural frequencies that can be defined for a rod. They are solutions of the equations

$$\sin n\ell = 0 \quad \text{(free-free)} \qquad (17)$$

$$\sin n\ell = 0 \quad \text{(clamped-clamped)} \qquad (18)$$

$$\cos n\ell = 0 \quad \text{(clamped-free)} \qquad (19)$$

$$n\ell = \sqrt{\rho/E_\omega} \; \ell \; \omega_n \qquad (20)$$

where ω_n = natural frequency

Discounting zero frequency, the natural frequencies for free-free and clamped-clamped are the same and occur when

$$n\ell = k\pi \quad (k = 1, 2, ---) \qquad (21)$$

so that

$$\omega_n = 2\pi f_n = \frac{k\pi}{\sqrt{\rho/E_\omega}\,\ell} \qquad (22)$$

The lowest free-free or clamped-clamped natural frequency is

$$f_1 = \frac{1}{2\ell\sqrt{\rho/E_\omega}} \qquad (23)$$

For clamped-free rods, the natural frequencies occur when

$$n\ell = (2k-1)\pi/2 \quad (k = 1, 2, ---) \qquad (24)$$

so that

$$\omega_n = 2\pi f_n = \frac{(2k-1)\pi/2}{\sqrt{\rho/E_\omega}\,\ell} \qquad (25)$$

The lowest clamped-free natural frequency is

$$f_1 = \frac{1}{4\ell\sqrt{\rho/E_\omega}} \qquad (26)$$

which is 1/2 the free-free or clamped-clamped natural frequency.

Define the lowest free-free or clamped-clamped natural frequency as the rod frequency f_r. Then, for constant $E_\omega = E$ and $\delta_{E\omega} = \delta$

$$n*\ell = \frac{\pi}{\sqrt{1+j\delta}} \; f/f_r \qquad (27)$$

To completely define a rod for the above analysis, only the values of M_r/m, f_r, and δ need be given.

For very low frequencies, the rod depicted in Figure (6a) acts like a mass M_r and that in Figure (6b) acts like a spring of stiffness
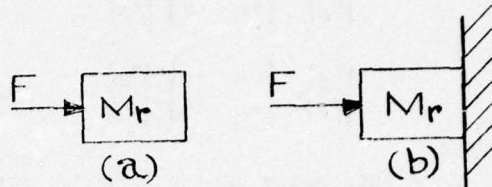
Fig. 6 - Low frequency models for a rod

$$K_r = 4M_r f_r^2 \qquad (28)$$

This relationship is obtained by expressing stiffness in terms of the four-pole parameter α_{21} as

$$K = \frac{j\omega}{\alpha_{21}} \qquad (29)$$

and using Eqs. (11) and (27) in the limit as ω approaches zero.

MATHEMATICAL MODEL FOR STRUCTUREBORNE NOISE

Representing the equipment, isolator, and foundation as rods, the mathematical model is derived from the block diagram in Figure 7.
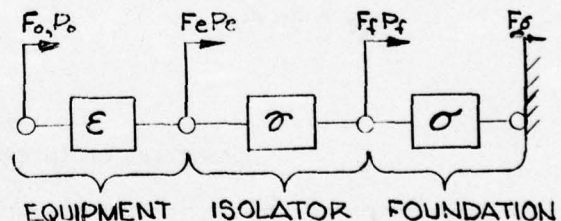
Fig. 7 - Four-pole parameter model of equipment, isolator and foundation

In this diagram ε, γ, and σ represent the modified four-pole parameters for the equipment, isolator, and foundation, respectively. In matrix form, the equations are

$$\begin{Bmatrix} F_o \\ P_o \end{Bmatrix} = \begin{bmatrix} \varepsilon_{11} & \varepsilon_{12} \\ \varepsilon_{21} & \varepsilon_{22} \end{bmatrix} \begin{Bmatrix} F_e \\ P_e \end{Bmatrix} \qquad (30)$$

$$\begin{Bmatrix} F_e \\ P_e \end{Bmatrix} = \begin{bmatrix} \gamma_{11} & \gamma_{12} \\ \gamma_{21} & \gamma_{22} \end{bmatrix} \begin{Bmatrix} F_f \\ P_f \end{Bmatrix} \qquad (31)$$

$$\begin{Bmatrix} F_f \\ P_f \end{Bmatrix} = \begin{bmatrix} \sigma_{11} & \sigma_{12} \\ \sigma_{21} & \sigma_{22} \end{bmatrix} \begin{Bmatrix} F_g \\ 0 \end{Bmatrix} \qquad (32)$$

where

F_o = internally generated force acting on equipment

P_o = acceleration times reference mass at the point of internal force generation

F_e = force acting at equipment-isolator interface

P_e = acceleration times reference mass at equipment-isolator interface

F_f = force acting at isolator-foundation interface

P_f = acceleration times reference mass acting at isolator-foundation interface

F_g = force acting at foundation-ground interface

The quantities of interest are summarized in Table 1.

Since F_g is not needed in the analysis, it is eliminated from Eq. (32) resulting in

$$F_f = \zeta_f \, P_f \qquad (33)$$

where

$$\zeta_f = \sigma_{11} / \sigma_{21} \qquad (34)$$

which is the normalized driving point impedance of the foundation. From Eqs. (31) and (33)

$$F_e = \left(\gamma_{11} \, \zeta_f + \gamma_{12} \right) P_f \qquad (35)$$

$$P_e = \left(\gamma_{21} \, \zeta_f + \gamma_{22} \right) P_f \qquad (36)$$

From Eqs. (30), (35), and (36)

$$F_o = \left[\varepsilon_{11} \left(\gamma_{11} \, \zeta_f + \gamma_{12} \right) \right.$$

$$\left. + \, \varepsilon_{12} \left(\gamma_{21} \, \zeta_f + \gamma_{22} \right) \right] P_f \qquad (37)$$

The <u>normalized equipment acceleration</u> is obtained from Eqs. (36) and (37) with $\zeta_f = \infty$, hence

$$S = \frac{\gamma_{21}}{\varepsilon_{11} \, \gamma_{11} + \varepsilon_{12} \, \gamma_{21}} \qquad (38)$$

The <u>force transmissibility</u> is obtained using Eqs. (33) and (37)

$$T = \frac{\zeta_f}{\varepsilon_{11} \left(\gamma_{11} \, \zeta_f + \gamma_{12} \right) + \varepsilon_{12} \left(\gamma_{21} \, \zeta_f + \gamma_{22} \right)} \qquad (39)$$

The <u>acceleration ratio</u> is obtained from Eq. (36)

$$A = \frac{1}{\gamma_{21} \, \zeta_f + \gamma_{22}} \qquad (40)$$

The <u>response ratio</u> is obtained as the ratio of the force transmissibility from Eq. (39) divided by the force transmissibility when the isolator is replaced by a rigid, massless rod. In this case the γ four-pole parameters are

$$\begin{bmatrix} \gamma_{11} & \gamma_{12} \\ \gamma_{21} & \gamma_{22} \end{bmatrix} = \begin{bmatrix} 1 & 0 \\ 0 & 1 \end{bmatrix} \qquad (41)$$

TABLE 1

QUANTITIES OF INTEREST IN THEORETICAL MODEL

SYMBOL	EQUATION	DESCRIPTION	PROBLEM OF INTEREST
S	$S = \dfrac{P_e}{F_o}\Big\|_{\text{rigid foundation}}$	Normalized Equipment Acceleration	MIL-STD-740B
T	$T = F_f/F_o$	Force Transmissibility	Ship Silencing
A	$A = P_f/P_e$	Acceleration Ratio	Common Mount Evaluation
R	$R = F_f/(F_f)_{\text{NO ISOLATOR}}$ $= P_f/(P_f)_{\text{NO ISOLATOR}}$	Response Ratio	Valid Mount Evaluation

168

so that

$$(T)_{\text{NO ISOLATOR}} = \frac{\zeta_f}{\varepsilon_{11} \zeta_f + \varepsilon_{12}} \qquad (42)$$

and

$$R = \frac{\varepsilon_{11} \zeta_f + \varepsilon_{12}}{\varepsilon_{11} \left(\gamma_{11} \zeta_f + \gamma_{12} \right) + \varepsilon_{12} \left(\gamma_{21} \zeta_f + \gamma_{22} \right)} \qquad (43)$$

One method of achieving better high frequency vibration isolation is to incorporate an additional mass within the isolator [Ref. 3] as shown schematically in Figure 8 and in block diagram form in Figure 9.
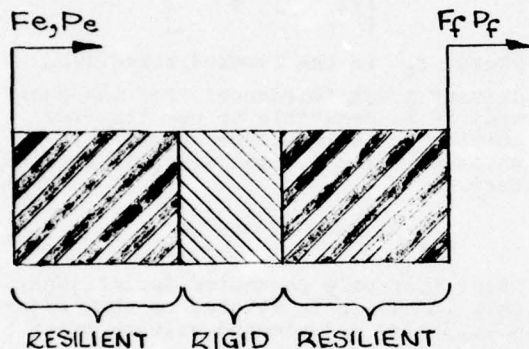
Fig. 8 - Rigid mass incorporated within isolator
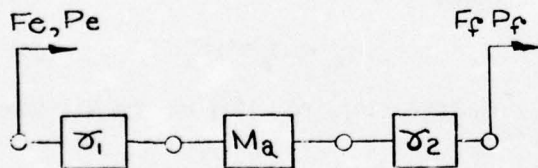
Fig. 9 - Four-pole parameter model of a rigid mass incorporated within isolator

The four-pole parameters for a mass are

$$\begin{bmatrix} 1 & j\omega m_a \\ 0 & 1 \end{bmatrix}$$

and the modified four-pole parameters are

$$\begin{bmatrix} 1 & m_a/m \\ 0 & 1 \end{bmatrix}$$

where m_a is the mass added to the isolator and m is the reference mass. As indicated by Eqs. (30) through (32), the manner in which the four-pole parameter blocks are combined is to multiply the matrices, so that

$$\begin{Bmatrix} F_e \\ P_e \end{Bmatrix} = \begin{bmatrix} \gamma_{11} & \gamma_{12} \\ \gamma_{21} & \gamma_{22} \end{bmatrix}_1 \begin{bmatrix} 1 & m_a/m \\ 0 & 1 \end{bmatrix} \begin{bmatrix} \gamma_{11} & \gamma_{12} \\ \gamma_{21} & \gamma_{22} \end{bmatrix}_2 \begin{Bmatrix} F_f \\ P_f \end{Bmatrix} \qquad (44)$$

where the subscripts 1 and 2 stand for the parts of the isolator on either side of the added mass. The product of the three matrices in Eq. (44) is the matrix of four-pole parameters for the isolator with an added mass and can be written as

$$\begin{bmatrix} \gamma_{11} & \gamma_{12} \\ \gamma_{21} & \gamma_{22} \end{bmatrix} = \begin{bmatrix} \gamma_{11} & \gamma_{12} \\ \gamma_{21} & \gamma_{22} \end{bmatrix}_1 \begin{bmatrix} \gamma_{11} & \gamma_{12} \\ \gamma_{21} & \gamma_{22} \end{bmatrix}_2$$
$$+ \frac{m_a}{m} \begin{Bmatrix} \gamma_{11} \\ \gamma_{21} \end{Bmatrix}_1 \{ \gamma_{21} \;\; \gamma_{22} \}_2 \qquad (45)$$

For the case where there is no added mass, define the four-pole parameters with a 0 subscript, so that

$$\begin{bmatrix} \gamma \end{bmatrix}_0 = \begin{bmatrix} \gamma \end{bmatrix}_1 \begin{bmatrix} \gamma \end{bmatrix}_2 \qquad (46)$$

Also, if the two resilient parts of the isolator are the same, then

$$[\gamma]_0 = [\gamma]_1^2 \qquad (47)$$

and the four-pole parameters for the complete isolator can be written in terms of the four-pole parameters of the isolator with no added mass.

$$\begin{bmatrix} \gamma_{11} & \gamma_{12} \\ \gamma_{21} & \gamma_{22} \end{bmatrix} = \qquad (48)$$

$$\begin{bmatrix} \gamma_{11} + \dfrac{m_a}{m} \dfrac{\gamma_{21}}{2} & \gamma_{12} + \dfrac{m_a}{m} \dfrac{1+\gamma_{11}}{2} \\[2ex] \gamma_{21} + \dfrac{m_a}{m} \dfrac{\gamma_{21}^2}{2(1+\gamma_{11})} & \gamma_{22} + \dfrac{m_a}{m} \dfrac{\gamma_{21}}{2} \end{bmatrix}_0$$

This relationship is obtained from Eq. (45) by equating the elements of the matrices in Eq. (47) and using the fact that $\gamma_{11} = \gamma_{22}$ for all γ matrices.

For the purpose of this analysis, it is convenient to take the mass of the equipment as the reference mass and also to define a reference frequency as the natural frequency of the equipment mass on the stiffness of the isolator. Using e and i as subscripts for equipment and isolator, respectively, the reference natural frequency is

$$f_n = \frac{1}{2\pi} \sqrt{\frac{K_i}{M_e}} \qquad (49)$$

and using Eq. (28)

$$f_n = \frac{1}{\pi} \sqrt{\frac{M_i}{M_e}} \, f_i \qquad (50)$$

Eq. (50) can be used to determine the first standing wave frequency of the isolator, given the natural frequency of the isolator system and the ratio of isolator mass to equipment mass.

In order to compare the equations given above for the quantities S, T, A, and R with results obtained by others [Refs. 4 and 5] in terms of impedances and transmissibilities, the four-pole parameters can be written in terms of these quantities. Referring to Figure 5 and the definitions of the four-pole parameters in Eqs. (2) through (5), the transmissibility and the input and output blocked driving point impedances are

$$T = 1/\alpha_{11} \qquad (51)$$

$$Z_1 = \alpha_{11}/\alpha_{21} \qquad (52)$$

$$Z_2 = \alpha_{22}/\alpha_{21} \qquad (53)$$

Using these equations and the four-pole parameter relationship given by Eq. (6) the four-pole parameters are

$$[\alpha] = \begin{bmatrix} \dfrac{1}{T} & \dfrac{Z_2}{T} - TZ_1 \\ \dfrac{1}{TZ_1} & \dfrac{Z_2}{TZ_1} \end{bmatrix} \qquad (54)$$

Defining an impedance normalized by the impedance of the reference mass as

$$\zeta = \frac{Z}{j\omega m} \qquad (55)$$

the modified four-pole parameters are

$$[\beta] = \begin{bmatrix} \dfrac{1}{T} & \dfrac{\zeta_2}{T} - T\zeta_1 \\ \dfrac{1}{T\zeta_1} & \dfrac{\zeta_2}{T\zeta_1} \end{bmatrix} \qquad (56)$$

and for the case where the transmission properties are the same in either direction (as in the case for a rod), $\zeta_1 = \zeta_2 = \zeta_B$ and the modified four-pole parameters are

$$[\beta] = \begin{bmatrix} \dfrac{1}{T} & (1-T^2) \, \dfrac{\zeta_B}{T} \\ \dfrac{1}{T\zeta_B} & \dfrac{1}{T} \end{bmatrix} \qquad (57)$$

where ζ_B is the blocked normalized driving point impedance. For the equipment it is desirable to use the free driving point impedance at point 2, which in terms of the four-pole parameters is

$$Z_{2F} = \alpha_{12}/\alpha_{11} \qquad (58)$$

Using four-pole parameter definitions, this impedance is related to the transmissibility and blocked driving point impedances according to

$$Z_{2F} = Z_2 - T^2 Z_1 \qquad (59)$$

and for the case where the transmission properties are the same in either direction the free and blocked normalized driving point impedance is related according to

$$\zeta_F = (1-T^2)\zeta_B \qquad (60)$$

Using Eq. (60), Eq. (52) can be written as

$$[\beta] = \begin{bmatrix} \dfrac{1}{T} & \dfrac{\zeta_F}{T} \\ \dfrac{1-T^2}{T\zeta_F} & \dfrac{1}{T} \end{bmatrix} \qquad (61)$$

Using Eq. (57) for the isolator and foundation, and Eq. (61) for the equipment, with Eqs. (38), (39), (40) and (43) given above for the quantities S, T, A, and R, they can be written as

$$S = \frac{T_e}{\zeta_e + \zeta_i} \qquad (62)$$

$$T = \frac{\zeta_f \, T_e \, T_i \, \zeta_i}{\left(\zeta_f + \zeta_i\right)\left(\zeta_e + \zeta_i\right) - \left(T_i \zeta_i\right)^2} \tag{63}$$

$$A = \frac{T_i \zeta_i}{\zeta_f + \zeta_i} \tag{64}$$

$$R = \frac{\left(\zeta_f + \zeta_e\right) T_i \zeta_i}{\left(\zeta_f + \zeta_i\right)\left(\zeta_e + \zeta_i\right) - \left(T_i \zeta_i\right)^2} \tag{65}$$

where ζ_e = free normalized driving point impedance of the equipment at the equipment-isolator interface.

  T_e = force transmissibility across the equipment.

  ζ_i = blocked normalized driving point impedance of the isolator.

  T_i = force transmissibility across the isolator.

  ζ_f = blocked normalized driving point impedance of the foundation.

Note that the normalized equipment acceleration S does not depend on the foundation, since it was defined on the basis of a foundation with infinite impedance. However, the acceleration ratio A does not depend on the equipment, although no assumptions concerning the equipment were made. The normalized equipment acceleration S and the force transmissibility T depend on equipment transmissibility as well as the equipment impedance, whereas the response ratio R is independent of the equipment transmissibility. Note also the similarity between the expressions for force transmissibility T and response ratio R.

For a rod, the transmissibility and the blocked and free normalized driving point impedances are obtained from Eqs. (16), (57), and (61), respectively, as

$$T = \frac{1}{\cos(n*\ell)} \tag{66}$$

$$\zeta_B = \frac{-M_r/m}{(n*\ell)\tan(n*\ell)} \tag{67}$$

$$\zeta_F = \frac{M_r}{m} \frac{\tan(n*\ell)}{n*\ell} \tag{68}$$

COMPUTER PROGRAM

The equations for the normalized equipment acceleration S, the force transmissibility T, the acceleration ratio A, and the response ratio R (Eqs. (38), (39), (40), and (43)) were used in a computer program, written in FORTRAN for the CDC computers, to obtain the graphs presented in the section THEORETICAL RESULTS below. The modified four-pole parameters for the rods representing equipment, isolator, and foundation were computed using Eq. (16). The graphs were produced using the DISSPLA plotting routines available at CDC computer centers. A listing of the program is given in the Appendix.

The input to the program consists of cards with field length of eight characters. The first card has the number of cases in field one. This is an integer value and must be right justified in the field (i.e., the number ends in column 8). The next four cards are repeated for each case.

Card 1 - The first card of the repeated set has the number of plots (an integer) for this case in field one, followed by as many integer values as the number of plots to determine which plots are to be obtained. The plots that can be obtained are the values of S, T, A, and R as described in Table 1 versus the frequency ratio (ratio of forcing frequency to reference frequency). The numbers designating the type of plot are 1 = A, 2 = R, 3 = S, 4 = T, (e.g., if all four plots are desired, this card would contain the integers 4, 1, 2, 3, and 4 in columns 8, 16, 24, 32, and 40, respectively).

Card 2 - This card contains values of mass ratios, frequency ratios, and loss factors for this case. The first four fields contain the values of mass ratios for foundation, isolator, equipment, and rigid mass included within the isolator, respectively. The next three fields (fields 5, 6, and 7) contain the frequency ratios for the foundation, isolator and equipment, respectively. The next two fields (fields 8 and 9) contain the values of loss factor for the foundation and equipment, respectively. The mass ratios are the values of the masses divided by the reference mass and the frequency ratios are the values of the fundamental rod frequencies divided by the reference frequency. The program is written generally so that the reference mass and reference frequency can be chosen arbitrarily (e.g., if it is desired to use actual values of the masses and frequencies, then a value of unity can be

assumed for the reference mass and the reference frequency). In the present analysis, it is desired to use the equipment mass as the reference mass and the isolation system natural frequency as the reference frequency so that in all cases the equipment mass ratio is set equal to unity and the relationship between isolator mass ratio and isolator frequency ratio, as given in Eq. (50), is maintained. Also, in order to relate to the physical situation, the fundamental rod frequencies are taken to be the free-free for the equipment, the clamped-clamped (which has the same value as the free-free) for the isolator, and the clamped-free (which has half the value of the free-free) for the foundation.

Card 3 - This card contains the number of values (an integer) of the isolator loss factor in field one, followed by the values in the succeeding fields. The program arbitrarily limits the maximum number of values to 5. The plots obtained have one curve for each value of isolator loss factor.

Card 4 - This card sets the range of the frequency ratio for which values of S, T, A, and R are to be plotted. It also sets the number of points per curve. The first two fields contain the low value and high value of the frequency ratio and the third field is an integer number equal to the number of divisions within the range.

The printed output from the computer program consists of a plot number and corresponding table of values for the mass ratios, frequency ratios, and loss factors. The plots are numbered consecutively and the plot numbers are also printed on the plot.

Each of the curves on a plot are marked by a symbol. The symbols correspond to the order in which the isolator loss factor values are input. The order in which the symbols are used is

$$\square \ , \ O \ , \ \triangle \ , \ + \ , \ X$$

THEORETICAL RESULTS

Using the computer program described above, theoretical results were obtained in graphical form for various combinations of system parameters. These results are presented in Figures 10 through 41. For all of the graphs, the loss factor for both the foundation and the equipment was taken to be 0.01. Three different isolator loss factor values were used in this analysis corresponding to the three curves in each

graph. They are 0.1 with the symbol O, 0.2 with the symbol □, and 0.3 with the symbol △. These correspond to isolation system resonant transmissibilities of 10, 5, and 3.3, respectively. The values of the other parameters as they relate to the various graphs are given in Table 2. Note that the equipment mass ratio is always unity so that the equipment mass is the reference mass. Also, the relationship between isolator mass ratio and isolator frequency ratio as given by Eq. (50) is always maintained so that the isolation system natural frequency is the reference frequency. Except for case 4, which simulates a massless isolator, the frequency ratio (the abscissa of the graphs) ranges from zero to six times the isolator frequency ratio so that the first six isolator standing wave frequencies are presented.

Except for those cases that simulate a massless isolator (case 4), a rigid equipment (cases 9 and 10), or a rigid foundation (cases 8 and 10), the fundamental rod frequencies representing equipment isolator and foundation were taken to be in the ratio of 2:3:2, respectively. Although the fundamental frequencies for equipment and foundation are the same, the higher resonant modes for the foundation occur at every other resonant mode of the equipment, since the foundation is modeled as a clamped-free rod and the equipment as a free-free rod. For the even numbered equipment resonant modes, the foundation has an anti-resonant condition. The purpose of choosing the isolator fundamental mode to be 1.5 times that of the equipment and foundation, is to have the isolator resonant modes sometimes coincide with the equipment and foundation modes and sometimes not. The values of the frequency ratios for which the resonant modes occur is given in Table 3 for cases 1, 2, and 3.

For cases 1 through 5 and case 9, the mass ratio of the foundation is unity. For this situation, the minimum values for the driving point impedances for the equipment and foundation are equal. The driving point impedances of the equipment and foundation are measured at the equipment-isolator and isolator-foundation interfaces, respectively, and the minimum values occur at the resonant modes.

DISCUSSION OF THEORETICAL RESULTS

Cases 1 and 2 represent the minimum and maximum values of isolator mass ratios, respectively, and correspond to isolator frequency ratios of 100 and 10, respectively. Isolator frequency ratios

TABLE 2

PARAMETER VALUES FOR GRAPHS

Case	FIG.No. FOR THE QUANTITY				MASS RATIOS				FREQUENCY RATIOS		
	S	T	A	R	Equipment	Isolator	Foundation	Added	Equipment	Isolator	Foundation
1	10	11	12	13	1	0.001	1	0	66.7	100	66.7
2	14	15	16	17	1	0.1	1	0	6.67	10	6.67
3	18	19	20	21	1	0.01	1	0	20	30	20
4	22	23	24	25	1	0.00001	1	0	20	1000	20
5	26	27	28	29	1	0.01	1	0.1	20	30	20
6	18	30	38	34	1	0.01	0.1	0	20	30	20
7	18	31	39	35	1	0.01	10	0	20	30	20
8	18	32	–	36	1	0.01	10^6	0	20	30	10^6
9	40	33	20	37	1	0.01	1	0	10^6	30	20
10	40	41	–	41	1	0.01	10^6	0	10^6	30	10^6

NOTE: Loss factor for equipment and foundation is 0.01.
Loss factor for isolator has values of 0.1, 0.2,
and 0.3 for the three curves on the graph indicated
by the symbols O, □, Δ, respectively.

TABLE 3

RESONANT MODES FOR EQUIPMENT, ISOLATOR, AND FOUNDATION

NATURAL FREQUENCY RATIOS			NATURAL MODE NUMBERS FOR		
CASE 1	CASE 2	CASE 3*	Equipment	Isolator	Foundation
66.7	6.67	20	1		1
100	10	30		1	
133	13.3	40	2		
200	20	60	3	2	2
267	26.7	80	4		
300	30	90		3	
333	33.3	100	5		3
400	40	120	6	4	
465	46.5	140	7		4
500	50	150		5	
534	53.4	160	8		
600	60	180	9	6	5

*Also applicable to cases 4 through 10.

Fig. 10 - Equipment acceleration of
case 1, table 2

Fig. 11 - Force transmissibility of
case 1, table 2
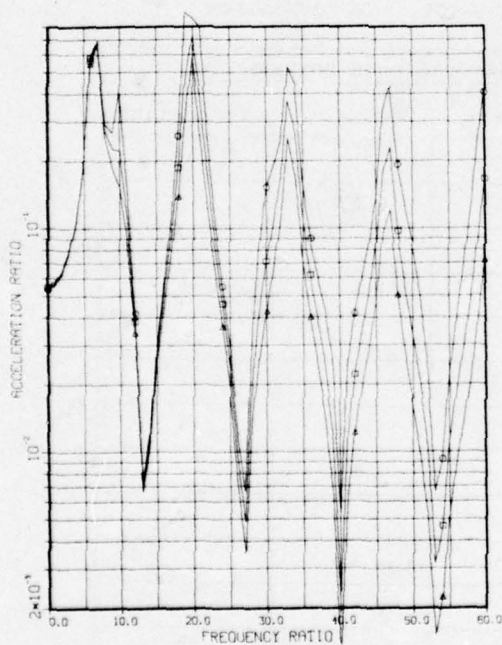
Fig. 12 - Acceleration ratio of
case 1, table 2

Fig. 13 - Response ratio of case 1,
table 2

174

Fig. 14 - Equipment acceleration of case 2, table 2

Fig. 15 - Force transmissibility of case 2, table 2

Fig. 16 - Acceleration ratio of case 2, table 2

Fig. 17 - Response ratio of case 2, table 2

175

Fig. 18 – Equipment acceleration of case 3, table 2
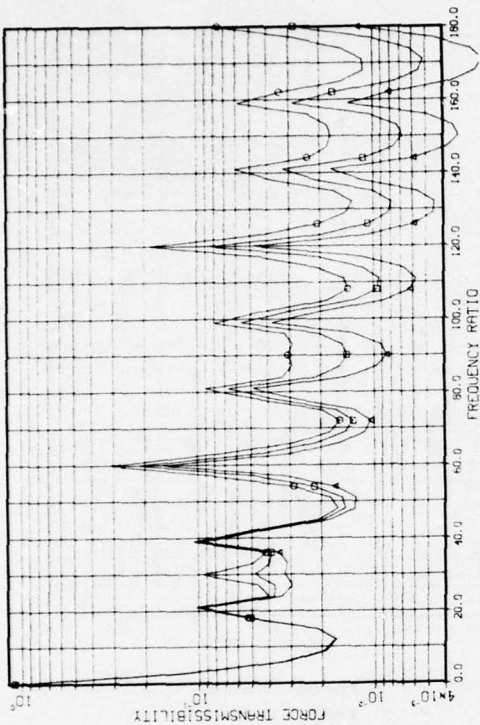
Fig. 19 – Force transmissibility of case 3, table 2

Fig. 20 – Force transmissibility of case 3, table 2

Fig. 21 – Response ratio of case 3, table 2

176

Fig. 22 - Equipment acceleration of Case 4, table 2

Fig. 23 - Force transmissibility of case 4, table 2

Fig. 24 - Acceleration ratio of case 4, table 2

Fig. 25 - Response ratio of case 4, table 2

177

Fig. 27 - Force transmissibility of case 5, table 2

Fig. 26 - Equipment acceleration of case 5, table 2
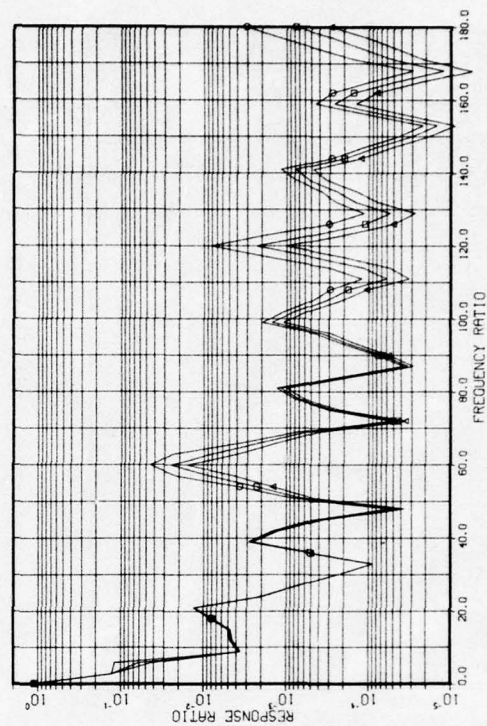
Fig. 29 - Response ratio of case 5, table 2

Fig. 28 - Acceleration ratio of case 5, table 2

178
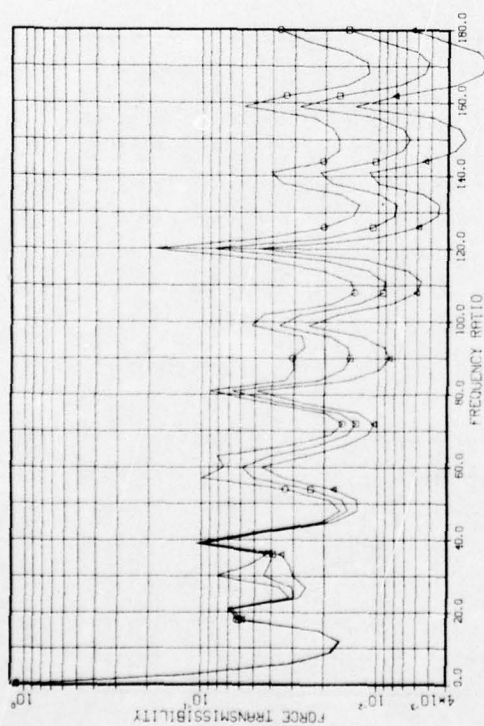
Fig. 30 – Force transmissibility of case 6, table 2
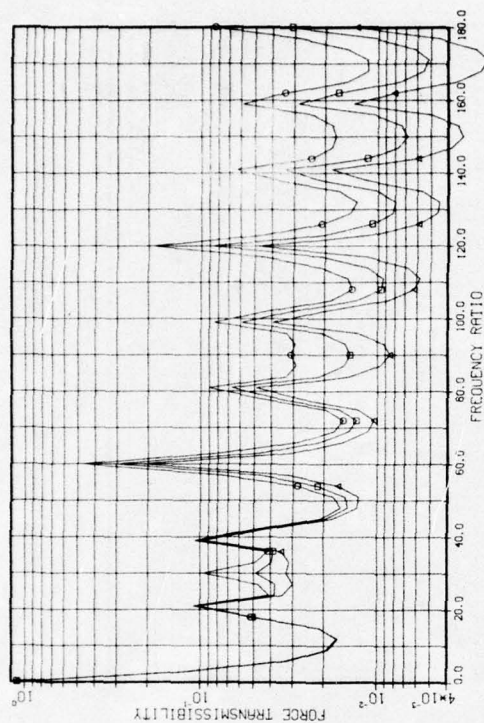
Fig. 31 – Force transmissibility of case 7, table 2
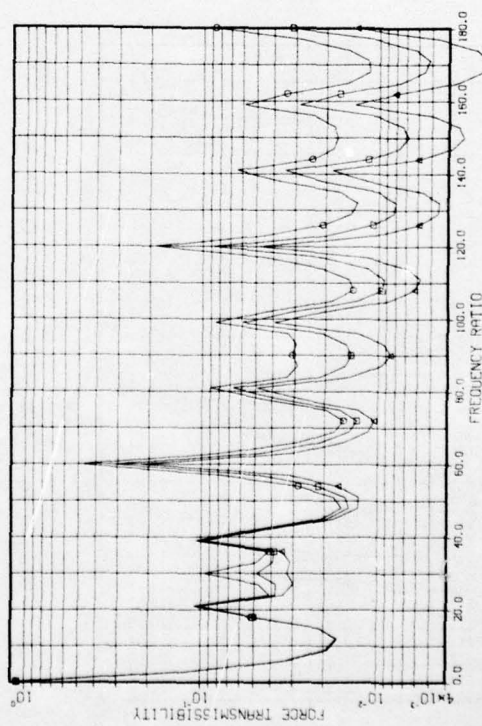
Fig. 32 – Force transmissibility of case 8, table 2
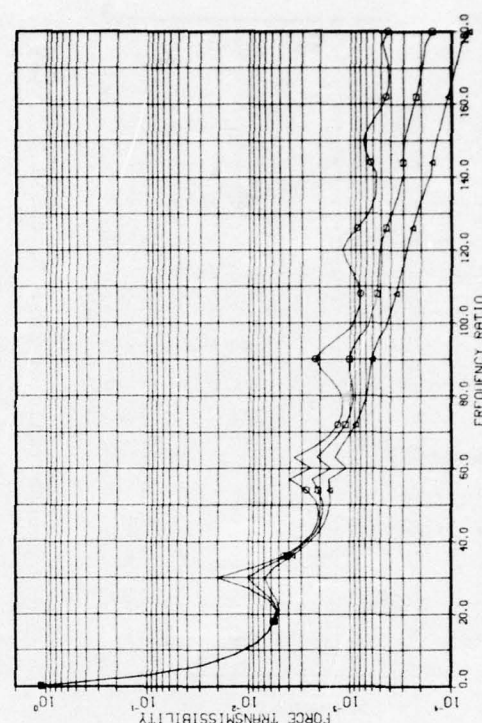
Fig. 33 – Force transmissibility of case 9, table 2

179

Fig. 34 – Response ratio of case 6, table 2

Fig. 35 – Response ratio of case 7, table 2
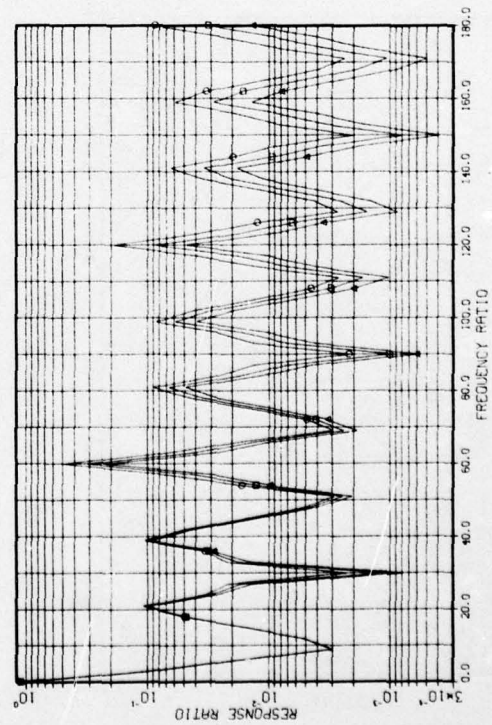
Fig. 36 – Response ratio of case 8, table 2

Fig. 37 – Response ratio of case 9, table 2
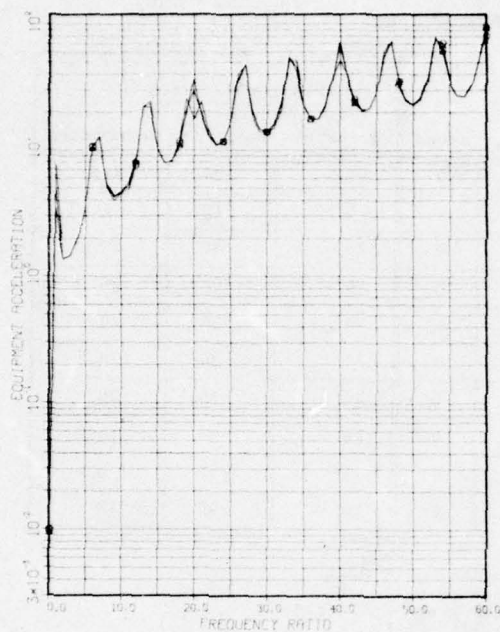
Fig. 39 - Acceleration ratio of case 7, table 2
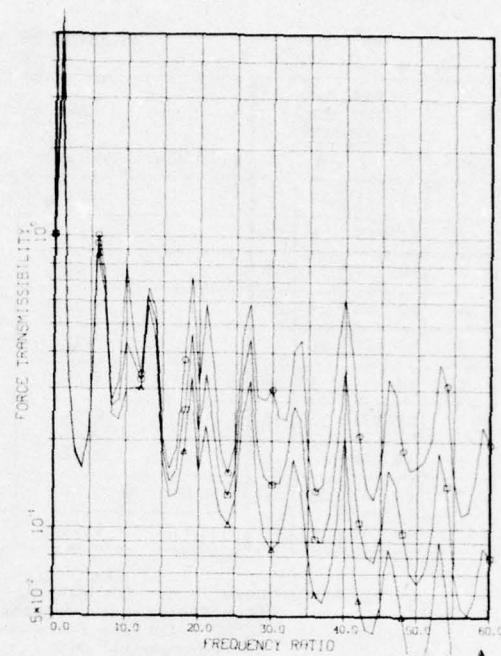

Fig. 41 - Force transmissibility of case 10, table 2
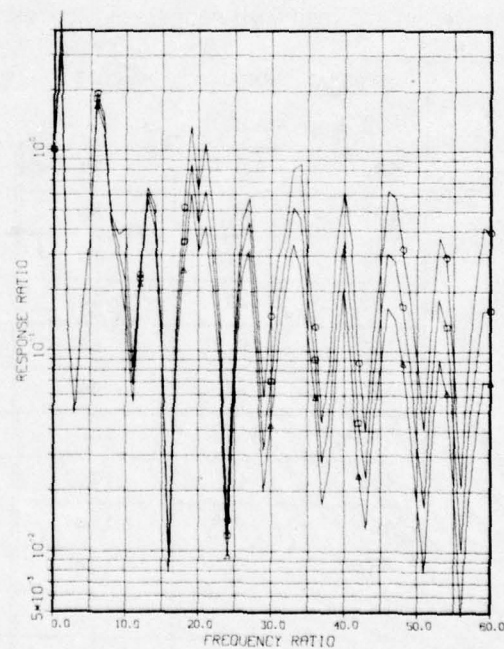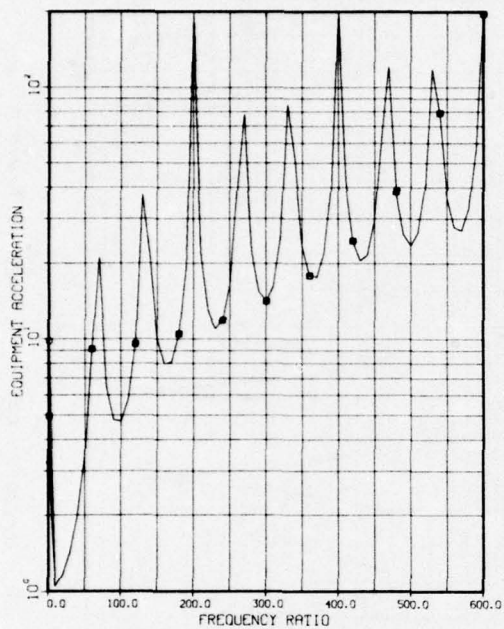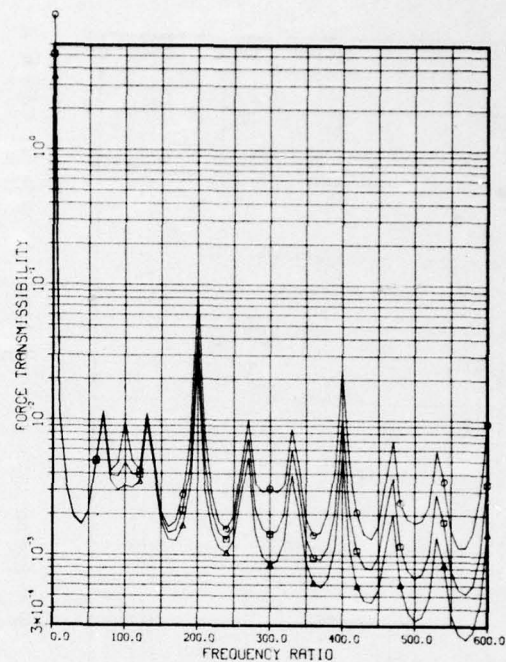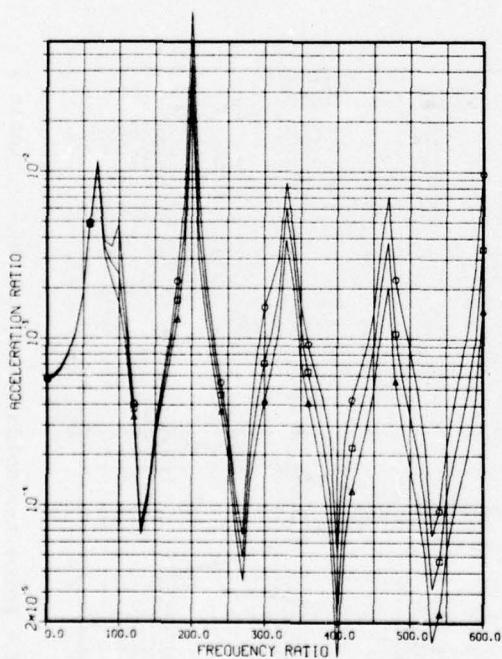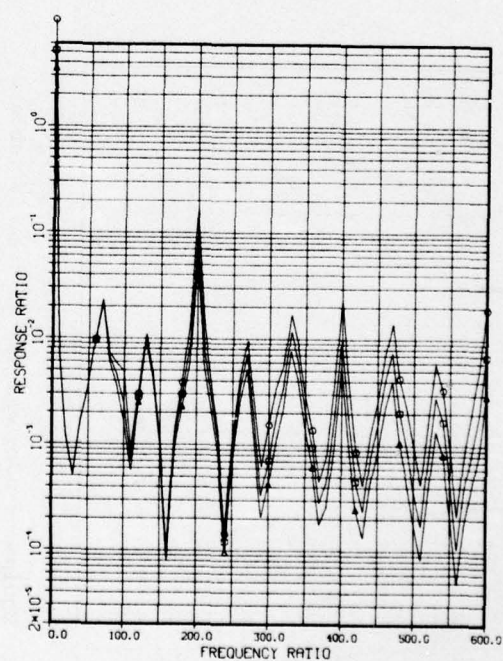

Fig. 38 - Acceleration ratio of case 6, table 2
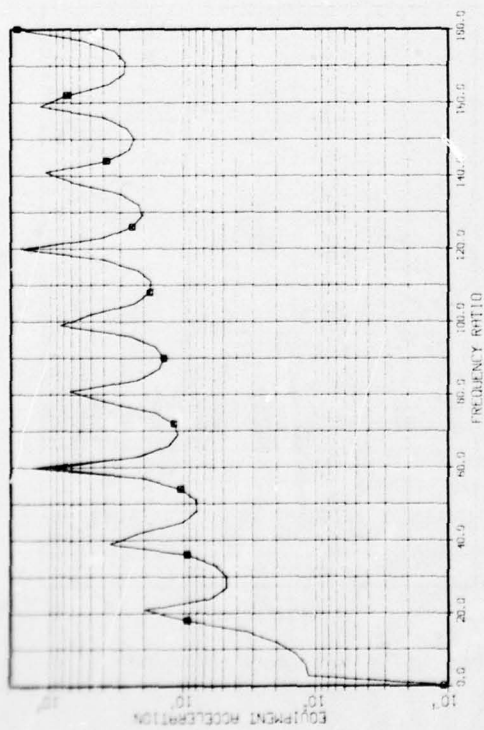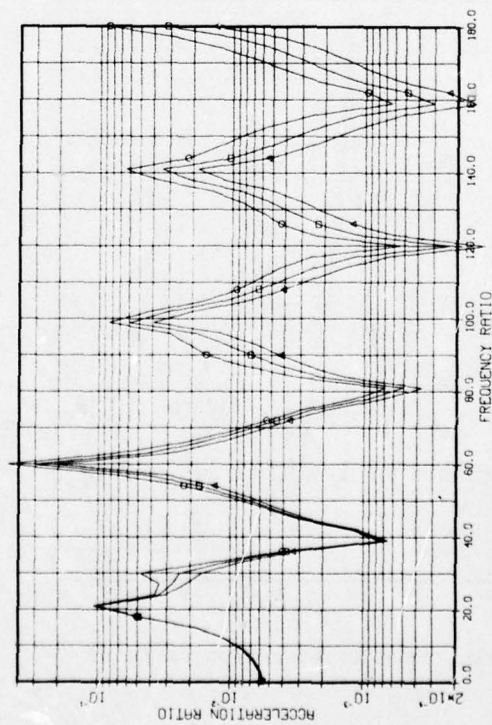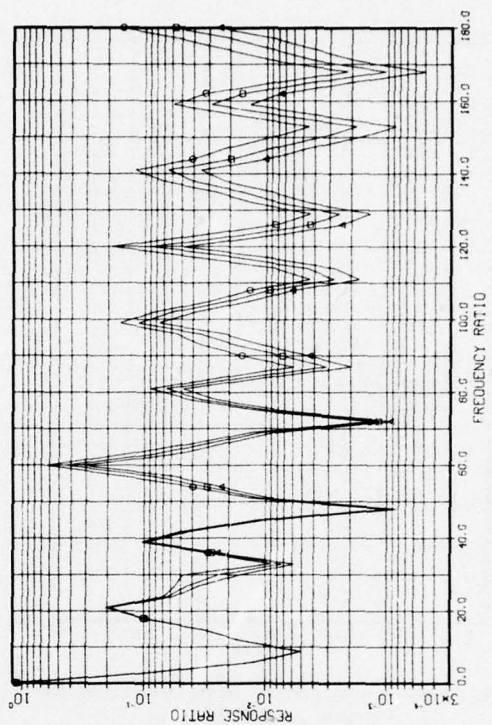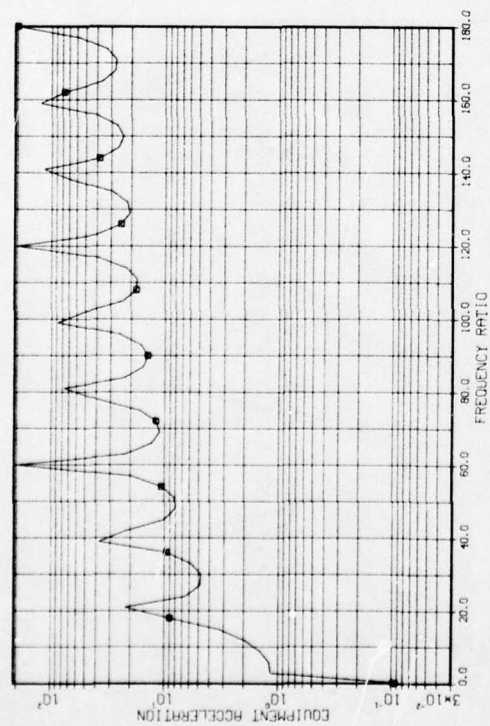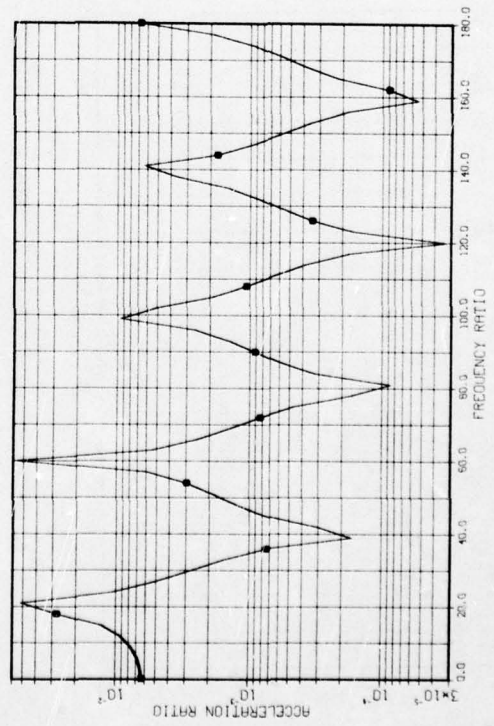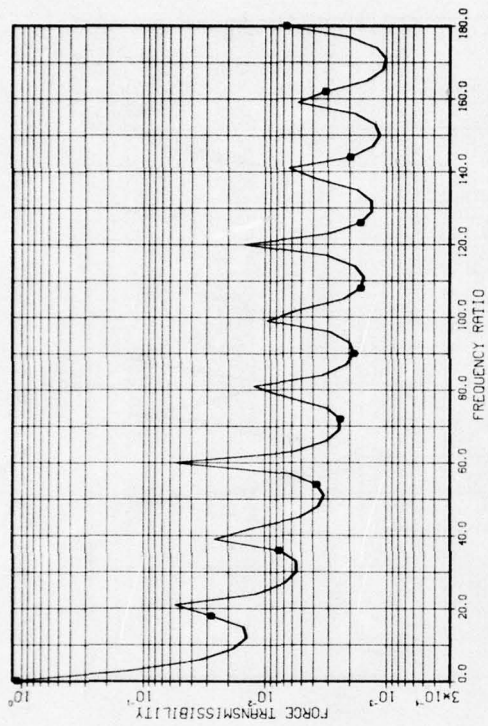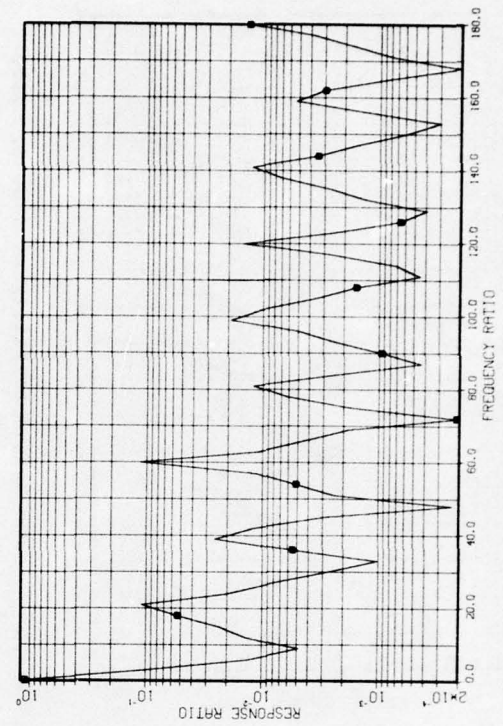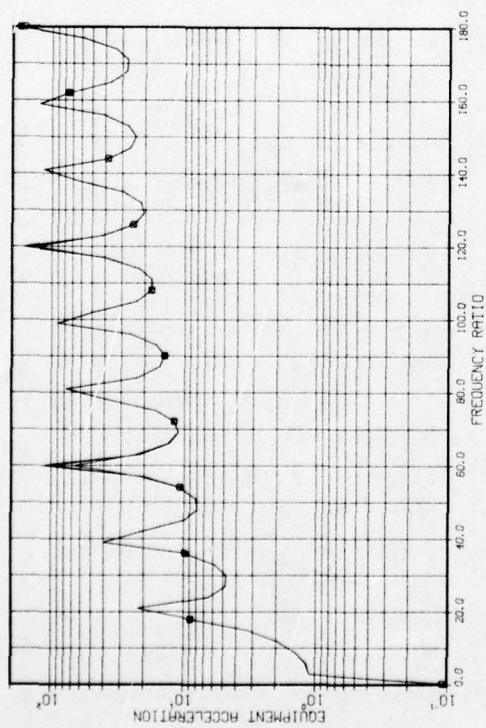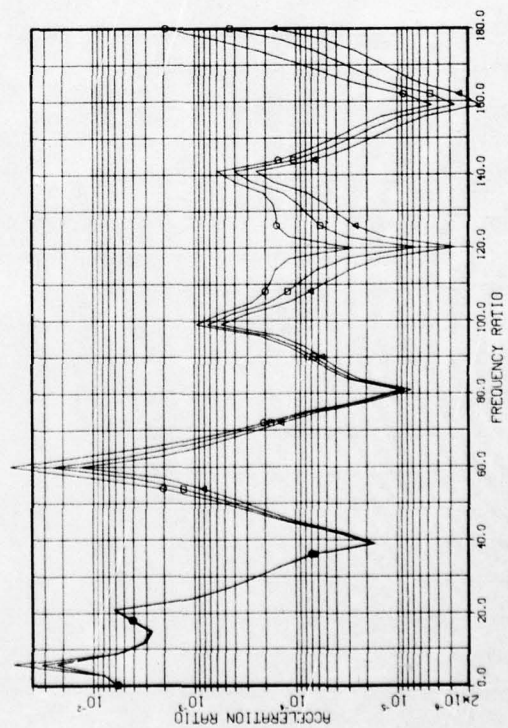

Fig. 40 - Equipment acceleration of case 9, table 2

181

(i.e., the ratio of the first standing wave resonance in the isolator to the isolation system natural frequency) will usually be between 10 and 100. Case 3 represents an intermediate value of isolator mass ratio, and hence isolator frequency ratio, and is used as a reference case to which the other cases are compared. For this case, the quantities S, T, A, and R, as described in Table 1, are graphically displayed in Figures 18, 19, 20, and 21, respectively.

The normalized equipment acceleration shown in Figure 18 indicates that isolator damping has no practical effect on the equipment acceleration. This holds true for all the other cases as well. The initial increase in equipment acceleration with frequency ratio can be considered as the effect of decreasing the isolation system natural frequency for a given forcing frequency. This is intuitively acceptable since the softer the isolator, the less constraint it puts on the equipment, thus allowing the equipment to vibrate freely. The situation is quite different for the force transmissibility shown in Figure 19. Here, the force transmitted to the foundation decreases with decreasing isolation system natural frequency. From the standpoint of being acceptable according to MIL-STD-740B, it is desirable to minimize the equipment acceleration, whereas from the standpoint of achieving ship silencing it is desirable to minimize the force transmitted to the foundation. However, making a choice between alternative isolators in order to decrease one of these quantities (equipment acceleration or force transmitted to the foundation), will increase the other. It is for this reason that the results of tests according to MIL-STD-740B should not be used to evaluate isolators. One method to evaluate isolators is based on the ratio of the acceleration on the foundation side to that on the equipment side of the isolator. This evaluation seems reasonable since if the isolator is replaced by a rigid, massless rod, the acceleration ratio would be unity. Any value less than unity would indicate a reduction in vibration. However, Eqs. (40) or (64) indicate that this ratio does not depend on the equipment. This situation is illustrated by the graph of the acceleration ratio shown in Figure 20. At a frequency ratio of 120, the equipment has a resonance and the effect of this resonance is to cause the force transmissibility to have a peak as shown in Figure 19. The acceleration ratio, on the other hand, has a trough at this frequency ratio, as shown in Figure 20.

The reason for the trough is the anti-resonance of the foundation at this frequency ratio. The true evaluation of the effectiveness of an isolator in reducing structureborne noise is the response ratio, which is the ratio of force transmitted to the foundation when the equipment is mounted on isolators to this force when the equipment is attached directly to the foundation. The response ratio for this case is shown in Figure 21. For frequencies above the first structural resonance, the response ratio has a maximum value of 0.6 and a minimum value of 0.0005. This wide range of values is due to the highly resonant equipment and foundation and to standing waves in the isolator. The maximum response ratio occurs at a frequency ratio of 60 where the equipment, isolator, and foundation all have a resonant mode. The minimum response ratio occurs at a frequency ratio of 168. There are anti-resonances of the equipment, isolator, and foundation at frequency ratios of 170, 165, and 160, respectively. Also, there is a general trend for the response ratio to decrease with increasing frequency ratio. At a frequency ratio of 180, the equipment, isolator, and foundation all have a resonant mode as they do at a frequency ratio of 60, but at 180 the amplitudes are considerably reduced and the effect of isolator damping is more pronounced. The average value of the response ratio over this frequency range is approximately 0.02, which is a 34 db reduction in structureborne noise.

The curves for force transmissibility, acceleration ratio, and response ratio in Figures 19, 20, and 21, respectively, indicate that the higher the value of damping, the lower the value of these quantities. The type of damping assumed in this analysis is hysteric damping (i.e., the loss factor is independent of frequency). This type of damping is commonly used to represent structural materials and elastomeric materials used in vibration isolators [Ref. 1]. For this type of damping, the high frequency transmissibility of a rigid equipment isolated from a rigid foundation by a massless isolator is essentially independent of isolator damping for values of loss factor ≤ 0.3 [Ref. 1]. The effect of damping shown in these graphs is due to the isolator mass. This conclusion is verified by the curves in Figures 23, 24, and 25, which are the same as Figures 19, 20, and 21, except for the assumption of a massless isolator. For the massless isolator, the effects of isolator damping are negligible. Also, the effects of damping are quite prominent in

Figure 41, which is the force transmissibility for a rigid equipment and rigid foundation, but with an isolator having mass.

The quantitative effects of the mass of the isolator can be seen by comparing the values of equipment acceleration (Figures 10, 14, 18), force transmissibility (Figures 11, 15, 19), acceleration ratio (Figures 12, 16, 20), and response ratio (Figures 13, 17, 21) for isolator mass ratios of 0.001, 0.1, and 0.01. This comparison must be done on the basis of mode numbers, not frequency ratio, since the ratio of equipment, isolator, and foundation fundamental resonant frequencies has remained constant. On this basis, there is essentially no difference in equipment acceleration for changes in isolator mass, however, the force transmissibility, the acceleration ratio and the response ratio are all increased proportional to the increase in isolator mass. The effect of isolator mass under the assumption that the equipment and foundation resonances remain constant (i.e., only the isolator resonances change with a change in isolator mass) can be seen by comparing Figures 18 through 21 for isolator mass ratio of 0.01 to Figures 22 through 25 for isolator mass of 0.00001. Here again, there is essentially no difference in equipment acceleration. The force transmissibility, acceleration ratio and response ratio are approximately 10 times greater for an isolator mass ratio of 0.01 than they are for an essentially massless isolator (isolator mass ratio of 0.00001).

The effect of inserting a rigid mass in the middle of the isolator (case 5 of Table 2) is shown in Figures 26 through 29. The mass ratio for the added mass is 0.1 and the mass ratio of the isolator mass is 0.01 so that these graphs can be compared to the corresponding graphs in Figures 18 through 21. Again, there is essentially no difference in equipment acceleration. However, a large reduction in force transmissibility, acceleration ratio, and response ratio is obtained.

The following discussion pertains to the effects of changing the foundation and equipment parameters (cases 6 through 9). The normalized equipment acceleration S does not depend on the foundation since it was assumed in the definition that the foundation is rigid. Its dependence on equipment is discussed below.

Force transmissibility T depends on both the foundation and equipment. Figures 30 through 33 show this

dependence and can be compared to Figure 19 as discussed above. Figures 30 and 31 have the same parameter values as for Figure 19, except for the mass ratio of the foundation which is 0.1 and 10, respectively, whereas that of Figure 19 is 1. From Eqs. (67) and (68) it can be ascertained that the ratio of foundation mass to equipment mass is equal to the ratio of the minimum impedance (troughs) of the foundation to that of the equipment for the same small value of damping in foundation and equipment. Therefore, the troughs of the foundation impedance are 1/10, the same, and 10 times that of the equipment in Figures 30, 19, and 31, respectively. There is remarkably little difference between these three figures indicating that the force transmissibility has very little dependence upon the magnitude of the foundation impedance. The force transmissibility curves shown in Figure 32 are for case 8 of Table 2, which has the same parameter values as those for Figure 19, except that the foundation is essentially rigid. These curves are almost identical to those of Figure 31 indicating that if the troughs of the foundation impedance are 10 times greater than those of the equipment, the foundation can be considered as a nonresonant rigid structure for the determination of force transmissibility. The force transmissibility for the case where the equipment is considered rigid is shown in Figure 33. Comparing these curves to those in Figure 19, which has the same parameter values except that the equipment is flexible, shows that the equipment structural resonances greatly increase the force transmitted to the foundation.

The acceleration ratio A does not depend on the equipment and is discussed below.

Response ratio R depends on the foundation and the equipment. Figures 34 through 37 show this dependence and can be compared to Figure 21. Similarly to the force transmissibility discussion above, Figures 34, 21, and 35 depict the response ratio where the troughs of the foundation impedance are 1/10, the same, and 10 times, respectively, that of the equipment. Comparing Figures 34 and 21 show that for a low impedance foundation the response ratio is predominantly influenced by the foundation and that performance is degraded compared to the case of equal minimum impedance values of foundation and equipment. The curves in Figure 21 are very little different to those in Figure 35, and also are quite similar to those of Figure 36, which is the case of infinite foundation impedance. This indicates that if

the troughs of the foundation impedance are equal or greater than those of the equipment, then the response ratio can be essentially determined by considering the foundation to be rigid. Comparing Figure 37, where the equipment is assumed to be rigid, to Figure 21, which is the corresponding case for flexible equipment, shows the influence of equipment structural resonances on the response ratio. This influence is significant, but not as drastic as for the force transmissibility.

Acceleration ratio A is shown in Figures 38 and 39 for the case where the troughs of the foundation impedance are 1/10 and 10 times that of the equipment, respectively. As in the discussions of force transmissibility and response ratio above, these should be compared to Figure 20, which is the case of equal impedance troughs for foundation and equipment. From these three figures, it can be seen that the average value of the acceleration ratio over the frequency range is approximately inversely proportional to the foundation mass ratio, which is the ratio of foundation to equipment minimum impedance. Also, comparing Figures 12, 16, and 20, the average acceleration ratio is proportional to isolator mass ratio and for all these cases can be taken as approximately one-half the ratio of isolator mass to foundation mass. The significance of this is that as the foundation impedance increases, the acceleration ratio decreases, becoming zero for a rigid foundation. Since the response ratio does not have this characteristic, the acceleration ratio cannot be used in general to evaluate isolators. However, for a low impedance foundation the acceleration ratio is similar to the response ratio as shown in Figures 38 and 34 for the case of foundation mass ratio equal to 0.1. The effects of the equipment do not show up for the acceleration ratio, but for this case the foundation is the prominent influence on response ratio as discussed above. Therefore, when the foundation impedance is much less than the equipment impedance, the acceleration ratio can be used as an estimate of the response ratio and hence to evaluate isolators. This situation can be determined from Eqs. (64) and (65) where, as the ratios of foundation and isolator impedances to equipment impedance approach zero, the expression for the response ratio R reduces to that for the acceleration ratio A. Conversely, for a large foundation impedance, the acceleration ratio is useless. This is the case when testing according to MIL-STD-740B where the foundation should be made as rigid as possible.

Normalized equipment acceleration S is shown in Figure 40 for the case of a rigid equipment. Above the isolation system natural frequency, this quantity is equal to unity as it should be for a rigid mass in space. While the isolation system resonance does have an influence, the standing wave isolator resonances do not. As discussed above, the only things that have a significant influence on the equipment acceleration are the isolation system natural frequency and the equipment itself. If the isolation system natural frequency is set well below the testing frequencies, and if the isolator has high frequency characteristics as is assumed in this analysis (see NONLINEAR EFFECTS below), then the equipment acceleration will depend only on the equipment itself, which is the purpose of testing according to MIL-STD-740B.

Finally, the case for which both equipment and foundation are rigid is depicted in Figures 40 and 41. Figure 40 is for equipment acceleration, which is identical to the case for rigid equipment (case 9) since it is assumed that the foundation is rigid for the equipment acceleration calculation. The force transmissibility is shown in Figure 41. These curves are almost identical to those of Figure 33, which is for the case of a rigid mass but a flexible foundation. From this and the discussion above, it is concluded that the force transmissibility is only slightly influenced by the flexibility of the foundation. The acceleration ratio for this case is zero for all frequencies since the foundation is rigid. The response ratio for this case is identical to the force transmissibility as can be determined from Eqs. (63) and (64) by setting $T_e = \zeta_e = 1$ for the rigid equipment and $\zeta_f = \infty$ for the foundation.

Conclusions based on these results are discussed below. However, two further considerations will be discussed first. One of these is the simplicity of the model used. Real structures are not solid as is the case for the rods used in this analysis. If a rod is to be used to represent a structure it is probably reasonable to assume that its density is much less than that of the material of the structure. Because of this, it may be more reasonable to assume an isolator mass ratio of 0.1 in predicting actual values that can be expected. Figures 14 through 17 show the normalized equipment acceleration, force transmissibility, acceleration ratio, and response ratio, respectively, for this case. Whereas there was an

average over the frequency range of 34 db reduction of vibration (based on the response ratio) for an isolator mass ratio of 0.01, there is approximately a 20 db reduction for the isolator mass ratio of 0.1. This is precisely the amount of vibration reduction attributed to the resilient mounts by the specification in MIL-STD-740B, which allows the acceptable vibration level for equipment that is to be isolation mounted to be 20 db higher than for equipment that is to be solidly mounted aboard ship. Another aspect of the simplicity of the model is that it considers only one mounting point and one directional vibration transmission. Actual structures have many mounting points with many degrees of freedom all interacting with one another. Although the model used for this analysis does not describe the actual situation, it is felt that it incorporates the salient features and that the general conclusions developed from this model are valid for the actual situation. The other consideration is the nonlinear effects of the isolator discussed in the following section.

NONLINEAR EFFECTS IN ISOLATORS

The analysis above assumes that the equipment, isolator and foundation behave linearly. For the small motions encountered for structureborne noise, this seems to be a reasonable assumption. However, in regards to the isolator certain precautions should be taken. The results above use the isolation system natural frequency as the reference frequency. The isolation system natural frequency is usually measured at large amplitudes whereas in the high frequency vibration isolation region, the amplitudes are quite small. Therefore, if the isolator properties are amplitude dependent, this must be taken into account in evaluating the results given above.

For isolators made of elastomeric materials, the amplitude dependence can be handled quite easily. In Ref. 6, a general expression (Eq. 2.20) is given relating elastomer shear modulus to shear strain. This relationship is corroborated by experimental data for many types of elastomers (Figure 2.24, Ref. 6). The curves in Figure 42 were computed based on this expression and show that the shear modulus approaches a constant value as strain goes to zero. This value is higher than the modulus value at large strains. The high and low values of shear modulus are dependent on the particular material
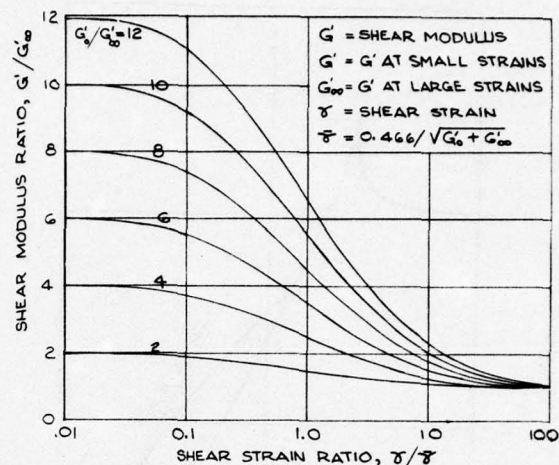
Fig. 42 - Variation of rubber shear modulus with shear strain

being used, but the manner in which the modulus varies from high to low as a function of strain is the same for all the materials. For the purpose of illustrating this effect in a manner applicable to this analysis, a transmissibility curve of a commonly used commercial isolator made of silicone elastomer is shown in Figure 43. This test was run with a very rigid mass to avoid structural resonances. The mass was mounted on the isolator which was attached rigidly to the vibration shaker head. Transmissibility is the ratio of mass acceleration to shaker head acceleration. The shaker head input was 0.036 inch D.A. from 15 to 74 Hz and 10 g's from 74 to 1000 Hz. Initially, the transmissibility starts to fall off at the rate of 12 db/octave as predicted by the linear theory. Beginning at approximately 74 Hz, the fall off is less than 12 db/octave until the curve reaches the high frequency asymptote at approximately 500 Hz where it again falls off at the rate of 12 db/octave. This transition is explained by the fact that the modulus is changing from a low value at the higher strains to a high value at the smaller strains. For frequencies higher than that at which the modulus reaches its maximum value, the transmissibility continues to fall off at the rate of 12 db/octave. Continuing the high frequency asymptote upward until it intersects the line where transmissibility is unity, indicates that an isolation system natural frequency of 100 Hz should be used rather than the measured value of 40 Hz. Since the measured transmissibility coincides with
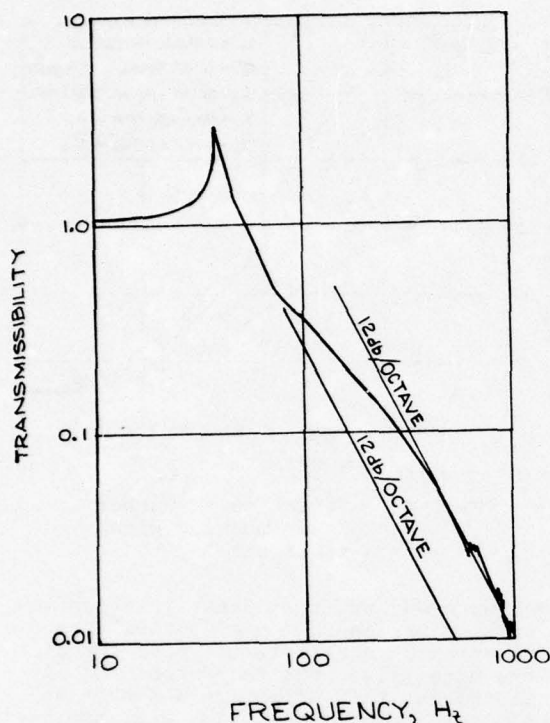
Fig. 43 - Transmissibility of a
common commercial
elastomeric isolator

the high frequency asymptote above 500
Hz, it behaves according to the theo-
retical model used in the analysis for
frequency ratios greater than 5, assum-
ing an isolation system natural fre-
quency of 100 Hz.

For isolators incorporating coulomb
friction type damping, the situation is
much worse than for elastomeric mater-
ials. Coulomb friction dampers tend to
"lock up" as the amplitude is decreased,
resulting in a degradation of high fre-
quency vibration isolation [Ref. 7].
Since it is necessary to include damping
in an isolator in order to control am-
plitudes at resonance, and since metals
have very low inherent damping, metallic
type isolators usually incorporate some
form of coulomb damping mechanism. This
type of isolator is more difficult to
analyze than elastomeric type so that
it may be necessary to perform high fre-
quency, low amplitude vibration testing
on them to determine their suitability
for use in isolating structureborne
noise.

In the linear analysis above, it
was concluded that the results of test-
ing according to MIL-STD-740B could not

be used to evaluate the effectiveness
of isolators in reducing structure-
borne noise. When considering non-
linear effects of isolators, this con-
clusion is more emphatic. An isolator
that "locks up" or is very stiff in the
high frequency region and does not have
significant standing waves will put a
constraint on the equipment, thus caus-
ing its acceleration to be diminished
compared to an isolator that is soft in
the high frequencies. This will help
equipment to pass the acceptance vibra-
tion level of MIL-STD-740B. However,
this type of isolator will transmit more
force into the foundation, thus defeat-
ing the purpose for which it was in-
tended. If this type of isolator also
has significant standing waves, these
will cause both the equipment accelera-
tion and the force transmitted to the
foundation to be larger than would be
obtained by an isolator of the type
assumed for this analysis.

CONCLUSIONS

Based on the results of the theo-
retical study and considerations of
nonlinear effects in the isolators, the
following conclusions are drawn:

1. The results of testing according to
   MIL-STD-740B should not be used to
   evaluate isolators. This is espe-
   cially true if the isolators have
   significant nonlinear effects.

2. Within the range of values considered,
   the isolator mass and damping have
   essentially no effect on the equip-
   ment acceleration and for frequencies
   greater than 4 or 5 times the system
   natural frequency, the equipment be-
   haves as though it were suspended in
   space. This conclusion may not be
   justified for nonlinear isolators.

3. The force transmissibility has very
   little dependence on the foundation
   structural resonances. For a given
   piece of equipment the force trans-
   mitted to a rigid foundation will be
   quite similar to the force transmitted
   to a flexible foundation so that this
   measurement can be used to evaluate
   the combination of equipment and
   isolators.

4. The acceleration ratio can be used to
   evaluate isolators for a very flexible
   foundation, but should not be used if
   the foundation impedance is greater
   than the equipment impedance.

5. The response ratio determines the
   effectiveness of the isolator in
   reducing structureborne noise. In
   the theoretical study, the isolator

186

achieved an average reduction of approximately 34 db for an isolator to equipment mass ratio of 0.01. For a mass ratio of 0.1 the reduction was approximately 20 db and considering the theoretical model used, this is probably more realistic.

6. The theoretical analysis presented is applicable to elastomeric type isolators, but is probably not good for metallic type isolators.

7. For elastomeric isolators, increasing damping decreases the values of the force transmissibility, acceleration ratio and response ratio. This is in contrast to the simple model that assumes rigid equipment and foundation, massless isolator, and viscous damping, where the opposite is true.

8. The lower the mass of the isolator, the greater is the reduction of vibration except for the case where a rigid mass is inserted in the middle of the isolator. In this case, the added mass greatly reduces the vibration transmitted to the foundation.

REFERENCES

1. Snowdon, J.C., Vibration and Shock in Damped Mechanical Systems, John Wiley & Sons, New York, 1968.

2. Hixson, E.D., "Mechanical Impedance and Mobility" in Shock and Vibration Handbook Edited by C.E.Crede and C.M. Harris, McGraw-Hill, New York, 1961, Vol. 1, Chap. 10, pp. 35-36.

3. Ungar, E.E.; and Dietric, C.W., "High Frequency Vibration Isolation", J. Sound Vib., v.4, n.2, 1966, pp 224-241.

4. Sykes, A.O., "Vibration Isolation When Machine and Foundation are Resilient and Wave Effects Occur in the Mounts", David Taylor Model Basin Report 1404, Sept. 1960.

5. Molloy, C.T., "Four-Pole Parameters in Vibration Analysis" in Mechanical Impedance Methods Edited by R. Plunkett, ASME, New York, 1958, Chap. 4, pp.43-68.

6. Davey, A.B.; and Payne, A.R., Rubber in Engineering Practice, Maclaren and Sons Ltd., London, 1964.

7. Ruzicka, J.E.; and Derby, T.F., Influence of Damping in Vibration Isolation, The Shock and Vibration Information Center, Naval Research Laboratory, Washington D.C., 1971, Chap. 3.

APPENDIX

```
      PROGRAM SBSP(INPUT,OUTPUT)
      COMPLEX C,NL,SNL,A11,A12,A21,A22,F0,ZF,CEM
      REAL M
      DIMENSION B(301),R(301,5,4),FB(301),DI(5)
     *          ,M(3),F(3),D(3),C(3),NL(3),SNL(3)
     *          ,A11(3),A12(3),A21(3),A22(3)
     *          ,M(4)
      DATA PI/3.14159/
      DATA IPLT/0/
      PRINT 602
      CALL BGNPL(-1)
      CALL XLABEL(15HFREQUENCY RATIO,15)
      READ 501, NC
      DO 10 IC=1,NC
      READ 502, NPLTS,(N(I),I=1,NPLTS)
      READ 503, (M(I),I=1,3), AM, (F(I),I=1,3),D(1),D(3)
      READ 504,NDI,(DI(I),I=1,NDI)
      READ 505,BL,BH,NDIV
      CALL XRANGE(BL,BH)
      IM=NDIV/10
      CALL MRKPLT(IM)
      NPTS=NDIV+1
      DIV=(BH-BL)/FLOAT(NDIV)
      B(1)=BL
      DO 1 I=2,NDIV
    1 B(I)=B(I-1)+DIV
      B(NPTS)=BH
      IF(BL .EQ. 0.) B(1)=.1*DIV
      F(1)=2.*F(1)
      DO 5 K=1,NDI
      D(2)=DI(K)
      DO 2 I=1,3
    2 C(I)=PI/(F(I)*CSQRT(CMPLX(1.,D(I))))
      DO 5 I=1,NPTS
      DO 3 J=1,3
      NL(J)=C(J)*B(I)
      SNL(J)=CSIN(NL(J))
      A11(J)=CCOS(NL(J))
      A22(J)=A11(J)
      A12(J)=M(J)*SNL(J)/NL(J)
    3 A21(J)=-NL(J)*SNL(J)/M(J)
      ZF=A11(1)/A21(1)
      IF(AM .EQ. 0.) GO TO 4
      A22(2)=A22(2)+.5*AM*A21(2)
      A21(2)=A21(2)+.5*AM*A21(2)**2/(1.+A11(2))
      A12(2)=A12(2)+.5*AM*(1.+A11(2))
      A11(2)=A22(2)
    4 F0=A21(2)*ZF+A22(2)
      DEN=A11(3)*(A11(2)*ZF+A12(2))+A12(3)*F0
      R(I,K,1)=CABS(1./F0)
      R(I,K,2)=CABS((A11(3)*ZF+A12(3))/DEN)
      R(I,K,3)=CABS(A21(2)/(A11(3)*A11(2)+A12(3)*A21(2)))
    5 R(I,K,4)=CABS(ZF/DEN)
      F(1)=F(1)/2.
      DO 10 J=1,NPLTS
      IPLT=IPLT+1
      PRINT 601, IPLT,(M(I),I=1,3),AM,(F(I),I=1,3)
     *          ,D(1),DI(1),D(3),(DI(I),I=2,NDI)
      NF=N(J)
      GO TO (101,102,103,104),NF
  101 CALL YLABEL(18HACCELERATION RATIO,18)
      GO TO 105
  102 CALL YLABEL(14HRESPONSE RATIO,14)
      GO TO 105
  103 CALL YLABEL(22HEQUIPMENT ACCELERATION,22)
      GO TO 105
  104 CALL YLABEL(22HFORCE TRANSMISSIBILITY,22)
  105 CALL OPNPLT
      DO 106 I=1,NPTS
  106 FB(I)=R(I,1,NF)
      CALL YLGPLT(B,FB,NPTS)
      IF(NDI .EQ. 1) GO TO 109
      DO 108 K=2,NDI
      DO 107 I=1,NPTS
  107 FB(I)=R(I,K,NF)
  108 CALL CURVE(B,FB,NPTS,IM)
  109 CALL GRID(2,1)
      CALL FRAME
      CALL ENDPL(IPLT)
   10 CONTINUE
  501 FORMAT(I8)
  502 FORMAT(5I8)
  503 FORMAT(9F8.0)
  504 FORMAT(I8,5F8.0)
  505 FORMAT(2F8.0,I8)
  601 FORMAT(//* PLOT*,I3,11X,*FOUNDATION*,5X
     *       ,*ISOLATOR*,4X,*EQUIPMENT*,6X,*ADDED*//
     *       * MASS RATIO*,5X,4E13.3/
     *       * FREQUENCY RATIO*,3E13.3/
     *       * DAMPING*,8X,3E13.3/(29X,E13.3))
  602 FORMAT(1H1)
      CALL EXIT
      END
```

POLYURETHANE FOAM ISOLATORS FOR SHOCK ISOLATED
EQUIPMENT FLOORS

William C. Gustafson
Boeing Aerospace Company
Seattle, Washington

This article presents the results of a large analytical and experimental program that was undertaken in the design and verification of a polyurethane foam isolator set for shock-isolated equipment floors. The operating environment which controlled the system design was ground motion induced by nuclear weapons; the major design constraints were the available space in an existing facility for dynamic floor excursion, and the level of shock attenuation that had to be achieved to ensure equipment survival. To achieve a high degree of confidence in the system design, a qualification program was configured where analytical design models would be qualified by correlation with a smaller floor segment test and then the operational floor would be qualified by detailed analytical data evaluation with these models.

INTRODUCTION

This article presents the results of a large analytical and experimental program that was undertaken in the design and verification of a horizontal isolator set for shock isolated equipment floors. Polyurethane foam blocks were chosen for the isolator set because of their unique shock absorption characteristics, reliability, and near optimum properties for the imposed design requirements. The operating environment which controlled the system was ground motion induced by nuclear weapons; the major design constraints were the available space in an existing facility for dynamic excursions, and the level of shock attenuation that had to be achieved to ensure equipment survival. One additional constraint was imposed by the requirement that the foam blocks had to form a continuous platform which could be walked on by maintenance personnel while servicing equipment.

This latter design constraint associated with maintenance functions, along with the allowable equipment operating equipment constraint, led to a foam isolator design with very little margin for change. Maintenance functions required a foam that was stiff enough to ensure reasonably natural walking and working conditions along with certain maximum deflection requirements when subject to heavy maintenance equipment loads. Safety requirements dictated that the foam surface had to be continuous along the floor edge and extend outward to the facility in order to eliminate open areas through which personnel could fall to the lower level. Walkability dictated the minimum density, 10 lbs/cu. ft., safety considerations dictated the foam area in the horizontal plane, and deflection limitations established a minimum vertical depth. Once these design constraints were met, very little design flexibility was left to size the isolator set for the design nuclear attack environment. Fortunately, by using a couple of mechanisms such as coring and tapering the foam, the isolator set design was tailored to meet attenuation characteristics necessary to meet the operating environment constraint.

The importance of the electronic equipment being shock isolated necessitated considerable system-level testing in order to qualify the floor system with high confidence. Practical limitations imposed by the size of the operational equipment floors precluded full-scale testing with inputs to the horizontal foam isolator set. Furthermore the immense set of parameter variations in attack conditions such as attack direction, weapon yield, height of burst, overpressure, etc., that must be dealt with in the design could not be handled in a system-level test program. In order to cope with all of these considerations and achieve a high degree of confidence in the system design, a qualificiation program was configured where the analytical design models would be qualified by correlation with a smaller floor segment test and then the operational floor would be qualified by a detailed analytical data evaluation with these models.

This article deals principally with the horizontal isolation system used on the electronic equipment floors. The vertical isolation system consisting of four liquid springs on the operational floor was the subject of much verification testing and analysis and is touched upon only briefly herein. This material is covered in discussions of both component level testing by Ashley (1) and full-scale testing by Milne (4). An overview of the design procedures, test programs, and their interrelationship in the overall floor system design is discussed by Luschei (3). The floor segment test discussed herein did provide valuable data on the vertical isolation system at the time it was conducted, but subsequent full-scale testing of the floor system provided the most important source of data for verification of the vertical isolation system. The absence of inputs to the horizontal isolators during the full-scale testing meant that the floor segment test under discussion was the only source of data for floor response evaluation with excitation to the horizontal isolators. Additionally, the full-scale test program lacked an actuation system for testing with direct-induced motion input; this also placed additional uniqueness on the data from this test program.

TEST DISCUSSION

The testing was done in a test fixture specifically designed for verification testing of a missile suspension system. The test fixture, along with a floor test specimen in place, is pictured in Fig. 1. The principal parts of the test fixture are the steel tower and the three driving rings along with their associated actuators. The bottom driving ring was not employed in this test program. The floor segment test specimen was suspended by its vertical liquid isolators from the upper driving ring, and the floor structure with its horizontal isolators set inside the middle driving ring. The upper driving ring was driven by two 1.5-million-pound force actuators, referred to as prime movers, and two smaller hydraulic actuators. The lower driving ring was driven by one prime mover and two of the smaller hydraulic actuators. The large prime movers input shock motion simulating the air-induced ground motion, and each pair of smaller hydraulic actuators produced motion simulating the direct-induced (crater induced) ground motion. The design and development of the large prime movers are discussed in detail by Burwell (2).

The upper driving ring could be driven at angles of 0 to 45 degrees from the horizontal plane for the air-induced effects. Upon completion of the air-induced motion, the driving ring decoupled from the prime movers and the direct-induced motion was induced by the two smaller actuators. The direct-induced motion was confined to the horizontal direction. Practical limitations had precluded the inclusion of vertical direct-induced motion input capability in the test fixture. Motion on the lower driving ring was confined to the horizontal plane. The limitations imposed by the horizontal-only constraint on the lower driving ring and the direct-induced motions were not significant to the floor test program. The reason for this was as stated previously; the test was being used to qualify the analytical tools and not an operational floor. A broader discussion of the test fixture can be found in works by Luschei (3) and Mortimer (5).

The test specimen is pictured in Fig. 2. The floor structure was a 5-foot-by-10-foot steel floor that had been developed for a prior transmissibility test program and now trimmed to fit into the lower driving ring. The floor was suspended from the upper driving rings by three of the operational-type liquid isolator assemblies. The liquid isolator assembly consisted of a wire rope cable approximately 45 inches long which was swagged into a fitting on the isolator rod, a pressure cylinder into which the rod fit, and a mono-ball mounting of the isolator pressure cylinder onto the floor. The assembly, along with some of its salient details, is illustrated in Fig. 3. On each side of the floor normal to the direction of test motion, two foam isolators were mounted. The size of each block was 36.5" x 16.5" x 23" with the 23-inch dimension in the direction of compression and the 16.5-inch dimension was the height. The blocks had been sized to limit the horizontal rigid-body response on the floor to approximately 3.0 g's. Mounted on the floor were two standard electronic equipment cabinets with mass-simulated electronics on the inside. A post structure with a tray on the upper end was employed to simulate an overhead tray for electronic cabling and an environmental control system duct that was present on the operational floor. The lower side of the floor had considerable lead ballast to bring the static load on each liquid spring up to the design range of the isolator which is 8.0 to 20.0 kips. For this test program each isolator was statically loaded to 8.0 kips.

The test specimen was instrumented with 84 channels of active instrumentation which were recorded on wideband, frequency-modulated tape recorders. In addition to the active instrumentation, a complete set of passive measurements were made. The test measurements that were made fell into two broad categories, test input motions and floor system dynamic response. The acceleration, velocity, and displacement input motions of the force actuators were important measurements for the test/analysis correlation that was to be done. The excursions of the floor segment were monitored with seven linear displacement transducers. Additionally numerous accelerometers were used to gather data on the rack and floor environments that were generated for each dynamic event. The liquid shock isolators were instrumented for loads determination and also a system of accelerometers to trace the transmission and attenuation of the input environment down to the floor and rack level.

The seven active displacement transducer recordings were digitized and placed on magnetic tape for a computerized mathematical transformation into time-history responses of the floor along a cartesian coordinate system. The transformation from transducer lengths to inertial coordinates of the moving floor was accomplished by

$$\ell_i^2 = (k_j - k_j')^T (k_j - k_j') \tag{1}$$

where

ℓ_i = transducer length

k_j = coordinates of moving floor

k_i' = coordinates of fixed ends of wires (test fixture reference).

The resulting system of equations is a system of nonlinear algebraic equations that must be solved by numerical techniques. In particular the Newton-Raphson iteration method is employed in the solution of this nonlinear system of algebraic equations. Since a redundant number of displacement transducers were employed, several solutions for various combinations of six gages were made and an average of the solutions was taken. Active and passive measurements were generally found to correlate within 0.2 inch; the highest discrepancy was about 1.0 inch. Aside from amplifications or attenuations of error that may take place in the mathematical transformation to cartesian body coordinates because of transducer geometry, it is felt that an accurate displacement time history of the dynamic event was obtained.

Out of a large series of tests, four tests were considered to be the most significant with respect to the test/analysis correlation effort for system excursions. These four tests provided the necessary confidence that floor excursions could be predicted analytically with and without the foam isolator set; and with the foam isolators the excursions could be predicted for the various forms of ground motion that were necessary for consideration in the design analysis. Two general types of air-induced ground motion were employed in these tests; these were a positive-only waveform and also a positive motion followed by a 50-percent return waveform. The positive-only motion is characteristic of a purely plastic medium where there is no recovery after deformation. The other form of air-induced motion considered was one with 50-percent recovery of the medium after positive deformation. The two types of air-induced waveforms that were achieved in the testing are displayed in Fig. 4. These velocity time histories represent the vertical motion of the upper driving ring and the horizontal motion of both the upper and lower driving rings. The upper ring moved down a track 45 degrees from the horizon to produce equal vertical and hori-

190

zontal motion. As the figure illustrates, the air-induced era was confined to approximately 0.3 seconds. The direct-induced waveform that was achieved in the testing is illustrated in Fig. 5. As can be noted in the figure, the direct-induced waveform had approximately a 50-percent return. The direct-induced waveform was initiated at approximately 0.7 to 0.8 seconds after initiation of the air-induced motion. Earlier initiation of the direct-induced event was difficult because of time required for decoupling the driving rings from the large prime movers.

The four tests treated in this dissertation were designated as Tests 1, 4, 5, and 8. Test 1 employed an air-induced input only with the 50-percent return; and for this test the *foam isolators were not driven. Data from this test established the baseline for determining the response created by the horizontal foam isolator set.* Test 4 provided nominally the same input to the test article as Test 1, with the addition of the lower driving ring exciting the horizontal foam isolators. Test 5 again was an air-induced only test with no return; the data from this test were a baseline for evaluating the effect of changes in waveform and also for comparison with other tests employing direct-induced waveform inputs. Test 8 employed nominally the same air-induced motion as Test 5 with the addition of the direct-induced waveform event. Both Tests 5 and 8 had the lower driving ring operating for excitation of the foam isolator set.

ANALYSIS DISCUSSION

The analytical modeling that was done for the design of these shock isolated floors does not in itself represent an unique approach; the material of real interest is the confi-*dence that has been achieved in analytical procedures for a* material with very strong nonlinear response characteristics. With this in mind, the analytical modeling will be discussed briefly to illustrate the complexity of the tools that had to be developed to achieve the desired confidence in predicted response of a system employing polyurethane foam isolators.

The analytical model used for the floor excursion analysis predicts three-dimensional excursions of an arbitrarily shaped floor supported by an arbitrary number of isolators and excited by a specified ground shock. The mathematical modeling uses six rigid-body degrees of freedom with the option of an additional five freedoms for flexible body modes. The rigidity of the floor structures that were being dealt with indicated that the inclusion of flexible body mode shapes to obtain accurate excursion data was not necessary. This factor greatly simplified the analysis and reduced computation time immensely. The resulting equations of motion for the reduced system may be expressed in the matrix form

$$M(q_k)\,\ddot{q}_k = B(q_k, \dot{q}_k) + Q \qquad (2)$$

where

M = 6 x 6 variable mass matrix

B = column matrix containing products of the velocities, $\dot{q}_k$, which represents centrifugal and coriolis forces in the rigid body

Q = column matrix containing the generalized forces containing the terms expressing floor weight, isolator forces, and sliding friction forces

The liquid isolator has been modeled by three elements: a *nonlinear elastic spring, a damping element where force is* proportional to the square of the velocity, and a friction ele-

ment. The equation representing the ith liquid isolator force is given by:

$$F_i = R_i + f_i(\delta_i) + Cv_i\dot{\delta}_i|\dot{\delta}_i| + fr_i(1-e^{-50|\dot{\delta}_i|})\frac{\dot{\delta}_i}{|\dot{\delta}_i|} \qquad (3)$$

where

R_i = static reaction calculated from solution of Eq(2) at time zero

$F_i(\delta_i)$ = spring force which can be calculated from isolator fluid compressibility equations or established by stroking the actual isolator

Cv_i = damping constant for the drag plate damper in fluid which was established during damper plate tests and verified during component testing of isolator

fr_i = friction which is created basically by the seals of the pressure cylinder mating against the isolator rod; the magnitude of the friction is assumed constant and established by stroking isolator

The term, $(1-e^{-50|\dot{\delta}_i|})$, is a smoothing function designed to avoid integration instability when the system isolator rod is coming to rest or changing directions. The expression is very nearly 1, even for very small velocities.

The foam isolators are modeled by three elements suggested by Sepcenko (6): a nonlinear inelastic spring, a Maxwell element, and a pneumatic element. A schematic of *the foam isolator representation is illustrated in Fig. 6.* One modification that has been made in the foam idealization over that suggested by Sepcenko (6) is the use of a single Maxwell element rather than the use of a series of Maxwell elements which Sepcenko (6) terms a relaxation spectra. This simplification greatly reduced the computational time for the analyses of the operational floor where as many as 24 foam isolators may be employed in the analysis.

The nonlinear inelastic spring element exhibits a stress which is a double-valued function of strain with separate loading and unloading branches; the features of which are shown in Fig. 7. The functional values for the loading and unloading curves are derived from static test data. Usually the first and second loading cycles of the foam are somewhat higher than subsequent cycles; but continued cycling produces a repeatable loading curve which *can be represented as a function of the instant value of strain.* The unloading curve is dependent on the value of the strain amplitude at the time unloading begins. For numerical computations data could be stored for a number of unloading branches for various maximum strain amplitudes and then interpolation utilized to obtain intermediate unloading branches as needed. A more convenient approach is to use an algorithm suggested by Sepcenko which derives the intermediate unloading branches from geometrical considerations of the static test data for loading and unloading for each maximum strain of interest. This expression is given by the following recurrence equation: (4)

$$\sigma_{H_{n+1}} = \left\{ [f_\ell(\epsilon_{n+1}) - f_u(\epsilon_{n+1})] \frac{f_u(\epsilon_1 - \Delta\epsilon)}{f_u(\epsilon_1)} \right\} \left\{ \frac{\sigma_{H_n} - f_u(\epsilon_n)}{f_\ell(\epsilon_n) - f_u(\epsilon_n)} \right\}^2$$

$$+ f_u(\epsilon_{n+1}) \frac{\sigma_{H_n} - f_u(\epsilon_n)}{f_\ell(\epsilon_n) - f_u(\epsilon_n)} + [\sigma_{H_n} - \Delta\epsilon \frac{\partial f_u}{\partial \epsilon}(\epsilon_n)] \frac{f_\ell(\epsilon_n) - \sigma_{H_n}}{f_\ell(\epsilon_n) - f_u(\epsilon_n)}$$

where

σ_{H_n}, ϵ_n = stress and strain at time t_n

$\sigma_{H_{n+1}}, \epsilon_{n+1}$ = stress and strain at time t_{n+1}

$\Delta\epsilon$ = $\epsilon_n - \epsilon_{n+1}$

If the foam begins to reload at some point (σ_p, ϵ_p) before completely unloading, the following relationship is used:

$$\sigma_H = \sigma_p + f_\ell(\epsilon - \epsilon_p) \tag{5}$$

If the strain in the foam exceeds the maximum value of strain for which static test data are available, a parabolic extrapolation of the available loading curve is employed. Unloading in this range of strain is assumed to occur along the same curve. The loading condition or direction changes whenever the strain rate becomes zero.

The stress present in the Maxwell element is governed by the differential equation

$$\dot{\sigma}_M + \frac{1}{\tau}\sigma_M = G\dot{\epsilon} \tag{6}$$

where

G and τ are constant. For zero initial conditions, $\sigma_M(0) \approx 0$ and $\epsilon(0) = 0$, the solution of Equation (6) is given by

$$\sigma_M(t) = G\epsilon(t) - \frac{G}{\tau}\int_0^t (\epsilon(t')) \, e^{-(t-t')/\tau} \, dt' \tag{7}$$

The integral in Equation (7) can be conveniently calculated from the following:

$$\int_0^t \epsilon(t') e^{-(t-t')/\tau} dt' = e^{-\Delta t/\tau}\int_0^{t-\Delta t} \epsilon(t') e^{-(t-\Delta t - t')/\tau} \, dt'$$

$$+ \int_{t-\Delta t}^t \epsilon(t') e^{-(t-t')/\tau} dt' \tag{8}$$

which leads to the recurrence formula

$$I_n = e^{-\Delta t/\tau} I_{n-1} + e^{-\Delta t/\tau} \epsilon(t)\Delta t \tag{9}$$

For acceptable convergence of Equation (9) the computational step Δt is taken to be at least an order of magnitude smaller than τ.

The final element in the foam model is the air spring. The stress in the air element is given by the two following equations for adiabatic conditions in air:

$$\sigma_A = P_o\left\{\left(\frac{\gamma - \Delta V/V}{\gamma - \epsilon}\right)^{1.38} - 1\right\}\alpha\gamma \tag{10a}$$

$$\Delta V/V \approx B\int_0^t (\gamma - \epsilon)^3 \left[\frac{\sigma_A/\alpha\gamma}{1 - (\gamma - \epsilon)}\right]^{1/2} dt' \tag{10b}$$

where

σ_A = stress in the air spring
P_o = atmospheric pressure (14.7 psi)
γ = initial porosity of foam block
V = initial volume of foam block
ΔV = volume of air having escaped from block
B = venting factor
α = shape factor

In both the Maxwell element and the air spring, the dummy variable t' is set equal to zero at time $t=0$ and at every time the foam has completely unloaded and then starts another loading cycle.

The set of mechanical properties for the 10-pcf foam that was used both in this test program and the operational floor system are given in Fig. 8. Shown graphically is a composite of many static tests on various foam blocks. This curve forms the basis for computation of stress in the nonlinear inelastic spring element. The properties chosen for the Maxwell element and the air spring were basically determined from a series of component level tests, Ashley (1), where individual foam blocks were tested dynamically by impacting a stationary foam block with a moving sled having sufficient mass and velocity to obtain the desired maximum strain level. For each specimen, a series of tests was run at different strain rates and various maximum values of strain. From this series of tests, it is possible to determine values for the various parameters in the Maxwell element and the air spring. The process is done much by trial and error because total separation of the effects could be achieved only if dynamic test data could be acquired for an evacuated environment.

When the strain rate is relatively low, the effect of air flow on the load in the foam is small. Choice of G and τ can be conveniently sized from time histories of such dynamic test data. Consider the constitutive relation for the nonlinear spring and the Maxwell elements at $t=0$:

$$\dot{\sigma}(0) = [E(0) + G]\dot{\epsilon}(0) \tag{11}$$

where

$$\sigma(0) = 0, \; \epsilon(0) = 0, \text{ and } E(0) = \frac{d\sigma_H(0)}{d\epsilon}$$

From Equation (11), an initial estimate of G is estimated as:

$$G = \frac{\dot{\sigma}(0)}{\dot{\epsilon}(0)} - E(0) \tag{12}$$

Now let $t=t_o$ be the time at which first cycle strain unloading is complete, i.e., $\epsilon(t_o)=0$; then

$$\sigma(t_o) + \tau\dot{\sigma}(t_o) = \tau[E(t_o) + G]\dot{\epsilon}(t_o) \tag{13}$$

Solving Equation (13) for τ and assuming that $E(t_o) \approx E(0)$, then

$$\tau = \frac{\sigma(t_o)}{\dfrac{\dot{\epsilon}(t_o)}{\dot{\epsilon}(0)}\dot{\sigma}(0) - \dot{\sigma}(t_o)} \tag{14}$$

Equations (12) and (14) provide an initial estimate of the two parameters for the Maxwell element. Further refinement

is generally the result of an iterative process designed not only to fit the dynamic stress-strain relationship, but also the dissipation energy observed in the test data.

At large strain rates the air effects become so dominant that no combination of nonlinear spring and Maxwell element parameters results in an acceptable degree of correlation with test data. Proceeding by trial and error with the complete model, it is found that at high strain amplitudes a wide range of values of B, G, and τ are able to fit well the hysteretic loop of a single test, while only a unique combination of these parameters results in a best fit in the entire range of strain amplitudes and strain rates. The parameter B or venting factor for the air must merely be chosen on an iterative process which results in the best match of experimental data. Tests employing high strain rates and amplitudes are most convenient for this purpose. The range of this parameter suggested by Sepcenko is $12 < B < 30$. The parameter α is a shape factor relating peak pressure difference to the average pressure difference experienced. It depends on the shape of the foam block and in general it will vary with the strain time history. In the present analysis, α is assumed to take on a constant value. The anticipated range of this parameter is $0.65 < \alpha < 0.95$. The lower values of B and α will correspond to the more dense foams.

As stated previously, the relaxation spectrum suggested by Sepcenko (6) was replaced by a single Maxwell element. The justification for this simplification was the ability to achieve the desired engineering design analysis confidence without this additional complexity. Sepcenko (6) found the relaxation spectrum necessary to obtain the best possible match of component-level test data. Subsequent system-level testing of suspension systems illustrated that only small changes in response are witnessed as a result of the relaxation spectrum rather than a single Maxwell element. The difference that was obtained did not accumulate with time, but maintained a relatively constant difference. The effect of the relaxation spectrum is illustrated in Fig. 9. The hysteretic stress-strain diagram in Fig. 9 is based on a component-level test and, as illustrated, an improved match of test data was obtained with the relaxation spectrum. The effect on system response was not large enough to warrant the additional complexity and computational effort in the computer analysis. Additionally, satisfactory analysis/test correlation was achieved without the added complexity.

DISCUSSION OF RESULTS

The principal motivation for this test program was the verification of the analysis tools to predict dynamic excursions of the shock isolation system which employed polyurethane foam isolators. The first step was to demonstrate the capability of predicting system response in the absence of the foam isolator set. This task did not prove to be as straightforward as originally postulated due to the unknown dissipation functions in the system. The first system test without excitation to the foam isolator set indicated a great deal more friction and dissipation in the system than anticipated. The source of this dissipation was identified as being present in the isolator upper and lower monoball of the isolator. Increased friction between the isolator rod and the cylinder, over that noted from load-stroke testing, was necessary to acceptably predict the vertical motion of the floor. Once satisfactory correlation was achieved in the absence of foam isolator excitation the next step, which was to predict test response with foam isolator excitation, was not difficult. The greatest problems were associated with the selection of the correct transverse friction between the foam isolator and the driving ring or wall.

In order to match the test predictions, the test inputs had to be evaluated and digitized for use in the computer analysis. The upper ring, as the reader will recall, had two prime movers, each of which provided a time history input for analysis. Additionally there were passive measurements taken on both the prime movers and the floor and the isolators' final positions and/or maximum responses. Small discrepancies were found between the active and passive measurements which had to be considered in the analysis/test correlation. In the final analysis, the input velocity time histories were scaled up or down to yield displacements which were equal to the maximum and minimum of the available measurements. In Figs. 10 through 13 where the analysis/test comparisons are made, often two analysis curves are shown corresponding to the two values of D. These represent the maximum and minimum of the available input measurements for that test.

Fig. 10 illustrates the analysis/test comparison for the test with no excitation to the foam isolators. The inputs were an air-induced waveform only with 50 percent ground return. In order to obtain the proper dissipation function for horizontal excursions in the analytical predictions for this test, a set of horizontal coulomb damper forces was necessary. A value of 100 pounds for the horizontal friction damping set in each principal orthogonal direction was found to be optimum for correlation. The damping elements were chosen to be 1000 inches long to negate the effect of dampers orthogonal to the principal plane of motion if there was no out-of-plane motion. The total friction force in the vertical isolators was found to be the predominant influence on the floor's vertical response. The total amount of vertical friction was sized with the thought of producing the best match of test data over a range of several cycles rather than just trying to reproduce the first peak response.

Differences in friction between isolators does not have a significant influence on the vertical motion of the floor, but a significant influence is seen on the pitching motion. Although the low rate load-stroke data do not fully reveal the dynamic dissipation present in the isolator, the data are valuable in ascertaining differences in friction between isolators. The load-stroke data provide a good estimate on friction differences between isolators which was taken into consideration in the design analysis of the operational floors. The dissipation forces created by the drag-plate damper had very little influence on the excursions of the floor. The drag-plate damper is present to temper the shock loads on the liquid isolator and was not designed to limit floor excursions.

Fig. 11 illustrates the test/analysis comparison for the same ground shock inputs as used in Test 1 (Fig. 10) with the addition of shock excitation to the foam isolator set. Obtaining a good match with test data for horizontal response was not found to be a difficult task. The best fit foam model developed on the basis of component-level testing proved to be satisfactory in the system-level test/analysis comparison. Several alternate foam models with various combinations of parametric representation in the Maxwell and air element that had been examined as candidate choices in the component-level test/analysis effort were once again examined for the test/analysis done here. Comparison of the responses indicated the modeling which was considered optimum for component-level sled testing appeared optimum at the system level.

The sliding friction between the foam isolator and the driving structure proved to be the most difficult to handle. In both the floor segment test program and on the operational system, the outer interfacing surface was covered with teflon

and a smoothness requirement was levied on the interfacing wall surface in an attempt to minimize this sliding friction. The coefficient that was used to represent the sliding friction was found to significantly influence the vertical and pitch motions of the floor. The first maximum downward vertical motion was independent of the friction, but subsequent maximums and minimums were the affected cycles. A coefficient of 0.15 times the normal pressure was selected as the friction magnitude that resulted in the best match of test data. This value of friction was higher than thought to be present on the basis of pull tests run on a plate sandwiched between two compressed foam blocks. The difference in the data was attributed to possible inadequacies of the foam model.

The inadequacies of the model were the failure to treat transverse bending and shearing deformations; the isolator model acted strictly as a compression member. The foam isolators had been sized to provide a slenderness ratio that precluded buckling of the isolator during compression and additionally provision had been made to avoid excessive deflection due to transverse static loading. In spite of these measures, considerable transverse bending and shear deformations were witnessed. Fortunately good test/analysis comparisons were possible for floor horizontal excursions without adding complexity to the foam modeling. The same quality of match with test results was difficult to obtain for pitching motion of the floor. A good match with the first couple peak responses was achieved, but subsequent responses were generally overpredicted. The problem could result from inadequate treatment of the interface friction or the shortcomings of the bending and shear deficiencies in the modeling. The current modeling was felt to be adequate for the floor design analysis and greater depth in foam modeling was not pursued.

The comparison shown for Test No. 5 in Fig. 12 covers a ground motion input for an air-induced waveform without ground return. Test No. 8 shown in Fig. 13 covers a ground motion input which includes both the air-induced and the direct-induced waveforms. Direct-induced waveforms result in a forcing function with much greater duration than the air induced which is very short in duration, and is characterized as a shock impulse. The ability to predict floor motions for the direct-induced waveform was important because the principal role of the horizontal foam isolator set was to overcome the large relative floor displacements associated with direct-induced ground motion.

In addition to establishing the credibility of analytically predicted floor excursions in this test program, a major objective was to examine the influence that the foam isolator set played on the operating environments experienced by the electronic equipment which is being isolated. This is readily done by comparing the test-induced floor environments from the equivalent tests with and without foam isolator excitation. This comparison is made in Fig. 14 in terms of floor shock spectra response. The comparison readily reveals the important fact that the foam isolators are not influencing the floor responses in the frequency range above 100 cps. The liquid isolators represent the loading path, which is principally responsible for the high-frequency floor environment which will be present. The response below 100 cps is in-

creased due to the large increase in the floor horizontal rigid-body acceleration caused by the foam excitation.

The large increase in horizontal floor acceleration due to the foam isolators is observed in Fig. 15. The large accelerations occur during the air-induced ground motion era where the ground motion accelerations and velocities are the most severe. The upper comparison in Fig. 15 shows the dramatic effect that the foam isolators have on reducing floor relative displacements during the direct-induced era. It is observed that the foam has little influence in reducing relative floor displacements during the air-induced era. Significant reductions in the displacement caused by the air-induced motion can only be achieved if the allowable low-frequency environment on the floor-mounted equipment was raised considerably.

CONCLUSIONS

The foregoing test/analysis comparisons lead to the conclusion that dynamic excursions for a shock isolation system utilizing polyurethane foam isolators can be adequately predicted for system design using analytical techniques. Secondly, the system environments above 100 cps are not significantly influenced by the foam isolators. This latter fact validated the response value of high-frequency environment data gathered on a subsequent full-scale test where only inputs to the vertical isolators were employed. The effectiveness of foam as an isolator is most dramatically seen where the accelerations associated with the ground motion are on the same order of magnitude as the allowable floor acceleration, as is often the case with direct-induced ground motion.

REFERENCES

1. J. P. Ashley, "Component Testing of Liquid Shock Isolators and Elastomers in Support of Recent Shock Isolation Systems Designs," 46th Shock and Vibration Bulletin, 1976.

2. G. R. Burwell, "Actuator Development for System-Level Shock Testing," 46th Shock and Vibration Bulletin, 1976.

3. L. L. Luschei, "An Introduction to the Design and Qualification of Large Shock Isolation Systems," 46th Shock and Vibration Bulletin, 1976 (Classified: SECRET).

4. W. R. Milne, "Analysis and Testing of Full Scale Shock Isolated Equipment Floors," 46th Shock and Vibration Bulletin, 1976.

5. H. R. Mortimer, "Shock Isolation System Design, Analysis and Testing for a Silo Based ICBM," 46th Shock and Vibration Bulletin, 1976 (Classified: SECRET).

6. Valentine Sepcenko, "Analysis of Open Cell Polyurethane Foam Under Impact Loading," 44th Shock and Vibration Bulletin, 1974.
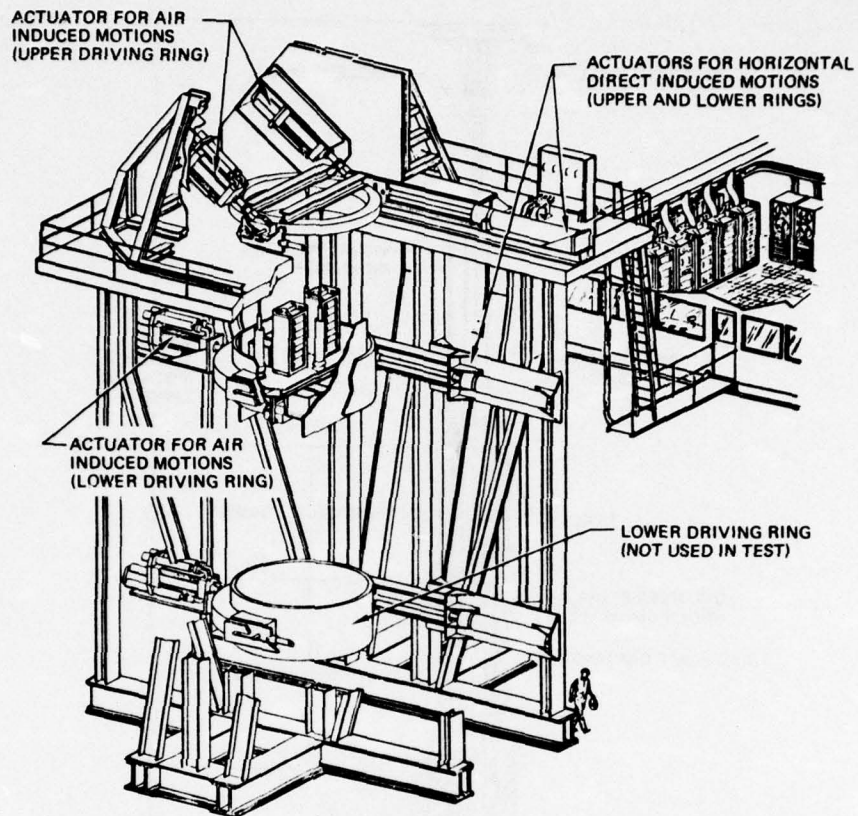
FIGURE 1   DYNAMIC TEST SETUP WITH FLOOR SEGMENT IN PLACE
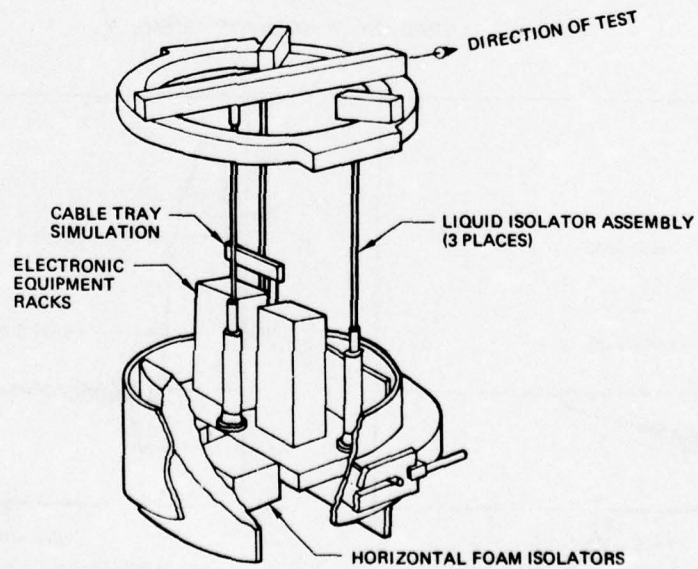
FIGURE 2   FLOOR SEGMENT TEST SPECIMEN SCHEMATIC
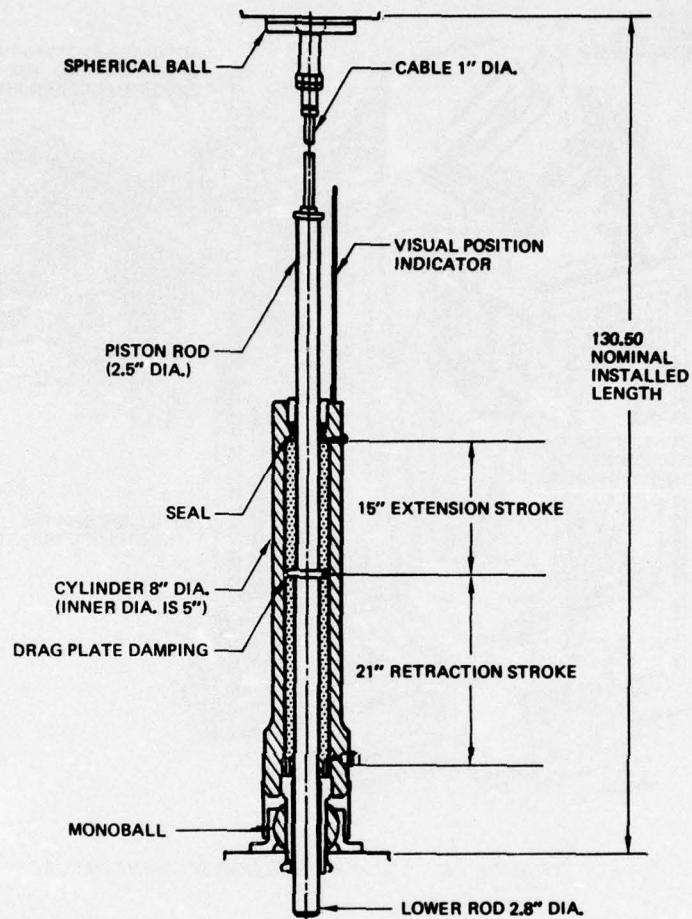
FIGURE 3   LIQUID SHOCK ISOLATOR ASSEMBLY
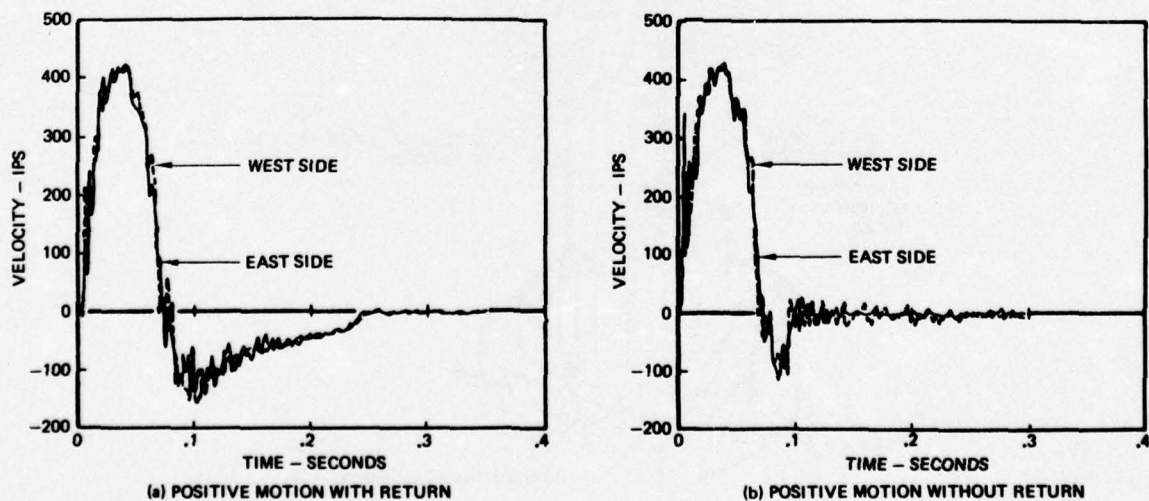
FIGURE 4   TYPICAL AIR INDUCED VELOCITY WAVEFORMS

196
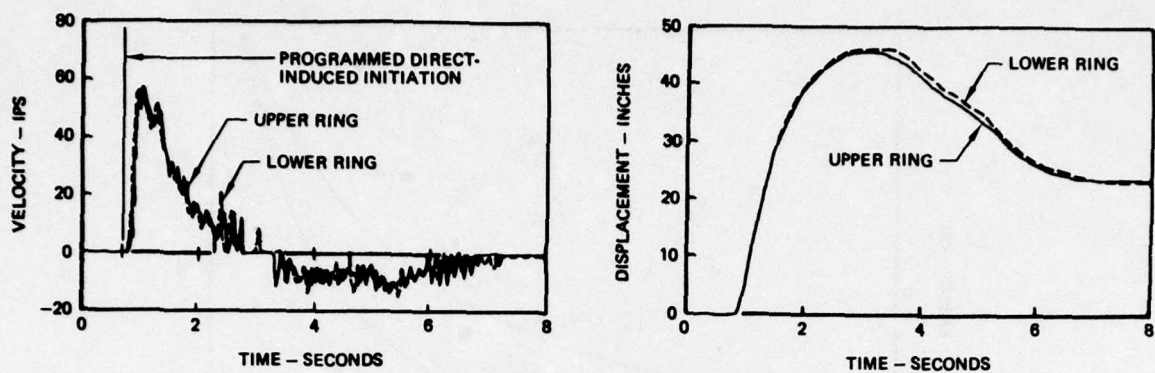
FIGURE 5   TYPICAL DIRECT INDUCED VELOCITY AND DISPLACEMENT WAVEFORMS
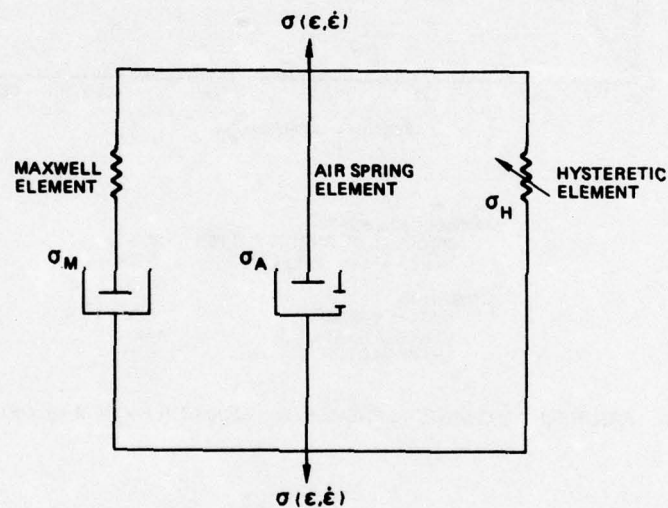
FIGURE 6   FORCE ELEMENTS IN FOAM ISOLATOR MODEL
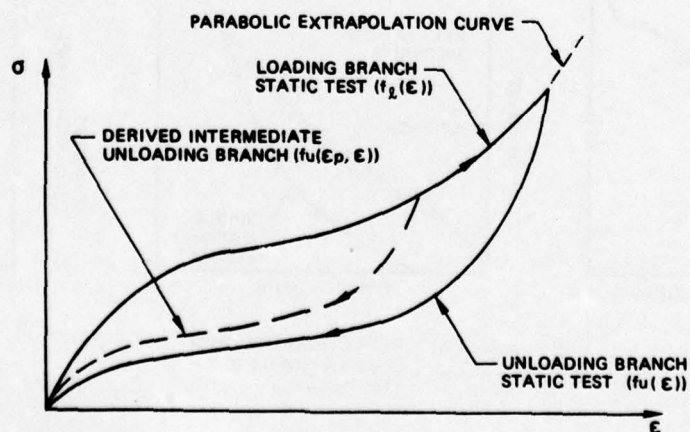
FIGURE 7   ANALYTICAL FEATURES OF HYSTERETIC ELEMENT

197
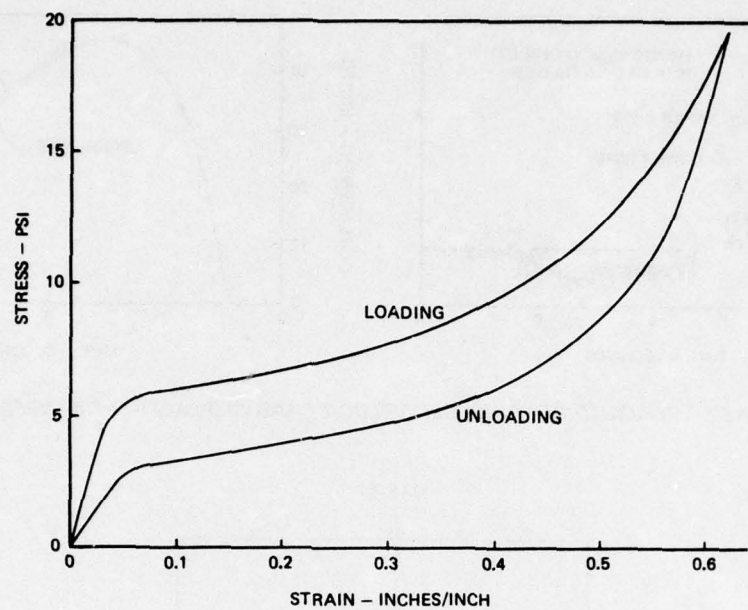
MAXWELL ELEMENT
    MODULUS OF RIGIDITY, G(PSI)   29.0
    RELAXATION TIME, τ (SEC)   0.35

AIR SPRING
    INITIAL POROSITY, γ 0.863
    VENTING FACTOR, β 16.0
    SHAPE FACTOR, α 0.95

FIGURE 8   MECHANICAL PROPERTIES FOR 10 PCF FOAM MODEL

———— RELAXATION SPECTRUM
- - - - SINGLE MAXWELL ELEMENT
⊙   TEST DATA
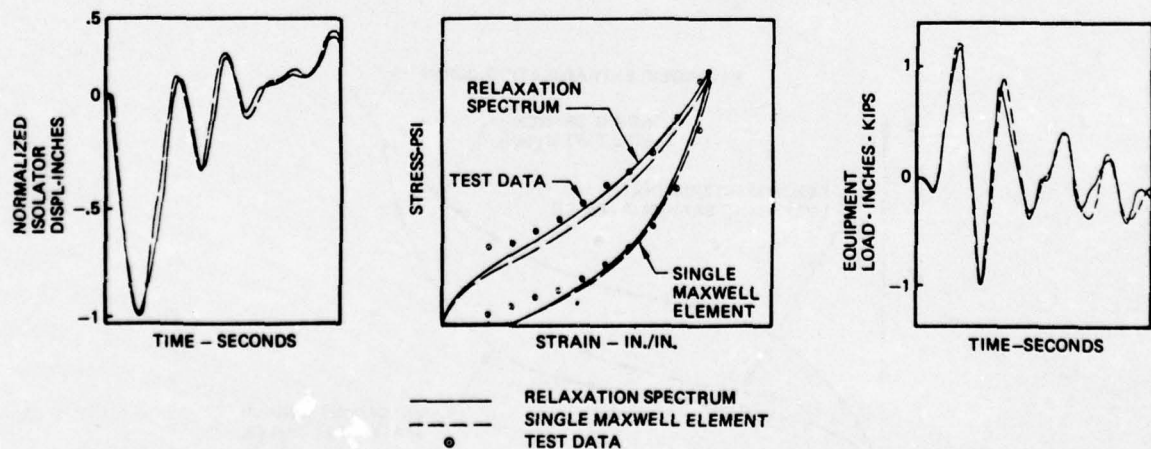
FIGURE 9   EFFECT OF RELAXATION SPECTRUM ON SYSTEM RESPONSE

198
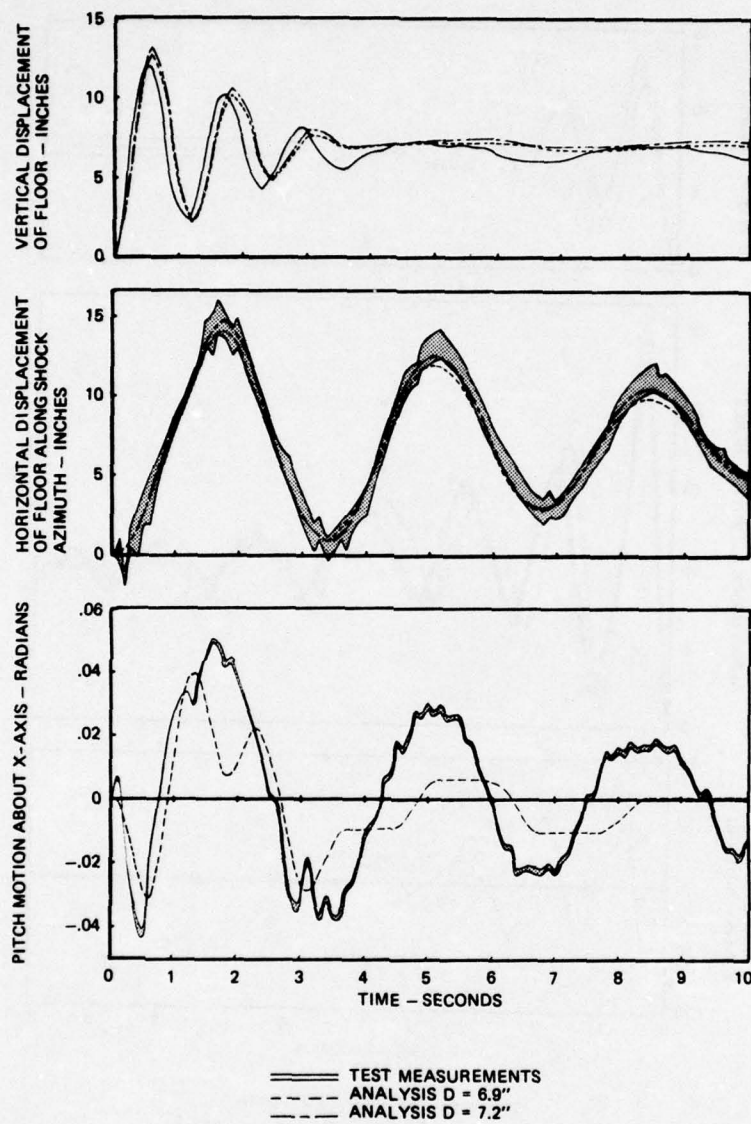
FIGURE 10   TEST/ANALYSIS COMPARISON FOR TEST NO. 1

199
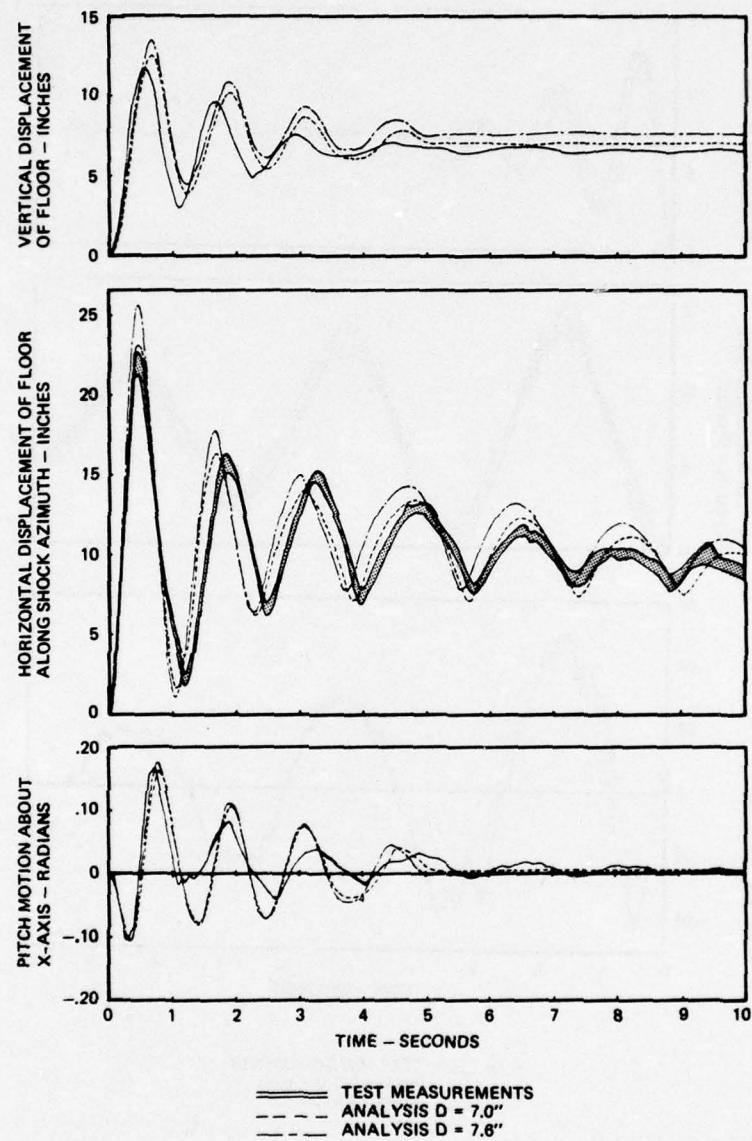
FIGURE 11   TEST/ANALYSIS COMPARISON FOR TEST NO. 4

200

VERTICAL DISPLACEMENT OF FLOOR – INCHES

HORIZONTAL DISPLACEMENT OF FLOOR ALONG SHOCK AZIMUTH – INCHES

PITCH MOTION ABOUT X-AXIS – RADIANS

TIME – SECONDS

TEST MEASUREMENTS
ANALYSIS D = 13.1"
ANALYSIS D = 14.6"
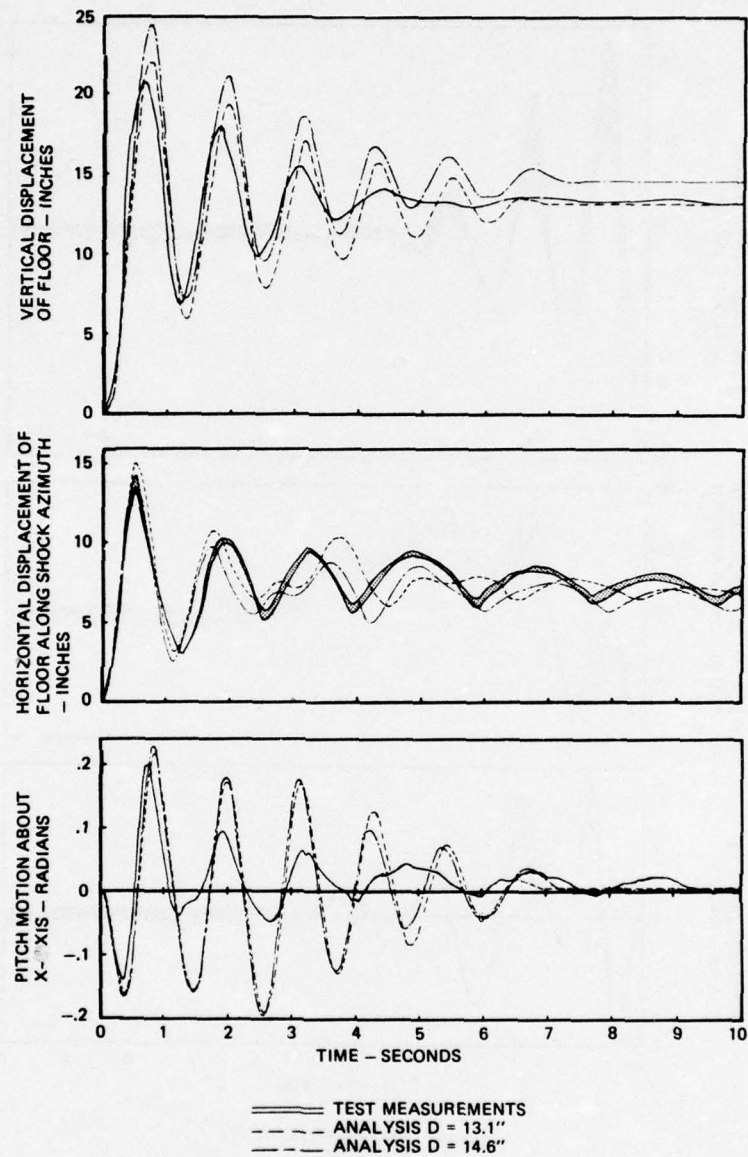
FIGURE 12   TEST/ANALYSIS COMPARISON FOR TEST NO. 5
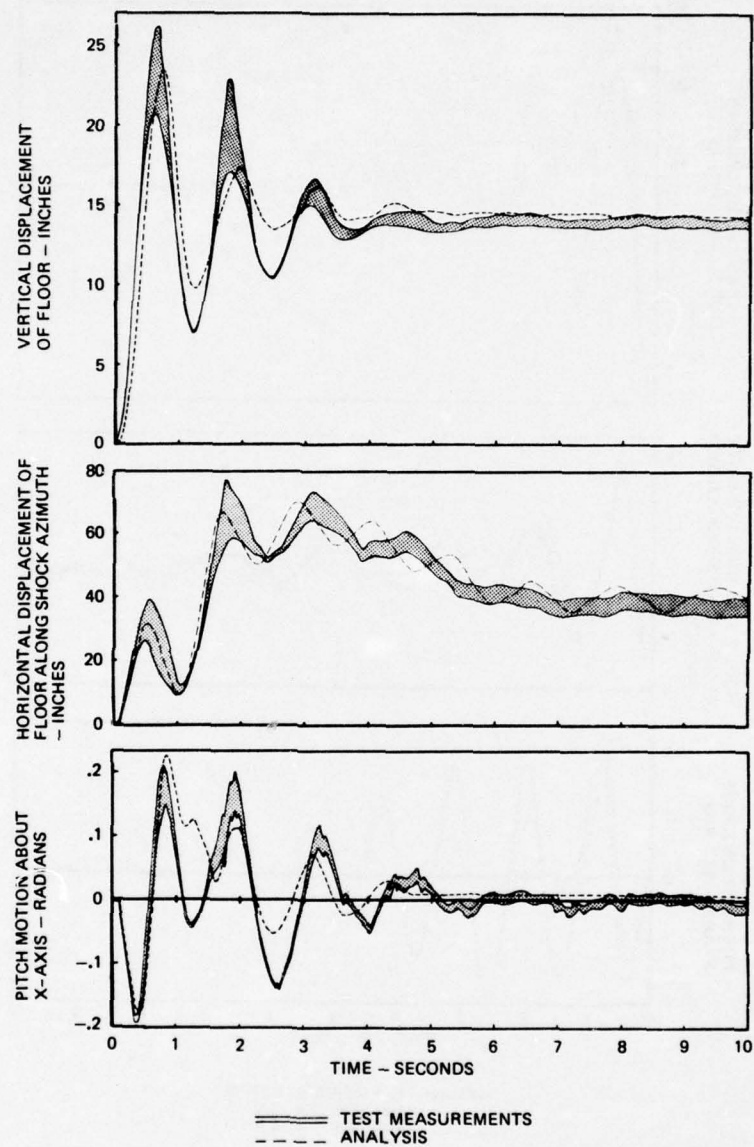
FIGURE 13   TEST/ANALYSIS COMPARISON FOR TEST NO. 8

202
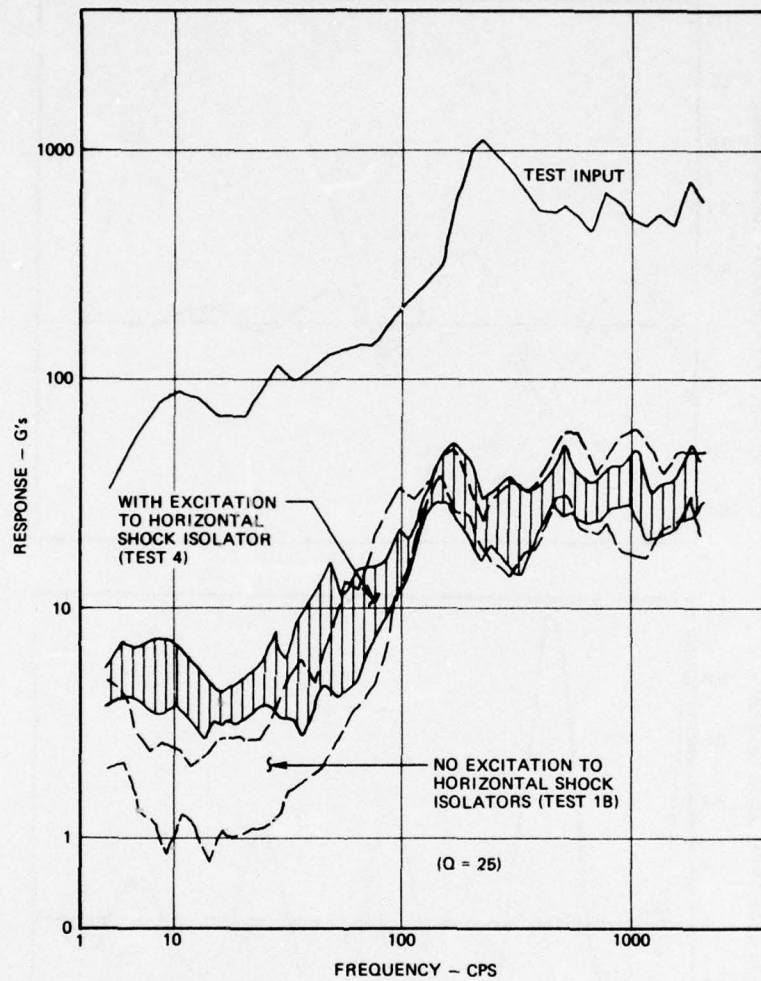
FIGURE 14   EFFECT OF FOAM ISOLATORS ON FLOOR
HORIZONTAL RESPONSE SHOCK SPECTRA
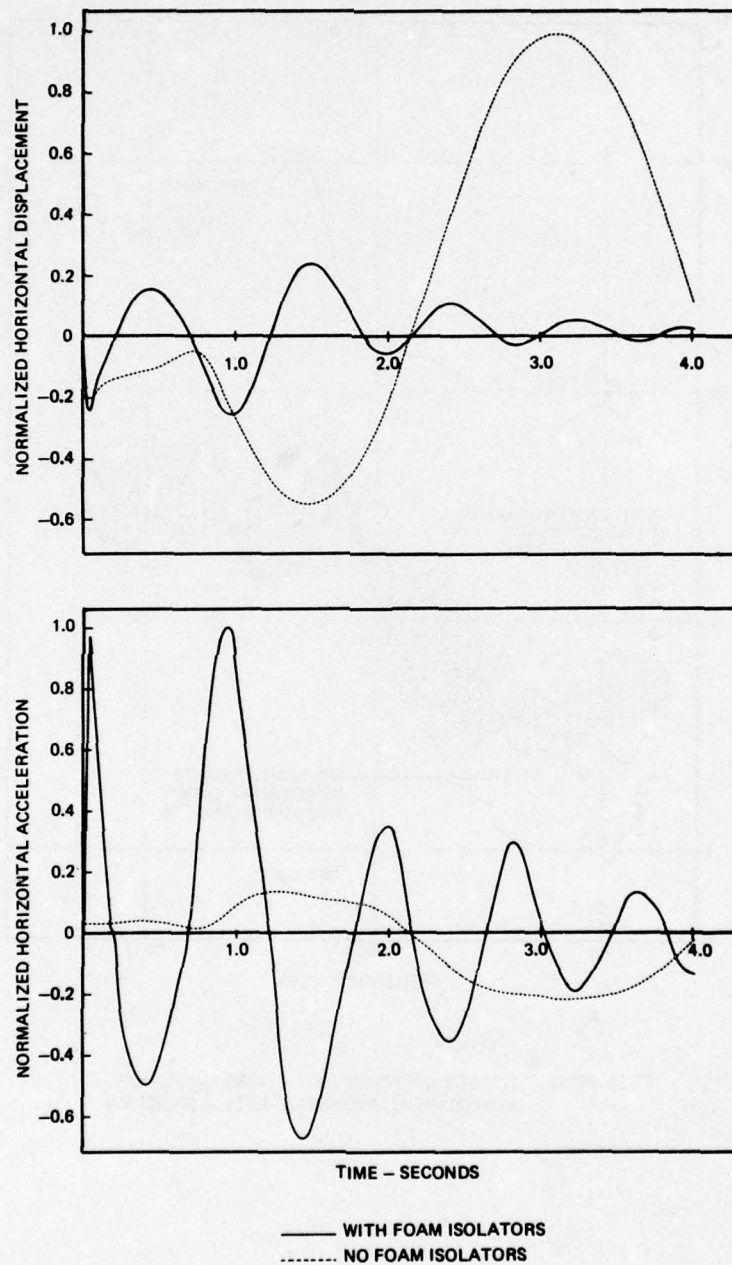
FIGURE 15   EFFECT OF FOAM ISOLATORS ON FLOOR RESPONSE

204

COMPONENT TESTING OF LIQUID SHOCK ISOLATORS AND ELASTOMERS
IN SUPPORT OF RECENT SHOCK ISOLATION SYSTEM DESIGNS

John P. Ashley
Boeing Aerospace Company
Seattle, Washington

Considerable component testing has been accomplished to support the design of new shock isolation systems. Early concept development transmissibility testing provided response characteristics for the most suitable candidate shock isolation systems. Tested elements included elastomeric foam, rubber pads, cables, liquid isolators and candidate floor structures. From these test results, optimum characteristics for shock isolation systems were established and subsequently applied toward specific design requirements and weapon system design specifications. Within required design constraints, prototype hardware was fabricated and subsequently subjected to development testing to provide design and analysis data in support of the system shock isolation designs. Computer analysis models were developed to calculate selected responses associated with these new shock isolation systems. This paper is devoted to describing the component dynamic development test and analysis efforts and resulting conclusions which ultimately led to the detail shock isolation system designs which are currently being deployed.

INTRODUCTION

In the last decade technology has produced larger yield and more accurate nuclear weapons, producing higher overpressures and increasing the crater-related ground motion effects. The result has been more severe nuclear weapons effects ground motion design criteria for a missile suspension system (MSS) that protects and provides a launch platform for an ICBM, and for a shock isolated floor that protects the operational ground equipment required for an ICBM launch. Luschei (a) briefly describes these two new shock isolation systems in an overview of the testing and analysis efforts that were accomplished in support of their qualification requirements.

This paper is devoted to a description of the dynamic testing of candidate isolation system components that has been accomplished in support of these two new shock isolation system designs which are currently being deployed. Testing was conducted over a six-year period, and consisted of candidate isolation system component tests, and subsequent development testing of components selected for consideration in the detail system design. Specific isolation system components for which dynamic response characteristics were investigated include: elastomer foams, rubber springs, steel cables, single and dual-chamber liquid isolator assemblies, floor platforms of several types of construction, and a liquid/mechanical shock isolator concept.

Computer analysis models were developed to calculate selected responses associated with the new shock isolation systems. These models were initiated during the candidate component tests and design phases of each isolation system, and were subsequently developed and improved as test data from the component development and full-scale test programs became available. Typical results from these analysis models are presented in this report.

CANDIDATE ISOLATION SYSTEM COMPONENT TESTS

Early concept development transmissibility testing, introduced by Grant (b), provided dynamic response characteristics for the most suitable candidate shock isolation systems. These concept tests provided a basis for early elimination of concepts with undesirable characteristics and influenced design details where concept feasibility was demonstrated. Empirical data and improved techniques for the prediction of shock isolation system dynamic performance also were obtained. From these test results, optimum characteristics for shock isolation systems were established and subsequently directed toward specific design requirement and weapons system design specifications. Five general shock isolation element categories were subjected to candidate component testing under conditions of shock, vibration, and impact loading. Tested elements included elastomeric foam, rubbers, cables, liquid isolators, and candidate floor structures. Test data were used to determine acceleration transmissibility for varying input levels for each of these elements.

Foam Testing

Initial testing during the concept feasibility studies for shock isolation programs consisted of an extensive foam vibration transmissibility test program. Test conditions included those to evaluate acceleration transmissibility and force transmissibility for both tension/compression and shear modes. The foam was excited by a controlled vibration input with slow sine sweeps and with transient vibration inputs. Static force deflection, vibration transmissibility and overall dynamic response characteristics were evaluated for each of the seven flexible foam specimens tested. Variations in response characteristics as they related to specimen density, specimen preload, specimen repeatability and variation in input test levels were investigated. The seven basic test specimens were as follows:

CANDIDATE FOAM SPECIMENS

Specimen No.	Approximate Density (Lbs/cu Ft)	Material Type
F1	3	Polyether Urethane (Open Cell)
F2	5	
F3	7	
F4	9	
F5	3	Latex Foam Rubber (Closed Cell)
F6	5	Poly-Vinyl-Chloride (Open Cell)
F7	2	Polyethylene (Closed Cell)

The initial goal of the foam test program was to establish a test sequence and standard specimen size in order to obtain the maximum information on foam transmissibility and dynamic response characteristics prior to failure of the specimens. A specimen size of 9.5 inches by 9.5 inches by 4 inches high blocks was selected for all foam testing. The foam blocks then were bonded to aluminum plates for accommodating attachment to the test fixtures and specimen preload when required. Five of the foam vibration test specimens were subsequently selected for impact (specimen drop) testing. Four impact velocities, up to 300 inches per second, and eight specimen preloads (0.05 to 1.5 psi—weight per specimen area) were used to evaluate the effect of load rate on the foam specimen responses.

Figs. 1 and 2 illustrate the representative compression and shear static force deflection characteristics respectively for each of the specimen types. The polyethylene closed cell foam (F7) was considerably less resilient than the other foams selected for this program, and is also inclined to have a more linear compression load deflection characteristic. The polyethylene foam specimens had somewhat higher damping characteristics than polyether urethane foams when loaded to give approximately the same natural frequency.

It was concluded during this concept development foam test program that the high-frequency response is not entirely attenuated by foam, as shown by the representative foam transmissibility curve on Fig. 3. As would be expected, however, the high-frequency attenuation characteristics did improve with decreasing stiffness, particularly for the polyether urethane open cell foam (types F1 through F4). The rubber latex foam (F5) and poly-vinyl-chloride foam (F6) exhibited good attenuation characteristics; however, they did not have sufficient stiffness to be considered candidates for further development toward anticipated shock isolation system design requirements.

The loading capability and major resonant frequency of a specific foam are important considerations in its selection for use as a shock isolation system. These parameters are compared in Fig. 4 for the seven foam specimens tested. Good repeatability in transmissibility response for a specific specimen type was observed, and a trend of decreasing response transmissibility for increased input acceleration was noted for all specimen types.

Rubber and Cable Tests

As part of the same candidate component test program, dynamic impact testing was conducted on selected rubber and cable specimens. The objectives of these tests were to determine dynamic force-deflection characteristics for specific rubber specimens and to obtain data necessary to describe acceleration transmissibility and dynamic deflection characteristics for various cable types and lengths.

Impact (specimen drop) testing of five candidate rubber specimens consisted of applying a near step velocity input utilizing the same drop test machine employed during the foam impact test program. The test articles were impact loaded separately in two orthogonal axes, simulating tension-compression and shear response loading. Each test article was preloaded to a percentage or specimen strain and tested at two input velocity levels (200 and 350 IPS). A single specimen consisted of rubber in the form of two disks (10-inch O.D. by 4-inch I.D. by 2 inches thick) which were vulcanized to aluminum end plates. A schematic of the test specimen and preloading mechanism is provided in Fig. 5. A summary of the rubber specimen material specifications is provided below:

CANDIDATE RUBBER SPECIMENS

Rubber Type	ASTM Designation	Chemical Identification	Shore Hardness Durometer
11 R Butyl	R	Isobutylene	32H
11 R Butyl	R	Isobutylene	52H
11 R Butyl	R	Isobutylene	74H
NBR	SB	Nitrile butadene	65H
Polyurethane	—	Polyurethane di-isocyanate	60H

The following observations were made from evaluation of the test results and apply only to the specific test articles described above:

Loading rate varied little with change in durometer under conditions of compression loading; however, it did increase with increasing durometer under the conditions of shear loading.

The rubber specimens evidenced an appreciable transmission of high-frequency vibrations for compression loading. For shear loading there was little transmission of high-frequency data.

The lower durometer rubbers have a higher apparent damping factor associated with the first mode response for both compression and shear. The higher durometer rubbers exhibited some amplification of the fundamental response mode.

Seven cable specimens were subjected to high-velocity vertical and horizontal impact testing. Vertical testing was accomplished by impulse loading the upper end of the test article in the longitudinal axis. Each cable was tested at three input levels for each of three static preloads (5, 15 and 30 KIPS) for a total of nine shocks per cable. A description of the cable specimens identification is summarized below:

CANDIDATE CABLE SPECIMENS

Cable No.	*Lay/Core	*Type/Class	*Construction	Diameter (Inches)	Length (Feet)
1	6 x 7/fiber	1/1	—	1-1/8	15
2	6 x 19/fiber	1/2	4	1-1/8	15
3	6 x 19/wire	1/2	4	1-1/8	15
4	6 x 37/wire	1/3	7	1-1/8	5
5	6 x 37/wire	1/3	7	1-1/8	15
6	6 x 37/wire	1/3	7	1-1/2	15
7	6 x 37/wire	1/3	7	1-1/8	10

*Standard notation describing cables and cable construction taken from RR-W-0041b.

Generally there was considerable transmission of high-frequency vibration observed down the length of the cable for the 3½-inch vertical input conditions. Lateral responses due to the vertical impact conditions were complex and multimodal. Slack cable conditions were achieved and the longitudinal cable modes and damping factors were determined for each cable configuration.

Horizontal impact testing was accomplished by impulse loading the cable upper end mounting plate and driving it laterally through a controlled displacement. Maximum input levels were: 15 inches displacement, 320 IPS velocity, and 220 g's acceleration. Complex lateral responses were excited in the cable specimens and measured response data revealed evidence of fundamental modes with higher frequencies superimposed. No apparent cable slack was introduced by the high lateral inputs and no cable damage was noted.

Liquid Isolator Testing

Candidate isolation system component testing included a comprehensive test program of evaluating liquid isolators. The program included vertical and horizontal shock testing on two dual-chamber isolator configurations, and on three single-chamber isolator configurations consisting of pressure-cylinder/rod assemblies which were designed and built by The Boeing Company. A limited amount of vibration testing was conducted on one dual-chamber isolator configuration.

Vertical and horizontal positive-only shock inputs were provided separately by two different force actuators that preceded the full-scale test facilities described in detail by Burwell (c). Fig. 6 depicts the vertical test configuration and Fig. 7 the horizontal test setup. Representative vertical and horizontal resulting input shock spectra levels are presented in Fig. 8.

To gain a diverse set of data on liquid springs, two single-chamber pressure cylinders were designed to be combined with two piston rods to give three different fluid isolator configurations. One pressure cylinder (designated Cylinder 1) was similar to the high-rate (lower) cylinder of the two dual-chamber isolators. The second pressure cylinder (Cylinder 2) was designed to investigate isolator geometry and the effect of pressure, independent of preload. Fig. 9 provides a schematic indicating the relative size differences in the single-chamber isolator configurations. Isolator Rod 1 had a piston area of 2.5 square inches and Rod 2 had a net piston area of 2.0 square inches. The cylinders and piston rods were combined into three basic isolator assemblies as delineated in the summary of total test configurations below:

| | Number of Configurations Tested | | |
	Vertical Shock	Horizontal Shock	Vibration
Dual-Chamber Isolator			
10, 15 and 20 kips preloads	5	3	4
33 to 60 kips preloads	2	2	---
Single-Chamber Isolators			
20, 25, 30 and 45 kips preloads			
Cylinder 1/Rod 1	20	6	---
Cylinder 2/Rod 1	8	---	---
Cylinder 2/Rod 2	2	---	---

Isolator volumes were varied by adding radial segments internal to the cylinder. Volume ranges accomplished in this manner were:

Cylinder 1—440—550— 660 cu. in.
Cylinder 2—660—930—1320 cu. in.

Fluid effects were evaluated by using silicone fluid viscosities of 0.65, 50, and 200 centistokes. In addition, water and alcohol were used as fluids for comparison with silicone performance. Static preloads were provided for the isolator configurations by attaching a responding structure which supported an appropriate number of lead weights to meet the desired preload mass. Fig. 6 shows the most frequently used preload support structure configuration.

The three basic structural arrangements depicted in Fig. 10 were employed to investigate the effects of isolator mounting technique on isolator transmissibility. The soft-mounted configuration utilized a cable assembly between the isolator rod and the load head. The hard-mounted rod configuration attached the isolator rod directly to the load head and placed the cable between the housing and the preload. The hard-mounted inverted configuration was essentially the reverse of the soft-mounted configuration with the lower housing attached to the load head and with the cable segment between the rod and the preload. Also, to evaluate the effects of secondary shock isolation on system transmissibility, two rubber mounting pad configurations were investigated; first, between the hard-mounted rod and the test input load heads, and second, between the lower cable fitting and the preload.

In total, 36 load-deflection tests, 94 vertical shock tests, and 27 horizontal shock tests were performed to evaluate the variations in system parameters including volume, fluid type, fluid viscosity, isolator damping, isolator mounting and isolator preloads, and their effects on transmissibility and performance.

Approximately 36 instrumentation input and response measurements were recorded during each dynamic test and can be summarized into the following categories:

1. Crystal accelerometers, input and response (high frequency)
2. Strain gage accelerometers, low-frequency response
3. Strain gages, axial and bending loads
4. Velocity, input and response
5. Displacement, input and response
6. Pressure, cylinder performance
7. Temperature, cylinder performance

Major conclusions obtained from the candidate liquid isolator component testing are summarized below.

Vertical floor responses for higher input levels are not significantly greater than for lower inputs to the same isolator configuration. Resulting transmissibilities are, therefore, lower for higher input levels. This result may be due to friction in seals and the conclusion only applies to vertical, down input shocks where the cable can go slack. Up pulses will see increasing response with increase in input.

Fig. 11 shows that for vertical response to a vertical input, the single-chambered isolators performed as well as or better than the dual-chambered isolator. Differences in

transfer functions between the two cases can be attributed primarily to differences in test setup since the dual-chambered isolator used a slotted fitting and the single-chambered isolator used a cable. Vertical response results from the horizontal testing (where a cable segment was used) verified this assumption.

The hard-mounted rod configuration (rod mounted to load head) had the lowest transmissibility of the three single-cylinder mounting configurations subjected to vertical testing. This was due to the ability of the cable between the isolator and the floor to decouple the floor. The soft-mounted rod configuration (cable between rod and load head) and the hard-mounted inverted configuration (isolator upside down and mounted to load head) had significantly higher transmissibilities. Vertical transfer functions for the three mounting configurations are shown on Fig. 12. The hard-mounted rod configuration demonstrated its ability to survive and perform in a high-shock environment when subjected to vertical or horizontal inputs; however large rod bending loads were experienced.

When rubber pads were placed between the load head and the hard-mounted rod, the vertical rod compressive loads and the horizontal rod bending loads were lowered. The transmissibility was observed to increase for this condition. The difficulties with rubber pads lie in trying to achieve the required horizontal pad flexibility while maintaining vertical load capability.

A major source of high-frequency environment above 800 Hz in liquid shock isolators is the standard one-direction damping valve. As the valve opens and closes, it slams against stops on the piston rod and, in doing so, it excites longitudinal modes of the isolator. Fig. 13 presents vertical transfer functions for a typical single-chambered isolator with and without a damper valve.

For a given input level, vertical transmissibility increases with preload for higher values of preload on the soft-mounted, single-chambered isolators. This increase in transmissibility is dependent on isolator friction since it is friction which transmits forces from the rod/cable/load head assembly to the shock isolated platform. Increasing the preload on a given isolator will result in increased friction and consequently, the transmitted environment will increase. However, this trend reaches a threshold and for lower values of preload, both single-cylinder and dual-cylinder isolators showed only small changes in transmissibility with preload. Fig. 14 compares transmissibilities for three different preloads on a single-chambered isolator.

The dual-chamber isolator test results showed reduced retraction rates for increasing fluid viscosity with the highest retraction rate for 0.65 centistokes silicone fluid. The dual-chamber isolator uses 50 centistokes in the field installation.

The relationship between static and dynamic isolator friction was observed to be complex. Friction appears to vary with velocity and for higher isolator pressures, dynamic friction is much lower than would be expected based on the static data.

No significant trend of transmissibility with variations in silicone viscosity was found for dual-chamber isolator testing. For single-chamber isolators tests (which compared silicone, water and alcohol) transmissibility data showed that no improvement can be gained by using either water or alcohol. Cylinders with highest length-to-diameter ratio for a given fluid volume tended towards lower transmissibility.

It must be emphasized here that the response trends indicated by the data presented above are for particular isolator configurations, subjected to a particular excitation. The interdependency between input pulse, isolator configuration and isolator rod retraction capability is complex, and the designer cannot be too careful in attempting to extrapolate these results to a different isolator subjected to a different excitation. From this test program, however, came the following design considerations for future use of liquid isolators in shock isolation systems:

Future design programs should give strong consideration to the use of a single-chambered isolator from a transmissibility and cost viewpoint.

Develop lower friction seals to reduce the effect of friction on transmissibility.

Develop an improved damping device to eliminate unwanted environment generated by valve impact.

Minimize slack cable wherever possible to keep system loads as low as possible.

Conduct additional testing to determine more precisely the variation of isolator friction with pressure and velocity.

Floor Structure Testing

A series of candidate floor structure tests was conducted to provide useful data for design and analysis of possible shock isolated floor subsystems. The test program emphasized construction concepts, fabrication, and material suitability. Dynamic characteristics in the flexible floor frequency range beyond the low fundamental "rigid body" modes were of concern. Dynamic performance comparisons constituted the basis for selected of materials and structural arrangements.

Dynamic testing of three steel, three wood, and five additive damped steel floors was accomplished on specimens approximately 11 feet long by 5 feet wide. The basic parameters under investigation were:
1. Stiffness—Bending and torsion
2. Damping—Free layer; additive for steel, and inherent for wood
3. Mass Loading—0, 2 and 3 equipment cabinets
4. Input—Magnitude and duration

Fig. 15 provides a schematic of the test configuration. Excitation of the floor was achieved by an electrodynamic vibrator. The test specimen was suspended at four corners by cables in series with airbags attached to a rigid superstructure. This system provided rigid body frequencies below 2 Hz. In addition, this approach provided easy floor height adjustment for leveling and attachment of the vibrator.

The test inputs included slow sine sweep, fast transient sweep, impulse, and complex shock simulating and liquid isolator transmitted environment. A modal survey was made during selected resonant dwell tests. A total of 196 tests, including modal survey tests, were conducted during the program. A maximum of 34 channels of acceleration and floor strain data were recorded on magnetic tape during each test. Transmissibilities and response shock spectra were the basic dynamic characterizations used in assessing the effect of each parameter variation on design.

Many detailed objectives were accomplished during the program, with the most significant being a recommended

floor design with the following characteristics:

1. The fundamental bending and torsion frequency of the floor should be below 25 Hz (below fundamental frequencies of floor mounted equipment).

2. The floor should be made of steel and be of continuous welded construction.

3. Structural elements such as plates, beam welds, and other large surfaces should have a fundamental frequency as high as practical, preferably in excess of 200 Hz (above predominant frequencies of floor-mounted equipment).

4. Free layer viscoelastic damping tile should be considered for application to the large plates and webs.

In conjunction with testing, several analytical tools were developed and correlated with the test results. Details of the analytical success achieved during this program were reported by Vail (d) in 1972. The test/analysis correlation showed the elemental modeling was a good tool for predicting dynamic characteristics out to a frequency of approximately 120 Hz. It was found that the equipment and floor structure weight, stiffness, and arrangement can affect the dynamic response characteristics of the system significantly in this frequency range. To account for these effects, design configurations can be analyzed to assess their relative merits in this frequency range. This test program provided the data to calculate the inherent damping needed for rational modeling in design trade studies. The classical damping values were too conservative in the frequency range corresponding to relatively large flexible cabinet motion.

The viscoelastic damping analysis was found to be a good tool for predicting the effect of floor damping on transmissibility characteristics.

Fast Fourier transform methods for response prediction by convolution of a known input with experimentally determined transmissibilities appear to be a good tool on the basis of analysis and test correlation that was accomplished. The test program provided the data to assess amplitude linearity and pulse duration effects needed to establish confidence levels for future dynamic analyses by this method. Two primary uses were envisioned for this analysis in floor design studies. The first is prediction of the high-frequency environment of a floor subsystem to establish compliance to existing criteria. The second is the establishment of future floor allowable dynamic environment criteria.

SHOCK ISOLATED PLATFORM—SELECTED COMPONENTS

Foam Development Tests

Based on satisfactory results achieved in foam testing during the concept development test program, additional static and dynamic tests were conducted to evaluate flexible foam as a suitable horizontal shock isolation system. Initial foam candidates were selected from earlier test data obtained during the shock isolation concept studies described earlier. The candidate specimen was a 7 pounds per cubic foot density, open-celled polyurethane foam (non-fire retardant).

Physical constraints of the existing platform installation required investigation of a larger size than previously tested. Static and dynamic tests were subsequently conducted to provide a comparison between the larger new specimens and three samples of the same type of foam that was tested during the concept development test series. The effects of size and age were investigated along with variations in load history, effects of precrushing and variations obtained from two vendor sources.

Fire-retardant foam was an additional requirement imposed for operational installations, necessitating additional evaluation. Fire-retardant foams of three different densities were investigated to determine which had the most similar static characteristics to the initial 7 pounds per cubic foot density candidate foam. Both compression and shear drop tests were conducted to evaluate the dynamic characteristics of these three densities of foam. From this evaluation, the most suitable foam candidate selected for further evaluation testing had a 10 pounds per cubic foot density. A second vendor selection was accomplished by specifying a static force deflection requirement, not density. The second selected vendor foam was a 7 pounds per cubic foot density, fire-retardant foam.

The new specimens consisted of 12 inch by 12 inch by 7.5 inch high blocks of open-celled, flexible, polyurethane, fire-retardant foam which had no previous static crushing. Using the two selected vendor sources, the specimens were subjected to a series of static force-deflection tests, compression and shear drop tests, and horizontal sled impact tests. Impact testing was conducted with the direction of impact normal to the face of the foam, 45 degrees from normal, and 60 degrees from normal. From the series of tests, static and dynamic response information was obtained. Additionally, one specimen was configured with a smooth teflon plate, 0.06 inches thick, bonded to one face of the foam, for evaluation as an antifriction device for possible use in conjunction with the foam. The use of grooved teflon sheets also was evaluated.

Significant conclusions resulting from the equipment platform horizontal shock isolator component development tests are summarized below.

Open-celled polyurethane foam is made up of cells and connecting structure. The density of the foam is a function of cell wall thickness and cell size. When foam is statically crushed there is certain cellular wall breakdown to the extent of the amount of deflection. The sketch below gives a good example of this phenomenon. Once the foam has been precrushed the force deflection characteristics remain fairly constant for a limited number of cycles, if the foam is allowed time to regain the air that was pushed out of it.
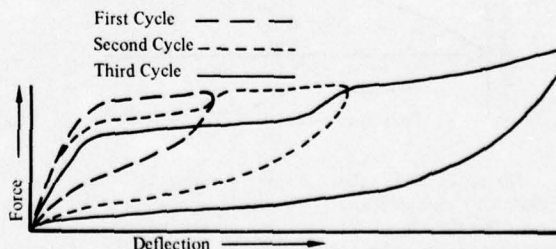
Repeated cycles during a short period of time show a reduction in force for a given deflection as can be seen on the sketch below. This force reduction is due to the loss of air which has been pushed out and has not had time to return.

First Cycle ——
Second Cycle ‒ ‒ ‒

Force

Shaded Area Is Temporary Change
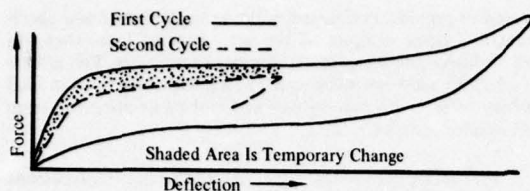
Deflection ——

If foam is crushed through many cycles, the increased cellular wall breakdown causes a reduction in the overall stiffness of the foam.

The second vendor, 7-PCF foam exhibited the same initial deflection characteristics as the first vendor, 10-PCF foam; however, the flat part of the force deflection curve is much flatter for the second vendor foam. These two facts indicate that the second vendor foam has larger cell size.

Comparison of static compression stress-strain results from both specimens, concept development and component development, resulted in the following conclusions:

1. The differences in size (within the limits of comparison) exhibited no significant effects.

2. Aging of polyurethane open-celled foam (at least within a 2-year period) does not degrade or significantly change the force characteristics.

It was concluded that foam should be selected on the basis of static force-deflection requirements rather than foam density. Also, dynamic force-deflection requirements should be considered for possible use when more rigid controls are desirable.

Dynamic drop-test data were utilized with static results for evaluation during the specimen selection phase of the foam test program. A comparison of drop test results with results from the sled impact test (normal to specimen face) demonstrates the validity of all comparisons made from drop test data during the subject foam testing.

The type of facing on the foam has definite influence on friction levels. Friction was higher for bare-faced foam than for teflon-faced foam.

Bare Faced ——
Teflon Faced ‒ ‒ ‒

(−) Friction Force (+)

Deflection ——
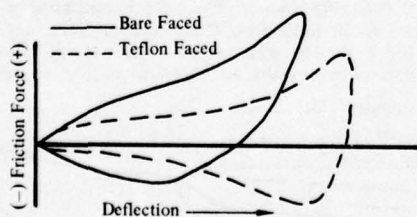
No appreciable influence of the teflon facing on the compressive characteristics was noted. Significant influence due to the bare-faced foam on compression and shear characteristics as the angle increased is due to the effect of increased friction on the foam specimen bending.

Increasing impact velocity causes a significant increase in compressive force for a given deflection due to the inability of trapped air in the foam specimen to escape; sketch A below gives a good example of this phenomenon.

A

Normal Force

Deflection ——

High Velocity ——
Low Velocity ‒ ‒ ‒

B

(−) Friction Force (+)

Deflection ——
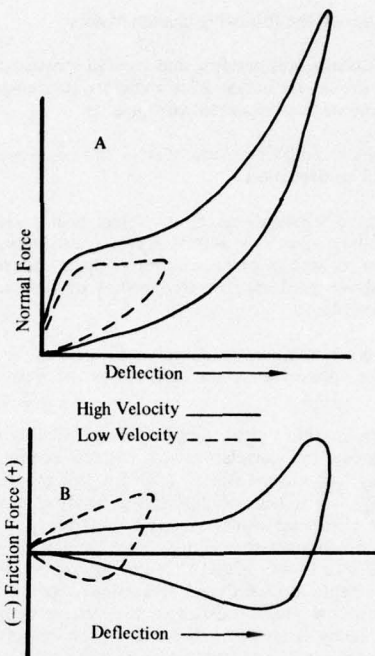
For smooth teflon-faced samples, the increased velocity tends to enhance the air cushion effect between the teflon and the reaction surface which decreases the friction force. Sketch B above gives a good example of this phenomenon. Increasing the sample impact angle tends to de-emphasize the foam trapped air phenomenon and increases specimen deformation due to increased friction.

The general trend in a comparison of the dynamic data is that the second vendor foam showed a much longer flat part of the dynamic force deflection curve. This difference is due to what appears to be a minor variation in the static force deflection and probably results from internal mechanical differences such as cell size, porosity and basic internal variation.

Friction tests were conducted with various surface finishes and teflon-faced form specimens to evaluate proposed facility interface requirements. It was determined that the existing facility enamel-painted surfaces were adequate.

Recommendations resulting from the horizontal shock isolator component (foam) development test program are summarized below.

1. Foam requirements should be specified on the basis of static load force deflection (or stress strain) characteristics rather than density alone. Specify a range of density which would be acceptable based on weight allowables. Static requirements should be selected after careful consideration of the probable range of dynamic responses for a given static response.

2. As part of the foam selection procedure, definite requirements should be specified for sample acceptance tests and also for delivery. For situations where it can be guaranteed that no crushing will exist prior to the intended use, uncrushed foam should be considered based on the increased hysteresis available.

3. For situations where sliding occurs between foam and its reaction surface, the foam surface should be lined with teflon (or similar material) to minimize transmitted shear loads and to eliminate the possibility of specimen failure. For compression-only situations, bare-faced foam should be adequate.

Additional static and dynamic foam tests were conducted to evaluate the effects of increased area and radial length requirements for a second equipment platform horizontal shock isolator design. The unique requirement for this design was that the foam blocks had to form a continuous platform which could be walked on by maintenance personnel while servicing equipment mounted on the platform.

The test articles were constructed from celled flexible poly (ether) urethane foam blocks of varying sizes and densities. The blocks were bonded to a half-inch aluminum plate on one end, a teflon sheet on the other end, and a fiberglass face on top. Fig. 16 shows a specimen with a rubber sheet laid over the fiberglass face. A typical test setup of the dynamic sled impact test condition is provided in Fig. 17. For these dynamic tests, a stationary foam block was impacted by the moving sled with sufficient mass and at several velocities to provide a suitable range of strain levels.

Testing provided answers to the following specific questions:

1. What is the effect of foam size upon the dynamic force deflection? Increasing the length of the foam sample tended to make the foam softer by increasing the amount of buckling. Increasing the area of the face of the foam sample, of course, made the foam stiffer.

2. Can foam blocks survive as shock isolators when used in operational conditions? During the 45-degree dynamic sled tests, foam blocks with a slenderness ratio of 0.50 or less failed. During the 60-degree dynamic sled test, foam blocks with a slenderness ratio of 0.60 or less failed. It became apparent that foam isolators should have a slenderness ratio larger than 0.60 to be failsafe. Slenderness ratio is the specimen width divided by specimen length.

3. What is the effect of loss of the air breathing capability of the foam specimens with both ends covered? The dynamic tests indicated that there was little change due to the blocking of the air flow from the foam.

4. To provide the walk-on/work platform capability, a foam protection cover was necessary, as seen in Fig. 16. What effect does the addition of this rubber protection sheet have on the dynamic force deflection characteristics? One test specimen had the rubber cover removed and was subjected to the same testing as the design verification test specimens. Virtually no change in the dynamic force deflection characteristics was observed.

The dynamic response characteristics obtained during these tests provided the basic properties in supporting the foam idealization analysis model developed by Sepcenko (e). The application of this analysis modeling to the ultimate qualification program of the horizontal isolation system presently used on electronic equipment platforms is covered in an article by Gustafson (f).

Liquid Isolator Development Tests

Based on the satisfactory performance exhibited during the single-chamber liquid isolator candidate testing, a prototype liquid shock isolator and cable assembly, duplicating functional characteristics of a new isolator design, was fabricated and tested to verify the functional performance of the isolator.

Proof pressure testing was conducted to demonstrate the structural integrity of the pressure cylinder and seal assemblies. Leak tests were conducted after each assembly of the isolator to verify fluid integrity and proper assembly of the seals. Load-deflection testing was performed to confirm the isolator predicted spring rates and establish the seal friction hysteresis.

Twang (initial displacement) tests were performed to define the isolator damped natural frequencies and dynamic force-deflection characteristics. Piston rod velocities were determined to establish the rod retraction/extension characteristics and assess damping for three preload (static pressure) conditions.

Vertical and horizontal shock tests were conducted on the prototype isolator to correlate isolator response with design requirements and verify performance for the design considerations. Isolator preload configurations of 8, 12 and 20 kips were subjected to input levels of 50, 75 and 100 percent of maximum force actuator capability and consisted of positive-only and positive-with-return-velocity waveforms. Typical 100-percent pulses achieved during testing are presented in Fig. 18.

Data evaluation of the test results was directed toward:

1. Defining rigid-body responses for a defined displacement, velocity, and acceleration input shock pulse.

2. Establishing slack cable/rod retraction rate capabilities for the various isolator configurations and input levels.

3. Verifying piston rod bending moment and resulting isolator horizontal load analytical predictions for horizontal shock pulses.

4. Establishing isolator and simulated floor response acceleration levels and identifying the source of the transmitted accelerations.

5. Defining the transmissibility characteristics of the liquid shock isolator for use in predicting the shock isolation system platform environment and subsequent equipment capability requirements.

The following performance characteristics were derived from the test results and compared well with analysis predictions.

Preload Configuration	Liquid Spring Rate	Rigid-Body Frequency
8 kips	600 lb/in.	0.84 Hz
12 kips	650 lb/in.	0.74 Hz
20 kips	810 lb/in.	0.65 Hz

Seal Friction = $\pm$ 500 lb
Dragplate Damping (C_V) $\approx$ 0.15

Shock test data exhibited no significant anomalies in the basic isolator performance, or low-frequency aspects of isolator responses. The prototype design liquid isolator assembly did exhibit satisfactory transmissibility characteristics as predicted from the candidate isolation system component isolator test program. Comparisons of shock spectra response levels and transmissibility ratios are shown in Figs. 19 and 20 respectively. It was also observed that the relationship of input pulse duration to rod retraction and the subsequent cable unslack condition significantly affects the resulting high-frequency environment levels.

Single Isolator Performance Limit Tests

Dynamic testing of a full-scale shock isolated equipment platform and its associated operational ground equipment was conducted to support qualification and validation of the system design. A description of the program and the achieved success is covered in a discussion by Milne (g). Immediately following, single isolator tests were conducted to determine the performance limits of the liquid shock isolators, including cables and attachments.

The test articles for this series of tests consisted of two shock isolator assemblies including the spherical nut/seat assembly, cable assembly, isolator cylinder, and flanged monoball bearing. The test article is depicted in Fig. 21; the only difference between assemblies is different cable assembly lengths (45 inches versus 81 inches, nominal). Attached to the base of each assembly, by means of the monoball flange, was a three-armed steel simulated floor structure as shown in the test setup photo of Fig. 22. The simulated floor structure supported the appropriate number of preload weights for the desired isolator configuration. The antirotation assembly noted in Fig. 22 restrained the mass from rotating during the dynamic loading and unloading of the isolator. Such a device was not required during full-scale testing because roll rotations are inhibited when more than one isolator supports the floor structure. This antirotation mechanism was designed to have low friction characteristics, with all metal-to-metal interfaces isolated by rubber pads.

Testing was accomplished at the test facility specifically designed for full-scale testing of shock isolated equipment platforms. Only one force actuator was utilized during each performance limit test as depicted in Fig. 22. Details of the force actuator capabilities and the parameter variations employed to achieve the desired inputs are provided in a discussion by Burwell (c).

The two specific objectives associated with the shock isolation system performance limits testing were:

1. Determine environment and loads due to rod impact with cylinder during full retraction, and relate to known failure levels of the platform-mounted equipment.

2. Determine input conditions which bring the isolator assembly to onset of failure—and actually cause failure.

Up to 63 instrumentation measurements were recorded on magnetic tape during each test condition. Also, a series of passive measurements was recorded to define the pre- and post-test conditions of the force actuator and test article. Oscillographs, shock spectra, Fourier transfer functions and time history/integration plots were generated for both quick-look and detailed analysis. Test and analysis results from these tests are not presented in this paper due to the classification level of such information.

Single Isolator Analysis

Analysis models were developed to calculate selected responses associated with the equipment floor shock isolation system. These models were initiated during the design and component testing phases and subsequently were developed and improved as test data from the various test programs became available. The analysis effort conducted in support of the full-scale equipment platform tests described by Milne (g), and the floor segment tests described by Gustafson (f), included the use of two analytic models. One model, described herein, is a planar analysis model of the detailed shock isolator assembly. The second model is a three-dimensional analysis model that calculates the rigid-body motions of the complete unsymmetrical equipment platform.

The single isolator model is composed of a number of elements which represent the isolator and a rigid simulation of the floor mass. The elements include the upper attachment fitting and integral spherical bearing attachment to the ceiling motion source, the support cable, the isolator piston rod, and isolator cylinder with monoball and the mass representing a floor segment. The horizontal foam isolators on the floor mass segment are modeled as described by Gustafson (f) but were not addressed in the isolator fragility test program.

The upper attach fitting is modeled as a rigid link on a pivot with one rotational degree of freedom in plane with the ceiling input motion. The cable is modeled as a series of five equally spaced, lumped masses, each representing one-fifth the total cable mass and connected by nonlinear spring, viscous damper and coulomb damper elements in parallel. Each cable mass element is allowed to move vertically and horizontally in the plane of the input motion. Spring and damper elements connect the uppermost cable mass with the lower end of the upper attach fitting.

The isolator rod is modeled as a rigid element that is attached to the end of the cable by the spring and damper elements and is allowed to displace relative to the cylinder. The isolator cylinder attaches to the floor mass on a pivot representing the lower monoball and has a rotational freedom in the plane of the input motion. The forces acting between the isolator rod and cylinder result from a nonlinear spring, velocity squared damping, coulomb damping, and a rod retraction and extension stop.

The floor element is modeled as a single mass that is allowed to move vertically and horizontally in the plane of the input motion. Pitching of the mass attached below the isolator monoball is not allowed in the model. This assumption is good for the full-up floor, but is not consistent with the single isolator test setup where the simulated floor mass was not restrained in pitch. This assumption significantly affects only one response used in the test/analysis comparisons: isolator cylinder rotation relative to the simulated floor mass. The initial rotation correlation is valid; however, the analysis response is significantly affected after the peak isolator rotation is reached.

The support cable is the most difficult isolator component to model accurately. This fact is important because the peak cable and rod axial loads and rod bending moment are affected significantly by the cable modeling. The cable modeling difficulty is associated with the spring rate and damping characteristics of the cable during the various levels of dynamic loading and the relationship of these characteristics to the measured static load/deflection curves. The static

load/deflection curves are a function of the cable end constraints. If the cable ends are allowed to rotate freely, the cable stiffness is much lower than if the ends are fixed to preclude rotation because the cable tends to "unwind" during loading. Also, the magnitude of the hysteresis loop is much greater for the former condition because of the greater friction associated with the relative sliding motion of the individual cable strands.

From the satisfactory test/analysis correlation achieved during the isolator performance limits testing, it was concluded that the single isolator analysis model does an adequate job of calculating the isolator dynamic responses and the correlation is generally well within the accuracy range of measured ceiling input motion and individual responses.

MISSILE SUSPENSION SYSTEM (MSS)–SELECTED COMPONENT TESTING

Concurrent with the development of the shock isolated equipment platform, an MSS was designed to ensure missile survival in today's nuclear attack environment. An overview of the test programs, and their interrelationship in the overall missile suspension system design, is discussed by Luschei (a).

Mortimer (h) addresses the initial trade studies which were accomplished to evaluate suspension system concepts for protecting the missile in existing silos. A single liquid/mechanical isolator and cable assembly was proposed as one such possible vertical shock isolation system concept, and subjected to development testing.

Liquid/Mechanical Isolator Development Testing

The primary objective of the test program was to demonstrate that the proposed liquid/mechanical concept would attenuate the ground motion design environments sufficiently to confirm its feasibility for use as a vertical isolation system. A secondary objective was to acquire sufficient data to allow verification of a preliminary vertical response analysis model of the test article.

The test setup for the development testing of the liquid/mechanical isolator concept is depicted on Fig. 23. The liquid isolator served to maintain tension in the cable while the mechanical spring provided the rigid-body dynamic stiffness. The liquid isolator was designed to be fully extended initially, then to retract as the cable tried to unload. For purposes of this test program, a tie-rod assembly extended from the simulated ring assembly to two weights representing the missile weight and the first missile longitudinal mode.

Testing was conducted in three parts:

Load-Deflection Testing–To determine the full-stroke, load-deflection characteristics of the composite liquid/mechanical spring specimen.

Vertical Shock Testing–To determine the transmissibility, the low-frequency dynamic response characteristics, and the associated loads when the system was subjected to a range of velocity pulses.

Impact Testing–To determine the high-frequency transmissibility and dynamic responses while the system was subjected to a 20-millisecond displacement pulse designed to simulate the worst possible slack cable condition.

A comparison of maximum input shock spectra levels achieved during the vertical shock and impact test conditions

is presented in Fig. 24. The shock test device and test specimen were instrumented with 37 channels of active data measurements which were recorded on wide-band, frequency-modulated tape recorders. Acceleration, velocity, and displacement of the input force actuators provided definition of the test inputs. Velocity, displacement and force measurements provided rigid-body response characteristics of the concept suspension system. Also, 20 acceleration measurements provided response data from which to evaluate high-frequency response attenuation characteristics and the source of transmitted environments.

On the basis of an excellent system performance demonstrated during this concept development test program, the liquid/mechanical isolator concept was recommended and subsequently approved for incorporation into the preliminary design of the MSS. Some of the significant results and conclusions observed during evaluation of system performance included:

The high-frequency performance of the system was equal to or better than expected, with a minimum of observed mechanical spring surge responses. Application of the 20-msec impact pulse to achieve longer slack cable conditions did not increase system responses significantly, as demonstrated in Fig. 25. Shock spectra levels measured on the simulated missile were within the missile aft skirt allowables. Also, as shown on Fig. 26, the liquid/mechanical system transmissibilities were determined to be generally better than comparable data for dual-rate liquid isolators with similar response characteristics.

At no time during the test program did the mechanical spring exceed the available rattlespace. Responses for both shock and impact testing were within the allowable excursions as demonstrated on Fig. 27. Also, at no time did the loads in the tie rods go to zero, which would have resulted in a potential for a missile aft skirt separation. Satisfactory verification of the preliminary vertical response analysis model was achieved during this program as demonstrated by the typical cable load/time histories presented on Fig. 28.

Two special conditions were included in the test program to evaluate the effects of possible test unique conditions: Adding 76 pounds of simulated cable ballast, to account for the longer operational cable configuration, increased the slack cable duration as seen in Fig. 29, without any notable change in missile response environment. The guide system noted on Fig. 23 was installed to restrict torsional motion resulting from cable loading or unloading. As shown in Fig. 30, the guide system did not contribute significantly to the overall response environments.

Suspension System Development Testing

Subsequent to the satisfactory performance exhibited during the single liquid/mechanical isolator tests, dynamic development tests were conducted on a prototype design MSS. The test specimen consisted of three liquid/mechanical shock isolators each supported by a cable, but only one of which was excited by a single force actuator. The liquid spring portion of the shock isolator was from an operational shock isolation system and was tested as part of the concept development tests described above. The mechanical spring portion of the isolator was prototype hardware. The missile cage assembly was representative of the final design with the exception of foam blocks and elastomeric springs which eventually were incorporated in the final system configuration for shock isolation from large horizontal motions. A simulated missile mass of 78,000 pounds was used supported by a

"boilerplate" skirt. A schematic of the test setup for the MSS single isolator development tests is provided in Fig. 31.

The primary objective of the test program was to provide design and analysis data for optimization of the system design by demonstrating the performance of one shock isolator when subjected to vertical and horizontal shock inputs. Specific objectives accomplished with this test program were: 1) establishing the full stroke load-deflection characteristics of the composite isolator assembly; 2) determining the high-frequency and low-frequency transmissibility; and 3) determining the rigid-body dynamic response characteristics, and the associated loads, when the upper cable attachment point of the prototype MSS was subjected to a range of vertical and horizontal simulated weapon system ground shock motions.

Testing was accomplished in a test fixture specifically designed for the eventual full-scale verification testing of an MSS. The test fixture with the development test article installed is depicted in Fig. 32. A more detailed discussion of the test fixture can be found in the work of Mortimer (h). Shock testing was accomplished by using a single pneumatic powered/hydraulically controlled actuator to provide a range of velocity waveforms to one of the three upper cable attachment points. Vertical testing was conducted by driving one cable attachment point in the vertical direction and dropping the other two attachment points through a crushable material. Horizontal testing was conducted by driving one cable attachment point in the horizontal direction while holding stationary the other two cable attachment points. For azimuth one, the input for the driven cable was directed toward the missile centerline. For azimuth two, the input for the driven cable was directed away from the missile centerline. Thirty-two total shock test conditions were conducted; 17 vertical axis tests, and 15 horizontal axis tests, including three levels of maximum velocity for both positive-only waveforms and positive-with-return-motion waveforms.

As in the liquid/mechanical concept development test program, the shock test device and the test article were instrumented to provide definition of the test inputs and the rigid-body and high-frequency response characteristics of the missile suspension system. An evaluation of the data from the tests conducted on the prototype design missile suspension demonstrated similar results and conclusions as delineated for the liquid/mechanical test program, namely:

1. Transmissibilities in the form of shock spectra measured at the simulated missile aft skirt were well within aft skirt allowables.

2. At no time during the test program did the mechanical spring exceed the available rattlespace.

3. The gimbal plate springs and aft skirt approached the unloaded condition for positive full-level vertical runs. The magnitude of this unloading condition did not appear to be large enough to justify concern.

4. There was a distinct increase in peak cable load for vertical return pulses over corresponding positive-only waveforms.

Test-analysis correlation of the MSS development was limited to two vertical and two horizontal shock tests. The two models used to obtain analysis correlation with the test data were a 12-degree-of-freedom single isolator model, and a 9-degree-of-freedom missile and suspension system model. The single isolator model simulated only vertical motion and

modeled the mechanical spring dynamics in detail; it also accurately models the liquid spring characteristics. This model was an updated version of the one used successfully to provide test-analysis correlation during the liquid/mechanical isolator concept development tests.

The 9-degree-of-freedom model simulated planar motion of the missile and suspension system. The liquid and mechanical isolators were not modeled to the same level of detail in this model which describes vertical/horizontal as well as pitching motions of the missile and suspension system, together with isolator freedoms which to a limited extent attempted to model the liquid/mechanical isolator assembly characteristics. Only the 9-degree-of-freedom model was used for test-analysis correlation of the horizontal shock tests, whereas both models were used for test-analysis correlation of the vertical shock tests. In general, the analysis results showed good agreement with test data as seen in Figs. 33 and 34. It was concluded, however, that modifications to the 9-degree-of-freedom analysis model, adding degrees of freedom, should be incorporated to better predict the gimbal excitations and skirt environment due to vertical shock inputs. Details of the final model and the degree of test correlation with the full-scale MSS design verification test program are discussed by Mortimer (h).

A limited vertical transmissibility analysis of the MSS development test setup also was performed. The purpose of this analysis was to gain a better understanding of the nature of the environment transmitted down the liquid/mechanical isolator to the missile interface. The analysis model is shown on Fig. 35. The mass and stiffness matrices were employed using the following equations:

$$[M] = \frac{d}{dt}\left(\frac{\partial T}{\partial \dot{q}}\right)$$
$$[K] = \frac{\partial U}{\partial q}$$

where T and U are the kinetic and potential strain energy respectively. The mass and stiffness matrices provided the system eigenvalues and eigenvectors. The first five mechanical spring modes were used in the analysis and the liquid spring was assumed to be operating. The analysis assumed a modal damping in the mechanical spring of 2 percent of critical, while the damping in the system modes was assumed to be 5 percent of critical. No optimization of damping values was attempted to provide a better analytical fit to the test data.

Fourier transfer functions were calculated using this analysis model, and an example of the results is provided in Fig. 36. The agreement between the test results and analysis was quite good up to 30 Hz. The frequency of the fundamental vertical mode (0.4 Hz) is not in the frequency covered by the test data. Other modes, apparent in the analysis-test correlation include: 1) the 5.5-Hz second mode, which is a highly damped mode predominantly involving the liquid spring cylinder oscillating between the liquid and mechanical springs; 2) the 10.6 Hz is the most predominant mode in the system principally involving the cage and missile oscillating between the gimbal springs; 3) there is no cage resonance response observed with the 16-Hz mode because this mode involves the load head vibrating on the hard rubber support pad, resulting in very little motion farther down in the system; and 4) the 19-Hz mechanical spring surge mode, defined very well by the analysis although there is a slight frequency shift to about 22 Hz for the test data. The analysis damping could be increased or decreased to better match the test amplitude.

214

It was concluded from this MSS development test and analysis program that the suspension system performance was quite satisfactory and that final design verification testing should be accomplished with the full-scale suspension system and missile.

Foam Testing

As described by Mortimer (h), the missile suspension system design also included a horizontal isolation system consisting of foamed polyurethane blocks. The foamed blocks were designed to prevent the suspension system cage from impacting the silo wall during crater-related ground motions. The analytical foam representation by Sepcenko (e), which was supported by the extensive development testing of foam discussed earlier, provided the preliminary design requirements. Tentative foam block dimensions and shape were established analytically from the in-silo launch loads and groundshock-induced loads at the various elements of the suspension system.

The resulting specimen, as shown in Fig. 37, consisted of two bonded polyurethane blocks, bonded lengthwise and with a teflon facing similar to the equipment platform design. Note the Nomex reinforcement at the specimen base, added to provide protection against gas dynamic loading during missile ignition. Two of these specimens were subjected to design verification dynamic and static compression loading tests. Each specimen was subjected to impacts resulting in both 40-percent strain and 25-percent strain conditions. The same specimens also were subjected to static compression loading in two axes, normal to the face and 20 degrees from normal. Dynamic testing was accomplished with the horizontal shock machine utilized during the equipment platform foam tests, with minor modifications to accommodate the larger specimen size. Static testing was conducted by using a universal static test machine. The specimen stress-strain relationship between dynamic loading and static loading is demonstrated in Fig. 38.

The successful performance during this program ultimately led to incorporating the design for qualification during the full-scale testing and detail analysis addressed by Mortimer (h).

Elastomeric Spring Testing

A secondary isolation system, also described by Mortimer (h), provides isolation between the missile and suspension system. The design consists of a shaped elastomeric spring assembly with buckling elements. Limiting static and dynamic force-deflection requirements were established on the basis of preliminary analysis of the missile suspension system. Elastomeric block configurations then were developed to achieve the required elastomer stiffness both normal and tangential to the spring surface. Preliminary design and testing resulted in the spring assembly configuration shown in Fig. 39. The assembly consists of three elastomeric spring components positioned radially in an assembly to achieve a ratio in spring constant (Knormal/Ktangential) approaching 1.0

Six elastomeric spring assemblies were subjected to static and dynamic acceptance testing prior to installing the assemblies in the full-scale suspension system test program. Testing was accomplished on the horizontal shock machine developed for foam testing, modified to accommodate an 8100-pound sled. Dynamic impacting of the spring assembly at an average velocity of 50 in./sec. was conducted at 0 (normal), 30 and 60 degrees. A typical comparison between dynamic and static loading results is provided on Fig. 39. Both dynamic and static tests provided consistent data which enabled Sepcenko (e) to achieve a satisfactory viscoelastic solution.

DISCUSSION

Analysis techniques can be used to predict magnitude of responses up to frequencies of 200 Hz, and some structural resonances to 600 Hz. All response predictions are based on assumed values of structural damping and/or stiffness and mass distributions from drawings, and it is known from experience that these parameters can be defined totally only by test, particularly for structural damping. High-frequency performance is historically sensitive to such design parameters as joint tolerances, means of attachment, assembly techniques and of higher modes of structural responses not readily identified by analytical means.

To have confidence that a complex shock isolation system ultimately will meet all design requirements, it is imperative that candidate isolator subsystems be subjected to a thorough development test program. For initial testing, the isolator assembly should be configured as closely as possible to the proposed design. Based on these results design changes may be implemented to improve the isolator transmissibility performance. The entire system response should be evaluated and any coupling effects of combining system components assessed, to determine possible changes to decouple undesirable system responses. The sources of environments should be defined and design changes be implemented to reduce them where possible.

The candidate selection and component development test programs described in this article proved to be very effective in that both shock isolation system designs ultimately demonstrated satisfactory performance.

ACKNOWLEDGEMENTS

REFERENCES

a. Loren L. Luschei, "An Introduction to the Shock Testing of Large Shock Isolation Systems," 46th Shock and Vibration Symposium, San Diego, 1975 (Classified Secret).

b. Richard L. Grant, "Initial Design Considering Statistical Fragility Assessment," 41st Shock and Vibration Symposium, December, 1970.

c. G. R. Burwell, "Actuator Development for System Level Shock Testing," 46th Shock and Vibration Symposium, San Diego, 1975.

d. Curtis F. Vail, "Effect of Additive Damping on Transfer Function Characteristics of Structures," Research Publication GMR-1255 dated October, 1972, published by the Society of Automotive Engineers, Inc.

e. Valentin Sepcenko, "Analysis of Open Cell Polyurethane Foam Under Impact Loading," 44th Shock and Vibration Symposium, December, 1973.

f. W. C. Gustafson, "Polyurethane Isolators for Shock Isolated Equipment Floors," 46th Shock and Vibration Symposium, San Diego, 1975.

g. W. R. Milne, "Analysis and Testing of Full-Scale Shock Isolated Equipment Floors," 46th Shock and Vibration Symposium, San Diego, 1975.

h. H. R. Mortimer, "Shock Isolation System Design, Analysis and Testing for a *Silo Based ICBM*," *46th Shock* and Vibration Symposium, San Diego, 1975 (Classified Secret).
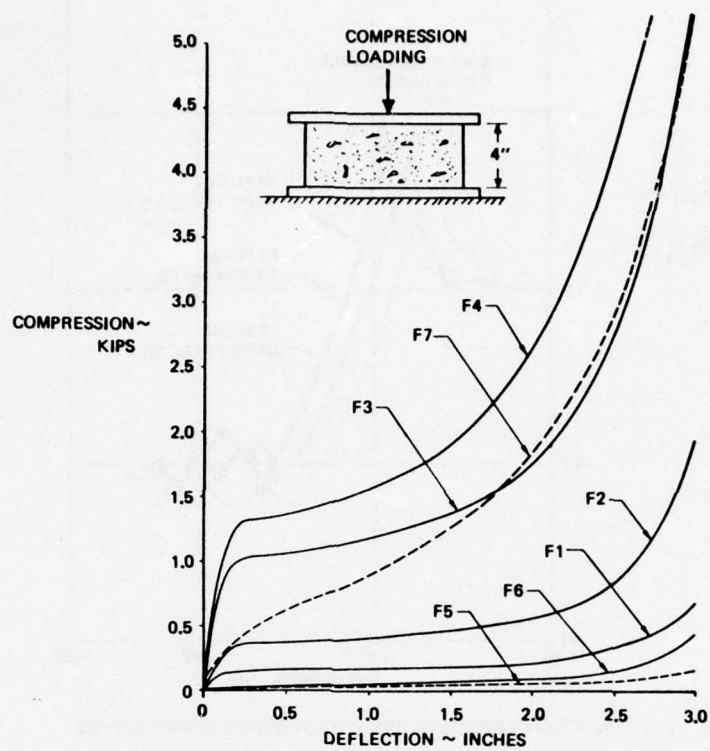
FIGURE 1   STATIC LOAD DEFLECTION COMPRESSION   (FIRST CYCLE LOADING ONLY)
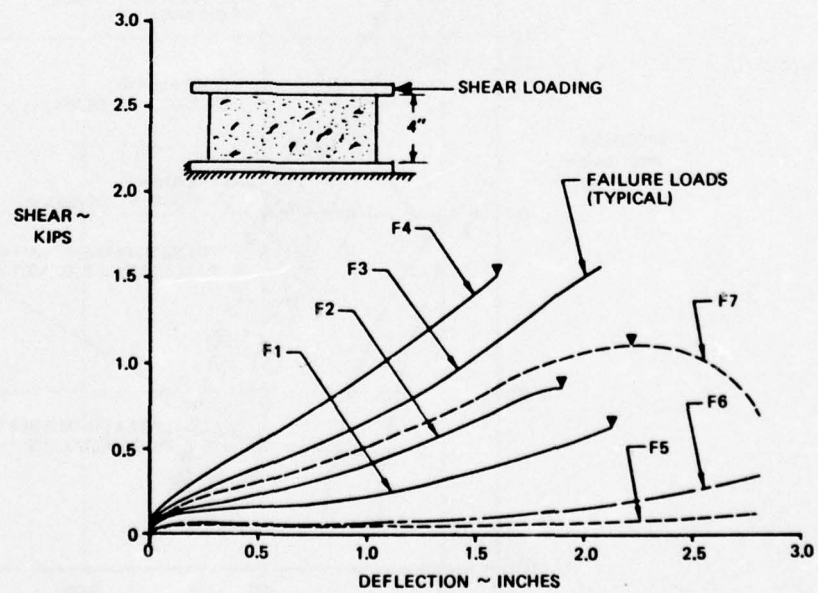
FIGURE 2   STATIC LOAD DEFLECTION–SHEAR

217
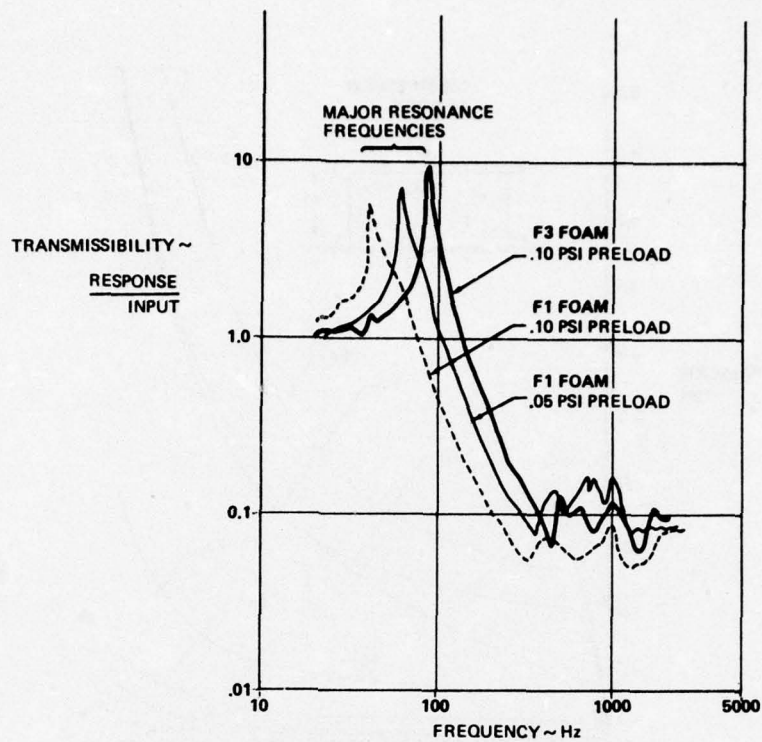
FIGURE 3   TYPICAL FOAM TRANSMISSIBILITY–TENSION-COMPRESSION
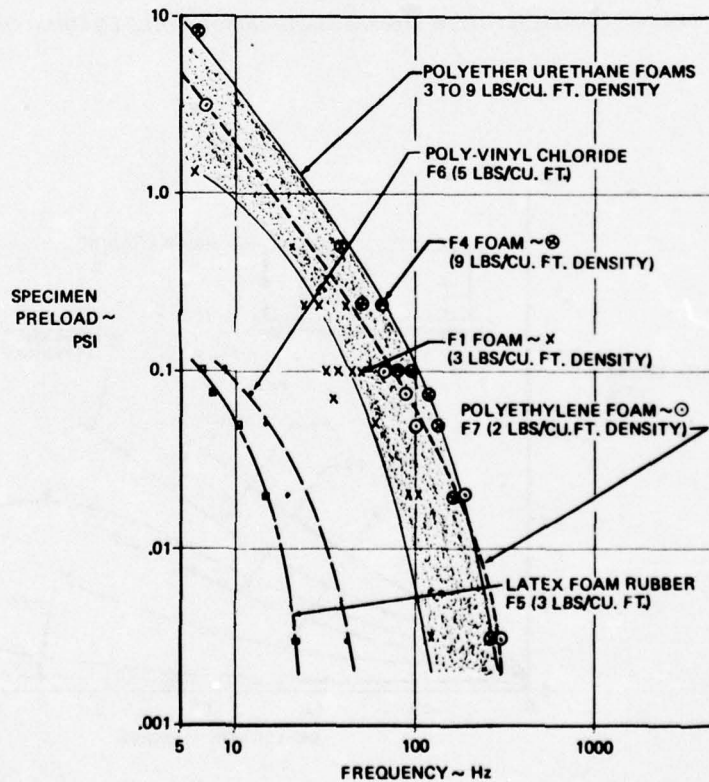
FIGURE 4   FOAM RESONANT FREQUENCIES VERSUS PRELOAD

218
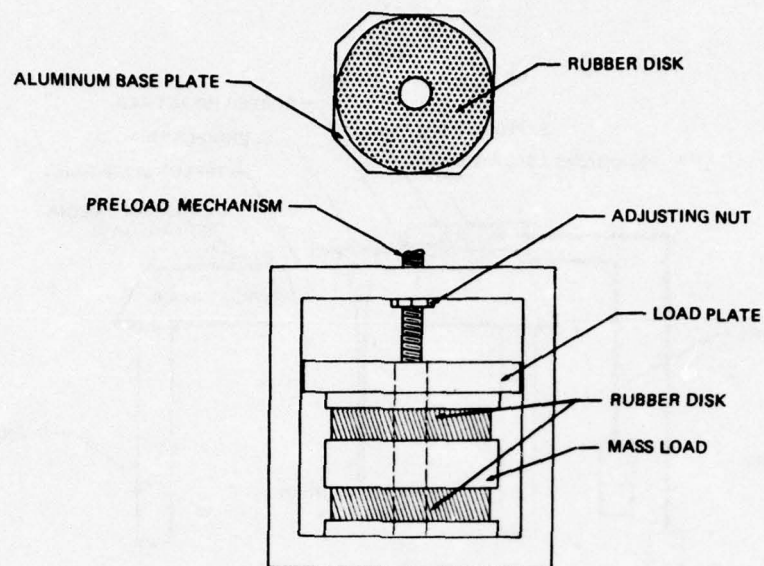
FIGURE 5   SCHEMATIC VIEW OF RUBBER TEST ARTICLE
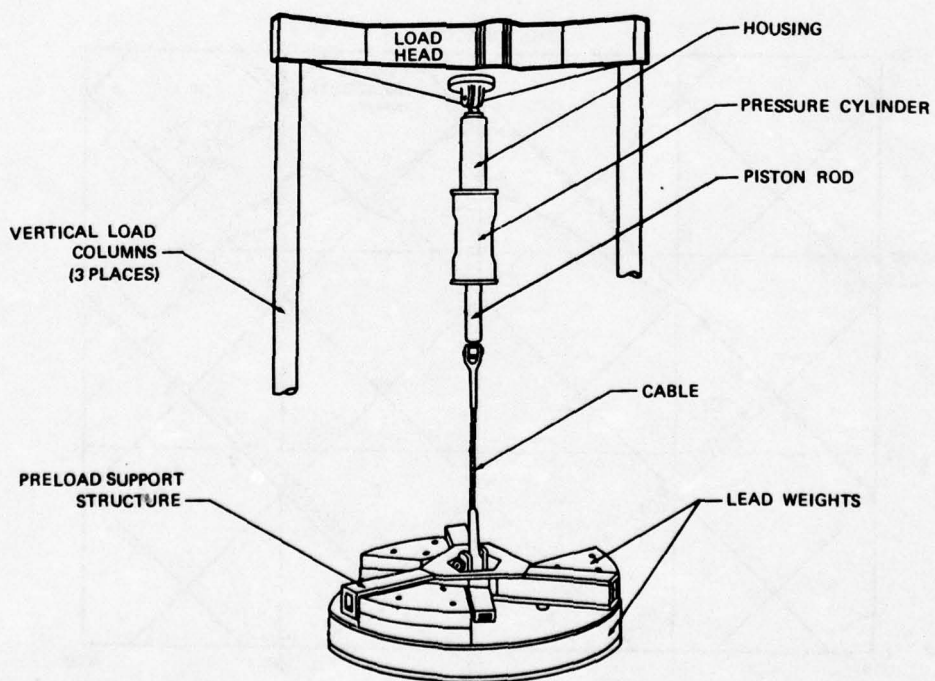
FIGURE 6   HARDMOUNTED INVERTED CONFIGURATION–VERTICAL SHOCK TESTING

219
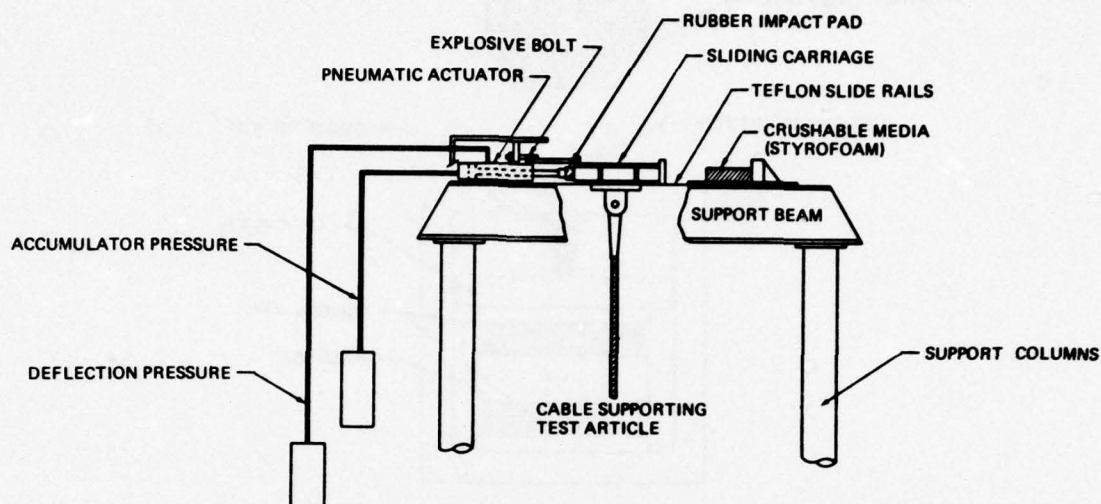
FIGURE 7   HORIZONTAL TEST FIXTURE

SHOCK SPECTRA
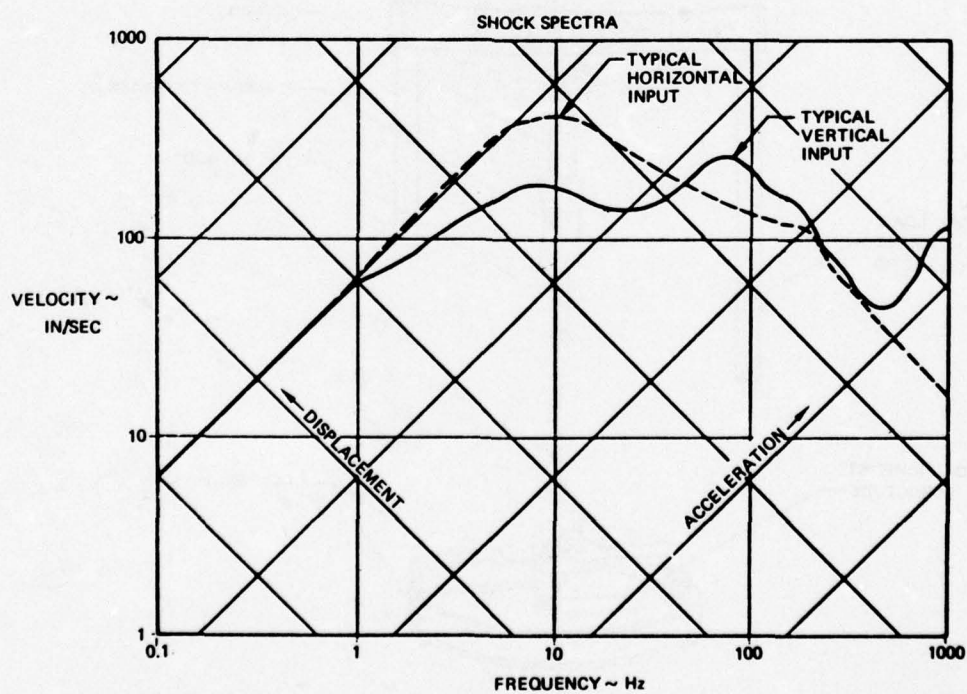
FIGURE 8   CANDIDATE ISOLATION SYSTEM COMPONENT TEST INPUTS—SINGLE ISOLATOR TESTS

220

CYLINDER II   CYLINDER I

PISTON ROD

PRESSURE
CYLINDER

UPPER
SEALS

STOP PLATE

LOWER SEALS

HOUSING
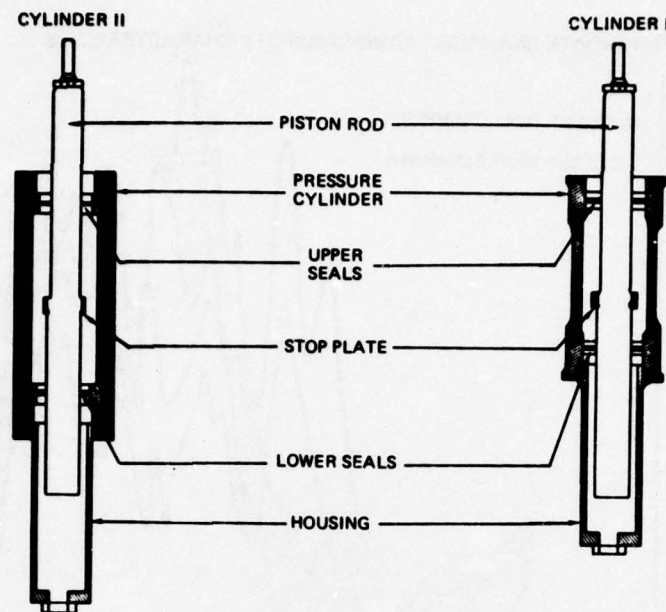
FIGURE 9   BASIC SINGLE CHAMBER LIQUID ISOLATOR COMPARISON

SOFTMOUNTED   HARDMOUNTED   HARDMOUNTED
                                                    INVERTED

CABLE   ISOLATOR   ISOLATOR
ASSEMBLY   ROD   HOUSING
ATTACHMENT   ATTACHMENT   ATTACHMENT
                                                                CEILING
                                                                ATTACHMENT

ISOLATOR   ISOLATOR   HOUSING
CABLE   PISTON
ASSEMBLY   ROD

                           ISOLATOR   ISOLATOR
                           PRESSURE   PRESSURE
                           CYLINDER   CYLINDER

ISOLATOR   HOUSING   ISOLATOR
PISTON   PISTON
ROD   ROD

ISOLATOR   ISOLATOR   ISOLATOR
PRESSURE   CABLE   CABLE
CYLINDER   ASSEMBLY   ASSEMBLY

HOUSING   SIMULATED
                                                    FLOOR –
                                                    PRELOAD
                                                    STRUCTURE

FIGURE 10   BASIC STRUCTURAL ARRANGEMENTS LIQUID ISOLATOR DEVELOPMENT TESTS

221

CANDIDATE ISOLATOR TRANSMISSIBILITY CHARACTERISTICS

VERTICAL RESPONSE / INPUT

FREQUENCY ~ Hz
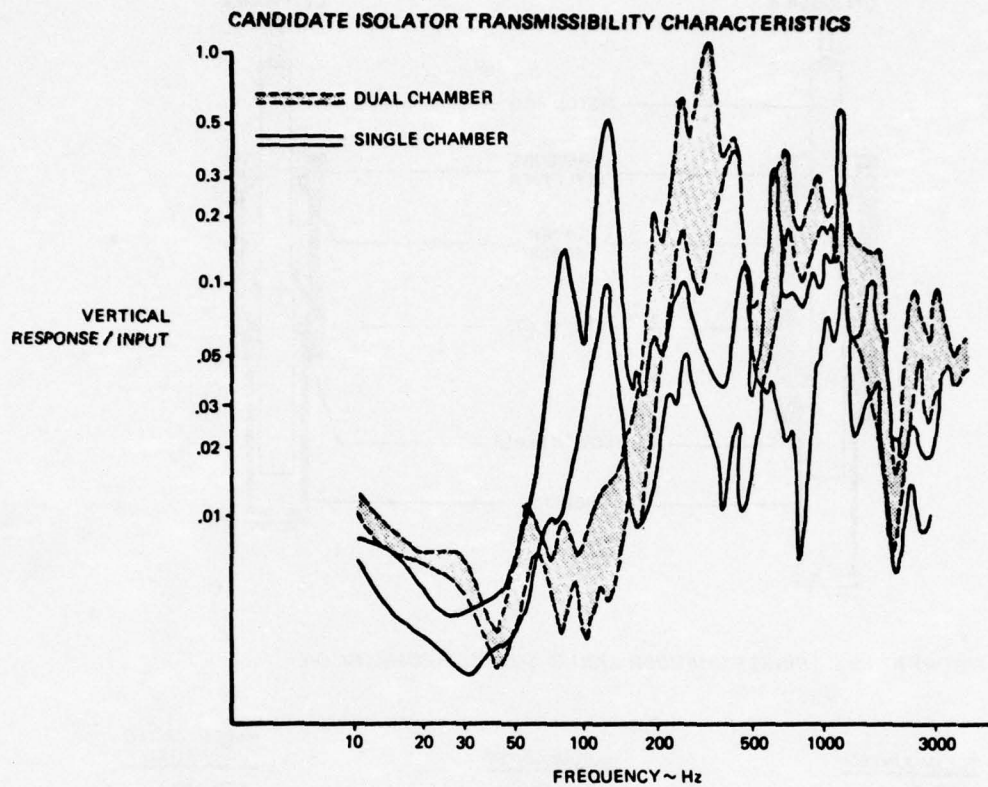
FIGURE 11   FOURIER TRANSFER FUNCTIONS

CANDIDATE ISOLATOR TRANSMISSIBILITY CHARACTERISTICS

FLOOR RESPONSE / INPUT

FREQUENCY ~ Hz
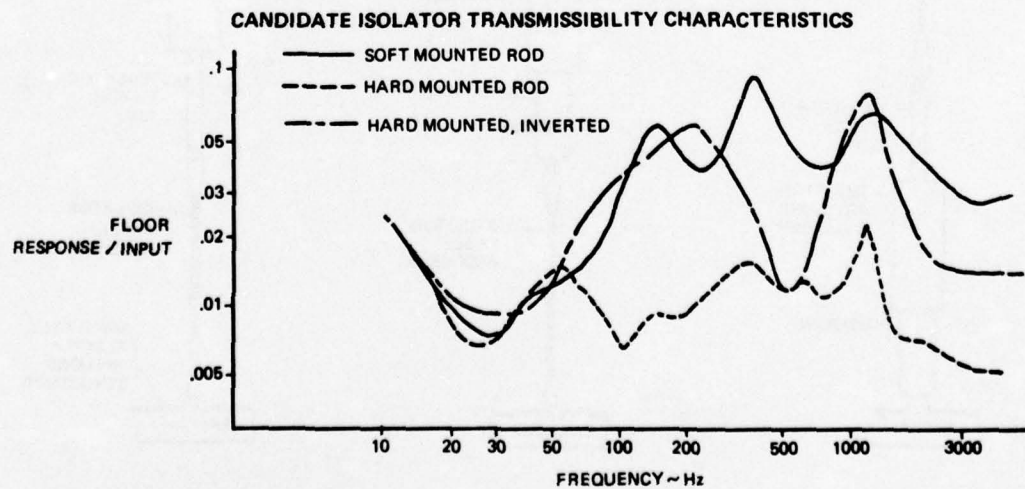
FIGURE 12   Q=5 SHOCK SPECTRA RATIOS

222

CANDIDATE ISOLATOR TRANSMISSIBILITY CHARACTERISTICS
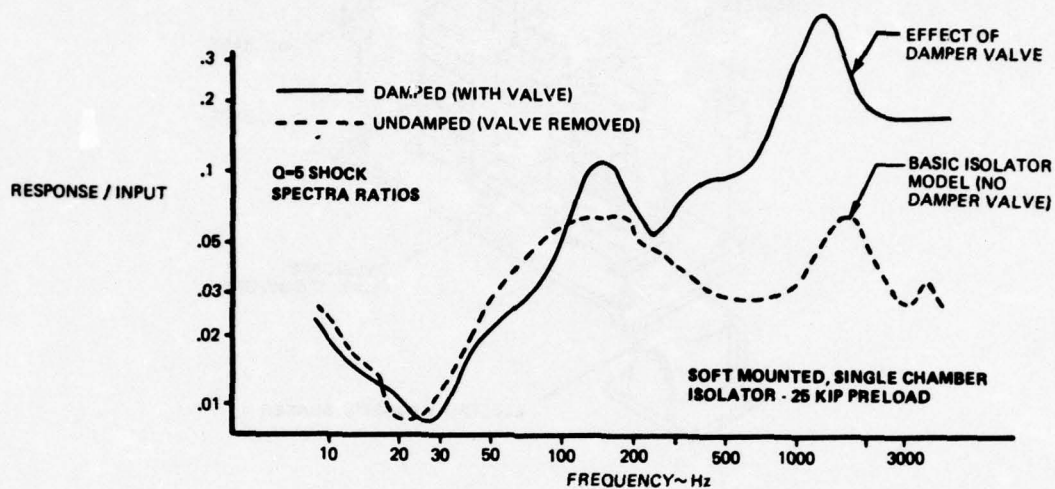
FIGURE 13 EFFECTS OF DAMPING VALVE

CANDIDATE ISOLATOR TRANSMISSIBILITY CHARACTERISTICS
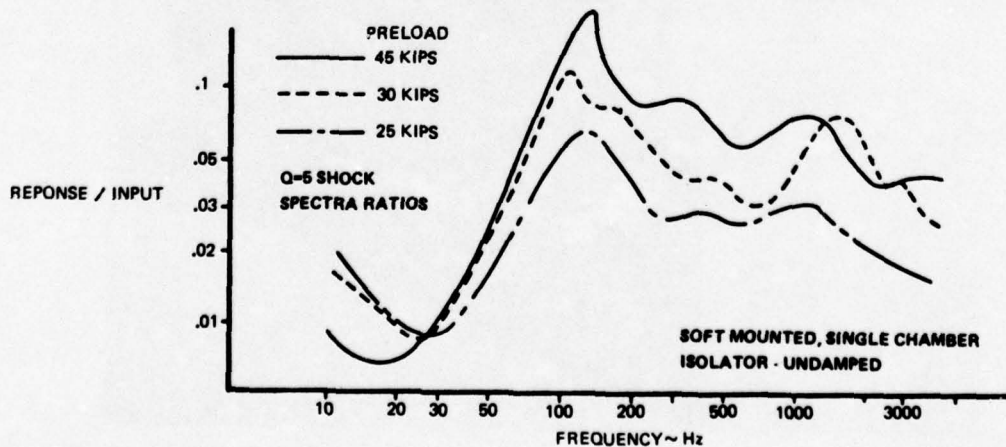
FIGURE 14 EFFECT OF ISOLATOR PRELOAD

223
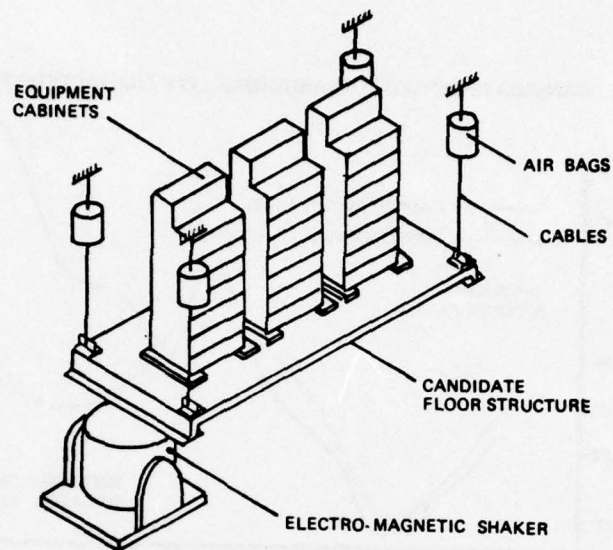
FIGURE 15   SCHEMATIC OF TEST ARRANGEMENT
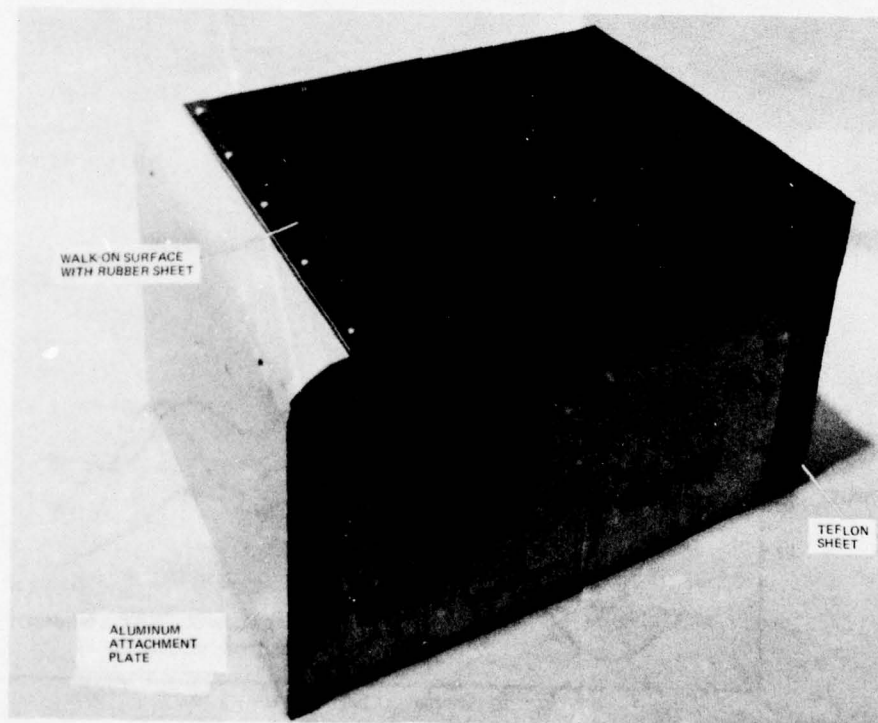
FIGURE 16   TEST SPECIMEN - HORIZONTAL SHOCK ISOLATOR

224

FIGURE 17   FOAM DYNAMIC LOADING CONDITION—SLED IMPACT DEVELOPMENT TESTING
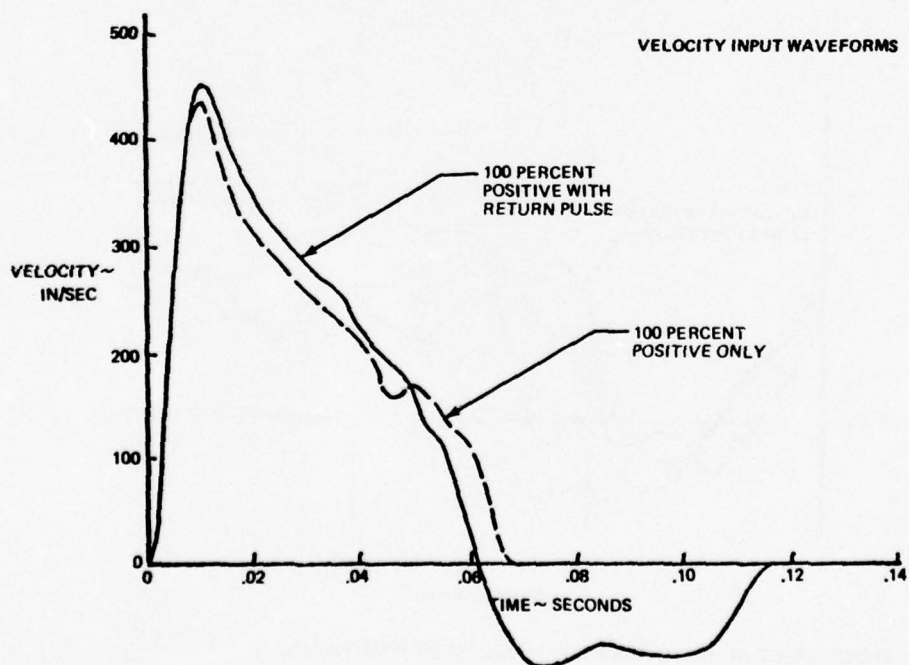
FIGURE 18   TYPICAL LIQUID ISOLATOR DEVELOPMENT TEST INPUT WAVEFORMS

225
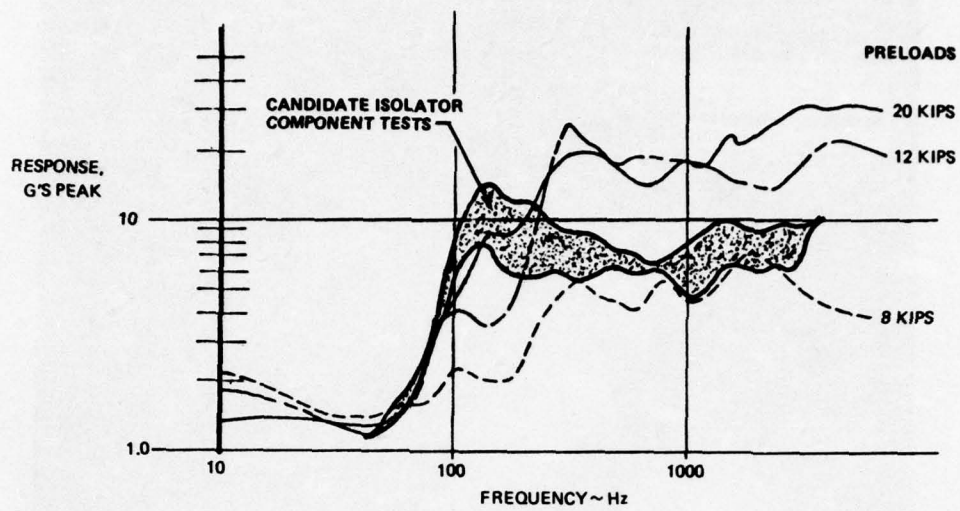
FIGURE 19 SHOCK SPECTRA RESPONSE FOR HIGH LEVEL INPUT POSITIVE PULSE
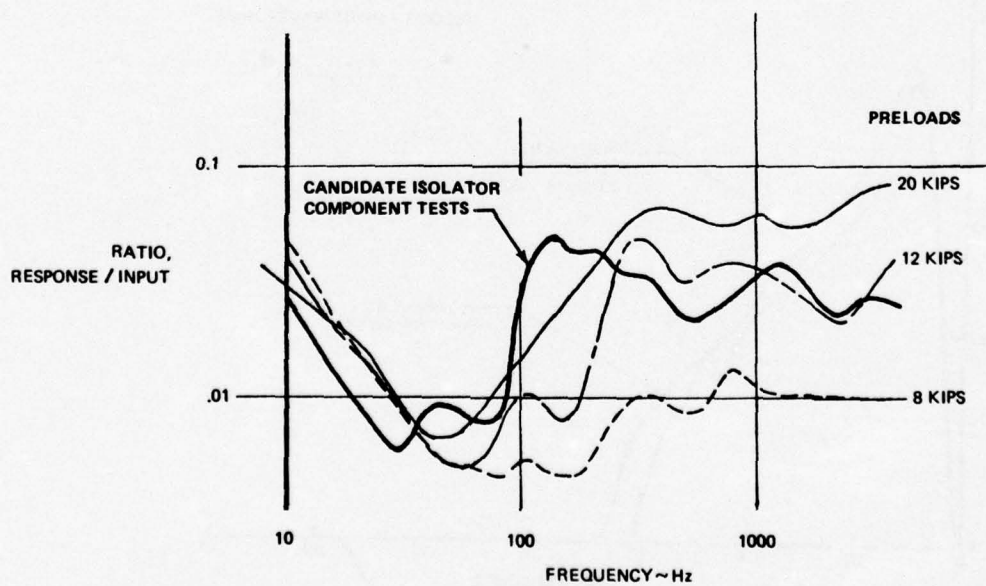
FIGURE 20 SHOCK SPECTRA RATIO FOR HIGH LEVEL INPUT POSITIVE PULSE

SPHERICAL BALL

CABLE 1" DIA.

VISUAL POSITION
INDICATOR

PISTON ROD
(2.5" DIA.)

SEAL

CYLINDER 8" DIA.
(INNER DIA. IS 5")

DRAG PLATE DAMPING

SILICONE FLUID

MONOBALL

LOWER ROD 2.8" DIA.

130 OR 166 INCHES
NOMINAL INSTALLED
LENGTH
(BASED ON CABLE LENGTH)

15" EXTENSION STROKE*

21" RETRACTION STROKE*

* BASED ON NOMINAL
STATIC POSITION
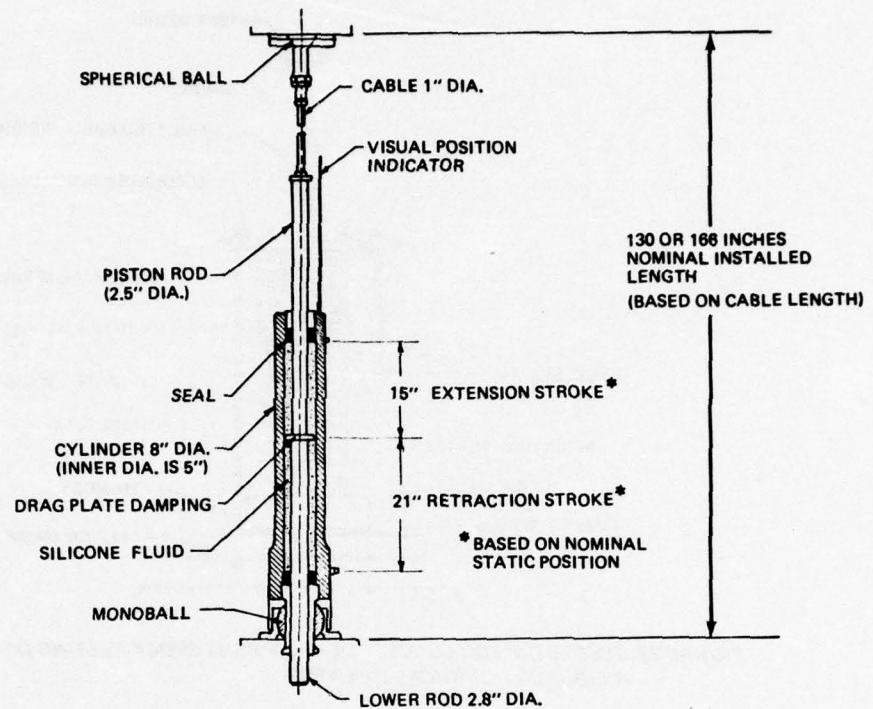
FIGURE 21   LIQUID SHOCK ISOLATOR ASSEMBLY
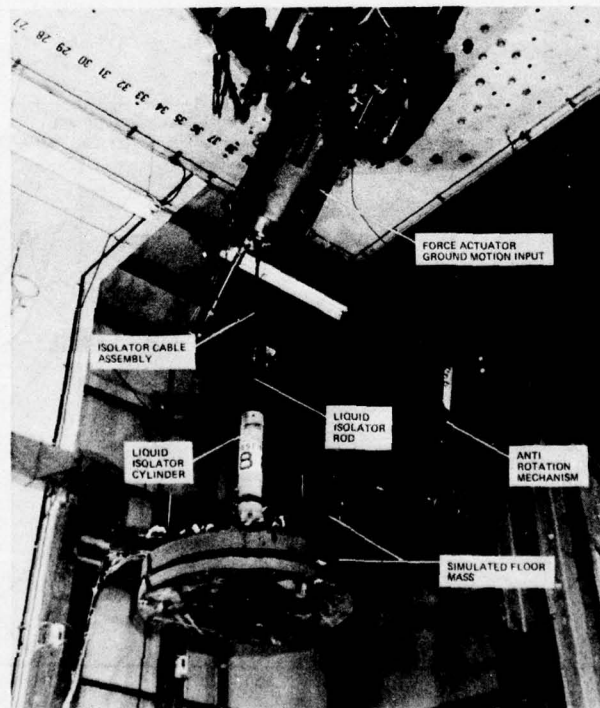
FIGURE 22   LIQUID ISOLATOR - PERFORMANCE LIMIT TESTING

227
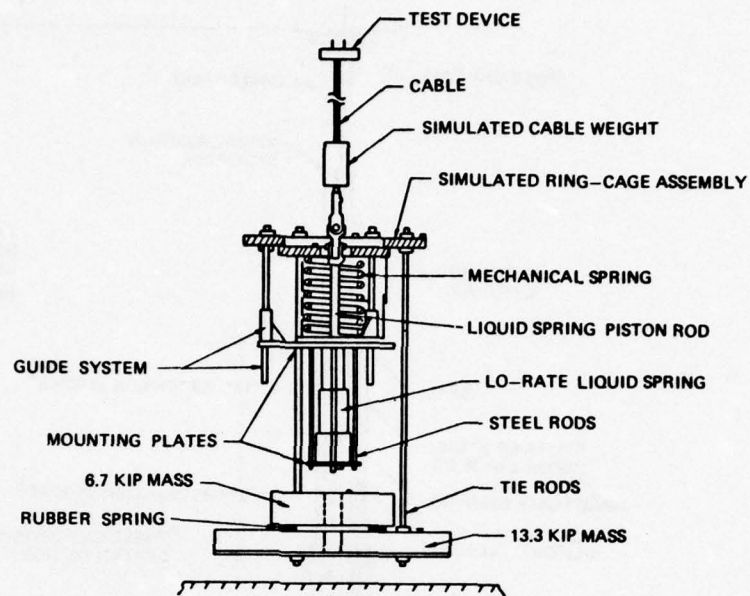
FIGURE 23 TEST SETUP FOR CONCEPT DEVELOPMENT SHOCK TESTING OF
A LIQUID/MECHANICAL ISOLATOR
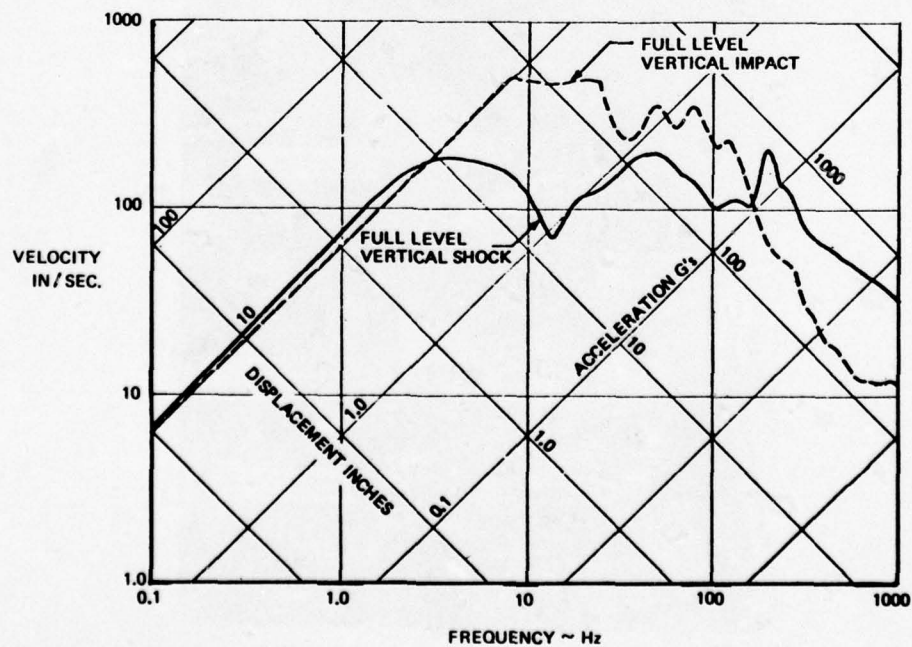
FIGURE 24 COMPARISON OF INPUT SHOCK SPECTRA LEVELS FOR LIQUID/MECHANICAL
ISOLATOR DEVELOPMENT TESTING

228
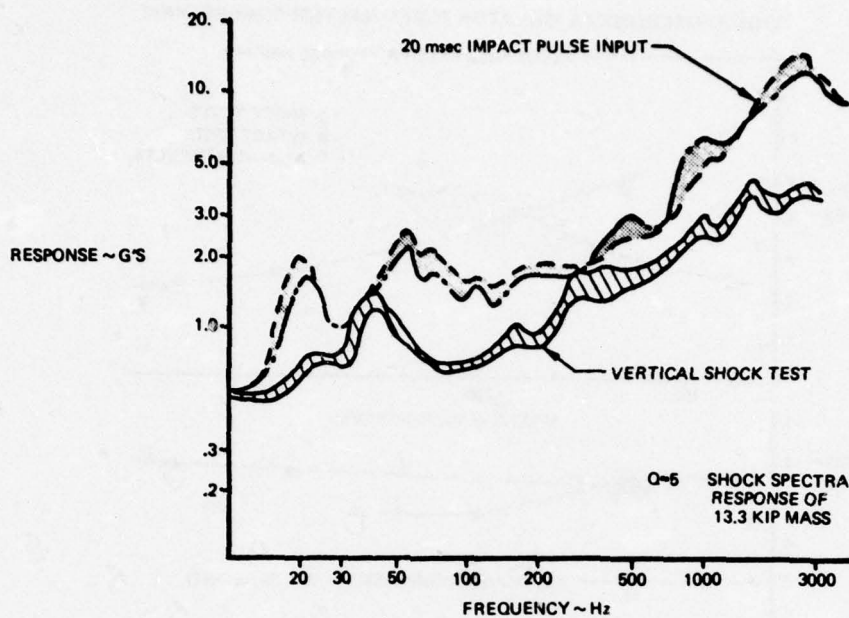
FIGURE 25   LIQUID/MECHANICAL ISOLATOR—VERTICAL RESPONSES
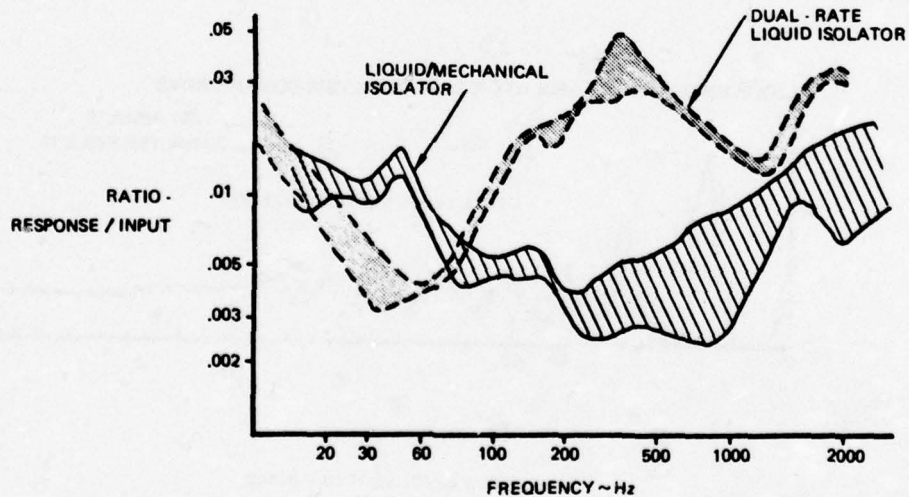
FIGURE 26   VERTICAL TRANSMISSIBILITY—SHOCK ISOLATOR

LIQUID/MECHANICAL ISOLATOR TEST/ANALYSIS COMPARISONS

ALLOWABLE EXTENSION (FREE HEIGHT)

○ SHOCK TESTS
▲ IMPACT TESTS
□ ANALYSIS RESULTS

EXTENSION ~ INCHES

MAXIMUM VELOCITY (IPS)

COMPRESSION ~ INCHES

ALLOWABLE COMPRESSION (SOLID HEIGHT)
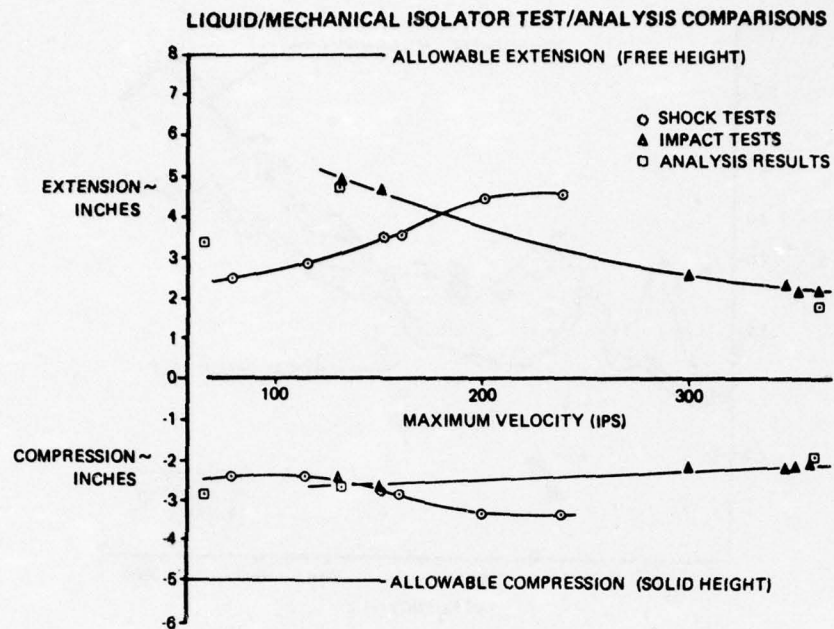
FIGURE 27   MECHANICAL SPRING EXCURSIONS

LIQUID/MECHANICAL ISOLATOR TEST/ANALYSIS COMPARISONS

—— TEST RESULTS
- - - ANALYSIS RESULTS

FULL LEVEL VERTICAL SHOCK

CABLE LOAD ~ KIPS

LOW LEVEL VERTICAL SHOCK

TIME ~ SECONDS
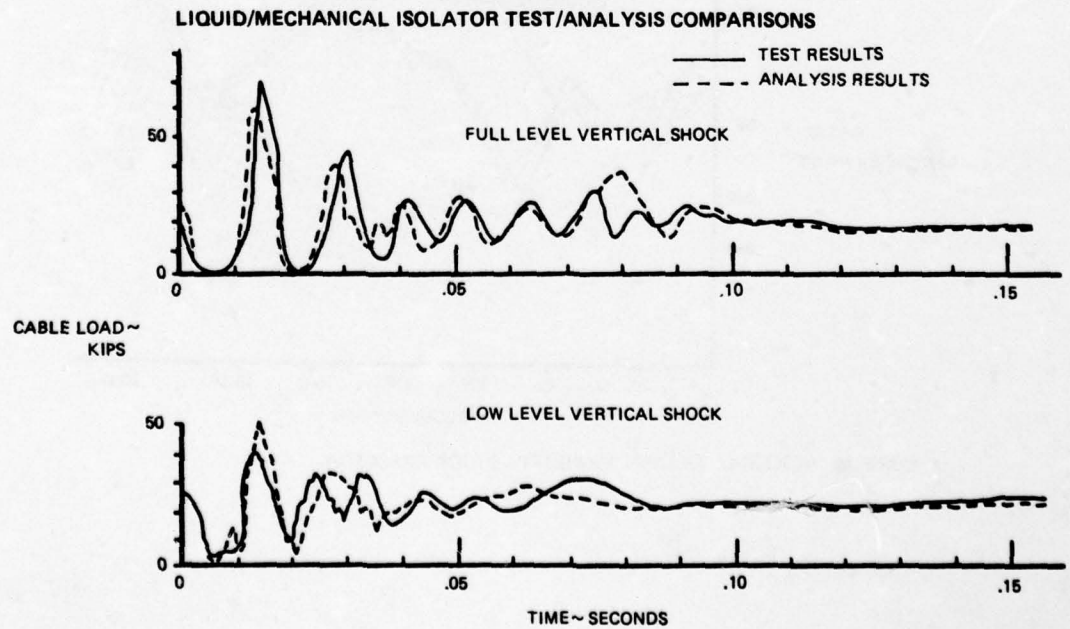
FIGURE 28   ISOLATOR ASSEMBLY CABLE LOADS

230

LIQUID/MECHANICAL ISOLATOR TEST RESULTS

FIGURE 29 CABLE LOADS

LIQUID/MECHANICAL ISOLATOR TEST RESULTS
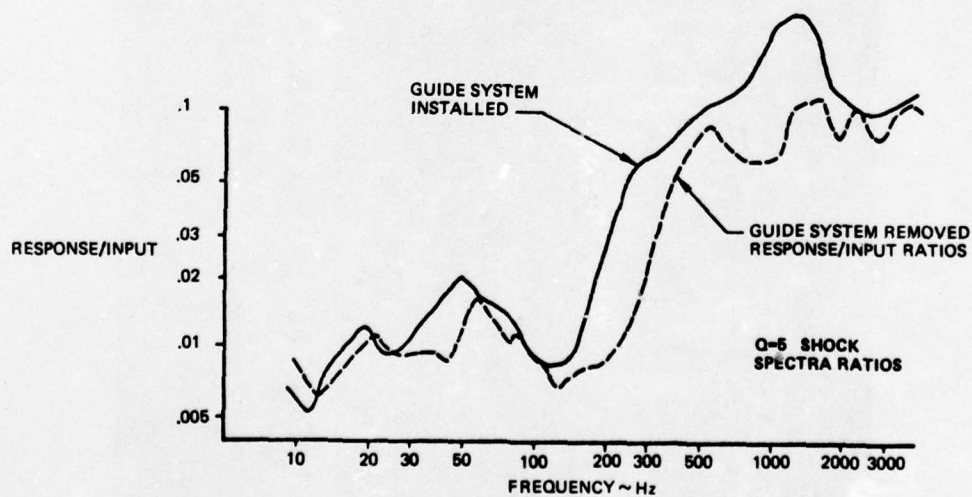
FIGURE 30 VERTICAL TRANSMISSIBILITY

231

CABLE GUIDE, CAGE

CABLE ASSEMBLY, PENDULUM

69.54"

(ARM ASSY, CAGE)
CABLE GUIDE STRUCTURE,
UPPER FOAM SUPPORT,
UPPER CASE RING, ARM ASSY,
LOWER CAGE RING, BOTTOM PLATE

223.22"

ADAPTER RING

RECEIVER RING
BASE SUPPORT RING

LOWER FOAM SUPPORT
MECHANICAL SPRING

PLATE (SUPPORT STRUCTURE SHOCK ISOLATOR)

COUPLING CABLE
SPRING CAN

LIQUID ISOLATOR
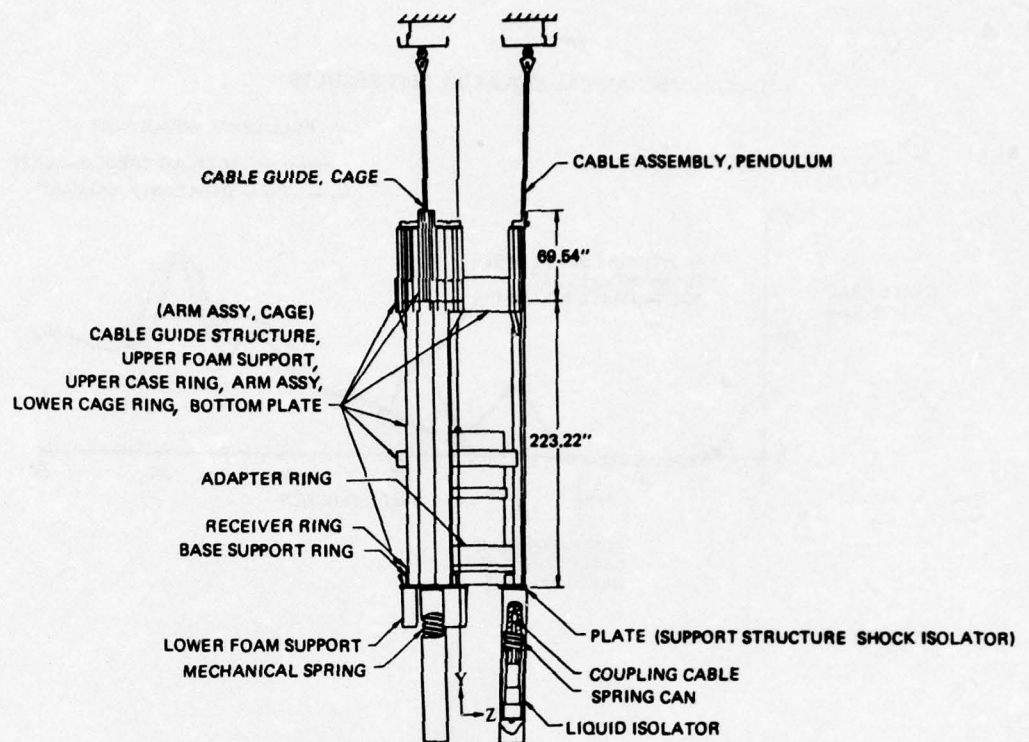
FIGURE 31 TEST SETUP FOR MISSILE SUSPENSION SYSTEM SINGLE ISOLATOR
DEVELOPMENT TEST PROGRAM
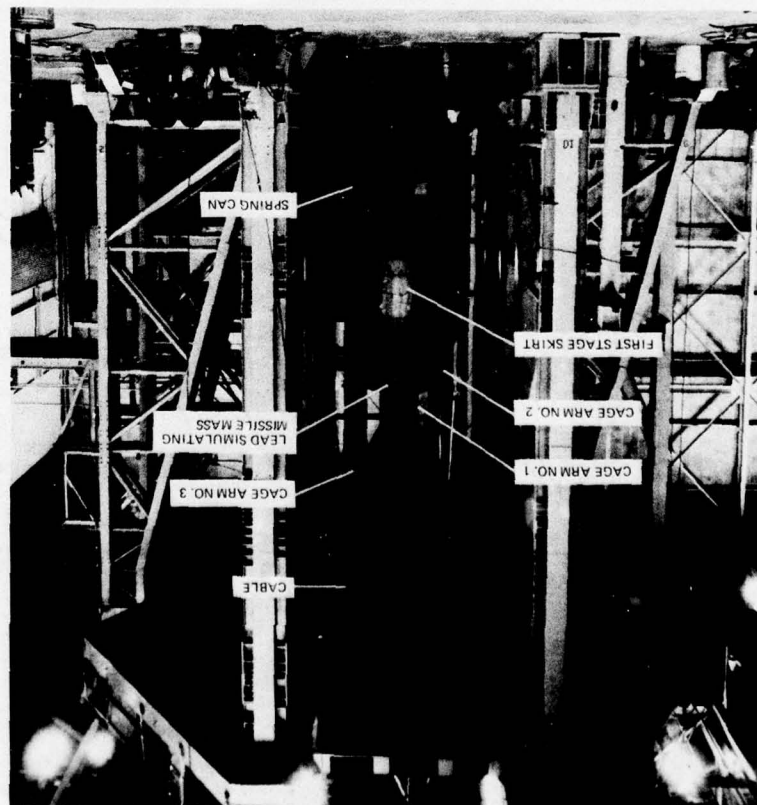
FIGURE 32 TEST SETUP FOR MISSILE SUSPENSION SYSTEM DYNAMIC DEVELOPMENT TESTS

232
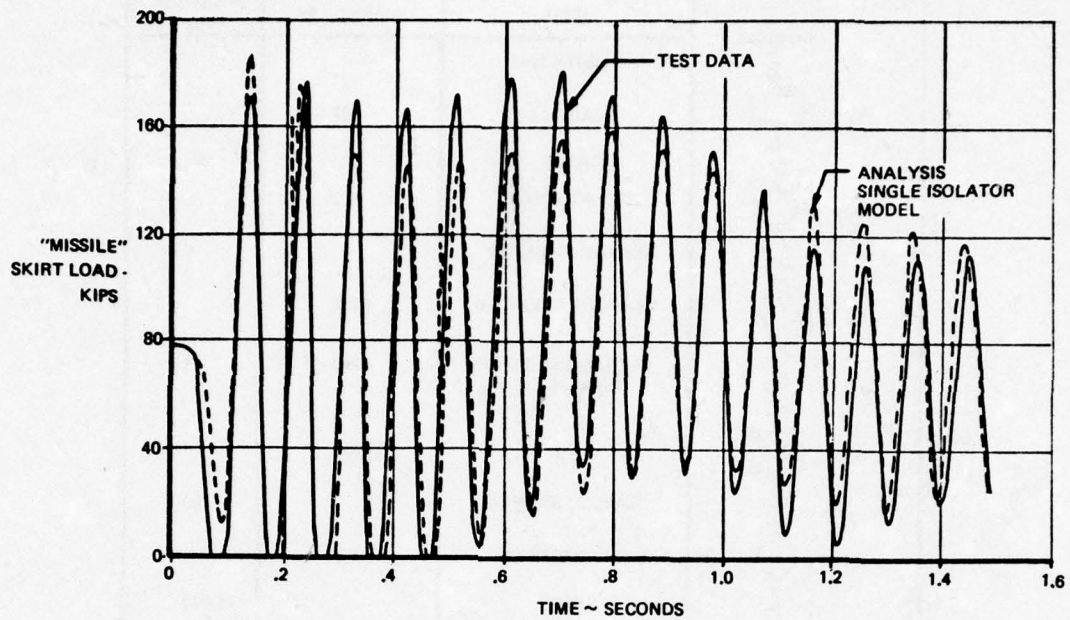
FIGURE 33   AFT SKIRT LOAD, SINGLE ISOLATOR MODEL
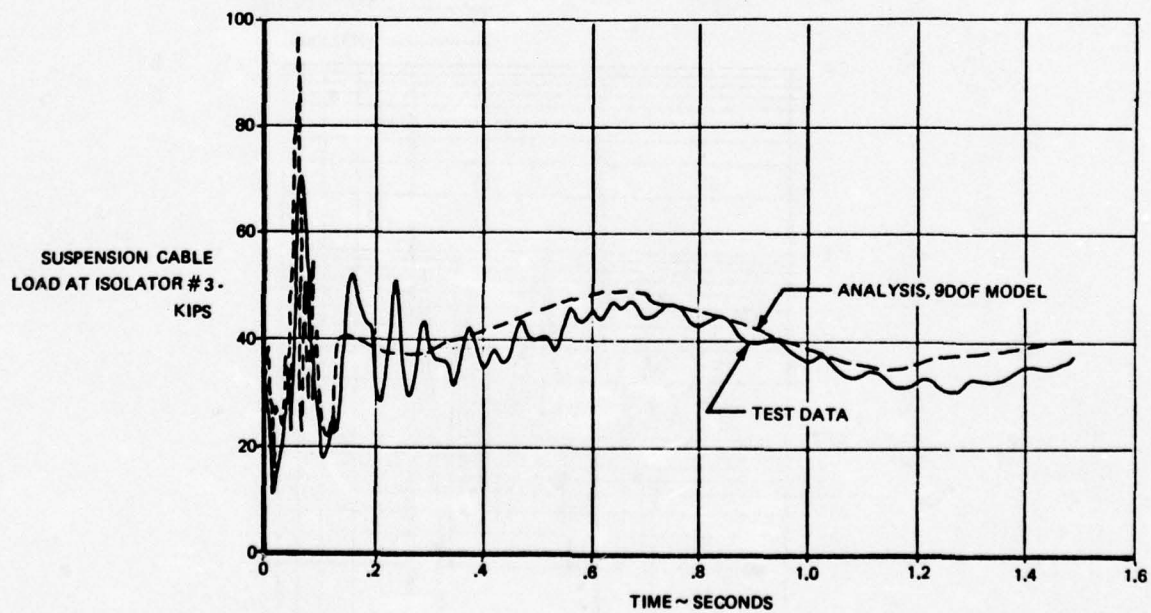
FIGURE 34   CABLE LOAD COMPARISON, 9DOF MODEL

233

	ITEM	WEIGHT, LBS	STIFFNESS, KIPS/IN
	RUBBER PAD		7
x_1	LOAD HEAD	212	
	CABLE		40
x_2	ISOLATOR ROD	102	
	LIQUID ISOLATOR		0.91
x_3	ISOLATOR CYLINDER	1,238	
	MECHANICAL SPRING $q_1, q_2, q_3, q_4, q_5,$	1,740	4.5
x_4	CAGE	11,500	
	GIMBAL SPRINGS		93.4
x_5	BASE ADAPTER RING	466	
	SKIRT		17,000
x_6	MISSILE	26,000	

FIGURE 35   TRANSMISSIBILITY ANALYSIS MODEL PROTOTYPE MISSILE SUSPENSION SYSTEM
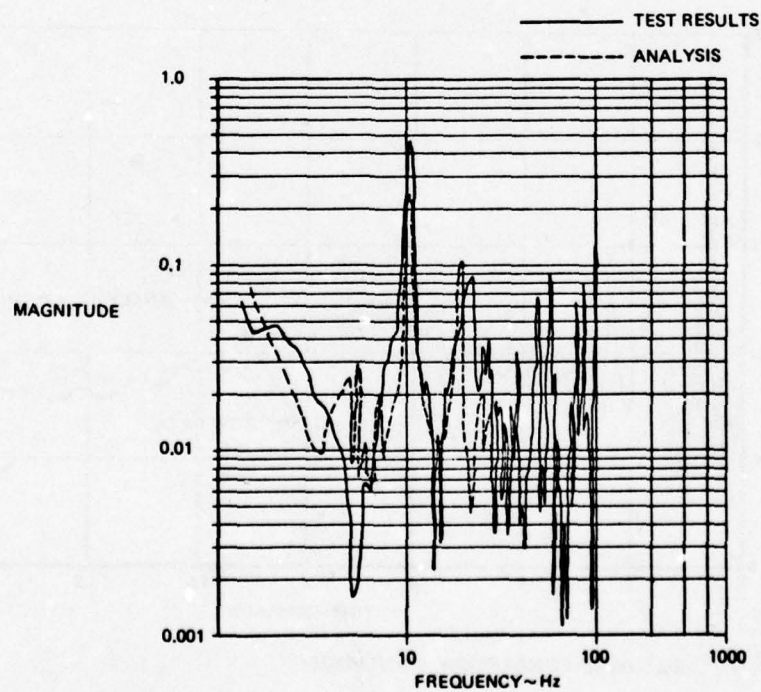
FIGURE 36   TEST–ANALYSIS COMPARISON OF FOURIER TRANSFER FUNCTIONS
BASE SUPPORT RING TO INPUT

234
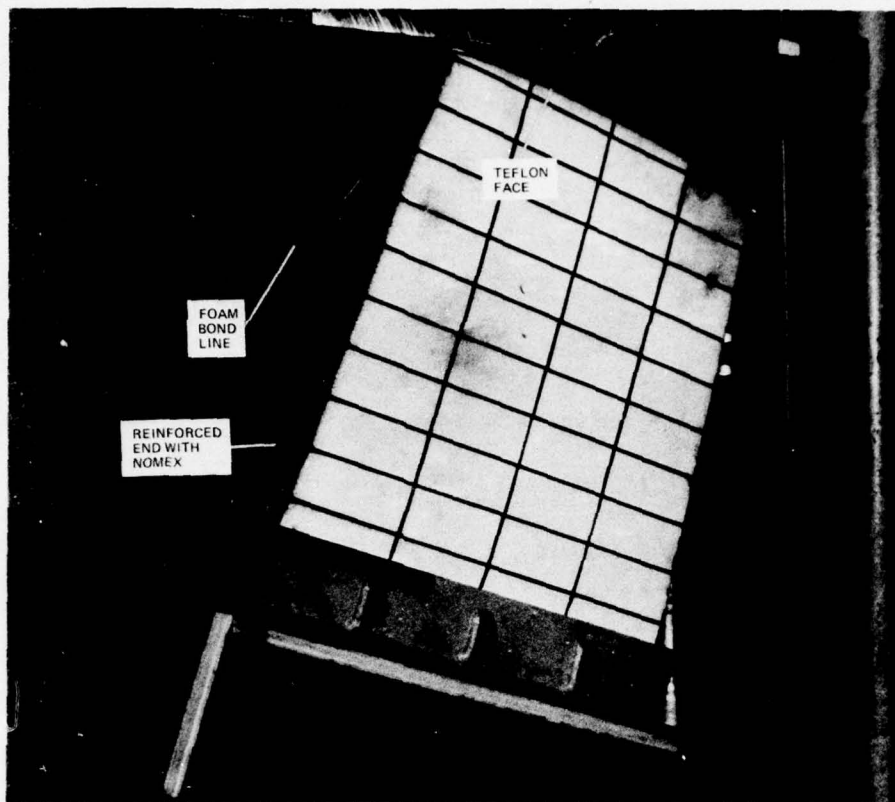
FIGURE 37   MISSILE SUSPENSION SYSTEM HORIZONTAL SHOCK ISOLATOR (FOAM) SPECIMEN
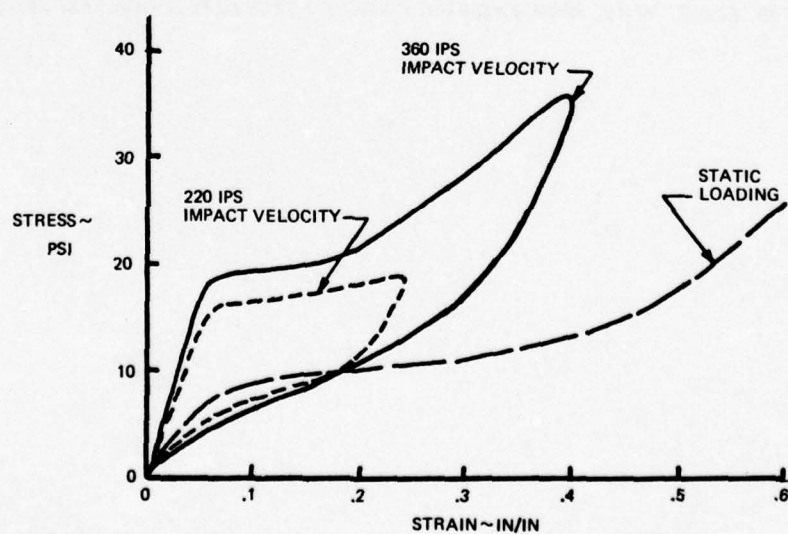
FIGURE 38   COMPARISON OF POLYURETHANE FOAM STRESS - STRAIN RELATIONSHIPS FOR
DYNAMIC AND STATIC COMPRESSION LOADING

235
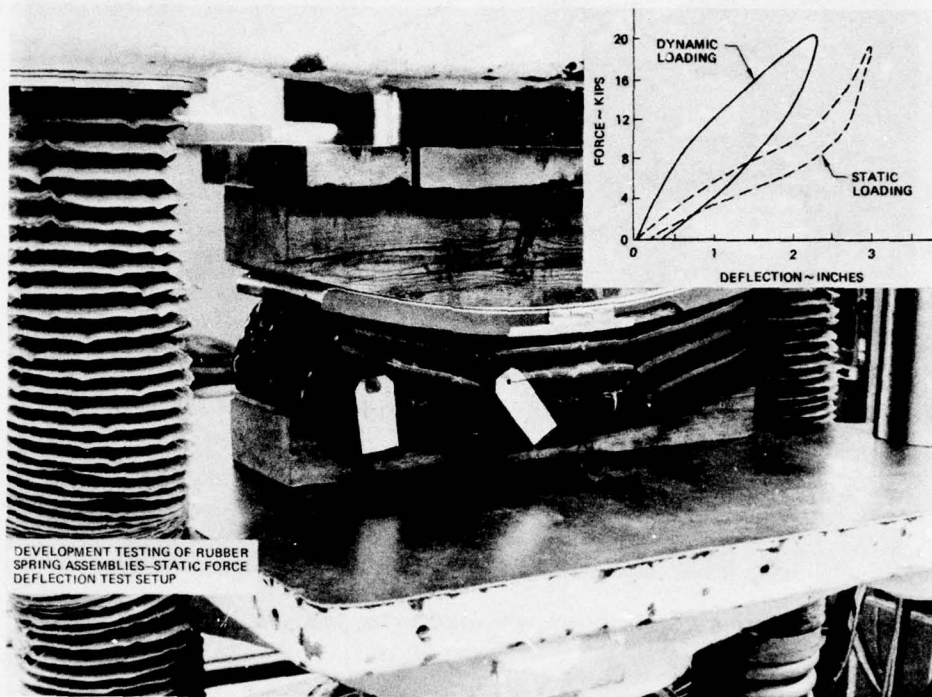
FIGURE 39 ELASTOMERIC SPRING ASSEMBLY STATIC FORCE DEFLECTION TEST SETUP

ANALYSIS AND TESTING OF FULL SCALE
SHOCK ISOLATED EQUIPMENT FLOORS

William R. Milne
Boeing Aerospace Company
Seattle, Washington

Increased nuclear threats have resulted in the need to design an improved equipment floor to ensure survival of electronic equipment critical to a silo-based ICBM system. The design problem was compounded by two constraints: to fit the new equipment floor into the existing facility, and to limit the floor response loads and environment to current equipment capabilities. The design criteria associated with the increased facility motion represented a composite shock requirement including motions induced by the airblast and ground-transmitted effects induced by cratering. A simplified analytical model for an equipment floor with idealized vertical and horizontal isolators was established to support selection of a candidate concept that would accommodate both air-induced and cratering response conditions. Component analyses of the liquid isolator and the horizontal foam restraints were developed separately and systematically improved by a series of component test programs. The overall system analysis then was accomplished using a single isolator model with the foam model added; a three-dimensional (six degree of freedom) loads and excursions analysis, known as the N-isolator program; and a linear transmissibility analysis using Fourier transform techniques which relate floor response to input motion or to responses at other floor locations. These models subsequently were used to qualify the operational suspension system to all aspects of the design criteria.

INTRODUCTION

Increased nuclear threats identified during the past decade have resulted in the need to design an improved equipment floor to ensure survival of electronic equipment critical to a silo-based ICBM system. The improved equipment floor design requirements limit loads on the sensitive equipment during the period when the suspension system is exposed to facility motions in excess of those used for the previous equipment floor design (Luschei, Ref. 1). The design problem was compounded by two design constraints: to fit the new equipment floor into the existing facility, and to limit the floor response loads and environment to current equipment capabilities. The design criteria associated with this increased facility motion were expressed in terms of shock spectra which represented a composite shock requirement including motions induced by the airblast and ground-transmitted effects induced by the cratering. Airblast-induced motions are characterized by a high velocity and acceleration and a relatively low displacement. The direct-induced (cratering) motions are characterized by a low acceleration, low velocity and a large displacement relative to that of the air-induced pulse.

A simplified analytical model for an equipment floor with idealized vertical and horizontal isolators was established to support the selection of a candidate concept. It became obvious as the study progressed that the airblast-induced motion had a significant influence on the floor loads while the direct-induced motion had a significant influence on the overall system motions. To accommodate both of these response conditions, a system concept was selected that had an annular steel equipment floor, with vertical isolation provided by four liquid isolators attached by cables to the facility ceiling and horizontal isolation provided by polyurethane foam blocks mounted on the sides of the floor. Existing equipment racks were mounted on the upper surface of the floor; batteries and a motor generator set were suspended by structure from the underside of the floor.

A detailed review of the analysis and testing requirements indicated the feasibility of dividing the activity into: (1) component analysis and testing which could be developed *separately and subsequently integrated into the system design*, and (2) the overall system analysis and testing which utilized results from the component-level work. The component analyses of the liquid isolator and the horizontal foam restraints were developed separately and systematically improved by a series of component test programs. The overall system analysis then was accomplished using the single isolator model with the foam model added; a three-dimensional (six degree of freedom) loads and excursions analysis known as the N-isolator program; and a linear transmissibility analysis using Fourier transform techniques, which relate floor response to input motion or to responses at other floor locations.

DESCRIPTION OF THE ANALYSIS MODELS

The full-scale suspension system analysis was accomplished by using three different but complementary models.

The single isolator model evolved as described by Ashley (Ref. 6), and was used to support the design by accurately defining loads and motions in the liquid isolator set. Fig. 1 shows a schematic of the model, and it can be seen that the horizontal foam shock isolators are included. This was done to account for the effects of horizontal motions (due to driven foam) at the base of the isolator on the isolator responses. Due to the complexity of the model, considerable computer time was used during computation and this model primarily was used to predict early time isolator loads and motions. The model used actual cable load-deflection data and the same isolator average load-stroke and friction-stroke characteristics which are identified in the following N-isolator discussion.

The N-isolator program is used to predict vertical and horizontal excursions of a three-dimensional body that is

suspended in space by massless, resilient support elements when the support attachment points can be displaced in any specified manner. The shape of the body, along with the number and location of supporting elements, is arbitrary within wide limits. Motions of the support attachment points are described by vertical and horizontal velocity time histories. The motion at each attachment point can be assumed to be independent of the motions at other attachment points. Rigid-body response motion is described by the six rigid-body degrees of freedom; i.e., three translations and three rotations.

Three types of isolators have been used to model the suspension system of the Wing V upgrade LER floor:

1. Four vertical isolators which possess stiffness, coulomb damping, and V^2 damping properties.

2. Ficticious horizontal isolators which have only friction properties. These isolators simulate the horizontal damping forces introduced by umbilical cables and by friction within the spherical bearings at the floor and ceiling attachment points of the vertical isolators.

3. A horizontal foam isolation system consisting of annular foam segments installed on the floor I.D. and O.D. and first analyzed by Specenko (Ref. 4).

The details of the model are discussed by Gustafson (Ref. 5), and they will not be repeated here. For the full-scale floor testing conducted at Vandenberg AFB, the horizontal foam isolation system was not driven during test and hence the horizontal foam model was not utilized in either the single isolator or in the N-isolator program. The equations of motion for the shock isolated floor were expressed in matrix form as:

$$|M| \begin{bmatrix} \ddot{X} \\ \ddot{Y} \\ \ddot{Z} \\ \ddot{\psi} \\ \ddot{\phi} \\ \ddot{\theta} \end{bmatrix} = \begin{bmatrix} B \end{bmatrix} + \begin{bmatrix} Q \end{bmatrix}$$

or, more simply:

$$M(q)\ddot{q} = B(q,\dot{q}) + Q$$

where

M = 6 x 6 mass matrix

B = column matrix containing centrifugal and coriolis forces in the rigid body

Q = generalized force matrix which includes floor weight and axial isolator loads

The integration of the above equations of motion was done by changing the six second-order differential equations to 12 equivalent first-order equations (six accelerations integrated to velocities and six velocities integrated to displacements). The program then used a fourth-order Runge-Kutta numerical integration technique with a variable time step.

Mass properties of the Block 1 floor (including the sprung weights of the isolators) were computed using the results obtained during the weighing of the Block 1 floor test specimen on 20 December 1972. Isolator load-stroke data were obtained from isolator acceptance tests conducted on each isolator as shown on Fig. 2. From curves like these, data on average load versus stroke (Fig. 3a) and friction versus stroke (Fig. 3b) were developed for use in the model. The N-isolator model subsequently was used to compute all shock isolated floor translations and rotations.

As part of the Wing V LER floor analysis for CDR, a semianalytical floor transmissibility model was employed to predict the high-frequency floor environment. This same technique was used to predict the floor environment for the tests in this program. One objective of the test program was to provide test data to verify or update the model to allow prediction of floor environments in the high-frequency range.

The term semianalytical reflects the fact that an analytically determined transfer function was employed for frequencies up to 50 Hz and experimental data from an earlier floor test program (Vail, Ref. 3) were employed for frequencies in excess of 50 Hz. Below 50 Hz the transfer function for the single-chamber isolator was obtained from data gathered during the isolator developmental testing, the transfer function for the floor structure was developed from the results of a finite-element model analysis, and cabinet transfer functions were developed from results of cabinet transmissibility tests conducted earlier. These transfer functions were then combined analytically to produce the overall transfer function. Convolutions of the appropriate transfer functions with the frequency response function of the input forcing function, and summation of the four isolator inputs in the frequency domain, results in a frequency response function for the floor environment at a location of interest on the floor. Transformation of the floor response back into the time domain enables computation of shock spectra of the floor environment for comparison with floor and equipment design criteria.

The employment of test data from floor-segment tests for frequencies greater than 50 Hz appeared reasonable because test data indicated that floors of varying primary stiffness and design had similar transmissibility characteristics above this frequency. This can be attributed to the structure acting as a collection of quasi-independent elements at the higher frequencies rather than as a structural unit. The test specimen used in Ref. 3 was the same steel floor modified and used during the floor segment test reported by Gustafson (Ref. 5). The heavier steel plates associated with the current floor design were expected to result in a more benign environment than was exhibited during the floor segment testing, thus representing a conservative approach to floor environment prediction.

TEST PROGRAM

As the analytical activities progressed, the requirement for a full-scale system-level test program was identified. The major goals of the test were to verify the vertical suspension system performance when it was exposed to criteria level inputs to the liquid isolator set. Key parameters that needed to be evaluated were isolator and floor loads, isolator set and floor damping, and floor and equipment high-frequency environment. The test program also would provide transmissibility data for a prototype floor structure which then could be used to update the transmissibility analysis model. Uncertainties in the transmissibility analysis and the im-

238

portance of the floor/equipment interface environment were the most important requirements for full-scale system testing. An additional goal was to evaluate the system response to input values at and in excess of the nominal design criteria without risking failure of the floor and the installed and functioning electrical equipment.

A two-part test program was planned for conduct in the full-scale test facility at Vandenberg AFB (Burwell, Ref. 2), which was designed specifically to test a complete shock isolated equipment floor. The horizontal foam isolators were not driven during the test because a prior floor segment test program (Gustafson, Ref. 5) had verified the ability to predict analytically the influence of the driven foam on the low-frequency floor response and the ability of the foam isolators to attenuate the high-frequency inputs. The first part of the test program (the Block 1 test program) varied input levels, input azimuth and input angle with the vertical and determined the isolator and floor responses including those at the interface with the attachment points of mass-simulated electronic equipment. Four test runs were conducted as shown in the matrix in Fig. 4. Runs 1 and 2 assessed the effects of increasing the vertical inputs to the floor. Runs 3 and 4 added a horizontal component of input motion and assessed the effects of varying the azimuth of the horizontal component of input motion.

The second portion of the test program (the Block 2 test program) repeated and then increased input velocities and displacements over those input conditions during the Block 1 test. Operating electronic equipment replaced the mass-simulated equipment used during Block 1. Six runs were conducted as shown in the matrix in Fig. 4. Runs 1 and 2 of Block 2 were repeats of runs 3 and 4 of Block 1, with the operating electronic equipment being the only difference in test specimen configuration. Run 3 was a low-level vertical test which simulated a distant attack condition. Runs 4 and 5 increased the vertical component of velocity over that used in runs 1 and 2 and used a 1:3 ratio of horizontal to vertical input (angle of 18.4 degrees with the vertical). Run 5 further increased the vertical component of velocity and used a 2:3 ratio of horizontal to vertical input (angle of 33.69 degrees with the vertical). Runs 4, 5 and 6 assessed the system performance when exposed to inputs which are site peculiar.

The matrix in Fig. 4 generally defines the input conditions for each test run, and goal pulse shapes then were chosen to meet the test spectrum requirements for each run. Since the primary actuators act in a single axis (Burwell, Ref. 2) vertical and horizontal components of input motion were always simple percentages of the goal pulse shapes.

The test programs were conducted according to approved test plans with detailed procedures prepared for each run identified in the test plan. Following each test run, a quick-look report was prepared and presented to the customer for approval. The report assessed the ability of the actual test run to meet the success criteria defined in the plan, and provided recommendations for any changes to the next planned test condition. At the conclusion of each block of testing, a detailed test report was prepared to present the test results, conclusions and recommendations.

TEST SPECIMEN

The Block 1 test specimen was a fully configured, prototype floor structure and isolator set with mass-simulated electronic equipment installed on the floor. The horizontal

isolator set was installed but not driven. A prototype environmental control system (ECS) duct assembly also was installed. The electronic equipment mass simulation was accomplished by installing standard equipment cabinets in their appropriate locations on the floor and then installing weighted drawers or plates in the different cabinet structures. Each piece of structure had the correct primary stiffnesses and center of gravity (c.g.) during the test. Items such as the motor generator set, VRSA and similar components were simulated by steel assemblies with their appropriate c.g.'s. Used batteries were installed on the underside of the floor and a cable assembly was routed to a fixed nearby structure to complete the simulation. When completely assembled, the test specimen was fully capable of providing data on all aspects of the shock isolated floor structural performance. Figs. 5 and 6 show overall views of the Block 1 and Block 2 test assemblies.

The Block 2 test specimen utilized the same floor structure and isolator set, but the mass-simulated electronic equipment was replaced by a complete set of operational electronic equipment shipped in from an operational facility and installed on the floor exactly as it would be installed in the facility. A launch control facility (LCF) simulator also was provided to allow direct communication with the electronic equipment and to assess the ability of this equipment to perform the required functions during and after each test event. After each test a simulated launch was performed and the electronic equipment performance was monitored.

INSTRUMENTATION AND DATA REDUCTION

The instrumentation system used on the Block 1 and 2 test program could record up to 250 channels of active data for any test run. During Block 1 testing, 175 to 222 data channels were multiplexed and recorded on magnetic tape. Twenty-eight channels (some of which were redundant to those on tape) were recorded on a direct-write visicorder to be used for immediate post-test assessment of primary actuator performance. Numerous passive measurements also were made to verify the peak values read on the active data records.

The types of data taken during Block 1 include acceleration, loads, velocities, strains, rotations, displacements, pressure and electrical events. Slow and high-speed color 16-mm movies were made of each test run. Figure 7 shows typical measurement locations used during Block 1 testing.

Block 2 testing used the same basic types and quantities of measurements as used during Block 1 with two major changes. Floor strain measurements were deleted because the Block 1 data showed low floor loads without the driven foam. Fifty electrical system performance measurements were added and recorded by the automatic sampled data instrumentation system (ASDIS) to assess the electronic equipment performance.

The same types of data reduction were used in support of both Block 1 and 2 test programs. Quick-look data were used for immediate (24-hour) assessment of test success. These data consisted of oscillograph data from dubs of the test tapes, analog shock spectra, and selected digital analyses run overnight at a nearby data reduction facility.

Permanent digital data were reduced at VAFB and shipped on plot tapes to Seattle for plotting and evaluation. These data included shock spectra, Fourier transforms and transfer functions, integrals and X-Y plots. Permanent

oscillograph records were prepared at VAFB and shipped to Seattle for annotation and evaluation.

TEST RESULTS

For ease of discussion, the test results have been divided into five categories: motions, loads, damping, environment and electronic equipment performance. These results have been derived from a thorough analysis of the test data with support from the analytical models as required to interpret the data. Block 1 and Block 2 test results will be discussed together unless it is appropriate to present the results separately.

Motions

System motions were derived by using sets of six wire-gage displacement measurements and reducing them to three translations and three rotations using the transformation technique described by Gustafson (Ref. 5). Isolator motions were measured using LVDT velocity and displacement transducers. System motions followed expected trends and peak translations were directly proportional to the final prime mover position. All vertical motions fell within the allowable values. Horizontal motions had to be evaluated with the knowledge that the foam was not driven. Floor rotations were low, and primarily in the direction of the input motion. Rotations were found to increase with increasing input displacement and with increasing components of horizontal input motion. Horizontal motions appeared to exhibit a change in frequency when the monoball at the isolator base locked up, but this effect was considered minor for cases where foam was driven horizontally. Isolator motions were found to be consistent with responses seen during floor-segment and single-isolator tests for preloads compatible with the 11,044-pound average isolator load seen on the Block 1 program. Rod retraction displacements were consistent with the increase in input motion and, after the first displacement cycle, rod cylinder displacements matched the vertical floor displacements described above. Rod retraction velocities were controlled by the drag plate damper as discussed below under damping. It was noted that adding a horizontal input motion component resulted in a modest decrease in rod retraction velocity due to the increase in lateral cable loading. Fig. 8 shows a comparison of isolator responses for a typical test condition. As the ceiling attach point moves down, the isolator rod retraction displacement cannot keep up with the input displacement (due to the influence of the drag plate damper) and the cable goes slack. As the ceiling motion slows down, the rod retraction continues to increase until the motion is terminated by a rapid buildup in axial cable load. This peak axial load is accompanied by a significant isolator rod bending moment (for inputs with horizontal components) and these loads excite a significant high-frequency environment on the floor. This environment was generally found to increase with increasing cable load.

Loads

Loads were measured in both the isolator set and in the floor structure using strain gages. Isolator loads were calibrated in terms of axial load and bending moment, while floor strains were recorded directly and converted to stresses analytically.

The VAFB floor test program provided the first opportunity to evaluate isolator axial loads and bending moments

under higher level input conditions. This was particularly important because the floor segment test program produced rod loads and moments which were higher than expected for the limited input capability of the floor segment test fixture.

The test results showed that vertical rod and cable loads were strongly dependent on the rod/ceiling relative velocity at the end of the slack cable period. For a given input level, rod bending moments were found to increase with increasing primary actuator angle with the vertical. The character of the load/moment signatures was found to be the same as that seen during floor segment test, but peak levels were generally lower on the full-scale tests for similar situations. In all cases, the loads and moments were below the allowables for the rod and/or the cable.

Floor loads were measured at different floor structure locations during the Block 1 test program. The floor loads were extremely low due to the lack of driven foam. The primary bending loads could be directly related to the isolator rigid-body motions as shown in Fig. 9. The strain-gage data showed a 7-Hz response superimposed on the rigid-body loads, which was verified as a low-amplitude floor flexible-response mode. The loads were compared with early estimates made for the floor without driven foam and found to be in reasonable agreement. Floor strain measurements were not made during Block 2 tests due to the low strain levels involved; the floor structure subsequently was qualified analytically.

Damping

A review of the system vertical and horizontal damping data indicated that coulomb damping was the primary source of system damping in both horizontal and vertical directions. Fig. 10 shows typical vertical responses to inputs of different levels. It can be seen that the amount of vertical damping is constant for the range of inputs considered. Comparisons with analysis showed that the amount of damping was higher than indicated by the measured friction deadband during the isolator acceptance tests. A review of the horizontal damping indicated that the value depended on whether relative motion existed in both the monoball and upper spherical fitting or only in the upper fitting. It was found that when the isolator monoball locked up due to friction, the horizontal damping dropped significantly and the pendulum frequency increased slightly. It is expected that these effects will be masked by the influences of the driven foam during design conditions. The system came to rest within the prescribed time period.

The liquid isolator has a "drag plate" damper attached to the piston rod to limit the rod retraction velocity, which will limit the impact loads occurring at the end of the slack cable period. The damping force is proportional to the square of the rod retraction velocity, i.e., $F = Cv\ V^2$ and a range of values for Cv was prescribed as part of the design process. Fig. 10 also shows values of damping force versus retraction velocity for Block 1 and 2 testing and for development tests conducted previously.

Environment

A major reason for conducting the full-scale floor test was to evaluate the high-frequency responses for the floor when it was subjected to high-level inputs at the ceiling attach point. The high-frequency data were thoroughly evaluated and subsequently used to update the empirical portion of the transmissibility model. The most significant

observations made from the data are touched on briefly in the following paragraphs.

The initial data evaluation activity involved a comparison of the results from each test condition with the floor allowables which were expressed in terms of Q=25 and Q=5 shock spectra. In all cases it was found that the floor data fell below the allowable levels. Fig. 11 shows an example of the comparison for run 4, Block 1.

Because operational electronic equipment was not available in time to support Block 1 tests, mass- and stiffness-simulated equipment were used. It was felt that this configuration would be more than adequate to assess the structural performance of the system. Fig. 12 shows a comparison of floor responses for run 4, Block 1 (mass-simulated electronic equipment) and run 1, Block 2 (operating electronic equipment) and little difference can be seen. This conclusion applies to all other responses also.

It was stated earlier that the floor segment test provided the first estimate of floor environment using a prototype isolator set with responding structure attached. One of the results of this test (Gustafson, Ref. 5) was the conclusion that the horizontal foam isolators did not contribute to the high-frequency environment on the floor. It also was concluded that the environment measured on the subscale test was an upper-bound environment and that it would be significantly lower during the actual full-scale test. This conclusion subsequently was verified on this program.

Earlier isolator component tests indicated that a lower threshold floor environment existed as a result of the isolator *rod breaking friction shortly after the start of the input* motion. For this program, the threshold was established as the floor responses associated with run 3 of the Block 2 test program which had an extremely low input level but where *the isolator rod broke friction. Once the isolator rod breaks* friction, floor environments increase with increasing cable load at the end of slack cable. A review of the input data reveals that a significant increase in ceiling input results in a *modest increase in floor environment. The resulting system* transmissibility (floor response divided by ceiling input) becomes a nonlinear function which is dependent on the input level as shown for the vertical direction in Fig. 13. As the preceding discussion applies to the relationship between ceiling input and floor locations. Comparisons between two locations on the floor and/or the cabinets show a highly linear relationship as also shown in Fig. 13. It is obvious that care must be exercised in selecting the appropriate system transfer function for use in the transmissibility analysis model.

Horizontal responses were found to increase significantly as the prime mover angle with the vertical was increased. The increase can be attributed to the increase in horizontal response of the isolator set and is illustrated by the response comparisons shown in Fig. 14.

A significant increase in floor environment was observed when sufficient input motion occurred (run 6, Block 2) to allow the isolator rods to bottom out in retraction. In this situation, the rod end fitting hits the isolator cylinder and sends a pulse down the cylinder, through the monoball and into the floor. Fig. 15 compares floor environment with and without rod/cylinder impact. This response will increase with increasing impact velocity and is limited by the terminal retraction velocity of the rod. This response mode must be considered when assessing the overall system capability.

The vertical floor environment was found to fall into a relatively narrow bandwidth for all floor locations, and hori-

zontal environment was found to be sensitive to orientation on the floor with respect to the radial or tangential floor axis. This sensitivity reflects the influence of the cabinet structure where the stiff cabinet axis is oriented radially and the soft cabinet axis is oriented tangentially on the floor.

Electronic Equipment Performance

A significant element of the Block 2 test program was the fact that a full set of operating electronic equipment was installed on the floor during the testing. It was required to demonstrate that the shock isolated floor and floor-mounted electronic equipment could survive attack and perform launch-critical functions after being subjected to selected ground motions. This requirement was satisfied by demonstrating that the weapon system survived and performed all required functions under the test conditions presented in Fig. 4.

TEST/ANALYSIS COMPARISONS

An important element of the Block 1 and 2 test programs was the use of the test data to verify and update the floor analysis models. Prior to each test condition, predictions were made using the appropriate models and the expected test inputs. Following the test, the actual test input motions were digitized and used as inputs to the models. The resulting responses then were compared with the test data to evaluate the model performance.

The single-isolator model was used primarily to define *isolator motions and loads as discussed above. The analysis* accurately predicted early time motions such as rod retraction displacement, as shown in Fig. 16. It was found that the values for vertical damping (Fig. 3) which were derived from isolator static load-stroke data (Fig. 2) needed to be increased to agree with the test data. This was typical for Block 1 and 2 testing.

The single-isolator model did a good job of defining vertical load signatures and amplitudes in the isolator rod and cable as shown in Fig. 17. Slack cable times and times to maximum rod and cable load were consistently close to values measured during test. Peak values of rod bending moment showed greater scatter on a run-by-run basis due to the complex nature of the input motion/cable/rod interaction as discussed by Ashley, Ref. 6. After a thorough review of the isolator moment data it was concluded that, for the range of inputs evaluated during Blocks 1 and 2, the single-isolator model satisfactorily predicted an upper-bound rod *bending moment, and no further modifications were made to* the model.

The N-isolator model was used to predict the long-term suspension system translations and rotations to assess the ability of the system to stay within the required rattle-space envelopes. Because the vertical system damping source is the same (isolator seal friction) for both the single isolator and the N-isolator models, the N-isolator friction values were updated to provide good agreement with the Block 1 test results. Fig. 18 shows a test/analysis comparison for vertical and horizontal floor translations and for floor rotations in the direction of the input motion.

The transmissibility analysis was expected to provide a conservative estimate of the floor environment for the various input conditions evaluated during the test program. Following Block 1 testing, the model was updated to utilize transfer functions developed from actual Block 1 test data.

The updated model is considered adequate for predicting floor responses for all conditions other than floor/wall impact and for isolator rod retraction impact where high impact velocities occur.

CONCLUSIONS

The full-scale test program, along with the floor segment test program and component tests on the foam and liquid isolators, all contributed to the development of a fully verified set of shock isolated platform analysis models. These three models subsequently were used to qualify the operational suspension system to all aspects of the design criteria. Qualification was accomplished by analysis using a group of input pulses which met the design criteria spectra and which were representative of the expected site-by-site variation in facility motions. As part of this qualification activity, floor excursions were compared with allowable rattlespace envelopes, floor and isolator loads were compared with the appropriate structural allowables, floor response spectra were compared with the appropriate $Q=5$ and $Q=25$ allowable spectra, and floor responses were shown to damp out within the allocated time. In all cases, the analytic models were able to demonstrate that the suspension system met or exceeded its requirements.

Following the qualification analyses, the same three models were used to establish the fragility levels of the floor suspension system with its complement of electronic equipment installed and operating. This activity was accomplished by increasing input motions in an orderly manner until onset of failure was identified in one of the following modes, as illustrated in Fig. 19:

a. Floor structure or cabinet impact with the rigid facility due to excessive foam crush or floor rotation. It was anticipated that this would result in potentially unacceptable structural loads and/or floor environment.

b. Isolator or floor loads exceed structural allowables under conditions where wall impact does not occur.

c. Predicted environments on the floor or equipment exceed OGE capabilities established during OGE fragility testing.

It can be seen that this technique can be used to identify potential capability growth for the system under consideration.

In conclusion, it can be seen that a comprehensive dynamic analysis, supported by well planned test programs of progressively increasing complexity, can provide an extremely powerful tool in the design, qualification and assessment of large shock isolation systems.

REFERENCES

1. Loren L. Luschei, "An Introduction to the Shock Testing of Large Shock Isolation Systems," 46th Shock and Vibration Symposium, San Diego, 1975 (Classified Secret).

2. G. R. Burwell, "Actuator Development for System Level Shock Testing," 46th Shock and Vibration Symposium, San Diego, 1975.

3. Curtis F. Vail, "Effect of Additive Damping on Transfer Function Characteristics of Structures," Research Publication GMR-1255, dated October 1972, published by the Society of Automotive Engineers, Inc.

4. Valentin Sepcenko, "Analysis of Open Cell Polyurethane Foam Under Impact Loading," 44th Shock and Vibration Symposium, 1973.

5. W. C. Gustafson, "Polyurethane Isolators for Shock Isolated Equipment Floors," 46th Shock and Vibration Symposium, San Diego, 1975.

6. J. P. Ashley, "Component Testing of Liquid Shock Isolators and Elastomers in Support of Recent Shock Isolation Systems Designs," 46th Shock and Vibration Symposium, San Diego, 1975.

LER ISOLATOR

RIGID ISOLATOR/FLEXIBLE CABLE ANALYSIS MODEL

LER CEILING

CABLE CEILING FITTING

CABLE

LOAD vs DEFLECTION

LOAD

DEFLECTION

ROD

ISOLATOR CYLINDER

FOAM ISOLATOR

LER FLOOR

RIGID LINK

AXIAL STIFFNESS

$K_C = K_S \left(1 + \dfrac{V_e}{CVF}\right)$

BENDING STIFFNESS (K_8)

ith CABLE MASS

CABLE IDEALIZATION

δ_E MAX (FROM STATIC)

δ_R MAX (FROM STATIC)
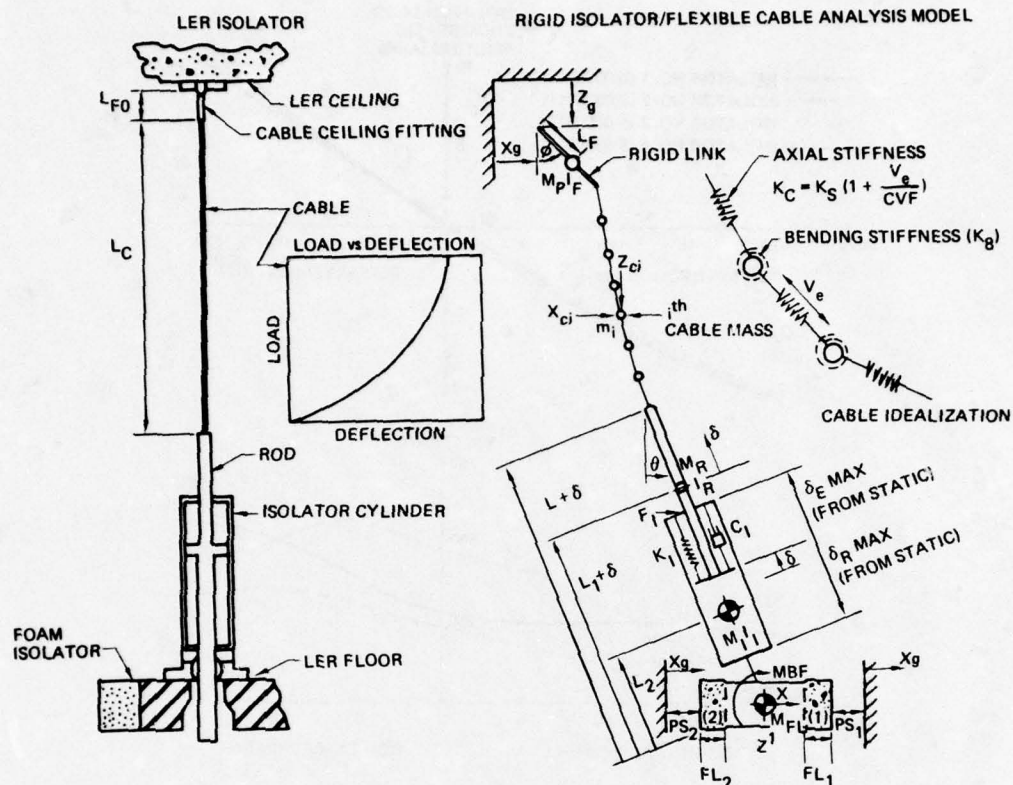
FIGURE 1   SINGLE ISOLATOR ANALYSIS MODEL

ISOLATOR ACCEPTANCE TEST DATA
SERIAL NO. 0000011

FRICTION DEAD BAND

START TEST
(BREAKAWAY
FRICTION = 500 LBS.)

ISOLATOR LOAD – KIPS

EXTENSION   ISOLATOR   RETRACTION
                 STROKE - IN
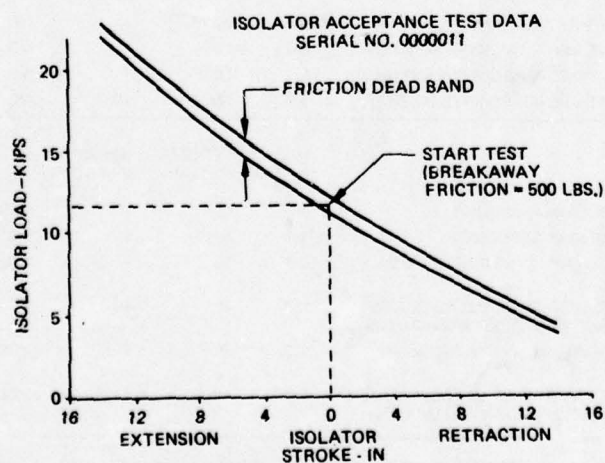
FIGURE 2   TOTAL LOAD-STROKE CHARACTERISTICS, ISOLATOR 2

a) ISOLATOR LOAD FROM STATIC POSITION (KIPS)

- ISOLATOR NO. 1 (#0000013)
- ISOLATOR NO. 2 (#0000011)
- ISOLATOR NO. 3 (#0000012)
- ISOLATOR NO. 4 (#0000010)

ROD RETRACTION (IN.) ROD EXTENSION (IN.)

b) ISOLATOR FRICTION (LB)

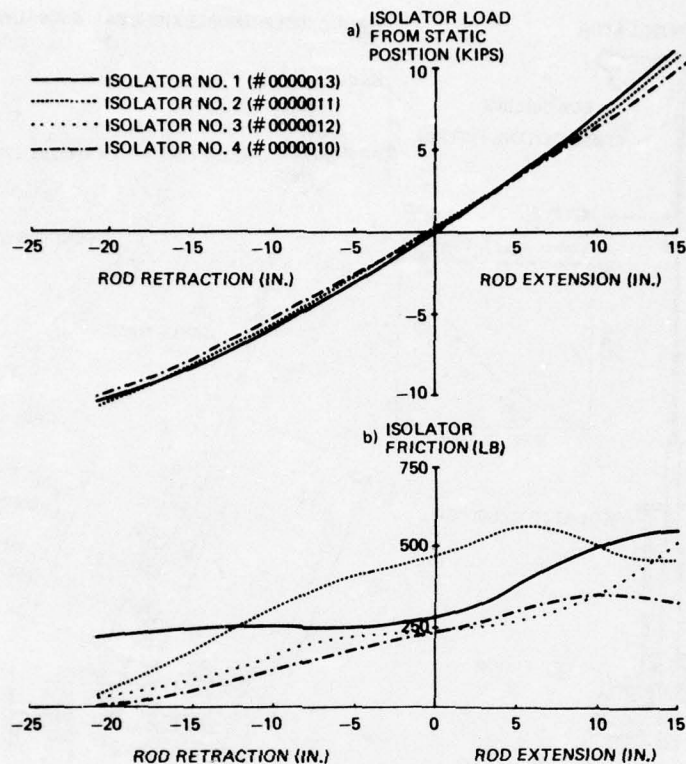ROD RETRACTION (IN.) ROD EXTENSION (IN.)

FIGURE 3   ISOLATOR AVERAGE LOAD AND FRICTION VS STROKE

BLOCK 1

RUN	INPUT	H/V RATIO	PERCENT RETURN	AZIMUTH VAFB ▷	EQUIPMENT POWER ON
1	50% INPUT VERTICAL WITH RETURN	0:1	50	–	NO
2	100% INPUT VERTICAL WITH RETURN	0:1	50	–	NO
3	100% INPUT VECTORED WITH RETURN	1:1	50	1	NO
4	100% INPUT VECTORED WITH RETURN	1:1	50	10	NO

BLOCK 2

RUN	INPUT	H/V RATIO	PERCENT RETURN	AZIMUTH VAFB ▷	EQUIPMENT POWER ON
1	REPEAT OF RUN 4, BLOCK 1	1:1	50	10	YES
2	REPEAT OF RUN 3, BLOCK 1	1:1	50	1	YES
3	LOW LEVEL INPUT - VERTICAL WITH RETURN	0:1	50	–	NO
4	INCREASED VERTICAL DISPLACEMENT OVER RUN 2, VECTORED WITH RETURN	1:3	25	10	YES
5	REPEAT OF RUN 4, VECTORED WITH RETURN	1:3	25	1	YES
6	INCREASED VERTICAL VELOCITY OVER RUN 5, VECTORED WITH RETURN	2:3	40	1	YES

▷ PRIME MOVER POSITION SPECIFIES THE HORIZONTAL DIRECTION THE PISTON WILL MOVE DURING THE INITIAL DOWNWARD MOTION (SEE FIGURE)

VAFB (NORTH) 10 1
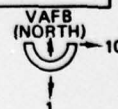
FIGURE 4   BLOCK 1 AND BLOCK 2 RUN MATRICES

244
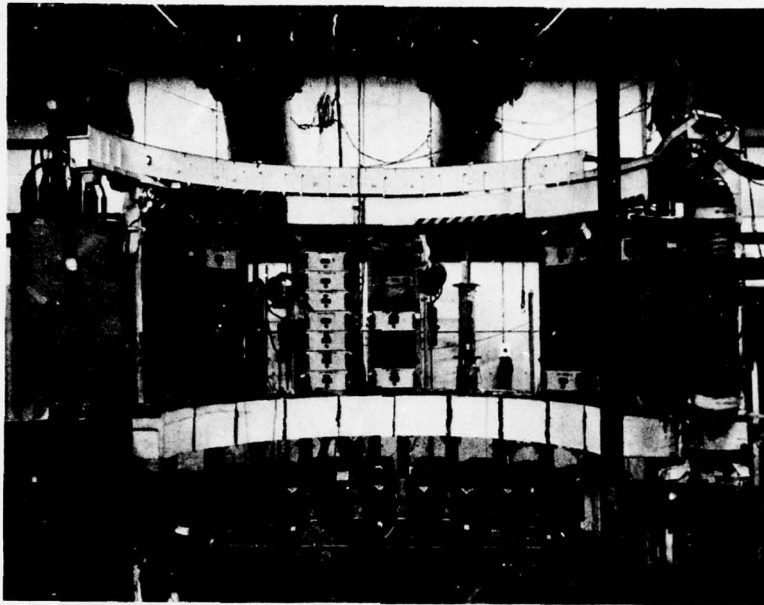
FIGURE 5   BLOCK 1 TEST ASSEMBLY

FIGURE 6   BLOCK 2 TEST ASSEMBLY

245
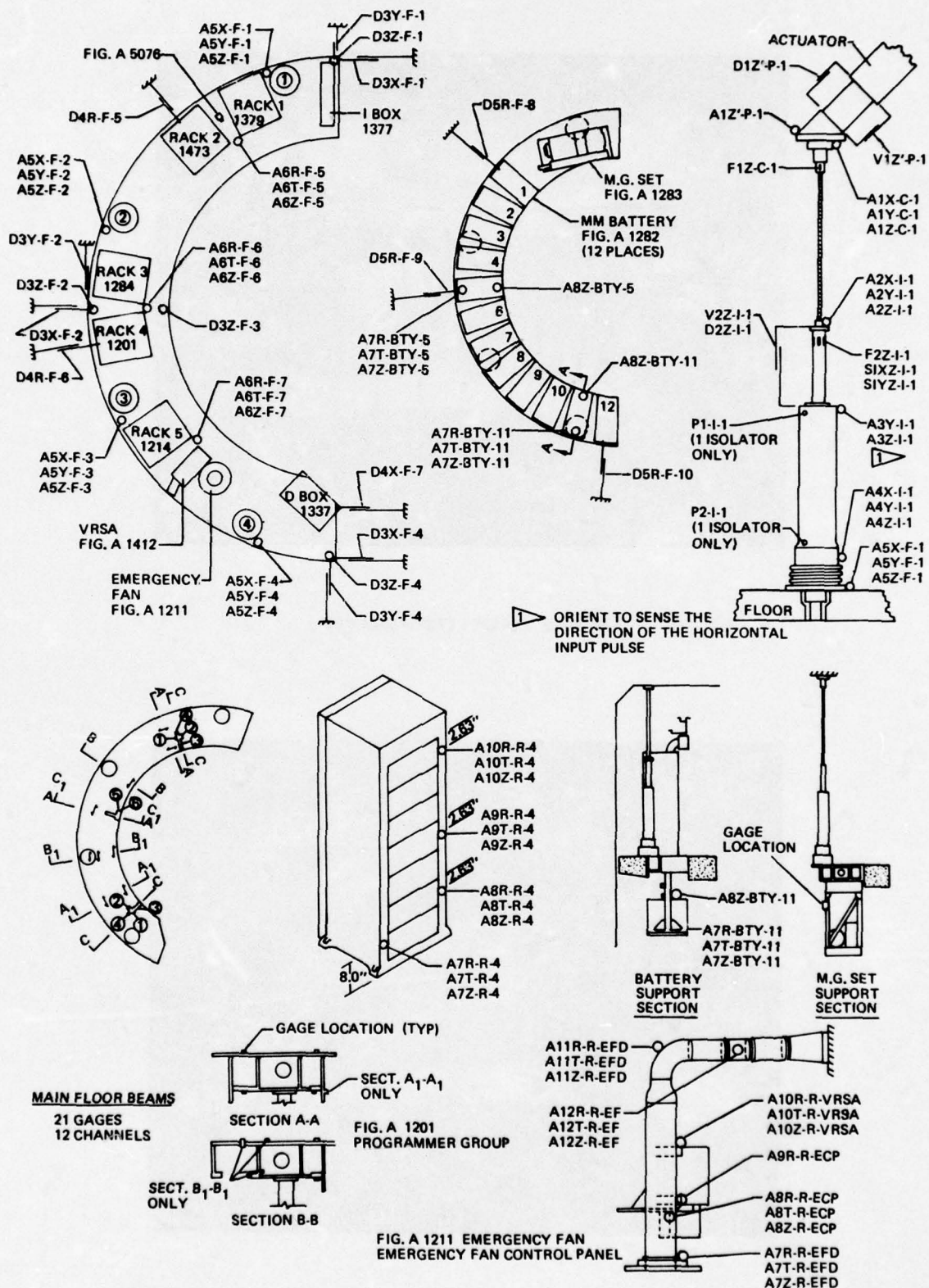
FIGURE 7 TYPICAL BLOCK 1 INSTRUMENTATION LOCATIONS
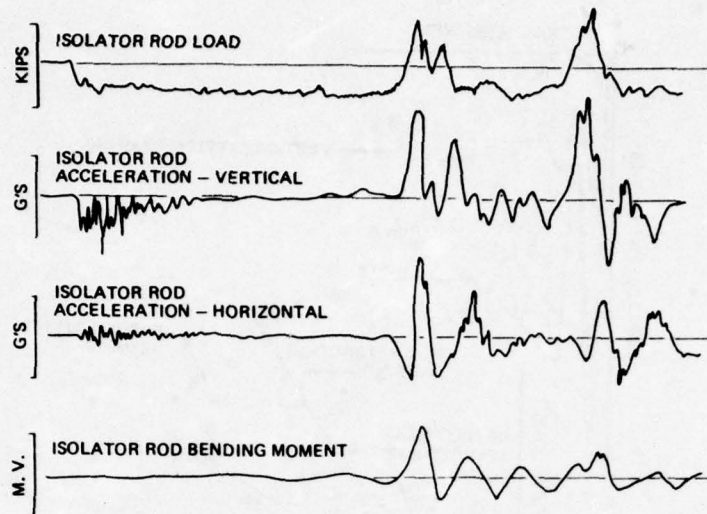
FIGURE 8 ISOLATOR RESPONSE COMPARISONS
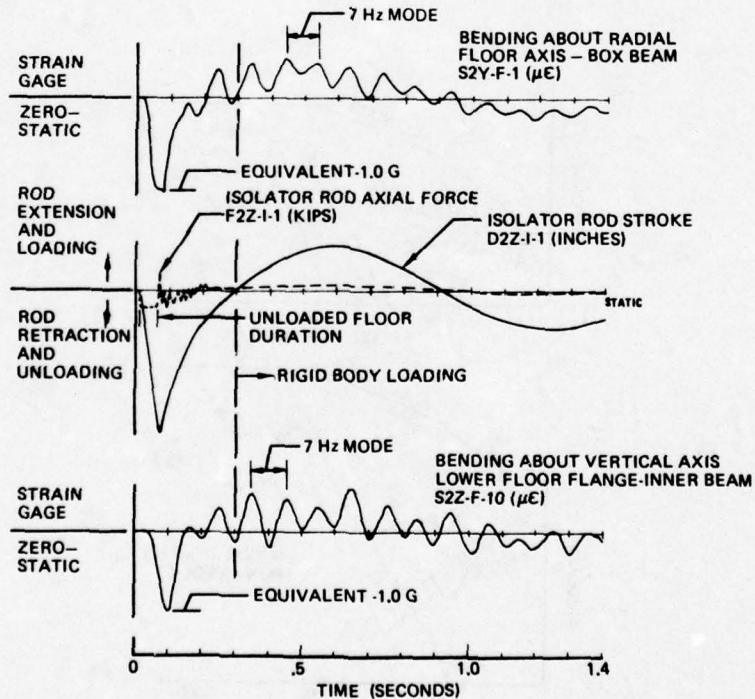
FIGURE 9 TYPICAL FLOOR LOAD HISTORIES

247
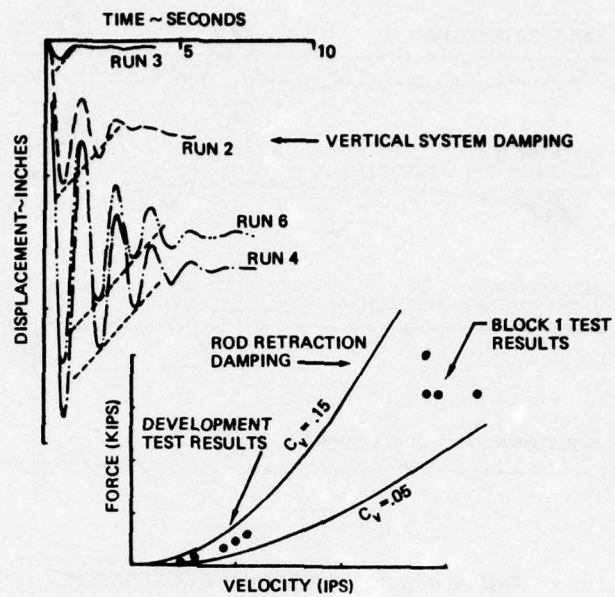
FIGURE 10   SYSTEM DAMPING COMPARISONS
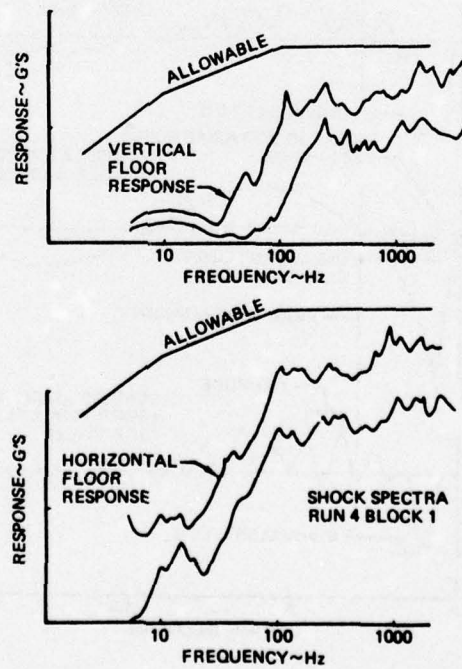
FIGURE 11   FLOOR RESPONSE VS ALLOWABLES
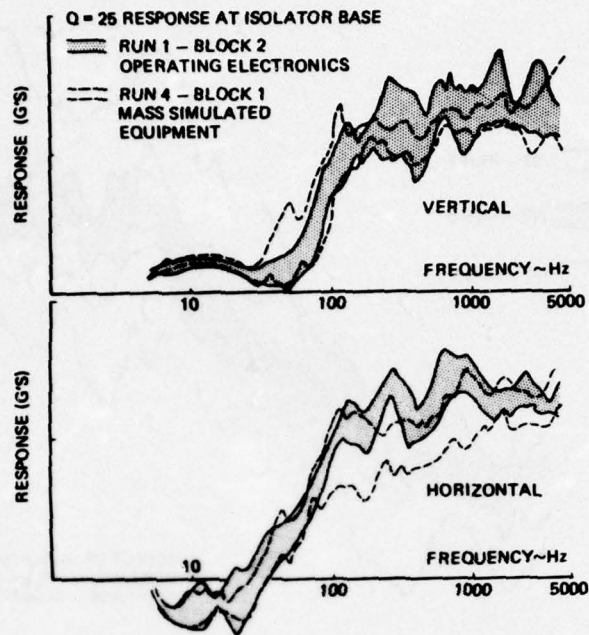
FIGURE 12   FLOOR ENVIRONMENT COMPARISON MASS SIMULATED VS OPERATING ELECTRONICS
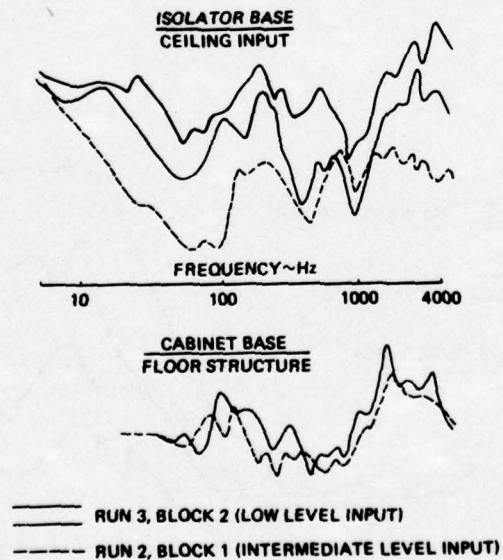
FIGURE 13   FLOOR TRANSMISSIBILITY COMPARISONS
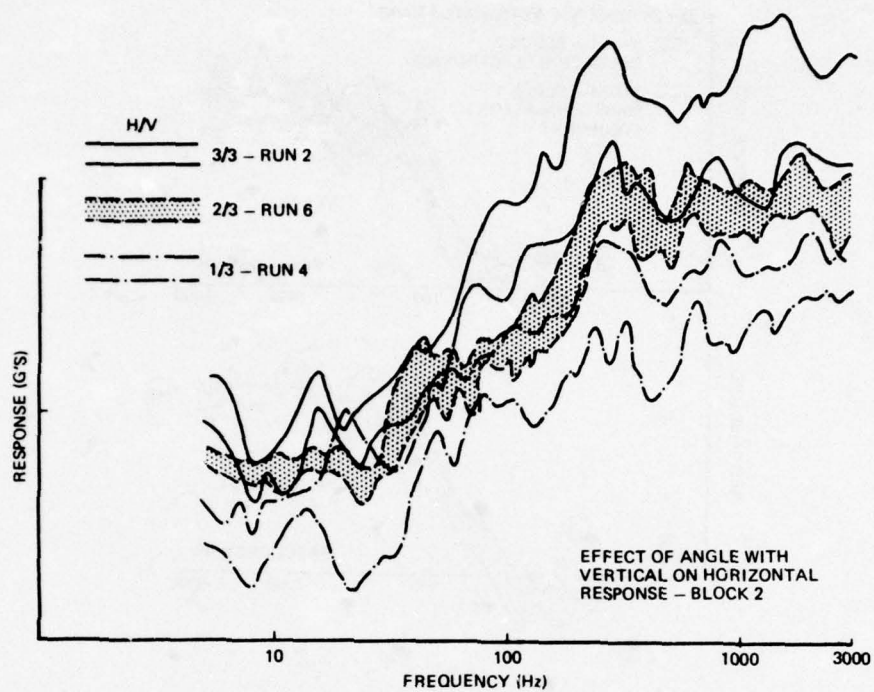
FIGURE 14   EFFECT OF ANGLE WITH VERTICAL ON HORIZONTAL RESPONSE—BLOCK 2
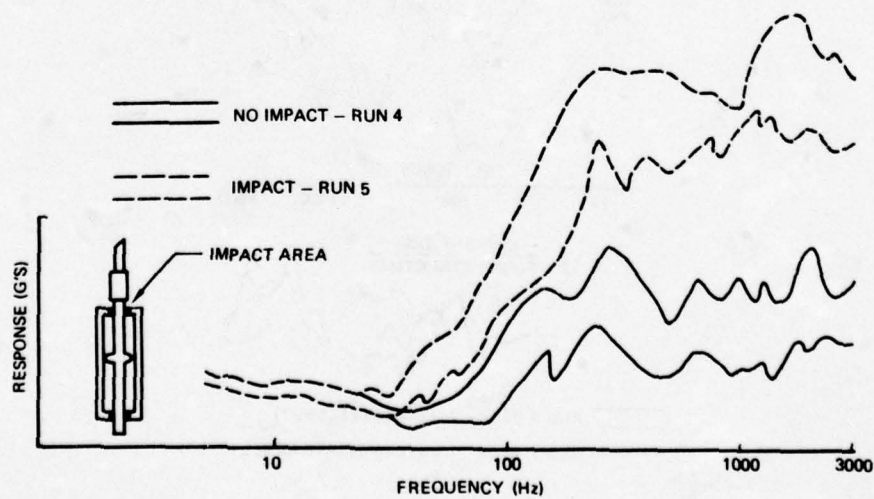
FIGURE 15   EFFECT OF ROD—CYLINDER IMPACT ON VERTICAL FLOOR RESPONSES—BLOCK 2

250
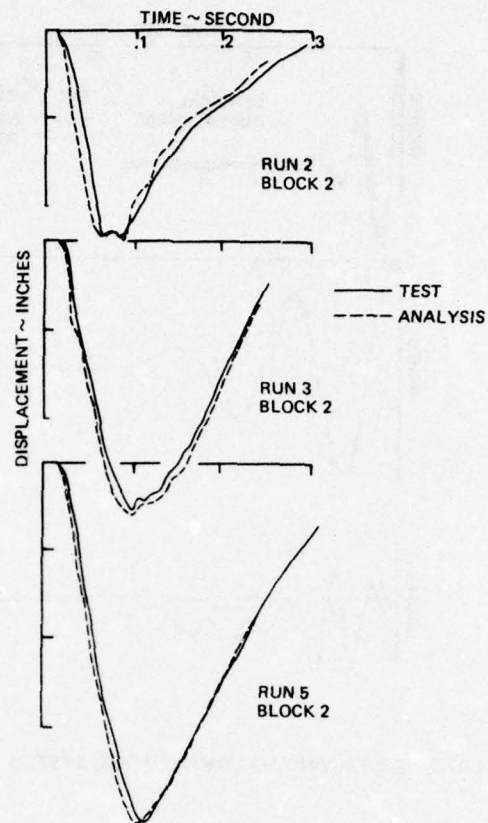
FIGURE 16   SINGLE ISOLATOR TEST—ANALYSIS COMPARISONS, EARLY TIME ROD RETRACTION DISPLACEMENT
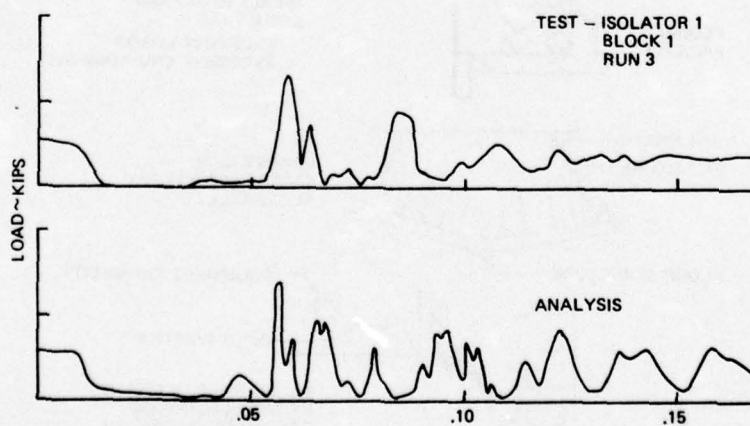
FIGURE 17   SINGLE ISOLATOR TEST—ANALYSIS COMPARISONS, ISOLATOR LOAD DATA

251
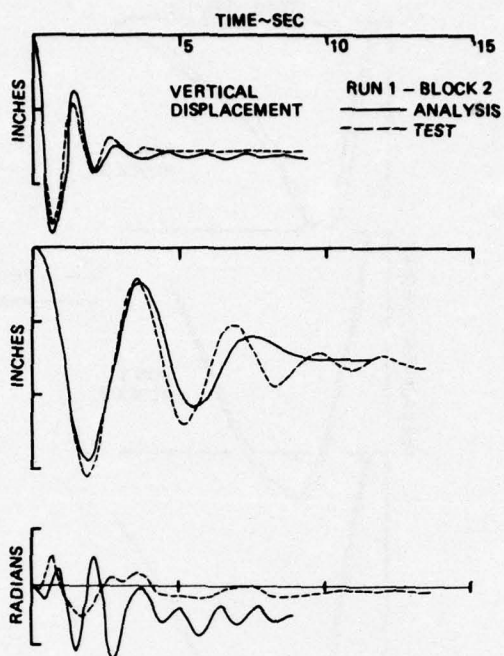
FIGURE 18 N-ISOLATOR TEST/ANALYSIS COMPARISONS, SYSTEM TRANSLATIONS AND ROTATIONS
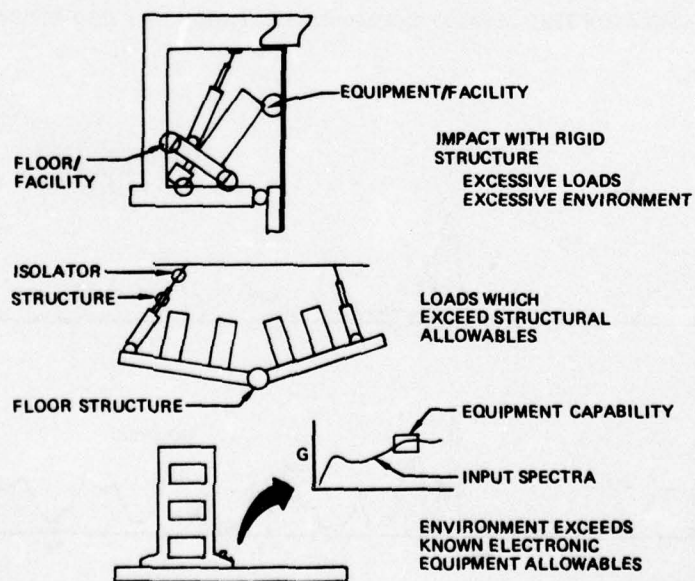
FIGURE 19 POSSIBLE FLOOR FAILURE MODES

252

FOCALIZATION OF SEMI-SYMMETRIC SYSTEMS

A. J. Hannibal
Lord Kinematics
Erie, PA

The focalization of a rigid body having one plane of symmetry and supported by a rigid foundation through four axisymmetric isolators is investigated. The isolators are divided into two sets having different elevations and lateral spreads. In each set, the isolator's stiffness characteristics are the same while their position and direction are symmetric about the body's plane of symmetry. A sequential unconstrained minimization technique is utilized as the solution method facilitating the constraint of spring rates, ratios of spring rates, directional characteristics of the isolators and the natural frequencies of the system. The existence of multiple solutions and the sensitivity of the focalization to parameter variations are discussed.

INTRODUCTION

The principle of decoupling the translational from the rotational degrees of freedom of a rigid body (re-

Fig.1 Top View of a Rigid Body Suspended by Four Equal, Axisymmetric, In-Plane Isolators Positioned in a Rectangular Pattern About its Center of Gravity

ferred to as focalization) has been understood and applied by analysts for many years. As treated in the literature [1], [2], [6], [7], focalization has been limited almost exclusively to symmetric systems in which four axisymmetric, in-plane isolators are positioned in a rectangular pattern about the c.g. of the suspended item per Fig. 1. One exception to the treatment of symmetric systems is the paper by Derby [3], in which the c.g. is arbitrarily placed with respect to the rectangular isolator pattern. All the isolators are the same and in-plane while their directional characteristics are manipulated to decouple the modes.

The approach described in this paper removes many of these limitations for it assumes that the package is suspended by two different isolator sets, front and rear, having different elevation and lateral spreads as shown on Fig. 2. To the designer, this means greater freedom to specify desirable isolator locations or to take advantage of those structurally available. In each set, the isolators' stiffness and damping characteristics are the same while their locations and directions are symmetric about the X-Z plane.

FRONT ISO. SET

ISO. #4

REAR ISO. SET

ISO.#3

γ_1

γ_2

X

e.c.

c.g.

A

b_1

γ_1

γ_2

b_2

B

A

ISO. #1

ISO.#2

B

ℓ

$2a-\ell$

Y

$2a$

TOP VIEW

Z

X

e.c.

h_1

c.g.

h_2

FRONT VIEW

θ_1

θ_2

VIEW A—A

VIEW B—B

γ_i - TOE-IN ANGLE

θ_i - ELEVATION ANGLE

Fig.2 Top and Front View of a Semi-Symmetric Rigid Body Suspended on Four Axi-Symmetric Isolators

It is also assumed that the body has one plane of symmetry (X-Z plane), which is not a serious limitation as many systems to which focalization is applicable have a plane of symmetry, such as prop-driven aircraft engines, cabs on trucks and tractors, shipping containers, optical and guidance systems, etc...

An important feature of this analysis is its ability to decouple the system with respect to an arbitrary point (referred to as the elastic center), usually the c.g., while constraining the spring rates of the isolators, their ratio, the toe-in and elevation angles (defined on Fig. 2), and the natural frequencies of the system.

The inclusion of constraints is facilitated by solving the problem using a sequential unconstrained minimization technique.

SYSTEM DESCRIPTION

The linear form of the equations of motion for the system described above and depicted in Fig. 2 is represented mathematically in matrix form as:

$$M\ddot{\vec{x}} + C\dot{\vec{x}} + K\vec{x} = \vec{F} \qquad (1)$$

where

254

$$\vec{\underline{X}} = (x, y, z)$$

$$\vec{\underline{\phi}} = (\alpha, \beta, \gamma)$$

and

$$\vec{x} = (\vec{\underline{X}}, \vec{\underline{\phi}}) \tag{2}$$

That is, the motion of a rigid body can be completely described with respect to an arbitrary point by three translations x, y, and z referred to as fore-aft, lateral and vertical respectively, and three rotations α, β and γ referred to as roll, pitch and yaw respectively. The rotations are defined as positive in the counterclockwise direction about the X, Y and Z axes respectively as illustrated on Fig. 3. Furthermore, they are assumed small to effect the linearity of the dynamic equations and to guarantee the commutative property necessary for their use as vectors.

The isolators are represented by three mutually-perpendicular springs along the principal axes of the isolator defined in Fig. 4 as X', Y' and Z'. They are assumed to be axisymmetric about the Z'-axis. For convenience, k_{ci}, the spring rate along the Z' axis, will be referred to as a compression spring rate and k_{si}, the spring rate along the X' and Y' axes, as a shear spring rate. It is further assumed that with respect

to the principal axes, the force-displacement relationship for each isolator can be represented in matrix form by:

$$k_{si} \begin{bmatrix} 1 & 0 & 0 \\ 0 & 1 & 0 \\ 0 & 0 & L_i \end{bmatrix} \quad i = 1, 2 \tag{3}$$

where L_i is defined as the ratio:

$$k_{ci}/k_{si}.$$
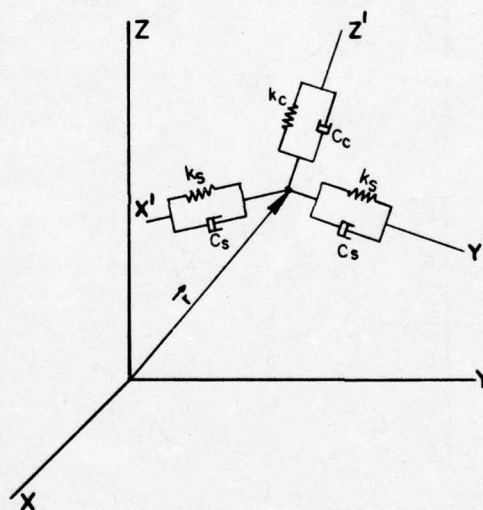
Fig.4 Schematic of an Isolator in Relation to the Fixed Coordinate System

Viscous dampers parallel to the springs as depicted in Fig. 4 are treated analogously. By pre and post multiplication of equation (3) by the proper transformation matrix (for the system under investigation here, equation (4) in the Appendix) will yield a force-displacement relationship of the isolator in terms of a general motion along the fixed body coordinates X, Y and Z. A thorough, detailed development of the general stiffness matrix resulting from an arbitrary positioned and oriented isolator represented by equation (3) is given in reference [8].
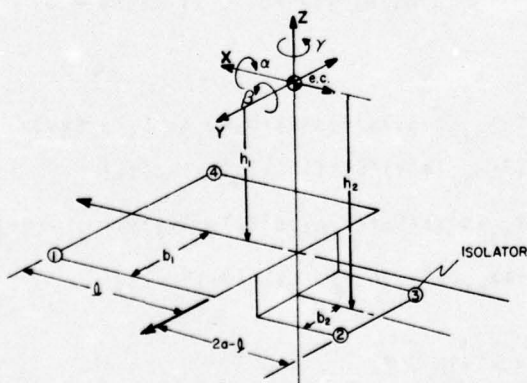

Fig.3 Isometric View of a Semi-Symmetric Body Showing the Position of the Isolators with Respect to the Elastic Center

Employing the above assumptions, the mass, damping, and stiffness matrices respectively are given by:

$$M = \begin{bmatrix} m & 0 & 0 & 0 & 0 & 0 \\ 0 & m & 0 & 0 & 0 & 0 \\ 0 & 0 & m & 0 & 0 & 0 \\ 0 & 0 & 0 & I_x & 0 & I_{xz} \\ 0 & 0 & 0 & 0 & I_y & 0 \\ 0 & 0 & 0 & I_{xz} & 0 & I_z \end{bmatrix}$$

(4a)

$$C = \begin{bmatrix} c_x & 0 & c_{xz} & 0 & c_{x\beta} & 0 \\ 0 & c_y & 0 & c_{y\alpha} & 0 & c_{y\gamma} \\ c_{xz} & 0 & c_z & 0 & c_{z\beta} & 0 \\ 0 & c_{y\alpha} & 0 & c_\alpha & 0 & c_{\alpha\gamma} \\ c_{x\beta} & 0 & c_{z\beta} & 0 & c_\beta & 0 \\ 0 & c_{y\gamma} & 0 & c_{\alpha\gamma} & 0 & c_\gamma \end{bmatrix};$$

(4b)

$$K = \begin{bmatrix} k_x & 0 & k_{xz} & 0 & k_{x\beta} & 0 \\ 0 & k_y & 0 & k_{y\alpha} & 0 & k_{y\gamma} \\ k_{xz} & 0 & k_z & 0 & k_{z\beta} & 0 \\ 0 & k_{y\alpha} & 0 & k_\alpha & 0 & k_{\alpha\gamma} \\ k_{x\beta} & 0 & k_{z\beta} & 0 & k_\beta & 0 \\ 0 & k_{y\gamma} & 0 & k_{\alpha\gamma} & 0 & k_\gamma \end{bmatrix}.$$

(4c)

The components of the stiffness matrix along with a sketch of their development is provided in the Appendix. The zeros in the stiffness and damping matrices are a consequence of the symmetry about the X-Z plane. Symmetry is also responsible for the fact that the products of inertia I_{xy} and I_{yz} are equal to zero.

FOCALIZATION

As mentioned in the introduction, the principles of focaiization are adequately recorded in the literature and, therefore, will not be repeated here.

Basically, to statically decouple the fore-aft, lateral, and vertical motions from roll, pitch and yaw, the submatrix

$$\begin{bmatrix} 0 & k_{x\beta} & 0 \\ k_{y\alpha} & 0 & k_{y\gamma} \\ 0 & k_{z\beta} & 0 \end{bmatrix}$$

(5)

of the stiffness matrix must be made identically zero; that is,

$$k_{x\beta} = k_{y\alpha} = k_{y\gamma} = k_{z\beta} = 0.$$

In most cases, "identically" zero is an impossibility and in the light of practical parameter identification "approximately" zero is sufficient. As derived in the Appendix, these terms are given by:

$$k_{x\beta} =$$

$$-2h_1 \, k_{s_1}[c^2\gamma_1(L_1+(1-L_1)c^2\theta_1)+s^2\gamma_1]*$$

$$-2h_2 \, k_{s_2}[c^2\gamma_2(L_2+(1-L_2)c^2\theta_2)+s^2\gamma_2]$$

$$-\ell\{k_{s_1}(1-L_1)s2\theta_1 c\gamma_1 - k_{s_2}(1-L_2)s2\theta_2 c\gamma_2\} \quad (6a)$$

$$-2ak_{s_2}(1-L_2)s2\theta_2 c\gamma_2$$

$$k_{y\alpha} =$$

$$2h_1 k_{s_1}[s^2\gamma_1(L_1+(1-L_1)c^2\theta_1) + c^2\gamma_1]$$

$$+2h_2 k_{s_2}[s^2\gamma_2(L_2+(1-L_2)c^2\gamma_2) + c^2\gamma_2] \quad (6b)$$

$$+b_1 k_{s_1}(1-L_1)s2\theta_1 s\gamma_1+b_2 k_{s_2}(1-L_2)s\gamma_2 s2\theta_2$$

$$k_{y\gamma} =$$

$$+b_1 k_{s_1}(1-L_1)s^2\theta_1 s2\gamma_1 - b_2 k_{s_2}(1-L_2)s^2\theta_2 s2\gamma_2$$

$$+2\ell\{k_{s_1}[s^2\gamma_1(L_1+(1-L_1)c^2\theta_1)+c^2\gamma_1]$$

$$+k_{s_2}[s^2\gamma_2(L_2+(1-L_2)c^2\theta_2)+c^2\gamma_2]\} \quad (6c)$$

$$-4ak_{s_2}[s^2\gamma_2(L_2+(1-L_2)c^2\theta_2)+c^2\gamma_2]$$

$$*s = \sin$$
$$\ c = \cos$$

256

$$k_{z\beta} =$$

$$-2h_1 k_{s_1}(1-L_1)s\theta_1 c\theta_1 c\gamma_1 + 2h_2 k_{s_2}(1-L_2)s\theta_2 c\theta_2 c\gamma_2$$

$$-2\ell\{k_{s_1}(L_1+(1-L_1)s^2\theta_1) + k_{s_2}(L_2+(1-L_2)s^2\theta_2)\}$$

$$+4ak_{s_2}(L_2+(1-L_2)s^2\theta_2) \qquad (6d)$$

Dynamic coupling, on the other hand, must also consider inertia and damping coupling. If the arbitrary point is taken as the center of gravity, the system is automatically inertia decoupled. The mass matrix expressed by equation (4a) and referenced hereafter in this paper reflects this situation. The coupling due to viscous damping will be assumed small or of the form $C = vM+wK$ so that it decouples simultaneously with the mass and stiffness matrices. In the case of hysteretic damping represented by a loss factor, η, damping can be modeled as the imaginary part of a complex stiffness[9],

$$k^* = k(1+j\eta). \qquad (7)$$

If the isolators are made of the same material, the damping matrix is given by $j\eta K$ and the damping forces again decouple simultaneously with the stiffness matrix. As a consequence of these assumptions, static and dynamic coupling are equivalent.

SOLUTION METHOD

The solution method is one of constrained minimization. Essentially, the constraints are combined with an objective function through a penalty function in the following manner:

$$h(\vec{\omega}) = f(\vec{\omega}) - P \; \Sigma \frac{1}{g_i(\vec{\omega})} \qquad (8)$$

where

$f(\vec{\omega})$ is the objective function.

$g_i(\vec{\omega}) < 0$ is an inequality constraint.

and

$\vec{\omega}$ is the vector of design parameters.

$h(\vec{\omega})$ is then minimized as an unconstrained objective function for an arbitrary positive value of P, which is sequentially reduced until $h(\vec{\omega}) \approx f(\vec{\omega})$. Details of this method referred to as the sequence of unconstrained minimizations technique as developed by Fiacco and McCormick can be found in references [5] and [10].

For the focalization problem, an objective function is formed as the sum of squares of the four non-zero coupling terms; that is,

$$\text{obj. function} = k_{x\beta}^2 + k_{y\alpha}^2 + k_{y\gamma}^2 + k_{z\beta}^2, (9)$$

which can be minimized with respect to an arbitrary subset of the following eight parameters: θ_1, θ_2, γ_1, γ_2, k_{s_1}, k_{s_2}, L_1 and L_2. Upper and lower bounds can be placed on these parameters as well as the natural frequencies of the system. By observing equations (6), it can be seen that when natural frequencies are not constrained, k_{s_2} can be factored from all four coupling terms. The optimum design, then, is only dependent on the ratio of shear spring rates, $R = k_{s_1}/k_{s_2}$, and not the values of k_{s_1} and k_{s_2}. The design parameters are reduced to the following seven: θ_1, θ_2, γ_1, γ_2, L_1, L_2, R. Similarly, the inertia properties of the system are not essential to the optimization unless frequency constraints are imposed.

The above constrained minimization problem is, then, submitted to an efficient computer program, called CONMIN, for solution. CONMIN is available from CHI Corp. in Cleveland, Ohio, although any equally efficient program utilizing the sequence of unconstrained minimization technique would suffice.

In some cases, the broad generality of the focalized system as presented may not be desirable or necessary, particularly in cases where the c.g. is only slightly off-center. Certainly the more symmetric the system, the more preferable the solution from both cost and manufacturability points of view. Therefore, equalities such as:

257

CONDITION	EQUALITIES
All isolators alike	$k_{s_1} = k_{s_2}$; $L_1 = L_2$
Equal toe-in angles	$\gamma_1 = \gamma_2$
Equal elevation angles	$\theta_1 = \theta_2$

or any design variable equal to a constant can be readily incorporated into the program by modifying the objective function, equation (9).

NATURAL FREQUENCY CONSTRAINTS

The natural frequencies are derived in closed form by assuming that minimization of the objective function has already been effected; that is, $k_{x\beta} = k_{y\alpha} = k_{y\gamma} = k_{z\beta} = 0$. In view of this assumption, the natural frequencies are given in Table 1.

For an arbitrary set of parameters, these equations do not truly represent the natural frequencies of the system. However, as the optimization progresses, they become more representative.

Constraining the predominant fore-aft mode is not immediately clear as it is coupled to the vertical, in which case it may be associated with either/or $\pm \sqrt{--}$ (see Table 1). A similar situation exists for roll-yaw coupling. To overcome this difficulty, two-dimensional eigenvectors are utilized as an identification vehicle in the following manner:

$$\begin{Bmatrix} x_{fa} \\ x_v \end{Bmatrix} = \begin{Bmatrix} 1 \\ \dfrac{-k_{xz}/m}{k_z/m - (2\pi f_+)^2} \end{Bmatrix} \quad (10a)$$

Fore-Aft & Vertical

$$\begin{Bmatrix} x_\alpha \\ x_\gamma \end{Bmatrix} = \begin{Bmatrix} 1 \\ \dfrac{-(I_x k_{\alpha\gamma} - I_{xz} k_\alpha)/D}{(I_x k_\gamma - I_{xz} k_{\alpha\gamma})/D - (2\pi f_+)^2} \end{Bmatrix} \quad (10b)$$

Roll & Yaw

TABLE 1

Natural Frequencies of a Decoupled System

Mode	Freq. (Hz)
Lateral	$\dfrac{1}{2\pi} \sqrt{k_y/m}$
Pitch	$\dfrac{1}{2\pi} \sqrt{k_\beta/I_y}$
Fore-Aft & Vertical	$\dfrac{1}{2\pi} \left(\left(\dfrac{k_x + k_z}{2m} \right) \pm \sqrt{\left(\dfrac{k_x - k_z}{2m} \right)^2 + (k_{xz}/m)^2} \right)^{\frac{1}{2}}$
Roll & Yaw	$\dfrac{1}{2\pi} \left(\left(\dfrac{I_z k_\alpha - 2 I_{xz} k_{\alpha\gamma} + I_x k_\gamma}{2D} \right) \pm \sqrt{\left(\dfrac{I_z k_\alpha - I_x k_\gamma}{2D} \right)^2 + \dfrac{1}{D^2} (I_x k_{\alpha\gamma} - I_{xz} k_\alpha)(I_z k_{\alpha\gamma} - I_{xz} k_\gamma)} \right)^{\frac{1}{2}}$ where $D = I_x I_z - I_{xz}^2$

TABLE 2
Geometry and Inertia Data of Five Sample Problems

SYSTEM	GEOMETRY						INERTIA				
	a	ℓ	b_1	b_2	h_1	h_2	m	I_x	I_y	I_z	I_{xz}
1,2,3,4	17.64	16.41	20.21	20.21	21.41	25.29	4.352	3161.	3719.	3139.	0
5	20.0	-4.0	10.0	10.0	15.0	15.0	-	-	-	-	-

where f_+ represents the frequency associated with the $+\sqrt{--}$ for fore-aft & vertical and roll & yaw coupling respectively.

The following inequalities establish the predominant mode. If $|x_V|<1$, f_+ is predominantly a fore-aft mode; otherwise, it is a vertical mode.

Similarly, if $|x_\gamma|<1$, f_+ is predominantly a roll mode; otherwise, it is a yaw mode.

Constraints in general must be approached with caution, for constraining system parameters has the advantage of producing a system which can be practically manufactured, but has the disadvantage of providing a lesser degree of focalization and, in some cases, no solution.

EXAMPLES

The following five systems are intended to demonstrate the broad application of the unconstrained minimization approach to focalization. Table 2 contains geometry and inertia information of the five systems being investigated. Systems 1, 2, 3, and 4 are the same with the exception for constraints which are given in Table 3. System 5 places the c.g. 4 inches outside of the isolator pattern.

Submitting these five systems for solution yielded the design variables found in Table 4.

Evaluating the stiffness matrices for the optimum design variables as presented in Table 5 demonstrates that although the coupling terms are not "zero", they are small relative to the diagonal elements, indicative of a decoupled system. A more meaningful measure of the degree of decoupling will be discussed later.

TABLE 3

Constraints Placed on Sample Problems

System	Constraints
1	Unconstrained
2	R = 1 (all isolators alike) $L_1 = L_2$
3	R = 1 $L_1 = L_2 \leq 10$
4	$36 < f(\text{fore-aft}) < 100$ (Hz) $36 < f(\text{lateral}) < 100$ $1000 < k_{s_1} < 10,000$ $1000 < k_{s_2} < 10,000$
5	Unconstrained

TABLE 4

Optimum Designs of Sample Problems

SYSTEM	STARTING VALUE									OPTIMUM DESIGN VARIABLES								
	θ_1^o	θ_2^o	γ_1^o	γ_2^o	k_{s_1}	k_{s_2}	R	L_1	L_2	θ_1^o	θ_2^o	γ_1^o	γ_2^o	k_{s_1}	k_{s_2}	$R=k_{s_1}/k_{s_2}$	L_1	L_2
1	45	45	50	50	-	-	1.0	10.	10.	43.92	39.33	51.25	56.88	3617.*	1000.*	3.617	13.2	27.8
2	45	45	50	50	-	-	1.0	10.	10.	45.75	43.85	52.73	48.34	1000.*	1000.*	1.0	26.35	26.35
3	45	45	50	50	-	-	1.0	5.	5.	20.80	20.40	44.94	23.84	1000.*	1000.*	1.0	9.38	9.38
4	43.92	39.33	51.25	56.88	1200	4320	.28	13.2	27.8	47.69	46.96	52.46	47.03	2700.	4408.	.613	56.43	121.76
5	30	30	100	60	-	-	1.0	5.	5.	35.6	46.72	119.0	35.3	5470.*	1000.*	5.47	68.93	16.83

*Not necessary for optimization

TABLE 5

Non-Zero Stiffness Terms of Sample Problems Using
The Optimum Design Variables

System	k_x	k_y	k_z	k_{xz}	k_α	k_β	k_γ	$k_{\alpha\gamma}$	$k_{x\beta}$	$k_{y\alpha}$	$k_{y\alpha}$	$k_{z\beta}$
1	.323	.502	.871	-.132	94.1	96.4	69.2	19.2	-.0035	.0058	.0001	.0059
2	.243	.341	.551	.015	41.2	38.8	29.1	-.027	0	-.0043	-.0001	.0012
3	.068	.054	.333	.011	108.	66.6	31.4	-10.1	-.0007	.0028	-.0004	.0006
4	3.39	4.22	6.46	2.71	143.	134.	105.	-24.7	-.0136	.0137	-.0047	-.0065
5	.833	2.11	5.19	1.83	43.9	270.	108.	-20.4	-.0004	-.0006	-.019	.0034

NOTE: All stiffness values to be taken times 10^5.

MULTIPLE SOLUTIONS

The existence of multiple solutions can most easily be demonstrated by analyzing the system having a rectangular isolator pattern with a centrally located c.g. per Figure 1. The simplifying assumptions: $k_{s_1}=k_{s_2}$; $L_1=L_2$, $\theta_1=\theta_2$, $\gamma_1=\gamma_2$, $h_1=h_2$, $b_1=b_2$, $\ell=a$, reduce the number of coupling terms from four to two, $k_{x\beta}$ and $k_{y\alpha}$, given by

$$k_{x\beta} = -4hk_{s_1}[\cos^2\gamma(L+(1-L)\cos^2\theta)$$
$$+\sin^2\gamma]-2ak_{s_1}(1-L)\sin2\theta\cos\gamma \tag{11}$$

$$k_{y\alpha} = 4hk_{s_1}[\sin^2\gamma(L+(1-L)\cos^2\theta)$$
$$+\cos^2\gamma]+2bk_{s_1}(1-L)\sin2\theta\sin\gamma \tag{12}$$

When equated to zero and combined to eliminate h/b, they can be written equivalently as:

$$a/b = \frac{\tan\gamma(C+\tan^2\gamma)}{1 + C\tan^2\gamma} \ , \tag{13}$$

where $\qquad C = 1+(L-1)\sin^2\theta$.

$$h/b = \frac{\frac{1}{2}(L-1)\sin2\theta\sin\gamma}{C\sin^2\gamma+\cos^2\gamma} \ . \tag{14}$$

Plots of γ versus θ are presented in Figure 5 for L = 5, 10, 20, 30, 50, 100; a/b = 1.0, 1.25, 1.5, 1.75, 2.0, 3.0; and h/b = .1, .25, .5, .75, 1.0, 2.0. Clearly a plethora of solution exists for most pairs of a/b and h/b. For demonstration purposes, the solutions for a/b = 1.25 and h/b = .5 are circled.
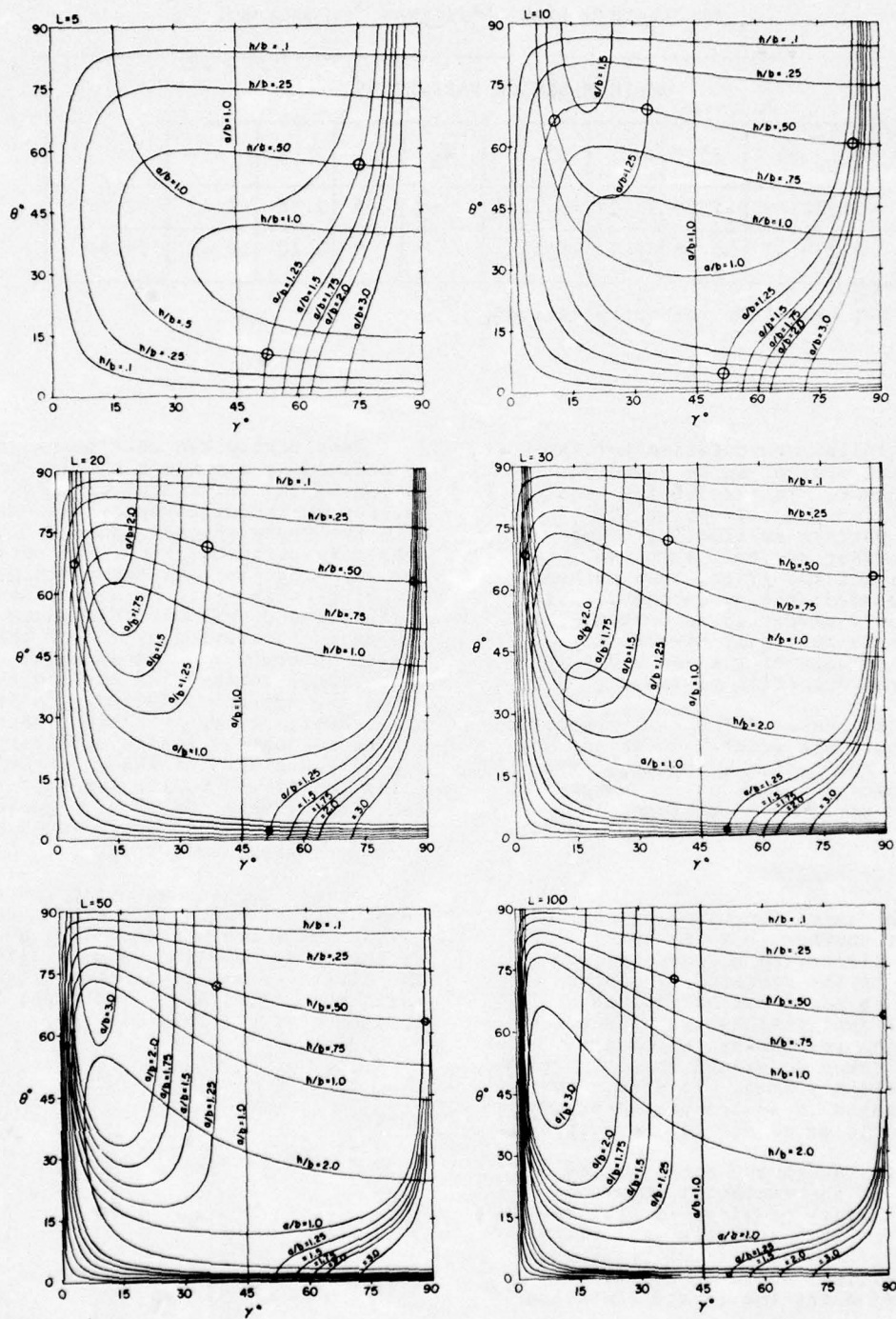
260

Fig.5 Focalization for Systems having a Rectangular Isolator Pattern and a Centrally Located C.G.

261

TABLE 6

Alternate Optimum Solutions for System 1

SOLU-TION	OPTIMUM DESIGN PARAMETERS								
	θ_1°	θ_2°	γ_1°	γ_2°	k_{S_1}	k_{S_2}	R	L_1	L_2
1	22.69	28.26	22.24	46.33	-*	-*	1.58	7.82	12.07
2	40.07	36.58	67.47	87.65	-*	-*	2.20	17.63	19.96

*Not necessary for optimization

A similar presentation for the symmetrical system can be found in Derby's paper. In fact, Derby uses solutions for the c.g. above the isolator pattern as starting values for the offset system. When the offset is not too great, this method is recommended; but, when the c.g. is dramatically offset as in System 5, it is better to initially direct the compression axis of the isolators in the general direction of the c.g.

In the case of the semi-symmetric system, multiple solutions are not so obvious. For System 1, however, two equally useful solutions to the one presented earlier can be found in Table 6.

SENSITIVITY ANALYSIS

The reason for choosing one solution over another, barring some physical limitation or personal preference, is the sensitivity of the solution to parameter variations. Practical applications are affected by fabrication tolerances, which are closely linked to system cost; therefore, if an optimum solution is sensitive to small changes in system parameters, it is of little or no use to the designer.

Even though the spring rates and L-values of the isolators impact on the sensitivity problem, it will be assumed for this analysis that their variation from the optimum requirement is negligible. Instead, emphasis will be placed on the toe-in and elevation angles.

Sensitivity can most meaningfully be defined as a measure of the participation of the rotational degrees of freedom in the eigenvectors associated with the translational modes for an arbitrary perturbation of the optimum design. The limit of the perturbation, Δ, being established by normal manufacturing and assembly tolerances. The parameterization of $+\Delta$ for the angles generate at most an eight dimensional rectangular enclosure about the optimum solution. Instead of an arbitrary perturbation, sensitivity can be adequately tested utilizing the 256 (2^8) "points" of the rectangular solid identified by the set {opt $+\Delta$}. Calculating this number of eigenvalue/vector solutions, however, would be time consuming and costly.

A less desirable, but physically meaningful approach is a static one in which unit forces in the x, y, and z direction are applied sequentially to the stiffness matrix of the design variation Δ (let $\Delta \equiv 0$ represent the optimum design); that is,

$$K(\Delta) \; \vec{x}_i^\Delta \; = \vec{B}_i \quad i = 1, 2, 3 \quad (15)$$

where

$$\vec{x}_i^\Delta = (x_i^\Delta, \; y_i^\Delta, \; z_i^\Delta, \; \alpha_i^\Delta, \; \beta_i^\Delta, \; \gamma_i^\Delta)$$

and
$$\vec{B}_1 = \begin{Bmatrix} 1 \\ 0 \\ 0 \\ 0 \\ 0 \\ 0 \end{Bmatrix}; \quad \vec{B}_2 = \begin{Bmatrix} 0 \\ 1 \\ 0 \\ 0 \\ 0 \\ 0 \end{Bmatrix}; \quad \vec{B}_3 = \begin{Bmatrix} 0 \\ 0 \\ 1 \\ 0 \\ 0 \\ 0 \end{Bmatrix}$$

262

The maximum fore-aft, lateral, vertical, roll, pitch, and yaw for the design variation Δ, independent of the sign of the force, are given by the absolute value of the sums,

$$x_\Delta = \sum_{i=1}^{3} \mid x_i^\Delta \mid , \quad \alpha_\Delta = \sum_{i=1}^{3} \mid \alpha_i^\Delta \mid ,$$

$$y_\Delta = \sum_{i=1}^{3} \mid y_i^\Delta \mid , \quad \beta_\Delta = \sum_{i=1}^{3} \mid \beta_i^\Delta \mid ,$$

$$z_\Delta = \sum_{i=1}^{3} \mid z_i^\Delta \mid , \quad \gamma_\Delta = \sum_{i=1}^{3} \mid \gamma_i^\Delta \mid .$$

$$\tag{16}$$

These values together with the geometry of the suspended body provide a measure of the "goodness" of the design. Imagine a rectangular solid with sides of length 2a, 2b, and 2c located symmetrically about the c.g. of the system as depicted on Figure 6. The dimensions of the box being established by a mounting location, an overhang or some other critical element of the system.
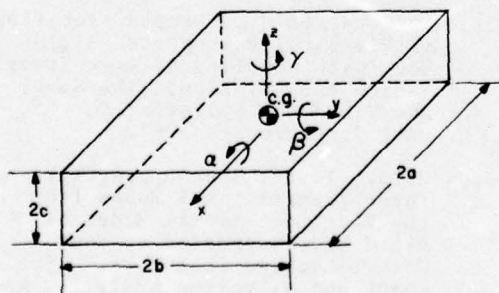
The maximum displacement in the x-direction due to rotations occurs at the point(s) ($+a$, $-b$, c), given by $c\beta+b\gamma$. By forming a ratio of this quantity to pure translation in the x-direction, a measure of the "goodness" of the optimum design can be defined as:

$$M_x^o \equiv \frac{c\beta_o + b\gamma_o}{x_o} ,$$

Likewise, for the y and z directions,

$$M_y^o \equiv \frac{c\beta_o + a\gamma_o}{y_o} ,$$

$$M_z^o \equiv \frac{b\alpha_o + a\beta_o}{z_o} . \tag{17}$$

Similarly, by finding the maximum values of the above defined ratio over the perturbation set {opt $\pm\Delta$}, given by

$$M_x^\Delta \equiv \max_{\{opt \pm \Delta\}} \frac{c\beta_\Delta + b\gamma_\Delta}{x_\Delta} ,$$

$$M_y^\Delta \equiv \max_{\{opt \pm \Delta\}} \frac{c\alpha_\Delta + a\gamma_\Delta}{y_\Delta} ,$$

$$M_z^\Delta \equiv \max_{\{opt \pm \Delta\}} \frac{b\alpha_\Delta + a\beta_\Delta}{z_\Delta} , \tag{18}$$

and comparing them with those of the optimum design a measure of the sensitivity of the optimum design to parameter variations is obtained. It should be understood, of course that M_x^Δ, M_y^Δ, and M_z^Δ are worst cases for they assume all motion due to rotation is cumulative.

The five systems described in Table 2, for which optimum designs have already been calculated, were subjected to the above sensitivity analysis for Δ's of $+2°$ and $+5°$. The results are presented in Table 7. In all cases, it can be seen that the optimum design truly decouples the system. In none of the systems does the motion due to rotation achieve 1% of that due to pure translation at the isolator

Fig.6 Imaginary Box Positioned About the Center of Gravity of the Suspended Item

TABLE 7

Sensitivity of Sample Problems to Parameter Variations

SYSTEM	a	b	c	M_x^{opt}	M_y^{opt}	M_z^{opt}	$\Delta = \pm 2°$			$\Delta = \pm 5°$		
							M_x^{Δ}	M_y^{Δ}	M_z^{Δ}	M_x^{Δ}	M_y^{Δ}	M_z^{Δ}
1	17.64	20.21	25.29	.001	.002	.003	.314	.719	.586	.875	1.95	1.36
2	17.64	20.21	25.29	.0005	.003	.004	.743	1.05	1.16	1.98	2.67	2.61
3	17.64	20.21	25.29	.0004	.0007	.004	.087	.062	.229	.244	.150	.564
4	17.64	20.21	25.29	.002	.003	.003	1.68	4.42	1.90	3.79	6.60	4.07
5	20.	10.	15.	.0002	.0055	.0006	.046	1.96	.212	.126	3.77	.601

locations. However, a relatively small variation in the direction angles causes a dramatic increase in M_x^{Δ}, M_y^{Δ}, and M_z^{Δ}. Sensitivity increases in the first four systems, which differ only in constraints, as a function of increasing L-values. Physically, this observation is not unexpected. It is prudent, therefore, on the designer's part to limit the L-value when and if possible. This limitation creates no problem for most systems in which frequency constraints are omitted.

The effect of tolerances on the natural frequencies should also be considered, especially if they are critical. In this case, the natural frequencies of the three "worst" case systems derived above or a cumulative "worst" system given by:

$$\max_{\{opt \pm \Delta\}} \sum_{i=1}^{3} (M_i^{\Delta})^2 \qquad i = x, y, z$$

$$(19)$$

can be calculated and compared with the constraints.

CONCLUSIONS

The sequential unconstrained minimization method applied to the focalization of rigid bodies suspended on isolators offers the designer flexibility heretofore unavailable. By constraining system parameters and, if necessary, the natural frequencies of the system, a physically realizable, optimal system can usually be obtained. Furthermore, two isolator sets, having different lateral spreads

and elevations permit the designer to take advantage of structurally available attachment locations. However, the application of constraints must be approached judiciously to avoid a "no solution" situation or one which is sensitive to parameter variations.

The sensitivity analysis as reported in this paper is not intended to be a complete study. However, its inclusion serves to point out that in many real systems, focalization can only be realized by exacting and often expensive fabrication tolerances.

REFERENCES

1. Andrews, G. J., "Vibration Isolation of a Rigid Body on Resilient Supports", The Journal of the Acoustical Society of America, Vol. 32, Number 8, August, 1960.

2. Collopy, F. H., "Damped Vibrations of Elastically Supported Rigid Body with Coupling Between Translation and Rotation," The Shock and Vibration Bulletin, No. 36, Part 7, February, 1967.

3. Derby, T. F., "Decoupling the Three Translational Modes From the Three Rotational Modes of a Rigid Body Supported by Four Corner-Located Isolators," The Shock and Vibration Bulletin, No. 4, Part 4, June, 1973.

4. Feinberg, Melvin, "Rigid Body Dynamics - Stable Platform Isolation Systems", AIAA Guidance and Control Conference, August, 1963.

5. Fox, R. L., "Optimization Methods for Engineering Design," Addison-Wesley, 1971.

6. Himelblau, H. Jr. and Rubin, S., "Vibrations of a Resiliently Supported Rigid Body," Shock and Vibration Handbook, Edited by C. M. Harris and C. E. Crede, Vol. 1, Chapter 3, McGraw-Hill, New York, 1961.

7. Pechter, L. S. and Kamei, H., "Design of Focalized Suspension Systems, Shock and Vibration Bulletin, No. 34, Part 3, December, 1964.

8. Smollen, L. E., "Generalized Matrix Methods for the Design and Analysis of Vibration-Isolation Systems," The Journal of the Acoustical Society of America, Volume 40, No. 1, 1966.

9. Snowdon, J. C., "Vibration and Shock in Damped Mechanical Systems," John Wiley and Sons, 1968.

10. Fiacco, A. V. and McCormick, G. P., "Nonlinear Programming: Sequential Unconstrained Minimization Techniques," Wiley, 1968.

APPENDIX

The stiffness matrix derived in this section is for a rigid body having one plane of symmetry and suspended on four isolators as shown on Figure 2. The arbitrary point about which the stiffness matrix is derived can be anywhere in the symmetric plane. References [4], [6], and [8] provide the foundation for this development.

The reactive forces, $\vec{Q}_i$, along the principal axes of the ith axisymmetric isolator per Figure 4 can be represented by the equation:

$$\vec{Q}_i = -\begin{bmatrix} k_{si} & 0 & 0 \\ 0 & k_{si} & 0 \\ 0 & 0 & k_{ci} \end{bmatrix} \vec{x}_i' = -K_i \vec{x}_i' \qquad (1)$$

where $\vec{x}_i'$ is the translatory motion of the isolator's elastic center along its principal axes.

The force applied to the body in terms of the arbitrary point and its corresponding motion, assuming small angles, is defined by:

$$\vec{F}_i = -T_i' K_i T_i \vec{x}_i \qquad (2)$$

where

$$\vec{x}_i = \underline{\vec{X}} - \vec{r}_i \times \underline{\vec{\phi}} \; ; \qquad (3)$$

$\vec{r}_i$ being given by (see Figure 3):

i	x	y	z
1	ℓ	b_1	$-h_1$
2	$\ell - 2a$	b_2	$-h_2$
3	$\ell - 2a$	$-b_2$	$-h_2$
4	ℓ	$-b_1$	$-h_1$

and the transformation T_i from the isolators' principal axes to the suspended body's coordinate system is given by:

$$T_i = \begin{bmatrix} c\theta_i \, c\gamma_i & -s\gamma_i & s\theta_i \, c\gamma_i \\ c\theta_i \, s\gamma_i & c\gamma_i & s\theta_i \, s\gamma_i \\ -s\theta_i & 0 & c\theta_i \end{bmatrix} \qquad (4)$$

$s = \sin$
$c = \cos$

where γ_i and θ_i are generalized rotations which are counterclockwise positive per Figure 7 and applied γ_i (about the Z-axis) before θ_i (about the Y'-axis). T_i' implies the transpose.
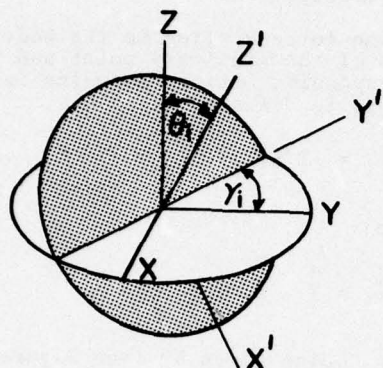
Fig.7 Generalized Rotations Which Define Isolator Orientations

For the four isolator's in question, γ_i and θ_i have the following signs:

Isolator	γ_i	θ_i
1	γ_1	$-\theta_1$
2	$-\gamma_2$	θ_2
3	γ_2	θ_2
4	$-\gamma_1$	$-\theta_1$

The total force applied to the suspended body through the isolators is given by:

$$\vec{F} = \sum_{i=1}^{4} \vec{F}_i = -\sum_{i=1}^{4} T_i' K_i T_i \vec{x}_i \ .$$

(5)

The moment about the arbitrary point is given by:

$$\vec{M} = \sum_{i=1}^{4} \vec{r}_i \times \vec{F}_i$$

(6)

Utilizing the definitions given above in the formulas (5) and (6) produces a stiffness matrix of the following form:

$$K = \begin{bmatrix} k_x & 0 & k_{xz} & 0 & k_{x\alpha} & 0 \\ 0 & k_y & 0 & k_{y\alpha} & 0 & k_{y\gamma} \\ k_{xz} & 0 & k_z & 0 & k_{z\beta} & 0 \\ 0 & k_{y\alpha} & 0 & k_\alpha & 0 & k_{\alpha\beta} \\ k_{x\alpha} & 0 & k_{z\beta} & 0 & k_\beta & 0 \\ 0 & k_{y\gamma} & 0 & k_{\alpha\beta} & 0 & k_\gamma \end{bmatrix}$$

(7)

whose elements are given by:

$$k_x = 2k_{s_1}\left[c^2\gamma_1(L_1+(1-L_1)c^2\theta_1)+s^2\gamma_1\right]+2k_{s_2}\left[c^2\gamma_2(L_2+(1-L_2)c^2\theta_2)+s^2\gamma_2\right] \tag{8}$$

$$k_{xz} = 2k_{s_1}(1-L_1)s\theta_1c\theta_1c\gamma_1-2k_{s_2}(1-L_2)s\theta_2c\theta_2c\gamma_2 \tag{9}$$

$$k_y = 2k_{s_1}\left[s^2\gamma_1(L_1+(1-L_1)c^2\theta_1)+2c^2\gamma_1\right]+k_{s_2}\left[s^2\gamma_2(L_2+(1-L_2)c^2\theta_2)+c^2\gamma_2\right] \tag{10}$$

$$k_z = 2k_{s_1}(L_1+(1-L_1)s^2\theta_1)+2k_{s_2}(L_2+(1-L_2)s^2\theta_2 \tag{11}$$

$$k_\alpha = 2h_1^2k_{s_1}\left[s^2\gamma_1(L_1+(1-L_1)c^2\theta_1)+c^2\gamma_1\right]+2b_1^2k_{s_1}(L_1+(1-L_1)s^2\theta_1 \tag{12}$$
$$+4b_1h_1k_{s_1}(1-L_2)s\theta_2c\theta_2s\gamma_2+2h_2^2k_{s_2}\left[s^2\gamma_2(L_2+(1-L_2)c^2\theta_2)+c^2\gamma_2\right]$$
$$+2b_2^2k_{s_2}(L_2+(1-L_2)s^2\theta_2)+4b_2h_2k_{s_2}(1-L_2)s\theta_2c\theta_2s\gamma_2$$

$$k_{\alpha\gamma} = 2b_1h_1k_{s_1}(1-L_1)s^2\theta_1s\gamma_1c\gamma_1-2b_1^2k_{s_1}(1-L_1)s\theta_1c\theta_1c\gamma_1 \tag{13}$$
$$+2\ell b_1k_{s_1}(1-L_1)s\theta_1c\theta_1s\gamma_1+2\ell h_1k_{s_1}\left[s^2\gamma_1(L_1+(1-L_1)c^2\theta_1)+c^2\gamma_1\right]$$
$$-2b_2h_2k_{s_2}(1-L_2)s^2\theta_2s\gamma_2c\gamma_2+2b_2^2k_{s_2}(1-L_2)s\theta_2c\theta_2c\gamma_2$$
$$-2(2a-\ell)b_2k_{s_2}(1-L_2)s\theta_2c\theta_2s\gamma_2$$
$$-2(2a-\ell)h_2k_{s_2}\left[s^2\gamma_2(L_2+(1-L_2)c^2\theta_2)+c^2\gamma_2\right]$$

$$k_\beta = 2h_1^2k_{s_1}\left[c^2\gamma_1(L_1+(1-L_1)c^2\theta_1)+s^2\gamma_1\right]+2\ell^2k_{s_1}(L_1+(1-L_1)s^2\theta_1) \tag{14}$$
$$+4\ell h_1k_{s_1}(1-L_1)s\theta_1c\theta_1c\gamma_1+2h_2^2k_{s_2}\left[c^2\gamma_2(L_2+(1-L_2)c^2\theta_2)+s^2\gamma_2\right]$$
$$+2(2a-\ell)^2k_{s_2}(L_2+(1-L_2)s^2\theta_2)+4(2a-\ell)h_2k_{s_2}(1-L_2)s\theta_2c\theta_2c\gamma_2$$

$$k_\gamma = 2\ell^2k_{s_1}\left[s^2\gamma_1(L_1+(1-L_1)c^2\theta_1)+c^2\gamma_1\right] \tag{15}$$
$$+2b_1k_{s_1}\left[c^2\gamma_1(L_1+(1-L_1)c^2\theta_1)+s^2\gamma_1\right]+4\ell b_1k_{s_1}(1-L_1)s^2\theta_1s\gamma_1c\gamma_1$$
$$+2(2a-\ell)^2k_{s_2}\left[s^2\gamma_2(L_2+(1-L_2)c^2\theta_2)+c^2\gamma_2\right]$$
$$+2b_2^2k_{s_2}\left[c^2\gamma_2(L_2+1+(1-L_2)c^2\theta_2)+s^2\gamma_2\right]+4(2a-\ell)b_2k_{s_2}(1-L_2)s^2\theta_2s\gamma_2c\gamma_2$$

where $s = \sin$
$c = \cos$

The terms $k_{x\beta}$, $k_{y\alpha}$, $k_{y\gamma}$ and $k_{z\beta}$ are given
by equation (6) in the text of the paper.

THE USE OF GENERAL PURPOSE COMPUTER PROGRAMS TO DERIVE EQUATIONS

OF MOTION FOR OPTIMAL ISOLATION STUDIES

W. D. Pilkey
Department of Engineering Science and Systems
University of Virginia
Charlottesville, Virginia 22901

Y. H. Chen
RCA/Astro-Electronics Division
P. O. Box 800
Princeton, New Jersey 08540

A. J. Kalinowski
Naval Underwater Systems Center
New London, Connecticut 06320

Techniques are developed which permit general purpose structural analysis computer programs to be used to generate the equations of motion necessary for limiting performance studies. The limiting performance characteristics of a system are useful in analyzing the optimal behavior of a dynamic system. In particular, the limiting performance characteristics are the essential ingredients in an efficient optimal design method for isolation systems.

INTRODUCTION

The use of conventional methods of optimal design has so far been limited to simple systems with few design parameters. This is primarily due to the overwhelming computational burdens of the methods which invariably require solving the system dynamics repeatedly. Recently a new approach that differs from the conventional methods in design methodology has been proposed and extensively explored (Reference 1, 2). The new approach, called the indirect synthesis method, selects the design parameters on the basis of a limiting performance study of the dynamic system being designed. In the process the system dynamics need be solved only once and thus the computational effort is greatly reduced. The method has been successfully applied to problems ranging from an infinite degree of freedom system with two design parameters (a beam) to a five degree of freedom system with six design parameters (an automobile model) (Reference 2). Frequently, only the limiting performance calculations are made for an isolation system as this provides useful information concerning the optimal system response. In particular, the limiting performance characteristics can be used as a yardstick for gauging the desirability of candidate system designs.

Several computer programs are now available for limiting performance studies. These are reviewed in Reference 3. Some of these programs, e.g., PERFORM (Reference 4) for transient systems and SYSLIPEC (Reference 5) for steady state systems, are virtually unlimited in terms of size and complexity of acceptable dynamic systems. PERFORM and SYSLIPEC are available through COSMIC as programs LAR-11930 and LAR-11931, respectively. The limiting performance computer programs usually require mass, stiffness, damping, and other characteristic matrices as input. The program then computes the limiting performance characteristics on the basis of this system information.

In view of the success as well as the extensive use of the finite element (FE) method in analyzing complex structures, it is important to develop the methodology necessary to couple available general purpose finite element structural programs to a limiting performance capability. This is the purpose of the work reported here. Once these general purpose programs can be used to develop input for a limiting

performance computer program, then the limiting performance and indirect synthesis can be applied to any system for which the general purpose FE program is appropriate.

Approaches for coupling general purpose programs to limiting performance capabilities will be considered. Primary emphasis is given to the use of the general purpose program to develop equations of motion in a form that can be used by the limiting performance program.

BACKGROUND

Consider a linear dynamic system whose equations of motion can be written in matrix form as

$$[M]\{\ddot{x}\} + [C]\{\dot{x}\} + [K]\{x\} = [F]\{\ddot{f}\} \quad (1)$$

where

{x} = displacement vector

[M] = N x N mass matrix, N being the number of degrees of freedom (DOF)

[C] = N x N damping matrix

[K] = N x N stiffness matrix

[F] = N x L coefficient matrix associated with the forcing function vector {f}, L being the number of forcing functions.

The optimal design problem is to choose portions of the system so that some index of performance is minimized (or maximized) and certain constraints are satisfied. It is assumed that both the performance index (ψ) and the constraint functions $C_k(x,t)$ on the response variables involve peak response variables, e.g., maximum stresses, displacements, accelerations. The performance index and the constraint functions can be written in the forms

$$\psi = \max_{r} \max_{t} |h_r|, \quad r = 1,2, \ldots R$$
$$C_k^L \leq C_k \leq C_k^U, \quad k = 1,2, \ldots K \quad (2)$$

where h_r's are the R response functions, and C_k^U, C_k^L are the prescribed upper and lower bounds of the kth constraint. We will restrict our consideration to cases wherein h_r and C_k are linear functions of the response (or state) variables.

The first step in using the indirect synthesis method is to calculate the limiting performance. Those portions of the system to be designed are replaced by generic (or control) forces {u(t)}, so that the equations of motion now become

$$[M]\{\ddot{x}\} + [C]\{\dot{x}\} + [\bar{K}]\{x\} + [V]\{u\}$$
$$= [F]\{\ddot{f}\} \quad (3)$$

where $[\bar{K}]$ is the new stiffness matrix, which omits any stiffness contributions from the design elements, and [V] is the N x J coefficient matrix associated with the generic forces {u}, J being the number of controllers. Such a general dynamical system is shown schematically in Figure 1. Two types of elements are considered; structural elements and isolator elements. There may be any number of each; in particular M structural elements and J isolator elements could be interconnected in an arbitrary fashion. A structural element may represent a discrete mass point, a rigid body of distributed mass, or a flexible structure such as a framework or a shell. The isolator elements, similarly, can represent either simple mechanisms without mass or models of more complicated devices. In general, the structural elements constitute the prescribed portions of the system (i.e., the base structure and the elements to be isolated) and the isolator elements are to be chosen in accordance with the design objectives. Note also that the control forces {u(t)}, being considered as explicit functions of time, do not contribute to the nonlinearity of the equations of motion even though they may have replaced nonlinear portions of the system, e.g., a nonlinear spring connection.

Once Equations (3) are established, and the performance index ψ and the constraints are placed in the form of Equations (2), then existing limiting performance capabilities can be used to obtain the limiting performance characteristics which are subsequently employed in selecting the design parameters.

As mentioned in Reference 1, the problem of establishing the coefficient matrices [M], [C], $[\bar{K}]$, [V], and [F] in Equation (3) for a particular dynamic system can be avoided by employing a general purpose dynamic program to generate impulse responses at isolator attachment points and then constructing h_r, C_k with Duhamel (convolution) integrals. That is, since
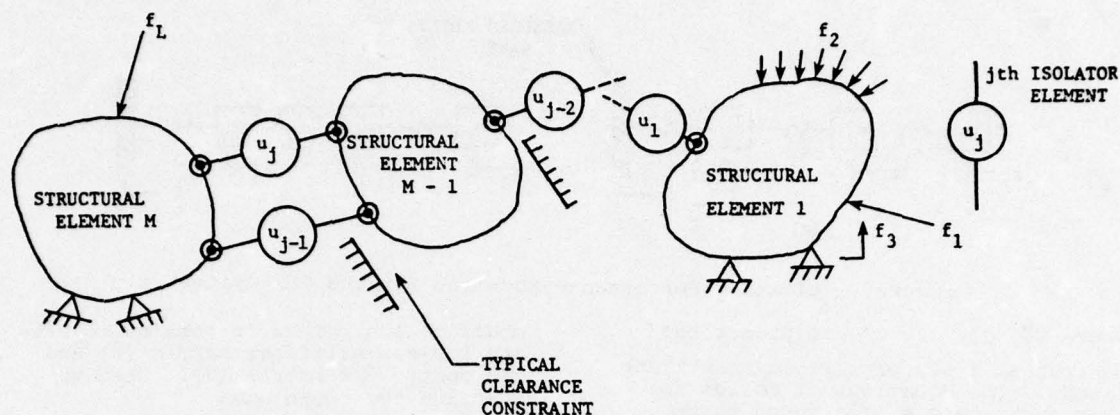
Figure 1 Structural Configuration for Determining Limiting Performance Characteristics

the system under consideration is linear, the response of the system excited by arbitrary forces u_j can be obtained by superimposing responses to unit impulses placed sequentially at each of the isolator attachment points, i.e.,

$$h_r(t) = h_{r0}(t) + \sum_{j=1}^{J} \int_0^t g_{rj}(t - \tau)u_j(\tau)d\tau$$

(4)

$$C_k(t) = C_{k0}(t) + \sum_{j=1}^{J} \int_0^t g_{kj}(t - \tau)u_j(\tau)d\tau$$

where g_{rj} and g_{kj} are the appropriate system responses to a unit impulse at the attachment point of the jth isolator, and $h_{ro}(t)$, $C_{k0}(t)$ are the responses to the L inputs $f_\ell(t)$. The g_{rj} and g_{kj} must be generated by the structural dynamics program. The advantage of this approach lies in the fact that an existing general-purpose structural dynamics code will be used to perform all of the system dynamics required for the limiting performance problem. However, in this work we are concerned with the situation whereby the system dynamics are to be solved by a limiting performance capability and not by the general purpose program. The general purpose program will be used to generate the coefficient matrices of Equations (3).

To illustrate the problems in-

volved in preparing the equations for a limiting performance solution, consider the simple example of a three degree of freedom spring-mass system as shown in Figure 2a. Let it be desired to select the spring constant k_2 such that the maximum acceleration transmitted to any mass is minimized while the three rattlespaces satisfy prescribed constraints. The k_1, k_3 spring rates remain at their prescribed values. For this example, the response functions that make up the performance index are

$$h_1 = \ddot{z}_1, \quad h_2 = \ddot{z}_2, \quad h_3 = \ddot{z}_3$$

and the constraint functions are

$$C_1 = z_1 - z_2,$$

$$C_2 = z_2 - z_3, \quad C_3 = z_3 - f$$

Therefore, Equations (2) become

$$\psi = \max_r \max_t |\ddot{z}_r|, \quad r = 1,2,3$$

or

$$\psi = \max\left[\max_t |\ddot{z}_1|, \max_t |\ddot{z}_2|, \max_t |\ddot{z}_3|\right]$$

$$c_1^L \leq |z_1 - z_2| \leq c_1^U$$

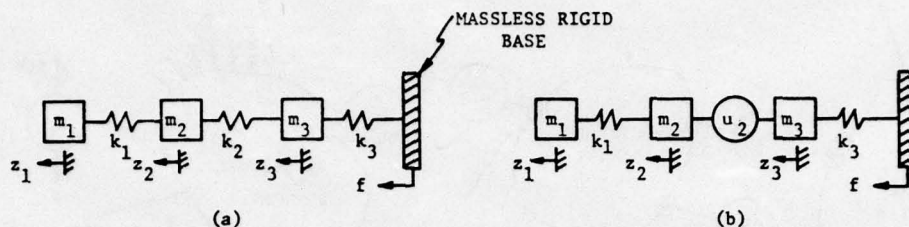$$c_2^L \leq |z_2 - z_3| \leq c_2^U$$

$$c_3^L \leq |z_3 - f| \leq c_3^U$$

271

MASSLESS RIGID BASE

(a)   (b)

Figure 2   Limiting Performance Modeling for a 3 DOF System

where C_1^L, C_1^U, ... C_3^U are prescribed constants, i.e., prescribed constraint bounds. The equations of motion for this system are easily found to be Equation (5) where $x_i = z_i - f$, $i = 1,2,3$.

modification. Thus it remains to create the new stiffness matrix $[\bar{K}]$ and the controller matrix $[V]$. Here we describe two techniques.

Technique 1

$$
\begin{bmatrix} m_1 & 0 & 0 \\ 0 & m_2 & 0 \\ 0 & 0 & m_3 \end{bmatrix} \begin{Bmatrix} \ddot{x}_1 \\ \ddot{x}_2 \\ \ddot{x}_3 \end{Bmatrix} + \begin{bmatrix} k_1 & -k_1 & 0 \\ -k_1 & k_1+k_2 & -k_2 \\ 0 & -k_2 & k_2+k_3 \end{bmatrix} \begin{Bmatrix} x_1 \\ x_2 \\ x_3 \end{Bmatrix} = - \begin{bmatrix} m_1 \\ m_2 \\ m_3 \end{bmatrix} \ddot{f} \tag{5}
$$

Now replace the middle spring by a generic force u_2 (Figure 2b). This results in a new set of equations.

The replacement of an isolator element k_i by a control force u_i amounts to substituting in the equation of mo-

$$
\begin{bmatrix} m_1 & 0 & 0 \\ 0 & m_2 & 0 \\ 0 & 0 & m_3 \end{bmatrix} \begin{Bmatrix} \ddot{x}_1 \\ \ddot{x}_2 \\ \ddot{x}_3 \end{Bmatrix} + \begin{bmatrix} k_1 & -k_1 & 0 \\ -k_1 & k_1 & 0 \\ 0 & 0 & k_3 \end{bmatrix} \begin{Bmatrix} x_1 \\ x_2 \\ x_3 \end{Bmatrix} + \begin{bmatrix} 0 \\ 1 \\ -1 \end{bmatrix} u_2 = - \begin{bmatrix} m_1 \\ m_2 \\ m_3 \end{bmatrix} \ddot{f} \tag{6}
$$

Equations (6) can be obtained either by applying the conditions of equilibrium to a configuration taken from Figure 2b or by directly making the substitution $u_2 = k_2(z_2 - z_3) = k_2(x_2 - x_3)$ in each row of Equation (5), which amounts to setting $k_2 = 0$ and taking the coefficients of k_2 in row 2 of the $[K]$ matrix as the column of the $[V]$ matrix. Obviously, the first approach becomes impractical when the system is complicated or when the system is being analyzed by FE codes since it contains unknown elements. In the following section, the second approach will be generalized and discussed further.

DEVELOPMENT OF THE EQUATIONS OF MOTION

As mentioned, in order to use most existing limiting performance computer capabilities, we must express the FE system equations of motion in the form of Equation (3) rather than in the usual FE form of Equation (1). Standard FE codes will always generate the mass matrix $[M]$, the damping matrix $[C]$, and the coefficient matrix $[F]$ which can be fed into the limiting performance codes with little or no

tion the relations

$$
u_i = k_i \sum a_j x_j \tag{7}
$$

where the summation is over the degrees of freedom that are connected with isolator k_i and the a_j's are the kinematical factors that are associated with each degree of freedom. This implies that isolator k_i no longer contributes to the assembly stiffness matrix and instead is replaced by an additional matrix $[V]$, whose individual columns consist of the coefficients of the term $k_i \sum a_j x_j$ in the equations of motion. With the aid of the element stiffness matrix written in assembly (global) coordinates, we can easily obtain the new stiffness matrix $[\bar{K}]$ and the controller matrix $[V]$ from $[K]$. From the node numbering scheme of a FE code, we know which elements of $[K]$ are contributed by isolator k_i so that the new stiffness matrix $[\bar{K}]$ is obtained by simply removing those contributions. In the FE program, set the spring elements to be optimized temporarily equal to zero and the desired $[\bar{K}]$ is produced by printing the

stiffness matrix. The controller matrix $[V]$ is formed by taking as its column the coefficients of k_i in a row (or column) of $[K]$, the row (or column) number being that of a degree of freedom which is enacted by the isolator.

Technique 2

Rewrite Equation (3) as

$$[M]\{\ddot{x}\} + [C]\{\dot{x}\} + [\bar{K}]\{x\}$$

$$= [F]\{\ddot{f}\} - [V]\{u\}$$

$$= [F]\{\ddot{f}\} - \begin{bmatrix} V_{11} & V_{12} & \cdots & V_{1J} \\ V_{21} & V_{22} & \cdots & V_{2J} \\ \vdots & & \vdots & \\ V_{N1} & V_{N2} & & V_{NJ} \end{bmatrix} \begin{Bmatrix} u_1 \\ u_2 \\ \vdots \\ u_J \end{Bmatrix}$$

$$= [F]\{\ddot{f}\} - \begin{Bmatrix} V_{11} \\ V_{21} \\ \vdots \\ V_{N1} \end{Bmatrix} u_1 - \begin{Bmatrix} V_{12} \\ V_{22} \\ \vdots \\ V_{N2} \end{Bmatrix} u_2 - \cdots - \begin{Bmatrix} V_{1J} \\ V_{2J} \\ \vdots \\ V_{NJ} \end{Bmatrix} u_J$$

$$\text{(8)}$$

The $[\bar{K}]$ is found as in technique 1. The columns of $[V]$ are obtained by noting that the elements of $[V]$ are simply the influence coefficients of the "loads" $\{u\}$. Thus to obtain the influence coefficients of a control force u_i (i.e., to obtain the ith column of $[V]$), set all u's equal to zero, save u_i which is set equal to 1 (Figure 3). The resulting load vector generated by FE program is the desired column. In practice, one must be careful to properly account for the constraints when generating the $[\bar{K}]$, $[V]$ matrices from a FE code, i.e. it is necessary to ascertain whether the matrices are printed before or after the displacement constraints have been applied to the problem.

Three Degree of Freedom System Example

Consider the problem of Figure 2 which was studied above. To treat a particular case, let $m_1 = 0.5$, $m_2 = 1.5$, $m_3 = 2.5$, $k_1 = 10$, $k_2 = 20$, $k_3 = 30$. Substitution of these values in Equation (5) gives

$$[M] = \begin{bmatrix} 0.5 & 0 & 0 \\ 0 & 1.5 & 0 \\ 0 & 0 & 2.5 \end{bmatrix},$$

$$[K] = \begin{bmatrix} 10 & -10 & 0 \\ -10 & 30 & -20 \\ 0 & -20 & 50 \end{bmatrix} \quad \text{(9)}$$

In terms of global coordinates the stiffness $[K_2]$ of the middle spring can be written as

$$[K_2] = \begin{bmatrix} 0 & 0 & 0 \\ 0 & 20 & -20 \\ 0 & -20 & 20 \end{bmatrix} \quad \text{(10)}$$

It follows from Equation (10) that the stiffness of the middle spring contributes to K_{22}, K_{23}, K_{32}, and K_{33}. Removing these contributions from $[K]$ of Equations (9) results in

$$[\bar{K}] = \begin{bmatrix} 10 & -10 & 0 \\ -10 & 10 & 0 \\ 0 & 0 & 30 \end{bmatrix} \quad \text{(11)}$$

and from the coefficients of elements in row 2 of $[K_2]$ we find

$$[V] = \begin{bmatrix} 0 \\ 1 \\ -1 \end{bmatrix}$$

which implies that $u = k_2(z_2 - z_3) = k_2(x_2 - x_3)$.

To generate the desired matrices $[M]$, $[\bar{K}]$, and $[V]$ with a general purpose program using the second technique, first compute $[M]$ as though a dynamics problem were to be run. Then run a static case to compute $[\bar{K}]$ and $[V]$ applying unit loads as shown in Figure 4.

PERFORMANCE INDEX AND CONSTRAINTS

Now that the equations of motion are in the proper form for a limiting performance study, we proceed to establish the performance index and constraints. Any linear combination of accelerations, velocities, displacements, or control forces can be used as a performance index or constraint function, i.e.

$$\{h\} \text{ or } \{C\} = [P]\{\ddot{x}\} + [Q]\{\dot{x}\} + [R]\{x\}$$

$$+ [S]\{u\} + [T]\{f\} \quad \text{(12)}$$

where $[P]$, $[Q]$, $[R]$, $[S]$ and $[T]$ are prescribed coefficient matrices.

The coefficient matrices in Equation (12) can be easily formed when using a FE code. For example, consider the discretized system shown in Figure 5. At each node, six degrees of freedom (DOF) (3 translational and 3 rotational) are specified. Suppose in Figure 5 that the accelerations along the y coordinate at node i and node j are to be constrained such that
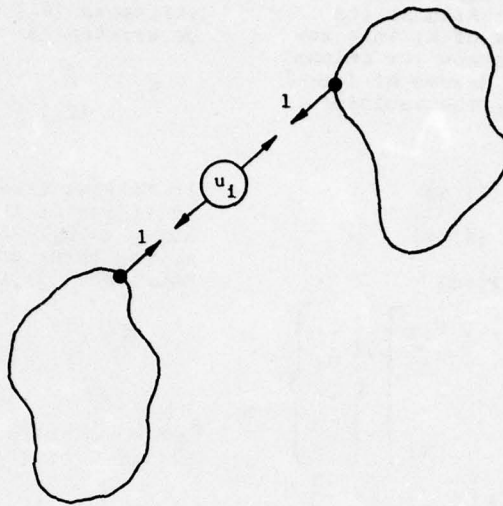
273

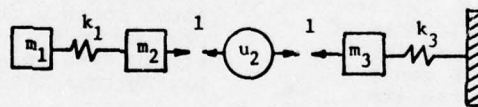Figure 3   Replacement of Generic Force by Unit Loads

Figure 4   Replacement of Generic Force by Unit Loads
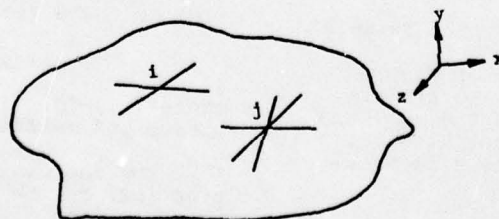for System of Figure 2

Figure 5   Configuration for Forming Constraints
and Performance Index

$$|a\ddot{y}_i + b\ddot{y}_j| \leq d \qquad (13)$$

where a, b, d are prescribed constants. To place the constraint function $a\ddot{y}_i + b\ddot{y}_j$ in the form of Equation (12), we need only input the node numbers, the nodal DOF, and the coefficients a, b, e.g., (i,2,a) and (j,2,b) where the 2 stands for the y degrees of freedom. In most general purpose FE codes, there is a printable connectivity array that identifies the nodal DOF to be constrained in terms of the independent assembly DOF. Suppose that (i,2) and (j,2) correspond to Ith and Jth assembly DOF. Then an appropriate kth row of the [P] matrix in Equation (12) will consist of the elements

$$P_{kI} = a, P_{kJ} = b, \text{ k being the row number}$$

$$P_{k\ell} = 0 \text{ for all } \ell \neq I, J. \qquad (14)$$

For this example the elements of the kth row of the matrices [Q], [R], [S], [T] are all zero since the constraint function of Equation (13) contains only accelerations. Similar reasoning permits Equation (12) to be formed for any acceptable type of performance index and constraint function.

Although we have chosen to describe a dynamic system by second order differential equations, Equations (3), some limiting performance programs work with first order differential equations. The second order equations are converted into a set of 2N first order linear differential equations

$$\{\dot{s}\} = [A]\{s\} + [B]\{\bar{u}\} + [D]\{\bar{f}\} \quad (15)$$

where

$$\{s\} = \begin{Bmatrix} \{\dot{x}\} \\ \{x\} \end{Bmatrix}$$

is a state vector with 2N components, and the coefficient matrices [A], [B], [D] are determined as functions of the coefficient matrices of Equation (3). Also, instead of Equation (12), the performance index and constraints are input to the limiting performance programs in the form

$$\{h\} \text{or} \{C\} = [E]\{s\} + [G]\{u\} + [H]\{f\}$$
$$(16)$$

where [E], [G], and [H] are prescribed coefficient matrices. Although the formation of Equation (15) using Equation (3) is a familiar manipulation, it is useful to consider in detail how Equation (16) is obtained from Equation

(12). This is accomplished by solving Equation (3) for $\{\ddot{x}\}$ and placing the result in Equation (12) to give

$$\{h\} \text{or} \{C\} = ([Q] - [P][M]^{-1}[C])\{\dot{x}\}$$

$$+ ([R] - [P][M]^{-1}[\bar{K}])\{x\}$$

$$+ ([S] - [P][M]^{-1}[V])\{u\}$$

$$+ ([T] + [P][M]^{-1}[F])\{f\}$$

$$(17)$$

A comparison of Equation (15) with Equation (17) shows that

$$[E] = \left[[Q]-[P][M]^{-1}[C] \quad [R]-[P][M]^{-1}[\bar{K}] \right]$$

$$[G] = [S] - [P][M]^{-1}[V]$$

and $\qquad (18)$

$$[H] = [T] + [P][M]^{-1}[F]$$

CLOSURE

The techniques have been established whereby a general purpose structural analysis program can be used to form the equations required for some available limiting performance programs. These techniques would permit a limiting performance study to be conducted on an arbitrary structural or mechanical system, which normally would involve finite element modeling for an analysis. The SAP IV general purpose FE computer program was employed to carry out a number of numerical examples to verify the formulation presented here.

REFERENCES

1. E. Sevin, W.D. Pilkey, Optimum Shock and Vibration Isolation, Shock and Vibration Information Center, Washington, D.C., 1971.

2. W.D. Pilkey, Y.H. Chen, A. J. Kalinowski, "Indirect Synthesis of Multidegree of Freedom Transient Systems," J. of Optimization Theory and Applications, to appear.

3. W.D. Pilkey, P. Smith, "Limiting Performance" in <u>Shock and Vibration Computer Programs</u>, Shock and Vibration Information Center, Washington, D.C., 1975.

4. W.D. Pilkey, B.P. Wang, Y. Yoo, and B. Clark, "PERFORM - A Performance Optimizing Computer Program for Dynamic Systems Subject to Transient Loadings," NASA CR-2268, 1973.

5. W.D. Pilkey, B.P. Wang, "SYSLIPEC - A Limiting Performance Computer Program for Linear Dynamics Systems Subject to Steady-State Sinusoidal Loading," Research Laboratories for the Engineering Sciences Report No. ESS-4085-109-73, University of Virginia, NASA Grant No. NGR 47-005-145, 1973.

PARTICULATE SILICONE RUBBER:
AN EFFECTIVE, REMOVABLE ENCAPSULANT FOR
ELECTRONIC PACKAGING

R. R. Palmisano and D. W. Neily
Harry Diamond Laboratories
Adelphi, Maryland

(U)A method of encapsulating electronic circuit board assemblies that enables rapid application and removal of the encapsulant was developed and evaluated. Low-density, inexpensive, foamed silicone rubber particles that are environmentally and electrically stable were used in lieu of conventional hard "potting." The silicone rubber particles can be easily applied by pouring and packing into electronic package voids; they are likewise easily removed from the package (and reusable), should circuit maintenance or rework be necessary.

Vibration tests of typical missile-borne applications indicate that, at resonance, electronic circuit board assemblies protected by this method experienced less than 10 percent of the acceleration measured before encapsulation.

INTRODUCTION

Epoxies and foamed polyurethanes are widely used, effective encapsulants for electronic circuits (1). When molded around circuit board assemblies and allowed to cure to a rigid state, they offer effective protection in shock and vibration environments by limiting excessive motion of the boards, components, and electrical connection; they also avert many unwanted microphonic effects in the circuit. However, once a subassembly or complete system is "potted," it becomes difficult and costly to make circuit repairs and modifications. To gain access to circuit components, one must tediously burrow into the rigid encapsulant. Even when the encapsulant is removed carefully, inadvertent component damage sometimes occurs.

AN ALTERNATIVE ENCAPSULATION CONCEPT

It has been found that if a loose fill of silicone-rubber particles is used as an encapsulation medium, the service and repair problems associated with rigid potting compounds are virtually eliminated. Discrete pellets or flakes of silicone rubber can be "poured" into available cavities surrounding circuit-board assemblies. The package is then sealed and ready to be used. Also noteworthy, there is no need for "potting" molds; nor are there lengthy cure cycles at elevated temperatures. Most importantly, if rework is necessary, the encapsulant can be easily dumped out or vacuumed from the electronic package.

Bulk pieces of foamed silicone rubber were reduced to particulate sizes by these laboratories. Two distinct particle shapes were derived, depending on how they were cut from the parent material:

a. Pellets were snipped from long lengths of 3/16-in. -dia. extruded strands of silicone foam rubber (Fig. 1).

b. Flakes were formed when chunks of silicone foam rubber were fed through a household meat grinder, giving the material the appearance of "rubber sawdust" (Fig. 2).

The physical properties of silicone foam rubber make it ideal for use in electronic packages. Several silicone compounds that were evaluated were found suitable because they have all of the following essential properties:

a. Chemical inertness: the compound must not decompose or initiate corrosion and must have long shelf life.

b. Temperature insensitivity: the compound must maintain properties

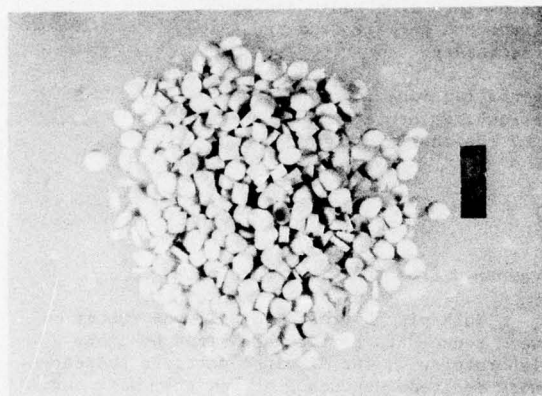Fig. 1(a) - Pellet formation: foam "spaghetti"

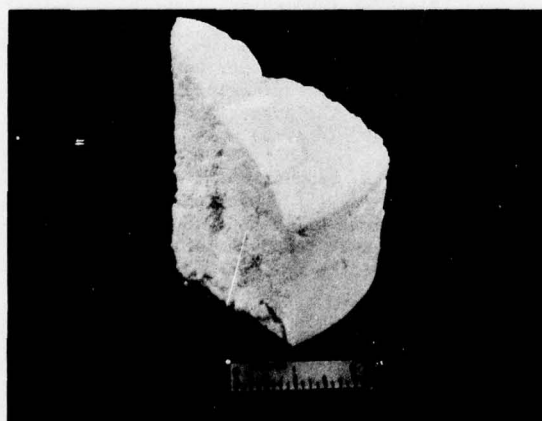Fig. 1(b) - Pellet formation: snipped pellets

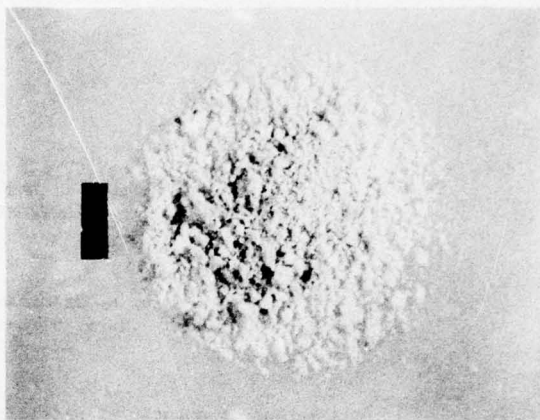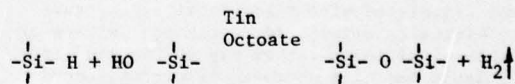Fig. 2(a) - Flakes formation: bulk foam rubber

Fig. 2(b) - Flakes formation: ground flakes ("rubber sawdust")

at high and low temperature extremes.

c. Removability: particle cohesion and adhesion to the circuitry and container should be negligible.

d. Good vibration damper: the compound must be able to mitigate the motion of the parts over a wider range of vibration frequencies and amplitudes.

e. Electrical inertness: the compound must not affect the circuit operation. This requires high dielectric strength, a small dielectric constant, high resistivity, and a low dissipation factor.

f. Light weight: the encapsulant should not significantly increase the total weight of the package.

g. Low moisture absorptivity: the encapsulant should not absorb or hold moisture.

h. Low cost: the cost should be small relative to the cost of the entire system.

A material that was found to possess these properties is a silicone foam rubber (polymer) resulting from the following chemcial reaction:

$$-\overset{|}{\underset{|}{Si}}- H + HO -\overset{|}{\underset{|}{Si}}- \xrightarrow{\text{Tin Octoate}} -\overset{|}{\underset{|}{Si}}- O -\overset{|}{\underset{|}{Si}}- + H_2 \uparrow$$

A prepolymer of the material consisting of a silane ($-\overset{|}{\underset{|}{Si}}- H$) plus a silanol (HO-$\overset{|}{\underset{|}{Si}}$-) structure react in the presence of the catalyst, tin octoate, as noted above; i.e. The silanic hydrogen and the hydroxyl group in the polymer react in the presence of the catalyst

278

to form a siloxane chain (-Si-O-Si-) with hydrogen (H_2) released. The hydrogen serves as a blowing agent and is instrumental in foaming the silicone polymer. A weak base such as amine is included to neutralize any free acid that may be present.

Typical, commercially available products that have been found to possess the aforementioned essential properties are Dow Corning RTV90-224, Emerson and Cumming Eccofoam SIL, and a silicone "spaghetti" made by Moldit Corporation. Manufacturers' data provided some of this information. Thermogravametric and corrosion tests verified chemical inertness. A loose fill of the particles of each weighed approximately the same, .014 lb/in^3. The ingredients to make bulk quantities of the foam rubber cost $5 to $13 per pound at the time of this report. The individual manufacturers can furnish other material specifications.

MEASUREMENT OF DAMPING EFFECTIVENESS

Sinusoidal vibration tests of electronic circuit-board assemblies were used to determine the effectiveness of foamed silicone-rubber particle encapsulation. A printed circuit-board assembly (2.09 x 4.096 in.) was mounted on standoffs in an aluminum fixture (Fig. 3, 4). This fixture was intentionally designed to provide a large unsupported span for the printed circuit-board. This configuration insured an exaggerated vibration response of the assembly. This assembly was subjected to sinusoidal vibration excitation of 2-g peak in the range of 10 - 2000 Hz. A miniature accelerometer, attached at the center of the circuit-board assembly, sensed the specimen's response. (Further details of the test configuration and instrumentation are given in App. A).

Test results are summarized in Figs. 5 and 6. The response is expressed as amplification factor or the ratio of the output to the input acceleration. A comparison of the results in Fig. 5 with those in Fig. 6 shows the beneficial damping effect at resonance of the foamed silicon-rubber particle encapsulant. The results show also that the four variations of the encapsulant were equally effective in vibration damping. Further noteworthy, a 1/3 overfill of encapsulant particles yields only a minor improvement in the vibration damping. The encapsulant materials were reused several times with no change in performance.

AN APPLICATION

Particulate silicone rubber encapsulants are in use in the XM818 Fuze electronic package for the SAM-D missile. For a small fraction of the fuze cost and fuze weight,

the electronic components are cushioned against excessive vibration. The package was subjected to a battery of environmental tests without a vibration or shock-induced malfunction. Results of experiments with sample hardware had given indications of this good functioning (App B).

CONCLUSIONS

The encapsulants described here offer several advantages over the conventional potting practice. Silicone-rubber flakes and pellets are removable, reusable, light-weight, inexpensive and offer high damping performance. They are environmentally and electrically inert. They should be considered in packaging problems similar to those described here, namely in missile fuzing applications. However, for applications that are considerably different -- for example, tube-fired munitions, the evaluations done here should be extended.
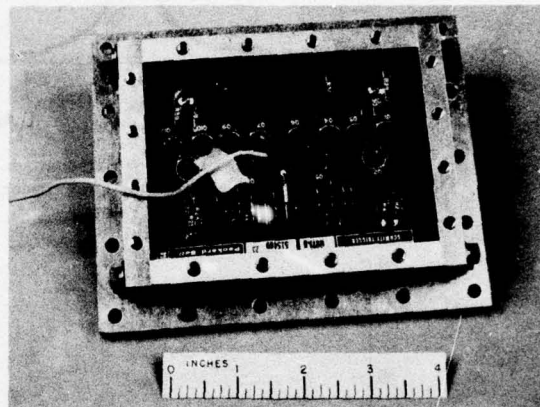

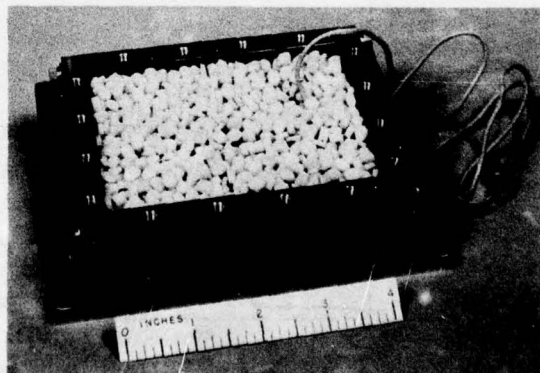Fig. 3 - Experimental package, unencapsulated

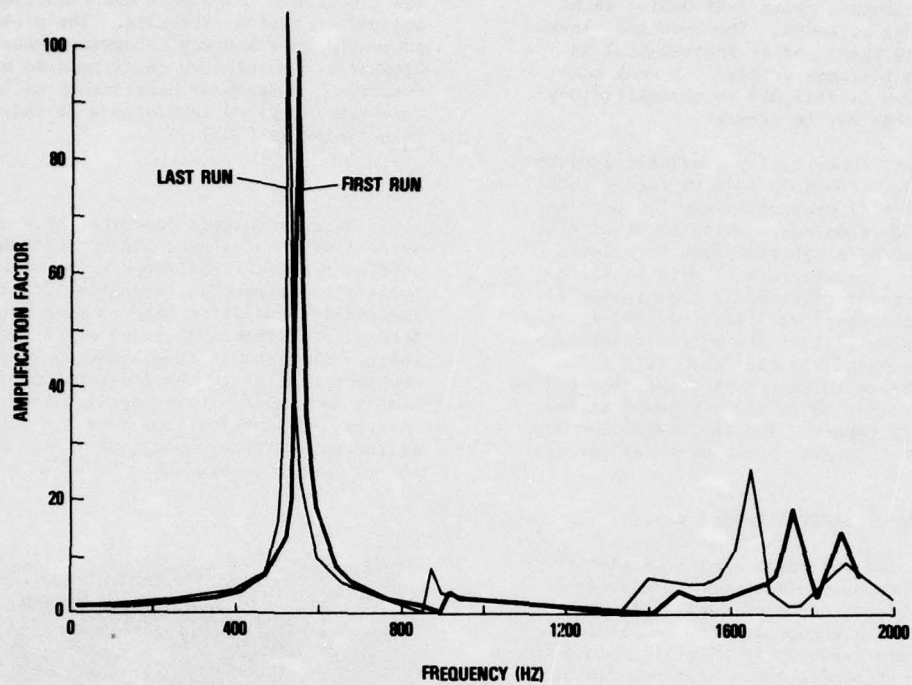Fig. 4 - Experimental package encapsulated (cover removed)

Figure 5: Response to 2 g sinusoidal vibration, amplification versus frequency, unencapsulated experimental package.
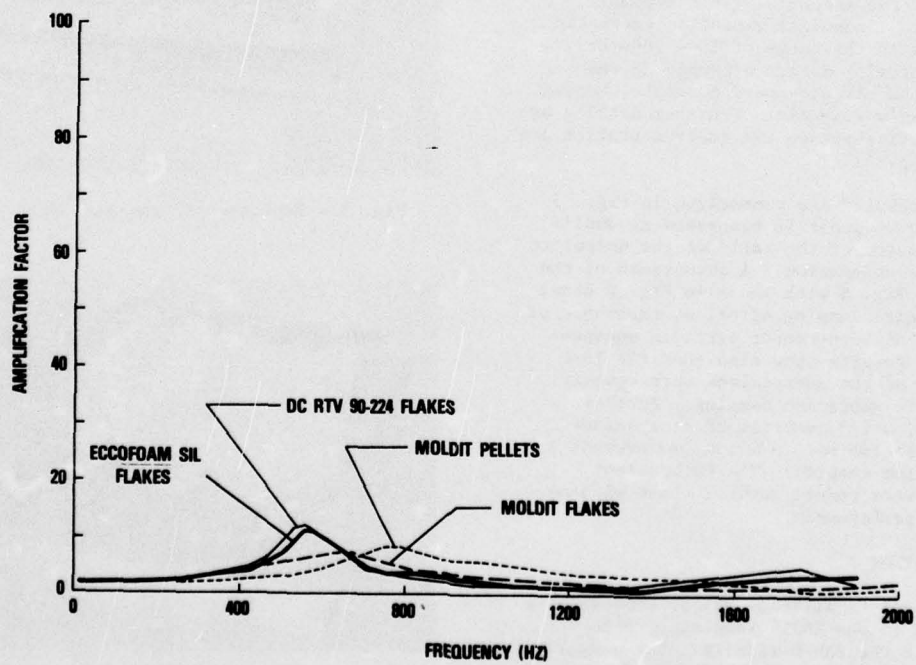

Figure 6: Response to 2 g sinusoidal vibration, amplification versus frequency, experimental package encapsulated with four different compounds.

REFERENCE

a. Charles A. Harper, ed., Handbook of
Electronic Packaging, McGraw-Hill,
New York, 1969

APPENDIX A

SPECIMEN (FIG.)
 	
EWT = 2.75 LB.
HOUSING:
    3/8 IN.–THICK AL. WALLS, LID, BASE
    18 MOUNTING HOLES, HOUSING TO SHAKER
    18 MOUNTING HOLES, LID TO HOUSING
CIRCUIT BOARD:
    PACKARD-BELL SCHMIOT TRIGGER
    SIZE: 2.75 + 4
    AVE WT'. DISTRIBUTION: 0.01 LB./IN. 2
    EWT = 0.11 LB.
	ACCELEROMETER
	
	WILCOXIN MOLDEL 103
	CHARGE SENSITIVITY 8.59 PC/G

ENDEVCO CHARGE AMPLIFIER

BRUSH STRIP-CHART RECORDER

MANUALLY DIGITIZED DATA

DESKTOP PLOTTER

EXCITATION

MB-GILMORE MODEL C-90 SHAKER
2G PEAK SINUSOIDAL VIBRATION
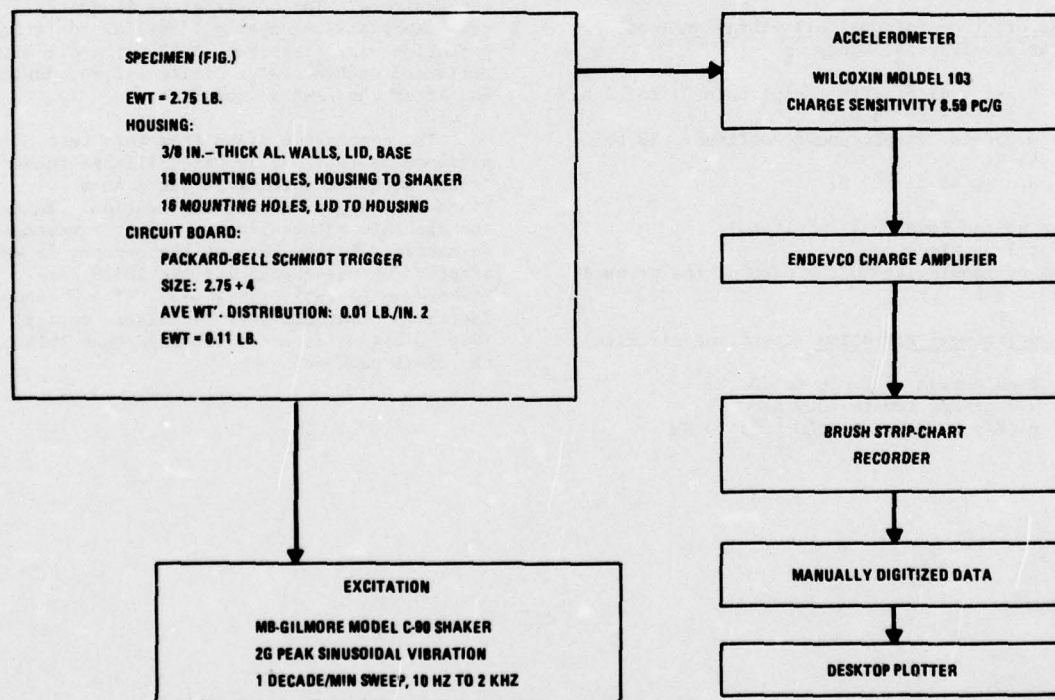1 DECADE/MIN SWEEP, 10 HZ TO 2 KHZ

Fig. A-1 - An Experiment for Evaluating the Vibration Damping Ability of Encapsulants

APPENDIX B--Evaluating Encapsulant in an XM818
Fuze Subassembly

Prior to the acceptance of silicone-rubber flakes as an encapsulant for the XM818 Electronic Assembly, tests were conducted to qualify this material and match it against the potting-in-place method. One electronic module was chosen as representative of the other fuze subassemblies (Fig. B-1). In this package five similar circuit boards sit in a housing of as many cells. These boards are held at the lateral edges by Birtcher tracks (spring-loaded clips).

A test series was programmed to simulate the transportation and flight environments of the fuze. The XM818 fuze is required to survive or operate in the following vibration environments:

Transportation (sinusoidal) vibration (non-operating circuits) Sweep up

    0.3-in. displacement amplitude, 5 to 13 Hz
    2.5 g, 13 to 38 Hz
    0.036-in. displacement amplitude, 38 to 44 Hz
    3.5 g, 44 to 500 Hz

Sweep up and down in 15 min total
Repeat four times
Input perpendicular to the pane of the printed circuit board

Flight (random) vibration (operating circuits)

    6-dB/octave rise, 50 to 100 Hz
    0.3 g^2/Hz, 100 to 2000 Hz
    6-dB/octave fall, 2000 to 3000 Hz

8.8 g RMS overall
3.4 min exposure time
Monitor circuit performance continuously

A mock-up of one cell of the assembly was used as the test specimen. A single circuit board, instrumented as in Fig. 3, was placed in the cell and encapsulated.

Two encapsulants were tested. The specimen was first filled with ground Moldit "spaghetti." The transportation and flight vibration tests outlined above were conducted. The encapsulant was then removed and replaced with a solid silicone foam potting (18 lb/cu ft). The potted-in-place sample was subjected to the same tests.

The test results show nearly equal performance for the particulate and the potted encapsulants. The acceleration frequency response plots are nearly identical for transportation vibration (Fig. B-2). The circuits performed within design limits before, during, and after the random vibration.

The conclusion drawn from this test sequence is that particulate silicone rubber is the equal of potting in place as a vibration damper in this application. Because the discrete encapsulant has other advantages as outlined in the body of the report, it was adopted for use throughout the XM818 Fuze Electronic Assembly (Fig. B-3). The encapsulant is poured into every available cavity (Fig. B-4) and accounts for less than 1 lb of the 15-lb package.
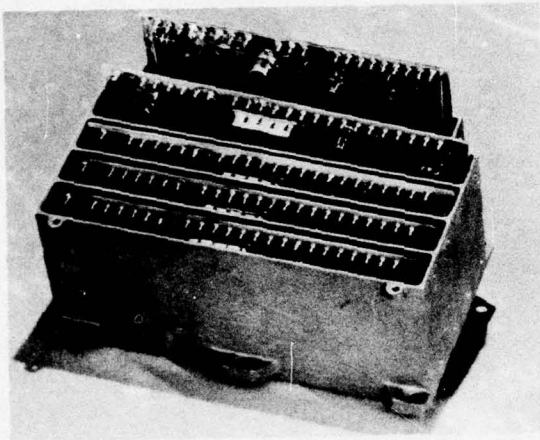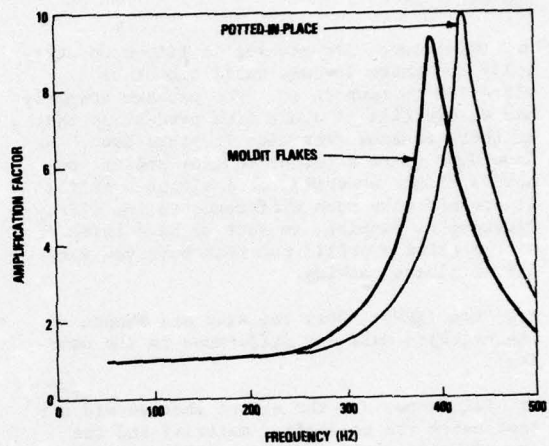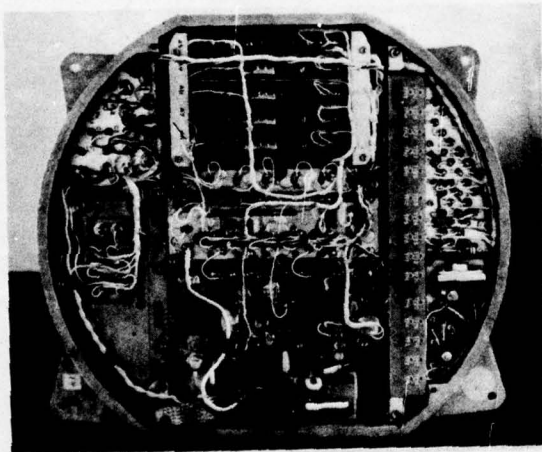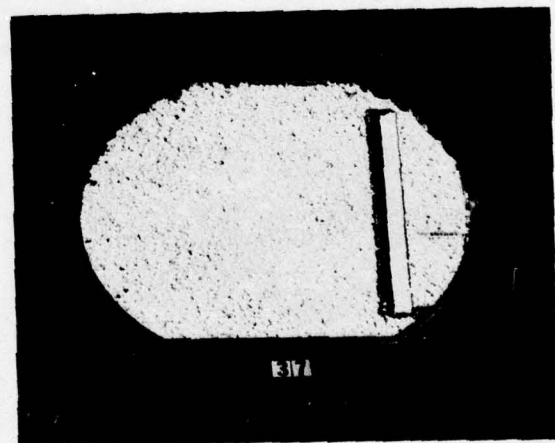
Figure B1

Figure B2

Figure B3

Figure B4

Discussion

Mr. Getline (Convair): How do you assure that
all cavities are filled with that material?
Do you have any control over the density of
the packing?

Mr. Palmisano: The package is filled up care-
fully and there is some small amount of
vibration to tamp it in. The package normally
has an overfill of about five percent so that
if there is some vibration it packs down. We
have done quite a bit of testing and if you
have a slight underfill or a slight overfill
it doesn't make much difference in the effec--
tiveness of damping; in fact we have tried it
with a third overfill and that buys you very
little almost nothing.

Mr. Chen (TRW): Does the size and shapes of
the granules make any difference in the damp-
ing?

Mr. Palmisano: To the extent that we did our
test using the pelletized material and the
ground material it made virtually no difference.

Voice: Where was the measurement taken?

Mr. Palmisano: At the center of the printed
circuit board. At the point of greatest
displacement.